Volume II.C

Midwestern Regional Carbon Sequestration Partnership (MRCSP) Phase III (Development Phase)

# Distributed Acoustic Sensing (DAS) Seismic Monitoring of $CO_2$ Injected for Enhanced Oil Recovery in Northern Michigan


Prepared by:

Battelle
505 King Avenue
Columbus, Ohio 43201

Principal Investigator: Dr. Neeraj Gupta

Authors: Mark Kelley, Liviu Grindei (VSProwess), Mary Humphries (VSProwess), Thomas Coleman (Silixa), Allen Modroo (Core Energy)



Submitted to:

The U.S. Department of Energy, National Energy Technology Laboratory
Program Manager: Andrea McNemar

DOE MRCSP Project #DE-FC26-05NT42589

September 2020

# Notice

This report was prepared by Battelle as an account of work sponsored by an agency of the United States Government and other project sponsors, including Core Energy, LLC and The Ohio Development Services Agency. Neither the United States Government, nor any agency thereof, nor any of their employees, nor Battelle and other cosponsors, makes any warranty, express or implied, or assumes any liability or responsibility for the accuracy, completeness, or usefulness of any information, apparatus, product, or process disclosed, or represents that its use would not infringe privately owned rights. Reference herein to any specific commercial product, process, or service by trade name, trademark, manufacturer, or otherwise does not necessarily constitute or imply its endorsement, recommendations, or favoring by the United States Government or any agency thereof. The views and the opinions of authors expressed herein do not necessarily state or reflect those of the United States Government or any agency thereof.

Battelle does not engage in research for advertising, sales promotion, or endorsement of our clients' interests including raising investment capital or recommending investments decisions, or other publicity purposes, or for any use in litigation.

Battelle endeavors at all times to produce work of the highest quality, consistent with our contract commitments. However, because of the research and/or experimental nature of this work the client undertakes the sole responsibility for the consequence of any use or misuse of, or inability to use, any information, apparatus, process or result obtained from Battelle, and Battelle, its employees, officers, or Trustees have no legal liability for the accuracy, adequacy, or efficacy thereof.

# Acknowledgements

**Sponsorships -** This report is part of a series of reports prepared under the Midwestern Regional Carbon Sequestration Partnership (MRCSP) Phase III (Development Phase). These reports summarize and detail the findings of the work conducted under the Phase III project. The primary funding for the MRCSP program is from the US Department of Energy's National Energy Technology Laboratory (NETL) under DOE project number DE-FC26-05NT42589 with Ms. Andrea McNemar as the DOE project manager. The past DOE project managers for MRCSP include Dawn Deel, Lynn Brickett, and Traci Rodosta. Many others in the DOE leadership supported, encouraged, and enabled the MRCSP work including but not limited to Kanwal Mahajan, John Litynski, Darin Damiani, and Sean Plasynski.

The Michigan Basin large-scale test received significant in-kind cost share from Core Energy, LLC, who also provided essential access to the field test site and related data. This contribution by Core Energy CEO Robert Mannes, VP Operations Rick Pardini, and Allan Modroo, VP Exploration, and the entire Core Energy staff is gratefully acknowledged. MRCSP work in Ohio has been supported by the Ohio Coal Development Office in the Ohio Development Services Agency under various grants (CDO D-10-7, CDO-D-13-22, CDO-D-D-13-24, and CDO-D-15-08) with Mr. Greg Payne as the OCDO project manager. Finally, several industry sponsors and numerous technical team members from State Geological Surveys, universities, and field service providers have supported MRCSP through cash and in-kind contributions over the years as listed in the individual reports.

**Program Leadership –** During the MRCSP Phase III project period, several Battelle staff and external collaborators contributed to the successful completion of the program through their efforts in field work, geological data analysis and interpretation, and/or reporting. The primary project managers over the MRCSP performance period have included Rebecca Wessinger, Neeraj Gupta, Jared Walker, Rod Osborne, Darrell Paul, David Ball. Additional project management support has been provided by Andrew Burchwell, Christa Duffy, Caitlin McNeil, and Jacqueline Gerst over the years.

**Principal Investigator:** Neeraj Gupta (614-424-3820/ gupta@battelle.org)

**Report Authors and Principal Technical Contributors**: Mark Kelley (Battelle), Liviu Grindei (VSProwess), Mary Humphries (VSProwess), Thomas Coleman (Silixa), Allen Modroo (Core Energy)

# Executive Summary

As part of the Midwest Regional Carbon Sequestration Partnership (MRCSP) Phase III project, a monitoring study was conducted to assess the effectiveness of DAS **(**Distributed Acoustic Sensing) - based VSP (Vertical Seismic Profiling) technology for delineating $CO_2$ injected into the Silurian-age pinnacle reefs in northern Michigan, the host rocks for the MRCSP Phase III demonstration project. The DAS VSP study was conducted in the Chester 16 reef, one of several reefs in Otsego County Michigan that is operated by Core Energy, LLC of Traverse City, Michigan.

Time-lapse DAS VSP was implemented at the Chester 16 reef to attempt to detect approximately 85,000 tonnes of $CO_2$ injected into the A-1 Carbonate and Brown Niagaran Formations. A baseline survey was conducted in February 2017 prior to injecting $CO_2$ and a repeat survey was conducted in August 2018. During the interim period between the baseline and repeat surveys, $CO_2$ was injected into the Chester 16 reef via the 6-16 injection well without production (withdrawal) of fluids from the reef. A grid of 181 source positions consisting of 44 vibrator positions, plus 137 dynamite shot locations, was used to give approximately continuous spatial coverage of the injection zone (A-1 Carbonate and upper Brown Niagaran) in the area between the two wells.

The processing approach implemented in this study focused on monitoring the change in the amplitude of the reflection coefficient (R) between the baseline and repeat surveys due to the introduction of $CO_2$. Reflection coefficient is defined as follows:

$$R = \frac{AI_1 - AI_2}{AI_1 + AI_2} = \frac{\rho_1 v_1 - \rho_2 v_2}{\rho_1 v_1 + \rho_2 v_2}$$

**Equation ES-1**

Where AI is acoustic impedance, which is the product of bulk density of the rock-fluid system and acoustic velocity of the rock. Introduction of $CO_2$ into a porous layer can cause changes in density and velocity of the rock-fluid system, resulting in a change in AI within the layer or interval receiving the $CO_2$. This can result in a change in the reflection coefficient at the interface between the $CO_2$-containing layer and the overlying or underlying layer that has not received $CO_2$. If the magnitude of the AI contrast between adjacent intervals is sufficiently large, the effect may be visually detectable by calculating/plotting the difference in R between the two surveys.

In the Chester 16 DAS VSP study, dynamite signals were weak compared to vibroseis so the two data types could not be combined. Doing so raised the lower limit of detection (i.e., reduced the overall signal-to-noise ratio). Therefore, the time-lapse (difference) analysis was done using only the higher quality vibroseis data. This constrained the image area to the immediate area surrounding the 6-16 and 8-16 wells rather than covering the area between the two wells as originally planned.

Results of the time-lapse VSP study are presented with two sets of figures: 1) 2D vertical pre-migration stack images showing reflection profile before and after $CO_2$ injection and the difference along a line extending from a single source point (101214) to the 6-16 injection well; and 2) a series of 2D plan view post-stack migration images that combine data from multiple (vibroseis) source locations showing time-lapse difference in R in the vicinity of the 6-16 injection well and the 8-16 monitoring well (post-migration). Ideally, the post-migration figures would have included data from all sources (i.e., vibroseis and dynamite) to provide the greatest spatial coverage of the reservoir. However, as previously discussed, due to the low signal-to-noise ratio (SNR) of the dynamite data compared to the vibroseis data, the two source types were not combined and only vibroseis data were used in the migration process to make the images.

Consequently, the spatial coverage of the image(s) is significantly smaller than the area that would have been imaged if dynamite data were included.

The difference images for the area near the 6-16 (injection) well show difference features within the injection interval (A-1 Carbonate Crest and upper Brown Niagaran) as expected; however, difference features with similar magnitude also appear above and below the injection interval, including areas where $CO_2$ is unlikely to exist. Therefore, these results are encouraging but not unequivocal. The difference image for the 8-16 monitoring well does not show a pattern (clustering) of difference features that suggests $CO_2$.

A 3D numerical reservoir fluid migration model was developed using the CMG GEM code to predict the spreading and distribution of the 85,000 tonnes of injected $CO_2$ at the time of the repeat DAS VSP, for comparison to the actual monitoring results. The reservoir model indicates that $CO_2$ likely would have reached to the 8-16 monitoring well by the time of the repeat VSP survey; therefore, if this is correct, it appears that the DAS VSP method might have failed to detect the $CO_2$ because the time-lapse post-stack migration difference images for the area surrounding the 8-16 well do not indicate the presence of $CO_2$.

A simple 1D vertical profile spreadsheet model was used to calculate expected change in R due to $CO_2$ injection to compare to actual monitoring results. The model is based on acoustic and density logs for the 6-16 well recorded after the well was drilled, but before commencing $CO_2$ injection. The model has seven geologic layers with homogeneous velocity and density. Seven different model scenarios were created to evaluate the effect of different magnitude changes in V and ρ on R. Only zones that received $CO_2$ directly via injection (A-1 Carbonate, upper portion of Brown Niagaran) and the A-2 Carbonate were adjusted. The results of the comparison indicate that the actual monitoring results compare well with the synthetic time-lapse results.

This DAS VSP study was partially successful for detecting $CO_2$ injected into the Chester 16 pinnacle reef. The DAS monitoring results indicate a measurable change (decrease) in seismic reflection coefficient in the A-1 Carbonate and Brown Niagaran Formation (i.e., the two injection intervals, in the area near the 6-16 injection well). However, difference features were also indicated in strata above and below the injection zone. The DAS data also produced reflection coefficient (RC) difference features in the vicinity of the 8-16 monitoring well, both within the injection zone and outside the injection zone, casting doubt on the results.

For DAS VSP technology to clearly detect the injected $CO_2$, the injected fluid must cause a change in AI (velocity and/or density) large enough to cause a change in RC that can be visibly detected. Laboratory tests and fluid substitution modeling both suggest the seismic response to $CO_2$ injection will be small (~5% change in acoustic velocity Vp). Such a small change in AI will have a minor effect on R. This is a physics-based limitation and therefore cannot be avoided.

Other “survey” factors likely limited the effectiveness of the DAS VSP technology. These include the following.

- Dynamite signals were weak compared to vibroseis so the two data types could not be combined. Doing so raised the lower limit of detection (i.e., reduced the overall SNR). Therefore, the time-lapse (difference) analysis was done using only the higher quality vibroseis data. This reduced the image area to the immediate area surrounding the 6-16 and 8-16 wells rather than the area between the two wells as originally planned. It also created the possibility that area(s) with $CO_2$ were missed.
- The well casings were not cemented completely to ground surface; consequently, only the cemented portion of the fiber optic DAS cable had sufficient acoustic coupling and provided useable data. This also reduced the image area compared to the originally planned image area.

- The vibroseis data from the repeat survey had significantly lower (better) SNR than the baseline vibroseis data. This is most likely because more sweeps were performed at each vibroseis source location in the repeat survey compared to the baseline survey. Vibroseis acquisition parameters were modified for the repeat survey. When repeated, the number of sweeps was increased from five to 10 (full force locations) and from 10 to 15 (reduced force locations).
- In this study, the injection tubing string in the 6-16 injection well vibrated during the acquisition of the VSP (due to dynamite or vibroseis energy waves impacting the tubing string), which adversely affected the acquired DAS data. In future DAS VSP surveys, it may be worthwhile to remove the injection tubing string, if present, prior to acquiring the data.
- A larger mass of injected $CO_2$ might have been easier to detect. The repeat DAS VSP survey was conducted after injecting only 85,000 tonnes of $CO_2$, which was earlier than originally planned. Originally, the repeat survey was planned after the fill-up phase, which occurred after injection 5.3 BCF of $CO_2$ (approximately 280,000 tonnes). It was necessary to conduct the repeat survey earlier than planned because Core Energy was considering converting the 8-16 monitoring well to a horizontal injection well, which would have precluded further DAS monitoring in this well.

These survey factors can be avoided in future DAS VSP studies if preventive measures are taken.

# Table of Contents



## List of Tables

## List of Figures

Page



## List of Equations

Page

# Acronyms and Abbreviations

| | |
|---|---|
| AI | Acoustic Impedance |
| A-1C | A-1 Carbonate Formation |
| A-2C | A-2 Carbonate Formation |
| BHG | Borehole Gravity |
| BN | Brown Niagaran Formation |
| $CO_2$ | Carbon Dioxide |
| CCUS | Carbon Capture, Utilization, and Storage |
| DAS | Distributed Acoustic Sensing |
| DOE | Department of Energy |
| DTS | Distributed Temperature Sensing |
| EOR | Enhanced Oil Recovery |
| GL | Ground Level |
| GPa | Gigapascals |
| INSAR | Interferometric synthetic aperture radar |
| MRCSP | Midwest Regional Carbon Sequestration Partnership |
| NETL | National Energy Technology Laboratory |
| OWC | Oil-Water Contact |
| PNC | Pulsed Neuron Capture logging |
| Psi | Per Square Inch |
| RC | Reflection Coefficient |
| RCSP | Regional Carbon Sequestration Partnership |
| RMS | Root Mean Square |
| SNR | Signal-to-Noise Ratio |
| VP | Compressional-wave Velocity |
| Vs | Shear-wave Velocity |
| VSP | Vertical Seismic Profile |
| WVSP | Walkaway VSP |
| ZVSP | Zero Offset VSP |

# 1.0 Introduction

## 1.1 Purpose

As part of the Midwest Regional Carbon Sequestration Partnership (MRCSP) Phase III project, a monitoring study was conducted to assess the effectiveness of ***DAS*** (Distributed Acoustic Sensing) - based VSP technology for delineating $CO_2$ injected into the Silurian pinnacle reefs in northern Michigan, the host rocks for the MRCSP Phase III study. The DAS VSP study was conducted in the Chester 16 reef, one of several reefs in Otsego County Michigan that is operated by Core Energy, LLC of Traverse City, Michigan. The study included a baseline DAS VSP in February 2017, prior to commencing $CO_2$ injection into the reef, and a repeat DAS VSP in July 2018 after approximately 85,000 tonnes of $CO_2$ had been injected. Prior to the baseline survey, MRCSP instrumented two new wells (Chester 6-16 and 8-16) in the Chester 16 field that had just been installed by Core Energy to conduct $CO_2$ Enhanced Oil Recovery (EOR).Both wells were equipped with a fiber optic cable attached to the outside of the deep casing string for distributed temperature sensing (DTS) and DAS. During the period between the baseline and repeat surveys, $CO_2$ was injected into the reef via the 6-16 well sans production in order to increase reservoir pressure above $CO_2$ miscibility pressure. The 8-16 well is an unperforated cased well that was used to support DAS VSP and other monitoring methods (DTS, Pulsed Neutron Capture Logging).

## 1.2 Organization of this Report

This report provides a high-level summary of the Chester 16 DAS VSP study, including background information (Section 1), data acquisition (Section 2), and results (Section 3). Details of the DAS VSP study are provided in a separate stand-alone report, included as Appendix A to this report, prepared by Silixa and VSProwess (VSProwess, 2019). Silixa, under contract to Battelle, recorded the DAS VSP data and VSProwess (under contract to Silixa) processed the data.

## 1.3 Geology of Chester 16 Reef

Figure 1-1 shows the outline of the Chester 16 reef and the location of the 6-16 and 8-16 wells. Both wells are deviated (i.e., different surface and bottomhole locations) as shown by the well traces (red lines) in Figure 1-1 that show the surface and bottomhole location for each well.

The area of the reef is approximately 216 acres, which includes formations that flank the reef. Figure 1-2 is a conceptual model of the geology of the Silurian pinnacle reefs in the northern reef trend based on lithostratigraphic units (i.e., formations). The Brown Niagaran (stratigraphically equivalent to the Guelph dolomite) and A-1 Carbonate are the hydrocarbon reservoirs in the Silurian reefs. The reefal buildups that occur within the Brown Niagaran are overlain and encased by cyclic carbonate and evaporite beds of the Salina Group that act as sealing units for the reefs. These include (in order of deposition) the A-0 Carbonate, A-1 Evaporite, A-1 Carbonate, A-2 Evaporite, A-2 Carbonate, and several salt units (B Unit through G Unit). The underlying Gray Niagaran (not shown), which forms the base of the reservoir (Gray Niagaran, is equivalent to the Lockport Dolomite).

An alternative more recent geologic conceptual model for the reefs that is based on depositional facies is shown in Figure 1-3. These depositional facies include windward reef flank, windward reef talus, reef core, leeward proximal reef apron, leeward distal reef apron, and leeward flank facies. Figure 1-4 is a “hybrid” geologic model for the Chester 16 reef based on depositional facies for the reef proper and lithostratigraphic units for the rocks surrounding the reef. Also shown are traces of the 6-16 and 8-16 wells and the depth of the perforations in the 6-16 (injection) well. As seen in Figure 1-4, the Chester 16

reef is composed of two pods with the two wells in different pods. Windward facies (not segregated) are situated on the northeast flank of both pods; leeward facies (not segregated) are situated on the southwest flank of both pods. The A-1 Carbonate occurs in three positions – above the reef core, (crest) where it has reservoir-quality properties, in the saddle region between the two pods (non-reservoir quality), and on the flanks (also non-reservoir). Also shown are the depths of five permanent pressure-temperature sensors (PT-1 through PT-5) in the 8-16 monitoring well. The conceptual model in Figure 1-4 was used to develop numerical reservoir models for simulating $CO_2$ injection, storage, and EOR in the Chester 16 reef. These models can be used to predict the $CO_2$ distribution in the reef at the time of the repeat DAS VSP. Figure 1-5 shows the predicted $CO_2$ distribution after injecting 85,000 tonnes of $CO_2$. It also shows that the injected $CO_2$ spread primarily into the A-1 Carbonate reef crest and the upper portion of the Brown Niagaran. $CO_2$ did not spread into the saddle region between the A-1 Carbonate and the Brown Niagaran, due to its low permeability and porosity. For a more in-depth explanation of the Chester 16 reef reservoir modeling methods and results, refer to the companion report on modeling (Mishra et al., 2020). Key descriptive statistics describing area, volume, thickness, and porosity of the Chester 16 (reef reservoir only) are provided in Table 1-1. These statistics were derived from the static earth model shown in Figure 1-4. For a more in-depth explanation of the geology of the Chester 16 reef, refer to the companion report on geologic characterization (Haagsma et al., 2020).

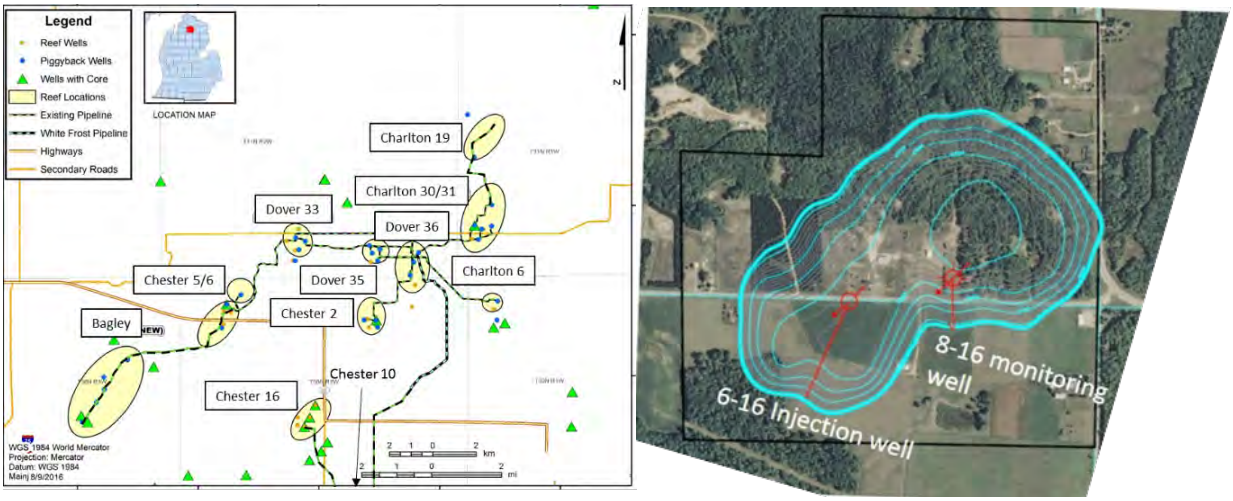


*Figure 1-1. Location and Outline of Chester 16 Reef and Location of the 6-16 and 8-16 wells.*

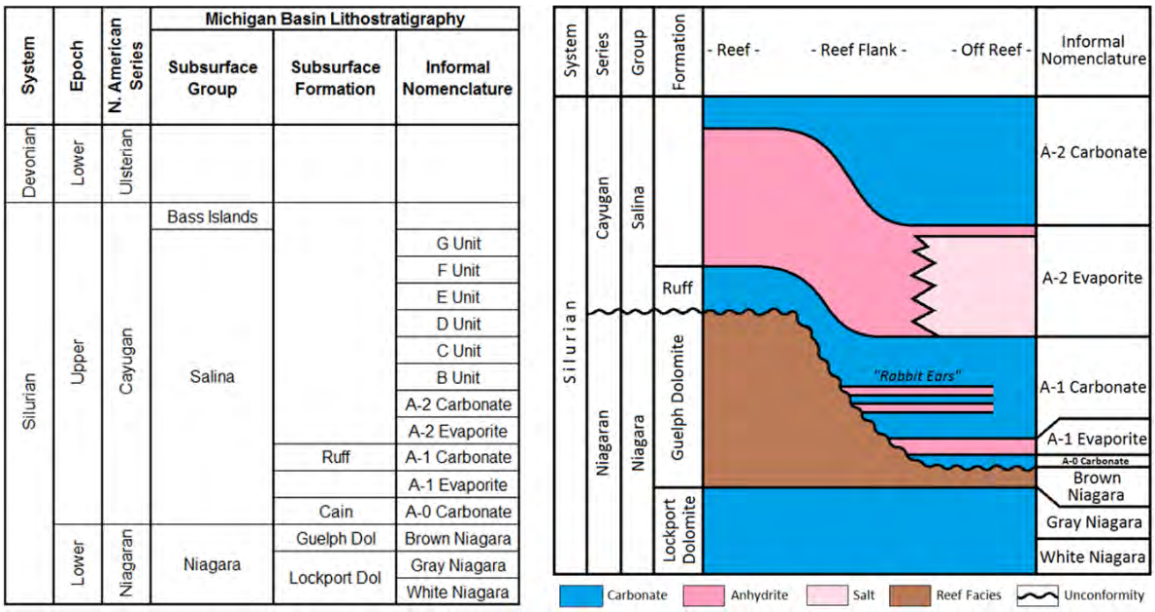


*Figure 1-2. Stratigraphy of the Silurian-age Niagaran and Salina Groups in the Michigan Basin. On left is the formal and informal Silurian stratigraphic nomenclature (modified from Trout, 2012, and Rine, 2015). On right is a conceptual model and stratigraphy of the Brown Niagaran reef interval (after Gill 1973, 1979; and Huh 1973).*

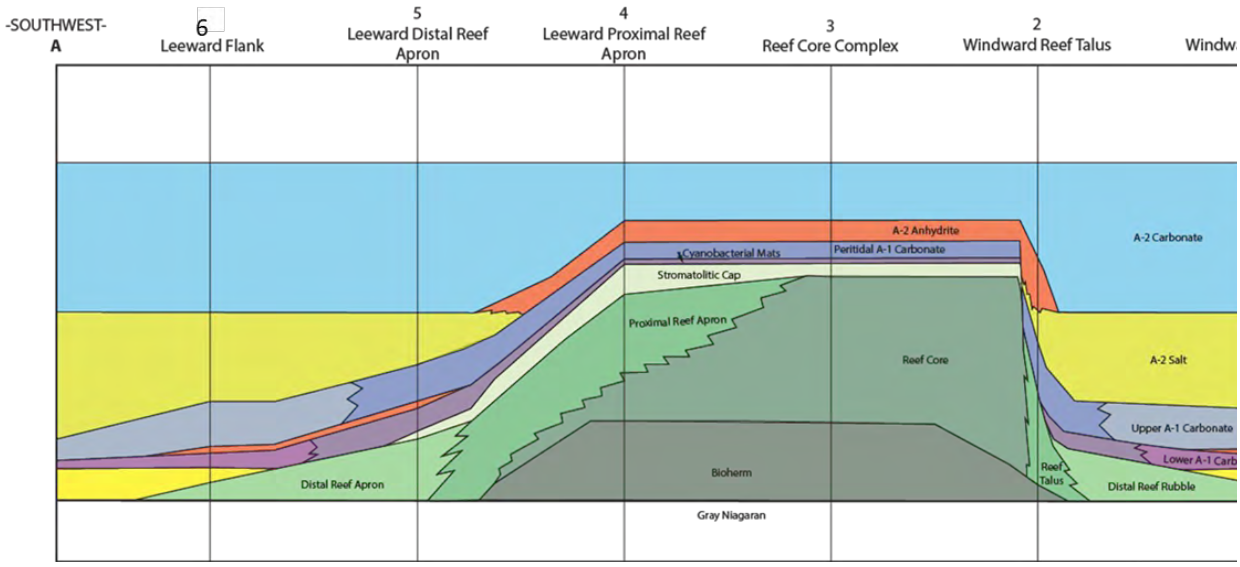


*Figure 1-3. Depositional facies model by Western Michigan University collaborators showing (1) windward flank, (2) windward reef talus, (3) reef core complex, (4) leeward proximal reef apron, (5) leeward distal reef apron, (6) leeward flank facies.*

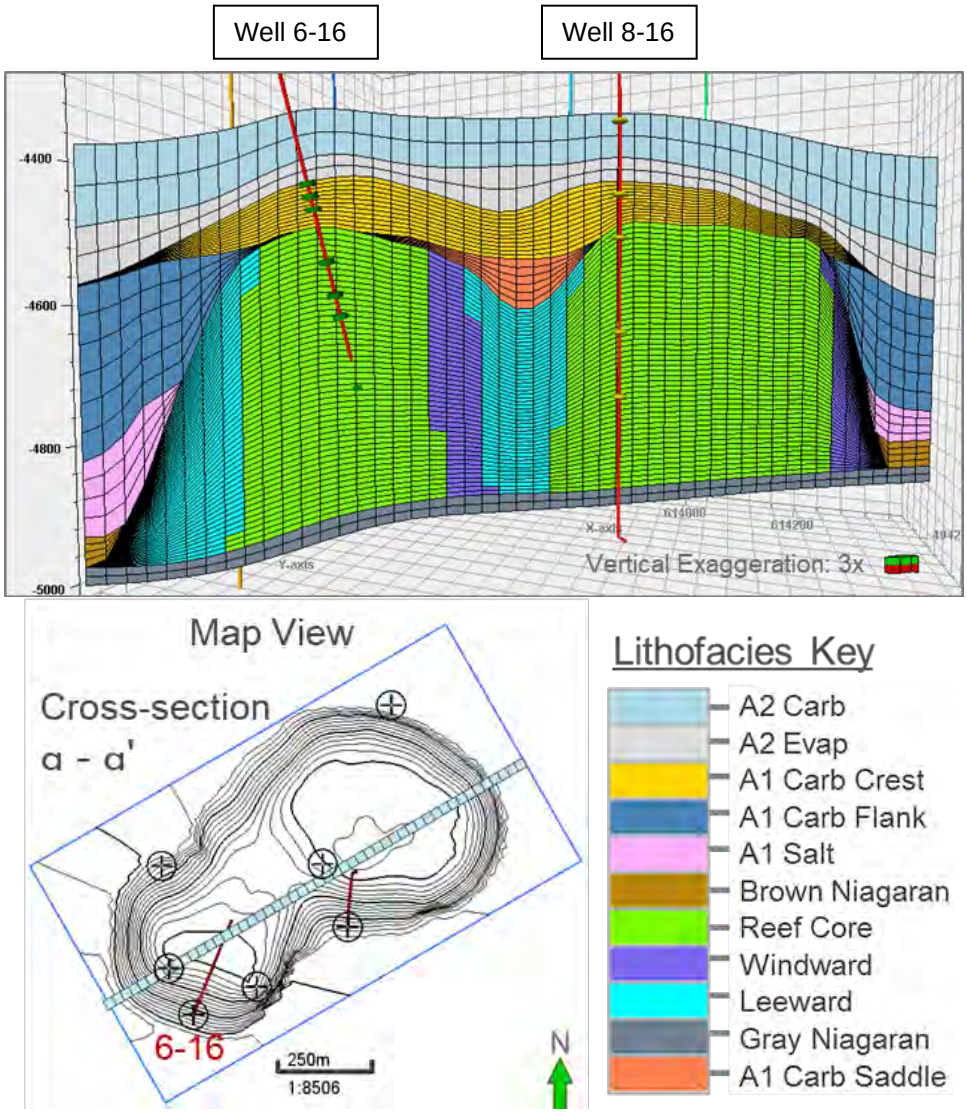


*Figure 1-4. Petrel Static Earth Model of Chester 16 Geology showing trace of the 6-16 and 8-16 wells and the depth of the perforations in the 6-16 well. Also shown are the depths of five permanent pressure-temperature sensors (PT-1 through PT-5) in the 8-16 monitoring well.*

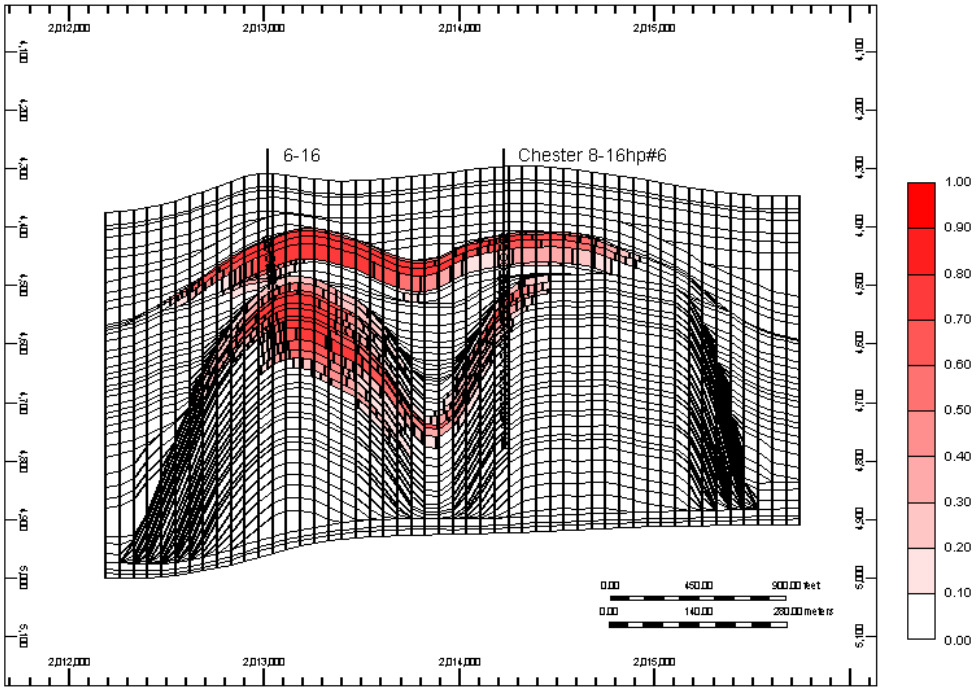


*Figure 1-5. Simulated percent $CO_2$ saturation after injecting 85,000 tonnes of $CO_2$. The 6-16 injection well is in the left pod and the 8-16 monitoring well is in the right pod.*

**Table 1-1. Key descriptive statistics describing area, volume, thickness, and porosity of the Chester 16 reservoir**

| Parameter | Value | Comment |
|---|---|---|
| Avg porosity A-1 Carb Crest, % | 11 | Based on total volume and pore volume estimates below |
| Avg porosity BN, % | 3.6 | Based on total volume and pore volume estimates below |
| Area, $ft^2$ | 6,560,100 | area of the A-1 Carb Crest out to where it eventually pinches-out to 0-feet thickness |
| Total volume of reservoir, $ft^3$ | 1,333,000,000 | A-1 Carb/Brown above oil-water interface |
| Total volume of A-1 Carb Crest, $ft^3$ | 224,747,445 | |
| Total volume of BN, $ft^3$ | 1,108,020,000 | Internal to the reef, above oil-water contact (OWC) |
| Pore volume of A-1 Carb Crest, $ft^3$ | 24,378,815 | |
| Pore volume of BN, $ft^3$ | 39,779,498 | Internal to the reef, above OWC |
| Avg. thickness of A-1 Carb Crest, ft | 33 | |
| Avg. thickness of the BN, ft | 217 | Internal to the reef, above OWC |

Note: A-1 Carbonate saddle region is not included in these statistics because it is not reservoir quality rock.

## 1.4 Objectives of the MRCSP Phase III Project

The MRCSP was formed to assess the technical potential, economic viability, and public acceptability of carbon sequestration within its region. The MRCSP is one of seven regional partnerships established in October 2003, which together make up the U.S. DOE's Regional Carbon Sequestration Partnership (RCSP) program. The RCSP program is led by DOE's National Energy Technology Laboratory (NETL).

The MRCSP Phase III Project is the Large Volume Sequestration Test Phase of the U.S. DOE Regional Carbon Sequestration Program that included two prior phases of study, including Phase I – Assessment of Regional $CO_2$ Emission Sources and Geological and Terrestrial Sequestration Opportunities and Capacity (October 1, 2003 through September 30, 2005) and Phase II, small-scale field sequestration demonstration tests (October 1, 2005 through February 4, 2011). Phase III began May 6, 2008 and ended at the end of 2020.

The goal of the MRCSP Phase III program is to implement a geologic injection test of sufficient scale to promote understanding of injectivity, capacity, and storage potential in reservoir types having broad importance to the region. In the process, it also will test and demonstrate important aspects of $CO_2$ storage technologies to key stakeholders, including the public, environmental groups, government officials, policymakers, and industry. The key aspects to be tested include permitting and stakeholder acceptance, $CO_2$ handling and compression, local transport, site assessment and development, injection and monitoring operations, site closure or transition to commercial operations, and institutional processes. Moreover, the project was required to achieve the large volume goal by injecting $CO_2$ continuously during several years of injection operations.

Between February 2013 and September 2019, the MRCSP Phase III large-scale test injected over 1 million tons of $CO_2$ into a group of Silurian-age (Niagaran) pinnacle reef reservoirs in Otsego County Michigan that are operated by Core Energy, LLC. There are over 800 pinnacle reefs in northern Michigan, and collectively, these geologic features have sufficient capacity to store several hundred million metric tons of $CO_2$. Moreover, most of the reefs are oil-bearing and went through primary production in the 1970s and 1980s; therefore, by injecting $CO_2$ into the reefs, there is a real opportunity to realize additional (enhanced) oil recovery (EOR) and to permanently store $CO_2$ after EOR. Core Energy currently operates several reefs for EOR using $CO_2$.

## 1.5 Overview of the Phase III Monitoring Program

A key objective of the MRCSP Phase III project is to evaluate the effectiveness of various technologies for monitoring $CO_2$ that has been injected into deep geologic formations (i.e., the Niagaran reefs), The MRCSP Phase III project included a comprehensive monitoring program in parallel with injecting over one\\ million tonnes of $CO_2$ into a subset of ten (10) Niagaran pinnacle reefs operated by Core Energy. Figure 1-6 and Table 1-2 identify the monitoring technologies conducted at each of ten pinnacle reefs. The monitoring program included the following:

- At all ten reefs, a basic monitoring suite consisting of $CO_2$ mass-balance accounting (i.e., injection rate, cumulative $CO_2$ injected, production rate, cumulative $CO_2$ produced) and reservoir pressure.
- At the Dover 33 reef, six additional monitoring techniques, including Vertical Seismic Profile (VSP) monitoring; geochemistry monitoring; borehole gravity (BHG) monitoring; pulsed neutron capture (PNC) logging; satellite monitoring (INSAR – Satellite); and micro-seismicity monitoring.
- At the Bagley reef and the Charlton 19 reef, two additional monitoring techniques, including geochemistry monitoring and PNC logging.

- At the Chester 16 reef, five additional monitoring techniques, including DAS VSP monitoring, cross-well seismic monitoring, DTS, geochemistry monitoring, and PNC logging.

Eleven (11) separate reports have been prepared for the (11) monitoring technologies listed in Table 1-2. Each report discusses the objectives of the monitoring study, methods that were used for measuring/ evaluating the effectiveness of the monitoring technology, and results of each monitoring technology. This report discusses the DAS VSP monitoring program that was implemented at the Chester 16 reef.

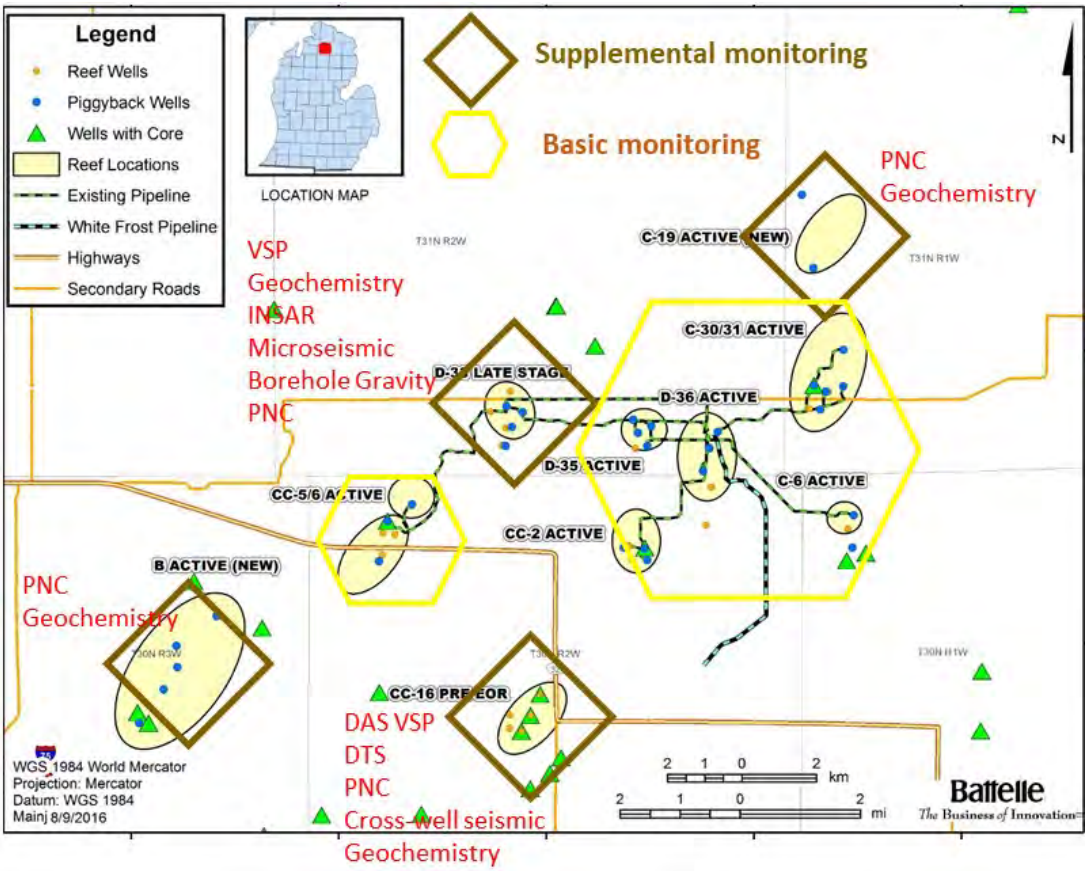


*Figure 1-6. Monitoring methods employed at various reefs during the MRCSP Phase III Program.*

**Table 1-2. Monitoring Technologies and Objectives as Implemented by Reef**

| | Monitoring Objective | | | | Monitoring by Reef | | | | |
|---|---|---|---|---|---|---|---|---|---|
| **Monitoring Technology** | **Mass-Balance Accounting** | **Leak Detection/ well integrity** | **$CO_2$ plume tracking/ interaction** | **Induced seismicity, uplift** | **Dover 33** | **Charlton 19** | **Chester 16** | **Bagley** | **Other reefs** |
| $CO_2$ injection/ production | X | | | | X | X | X | X | X |
| Reservoir Pressure | | | X | | X | X | X | X | X |
| Temperature (DTS) | | X | X | | | | X | | |
| PNC Logging | | X | X | | X | X | X | X | |
| Borehole Gravity | | | X | | X | | | | |
| Geochemistry | | | X | | X | X | X | X | |
| VSP – Geophone[a] | | X | X | | X | | | | |
| VSP – DAS[a] | | X | X | | | | X | | |
| Cross-well Seismic | | | X | | | | X | | |
| Microseismicity | | | | X | X | | | | |
| InSAR (Satellite radar) | | | | X | X | | | | |

a. Two varieties of VSP were implemented, including conventional VSP using geophones conveyed on a tubing string (Dover 33) and DAS VSP using fiber optic cable permanently mounted to the outside of the deep casing string (Chester 16).

## 1.6 Description of VSP

VSP is a type of borehole geophysical survey in which the receivers are placed in a borehole or well instead of on surface. A VSP produces a collection of seismograms recorded from land surface to a borehole. In terms of data acquisition, the defining characteristic of a VSP is that the receivers (e.g., hydrophones, geophones, accelerometers) are positioned either in a borehole or in a cased well (usually on a wireline or a tubing string) rather than on land surface; the receivers record downgoing and reflected (upgoing) seismic energy originating from a seismic source at the surface (DiSiena et al., 1984) (Figure 1-7).

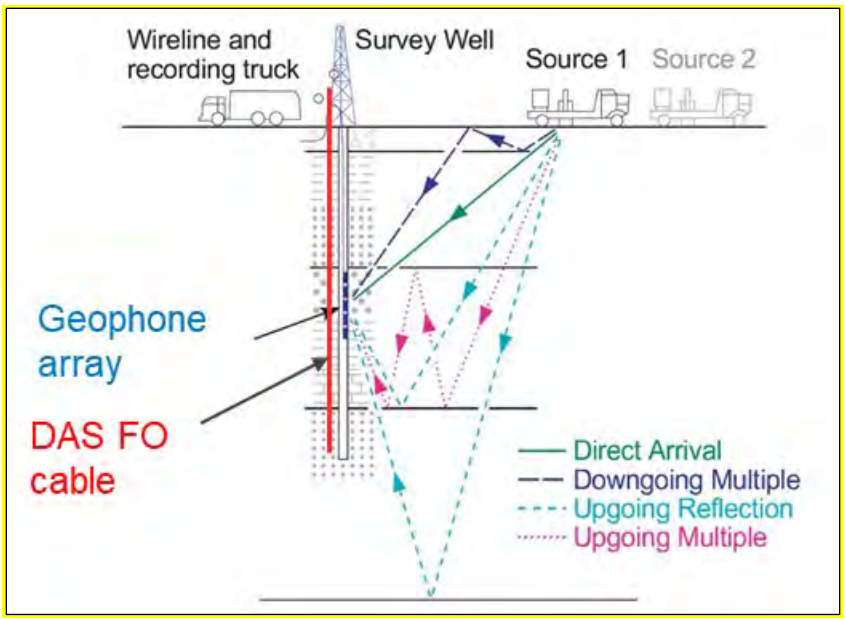


*Figure 1-7. Schematic diagram of a conventional and DAS VSP survey indicating a survey well, seismic source, receiver, wireline, and recording trucks (from DiSiena et al., 1984).*

A typical geophone VSP consists of five to 100 receivers (geophones) with a vertical spacing between successive stations of a few tens of feet. The horizontal distance between the surface source and the downhole receiver is the “offset” and can assume different magnitudes, depending on the specific VSP imaging application. Because the receiver stations are aligned vertically, the data-recording procedure is called VSP to distinguish the technique from conventional surface seismic profiling, in which seismic receivers are deployed across the surface and only upgoing seismic wavefields are recorded.

There are many types of VSPs. A walkaway VSP (WVSP) features a source that is moved to progressively farther offset locations away from the well that houses the geophones that are held in a fixed location in the borehole. Several sources deployed at various offsets might be called a multi-offset VSP, or if at different directions from the well, a multi-azimuth survey. In this study, sources were arranged in a grid pattern that surrounded the two wells with fiber optic cable installed for conducting the DAS VSP surveys. WVSPs provide vertical 2D seismic images extending away from the well. A sufficiently dense grid of shots on the surface provides s a 3D VSP. The use of downhole receivers in VSPs provides some advantages over surface seismic surveys, in particular:

- Increased frequency content improves vertical and lateral resolution; and,
- Improved SNR makes it possible to measure and quantify time-lapse changes in the reservoir with a greater degree of confidence.

## 1.7 Description of DAS VSP Monitoring

In conventional VSPs, geophones are placed in the borehole or well for the receivers. In a DAS VSP, a fiber optic cable replaces the geophones. Conventional geophones are point sensors, whereas with DAS, the optical fiber is the sensing element. A series of pulses are sent into the fiber and the naturally occurring backscattered light is recorded against time. A DAS system also includes a coherent optical time domain interferometer (instrument), commonly referred to as a lightbox or interrogator unit, at the surface connected to the fiber optical cable installed in the well. Seismic signals cause vibration, which in

turn cause microscopic elongation or compression of the fiber (micro-strain). The amount of strain is measured by recording/interpreting Rayleigh backscatter light from an optical laser pulse sent through the fiber and reflected to the transmitting end. In doing this, the distributed sensor measures at all points along the fiber. DAS seismic acquisition has some significant advantages over acquisition with geophones.

- DAS data can be acquired over the entire well at one instant whereas geophones are deployed in arrays that typically cover only a portion of the well, thus requiring array moves to span the entire well. Thus, geophones are not ideally suited for making instantaneous measurements.
- Fiber optic cables can be permanently installed behind casing, which facilitates making repeat measurements while allowing the well to be used for other purposes (e.g., fluid injection) and ensures a high degree of comparability (e.g., position of the receivers) between measurements, a key requirement for time-lapse monitoring techniques. Geophones can also be permanently installed but is costly compared to optic fiber.
- It is simpler and less costly to acquire seismic data from multiple wells simultaneously using DAS compared to geophones.

DAS has some limitations compared to (3-component) geophones, namely:

- DAS has a lower signal-to-noise ratio (SNR) compared to geophones (Mestayer et al., 2012). This limits the use of DAS in projects with weak signals. Stacking multiple (vibroseis) sweeps can improve SNR (stacking is possible if vibroseis is used as the source but not if dynamite is used).
- Fiber optic cables used for DAS are more sensitive to strain along the length of the fiber than strain perpendicular to the fiber (broadside to the fiber). Therefore, DAS does not record the full range of vibrations that can be recorded by a tool equipped with 3-component sensors.
- DAS has an uncertainty in receiver depths. Strain measurements from backscattered energy are associated with a certain depth along the fiber based on the arrival time of the backscattered energy, assuming a certain velocity of light in the fiber. The optical length (along the fiber) can be greater than the actual measured length (depth) of the well if the fiber length is made longer than the well length to prevent snapping when stretched. This leads to uncertainty in the optical length and depth errors that grow with depth. In addition, the length of the cable above the wellhead is not always accurately known.

## 1.8 Seismic Monitoring Basic Principles

Seismic monitoring, including time-lapse VSP, has been applied in the oil and gas industry since the 1990s to evaluate production parameters such as reservoir sweep efficiency, perform detailed history matching, and identify the presence of bypassed oil (Calvert, 2005). The amplitude, phase, and velocity of seismic waves recorded at the receiver are a function of the physical properties of both the rock matrix and the fluids contained within the pore spaces. When the fluids in the pore space are exchanged, the seismic signal also changes in a predictable manner. In the context of traditional oil and gas production, the pore fluids would change from oil/gas to water as the reservoir is depleted. In carbon capture, utilization, and storage (CCUS) settings, the goal is to displace pre-existing pore fluids with injected $CO_2$. An example fluid exchange relationship in the CCUS environment is one where $CO_2$ displaces water, thus reducing the bulk modulus and density of the rock/pore fluid unit (Purcell et al., 2010; Yang et al., 2014).

The fundamental property measured by seismic technologies is reflectivity. Sound energy travels through different media (rocks) at different velocities and is reflected at interfaces where the media velocity and/or

density changes. The amplitude and polarity of the reflections is proportional to the AI change across an interface. A seismic *trace* records the events (the arrival of energy at a receiver). AI is the product of velocity and bulk density; reflection (R) coefficient is defined as follows:

$$R = \frac{AI_1 - AI_2}{AI_1 + AI_2} = \frac{\rho_1 v_1 - \rho_2 v_2}{\rho_1 v_1 + \rho_2 v_2}$$

**Equation 1-1**

If the magnitude of the AI change is sufficiently large, the effect may be visually observed by comparing an image of the VSP monitor survey obtained after $CO_2$ injection to an image of a baseline VSP image obtained before $CO_2$ injection.

The deployment of time-lapse VSP for detecting/monitoring $CO_2$ in deep geologic strata is most effective in rocks that are highly compressible (low dry bulk modulus) and where there is a high contrast in the compressibility of fluids being substituted, i.e., saltwater with a fluid modulus of 2.25 gigapascals (GPa) 326,335 pounds per square inch (psi) compared to live oil (oil containing dissolved gas) with a fluid modulus of 1.0 GPa (145,038 psi) or gas phase of $CO_2$ (Lumley et al., 1997; Lumley, 2010). Additionally, the host rock must have sufficient porosity to allow pathways for migration and subsequent storage space for the secondary fluids (Lumley, 2010). If these variables are suboptimal, the seismic signal (impedance) caused by changes in pore fluids is far less likely to be detectable above the background noise of the dataset. The bulk modulus for supercritical $CO_2$ ranges from approximately 2 to 4 GPa, depending on pressure and temperature conditions; therefore, if VSPs are conducted over a period in which pressures and temperatures change, resulting in $CO_2$ undergoing a phase change (e.g., gas to liquid or supercritical liquid), this could provide adequate compressibility offset for detection (Yam and Schmitt, 2011).

# 2.0 Data Acquisition

## 2.1 DAS VSP Design

Pre-acquisition ray tracing was done to determine a set of source positions that would acceptably illuminate the reservoir zone in the target region. A grid of 181 source positions consisting of 44 vibrator positions and 137 dynamite shot locations was designed to give approximately continuous coverage of the zone of interest when recorded simultaneously using optical cables deployed on the production casing of the two deviated wells.

Figure 2-1 shows one plan view and one perspective view showing the well trajectories, the reef topography interpreted from well logs and 3D surface seismic data, and the shotpoints that were chosen. The underlay shows the zone at the top-of-reef level (5700 ft sub GL) where specular reflections from a nominal horizontal reflector are within the aperture determined by the available shot and receiver locations. The calculation for the aperture shown in Figure 2-1 assumed that only receivers below a depth of 2000 ft would provide useable data because the fiber optic cable above this depth was not cemented.

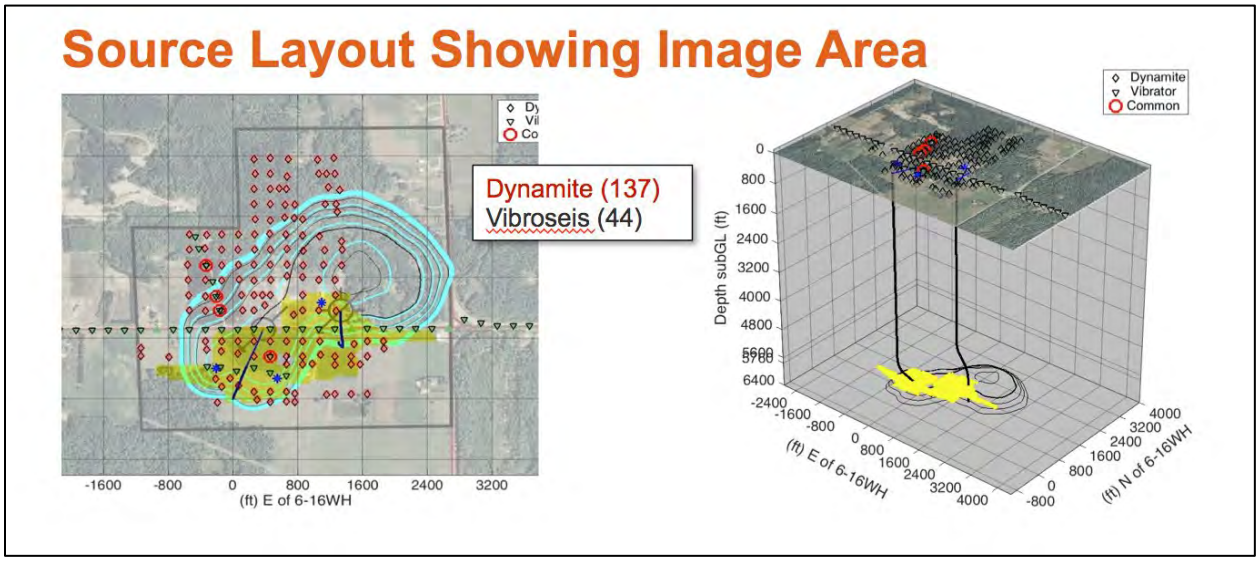


*Figure 2-1. Plan view and perspective view showing the well trajectories, the reef topography interpreted from well logs and 3D surface seismic data, and the shotpoints that were chosen based on pre-job ray tracing.*

## 2.2 Source Locations

The baseline DAS VSP data were acquired from February 17 through February 19, 2017. The survey included 45 vibroseis locations and 137 dynamite shot locations. A map showing the locations of vibroseis and dynamite source points is shown in Figure 2-2. Location coordinates, elevation, and other pertinent information for each source point is provided in Appendix A.

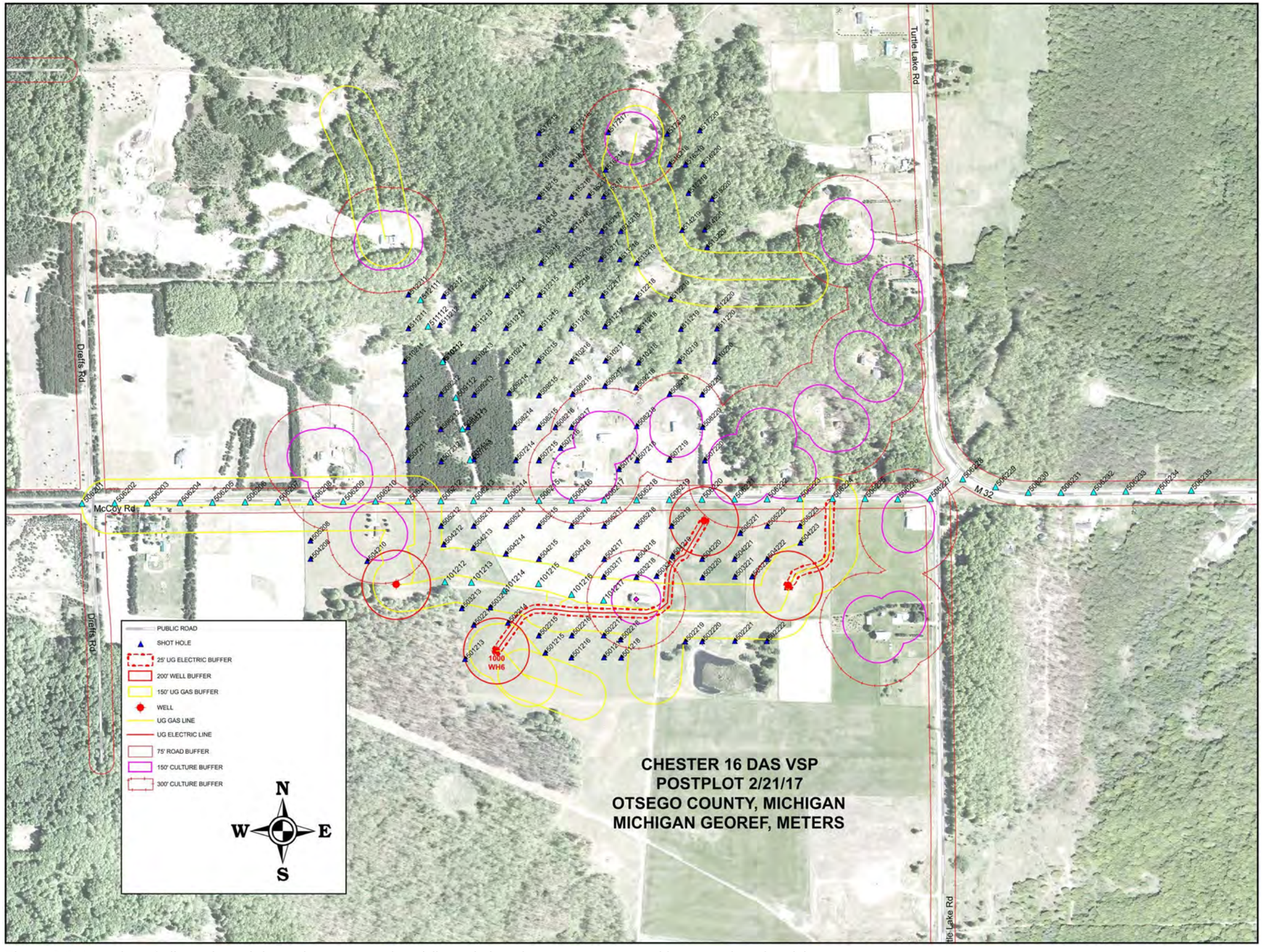


*Figure 2-2. Location of vibroseis and dynamite source points (vibroseis locations are represented by turquoise triangle)*

One position (SP 504216) was used as both a dynamite and a vibrator shot point to compare dynamite and vibroseis. One dynamite shot point (SP 502214) data was unusable due to a synchronization error. Vibroseis force was reduced at several shot points that are close to houses (full force was 78% of maximum capability of vibroseis trucks; reduced force was 40% of maximum). Dynamite source points were mostly a 1 kg load in a 20-ft deep boring. Load was reduced to 0.5 kg near houses. At several locations, it was not possible to drill to a depth of 20 ft due to saturated-ground conditions; therefore, at these locations, four 5-ft deep borings with a combined load of 0.65 kg were used. The monitor survey was recorded from August 20 to 22, 2018 using the same source points as the baseline survey. Vibroseis acquisition parameters were modified for the repeat survey in the following way: The number of sweeps was increased from five to 10 (full force locations) and from 10 to 15 (reduced force locations). Dynamite parameters (i.e., depth of borehole, load size) for the repeat survey were identical to the dynamite parameters for the baseline survey with the following exception—at the four locations where a cluster of four 5-ft deep borings with 0.65 kg charge was done twice during the baseline survey, they were not done twice in the repeat survey.

**Table 2-1. Vibroseis Acquisition Parameters**

| Parameter | Baseline Survey | Repeat Survey |
|---|---|---|
| Number of sweeps | 5 (full force)<br>10 (reduced force) | **10 (full force)**<br>**15 (reduced force)** |
| Number vibroseis trucks | 3 | **3** |
| Type | Linear | **Linear** |
| Frequency | 10-150 Hz | **10-150 Hz** |
| Start / end tapers | 0.5 s | **0.5 s** |
| Length | 30 s | **30 s** |
| Listen time | 4 s | **4 s** |

# 3.0 Results

Time-lapse DAS VSP was implemented at the Chester 16 reef to attempt to detect approximately 85,000 tonnes of $CO_2$ injected into the A-1 Carbonate and Brown Niagaran Formations. The baseline survey was conducted in February 2017 prior to injecting $CO_2$ and the repeat survey was conducted in August 2018. During the interim period between the baseline and repeat surveys, $CO_2$ was injected into the Chester 16 reef via the 6-16 injection well without production (withdrawal) of fluids from the reef. A numerical reservoir model of the Chester 16 reef was used to predict the $CO_2$ saturation distribution at the time of the repeat DAS VSP (see Figure 1-5).

The processing approach implemented in this study focused on monitoring the change in the amplitude of the reflectivity (RC) between the baseline and repeat surveys due to the introduction of $CO_2$. RC, a property of the interface between two intervals, is affected by the AI of the two intervals, where AI is the product of the bulk density and acoustic velocity of the rock-fluid system. Introduction of $CO_2$ into a layer can cause changes in density and velocity, resulting in a change in AI within the layer or interval receiving the $CO_2$. This can result in a change in the RC at the interface between the $CO_2$-containing layer and the overlying or underlying area that has not received $CO_2$.

## 3.1 Predicted Change in R Due to $CO_2$ Injection

Change in R due to injection of $CO_2$ was estimated using a simple spreadsheet model that calculates R using Equation 1-1 (note that this simplified equation for R does not include a term for incidence angle because it was shown through the use of Zoeppritz equation that for the range of recorded incidence angles the reflection response was fairly constant for the expected velocity and density variations). Figure 3-1 shows the velocity-density 1D model that was used to calculate change in R in response to $CO_2$ injection. The baseline (pre-$CO_2$ injection) model is based on well 6-16 acoustic and density logs recorded before commencing $CO_2$ injection. It is a seven-layer 1D model with constant velocity and density layers. Input values for velocity and density were computed by averaging the well log over the interval (the model value for each layer is shown by the black curves in Figure 3-1 overlain on the actual well log curve).

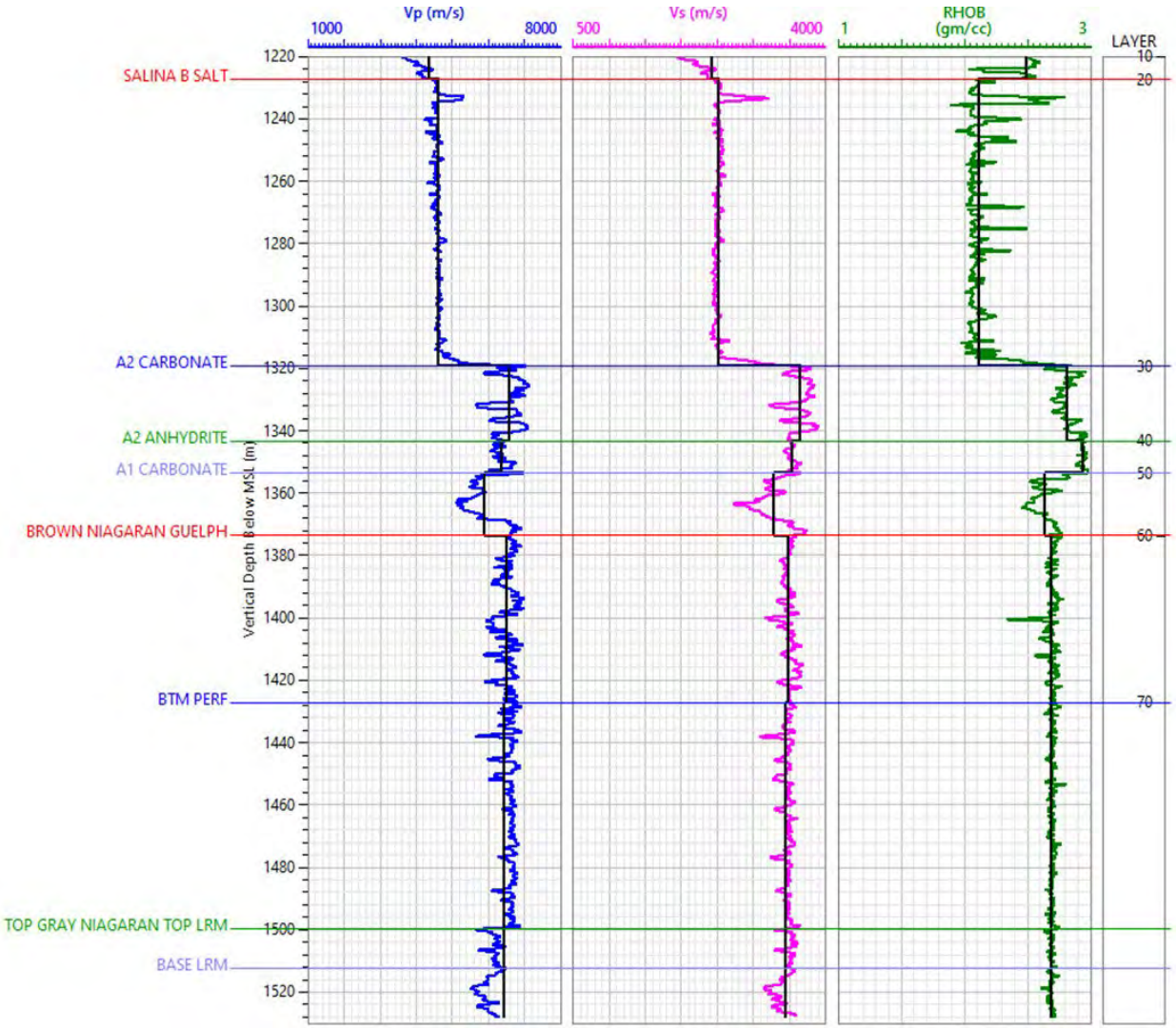


*Figure 3-1. Velocity-Density Model based on the well 6-16 acoustic and density logs recorded after the well was drilled and before $CO_2$ injection.*

Post-$CO_2$ injection values of R were calculated for seven different scenarios where each scenario is defined as a different percent change in V and ρ for the A-1 Carbonate, Brown Niagaran, and A-2 Carbonate. Each of the seven scenarios included two cases, a and b. The “a” cases involved an increase in Vp and/or density between the baseline and repeat VSP. The “b” cases involved a decrease in Vp and/or an increase in density between the baseline and repeat VSP. The model scenarios are described in Table 3-1, Figure *3-2* (a cases), and Figure 3-3 (b cases).

Values for ΔV were based on fluid substitution modeling and laboratory testing (details of the fluid substitution modeling and the laboratory tests are discussed in the companion report *Dover 33 Time-Lapse Vertical Seismic Profiling [VSP] Study*([Battelle, 2019]). Fluid substitution modeling suggests that for a reservoir with 10% porosity, the effect of fluid substitution with $CO_2$ is a ~1% decrease in Vp and Vs. In addition to fluid substitution modeling, laboratory tests were performed on reservoir core samples from the Dover 33 reef to assess the effect of $CO_2$ injection (fluid substitution) on acoustic velocities. Vp and Vs were measured for four different $CO_2$ saturations (5%, 35%, 70%, and 95%) for low pore pressure (500 psi) and high pore pressure (3,200 psi). The results show that P-wave and S-wave velocity are both sensitive to %$CO_2$ saturation; both decreased with an increase in $CO_2$ saturation. However, the

magnitude of the velocity change was less than 1%. Because fluid substitution modeling and laboratory tests both suggest that $CO_2$ injection will cause a very small change in acoustic velocities, an additional laboratory test was conducted to assess the effect of reservoir pressure (stress) on Vp and Vs. Core samples were subjected to 10 values of effective pressure ranging from 100 psi to 2,300 psi. The results of the laboratory test show that both P-wave velocity and S-wave velocity will decrease with decreasing effective pressure (increasing pore pressure) – i.e., both P-wave velocity and S-wave velocity increase with increasing effective pressure (decreasing pore pressure). The change in velocity was between 1% and 6% (details of the laboratory tests are discussed in the companion report Kelley et al., 2020)

Results of the synthetic modeling scenarios are summarized below:

### *Change in density with no change in velocity*

Scenarios 4, 5, and 6 predict the change in R due to an increase in density alone (no change in velocity) in the A-1 Carbonate (2%, 5%, 5%), Brown Niagaran (2%, 5%, 5%), and A-2 Carbonate (0%, 0%, 1%). The corresponding change in R is 4%, 10%, and 10%, respectively.

### *Change in velocity, no change in density*

**Increase in velocity –** Scenario 1a, 2a, and 3a predict the change in R due to an increase in velocity alone (no change in density) in the A-1 Carbonate (2%, 5%, 5%), Brown Niagaran (2%, 5%, 5%), and A-2 Carbonate (0%, 0%, 1%). The corresponding change in R for these three scenarios is 6%, 15%, and 16%, respectively.

**Decrease in velocity –** Scenario 1b, 2b, and 3b predict the change in R due to a decrease in velocity alone (no change in density) in the A-1 Carbonate (-1%, -6%, -6%), Brown Niagaran (-1%, -6%, -6%), and A-2 Carbonate (0%, 0%, -1%). The corresponding change in R for these three scenarios is 3%, 16%, and 17%, respectively.

### *Change in velocity and Density*

**Increase in velocity and density –** Scenario 7a predicts the change in R due to an increase in velocity and an increase in density in the A-1 Carbonate (5%, 5%), Brown Niagaran (5%, 5%), and A-2 Carbonate (1%, 1%), respectively. Corresponding change in R is 25% for this scenario.

**Decrease in velocity and increase in density –** Scenario 7b predicts the change in R due to a decrease in velocity and an increase in density in the A-1 Carbonate (-6%, 5%), Brown Niagaran (-6%, 5%), and A-2 Carbonate (-1%, 1%), respectively. Corresponding change in R is 9% for this scenario.

The increase in reservoir pressure will result in an increase in Vp and a Vs of up to 5%. To estimate the expected seismic response of the $CO_2$ injection into the carbonate reservoir, seven (7) scenarios were modeled and analyzed. The models were built using the well logs and information from the lab tests.

**Table 3-1. Model Scenarios and Results**

| Title | Description[a] | %Change in R (averaged across all layers) |
|---|---|---|
| Case 0 | Baseline | NA |
| Case 1a | +2% velocity change in A-1C and BN | 6% |
| 1b | -1% velocity change in A-1C and BN | 3% |
| Case 2 | +5% velocity change in A-1C and BN | 15% |
| 2b | -6% velocity change in A-1C and BN | 16% |
| Case 3a | +5% velocity change in A-1C and BN and +1% velocity increase in A-2C | 16% |
| 3b | -6% velocity change in A-1C and BN and -1% velocity change in A-2C | 17% |
| Case 4a | +2% density change in A-1C and BN | 4% |
| 4b | +2% density change in A-1C and BN | 4% |
| Case 5a | +5% density change in A-1C and BN | 10% |
| 5b | | 10% |
| Case 6a | +5% density change in A-1C and BN and +1% density change in A-2C | 10% |
| 6b | | 10% |
| Case 7a | +5% velocity and density change in the A-1C and BN and a +1% change in velocity and density in A-2C | 25% |
| 7b | -6% velocity change in the A-1C and BN and -1% velocity change in A-2C; +5% change in density in A-1C and BN and 1% change in density in A-2C | 9% |

a. A-1C: A-1 Carbonate; BN: Brown Niagaran; A-2C: A-2 Carbonate

The effect of a Vp increase and a Vp decrease was modeled for each scenario; a is the case of an increase in Vp,
b. is the case of a decrease in Vp.

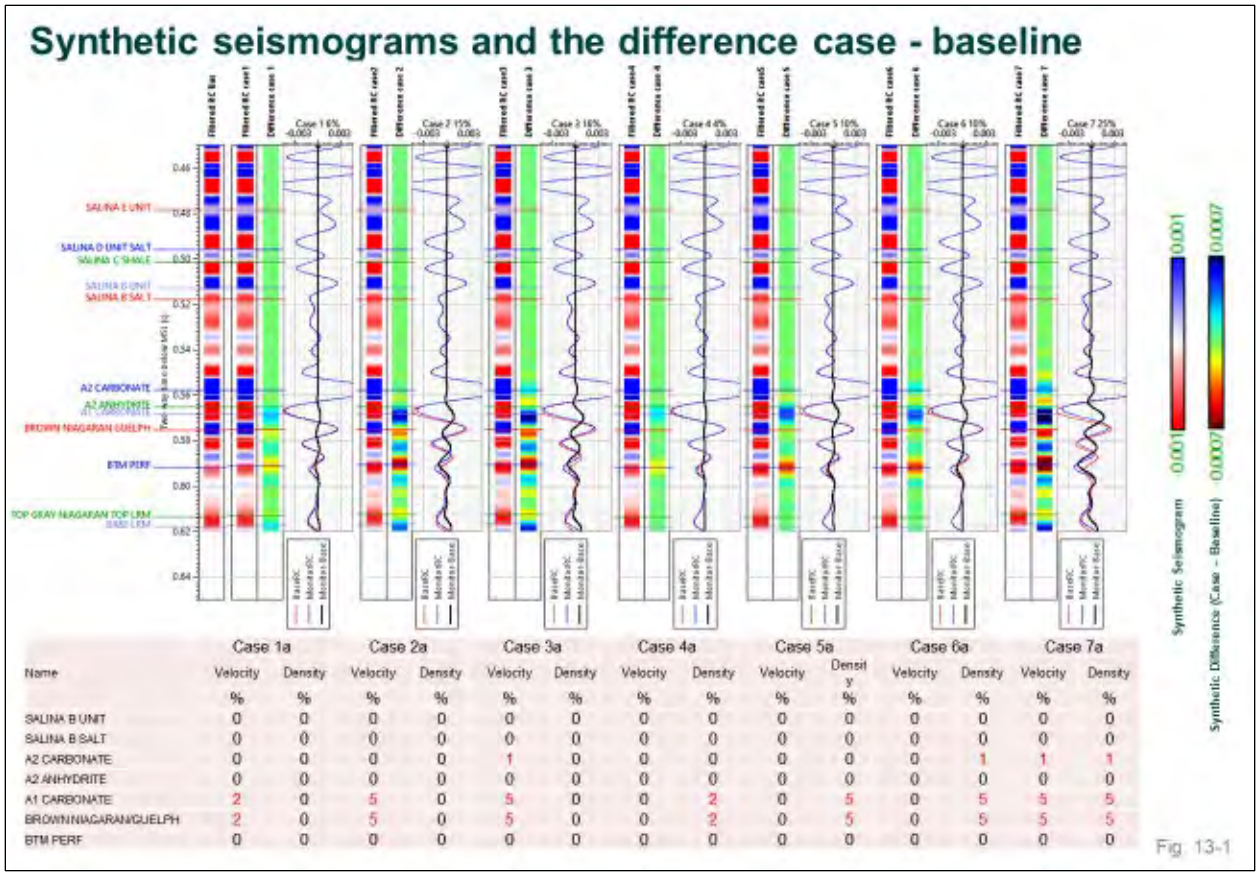


| | Case 1a | | Case 2a | | Case 3a | | Case 4a | | Case 5a | | Case 6a | | Case 7a | |
|---|---|---|---|---|---|---|---|---|---|---|---|---|---|---|
| Name | Velocity | Density | Velocity | Density | Velocity | Density | Velocity | Density | Velocity | Density | Velocity | Density | Velocity | Density |
| | % | % | % | % | % | % | % | % | % | % | % | % | % | % |
| SALINA B UNIT | 0 | 0 | 0 | 0 | 0 | 0 | 0 | 0 | 0 | 0 | 0 | 0 | 0 | 0 |
| SALINA B SALT | 0 | 0 | 0 | 0 | 0 | 0 | 0 | 0 | 0 | 0 | 0 | 0 | 0 | 0 |
| A2 CARBONATE | 0 | 0 | 0 | 0 | 1 | 0 | 0 | 0 | 0 | 0 | 0 | 1 | 1 | 1 |
| A2 ANHYDRITE | 0 | 0 | 0 | 0 | 0 | 0 | 0 | 0 | 0 | 0 | 0 | 0 | 0 | 0 |
| A1 CARBONATE | 2 | 0 | 5 | 0 | 5 | 0 | 0 | 2 | 0 | 5 | 0 | 5 | 5 | 5 |
| BROWN/NIAGARAN/GUELPH | 2 | 0 | 5 | 0 | 5 | 0 | 0 | 2 | 0 | 5 | 0 | 5 | 5 | 5 |
| BTM PERF | 0 | 0 | 0 | 0 | 0 | 0 | 0 | 0 | 0 | 0 | 0 | 0 | 0 | 0 |

*Figure 3-2. Predicted change in RC (shown in the upper part of the figure) for different changes in Vp and density (in these scenarios, all changes in Vp were positive).*

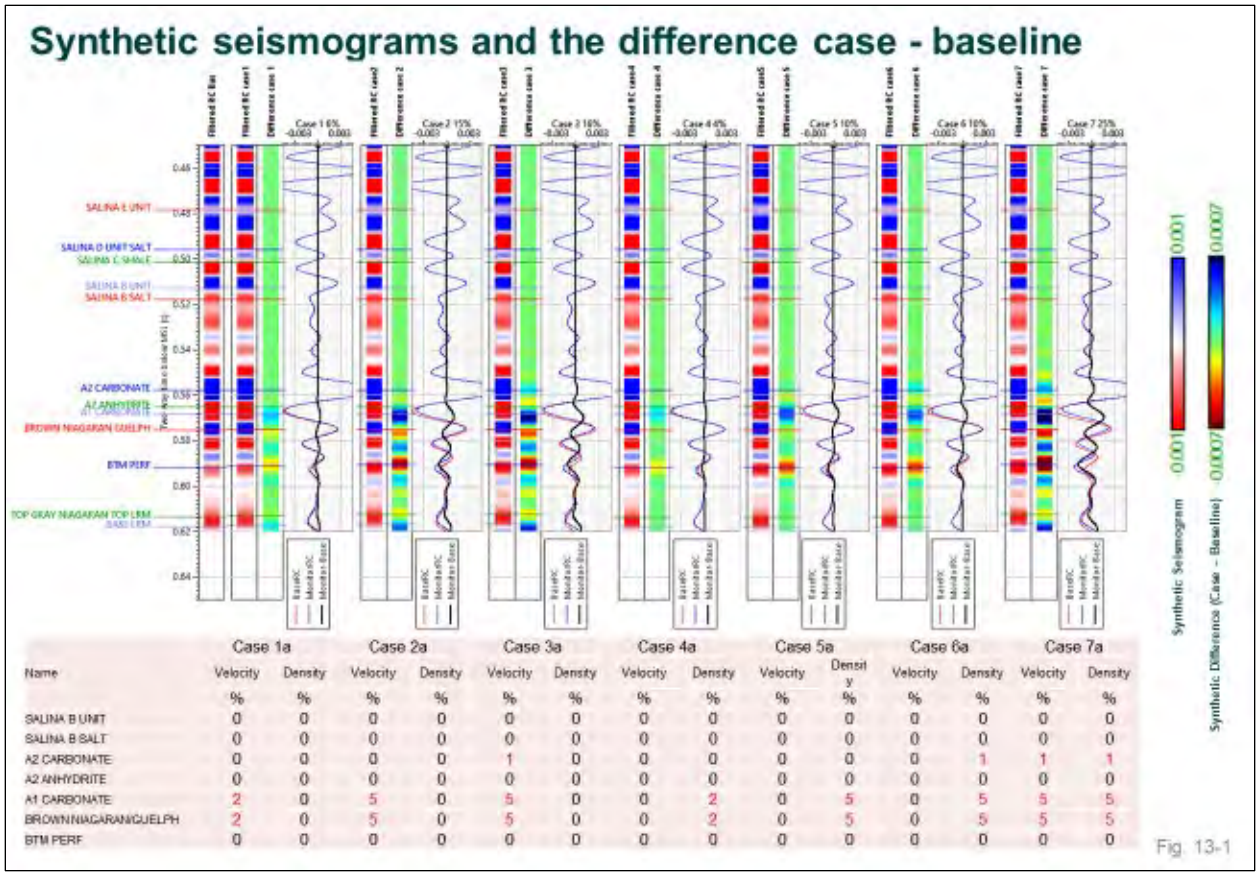


*Figure 3-3. Predicted change in RC (shown in the upper part of the figure) for different changes in Vp and density. In these scenarios, all changes in Vp were negative. Yellow shading indicates where input velocity is different than the scenario in Figure* 3-2 *Scenarios 4, 5, and 6 are identical to Figure* 3-2.

## 3.2 Recorded Time-Lapse Change in RC Due to $CO_2$ Injection

This section presents the results of the time-lapse VSP surveys for a single source point (101214) located near one of the wells instrumented with fiber compared to the predicted results from the previous section.

### 3.2.1 Pre-Migration Zero Offset VSP (ZVSP) Single Source Point Time-Lapse Results

For each model scenario/case, a figure was prepared that compares repeat-baseline to the synthetic difference and repeat R data and the difference between baseline and repeat (repeat survey minus baseline survey corridor stack difference— see Track 5 labeled Stack Difference), to the predicted R change (Track 6 labeled Synthetic Case) for one source point (101214) located close to the 6-16 well. Example figures of this type are shown in Figure 3-4 (Scenario 1b) and Figure 3-5 (Scenario 2b).

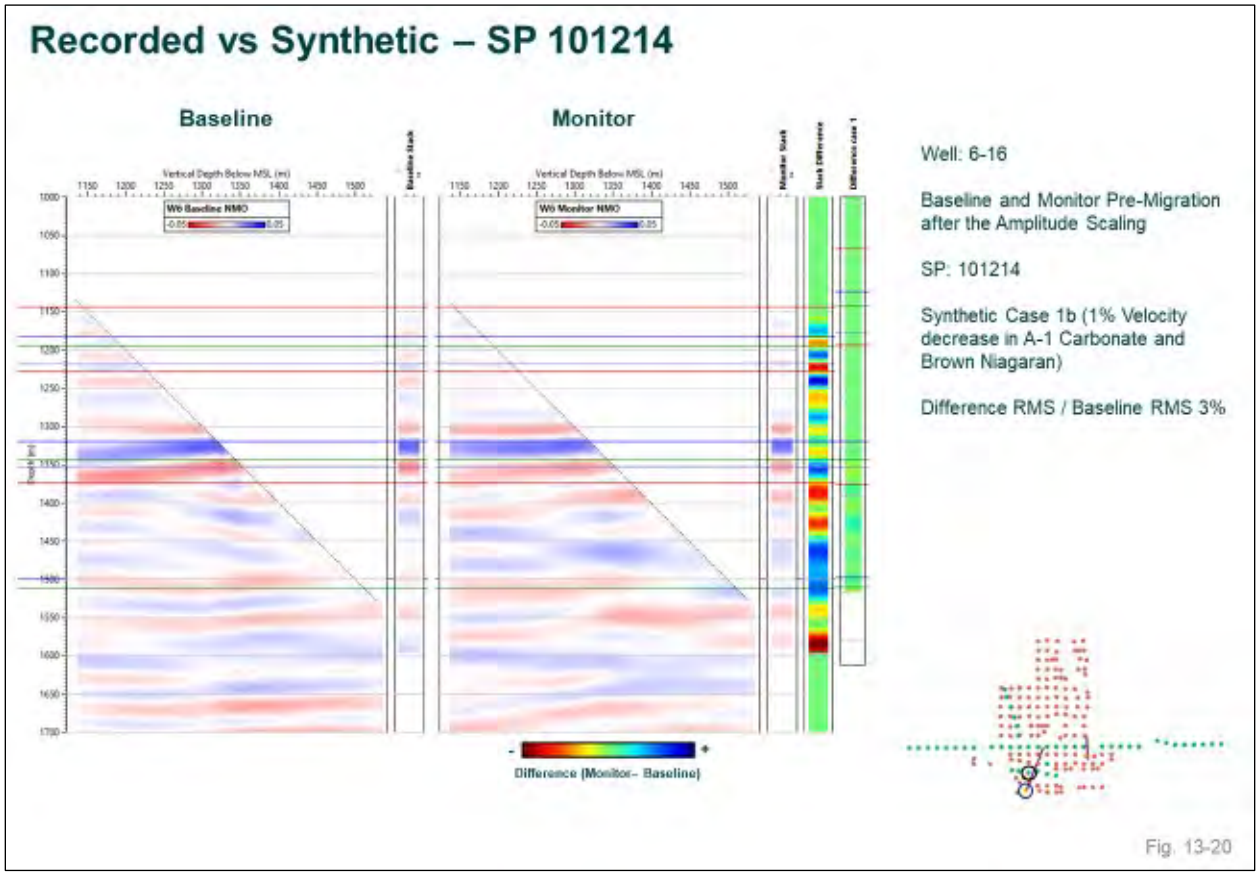


*Figure 3-4. Difference between actual recorded repeat VSP minus baseline VSP for vibroseis source point SP 101214 and synthetic ZVSP difference (model case 1b).*

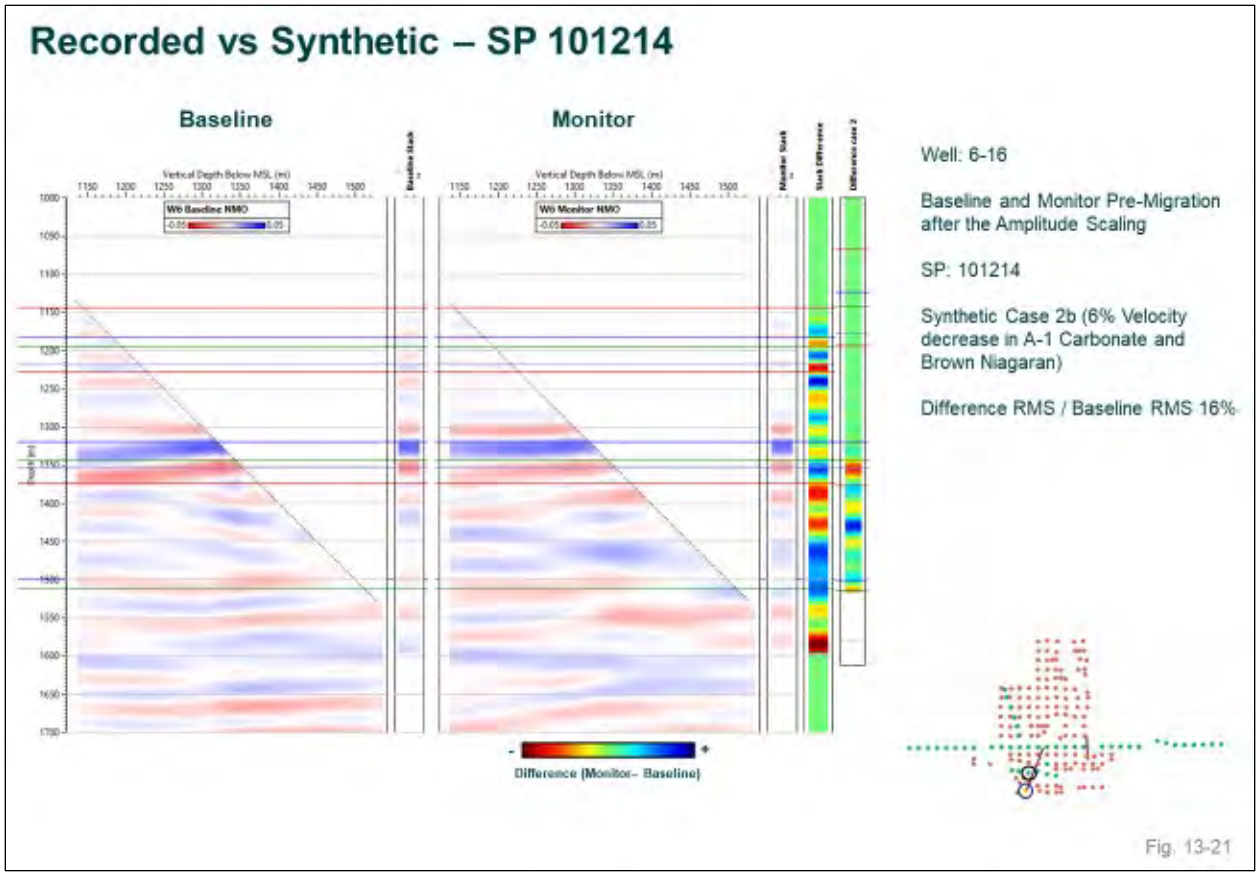


*Figure 3-5. Difference between actual recorded repeat VSP minus baseline VSP for vibroseis source point SP 101214 and synthetic ZVSP difference (model case 2b).*

### 3.2.2 Post-Migration Time-Lapse Results

Results of the DAS VSP study are time-lapse images that show the difference in R between the repeat survey and the baseline survey. Unlike the images in the previous section, which are based on a single source location, the images shown in this section combine data from multiple source locations. Ideally, the figures would have included data from all sources (i.e., vibroseis and dynamite) to provide the greatest spatial coverage of the reservoir. However, as previously discussed, due to the low SNR of the dynamite data compared to the vibroseis data, the two source types were not combined and only vibroseis data were used in the migration process (i.e., to make the images). Consequently, the spatial coverage of the images is significantly smaller than the area that would have been realized if dynamite data were included. The well casings were not cemented completely to ground surface; consequently, only the cemented portion of the fiber optic DAS cable had sufficient acoustic coupling and provided useable data. This also reduced the image area compared to the originally planned image area.

The time-lapse difference results are presented in Figure 3-6 and Figure 3-7. Additional images are provided in the comprehensive DAS VSP report in Appendix A.

Figure 3-6 shows a baseline and repeat RC vertical cross section image through each well, along with a (repeat survey minus baseline survey) “difference image” for each pair of time-lapse images. The limited coverage of each image is because the images were produced from only vibroseis data. The images cover an area close to the 6-16 injection well and the 8-16 monitor well. The imaged area near the injection well is particularly small. The difference image for the area near the 6-16 well shows difference features within the injection interval (A-1 Carbonate Crest and upper Brown Niagaran); however, difference features with similar magnitude also appear above and below the injection interval. Therefore, these results are encouraging but not unequivocal. The difference image for the 8-16 monitoring well does not show a pattern (clustering) of difference features associated with the injection interval.

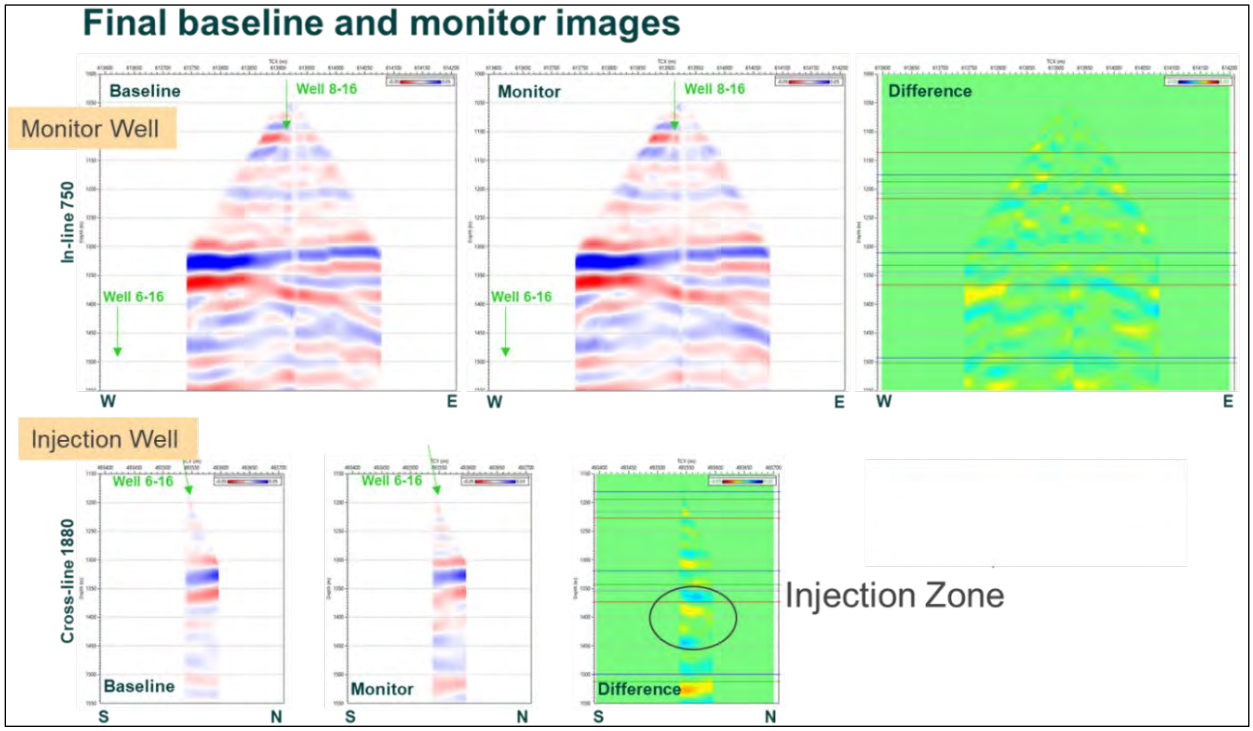


*Figure 3-6. Final baseline and repeat migrated images for well 8-16 and well 6-16.*

Another way to quantify the amplitude difference is to compute the difference amplitude root mean square (RMS) over a short vertical interval (i.e., from 5 m above to 5 m below a horizon). Figure 3-7 presents the difference amplitude RMS with the center of the analysis window at the A-1 Carbonate top surface and at 10 m, 20 m, 40 m and 60 m below the A-1 Carbonate surface. It is not a clear delineation, but higher RMS values are noticed close to the well 6-16 perforations.

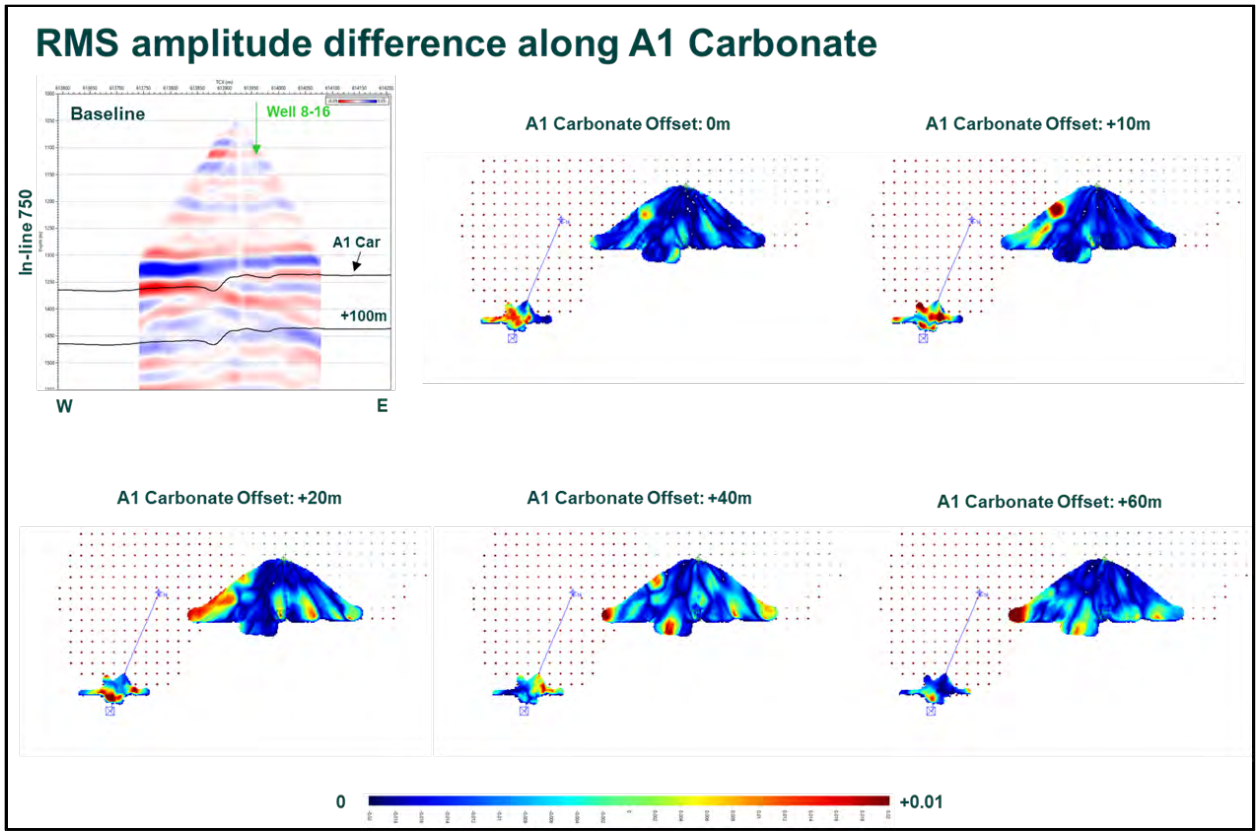


*Figure 3-7. The difference amplitude RMS with the center of the analysis window at the A-1 Carbonate top surface and at 10 m, 20 m, 40 m and 60 m below the A-1 Carbonate surface. It is not a clear delineation, but higher RMS values are noticed close to the well 6-16 perforations.*

## 3.3 Conclusions

This study evaluated the use of DAS VSP technology for delineating $CO_2$ injected into the A-1 Carbonate and Brown Niagaran Formations at the Chester 16 Reef in Otsego County Michigan. A baseline DAS VSP survey was acquired in February 2017 prior to commencing injecting $CO_2$ into the Chester 16 reef. In August 2017, after injecting 85,000 tonnes of $CO_2$ into the reef, a repeat (monitor) DAS VSP survey was acquired. Both surveys were nearly identical in design (i.e., number of sources, locations, parameters) and were processed using the same workflow so that the replacement of the native oil-water mixture with $CO_2$ was the primary change that occurred between the baseline and repeat surveys. Images were made showing the calculated difference between the baseline and repeat R distribution. The results, while encouraging, are not unequivocal. Areas where R changed between the baseline and repeat surveys were detected within the A-1 Carbonate and upper Brown Niagaran injection interval. However, the results also produced similar difference features outside the injection interval suggesting this technology is prone to producing false positives when conditions are not highly conducive for its use. In this study, the following factors contributed to the ambiguity in the results:

- Factor #1 Rock physics – in order for DAS VSP technology to clearly detect the injected $CO_2$, the injected fluid has to cause a change in AI (velocity and/or density) large enough to cause a change in RC that can be visibly detected. Laboratory tests and fluid substitution modeling both suggest the seismic response to $CO_2$ injection will be small (~5% change in acoustic velocity Vp). Such a small

change in AI will have a minor effect on R. Issue #1 is a physics-based limitation and therefore cannot be overcome.

- Factor #2 Survey factors – Several survey factors reduced the effectiveness of the DAS VSP technology. These can be avoided in future DAS VSP studies if preventive measures are taken.
  - Dynamite signals were weak compared to vibroseis so the two data types could not be combined. Doing so raised the lower limit of detection (i.e., reduced the overall SNR). Therefore, the time-lapse (difference) analysis was done using only the higher quality vibroseis data. This reduced the image area to the immediate area surrounding the 6-16 and 8-16 wells rather than the area between the two wells as originally planned. It also created the possibility that area(s) with $CO_2$ were missed.
  - The well casings were not cemented completely to ground surface; consequently, only the cemented portion of the fiber optic DAS cable had sufficient acoustic coupling and provided useable data. This also reduced the image area compared to the originally planned image area.
  - The vibroseis data from the repeat survey had significantly lower (better) SNR than the baseline vibroseis data. This is most likely because more sweeps were performed at each vibroseis source location in the repeat survey compared to the baseline survey. Vibroseis acquisition parameters were modified for the repeat survey in the following way: The number of sweeps was increased from five to 10 (full force locations) and from 10 to 15 (reduced force locations).
  - In this study, the injection tubing string in the 6-16 injection well vibrated during the acquisition of the VSP (due to dynamite or vibroseis energy waves impacting the tubing string), which adversely affected the acquired DAS data. In future DAS VSP surveys, it may be worthwhile to remove the injection tubing string, if present, prior to acquiring the data.
  - A larger mass of injected $CO_2$ might have been easier to detect. The repeat DAS VSP survey was conducted after injecting only 85,000 tonnes of $CO_2$, which was earlier than originally planned. Originally, the repeat survey was planned after the fill-up phase, which occurred after injection 5.3 BCF of $CO_2$ (approximately 280,000 tonnes). It was necessary to conduct the repeat survey earlier than planned because Core Energy was considering converting the 8-16 monitoring well to a horizontal injection well, which would have precluded further DAS monitoring in this well.

This DAS VSP study was partially successful for detecting $CO_2$ injected into the Chester 16 pinnacle reef. The DAS data indicate a measurable change (decrease) in seismic RC in the A-1 Carbonate and Brown Niagaran Formation, the two injection intervals, and near the 6-16 injection well. However, difference features were also indicated in strata above and below the injection zone. The DAS data also produced RC difference features in the vicinity of the 8-16 monitoring well, both within the injection zone and outside the injection zone, casting doubt on the results.

# 4.0 References

Mishra, S., Kelley, M., Ravi Ganesh, P., Haagsma, A., Raziperchikolaee, S., Main, J., Pasumarti, A., Smith, V., Mawalkar, S., and Gupta, N. 2020. I Integrated Modeling Report for $CO_2$ Storage with Enhanced Oil Recovery in Northern Michigan MRCSP topical report prepared for DOE-NETL project DE-FC26-05NT42589, Battelle Memorial Institute, Columbus, OH

Haagsma, A., Conner, A., Cotter, Z., Grove, B., Main, J., Scharenberg, M., Larsen, G., Raziperchikolaee, S., Goodman, W., Sullivan, C., and Gupta, N. 2020. Geologic Characterization for $CO_2$ Storage with Enhanced Oil Recovery in Northern Michigan. MRCSP topical report prepared for DOE-NETL project DE-FC26-05NT42589, Battelle Memorial Institute, Columbus, OH.

Kelley, M., Haagsma, A., and Gupta, N. 2020. Time-Lapse Vertical Seismic Profiling (VSP) for $CO_2$ Storage in a Depleted Oil Field in Northern Michigan MRCSP topical report prepared for DOE-NETL project DE-FC26-05NT42589, Battelle Memorial Institute, Columbus, OHCalvert, R., 2005, Insights and methods for 4D reservoir monitoring and characterization, Society of Exploration Geophysicists and European Association of Geoscientists and Engineers, Distinguished Instructor Series

DiSiena, J. P., Byun, B. S., Fix, J. E., Gaiser, J. E., Toksoz, N. M., and Stewart, R. R., 1984, FK analysis and tube wave filtering, Vertical seismic profiling, part B: Advanced concepts, p. 288-301.

Lumley, D., 2010, 4D Seismic monitoring of $CO_2$ sequestration, Geophysics, 29, doi:10.1190/1.3304817.

Lumley, D. E., Behrens, R. A., and Wang, Z., 1997, Assessing the technical risk of a 4-D seismic project: The Leading Edge, v. 16, no. 9, p. 1287-1292.

Purcell, C., Mur, A., Soong, Y., McLendon, T. R., Haljasmaa, I. V., and Harbert, W., 2010, Integrating velocity measurements in a reservoir rock sample from the SACROC unit with an AVO proxy for subsurface supercritical $CO_2$: The Leading Edge, v. 29, no. 2, p. 192-195.

VSProwess, 2019. Chester 16 Time-lapse DAS VSP Final report October 18, 2019; Prepared by VSProwess Ltd under subcontract with Silixa, LLC.; prepared for Battelle 505 King Avenue Columbus, Ohio 43201 under Purchase Order 566422.

Yam, H., and Schmitt, D., 2011, $CO_2$ rock physics: A laboratory study, CSPG CSEG CWLS Convention.

Yang, D., Malcolm, A., Fehler, M., and Huang, L., 2014, Time-lapse walkaway vertical seismic profile monitoring for $CO_2$ injection at the SACROC enhanced oil recovery field: A case study: Geophysics, v. 79, no. 2, p. B51-B61.

# Appendix A.

# Chester 16 Time-lapse DAS VSP Final Report

## Oct. 18, 2019

Battelle

# Chester 16
# Time-lapse DAS VSP

Final report

| | |
|---|---|
| **Revision 0** | **2019-10-18** |
| **Revision 1** | |
| **Revision 2** | |

Liviu.Grindei@vsprowess.com
Mary.Humphries@vsprowess.com
VSProwess Ltd

This report was developed by VSProwess under subcontract with Silixa, LLC.

Prepared for
Battelle
505 King Ave
Columbus, OH. 43201
Technical Lead: Mark Kelley
kelleym@battelle.org

VSProwess Ltd

Somerset UK TA4 2UX

www.vsprowess.com

## Summary

Battelle is leading the Midwest Regional Carbon Sequestration Partnership (MRCSP) multi-year research program to evaluate the suitability of Silurian-aged carbonate pinnacle reefs in northern Michigan for carbon dioxide ($CO_2$) utilization and storage (CCUS). The study is conducted under the U.S. Department of Energy National Energy Technology Laboratory (DOE/NETL) Regional Carbon Sequestration Program (RCSP). A key objective of the program is to test several monitoring technologies for detecting and delineating the $CO_2$ that has been injected into the carbonate-reef reservoirs. This report presents the results of a time-lapse Distributed Acoustic Sensing (DAS) Vertical Seismic Profiling (VSP) monitoring study at the Core Energy Chester 16 reef in Otsego County, Michigan. DAS VSP is as geophysical technique that has been used to monitor $CO_2$ injected into deep geologic reservoirs; however, this is the first time the technology has been applied to carbonate pinnacle reefs.

As part of this project, CORE Energy drilled two new wells in the late 2016/early 2017. Well 6-16 was equipped with injection tubing and used to inject $CO_2$ into the reservoir while a second well, 8-16, a future production well, was used to monitor the reservoir. A 3D DAS VSP survey was designed to illuminate the area between the two new wells. Due to surface access restrictions, a combination of vibroseis and dynamite sources was used.

Battelle, Silixa, and Core Energy carried out the first (baseline) survey in February 2017 prior to commencing injection of $CO_2$ into the reservoir, when reservoir pressure was low (approximately 700 psi). The second (repeat) survey was acquired 16 months later in July 2018 after 86,000 tons of $CO_2$ had been injected, raising the reservoir pressure to approximately 1500 psi.

Silixa processed the baseline VSP but later hired VSProwess Ltd to perform the processing, including both the baseline and repeat surveys. This report presents the processing performed on the baseline and monitor data surveys. The main objective was to determine the time-lapse effect on the seismic response by examining the difference between the two surveys. Therefore, the two surveys were processed in parallel using the same workflow and parameters. For each survey, dynamite source data was processed separately from vibroseis source data. The report presents the additional pre-processing workflow design for DAS surveys and a comparison between the dynamite and vibroseis datasets.

The 3D velocity model used for VSP processing was constructed using the well acoustic logs and the well 8-16 ZVSP data. The velocity model building and calibration is presented in this report. The quality of the data recorded using the vibroseis source was significantly better than that from the dynamite source and the imaging was therefore focused on the vibroseis data, as was the time-lapse analysis.

Synthetic (wave propagation) models were constructed to predict the time-lapse seismic response (i.e., change in reflection coefficients) due to $CO_2$ injection and the corresponding time-lapse change in the velocity of the acoustic waves and bulk density of the rock-fluid system, the primary parameters that effect reflectivity. The magnitude of the seismic response (change in velocity, density) depends on factors such as the rock porosity and bulk modulus (inverse of compressibility) – higher porosity and lower bulk modulus leads to a larger seismic change. If the change in velocity and/or density is too small, it may not be detectable with the time-lapse VSP method. The velocity changes were taken from laboratory fluid substitution tests conducted on reservoir cores from a nearby pinnacle reef. In general, the measured time-lapse results were consistent with the modelled results in the injection interval (A-1 Carb and upper Brown Niagaran). However, the model predicts the occurrence of

difference features above and below the injection interval, which were not observed in the monitoring results.

The time-lapse effect between the baseline and monitor survey was analysed to determine if the $CO_2$ plume can be mapped.

| Abbreviation | Description |
|---|---|
| VSP | **Vertical Seismic Profile** |
| DAS | **Distributed Acoustic Sensing** |
| WRE | **Well Reference Elevation** |
| SDE | **Seismic Datum Elevation** |
| MD | **Measured Depth below WRE** |
| TVD | **True Vertical Depth below WRE** |
| TVDSD | **True Vertical Depth below SDE** |
| KB | **Kelly Bushing** |
| GL | **Ground Level** |
| TT | **Transit Time** |
| OWT | **One Way Time** |
| TWT | **Two Way Time** |
| | |
| P-wave | **Compression (Primary) wave with particle motion along direction of travel** |
| S-wave | **Shear (Secondary) wave with particle motion perpendicular to direction of travel** |
| P-down | **P-wave in a downward direction** |
| PS-down | **P-down mode-converted on transmission to S-wave** |
| PP-up | **P-down reflected upward as P-wave** |
| PS-up | **P-down reflected upward as S-waved** |
| PSS-up | **PS-down reflected upward as S-wave** |
| | |
| SNR | **Signal to Noise Ratio** |

*Common abbreviations*

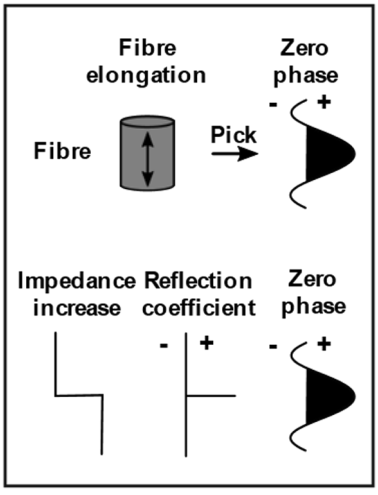


Polarity description

# Contents

# 1 Introduction

Fibre optic cable was installed in Chester 6-16 (injection) and 8-16 (monitor) wells outside the 5½" production casing and was cemented. Silixa LLC was in charge of recording the DAS VSP data using the iDAS v2 optical interrogator for the baseline and monitor survey. The dynamite and vibroseis sources were provided by Emerson Geophysical LLC for both baseline and monitor surveys. The DAS VSP data were processed by VSProwess Ltd.

The baseline survey was recorded from 18th February to 20th February 2017 and the monitor survey was recorded from 20th August to 22nd August 2018.

All measured depths within a borehole are referenced to the elevation above MSL of the Kelly Bushing (KB) for that borehole at the time of the survey: Well 6-16 KB was at 402.64 m (1321.0 ft) and well 8-16 KB was at 407.21 m (1336.0 ft).

The processed VSP results are referenced to Mean Sea Level (MSL).

The polarity convention used for results is an increase in acoustic impedance represented by a positive number on the trace and displayed as a peak. This is commonly known as SEG normal polarity

# 2 Pre-survey modelling

The Chester 16 license covers the pinnacle reef. Pre-survey modelling was performed by Silixa LLC to establish the best source geometry required to illuminate the area of interest. Permission was available to place seismic sources to the south of the Chester 16 EOR unit boundaries (Fig. 2-1) but pre-survey modelling showed this to be unnecessary (Fig. 2-3 left).

Chester 16 is an old depleted field, now in the enhanced oil recovery (EOR) phase. There are a number of old wells but only the new wells, drilled in the late 2016 to earlier 2017, have fibre optic cable installed and were to be used in this study.

Before the baseline seismic survey took place, several acquisition surveys had been designed.

The vibroseis source could be placed only along the road or connected tracks. Pre-survey modelling indicated this was not sufficient to illuminate the area of interest (Fig. 2-2 left). To achieve the desired illumination additional dynamite source locations would be required (Fig. 2-2 right).

The final source geometry design is shown in Fig. 2-3.

| Title | Description | Figure |
|---|---|---|
| **2 Pre-survey modelling** | | |
| Basemap | Allowed source position area | **2.1** |
| Acquisition design | Vibroseis and combined source survey | **2.2** |
| Imaging area | Combined sources survey imaging area | **2.3** |

*Table 2-1. Pre-survey modelling figures*

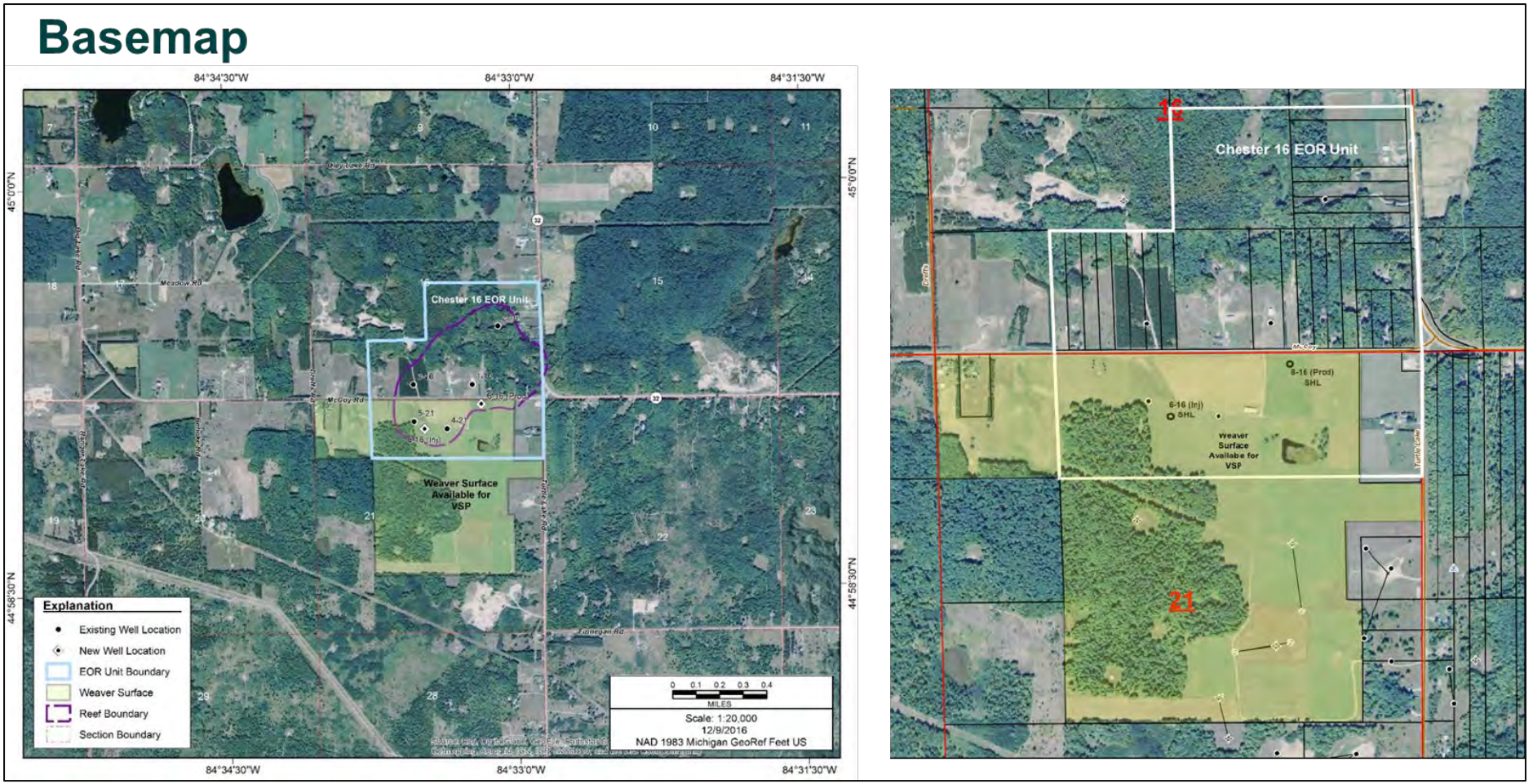


*Figure 2-1. Basemap of the Unit 16 permit area. Permission was available to place seismic sources to the south of the Chester 16 EOR unit boundaries.*

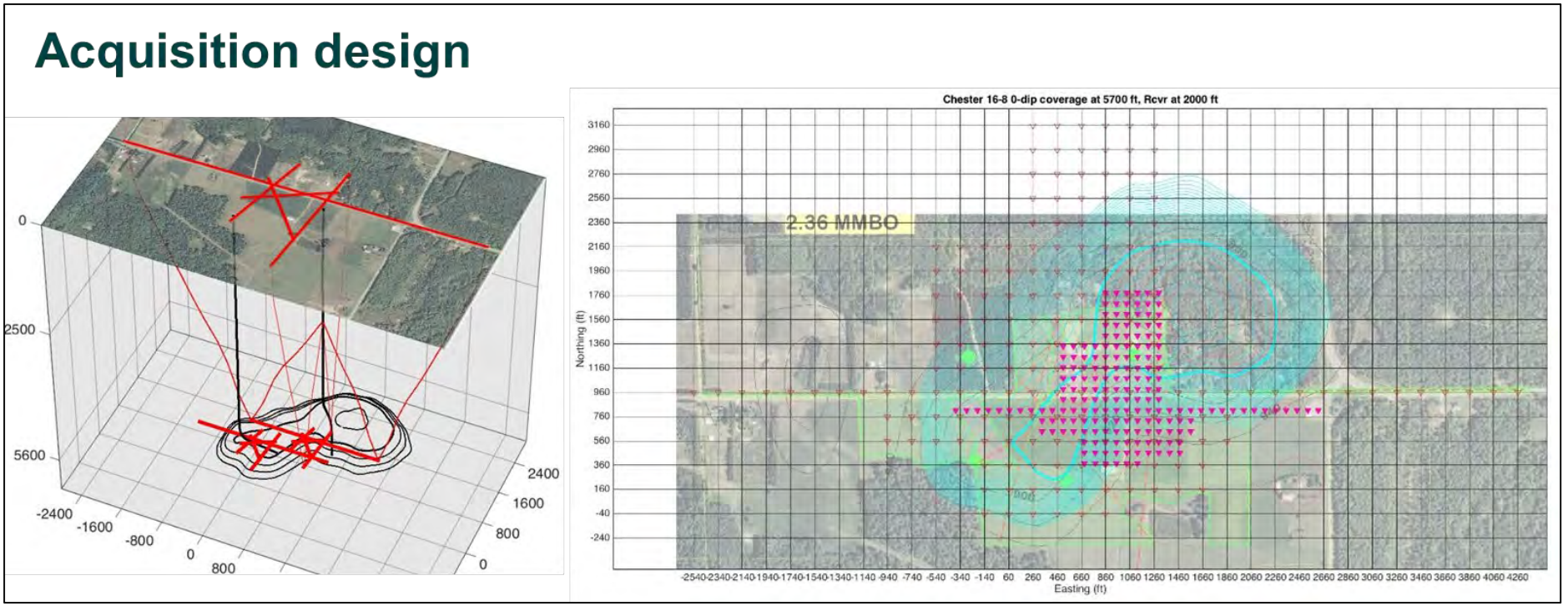


*Figure 2-2. Before the baseline seismic survey took place, several acquisition surveys had been designed. The vibroseis source could be placed only along the road or connected tracks. Pre-survey modelling indicated this was not sufficient to illuminate the area of interest (Fig. 2-2 left). To achieve the desired illumination additional dynamite source locations would be required (Fig. 2-2 right).*

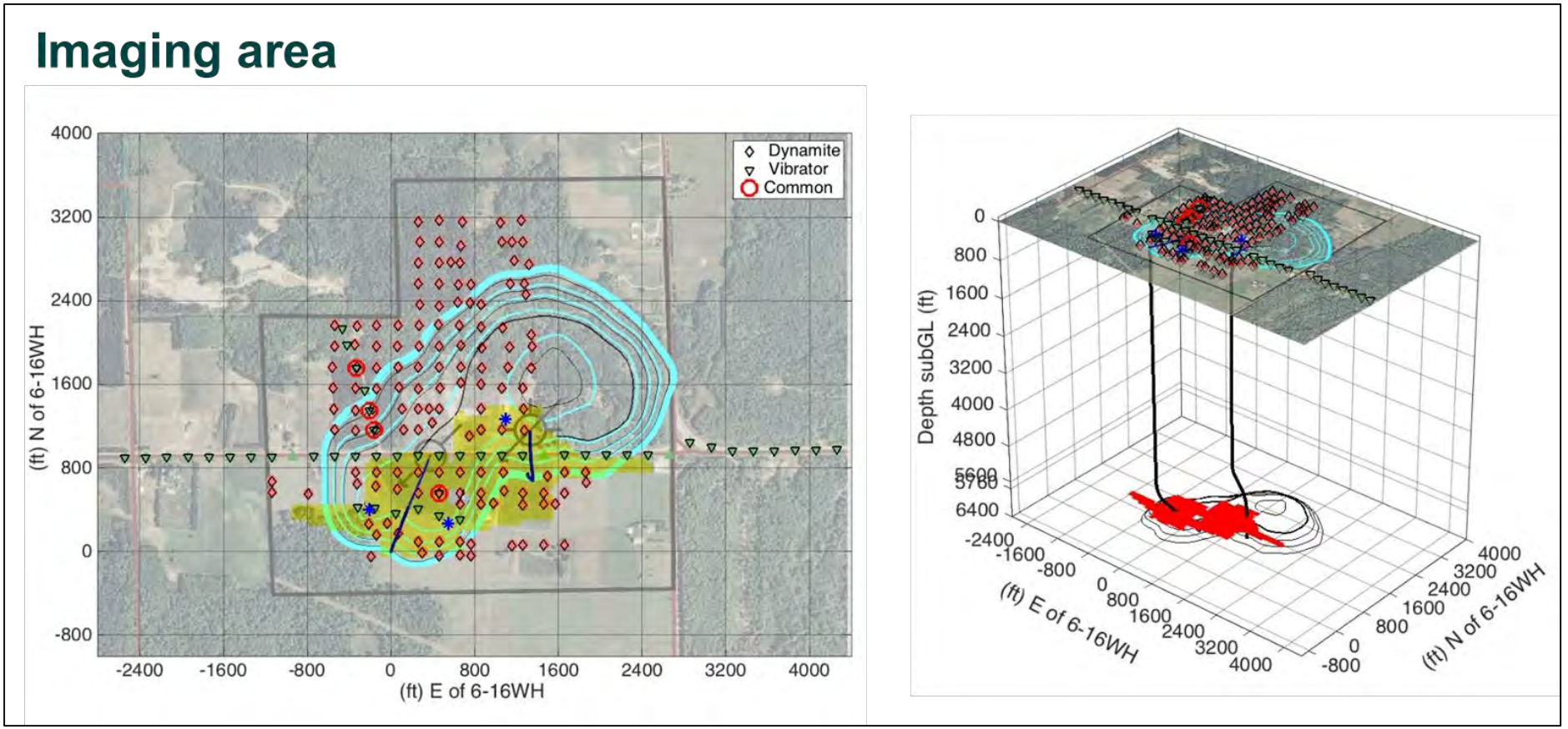


*Figure 2-3. Final source geometry design with vibroseis and dynamite. Pre-survey modelling showed that sources outside the Unit 16 permit are unnecessary to illuminate the southern part of the reef between the wells.*

# 3 Acquisition

Figure 3-1 shows the final source positions relative to the well head location shown in yellow. In blue are the vibroseis source points and in red are the dynamite source points.

Near the perimeter are exclusion zones due to existing gas pipelines and buildings (Fig. 3-2). The maximum vibroseis force was reduced inside the buffer zones near to the buildings to avoid any potential damage.

Figures 3-3 and 3-4 show the casing diagrams for injection well 6-16 and monitor well 8-16 respectively. The casing designs are similar, following the state oil & gas regulations, with 11 ¾" casing cemented to surface and the intermediate 8 5/8" casing and production 5 ½" casing only partially cemented. The injection well only is equipped with an injection string.

The lower part of each well is highly deviated to the north. Figures 3-5 and 3-6 present the well deviation projections in west-east, south-north and horizontal plans.

| 1 | Injection well | | |
|---|---|---|---|
| 2 | Name | **3** | **6-16 Pilot** |
| 4 | Client | **5** | **Core Energy, LLC** |
| 6 | Field | **7** | **Chester 16 Unit** |
| 8 | Location | **9** | **Michigan, USA** |
| 10 | Wellhead | **11** | **613517.8041 m E, 493519.9328 m N** |
| 12 | Coordinate system | **13** | **NAD83, GeoRef Hotine Oblique for whole state (meter)** |
| 14 | Kelly bushing | **15** | **1321.0 ft (402.64 m) above MSL** |
| 16 | Ground level | **17** | **1307.4 ft (398.50 m) above MSL** |

*Table 3-2 Well 6-16*

| 18 | Monitor well | | |
|---|---|---|---|
| 19 | Name | **20** | **8-16 HD1** |
| 21 | Client | **22** | **Core Energy, LLC** |
| 23 | Field | **24** | **Chester 16 Unit** |
| 25 | Location | **26** | **Michigan, USA** |
| 27 | Wellhead | **28** | **613916.8413 m E, 493745.3098 m N** |
| 29 | Coordinate system | **30** | **NAD83, GeoRef Hotine Oblique for whole State (meter)** |
| 31 | Kelly bushing | **32** | **1336.0 ft (407.21 m) above MSL** |
| 33 | Ground level | **34** | **1322.6 ft (403.13 m) above MSL** |

*Table 3-3 Well 8-16*

| 35 | Name | 36 | Measure Depth | | |
|---|---|---|---|---|---|
| | | **37** | **feet** | **38** | **meter** |
| 39 | Total depth | 40 | 6697 | **41** | **2041** |
| 42 | Top of cement 5-1/2" casing | 43 | 5420 | **44** | **1652** |
| 45 | 8-5/8" casing shoe | 46 | 4047 | **47** | **1234** |
| 48 | Top of cement 8-5/8" casing | 49 | 3050 | **50** | **930** |
| 51 | 11-3/8" casing shoe | 52 | 993 | **53** | **303** |
| 54 | 16" conductor shoe | 55 | 61 | **56** | **19** |

*Table 3-4 Well 6-16 casing*

| 57 | Name | 58 | Measure Depth | | |
|---|---|---|---|---|---|
| | | 59 | feet | 60 | meter |
| 61 | Total depth | 62 | 6316 | **63** | **1925** |
| 64 | Top of cement 5-1/2” casing | 65 | 5300 | **66** | **1615** |
| 67 | 8-5/8” casing shoe | 68 | 4000 | **69** | **1219** |
| 70 | Top of cement 8-5/8” casing | 71 | 2300 | **72** | **701** |
| 73 | 11-3/8” casing shoe | 74 | 960 | **75** | **293** |
| 76 | 16” conductor shoe | 77 | 80 | **78** | **24** |

*Table 3-5 Well 8-16 casing*

| 79 | Name | 80 | Measure Depth | | |
|---|---|---|---|---|---|
| | | 81 | feet | 82 | meter |
| 83 | Perforation 1 Top | 84 | 6274 | **85** | **1912** |
| 86 | Perforation 1 Bottom | 87 | 6284 | **88** | **1915** |
| 89 | Perforation 2 Top | 90 | 6135 | **91** | **1870** |
| 92 | Perforation 2 Bottom | 93 | 6145 | **94** | **1873** |
| 95 | Perforation 3 Top | 96 | 6094 | **97** | **1857** |
| 98 | Perforation 3 Bottom | 99 | 6104 | **100** | **1860** |
| 101 | Perforation 4 Top | 102 | 6033 | **103** | **1839** |
| 104 | Perforation 4 Bottom | 105 | 6043 | **106** | **1842** |
| 107 | Perforation 5 Top | 108 | 5937 | **109** | **1810** |
| 110 | Perforation 5 Bottom | 111 | 5947 | **112** | **1813** |
| 113 | Perforation 6 Top | 114 | 5914 | **115** | **1803** |
| 116 | Perforation 6 Bottom | 117 | 5924 | **118** | **1806** |
| 119 | Perforation 7 Top | 120 | 5892 | **121** | **1796** |
| 122 | Perforation 7 Bottom | 123 | 5902 | **124** | **1799** |

*Table 3-6 Well 6-16 perforations*

For both surveys, Emerson Geophysical, LLC used the same seismic source design. The source setup is presented in figure 3-7. The vibroseis source comprised three AHV-II vibrators (65,000 lb peak force) shaking in synchronised mode. Each vibrator was equipped with a Force II decoder. BoomBox I equipment was used to ignite the dynamite sources. The sources were radio-controlled using Universal Encoder I. The seismic encoder was connected by cable to the fibre optic interrogator.

The source observer used the SourceLink software to monitor the source position and parameters and to send the fire command. The observer computer connected to the Universal Encoder negotiate the starting time with the source controllers, generates the pilot sweep, sends the sweep over the radio and receives the source monitoring data while the Universal Encoder triggers the interrogator to start the acquisition. The source controllers and the fibre optic interrogators record the GPS timestamps at the sweep start and dynamite blast.

A dynamite charge of 1.0 kg was used at 20 ft depth below ground level for 97 locations. For 22 locations, near to the buildings or gas pipelines, only 0.5 kg charges were used at 20 ft depth. For 18 locations with difficult access a charge weight of 0.65 kg was used in groups of 4 holes drilled at 5 ft below ground level.

In each well a single ended fibre optic cable was clamped behind the 5-1/2” production casing. The seismic response of the DAS cable was however poor above the deviated section, probably because of poor coupling in the vertical section. The fibre optic cable terminates at the surface in the data shed

located near to the 8-16 well head (Figure 3-8). Each cable contains three single-mode fibres. Before each survey, and for each well, the fibre with the best reflectivity was chosen based on an optical time-domain reflectometer (OTDR) test. For the baseline survey, iDAS unit serial number 15041 was connected to SM1 fibre from well 6-16 and iDAS unit 16043 was connected to SM2 fibre from well 8-16. For the monitor survey, the iDAS unit 18067 was connected to SM1 fibre from well 6-16 and iDAS unit 17053 was connected to SM1 fibre from well 8-16. An anti-vibration table was used during the monitor survey to reduce the recorded noise due to vibration of the iDAS interrogator unit. The anti-vibration was not available during the baseline survey.

The data recording was supervised from the dog house located near the data shed. The interrogators were linked to the processing computers by a LAN connection.

| 125 | Parameter | 126 | Value |
|---|---|---|---|
| 127 | Type | **128** | **Linear** |
| 129 | Frequency | **130** | **10-150 Hz** |
| 131 | Start / End tapers | **132** | **0.5 s** |
| 133 | Length | **134** | **30 s** |
| 135 | Listen time | **136** | **4 s** |

*Table 3-7 Sweep parameters*

| 137 | Parameter | 138 | Value |
|---|---|---|---|
| 139 | Sampling frequency | **140** | **1 kHz** |
| 141 | Laser rate | **142** | **16 kHz** |
| 143 | Spatial resolution | **144** | **0.25m** |
| 145 | Acquisition mode | **146** | **Triggered** |

*Table 3-8 iDAS system parameters*

| 147 | Title | 148 | Description | 149 | Figure |
|---|---|---|---|---|---|
| **150** | **3 Acquisition** | | | | |
| 151 | Source position | 152 | Vibroseis and dynamite source position | **153** | **3.1** |
| 154 | 3D VSP Acquisition plan | 155 | Final 3D survey source position | **156** | **3.2** |
| 157 | Well 6-16 sketch | 158 | Casing diagram | **159** | **3.3** |
| 160 | Well 8-16 sketch | 161 | Casing diagram | **162** | **3.4** |
| 163 | Well 6-16 deviation | 164 | | **165** | **3.5** |
| 166 | Well 8-16 deviation | 167 | | **168** | **3.6** |
| 169 | Seismic source setup | 170 | Diagram | **171** | **3.7** |
| 172 | Acquisition setup | 173 | iDAS setup | **174** | **3.8** |

*Table 3-9 Acquisition figures*

# Source positions


*Figure 3-1. Source position - vibroseis and dynamite source position overlay on aerial view. The final source positions relative to the well head location is shown in yellow. In blue are the vibroseis source points and in red are the dynamite source points.*

# 3D VSP Acquisition plan

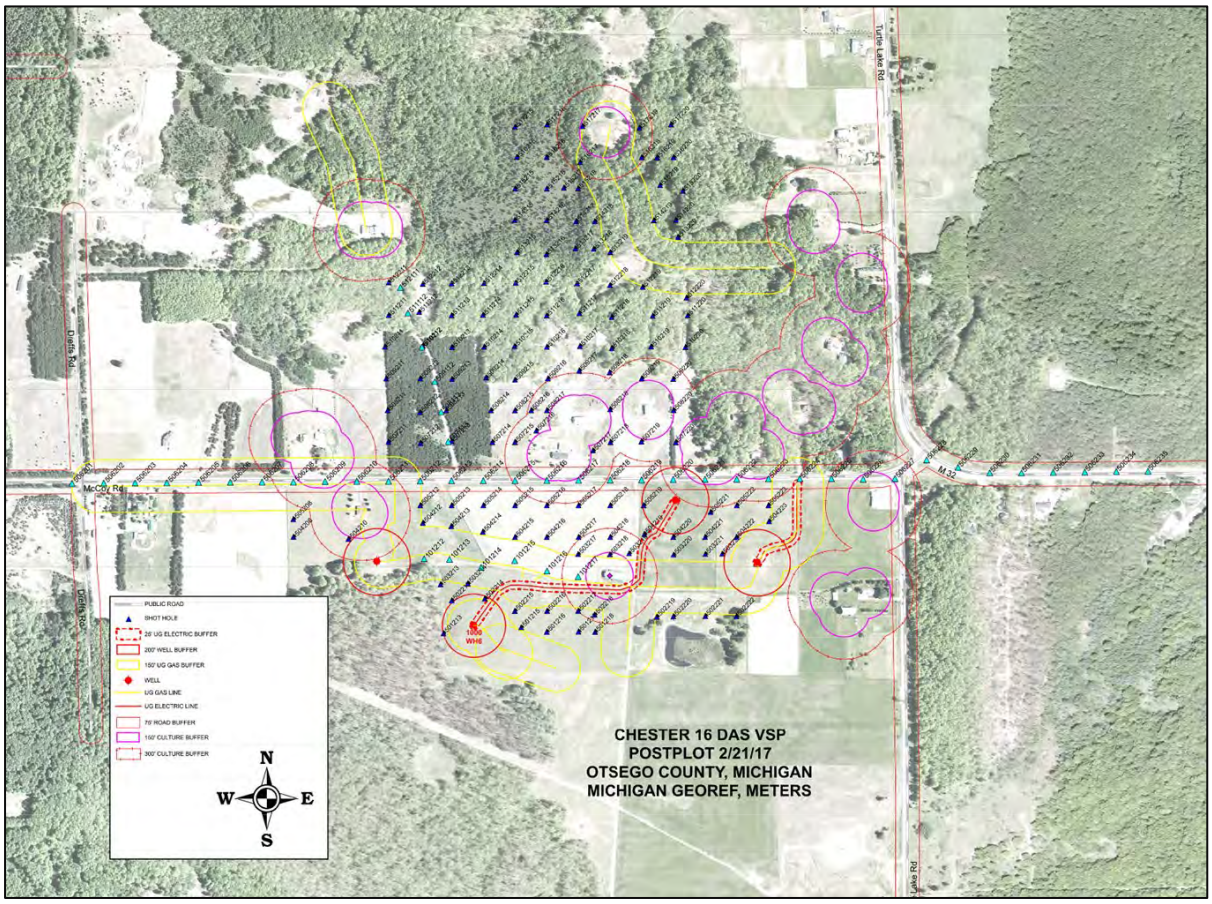


*Figure 3-2. 3D VSP Acquisition plan - the final 3D survey source position. Near the perimeter are exclusion zones due to existing gas pipelines and buildings. The maximum vibroseis force was reduced inside the buffer zones near to the buildings to avoid any potential damage.*

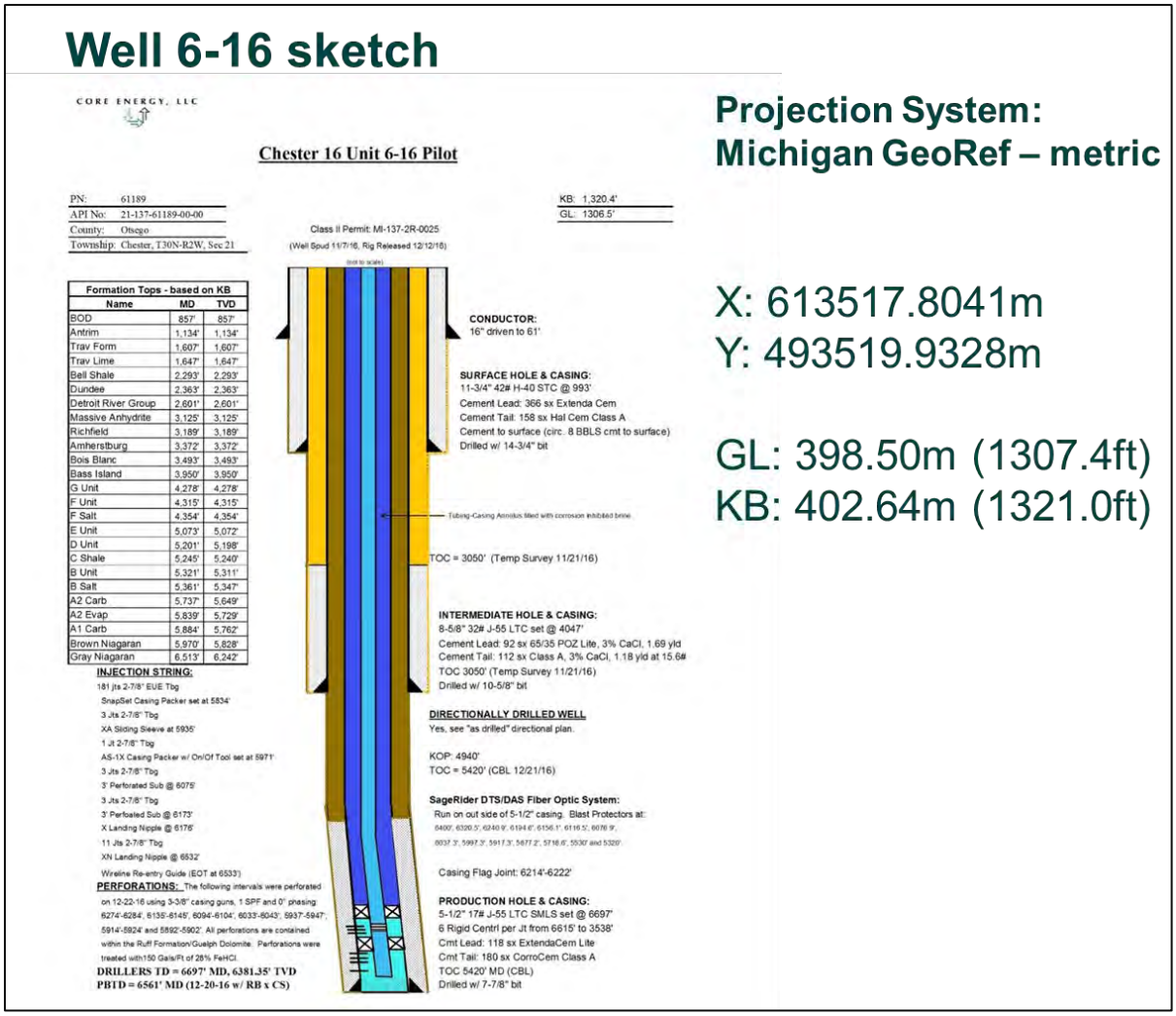


*Figure 3-3. Well 6-16 sketch - Casing diagram.*

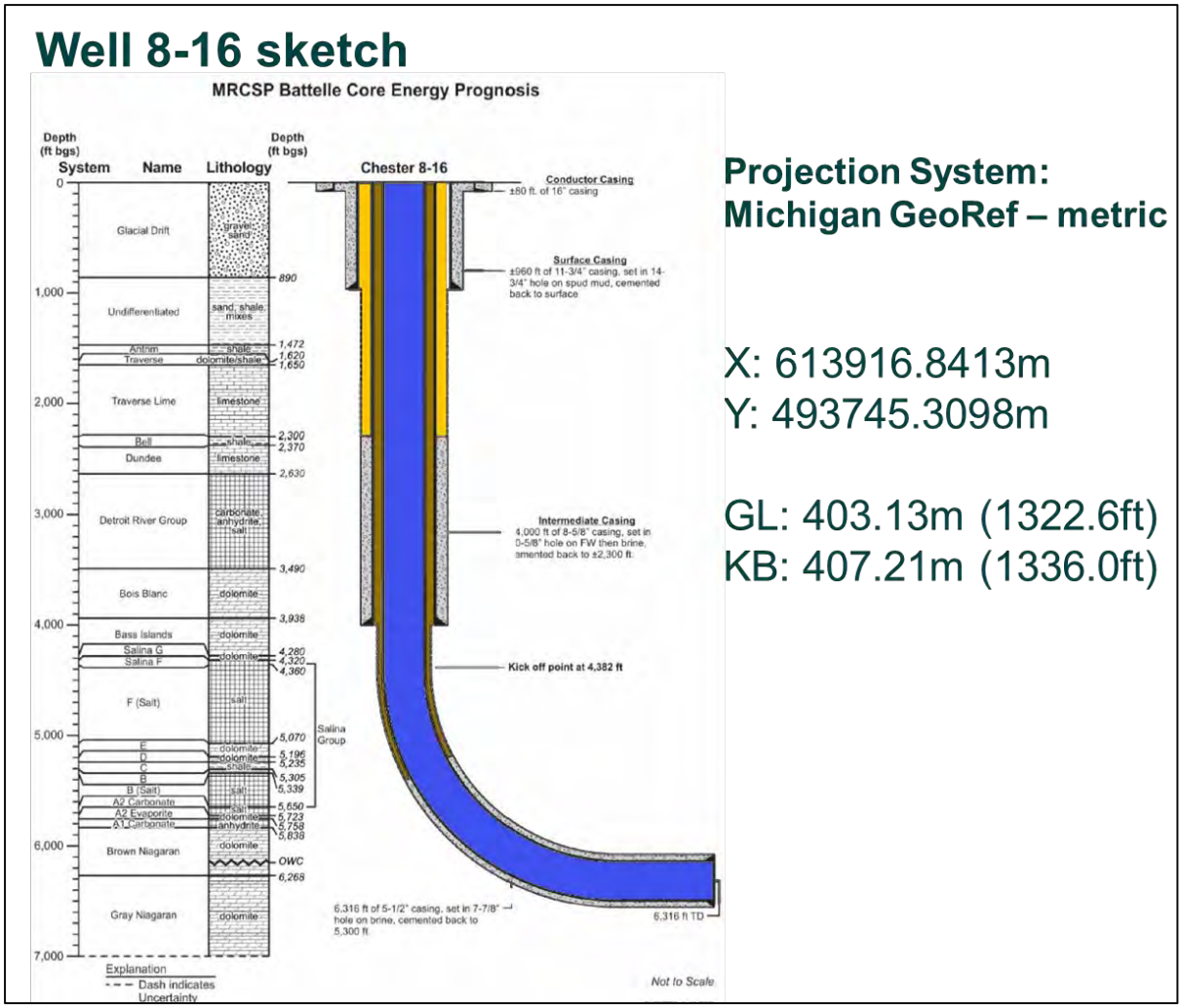


*Figure 3-4. Well 8-16 sketch - Casing diagram.*

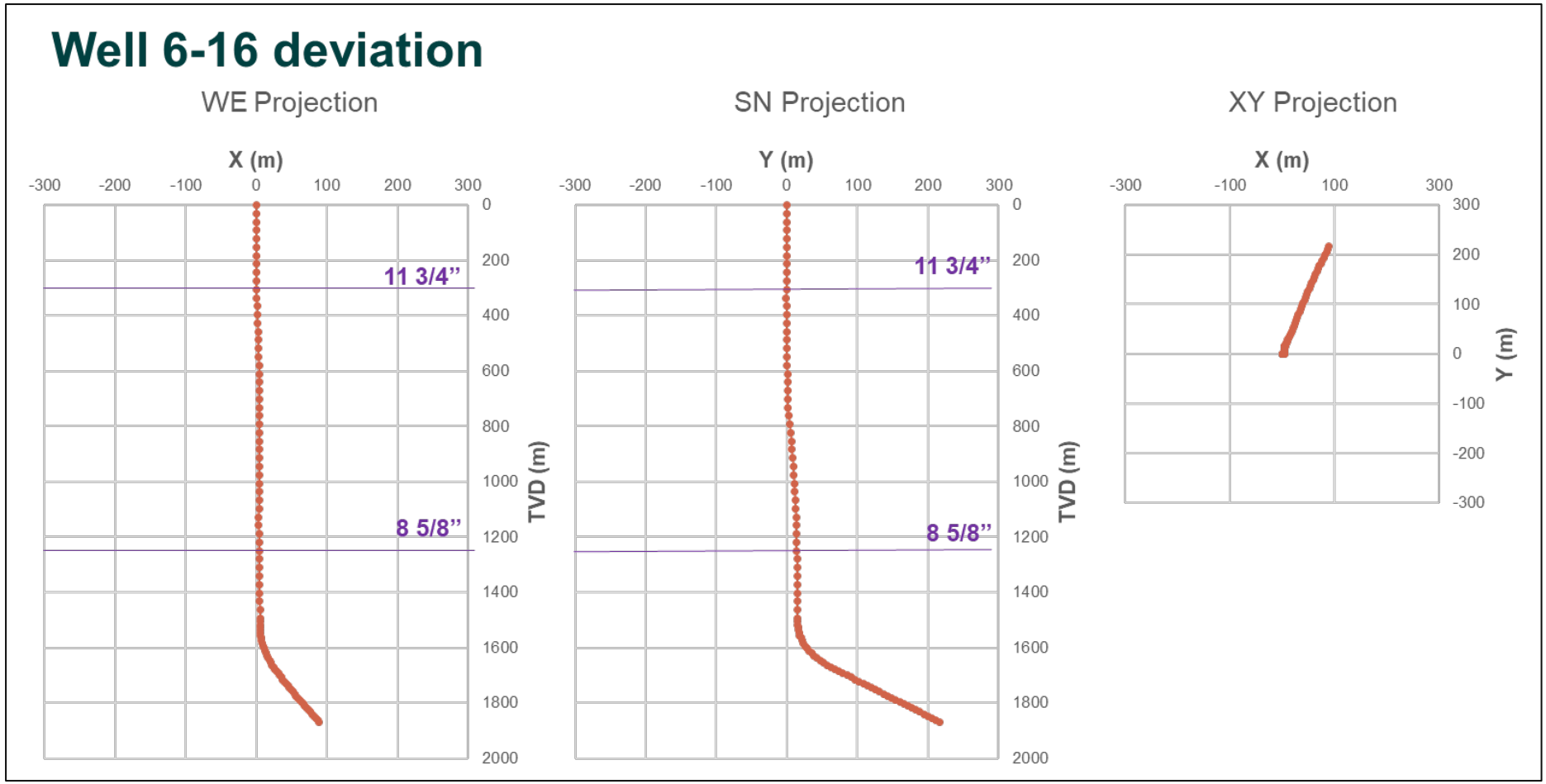


*Figure 3-5. Well 6-16 deviation.*

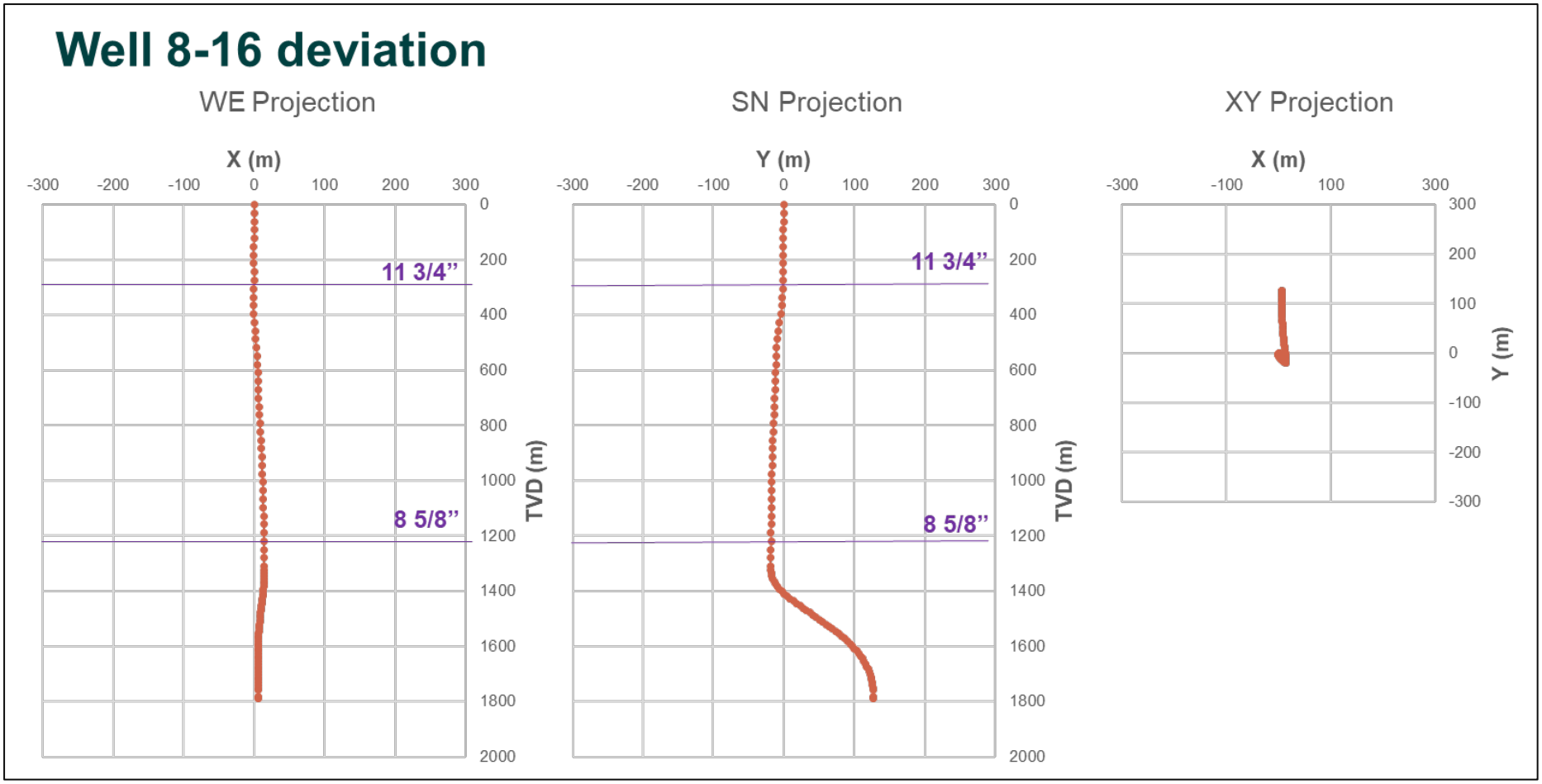


*Figure 3-6. Well 8-16 deviation.*

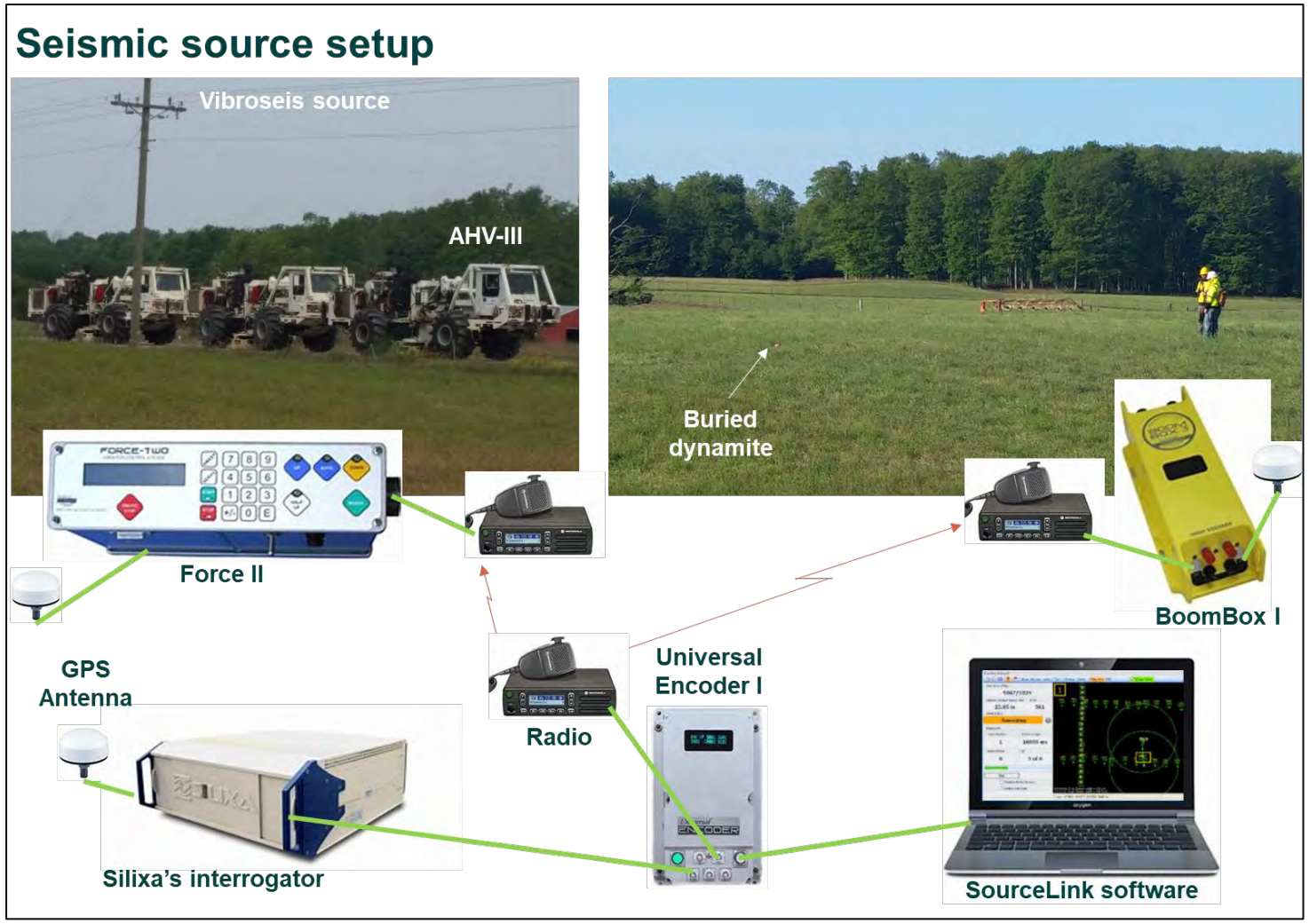


*Figure 3-7. Seismic source setup – diagram. For both surveys, Emerson Geophysical, LLC used the same seismic source design. The vibroseis source comprised three AHV-II vibrators (65,000 lb peak force) shaking in synchronised mode. Each vibrator was equipped with a Force II decoder. BoomBox I equipment was used to ignite the dynamite sources. The sources were radio-controlled using Universal Encoder I. The seismic encoder was connected by cable to the fibre optic interrogator.*

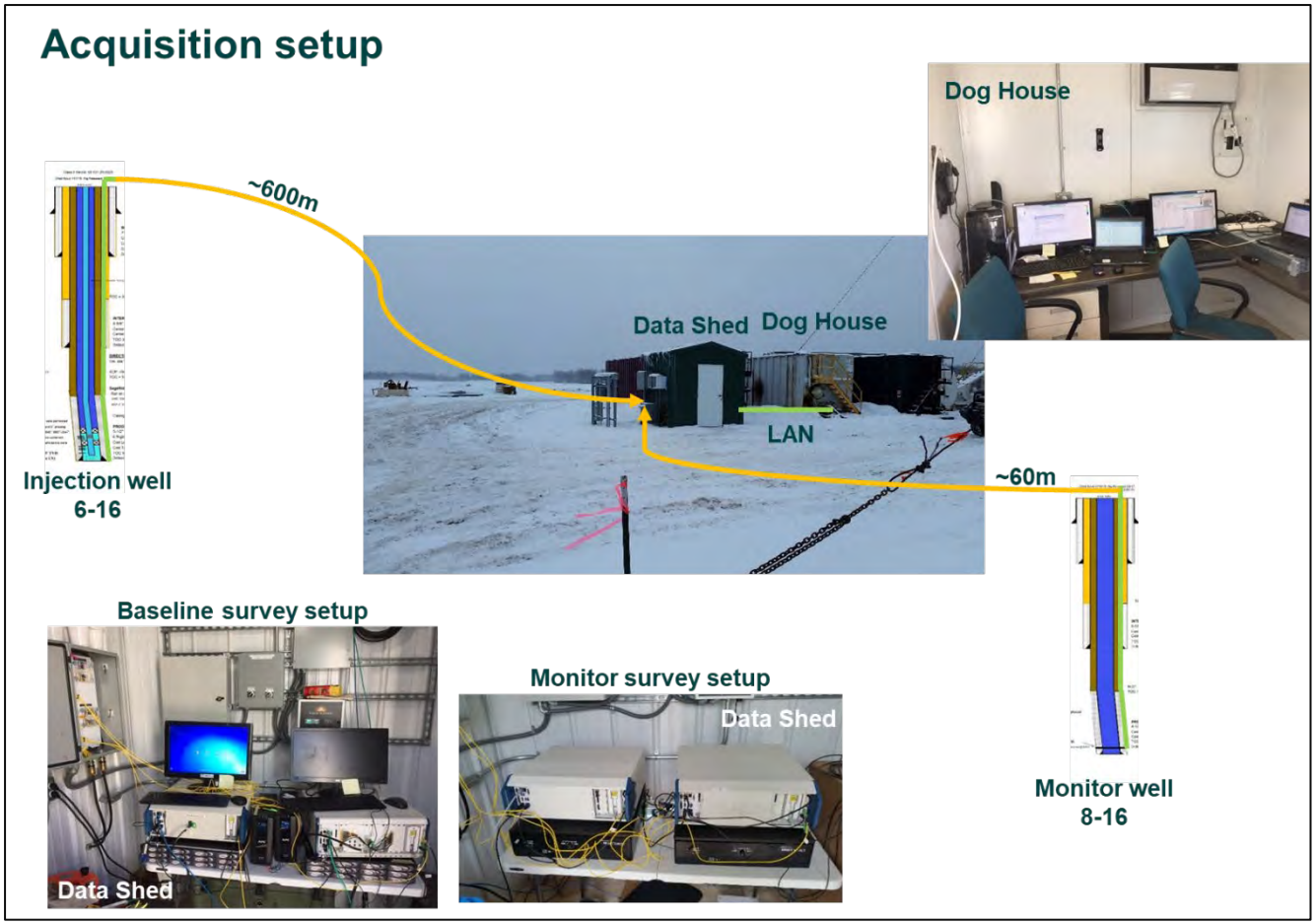


*Figure 3-8. Acquisition setup - iDAS setup. In each well a single ended fibre optic cable was clamped behind the 5-1/2" production casing. The seismic response of the DAS cable was however poor above the deviated section, probably because of poor coupling in the vertical section. The fibre optic cable terminates at the surface in the data shed located near to the 8-16 well head (Figure 3-8). An anti-vibration table was used during the monitor survey to reduce the recorded noise due to vibration of the iDAS interrogator unit. The anti-vibration was not available during the baseline survey. The data recording was supervised from the dog house located near the data shed. The interrogators were linked to the processing computers by a LAN connection.*

# 4 Depth calibration

The DAS interrogator records data sampled on channels distributed regularly along the total length of the fibre. Based on the speed of light in the glass fibre, the recorded data is positioned along the fibre relative to the box connector. This is known as Fibre Distance (FD). To locate the data along the well trajectory, a relationship is required between the fibre distance and Measured Depth (MD) along the well path. The depth calibration requires at least two points along the fibre with known FD and MD values. One point is the end of the fibre which generates a large light reflection and the second point is the entrance of the fibre into the well head which can be found by gently striking the cable at this point (the procedure is called a “Tap test”).

Figures 4-1 and 4-2 present the raw vibroseis stack data in fibre distance recorded in well 8-16 for the same source position, shot point (SP) 506212, during the baseline and the monitor survey respectively.

The well 8-16 fibre distance between the box connector and well head GL was determined as 62.6 m for the baseline survey (Fig. 4-3) and 61.6 m for the monitor survey (Fig. 4-4).

The end of the fibre distance downhole was determined from a vibroseis single shot recorded at SP 506212. For the baseline survey the fibre end is at 2011.1 m (Fig. 4-5) and for the monitor survey the fibre end is at 2010.1 m (Fig. 4-6). There is a 1 m difference between the baseline and the monitor survey fibre distance because different fibres were used and the length of each fibre from the same cable may vary by as much as 1%.

Figures 4-7 and 4-8 show the SP 506212 traces displayed in measured depth after the depth calibration.

| 175 | Calibration point | 176 | Fibre Distance (m) | | | 177 | Measured Depth (from KB) |
|---|---|---|---|---|---|---|---|
| | | 179 | Baseline | 180 | Monitor | 178 | |
| 181 | Ground level | 182 | 62.6 m | 183 | 61.6 m | **184** | **4.08 m** |
| 185 | Fibre TD | 186 | 2011.1 m | 187 | 2010.1 m | **188** | **1935.48 m** |

*Table 4-10 Well 8-16 depth calibration*

The depth calibration for the injection well 6-16 was performed using the vibroseis data recorded for SP 101214. The stack data for the baseline and monitor survey in fibre distance are presented in figures 4-9 and respectively 4-10.

The fibre well head entry point near GL was estimated at 597.8 m away from the interrogator connector for both surveys (Fig. 4-11 and 4-12).

Figures 4-13 and 4-14 show a zoom of SP 101214 single shot data recorded during the baseline and the monitor survey. The fibre end was determined at 2625.0 m fibre distance.

Figures 4-15 and 4-16 show the SP 101214 traces in measured depth, after the depth calibration. Figures 4-17 and 4-18 present the same features at the same depth on the baseline and monitor survey. This is a validation of the consistency between the baseline and monitor depth calibration.

| 189 | Calibration point | 190 | Fibre Distance (m) | | | 191 192 | Measured Depth (from KB) |
|---|---|---|---|---|---|---|---|
| | | 193 | Baseline | 194 | Monitor | | |
| 195 | Ground level | 196 | 597.8 m | 197 | 597.8 m | **198** | **4.24 m** |
| 199 | Fibre TD | 200 | 2625.0 m | 201 | 2625.0 m | **202** | **2026.92 m** |

*Table 4-11 Well 6-16 depth calibration*

| 203 | Title | 204 | Description | 205 | Figure |
|---|---|---|---|---|---|
| **206** | **4 Depth calibration** | | | | |
| 207 | Baseline Survey – Vibroseis Stack | 208 | SP 506212, well 8-16, fibre distance | **209** | **4.1** |
| 210 | Monitor Survey – Vibroseis Stack | 211 | SP 506212, well 8-16, fibre distance | **212** | **4.2** |
| 213 | Baseline Survey – Vibroseis Single Stack | 214 | SP 506212, well 8-16, calibration at GL | **215** | **4.3** |
| 216 | Monitor Survey – Vibroseis Single Stack | 217 | SP 506212, well 8-16, calibration at GL | **218** | **4.4** |
| 219 | Baseline Survey – Vibroseis Single Shot | 220 | SP 506212, well 8-16, calibration at fibre TD | **221** | **4.5** |
| 222 | Monitor Survey – Vibroseis Single Shot | 223 | SP 506212, well 8-16, calibration at fibre TD | **224** | **4.6** |
| 225 | Baseline Survey – Depth Calibrated Vibroseis Stack | 226 | SP 506212, well 8-16, measured depth | **227** | **4.7** |
| 228 | Monitor Survey – Depth Calibrated Vibroseis Stack | 229 | SP 506212, well 8-16, measured depth | **230** | **4.8** |
| 231 | Baseline Survey – Vibroseis Stack | 232 | SP 101214, well 6-16, fibre distance | **233** | **4.9** |
| 234 | Monitor Survey – Vibroseis Stack | 235 | SP 101214, well 6-16, fibre distance | **236** | **4.10** |
| 237 | Baseline Survey – Vibroseis Single Stack | 238 | SP 101214, well 6-16, calibration at GL | **239** | **4.11** |
| 240 | Monitor Survey – Vibroseis Single Stack | 241 | SP 101214, well 6-16, calibration at GL | **242** | **4.12** |
| 243 | Baseline Survey – Vibroseis Single Shot | 244 | SP 101214, well 6-16, calibration at fibre TD | **245** | **4.13** |
| 246 | Monitor Survey – Vibroseis Single Shot | 247 | SP 101214, well 6-16, calibration at fibre TD | **248** | **4.14** |
| 249 | Baseline Survey – Depth Calibrated Vibroseis Stack | 250 | SP 101214, well 6-16, measured depth | **251** | **4.15** |
| 252 | Monitor Survey – Depth Calibrated Vibroseis Stack | 253 | SP 101214, well 6-16, measured depth | **254** | **4.16** |
| 255 | Baseline Survey – Depth Calibrated Vibroseis Stack | 256 | SP 101214, well 6-16, measured depth QC | **257** | **4.17** |
| 258 | Monitor Survey – Depth Calibrated Vibroseis Stack | 259 | SP 101214, well 6-16, measured depth QC | **260** | **4.18** |

*Table 4-12 Acquisition figures*

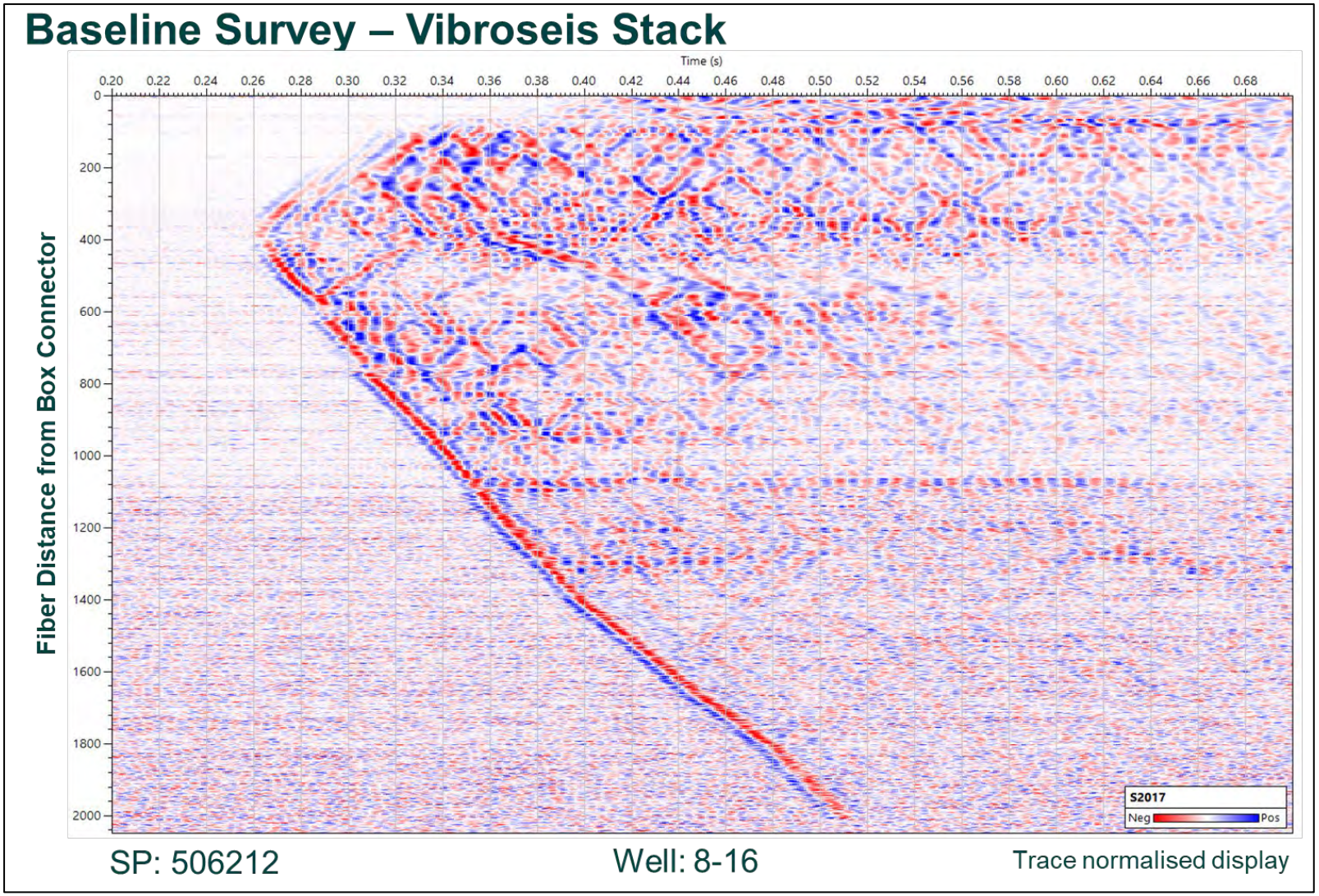


*Figure 4-1. Baseline Survey – Vibroseis Stack - SP 506212, well 8-16, fibre distance. Raw vibroseis stack data in fibre distance recorded in well 8-16 for the same source position, shot point (SP) 506212, during the baseline and the monitor survey respectively.*

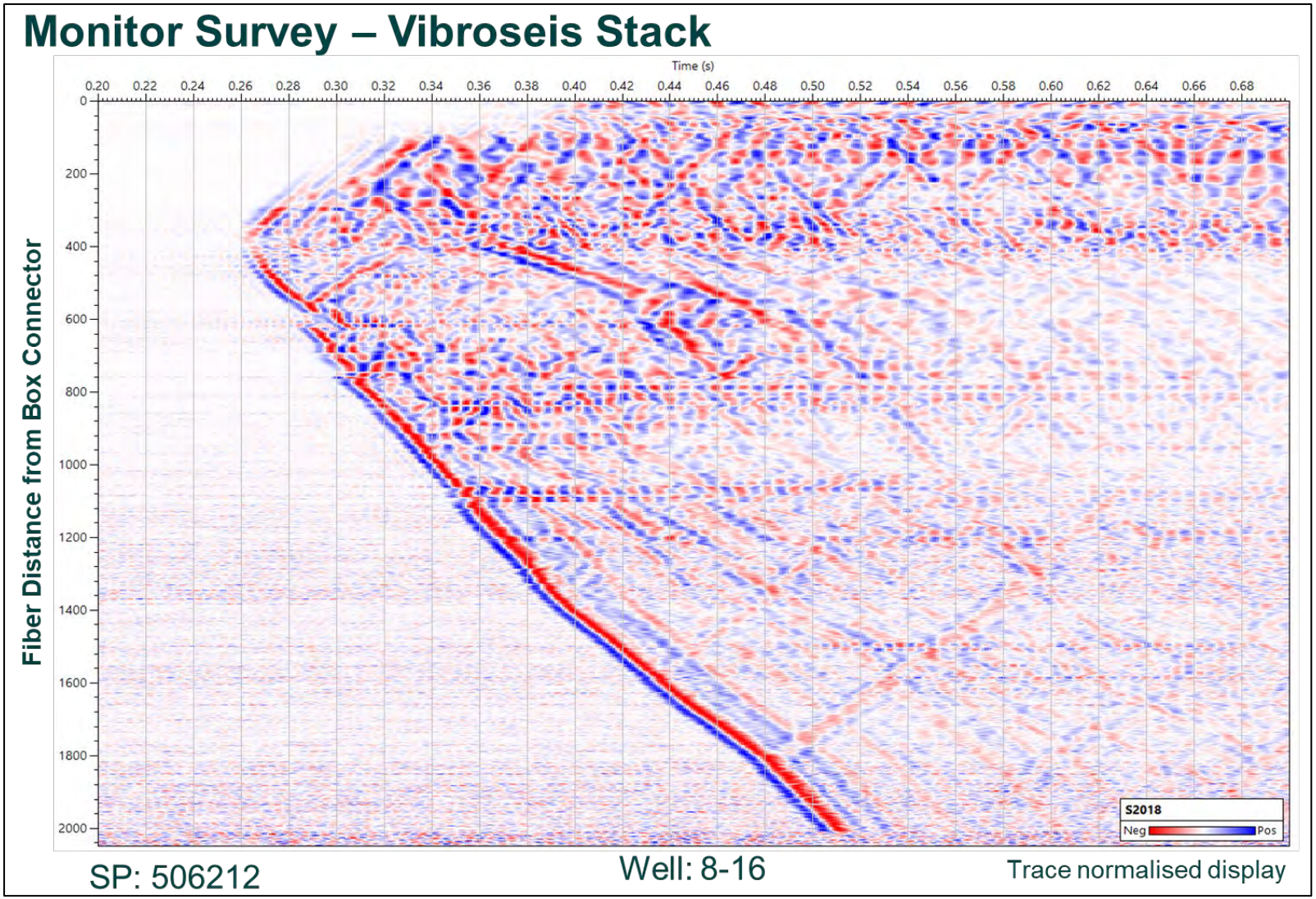


*Figure 4-2. Monitor Survey – Vibroseis Stack - SP 506212, well 8-16, fibre distance.*

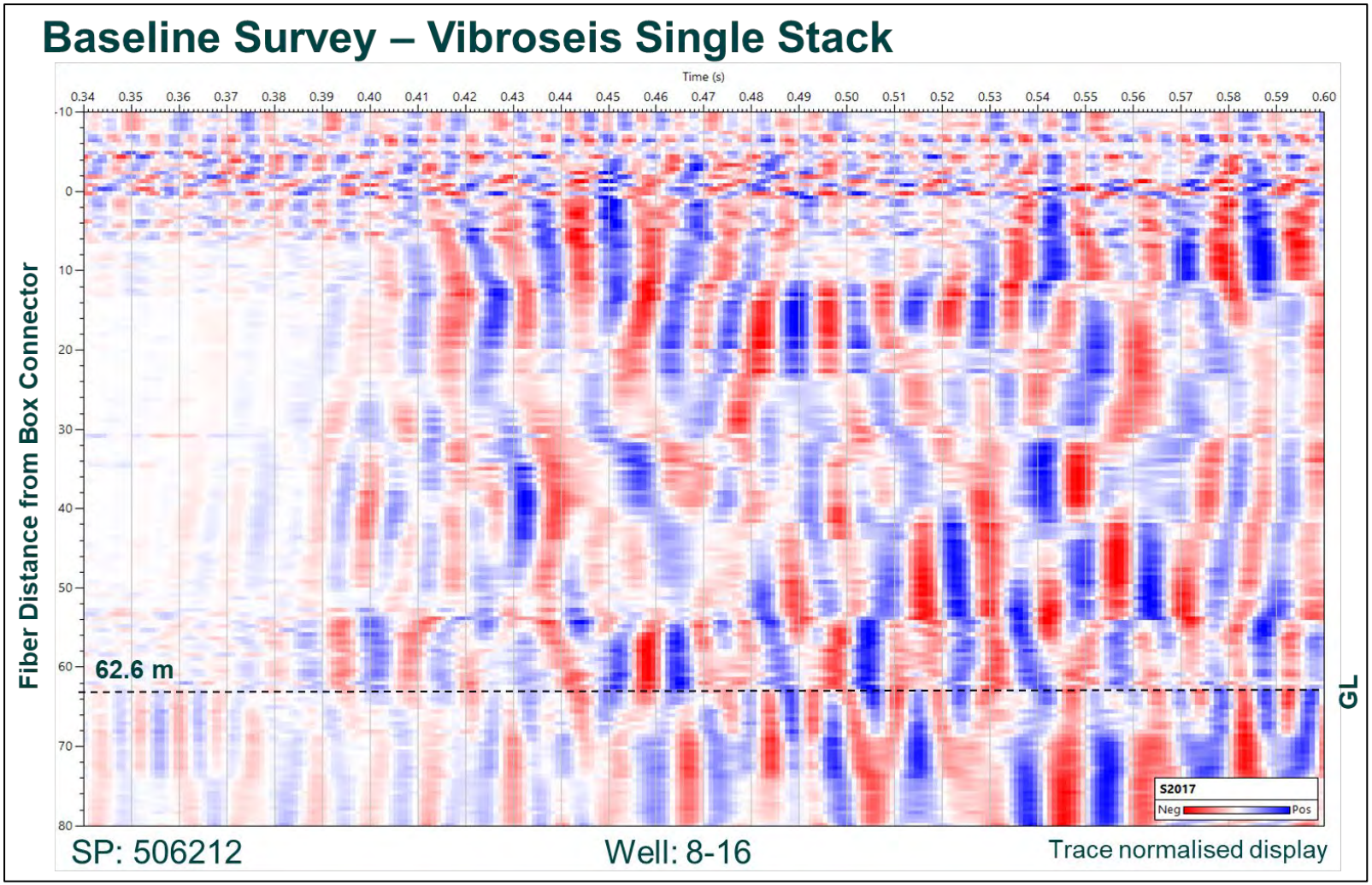


*Figure 4-3. Baseline Survey – Vibroseis Single Stack - SP 506212, well 8-16, calibration at GL. The well 8-16 fibre distance between the box connector and well head GL was determined as 62.6 m for the baseline survey.*

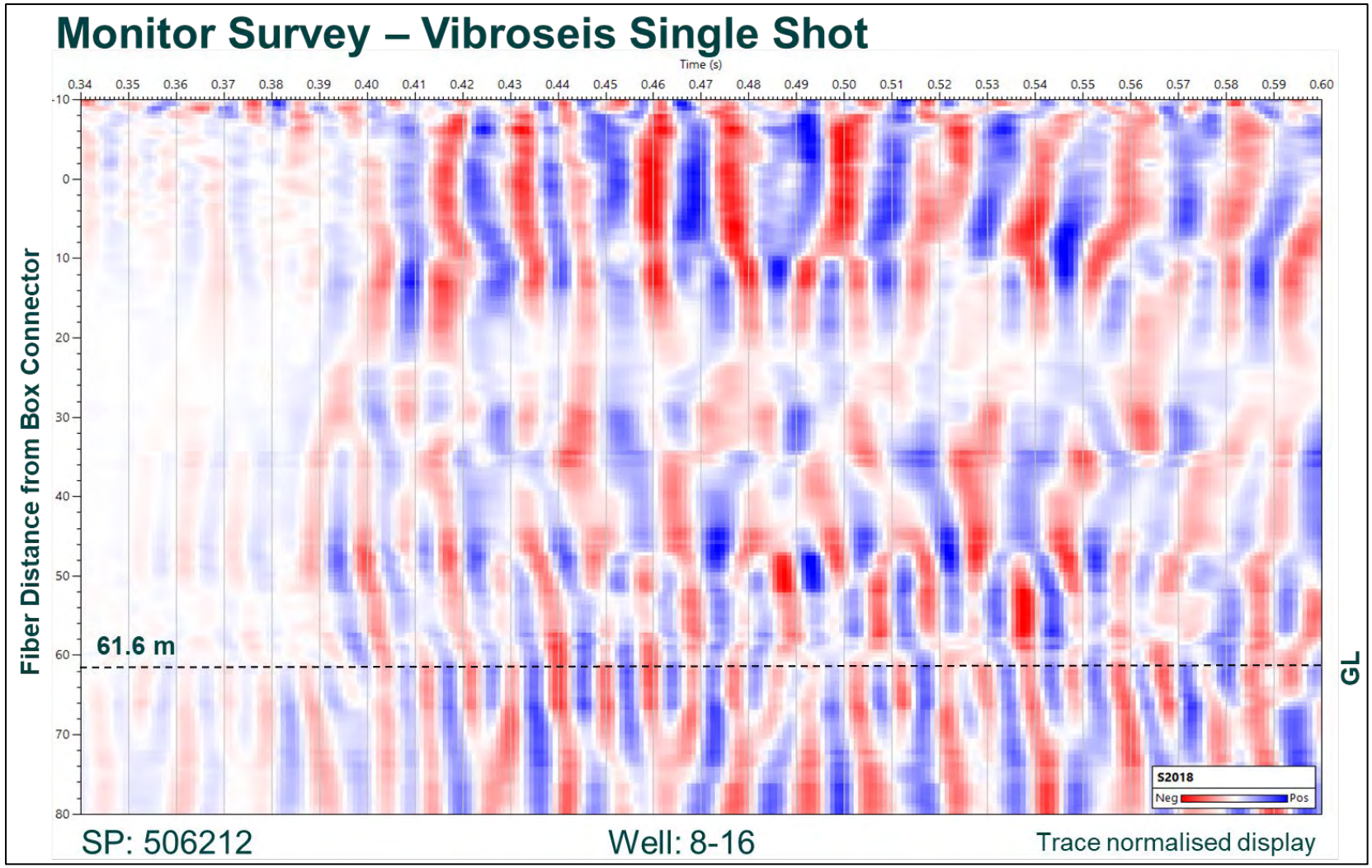


*Figure 4-4. Monitor Survey – Vibroseis Single Stack, SP 506212, well 8-16, calibration at GL. The well 8-16 fibre distance between the box connector and well head GL was determined as 61.6 m for the monitor survey.*

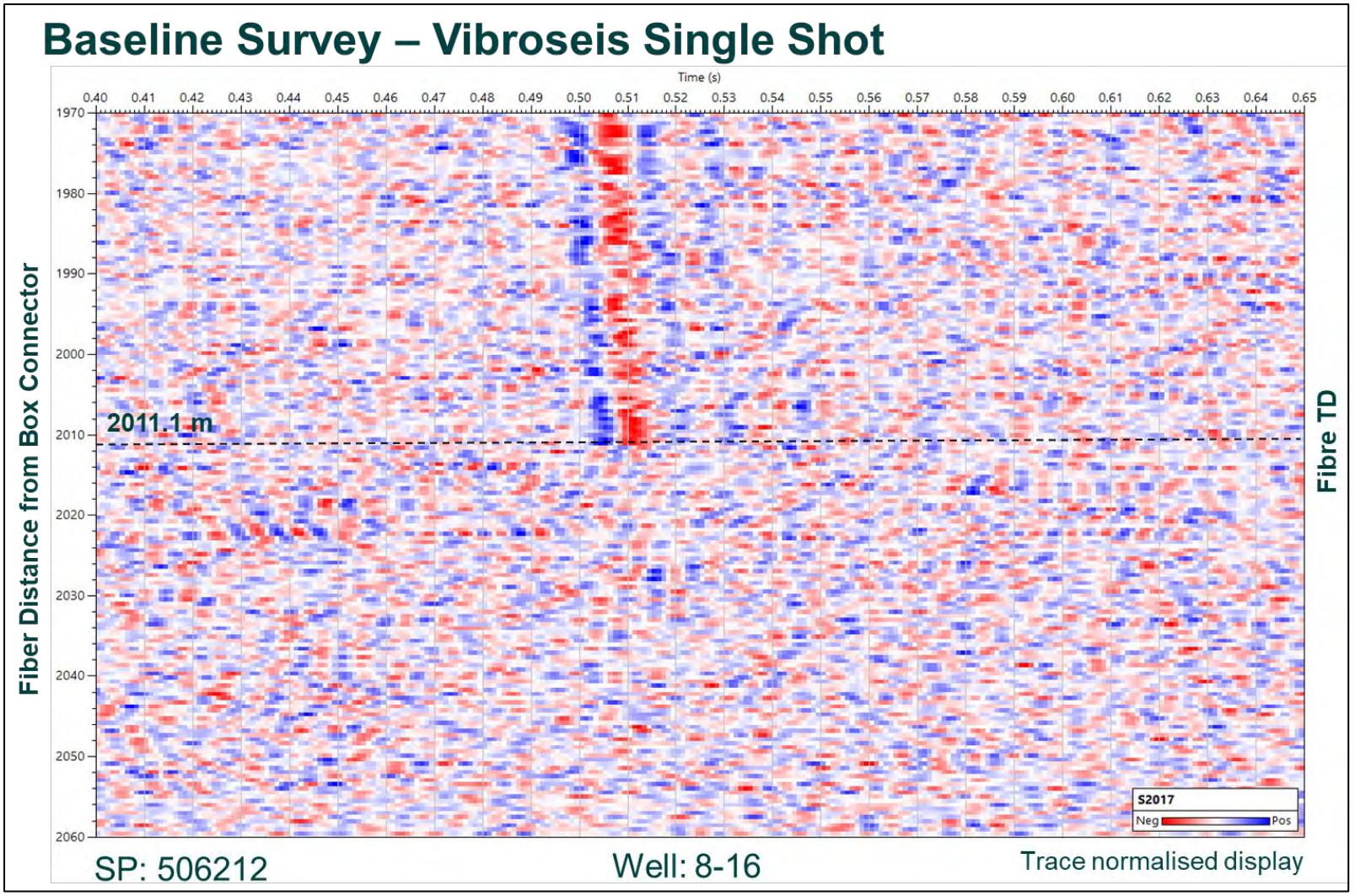


*Figure 4-5. Baseline Survey – Vibroseis Single Shot - SP 506212, well 8-16, calibration at fibre TD. The end of the fibre distance downhole was determined from a vibroseis single shot recorded at SP 506212. For the baseline survey the fibre end is at 2011.1 m.*

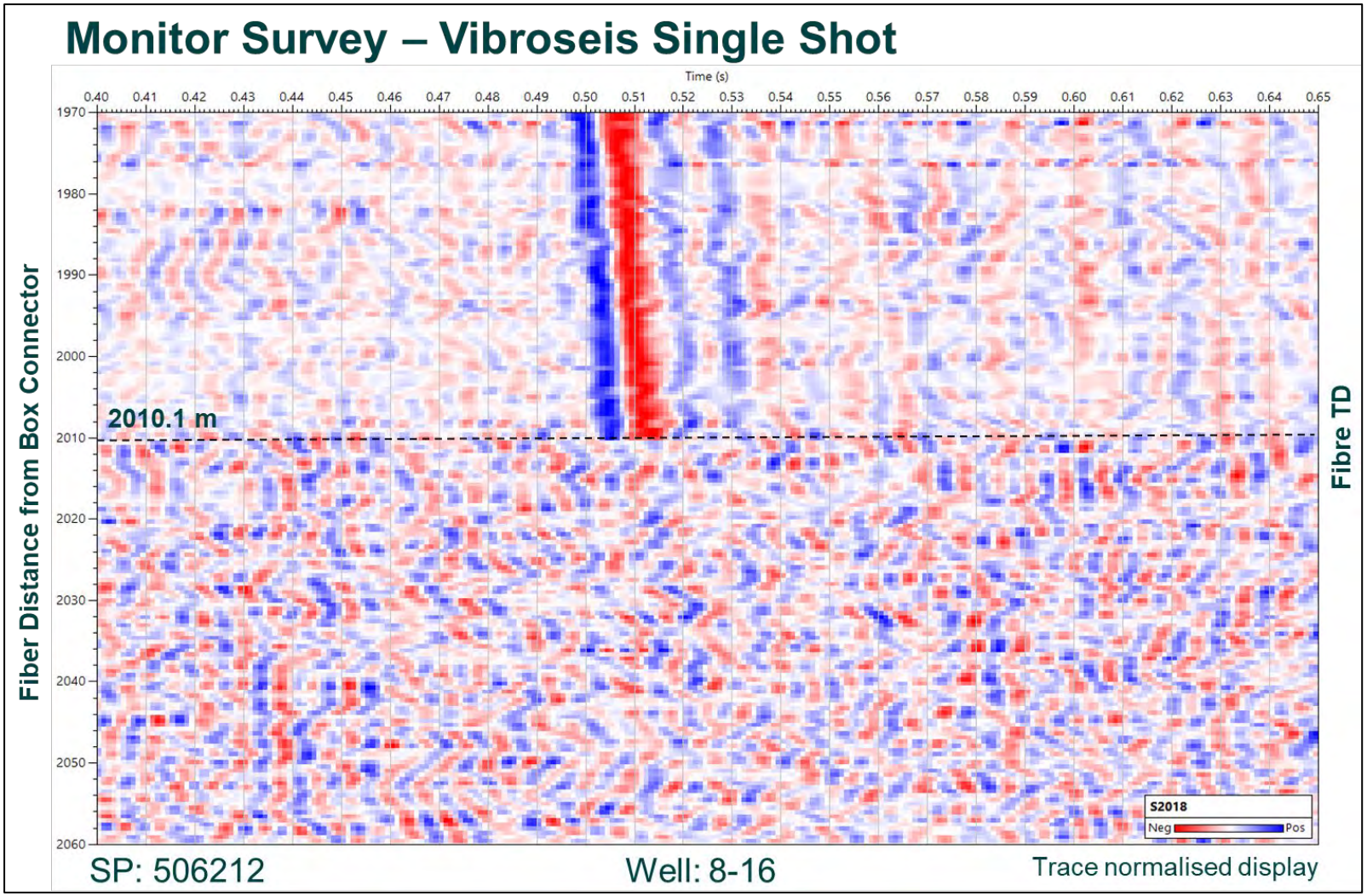


*Figure 4-6. Monitor Survey – Vibroseis Single Shot - SP 506212, well 8-16, calibration at fibre TD. For the monitor survey the fibre end is at 2010.1 m. There is a 1 m difference between the baseline and the monitor survey fibre distance because different fibres were used and the length of each fibre from the same cable may vary by as much as 1%.*

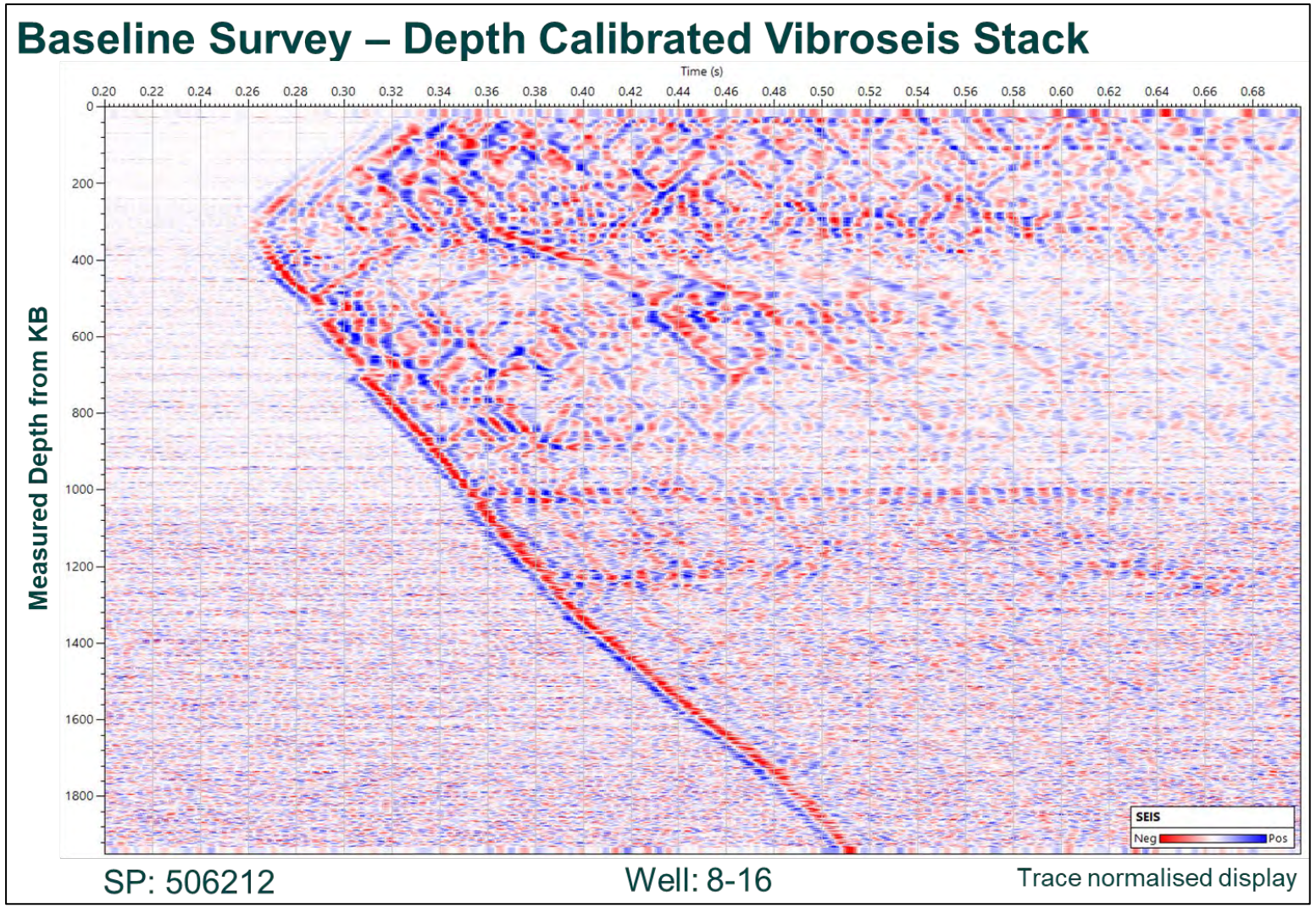


*Figure 4-7. Baseline Survey – Depth Calibrated Vibroseis Stack - SP 506212, well 8-16, measured depth.*

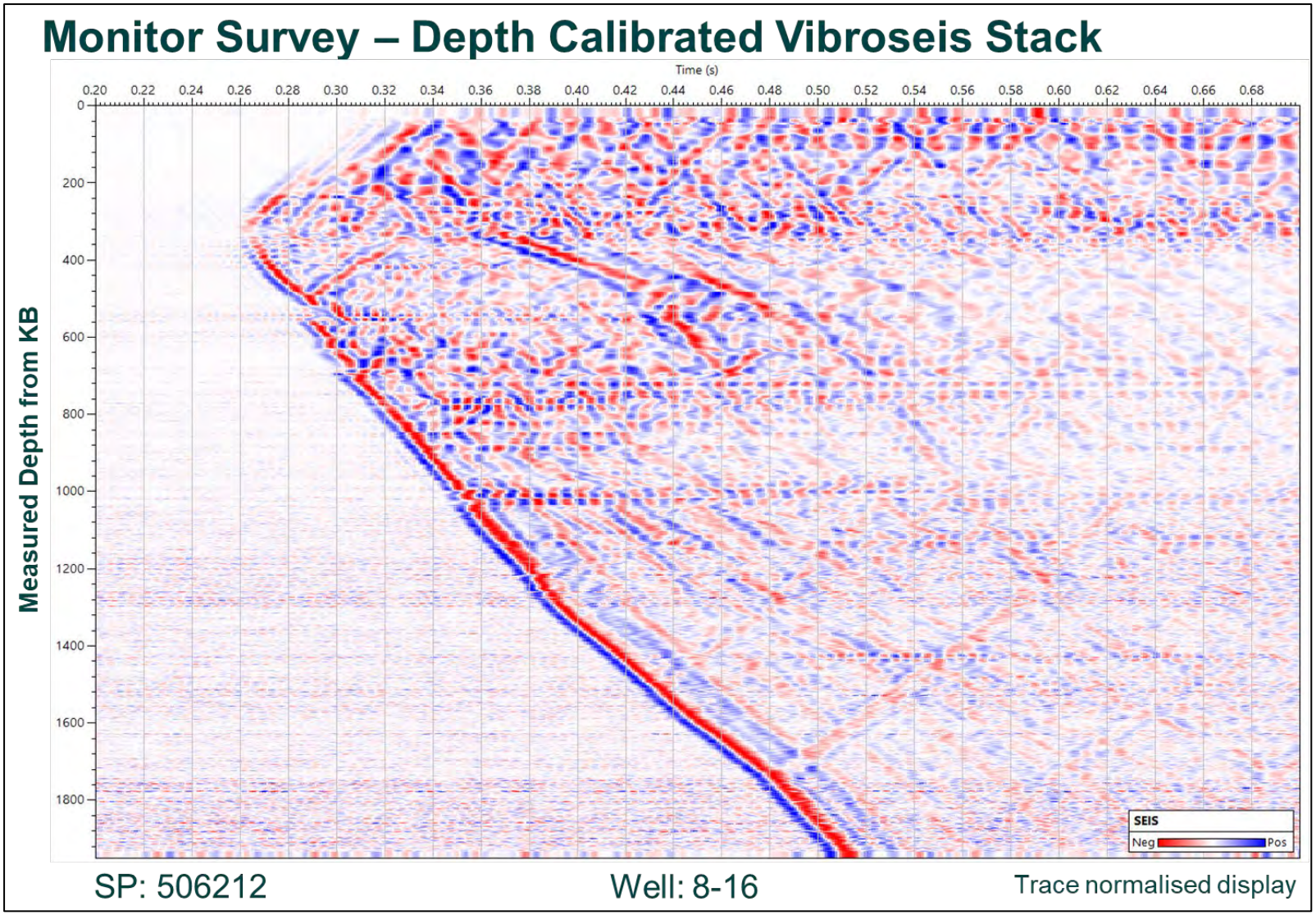


*Figure 4-8. Monitor Survey – Depth Calibrated Vibroseis Stack - SP 506212, well 8-16, measured depth.*

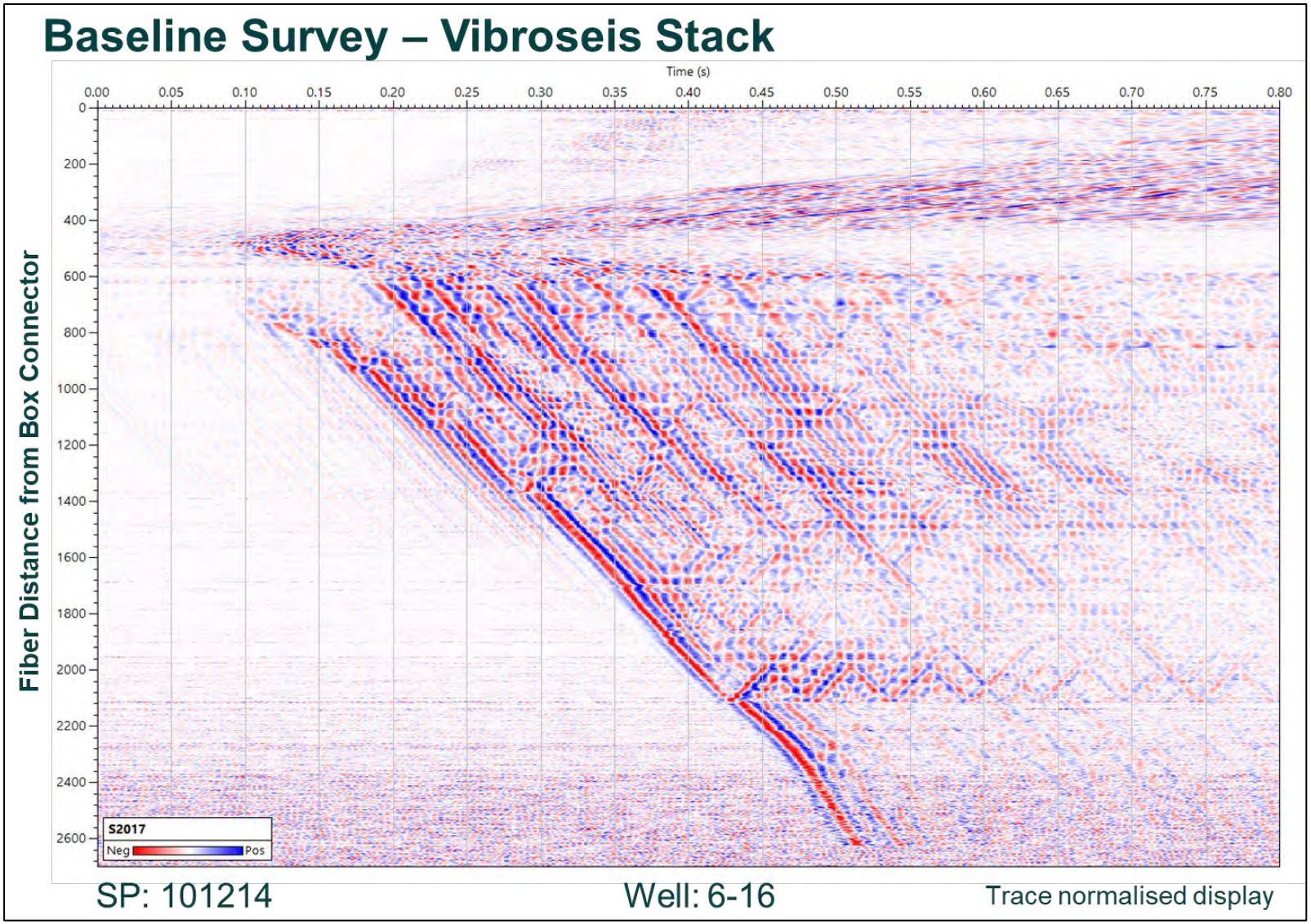


*Figure 4-9. Baseline Survey – Vibroseis Stack - SP 101214, well 6-16, fibre distance.*

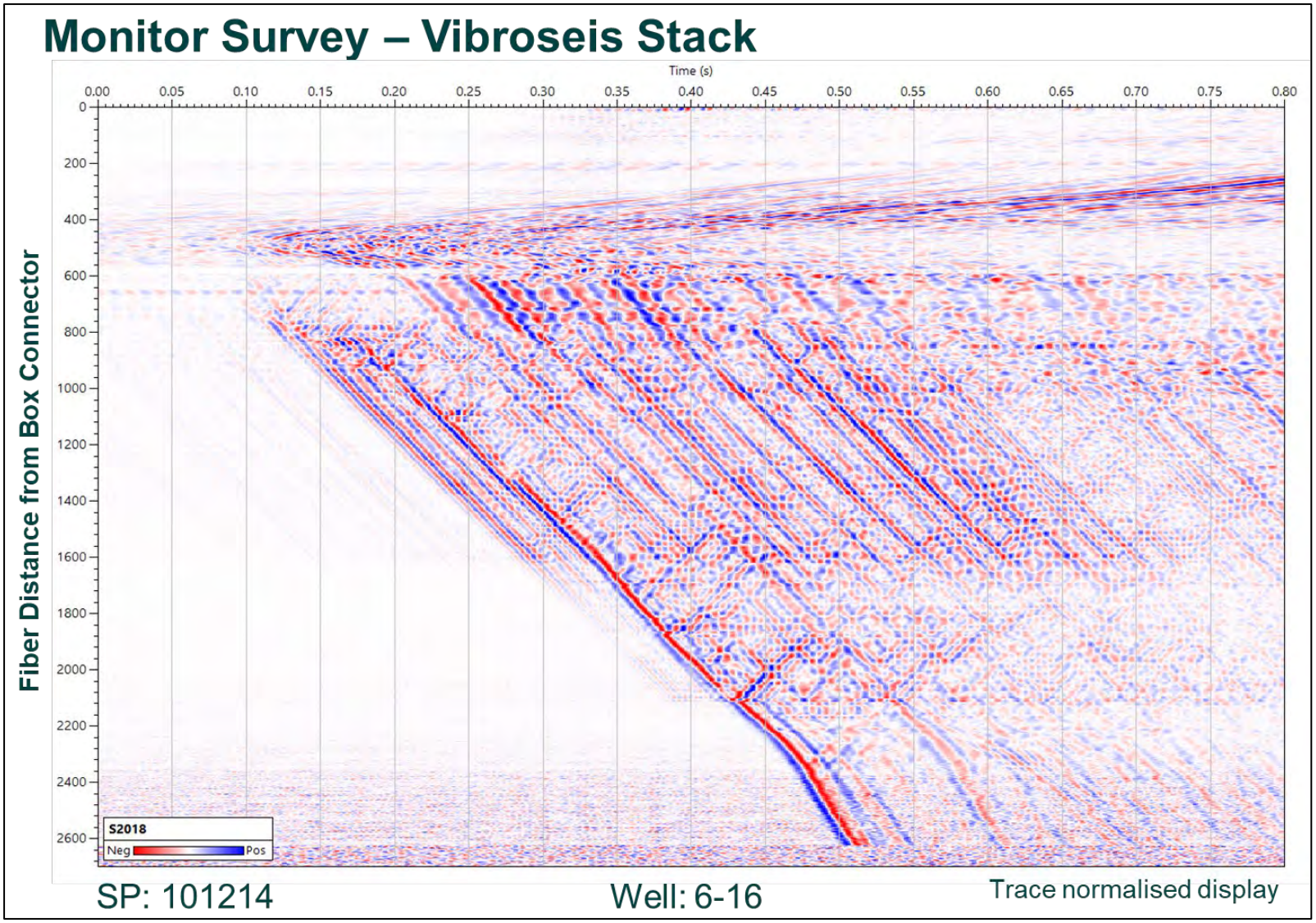


*Figure 4-10. Monitor Survey – Vibroseis Stack - SP 101214, well 6-16, fibre distance.*

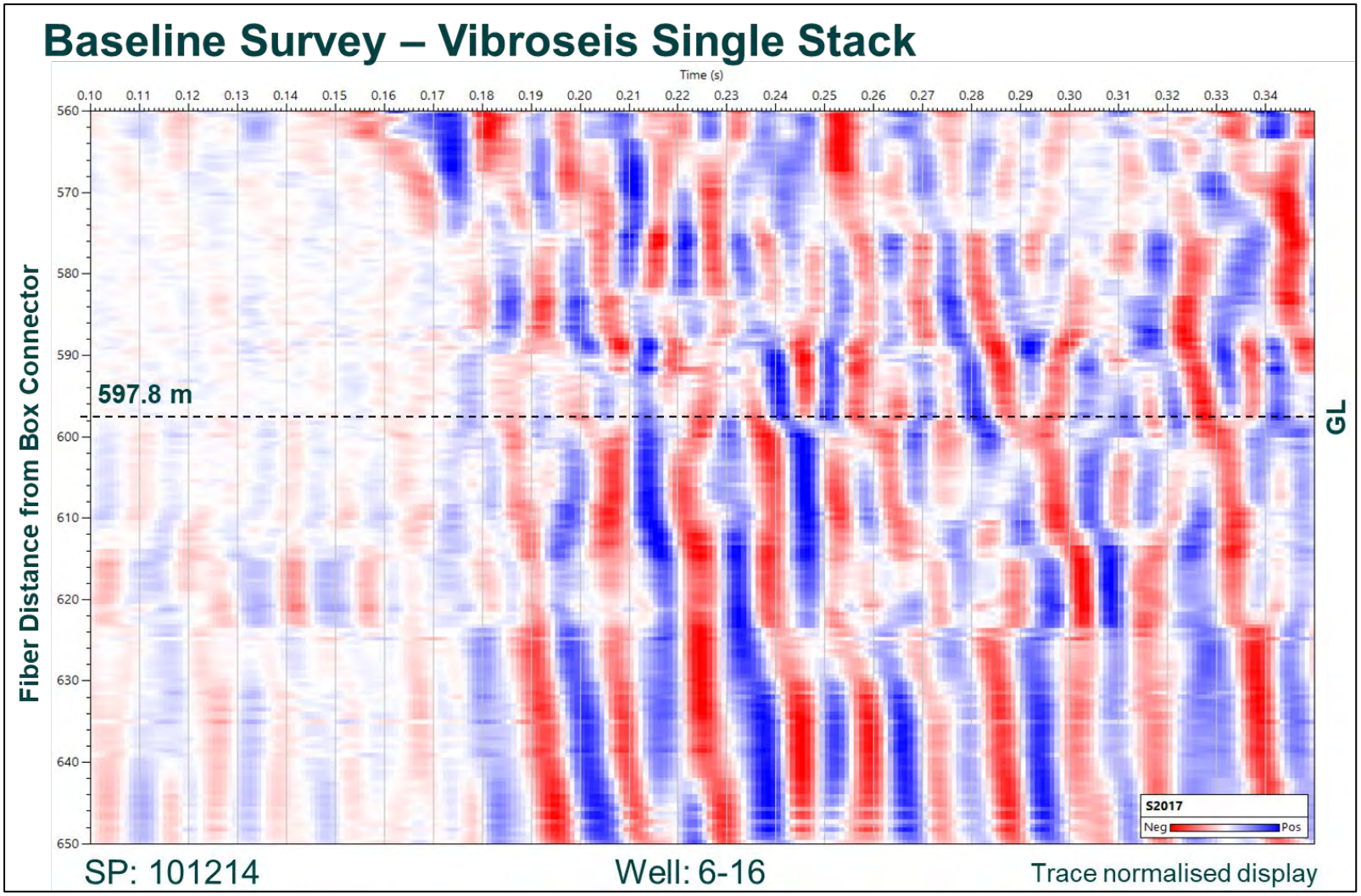


*Figure 4-11. Baseline Survey – Vibroseis Single Stack - SP 101214, well 6-16, calibration at GL. The fibre well head entry point near GL was estimated at 597.8 m away from the interrogator connector for both surveys (Fig. 4.11 and 4.12).*

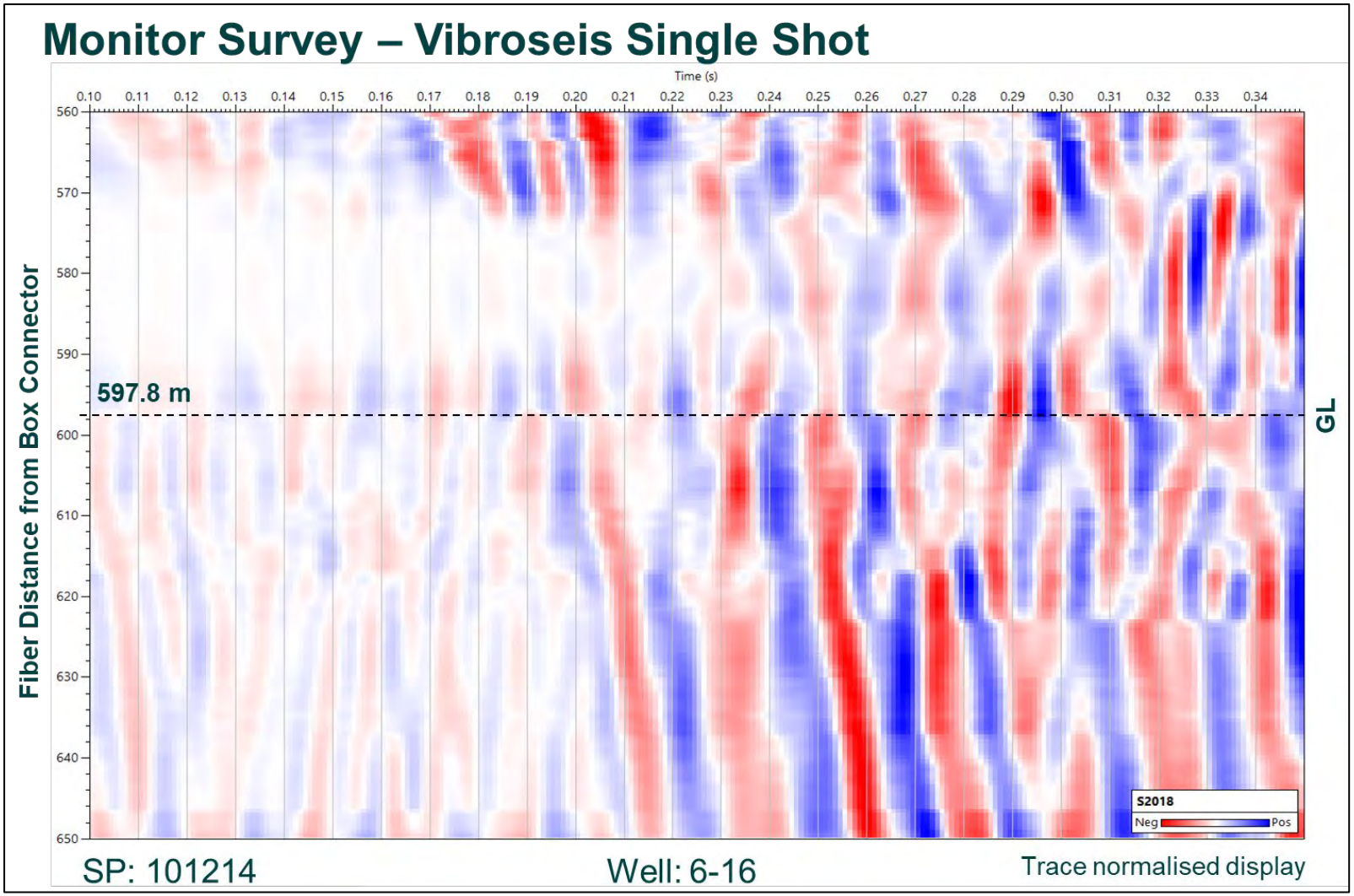


*Figure 4-12. Monitor Survey – Vibroseis Single Stack - SP 101214, well 6-16, calibration at GL.*

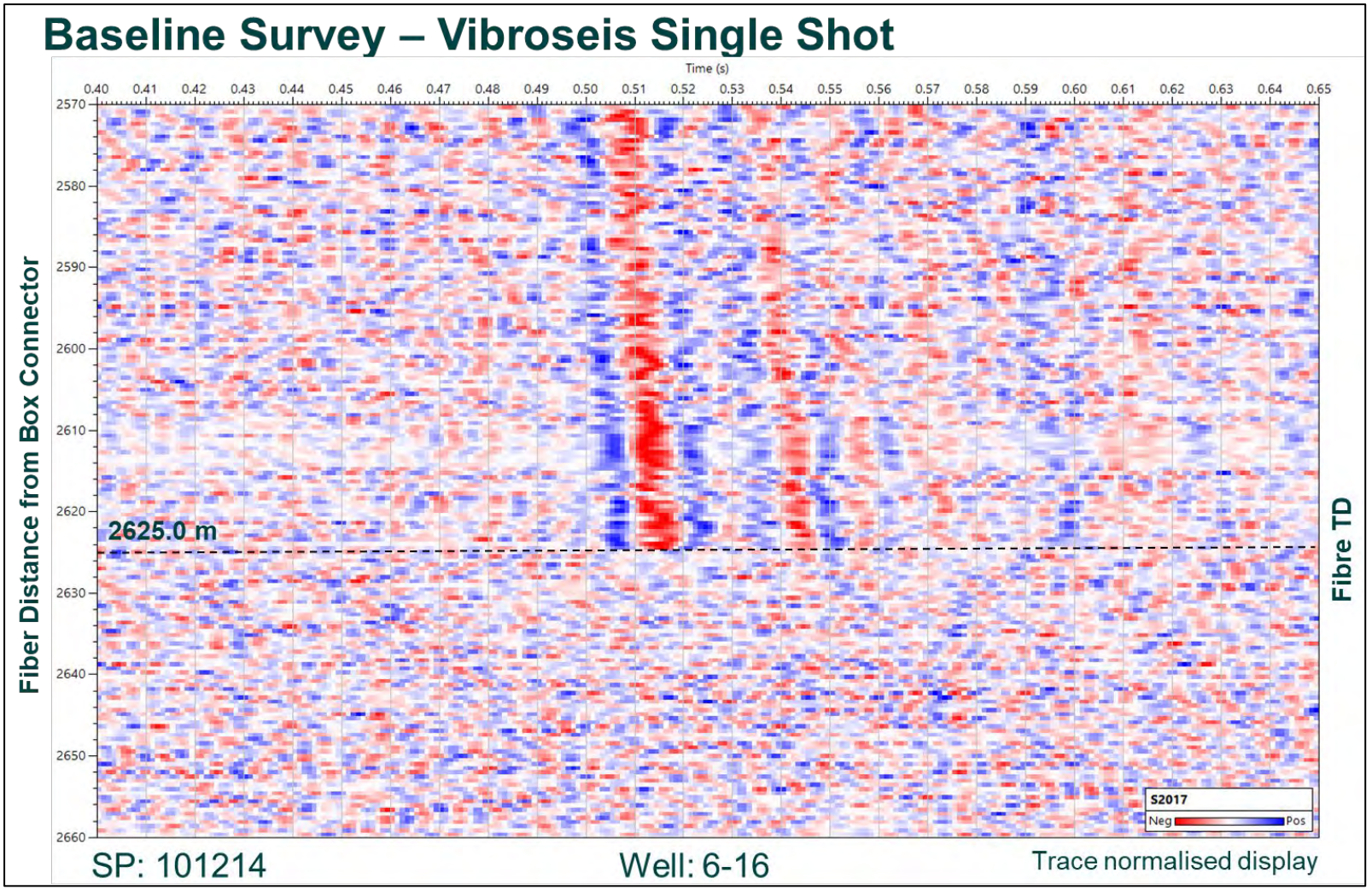


*Figure 4-13. Baseline Survey – Vibroseis Single Shot - SP 101214, well 6-16, calibration at fibre TD. This figure and the next one (4.14) show a zoom of SP 101214 single shot data recorded during the baseline and the monitor survey. The fibre end was determined at 2625.0 m fibre distance for the both surveys.*

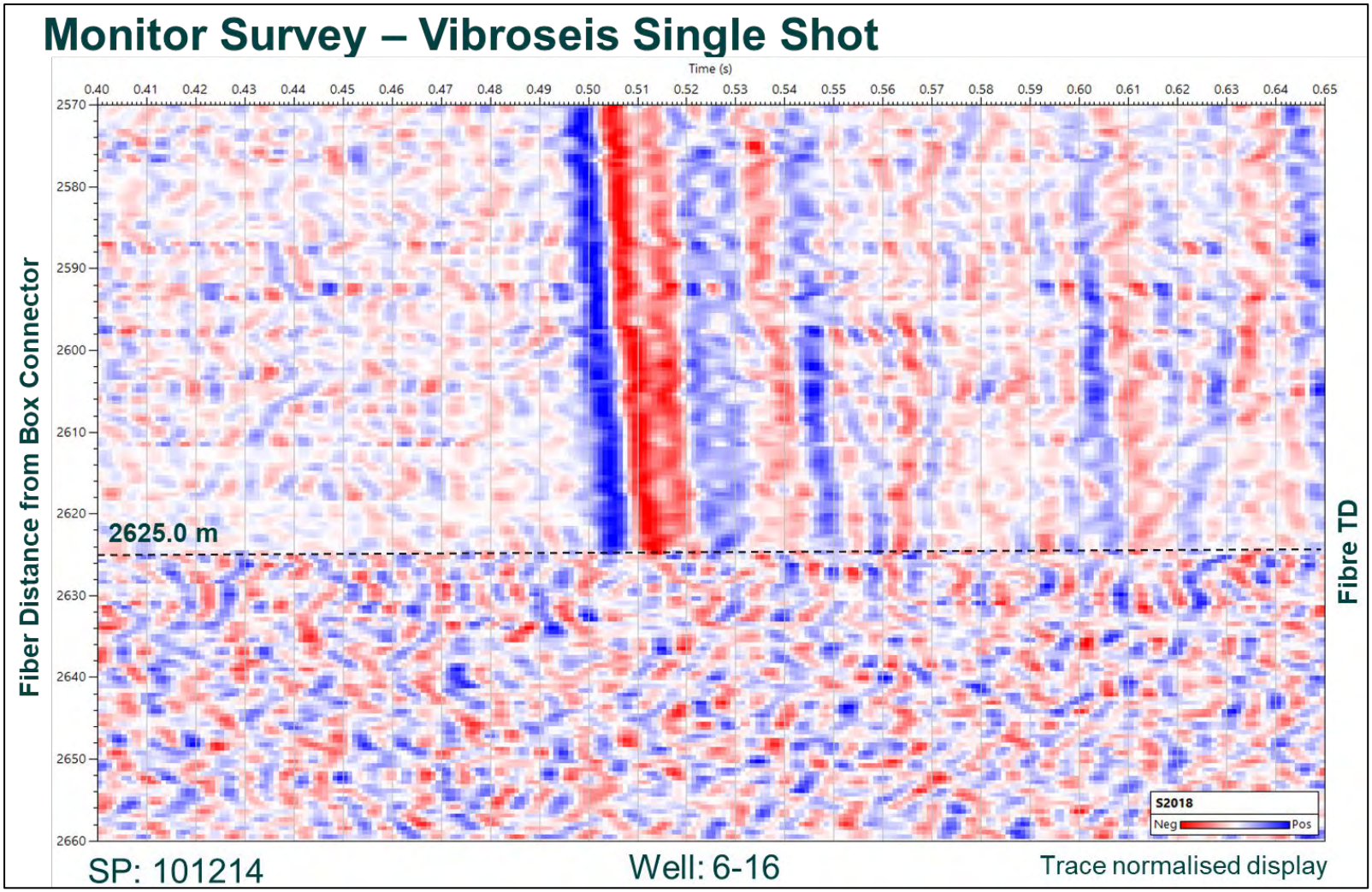


*Figure 4-14. Monitor Survey – Vibroseis Single Shot - SP 101214, well 6-16, calibration at fibre TD.*

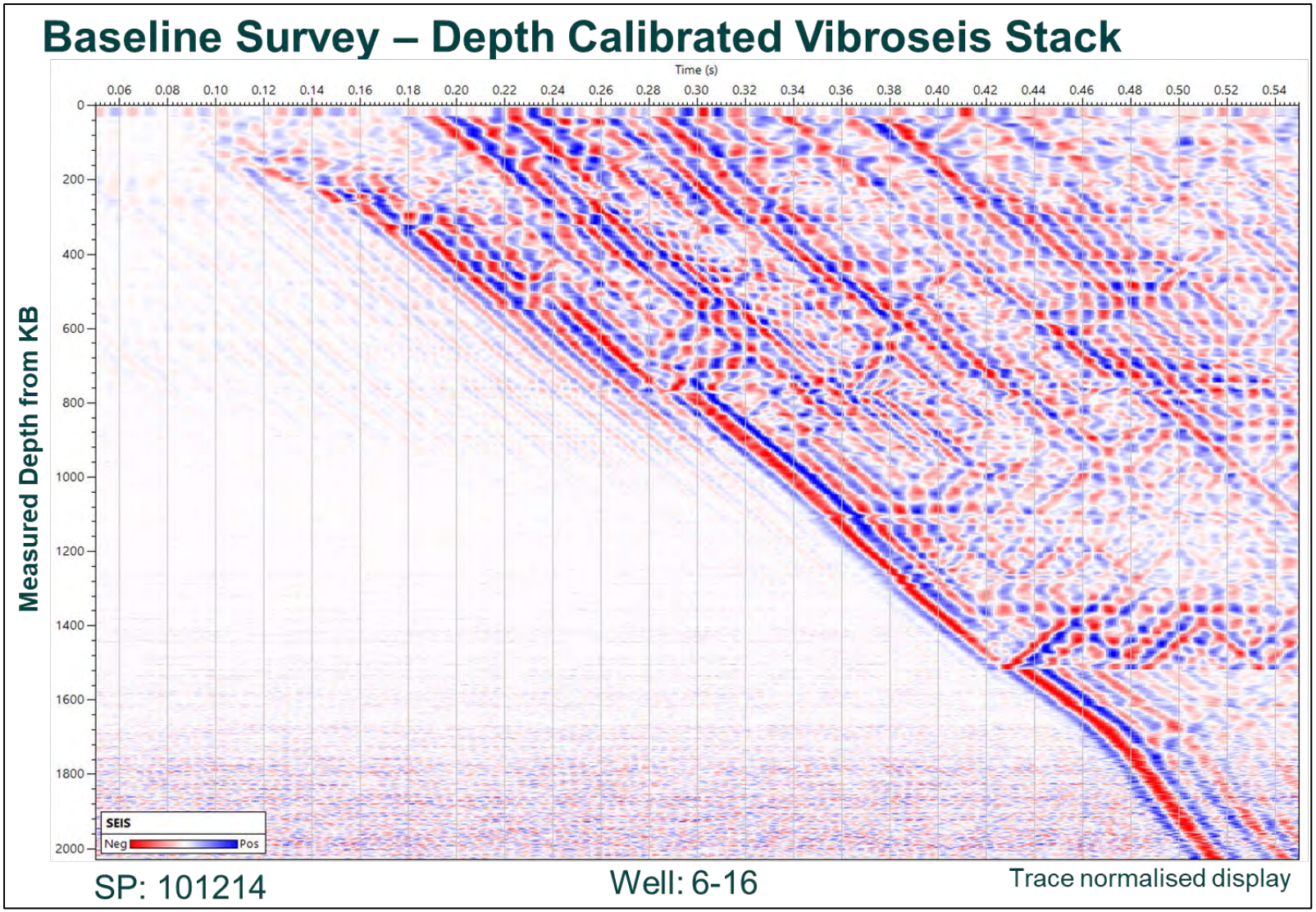


*Figure 4-15. Baseline Survey – Depth Calibrated Vibroseis Stack - SP 101214, well 6-16, measured depth.*

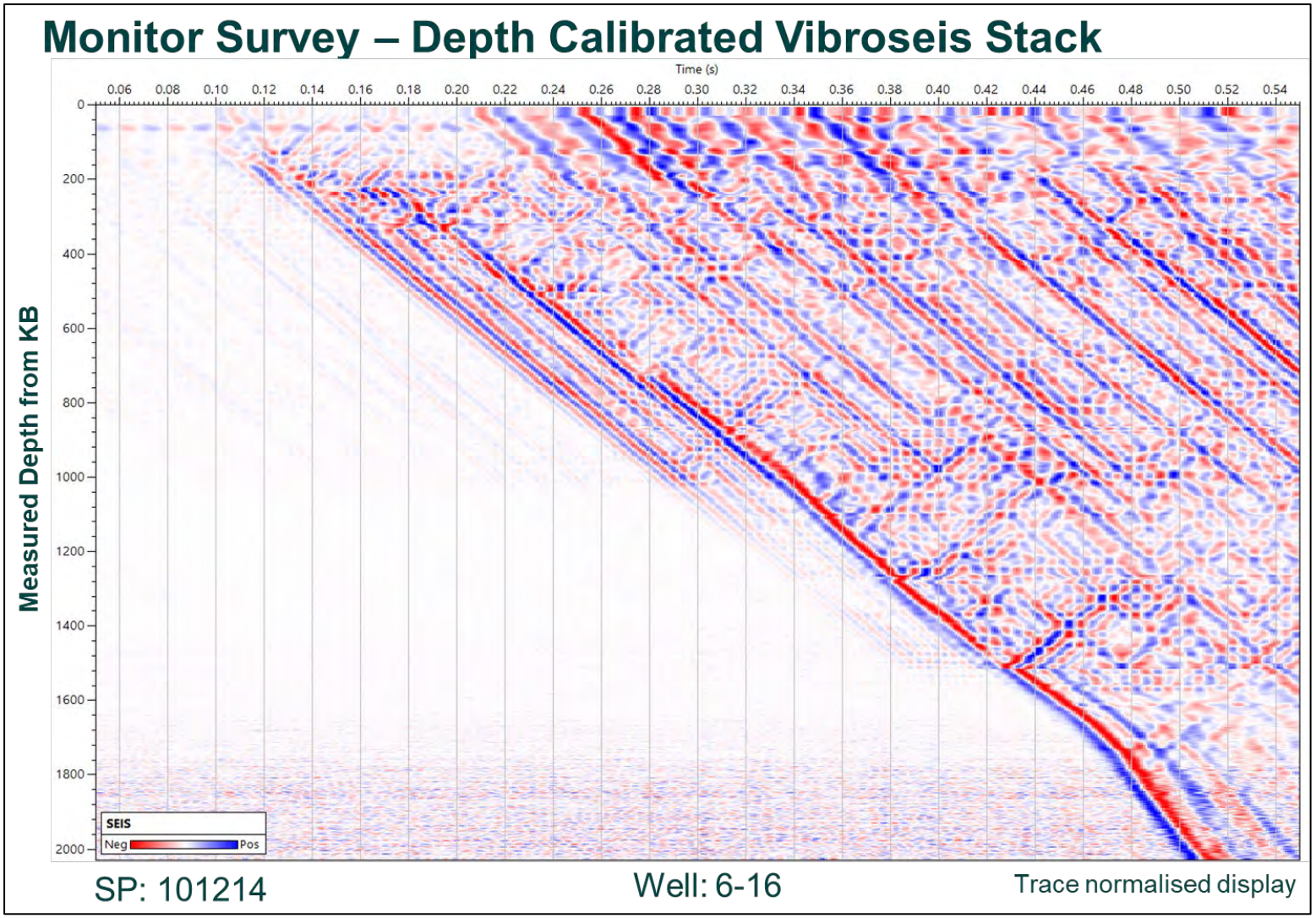


*Figure 4-16. Monitor Survey – Depth Calibrated Vibroseis Stack - SP 101214, well 6-16, measured depth.*

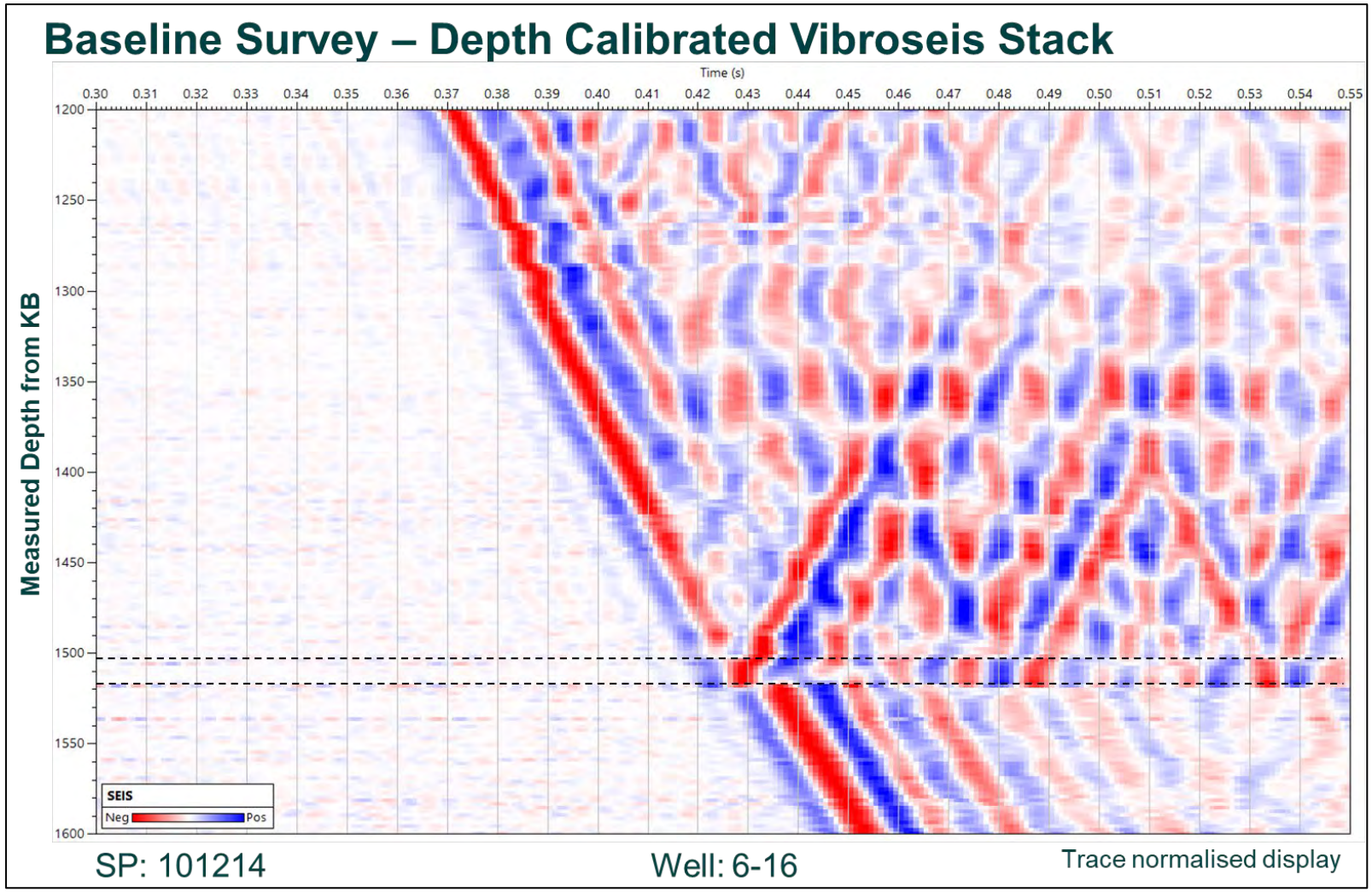


*Figure 4-17. Baseline Survey – Depth Calibrated Vibroseis Stack - SP 101214, well 6-16, measured depth QC.*

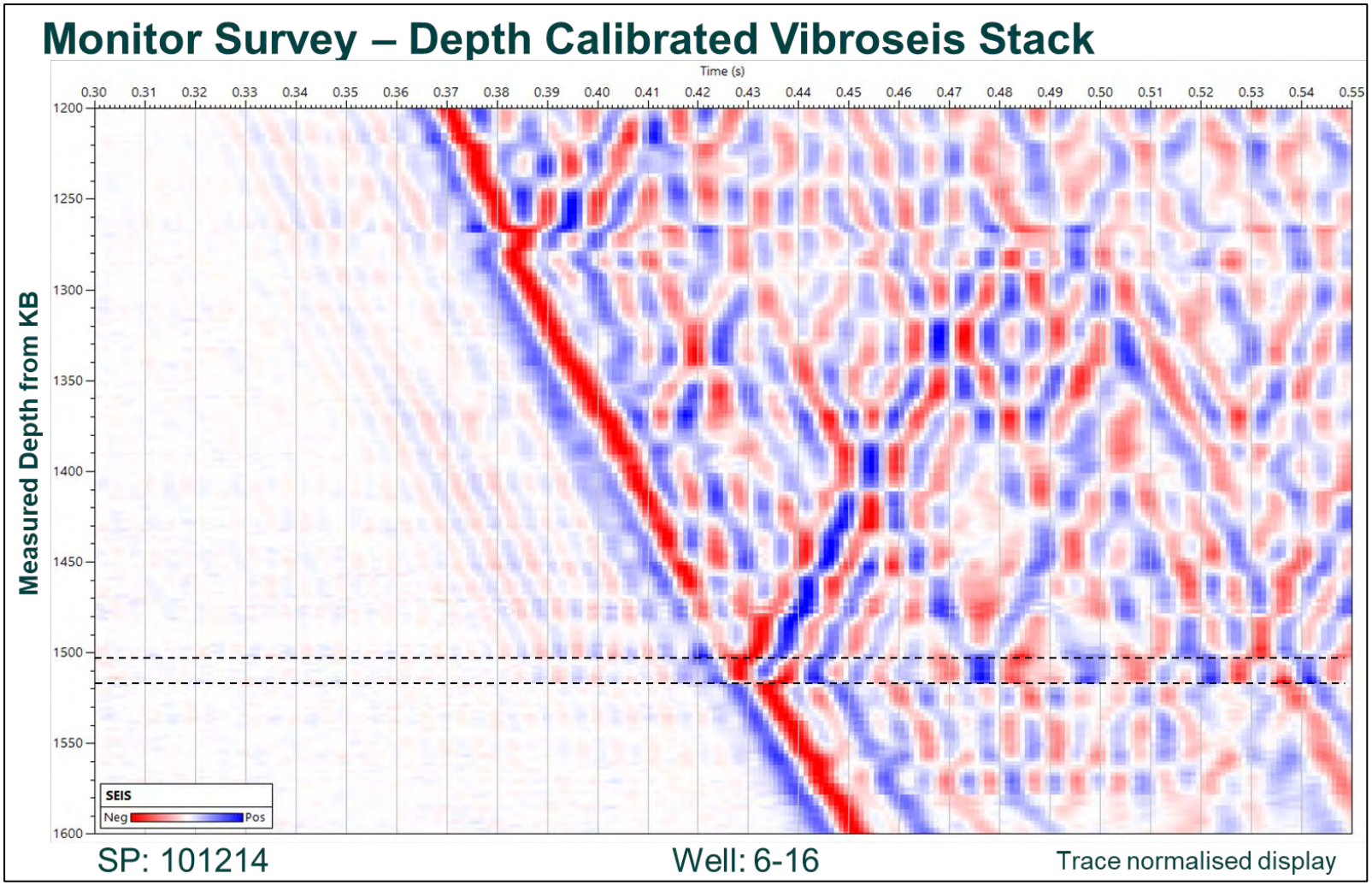


*Figure 4-18. Monitor Survey – Depth Calibrated Vibroseis Stack - SP 101214, well 6-16, measured depth QC.*

# 5 Pre-Processing

The pre-processing phase consists of several steps: compute the receiver position in depth, update the headers with the source position, reduce the noise, correlate sweep and stack (vibroseis data only). First the raw data is uploaded into the VSProwess database format (Silixa's iDAS interrogator records the seismic data in TDMS format). The fibre distance computation and depth calibration used to compute the receiver depth were presented in the previous chapter. The vibroseis and dynamite SP positions were updated using the coordinates provided by Emerson. The pre-processing workflow used is presented in figure 5-1.

## 5.1 Vibroseis Shot Points

The raw vibroseis data was correlated with a synthetic sweep generated by the VSProwess software. Figure 5-2 shows the synthetic sweep in the time and frequency domains. Figure 5-3 shows the single shot vibroseis uncorrelated traces recorded for SP 506220 and figure 5-4 shows the same traces after the correlation.

The DAS interrogator is sensible to external vibration producing a phase coherent noise along all the channels called Common Mode Noise (CMN). A long median filter along all the channels was applied to reduce the CMN (Fig. 5-5).

Some channels are noisier compared with the neighbouring ones. A median filter of 5 traces was applied to reduce the noise level (Fig. 5-6) followed by channels down sampling from 0.25 m to 2 m (factor of 8) (Fig. 5-7). An anti-aliasing filter was used during the down sampling process. A second CMN suppressing filter was applied before stacking (Fig. 5-8).

To increase the Signal to Noise Ratio (SNR) multiple sweeps were stacked together for the same SP (Fig. 5-9). On the baseline survey 5 sweeps were recorded per SP with full power vibroseis source and 10 sweeps for SPs with low power vibroseis source and on the monitor survey 10 sweeps have been recorded per SP with vibroseis at full power and 15 sweeps for SPs with vibroseis at low power.

A third CMN suppress was applied after the stacking (Fig. 5-10).

## 5.2 Dynamite Shot Points

Dynamite shot points have only one shot per location. Like vibriosis data the dynamite shots are affected by CMN (Fig. 5-11). The CMN is attenuated using a very long median filer (Fig. 5-12).

To remove the random noise generated by channels with high noise level, a median filter over 5 traces was applied (Fig. 5-13).

Figure 5-14 show the dynamite SP 502213 after down sampling from 0.25 m channel spacing to 2 m channel spacing.

| Title | Description | Figure |
|---|---|---|
| **5 Pre-processing** | | |
| Pre-Processing Workflow | For vibroseis and dynamite SPs | **5.1** |
| **5.1 Vibroseis SP** | | |
| Vibroseis Sweep | Theoretical sweep used for correlation | **5.2** |
| Raw Uncorrelated Vibroseis Shot | SP 506220, well 8-16, monitor srv., FID 424 | **5.3** |
| Correlated Raw Vibroseis Shot | SP 506220, well 8-16, monitor srv., FID 424 | **5.4** |
| Correlated Vibroseis Shot after Removing CMN | SP 506220, well 8-16, monitor srv., FID 424 | **5.5** |
| Correlated Vibroseis Shot after Enhancement | SP 506220, well 8-16, monitor srv., FID 424 | **5.6** |
| Correlated Vibroseis Shot after Depth Down-sampling | SP 506220, well 8-16, monitor srv., FID 424 | **5.7** |
| Correlated Vibroseis Shot after Second CMN Suppress | SP 506220, well 8-16, monitor srv., FID 424 | **5.8** |
| Correlated Vibroseis Stack | SP 506220, well 8-16, monitor srv., FID 424 | **5.9** |
| Correlated Vibroseis Stack – CMN Suppress | SP 506220, well 8-16, monitor srv., FID 424 | **5.10** |
| **5.2 Dynamite SP** | | |
| Raw Dynamite Shot | SP 502213, well 8-16, baseline srv., FID 1006 | **5.11** |
| Raw Dynamite Shot after Removing CMN | SP 502213, well 8-16, baseline srv., FID 1006 | **5.12** |
| Raw Dynamite Shot after Enhancement | SP 502213, well 8-16, baseline srv., FID 1006 | **5.13** |
| Raw Dynamite Shot after Depth Down-sampling | SP 502213, well 8-16, baseline srv., FID 1006 | **5.14** |

*Table 5-13 Pre-processing figures*

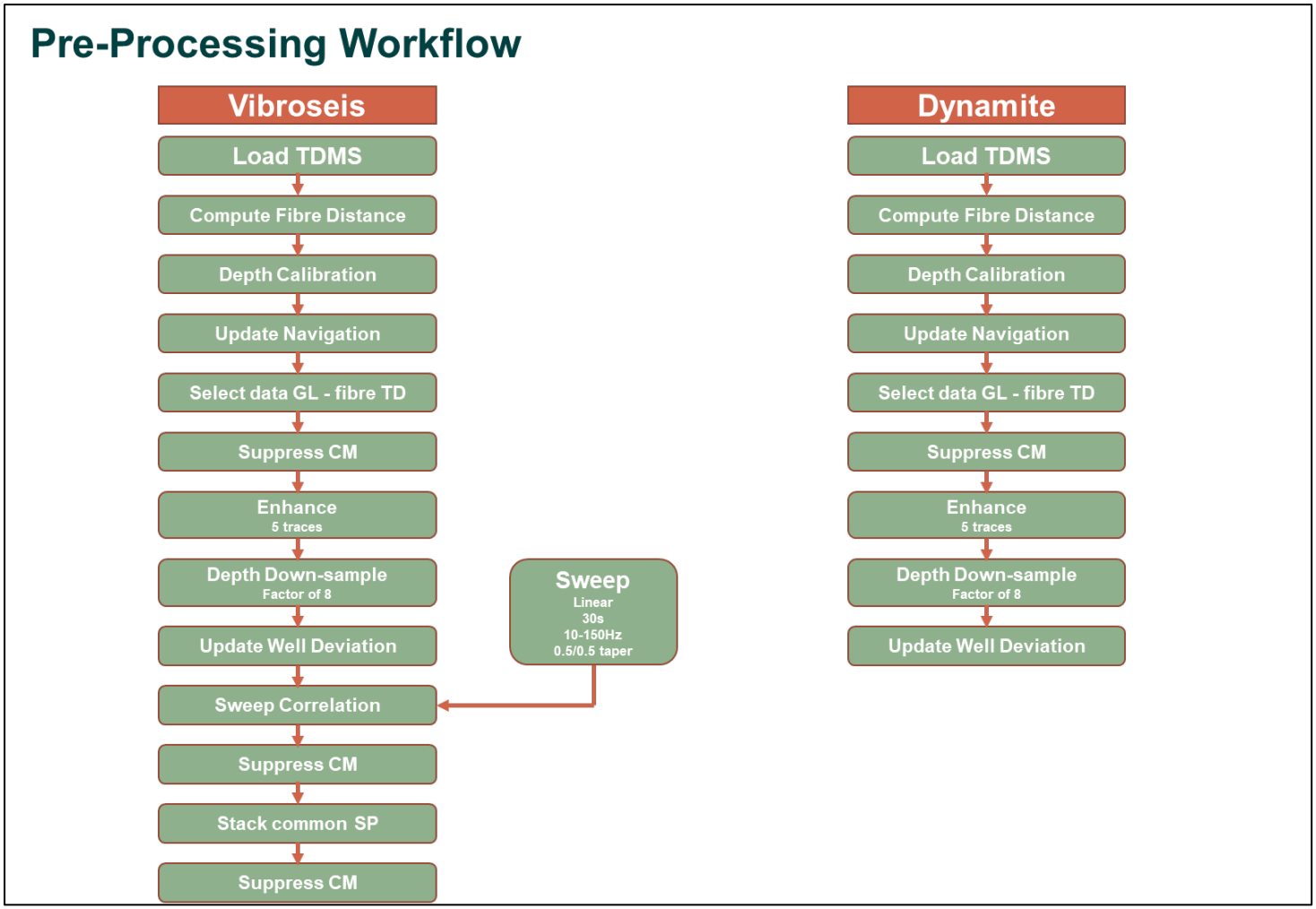


*Figure 5-1. Pre-Processing Workflow - For vibroseis and dynamite SPs. The pre-processing phase consists of several steps: compute the receiver position in depth, update the headers with the source position, reduce the noise, correlate sweep and stack (vibroseis data only). First the raw data is uploaded into the VSProwess database format (Silixa's iDAS interrogator records the seismic data in TDMS format). The fibre distance computation and depth calibration used to compute the receiver depth were presented in the previous chapter. The vibroseis and dynamite SP positions were updated using the coordinates provided by Emerson.*

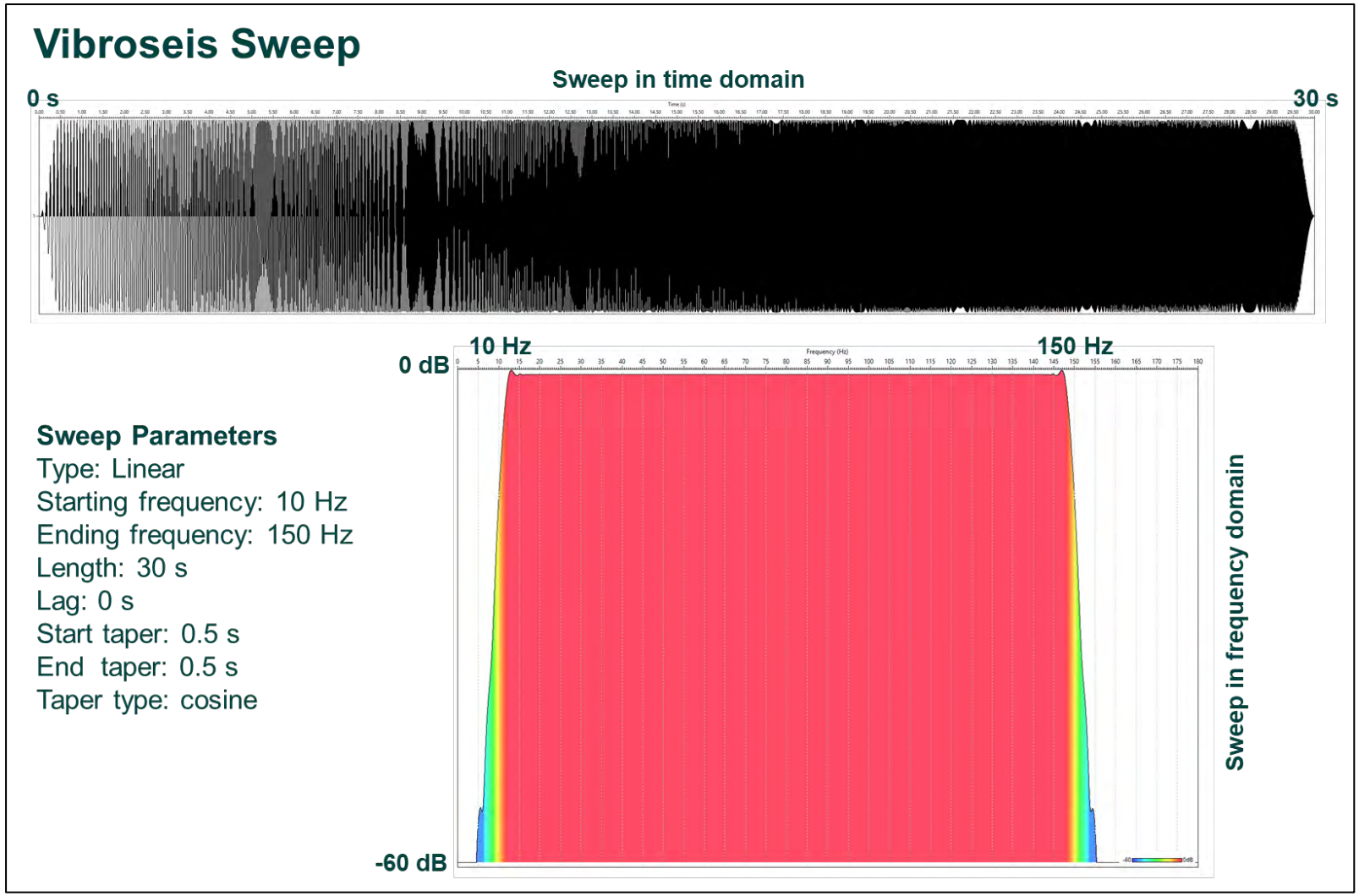


*Figure 5-2. Vibroseis Sweep - Theoretical sweep used for correlation. The raw vibroseis data was correlated with a synthetic sweep generated by the VSProwess software. Figure 5-2 shows the synthetic sweep in the time (up) and frequency domains (down).*

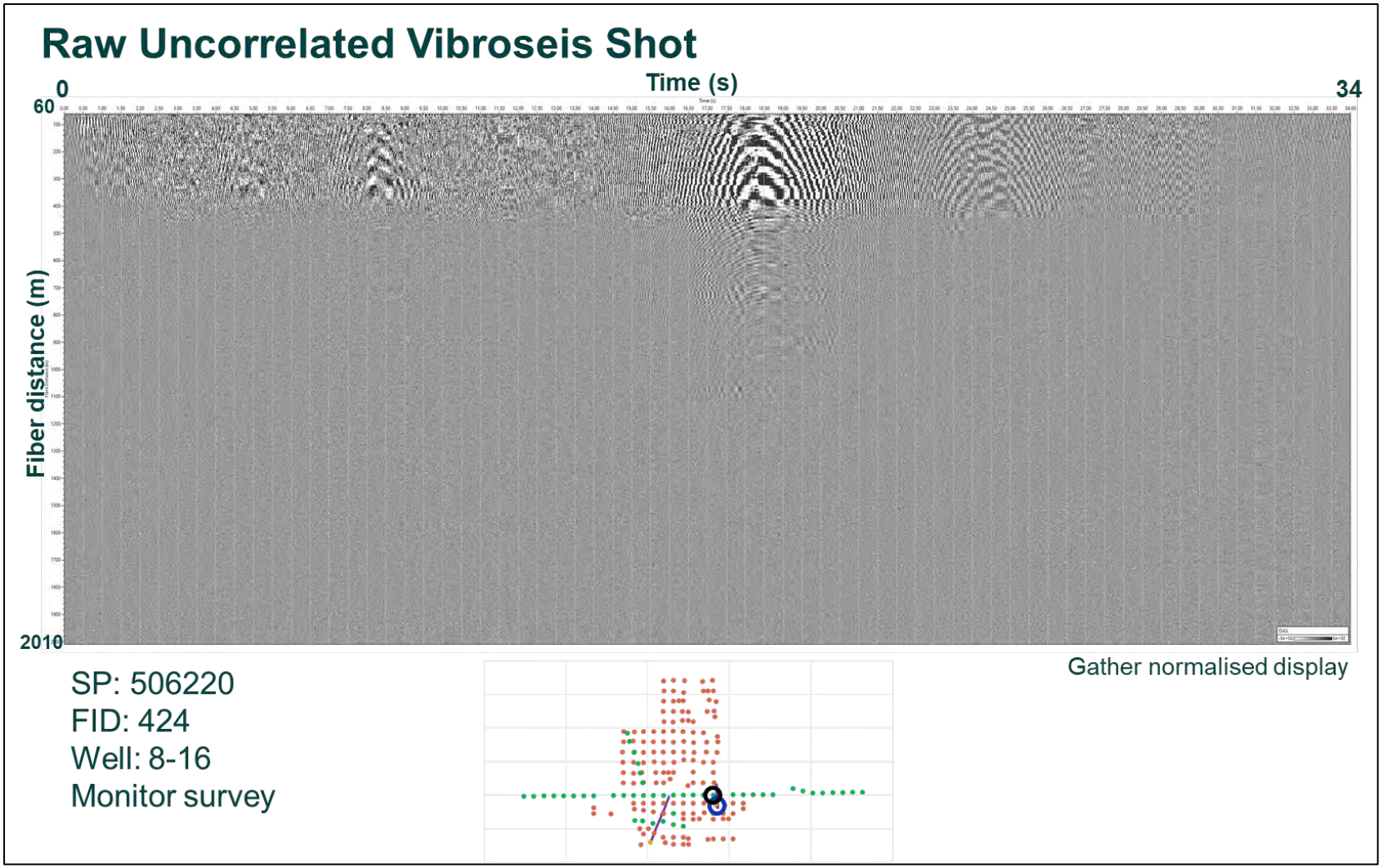


*Figure 5-3. Raw Uncorrelated Vibroseis Shot - SP 506219, well 8-16, monitor survey, FID 404. Figure 5-3 shows the single shot vibroseis uncorrelated traces recorded for SP 506219.*

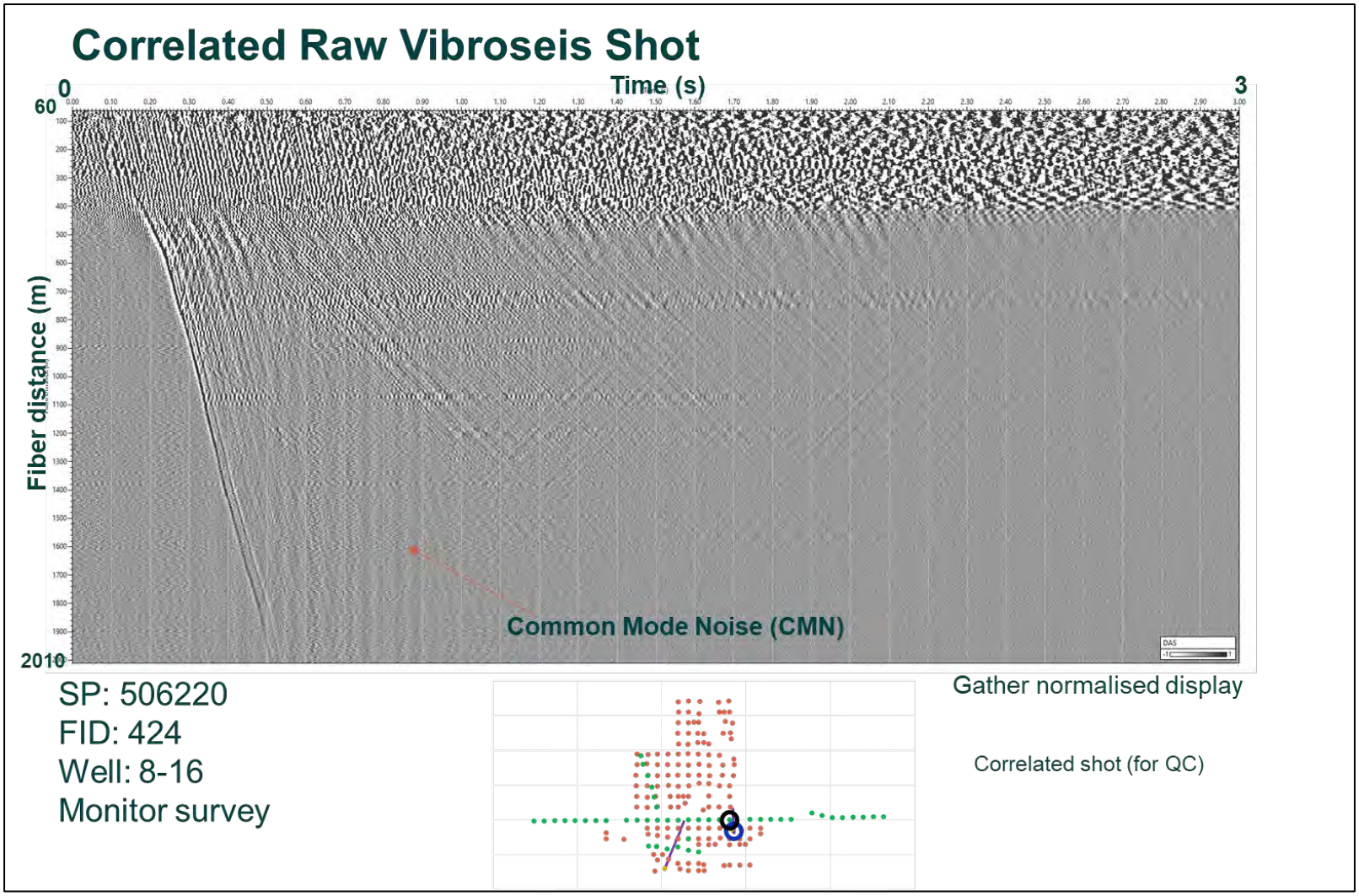


*Figure 5-4. Correlated Raw Vibroseis Shot - SP 506219, well 8-16, monitor survey, FID 404. Here are presented the same traces after the correlation.*

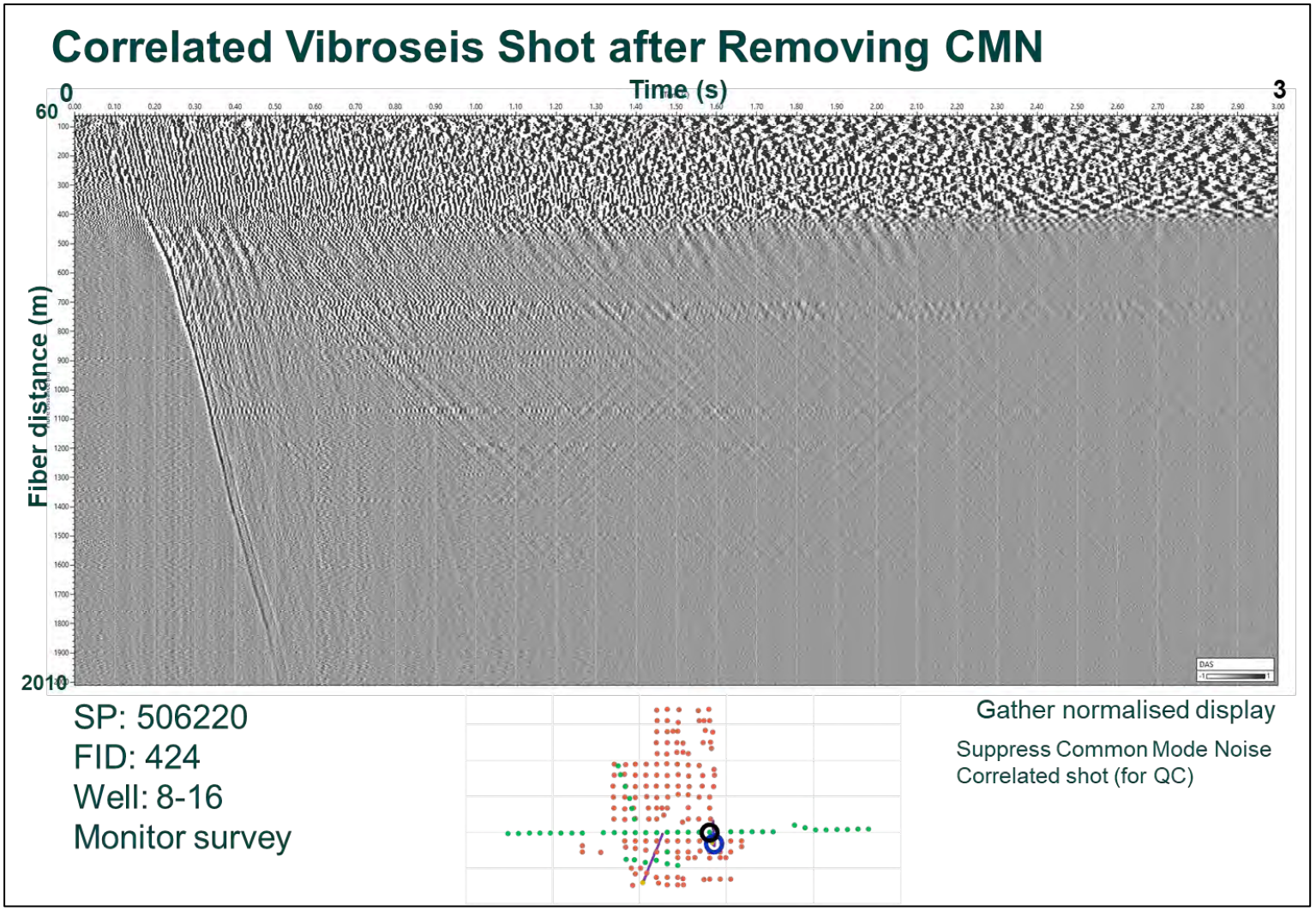


*Figure 5-5. Correlated Vibroseis Shot after Removing CMN - SP 506219, well 8-16, monitor survey, FID 404. The DAS interrogator is sensible to external vibration producing a phase coherent noise along all the channels called Common Mode Noise (CMN). A long median filter along all the channels was applied to reduce the CMN.*

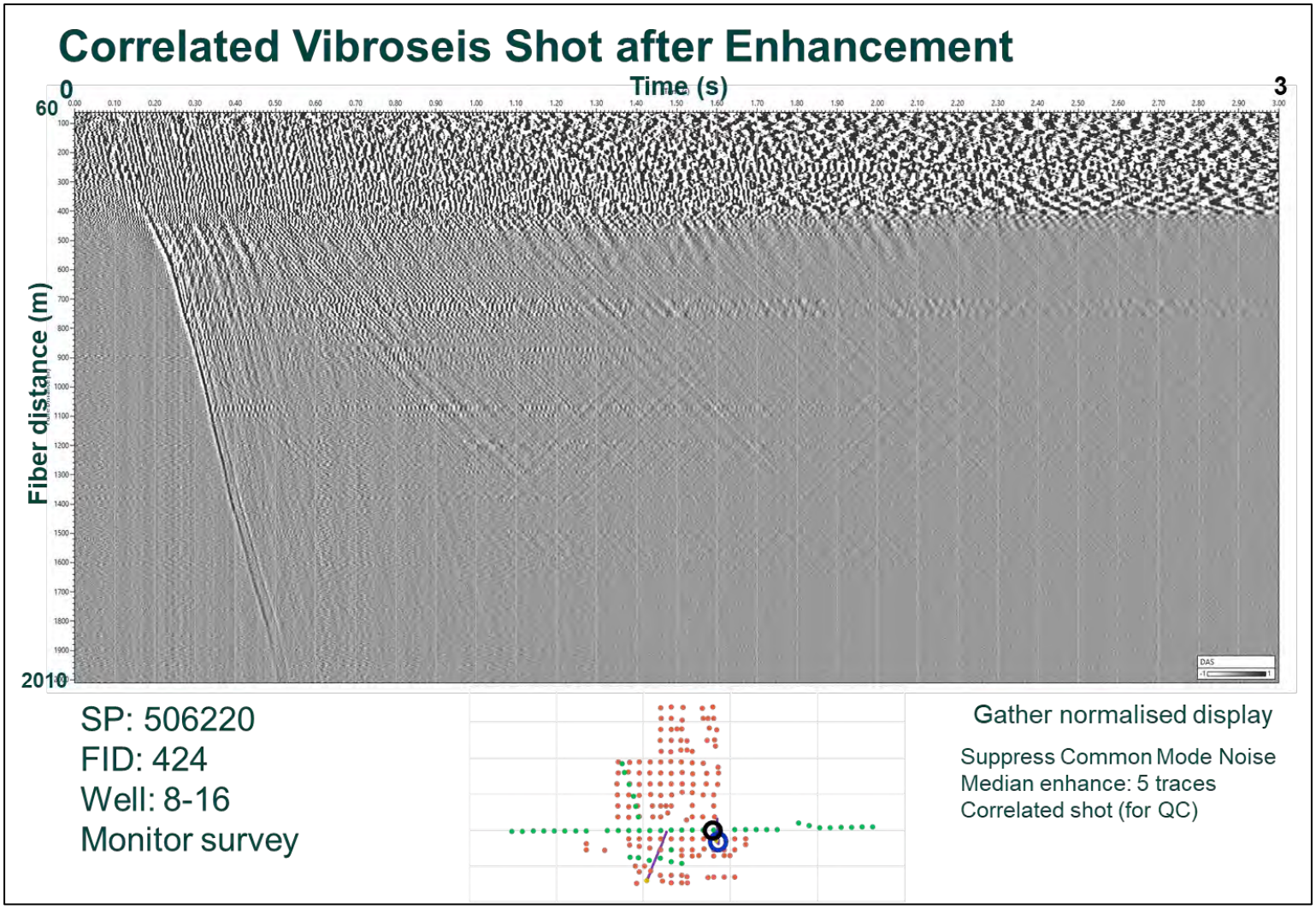


*Figure 5-6. Correlated Vibroseis Shot after Enhancement - SP 506219, well 8-16, monitor survey, FID 404. Some channels are noisier compared with the neighbouring ones. A median filter of 5 traces was applied to reduce the noise level.*

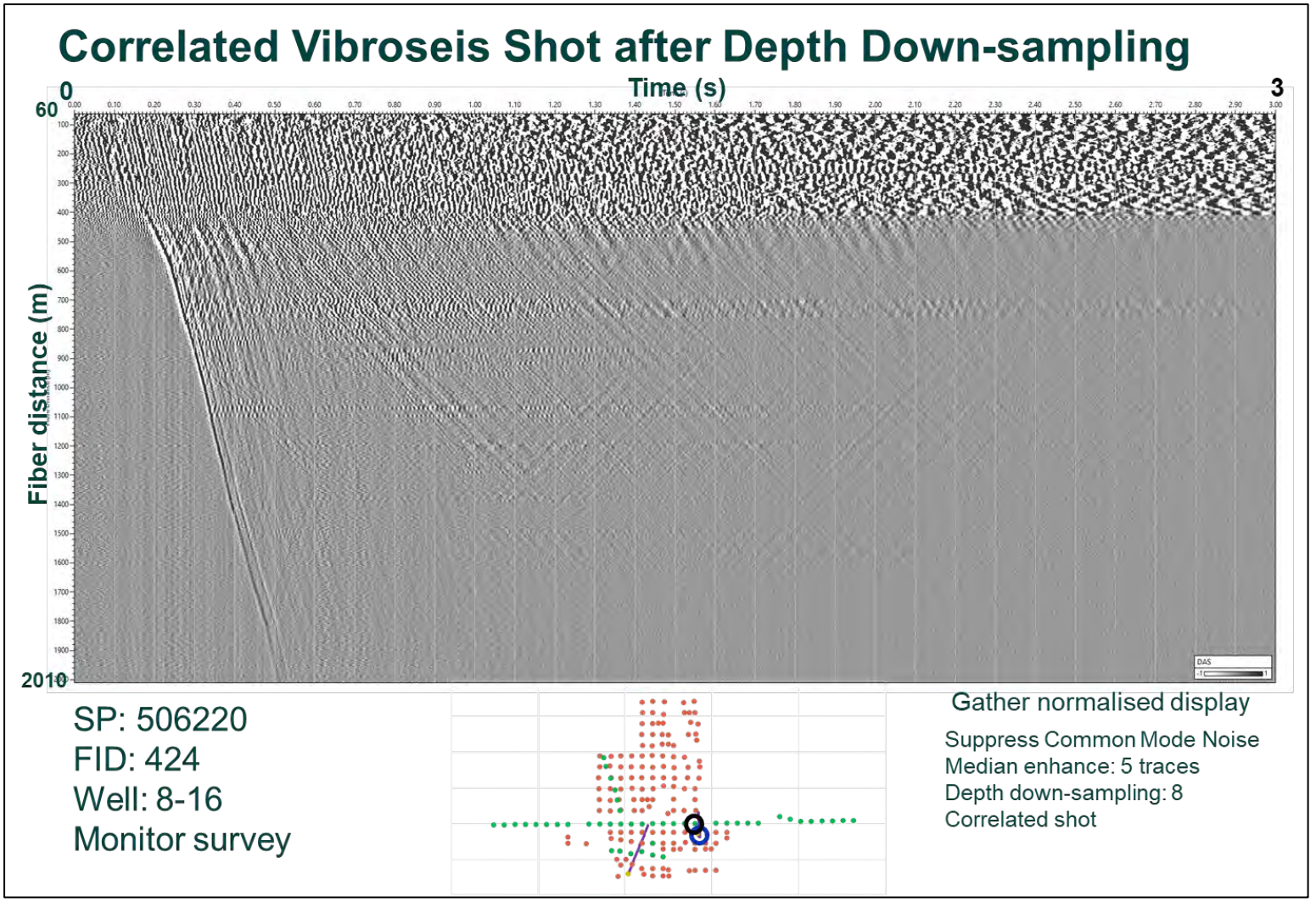


*Figure 5-7. Correlated Vibroseis Shot after Depth Down-sampling - SP 506219, well 8-16, monitor survey, FID 404. Channels down sampling from 0.25 m to 2 m (factor of 8). An anti-aliasing filter was used during the down sampling process.*

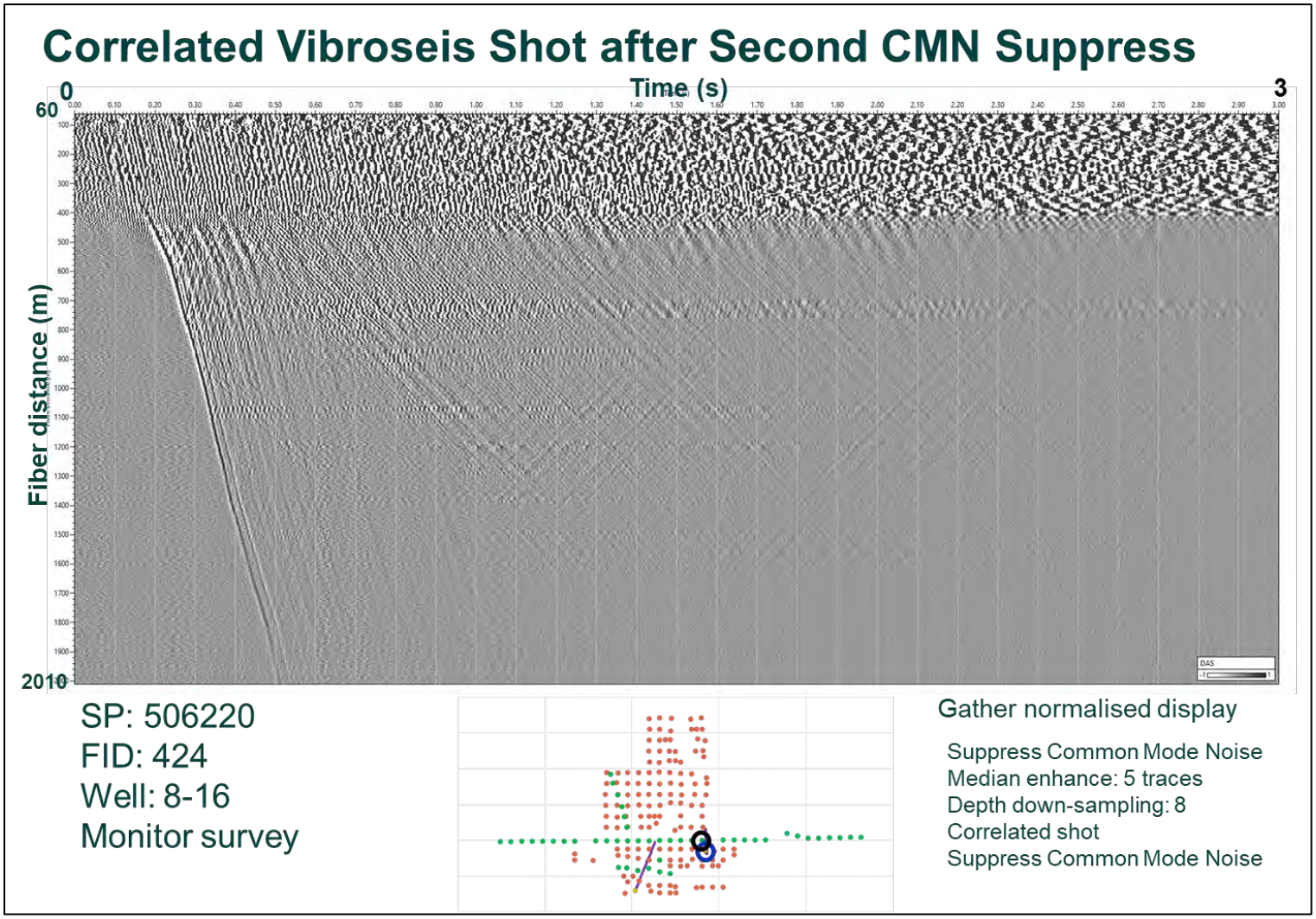


*Figure 5-8. Correlated Vibroseis Shot after Second CMN Suppress - SP 506219, well 8-16, monitor survey, FID 404. A second CMN suppressing filter was applied before stacking.*

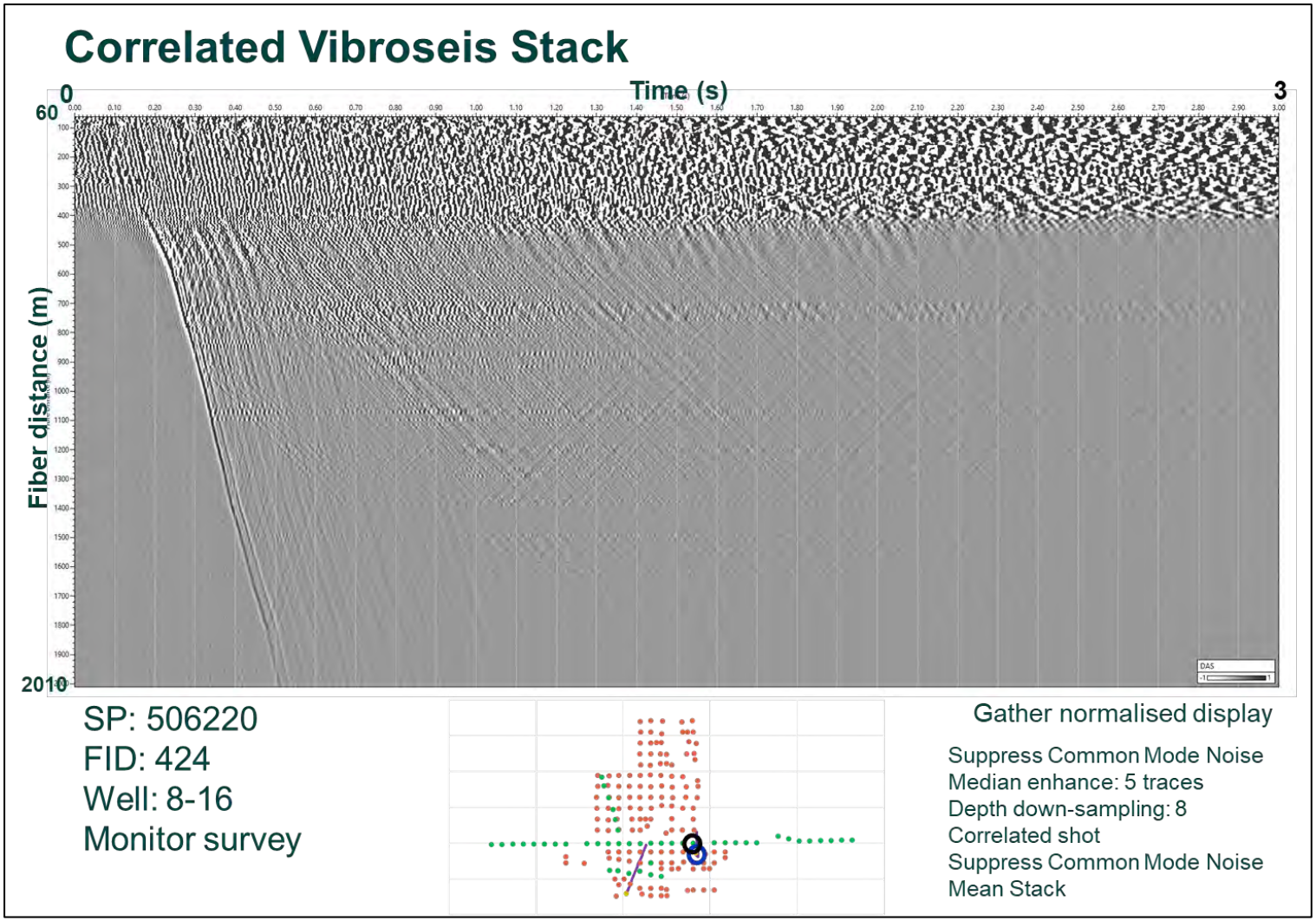


*Figure 5-9. Correlated Vibroseis Stack - SP 506219, well 8-16, monitor survey, FID 404. To increase the Signal to Noise Ratio (SNR) multiple sweeps were stacked together for the same SP.*

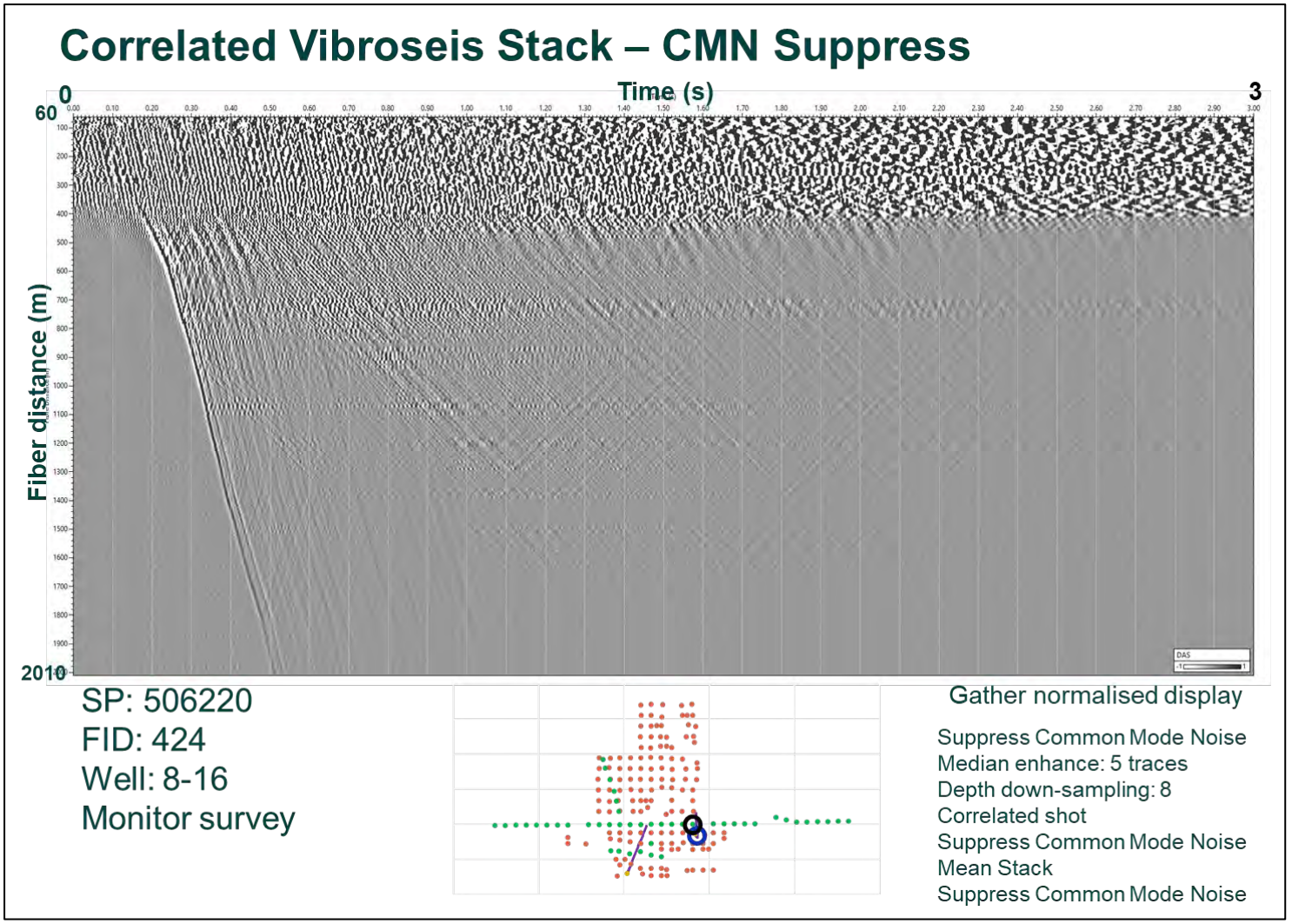


*Figure 5-10. Correlated Vibroseis Stack – CMN Suppress - SP 506219, well 8-16, monitor survey, FID 404. A third CMN suppress was applied after the stacking.*

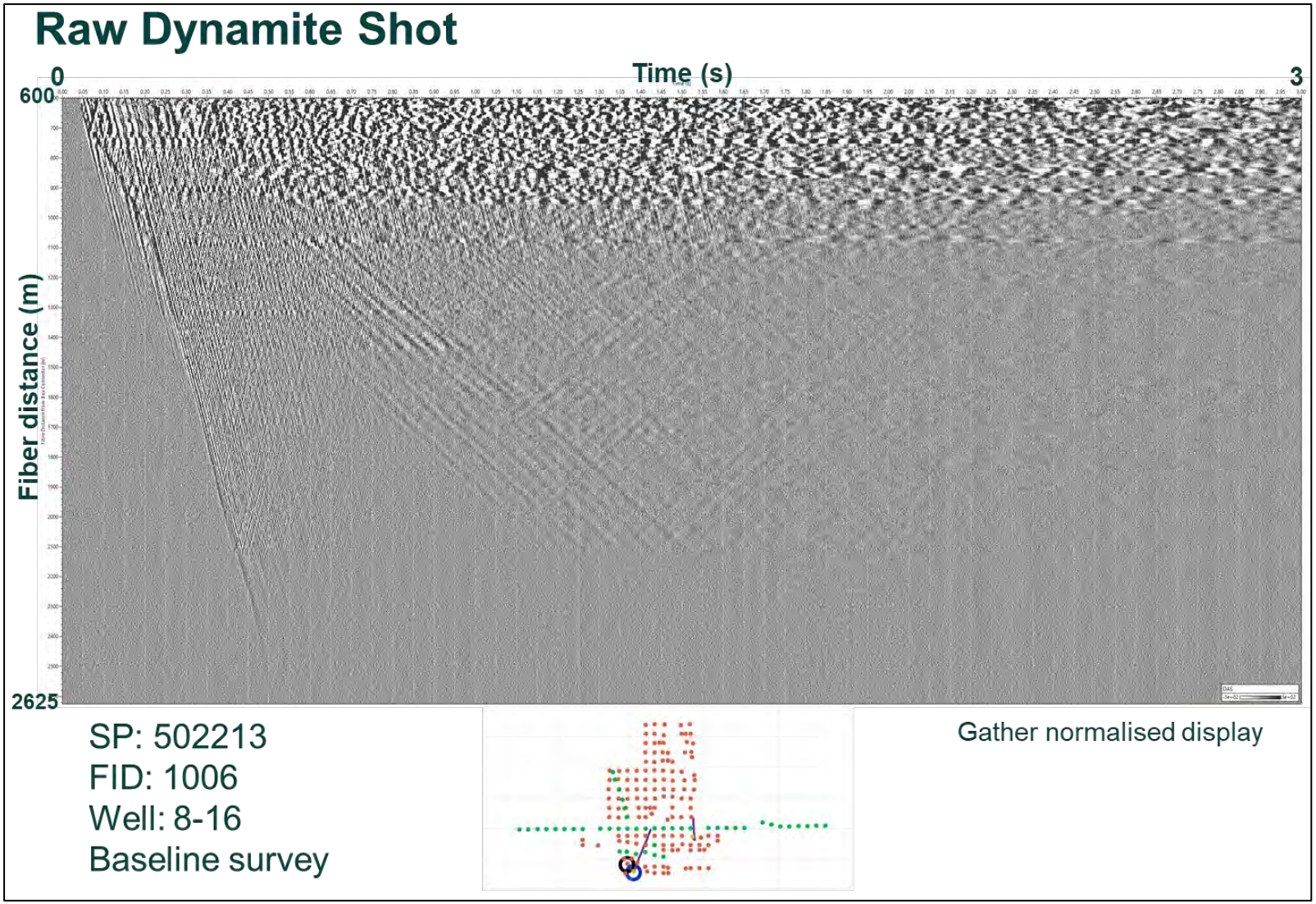


*Figure 5-11. Raw Dynamite Shot - SP 502213, well 8-16, baseline survey, FID 1006. Dynamite shot points have only one shot per location.*

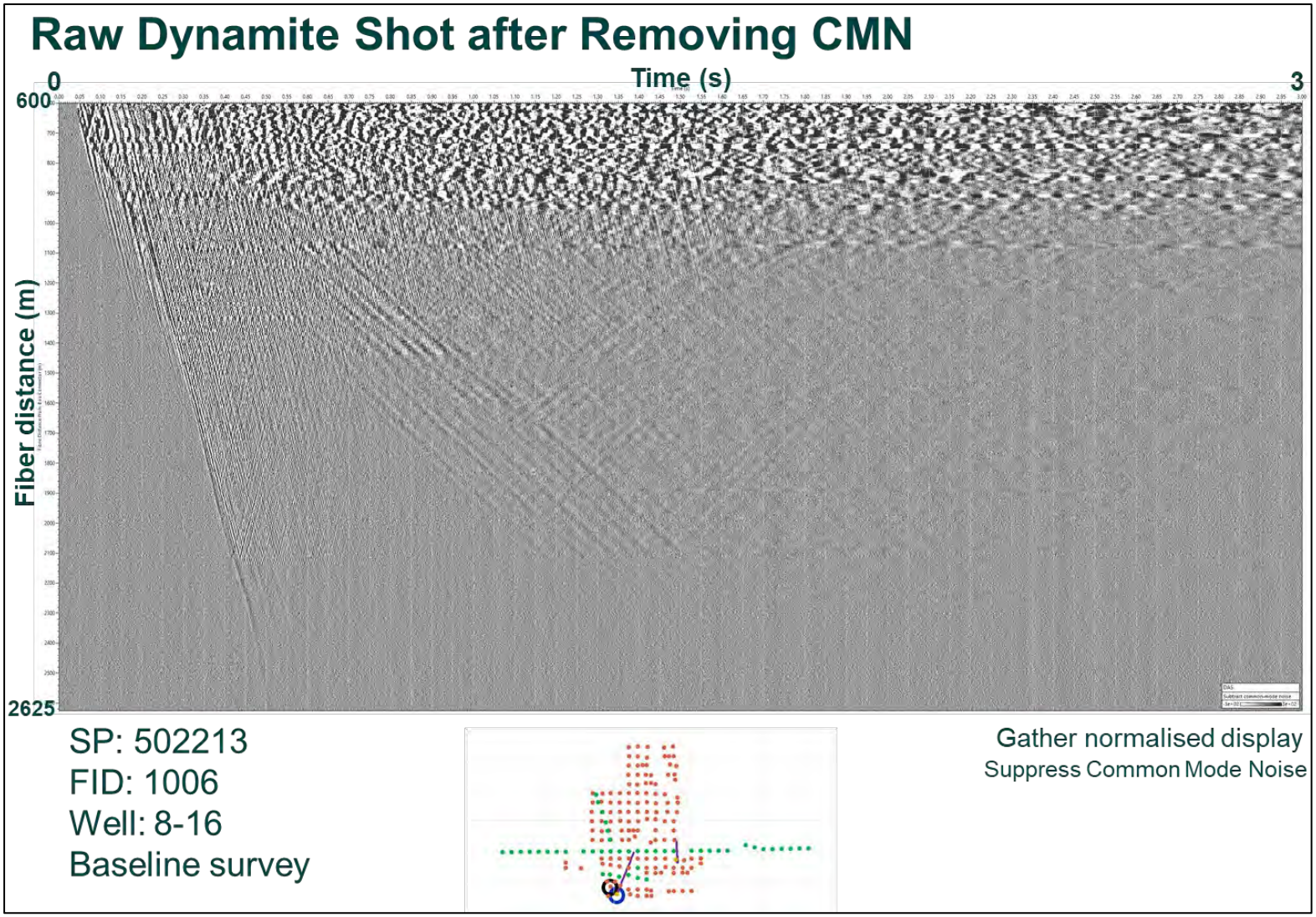


*Figure 5-12. Raw Dynamite Shot after Removing CMN - SP 502213, well 8-16, baseline survey, FID 1006. Like vibriosis data the dynamite shots are affected by CMN. The CMN is attenuated using a very long median filer.*

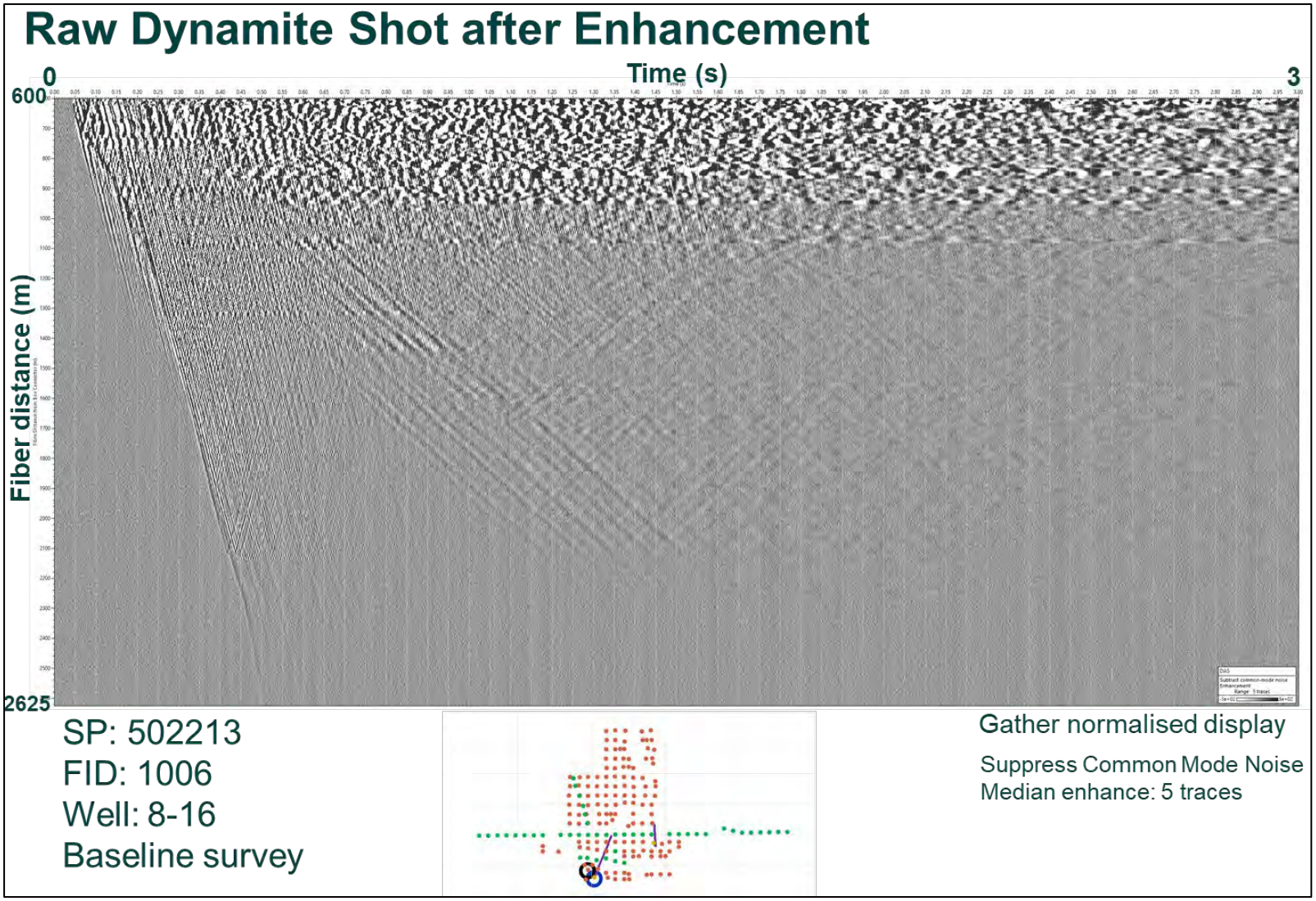


*Figure 5-13. Raw Dynamite Shot after Enhancement - SP 502213, well 8-16, baseline survey, FID 1006. To remove the random noise generated by channels with high noise level, a median filter over 5 traces was applied.*

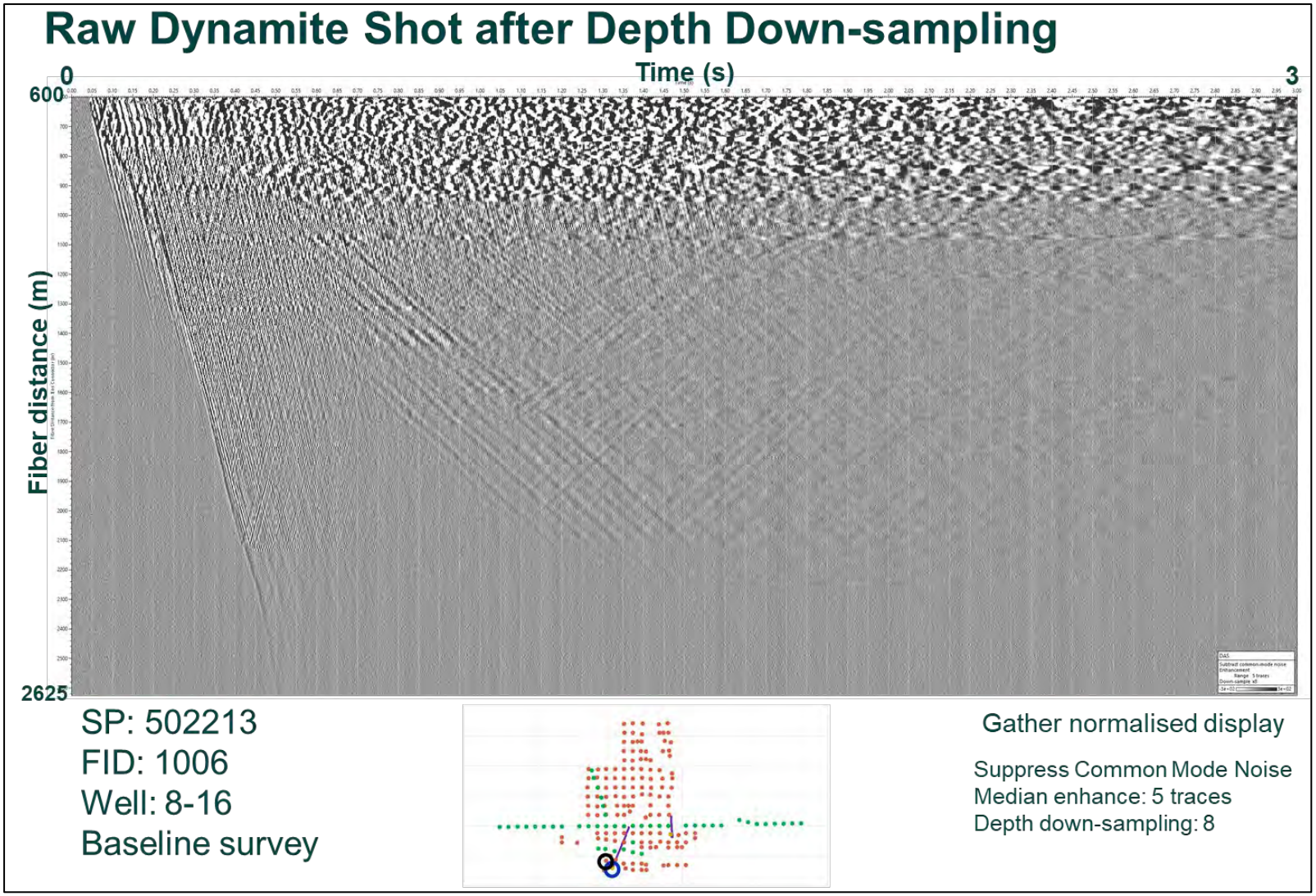


*Figure 5-14. Raw Dynamite Shot after Depth Down-sampling - SP 502213, well 8-16, baseline survey, FID 1006. Down sampling from 0.25 m channel spacing to 2 m channel spacing. An anti-aliasing filter was used during the down sampling process.*

# 6 Data QC

After data loading and the pre-processing stage, the data and metadata were quality checked. We verify the navigation information, check the coherency between the sweeps of the same SP and set the trace header data.

In figures 6-1 and 6-2 are displayed the planned and the recorded SP positions for baseline and monitor surveys. For vibroseis data the average shots position is displayed. Dynamite SPs have only one set of coordinates available; we assume that for the monitor survey the charges were placed in boreholes drilled in the same locations as those for the baseline. For the majority of the vibroseis shots acquired during the baseline survey the acquisition system recorded a GPS position only for two shot locations (Fig. 6-1 bottom right); for this reason, the source location weight centre provided by the SourceLink software has an error of a few meters. The location of each individual vibroseis shot and the flag position are presented in figure 6-3. For all the shots the location of the vibroseis source weight centre is very close to the flag position except for SP 506224, but for this SP the recorded position is consistent between the baseline and the monitor surveys. We notice also that the GPS signal is lower on the dirt road located in the forest.

The SeismicLink source location log provided by Emerson for some dynamite shot points is missing some values (Fig. 6-4). These gaps were filled using Silixa's handwritten field log.

At the SP 510112 the average GL elevation value recorded by the system for vibroseis is not in line with the dynamite elevation value located on the same position and also, with the neighbour SP's elevation (Fig. 6-5). The vibroseis elevation was corrected for this SP.

## 6.1 Vibroseis data

Figure 6-6 shows the number of sweeps for each vibroseis SP. On the baseline survey 5 sweeps were acquired at locations where the vibroseis sources shook at full force and 10 sweeps at locations with lower force. On the monitor survey at least 10 sweeps were acquired at the full force locations and at least 15 with at the locations with low force or with difficult coupling.

In the area with less consolidated shallow formation, for the same SP, time shifts between consecutive sweeps could occur due to vibroseis subsidence. To detect this, a cross-correlation between each shot and the stack at the same position was made. The cross-correlation peak was picked. The time delay of the central wavelet peak measures the time shift between the shot and the stack.

The QC analysis for the baseline survey recorded at well 6-16 for five shots: SP 506215 (close to well 6-16 TD), SP 101215 (close to well 6-16 well head), SP 506201 (far west), SP 506235 (far east) and SP 512211 (far north) is presented in Figures 6-7 to 6-14. Figures 6-7 to 6-12 present: the correlated shot (top – track 3), the stack (top – track 4), the shot – stack cross-correlation (top – track 2), the time shift between the shot and the stack (top – track 1) and all the shot – stack cross-correlations at 1550m MD (bottom centre).

In figure 6-12 is a QC of the five stacks and figure 6-13 shows the shot-stack cross-correlation wavelet (bottom row) at 1550 m MD and the time difference (top row) for all the shots of the well 6-16 baseline survey. Time shifts between them due to source subsidence were not noticed in the data above. The SPs on the far eastern side (506229 to 506235) have a lower shot-stack correlation due to the offset and weaker SNR.

Figure 6-14 shows the same data from figure 6-12 in the frequency domain. The noise level increases with frequency and the main frequency bandwidth is below 90 Hz.

The QC analysis for the baseline survey well 8-16, SP 506220 (close to well 8-16), SP 101217 (south to well 8-16 well head), SP 506201 (far west), SP 506235 (far east) and SP 512211 (far north) is presented in Figures 6-15 to 6-22. Figures 6-15 to 6-19 present: the correlated shot (top – track 3), the stack (top – track 4), the shot – stack cross-correlation (top – track 2), the time shift between the shot and the stack (top – track 1) and all the shot – stack cross-correlations at 1550m MD (bottom centre).

Figure 6-20 shows a QC of the five stacks and figure 6-21 shows the cross-correlation shot-stack wavelet (bottom row) at 1550 m MD and the time difference (top row) for all the shots of well 8-16, baseline survey. No time shift due to source subsidence was noticed in the data above. The cross-correlation between the shot and stack at well 8-16 is better than at well 6-16 due to a better SNR.

Figure 6-22 presents the same data from figure 6-20 in the frequency domain. The noise level increases with frequency and the main frequency bandwidth is below 110 Hz.

The QC analysis for the monitor survey, well 6-16, SP 506215 (close to well 6-16 TD), SP 101215 (close to well 6-16 well head), SP 506201 (far west), SP 506235 (far east) and SP 512211 (far north) is shown in Figures 6-23 to 6-30. Figures 6-23 to 6-27 present: the correlated shot (top – track 3), the stack (top, track 4), the shot – stack cross-correlation (top – track 2), time shift between the shot and the stack (top – track 1) and all the shot – stack cross-correlations at 1550m MD (bottom centre). Above 1540m MD due to the ringing the time shift exceeds 1ms.

Figure 6-28 shows a QC of the five stacks and figure 6-29 shows the shot-stack cross-correlation wavelet (bottom row) at 1550 m MD and the time difference (top row) for all the shots of well 8-16, monitor survey. A pattern of small time shifts was noticed between the shots, more obvious on the western part, but is below 0.5 ms.

Figure 6-30 shows the same data from figure 6-28 in the frequency domain. The noise level increases with frequency and the main frequency bandwidth is below 100 Hz. Below the top of the A2 Carbonate is a drop in low frequencies.

The QC analysis for the monitor survey, well 8-16, SP 506220 (close to well 8-16), SP 101217 (south to well 8-16 well head), SP 506201 (far west), SP 506235 (far east) and SP 512211 (far north) is shown in Figures 6-31 to 6-38. Figures 6-31 to 6-35 present the correlated shot (top – track 3), the stack (top – track 4), the shot – stack cross-correlation (top – track 2), the time shift between the shot and the stack (top – track 1) and all the shot – stack cross-correlations at 1550m MD (bottom centre).

Figure 6-36 shows a QC of the five stacks and figure 6-37 shows shot-stack cross-correlation wavelet (bottom row) at 1550 m MD and the time difference (top row) for all the shots of well 8-16, baseline survey. There is a small pattern of time shifts similar to those seen in well 6-16. Because we don't see the amplitude of changes in both wells we cannot assume it is due to subsidence. The cross-correlation between the shot and the stack at well 8-16 is better than at well 6-16 due to a better SNR.

Figure 6-38 presents the same data from figure 6-36 in the frequency domain. The noise level increases with frequency and the main frequency bandwidth is below 110 Hz. Also, the top of A2 Carbonate can be identified on the frequency displays.

Figures from 6-39 to 6-42 present the well 6-16 baseline stack (left) and the monitor stack (right) for SP: 506201 (far west), 506235 (far east), 506218 (between the well 6-16 TD and well 8-16) and 512111(far north). Figures from 6-43 to 6-46 shows stack data recorded in the well 8-16 for the same SP: 506201 (far west), 506235 (far east), 506218 (between the well 6-16 TD and well 8-16) and 512111(far north). For all the presented SPs the seismic response is similar between the baseline and

monitor survey; nevertheless, the baseline data noise level is higher due to the lower number of shots per SP. Both surveys are affected by ringing at similar intervals and those intervals may vary with offset. All well 6-16 SPs data is affected by tubing ringing above 1520 m MD. This level corresponds to the increase of the well deviation above 5°. Optic fibre is an omnidirectional sensor with the maximum response for movement along it. For this reason the down shear wavefield is stronger on the far offsets. The reflector at top A2 Carbonate is visible on all the vibroseis SPs.

Figure 6-47 presents the average signal to noise ratio at each SP location for: well 6-16 baseline survey (top left), well 8-16 baseline survey (middle left), well 6-16 monitor survey (top right) and well 8-16 monitor survey (middle right). For each stack we defined the signal window from 15 ms before First Break (FB) pick to 35 ms after the FB. The elevated noise window starts at 200 ms before FB and continues for 50 ms. For each channel below 1700 m MD a SNR value is computed as the ratio of the signal window RMS and the noise window RMS (Fig. 6-47 bottom left). Finally, an average value is computed for each SP. Figures 6-48 (well 6-16) and 6-49 (well 8-16) show a single stack trace at 1700 m MD for each SP and the signal to noise ratio (linear and in dB) for the baseline (left) and the monitor (right) surveys.

The monitor survey has an approximately three-time better SNR compare with the baseline survey. Also, the SNR decreases with offsets and is lower for locations with vibroseis sources shaking at low power. |There is a good first break definition with similar response on the baseline and monitor survey.

## 6.2 Dynamite data

Only one shot was acquired per shot location, for this reason the SNR is lower compared with the vibroseis data.

Figures from 6-50 to 6-55 present the well 6-16 baseline (left) and the monitor (right) in time and frequency domain for SP: 504214 (above the well 6-16 trajectory), 517215 (far north) and 502222 (far east). The baseline shots are affected to a higher degree by the high frequency noise. In the near offset shot data only the ringing is visible above the noise, while for the far offsets the signal is very week in the upper section of the well and below the noise level in the lower section. This may suggest that most of the source energy is absorbed in the unconsolidated shallow levels.

Figures from 6-56 to 6-61 present the well 8-16 baseline (left) and the monitor (right) in time and frequency domain for SP: 505221 (close to 8-16 well), 517220 (far north) and 501213 (far west). Similar to well 6-16, the baseline shots are affected to a higher degree by the high frequency noise. The signal is very week in the upper part of the well and below the noise level in the lower part of the well.

In figure 6-62 we show the average SNR computed in the same window interval as in figure 6-47 for the for well 6-16 baseline survey (top left), well 8-16 baseline survey (middle left), well 6-16 monitor survey (top right) and well 8-16 monitor survey (middle right). We applied a band pass filter (BPF) of 5,10 – 90,110Hz to the input data before the computation.

Figure 6-63 shows also the average SNR per SP but computed in a window from 5 ms before FB to 20 ms after FB for the signal and a 20 ms window starting 100 ms before FB for the noise; the average SNR value is computed using the channels from 1650 m to 1850 m MD. Excepting the close offsets, the signal level is below or very close to the noise level; the monitor survey has a better SNR.

Figures 6-64 (well 6-16, baseline), 6-65 (well 6-16, monitor), 6-66 (well 8-16, baseline) and 6-67 (well 8-16 monitor) show a single shot trace at 1700 m MD for each SP and the signal to noise in ratio and dB computed using the algorithm presented in figure 6-63. In the well 6-16 data, for the both surveys, the first break is weak. Well 8-16 has a better first break definition.

Two shot point locations have both vibroseis and dynamite data (Fig. 6-68). Figures from 6-69 to 6-76 present SP 510112 (on the north dirt road) and SP 504216 (close to well 6-16) common vibroseis-dynamite data recorded in both wells during the baseline and monitor surveys. The vibroseis data has a better SNR compared to dynamite data. Dynamite SP 510112 has a better SNR compared to dynamite SP 504216. The baseline survey has a higher noise level compared to the monitor survey. In well 6-16 the dynamite data are less affected by the ringing above 1520 m MD.

| Title | Description | Figure |
|---|---|---|
| | | |
| **6 Data QC** | | |
| Baseline survey – plan source vs actual source position | Vibroseis stack and dynamite shots | **6.1** |
| Monitor survey – plan source vs actual source position | Vibroseis stack and dynamite shots | **6.2** |
| Vibroseis GPS position vs Plan Location | Each vibroseis shots location | **6.3** |
| Monitor survey – Navigation QC | Silixa's handwrite log used to fill the software logs gaps | **6.4** |
| Shot Points Elevation | | **6.5** |
| | | |
| **6.1 Vibroseis SP** | | |
| Sweeps per Vibro Point | Baseline and monitor survey | **6.6** |
| Shot Points QC – Baseline – Vibroseis – Well 6-16 – SP 506215 | Cross-correlation between the shot and stack | **6.7** |
| Shot Points QC – Baseline – Vibroseis – Well 6-16 – SP 101215 | Cross-correlation between the shot and stack | **6.8** |
| Shot Points QC – Baseline – Vibroseis – Well 6-16 – SP 506201 | Cross-correlation between the shot and stack | **6.9** |
| Shot Points QC – Baseline – Vibroseis – Well 6-16 – SP 506235 | Cross-correlation between the shot and stack | **6.10** |
| Shot Points QC – Baseline – Vibroseis – Well 6-16 – SP 512211 | Cross-correlation between the shot and stack | **6.11** |
| Stacks QC – Baseline – Vibroseis – Well 6-16 | Stack in time domain | **6.12** |
| Baseline – Vibroseis – Well 6-16 – Shot * Stack Cross-Correlation | All the shots at 1550 m MD | **6.13** |
| Stacks QC – Baseline – Vibroseis – Well 6-16 – Frequency | Stack in frequency domain | **6.14** |
| Shot Points QC – Baseline – Vibroseis – Well 8-16 – SP 506220 | Cross-correlation between the shot and stack | **6.15** |
| Shot Points QC – Baseline – Vibroseis – Well 8-16 – SP 101217 | Cross-correlation between the shot and stack | **6.16** |
| Shot Points QC – Baseline – Vibroseis – Well 8-16 – SP 506201 | Cross-correlation between the shot and stack | **6.17** |
| Shot Points QC – Baseline – Vibroseis – Well 8-16 – SP 506235 | Cross-correlation between the shot and stack | **6.18** |
| Shot Points QC – Baseline – Vibroseis – Well 8-16 – SP 512211 | Cross-correlation between the shot and stack | **6.19** |
| Stacks QC – Baseline – Vibroseis – Well 6-16 | Stack in time domain | **6.20** |
| Baseline – Vibroseis – Well 8-16 – Shot * Stack Cross-Correlation | All the shots at 1550 m MD | **6.21** |
| Stacks QC – Baseline – Vibroseis – Well 8-16 – Frequency | Stack in frequency domain | **6.22** |
| Shot Points QC – Monitor – Vibroseis – Well 6-16 – SP 506215 | Cross-correlation between the shot and stack | **6.23** |

| Title | Description | Figure |
|---|---|---|
| Dynamite Shot QC – Well 6-16 – SP 517215 | Baseline and monitor survey | **6.52** |
| Dynamite Shot QC – Well 6-16 – SP 517215 – Frequency | Baseline and monitor survey | **6.53** |
| Dynamite Shot QC – Well 6-16 – SP 502222 | Baseline and monitor survey | **6.54** |
| Dynamite Shot QC – Well 6-16 – SP 502222 – Frequency | Baseline and monitor survey | **6.55** |
| Dynamite Shot QC – Well 8-16 – SP 505221 | Baseline and monitor survey | **6.56** |
| Dynamite Shot QC – Well 8-16 – SP 505221 – Frequency | Baseline and monitor survey | **6.57** |
| Dynamite Shot QC – Well 8-16 – SP 517220 | Baseline and monitor survey | **6.58** |
| Dynamite Shot QC – Well 8-16 – SP 517220 – Frequency | Baseline and monitor survey | **6.59** |
| Dynamite Shot QC – Well 8-16 – SP 501213 | Baseline and monitor survey | **6.60** |
| Dynamite Shot QC – Well 6-16 – SP 501213 – Frequency | Baseline and monitor survey | **6.61** |
| Signal to Noise Ratio – Dynamite | Computing window below 1700 m MD | **6.62** |
| Signal to Noise Ratio – Dynamite | Computing window 1650-1850 m MD | **6.63** |
| Dynamite – Signal to Noise Ratio – Baseline – Well 6-16 | Common Receiver Gather 1700mMD@KB | **6.64** |
| Dynamite – Signal to Noise Ratio – Monitor – Well 6-16 | Common Receiver Gather 1700mMD@KB | **6.65** |
| Dynamite – Signal to Noise Ratio – Baseline – Well 8-16 | Common Receiver Gather 1700mMD@KB | **6.66** |
| Dynamite – Signal to Noise Ratio – Monitor – Well 8-16 | Common Receiver Gather 1700mMD@KB | **6.67** |
| Vibroseis – Dynamite common SPs | Basemap | **6.68** |
| Vibroseis vs Dynamite – Baseline – Well 6-16 – SP 510112 | Total wavefield | **6.69** |
| Vibroseis vs Dynamite – Baseline – Well 6-16 – SP 504216 | Total wavefield | **6.70** |
| Vibroseis vs Dynamite – Baseline – Well 8-16 – SP 510112 | Total wavefield | **6.71** |
| Vibroseis vs Dynamite – Baseline – Well 8-16 – SP 504216 | Total wavefield | **6.72** |
| Vibroseis vs Dynamite – Monitor – Well 6-16 – SP 510112 | Total wavefield | **6.73** |
| Vibroseis vs Dynamite – Monitor – Well 6-16 – SP 504216 | Total wavefield | **6.74** |
| Vibroseis vs Dynamite – Monitor – Well 8-16 – SP 510112 | Total wavefield | **6.75** |
| Vibroseis vs Dynamite – Monitor – Well 8-16 – SP 504216 | Total wavefield | **6.76** |

*Table 6-14 Data QC figures*

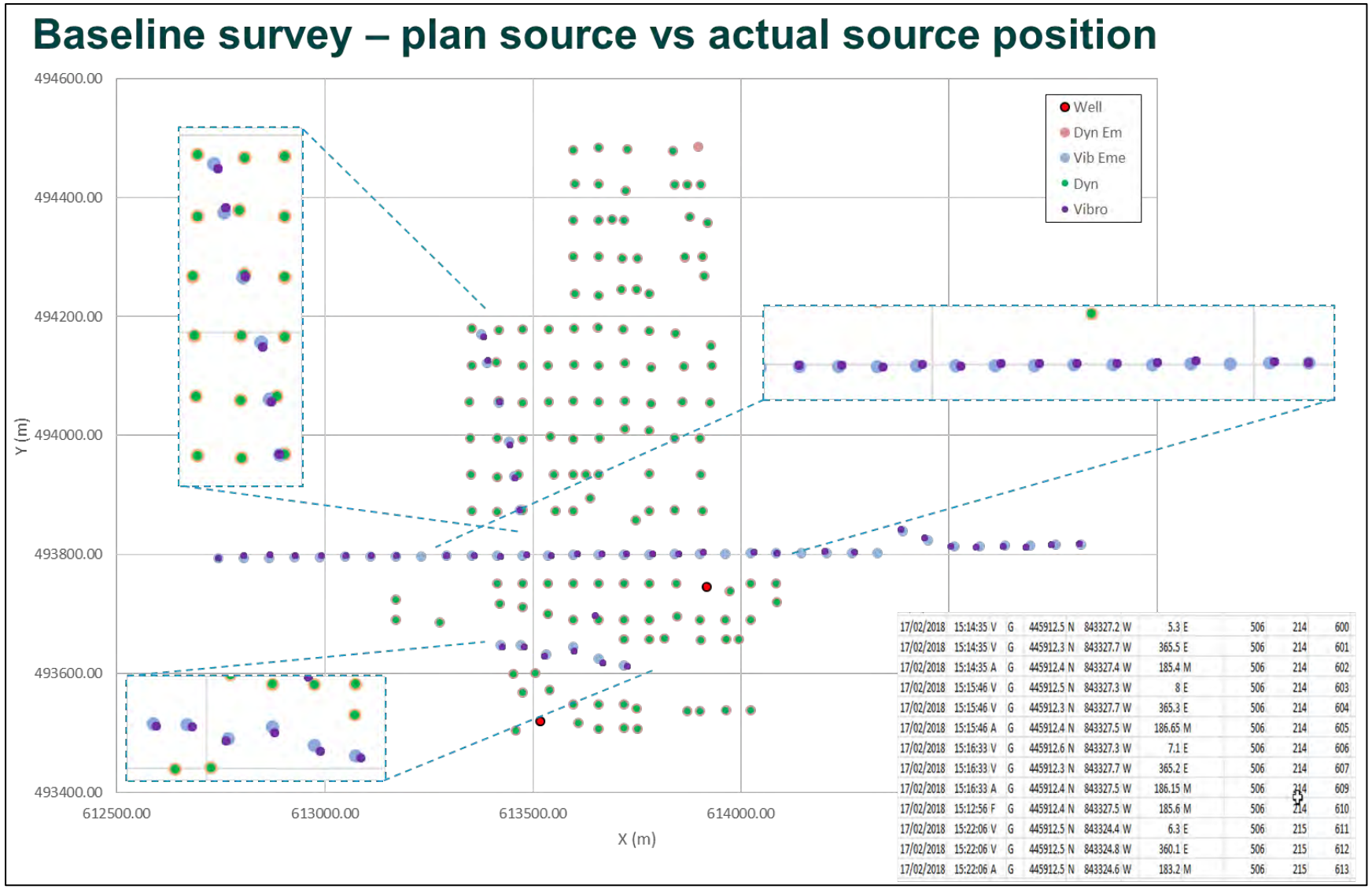


*Figure 6-1. Baseline survey – plan source vs actual source position - Vibroseis stack and dynamite shots. (Note: Em and Eme = Emerson)*

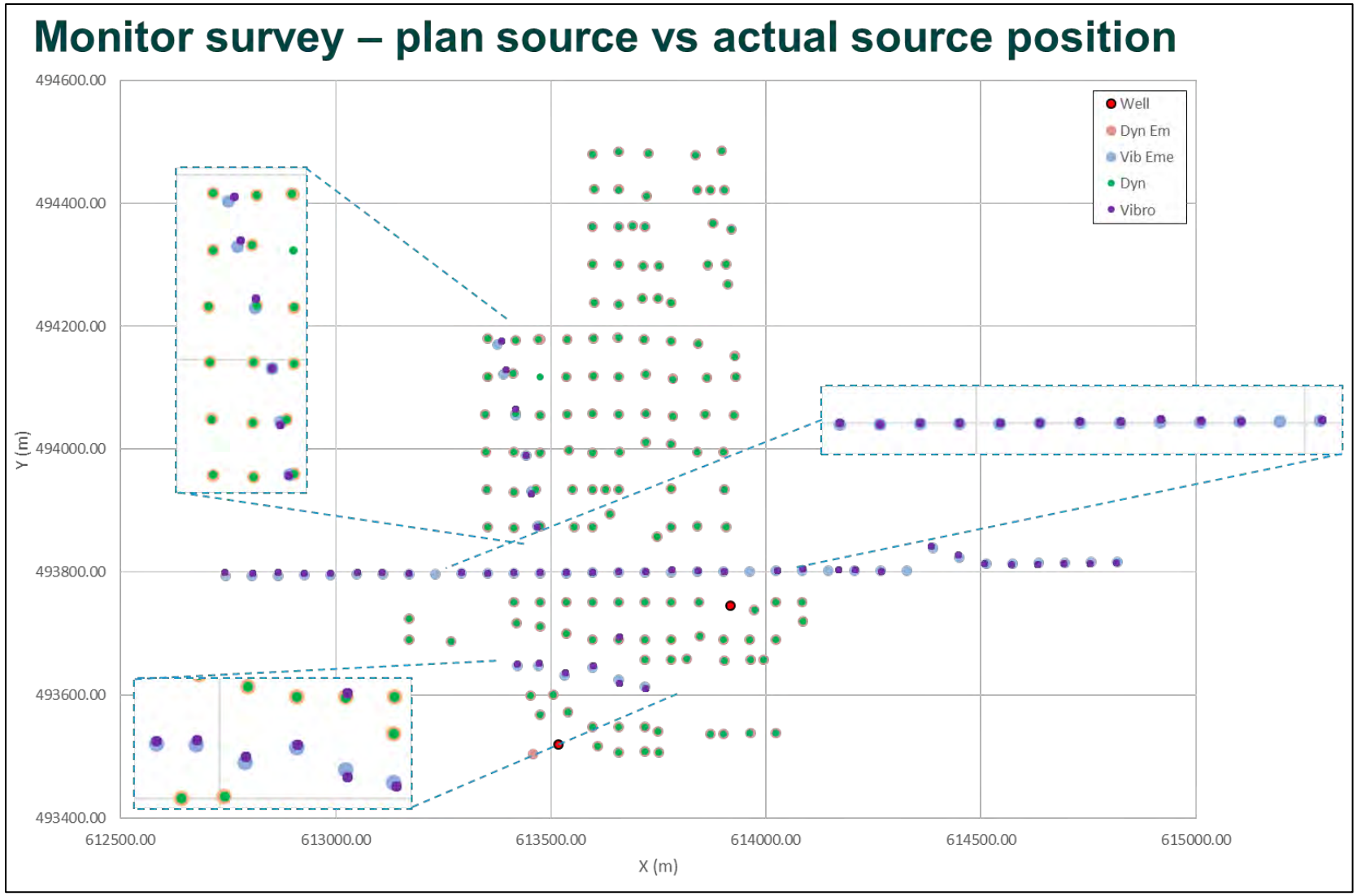


*Figure 6-2. Monitor survey – plan source vs actual source position - Vibroseis stack and dynamite shots. (Note: Em and Eme = Emerson)*

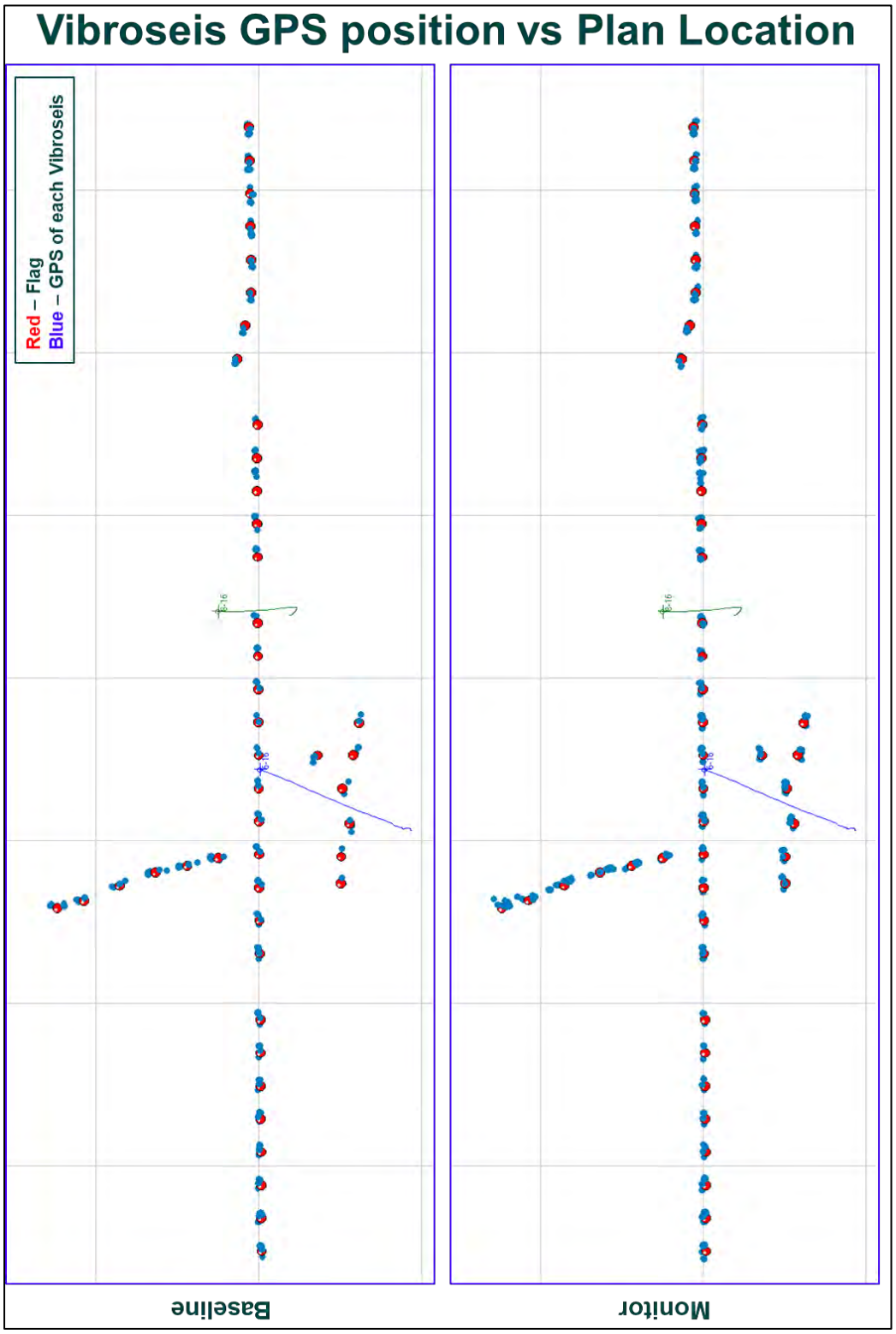


*Figure 6-3. Vibroseis GPS position vs Plan Location - Each vibroseis shots location. The location of each individual vibroseis shot and the flag position are presented in figure 6-3. For all the shots the location of the vibroseis source weight centre is very close to the flag position except for SP 506224, but for this SP the recorded position is consistent between the baseline and the monitor surveys. We notice also that the GPS signal is lower on the dirt road located in the forest.*

# Monitor survey – Navigation QC

| | | | | | | | |
|---|---|---|---|---|---|---|---|
| 22/08/2018 | 21:51:43 | 21:51:47 | | 09:51:46 | 507 | 219 | 0 |
| 22/08/2018 | 21:52:13 | 21:52:17 | | | 502 | 220 | 0 |
| 22/08/2018 | 21:53:13 | 21:53:17 | | 09:53:16 | 508 | 220 | 0 |
| | | | | | | | |
| 22/08/2018 | 00:41:00 | 00:41:04 | | 12:41:04 | 507 | 216 | 0 |
| 22/08/2018 | 00:41:59 | 00:42:03 | | | 507 | 215 | 0 |
| 22/08/2018 | 00:43:01 | 00:43:05 | | 12:43:04 | 512 | 212 | 0 |
| | | | | | | | |
| 22/08/2018 | 01:15:42 | 01:15:46 | | 13:15:46 | 513 | 216 | 0 |
| 22/08/2018 | 01:19:34 | 01:19:38 | | | 511 | 213 | 0 |
| 22/08/2018 | 01:22:51 | 01:22:55 | | | 514 | 216 | 0 |
| 22/08/2018 | 01:23:17 | 01:23:21 | | 13:23:20 | 512 | 213 | 0 |

Silixa's handwrite log used to fill the software logs gaps

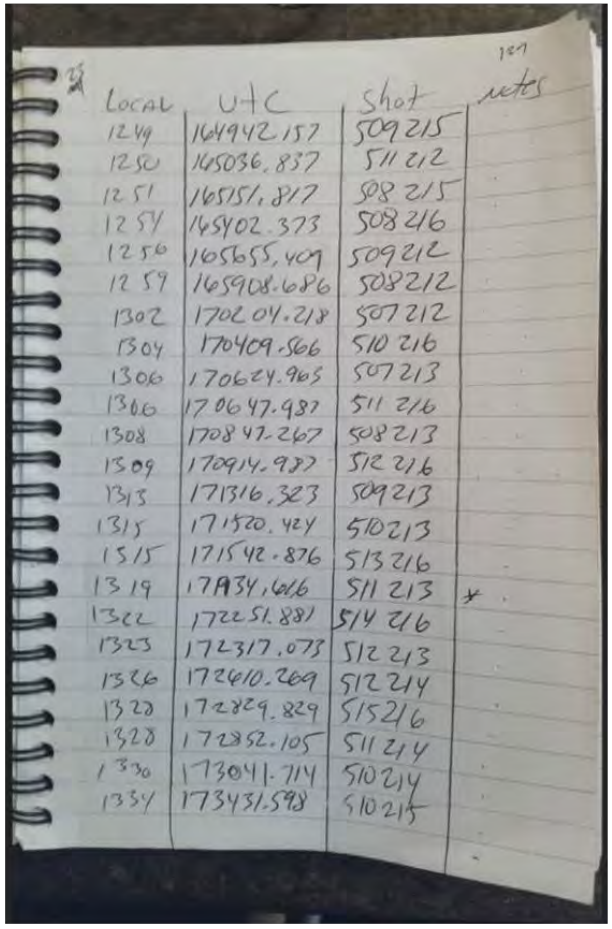


*Figure 6-4. Monitor survey – Navigation QC - Silixa's handwritten log used to fill the software logs gaps. The SeismicLink source location log provided by Emerson for some dynamite shot points is missing some values. These gaps were filled using Silixa's handwritten field log.*

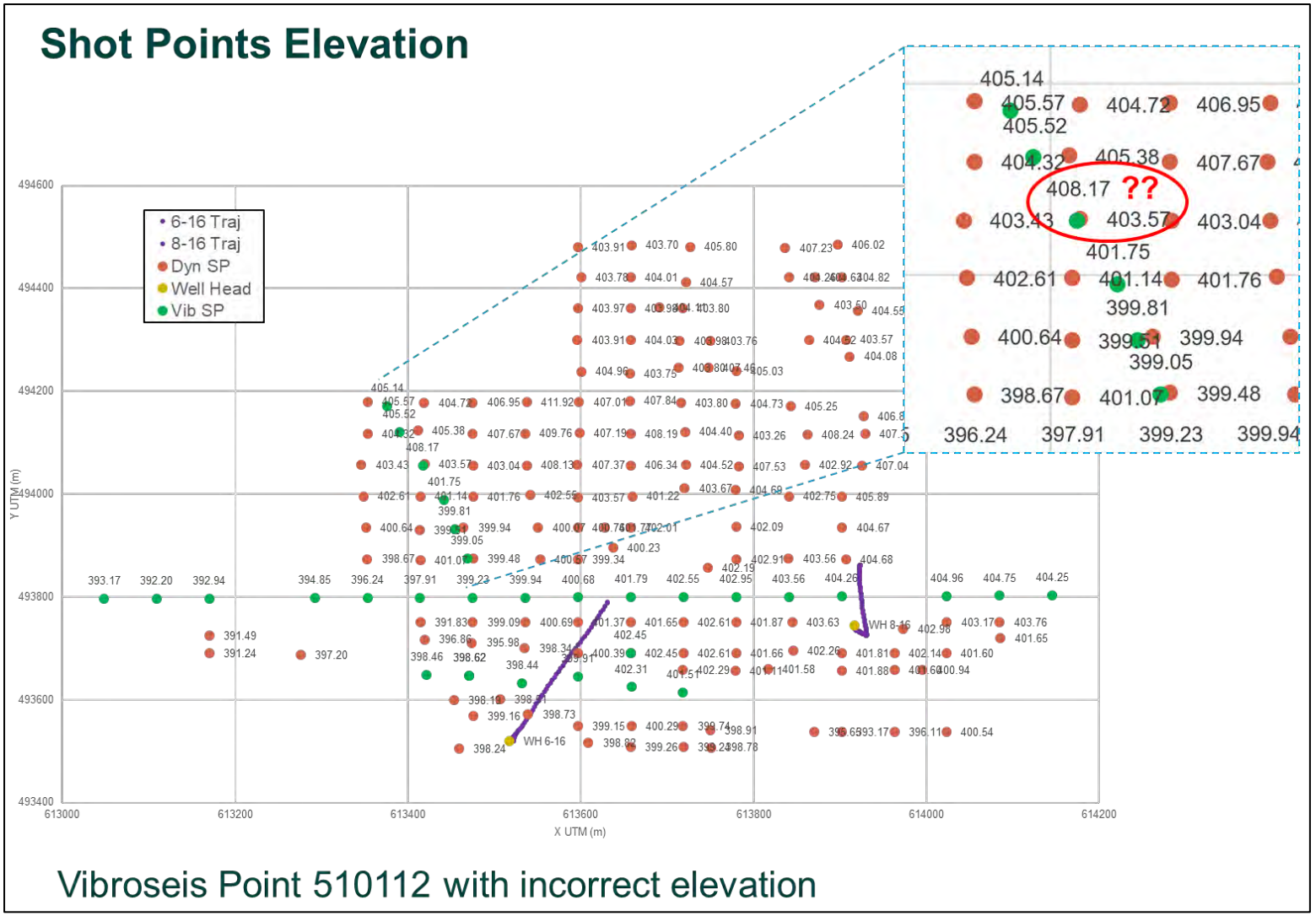


*Figure 6-5. Shot Points Elevation - At the SP 510112 the average GL elevation value recorded by the system for vibroseis is not in line with the dynamite elevation value located on the same position and, with the neighbour SP's elevation. The vibroseis elevation was corrected for this SP.*

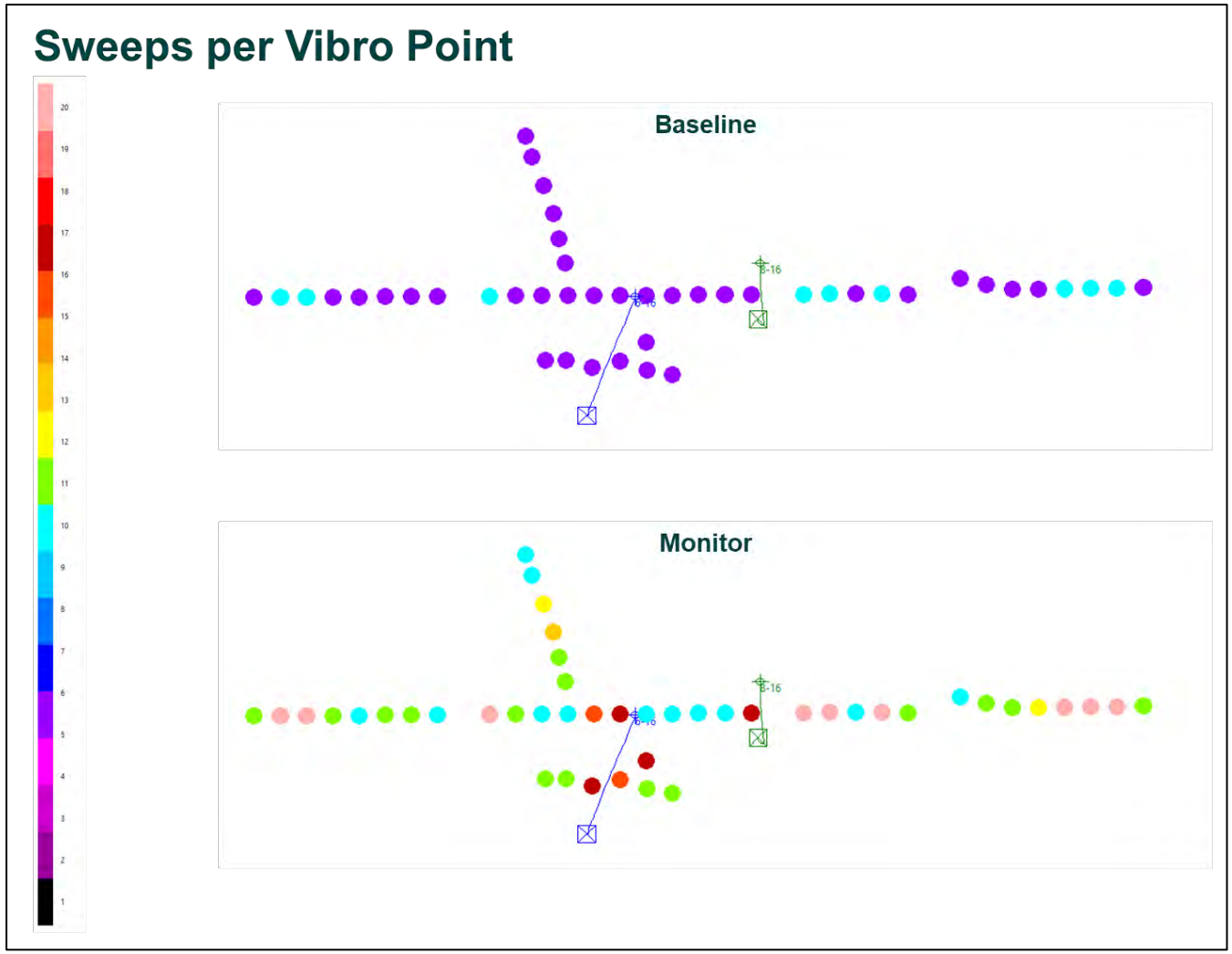


*Figure 6-6. Sweeps per Vibro Point - Baseline and monitor survey. Figure 6-6 shows the number of sweeps for each vibroseis SP. On the baseline survey 5 sweeps were acquired at locations where the vibroseis sources shook at full force and 10 sweeps at locations with lower force. On the monitor survey at least 10 sweeps were acquired at the full force locations and at least 15 with at the locations with low force or with difficult coupling.*

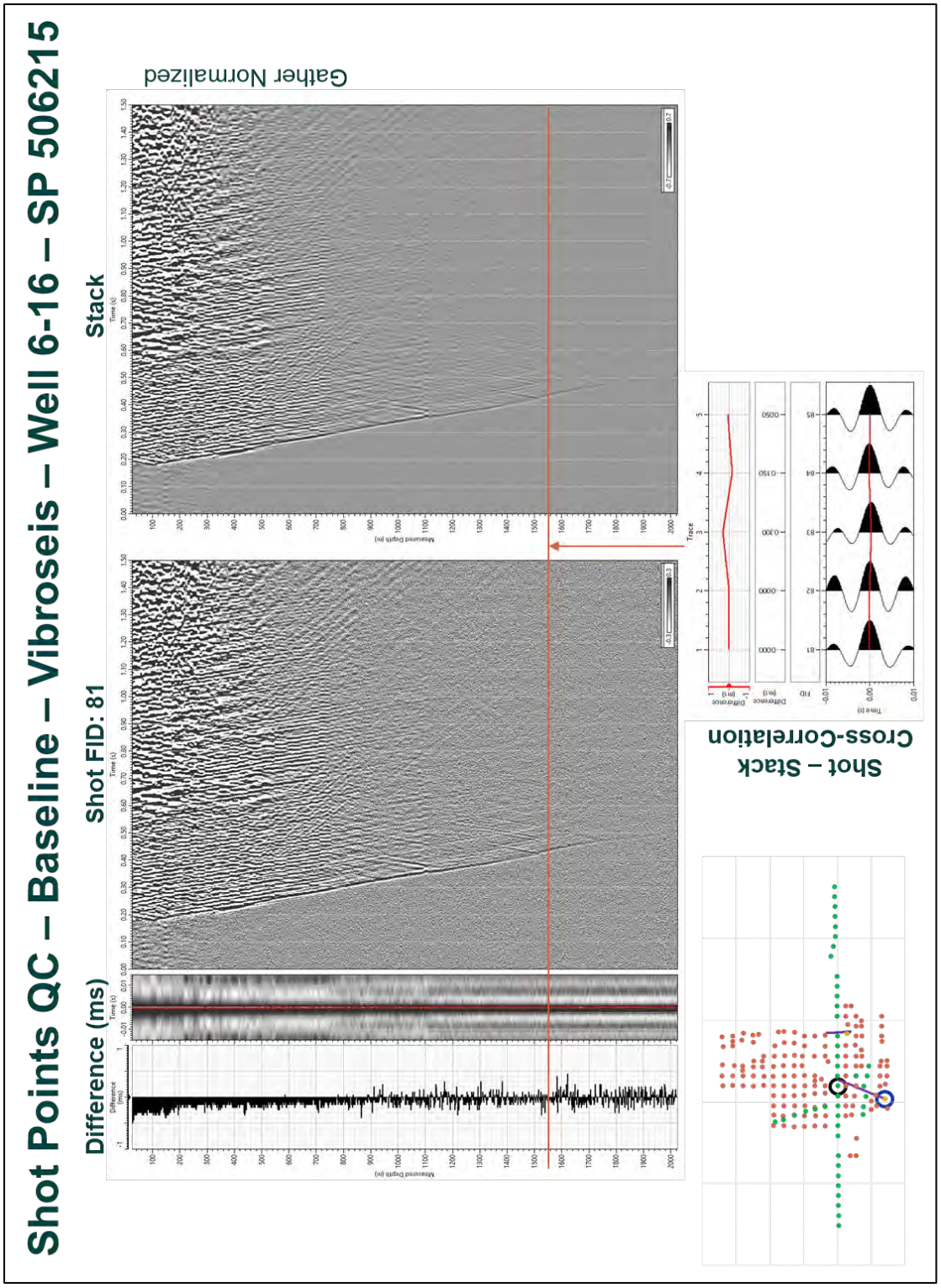


*Figure 6-7. Shot Points QC – Baseline – Vibroseis – Well 6-16 – SP 506215 - Cross-correlation between the shot and stack.*

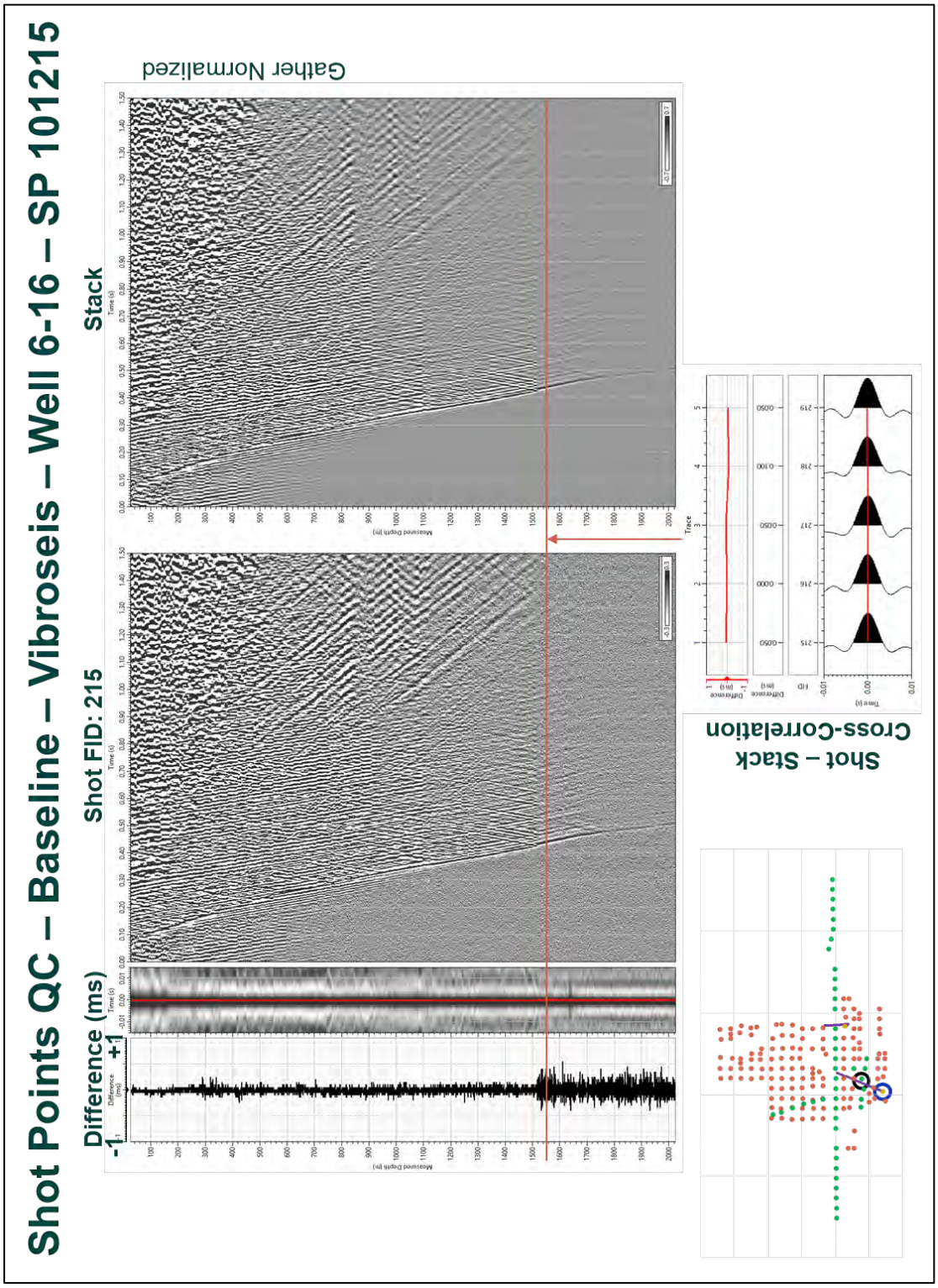


*Figure 6-8. Shot Points QC – Baseline – Vibroseis – Well 6-16 – SP 101215 - Cross-correlation between the shot and stack.*

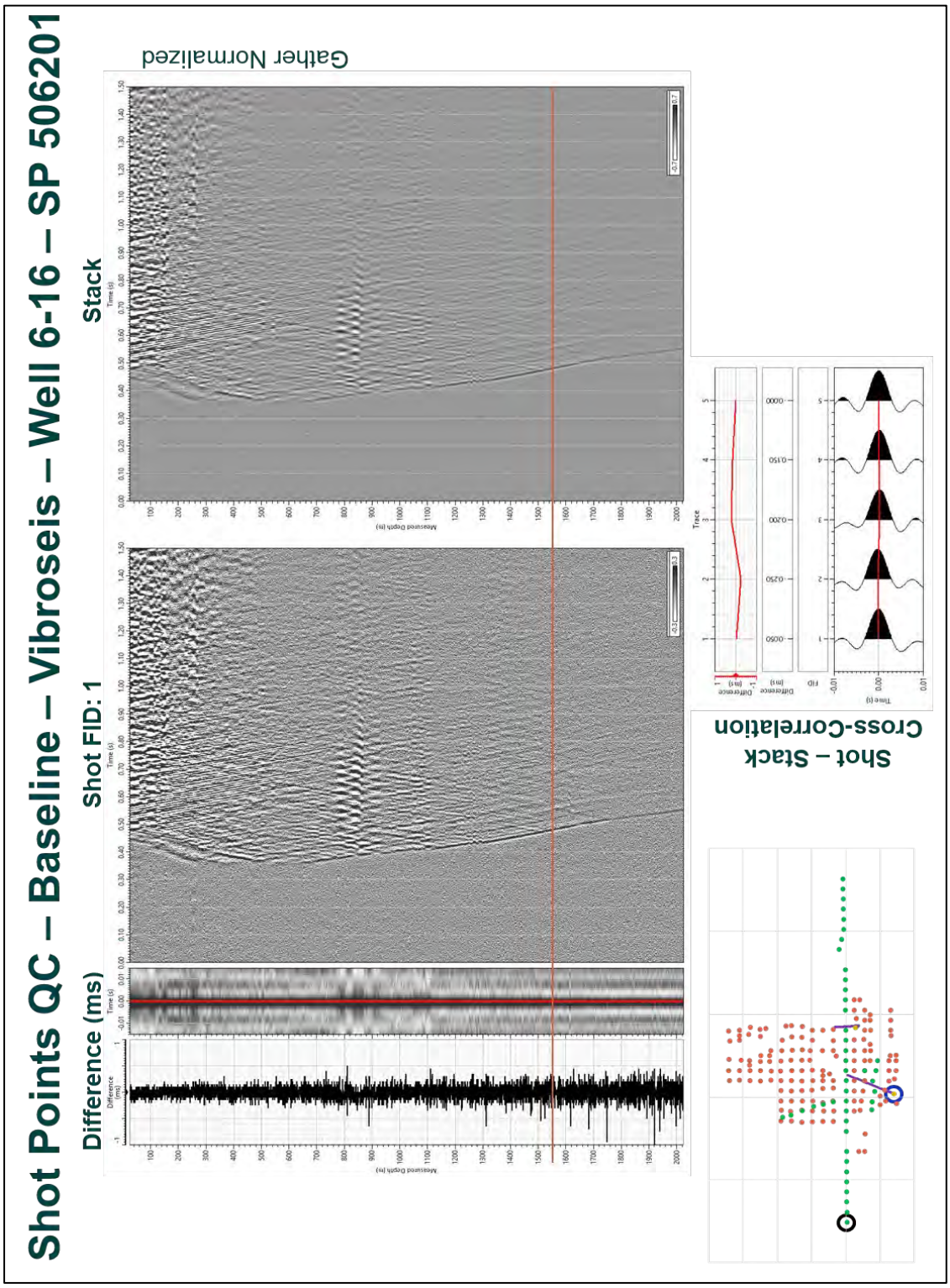


*Figure 6-9. Shot Points QC – Baseline – Vibroseis – Well 6-16 – SP 506201 - Cross-correlation between the shot and stack.*

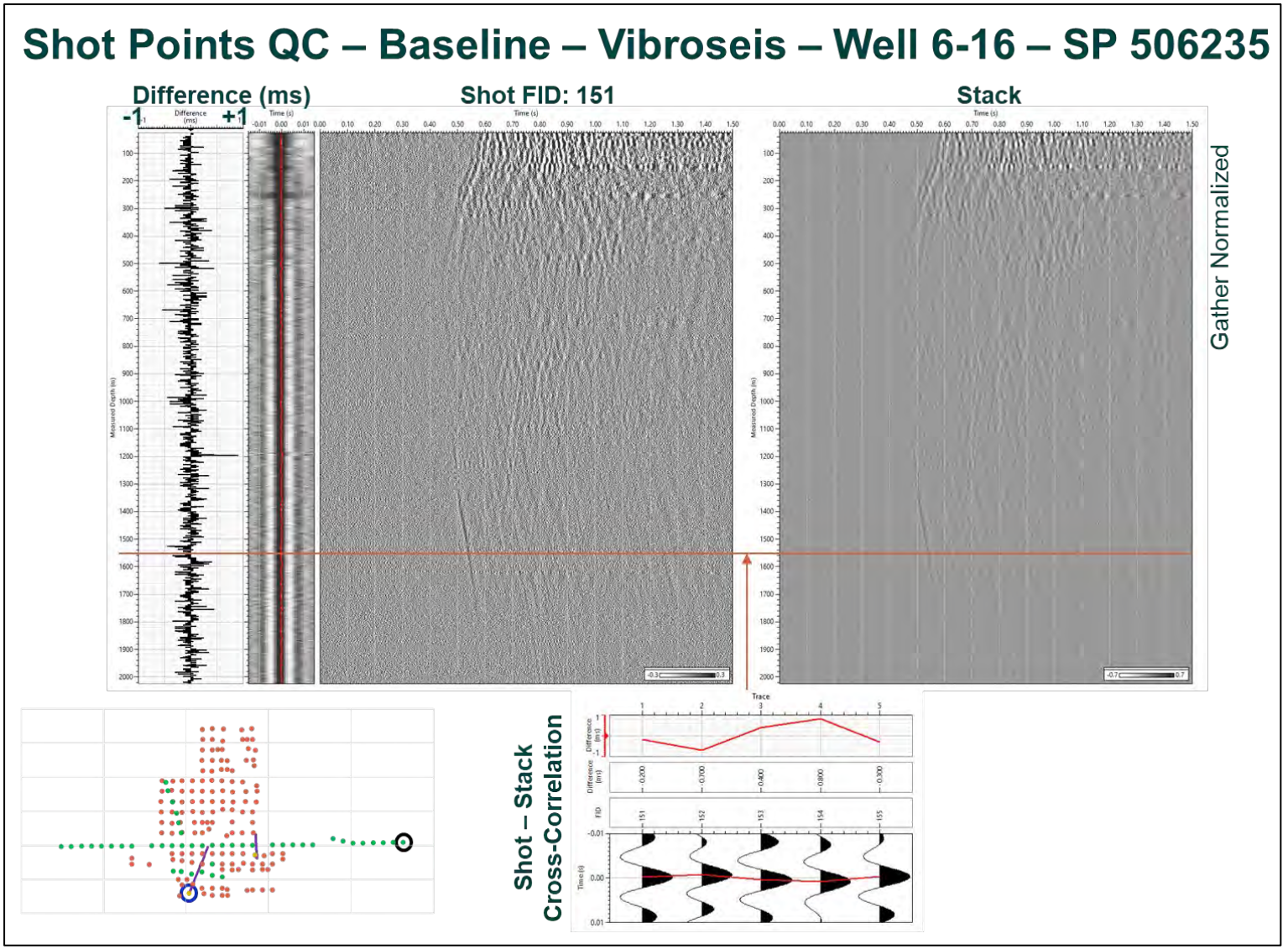


*Figure 6-10. Shot Points QC – Baseline – Vibroseis – Well 6-16 – SP 506235 - Cross-correlation between the shot and stack.*

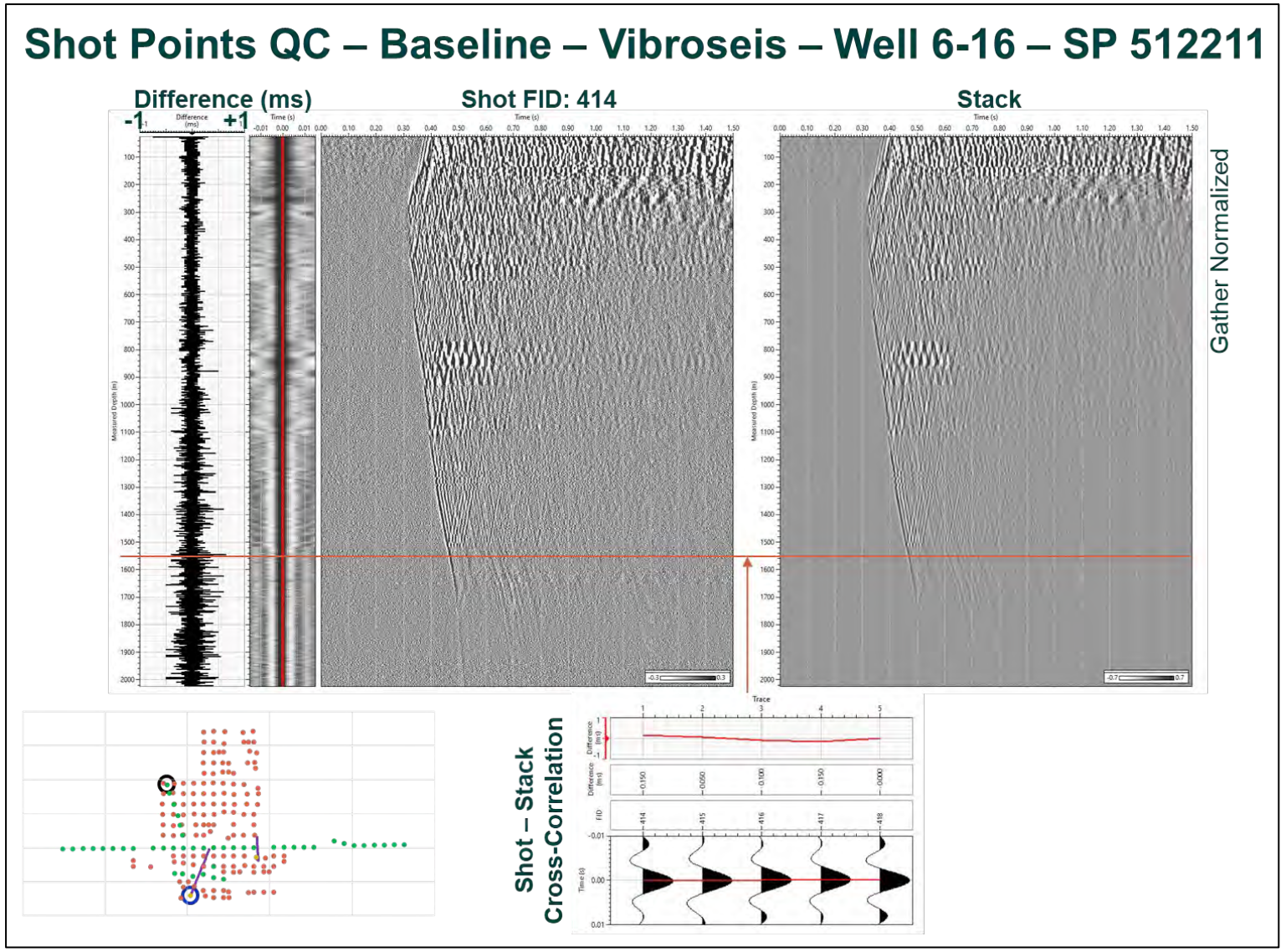


*Figure 6-11. Shot Points QC – Baseline – Vibroseis – Well 6-16 – SP 512211 - Cross-correlation between the shot and stack.*

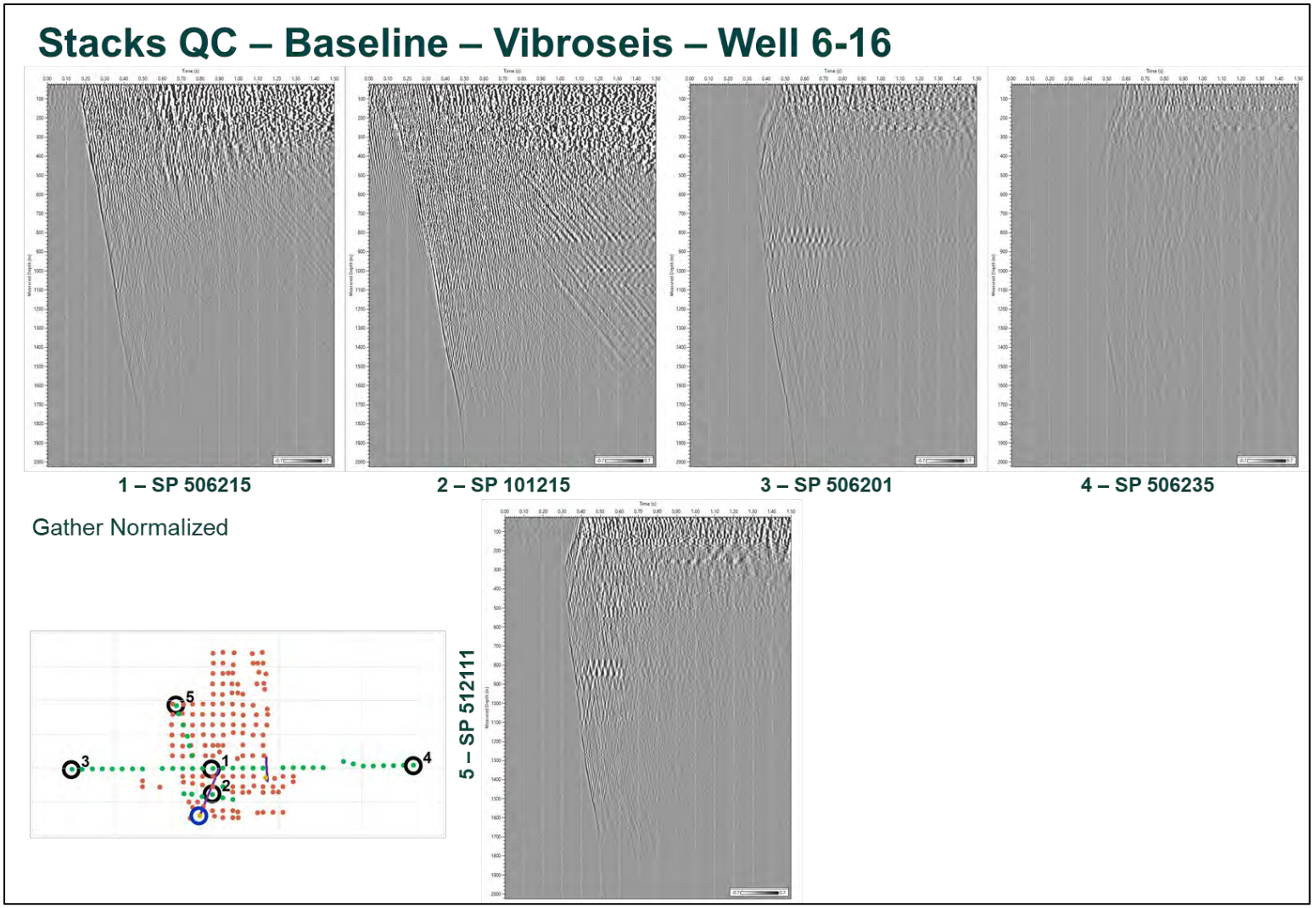


*Figure 6-12. Stacks QC – Baseline – Vibroseis – Well 6-16 - Stack in time domain. Figure 6-12 presents a QC of the five stacks presented above.*

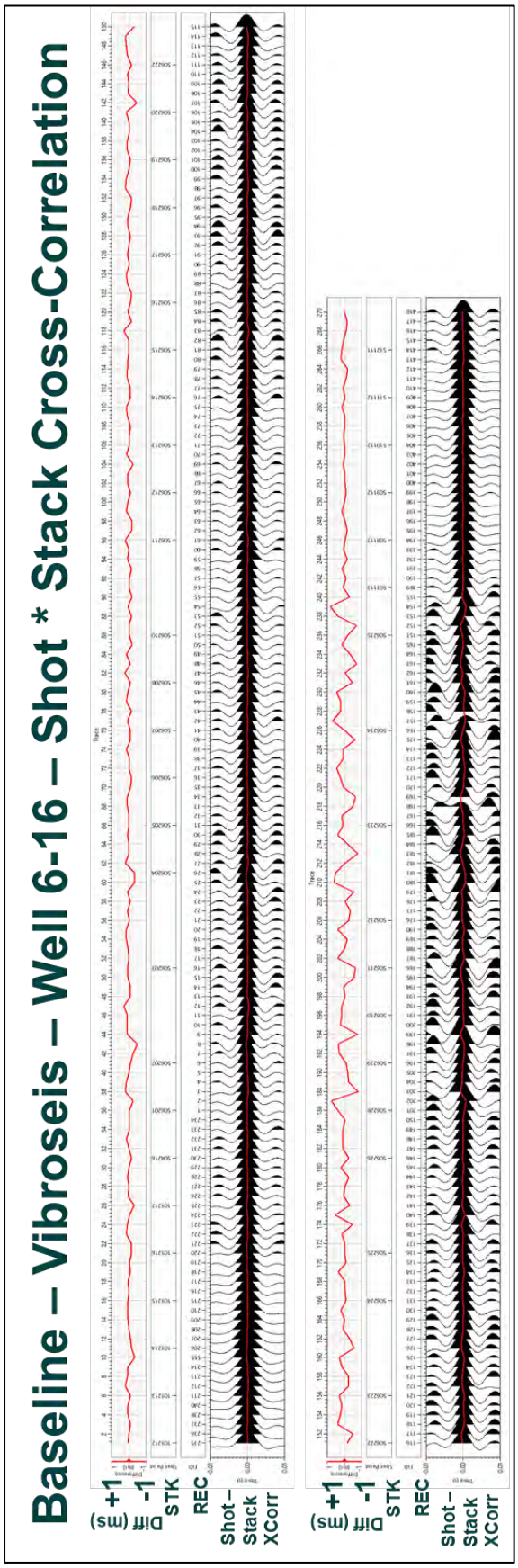


*Figure 6-13. Baseline – Vibroseis – Well 6-16 – Shot * Stack Cross-Correlation - All the shots at 1550 m MD. This figure shows the shot-stack cross-correlation wavelet (bottom row) at 1550 m MD and the time difference (top row) for all the shots of the well 6-16 baseline survey. Time shifts between them due to source subsidence were not noticed in the data above. The SPs on the far eastern side (506229 to 506235) have a lower shot-stack correlation due to the offset and weaker SNR.*

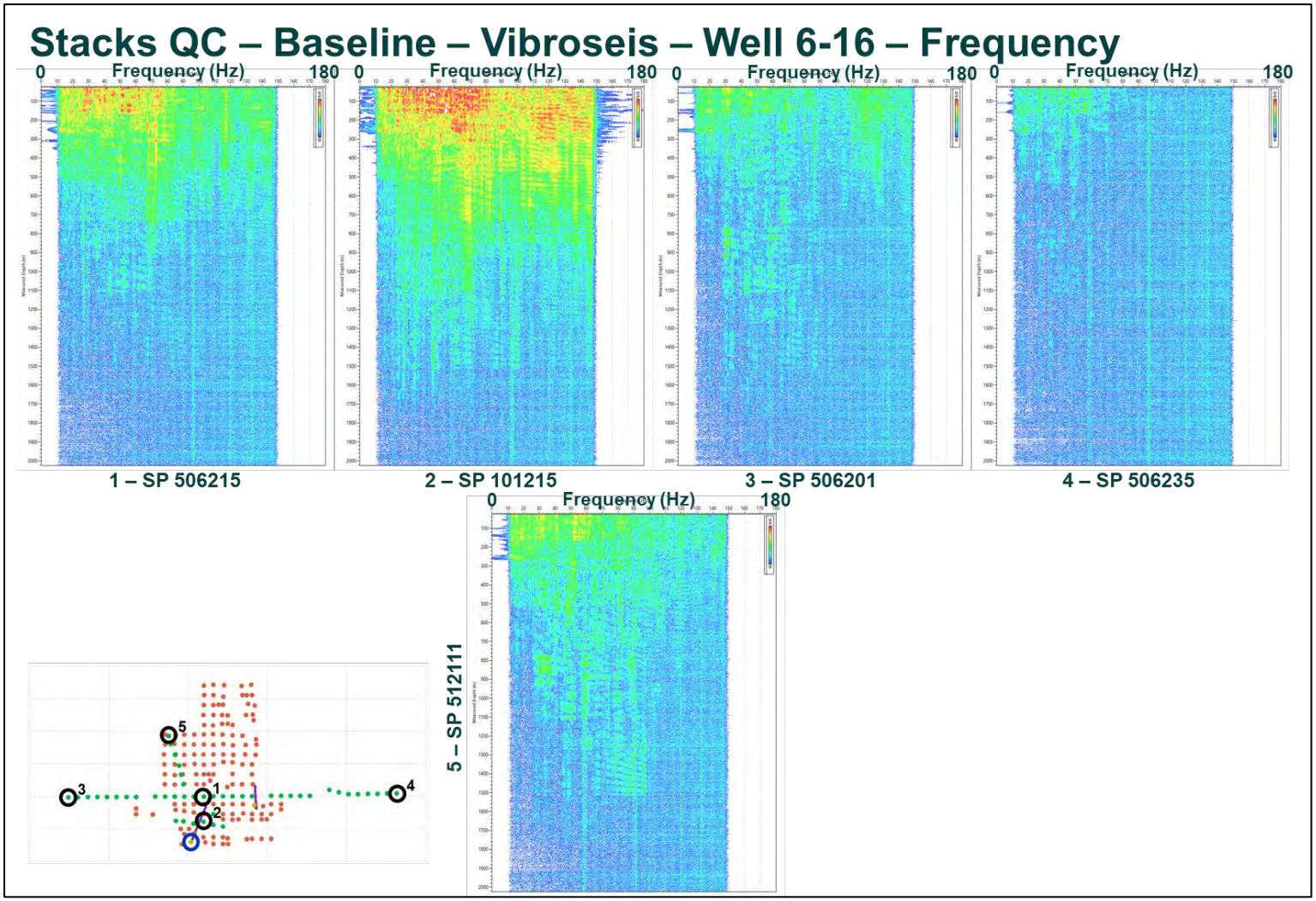


*Figure 6-14. Stacks QC – Baseline – Vibroseis – Well 6-16 – Frequency - Stack in frequency domain. This figure shows the same data from figure 6-12 in the frequency domain. The noise level increases with frequency and the main frequency bandwidth is below 90 Hz.*

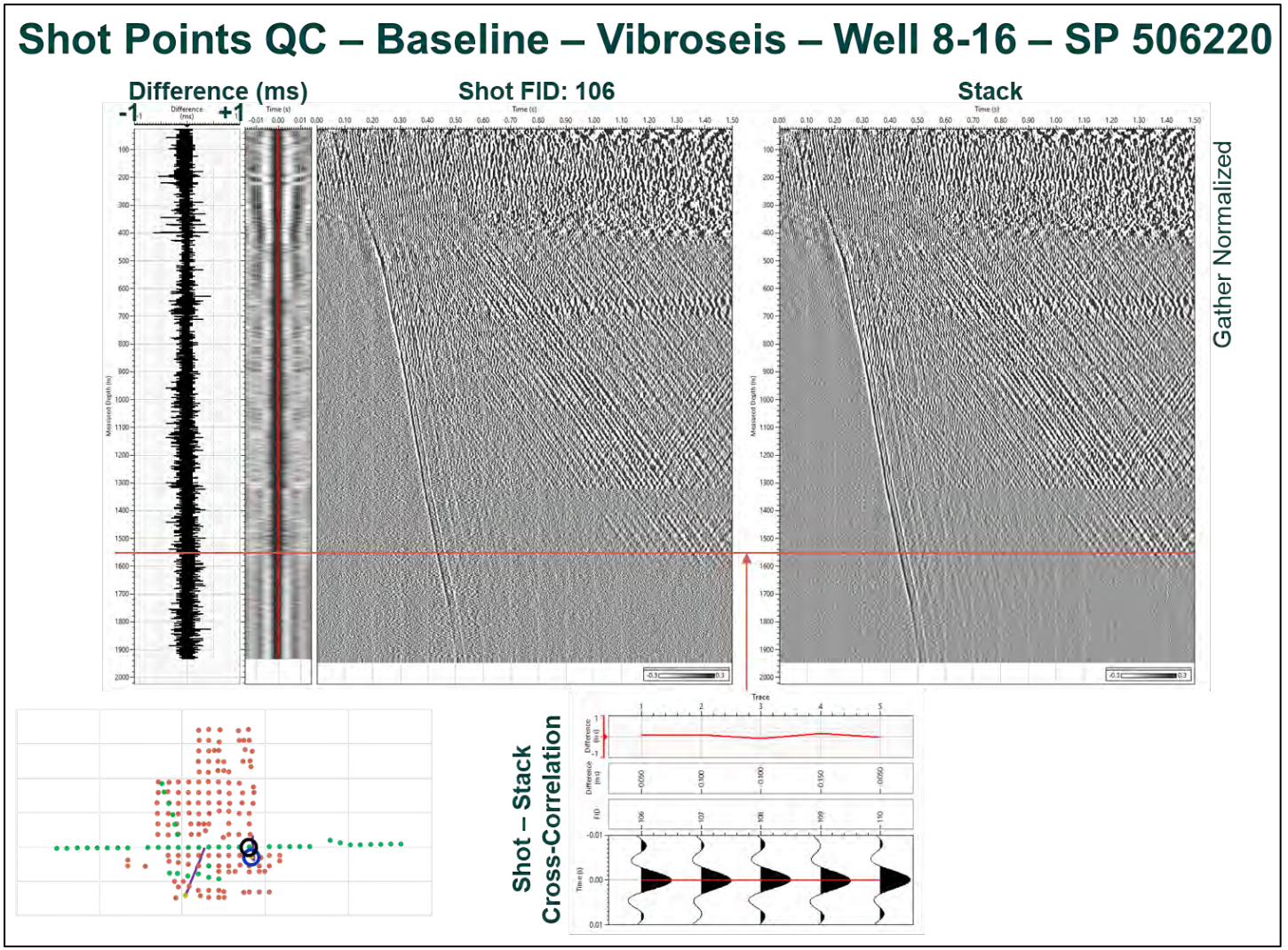


*Figure 6-15. Shot Points QC – Baseline – Vibroseis – Well 8-16 – SP 506220 - Cross-correlation between the shot and stack.*

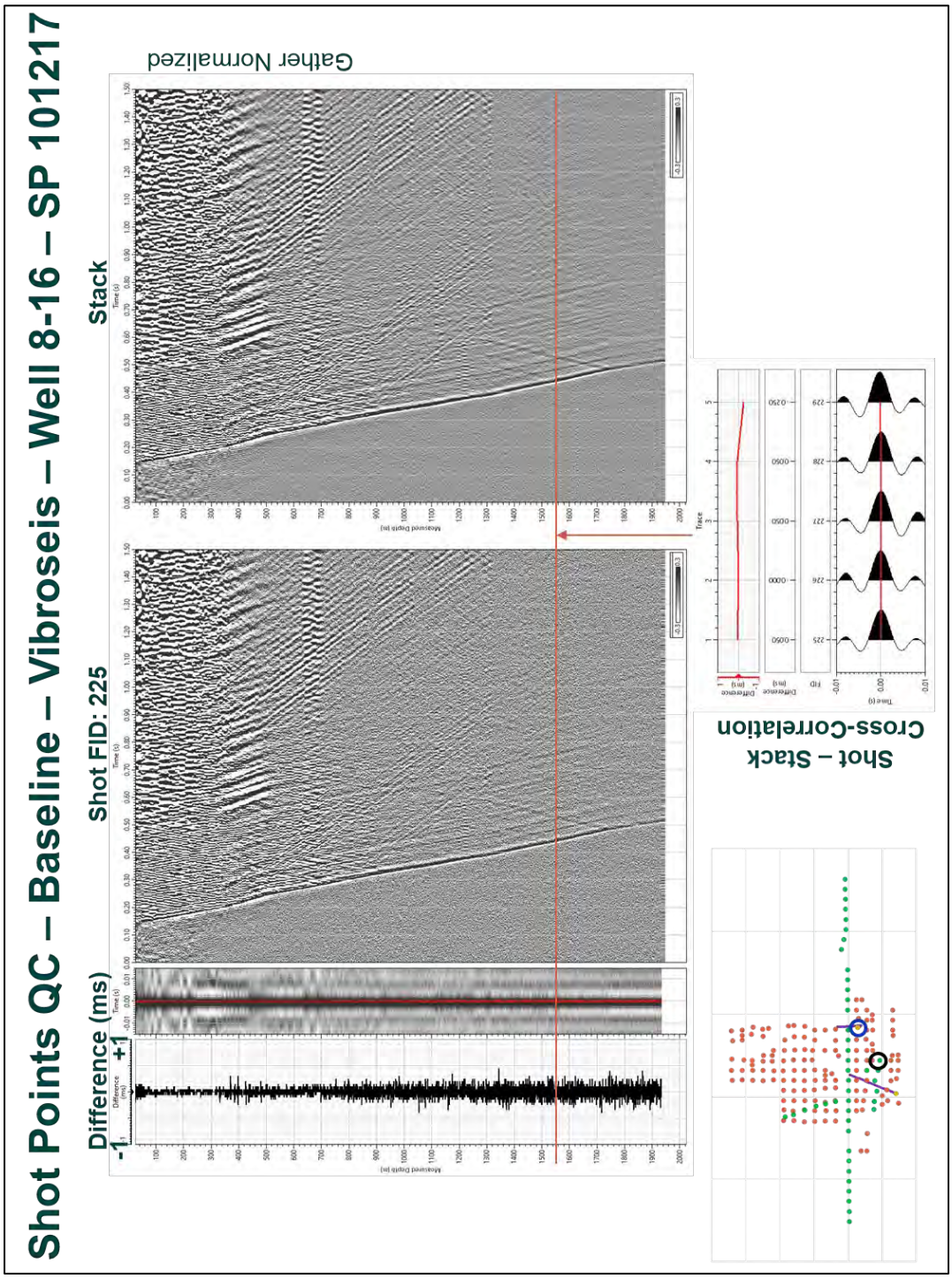


*Figure 6-16. Shot Points QC – Baseline – Vibroseis – Well 8-16 – SP 101217 - Cross-correlation between the shot and stack.*

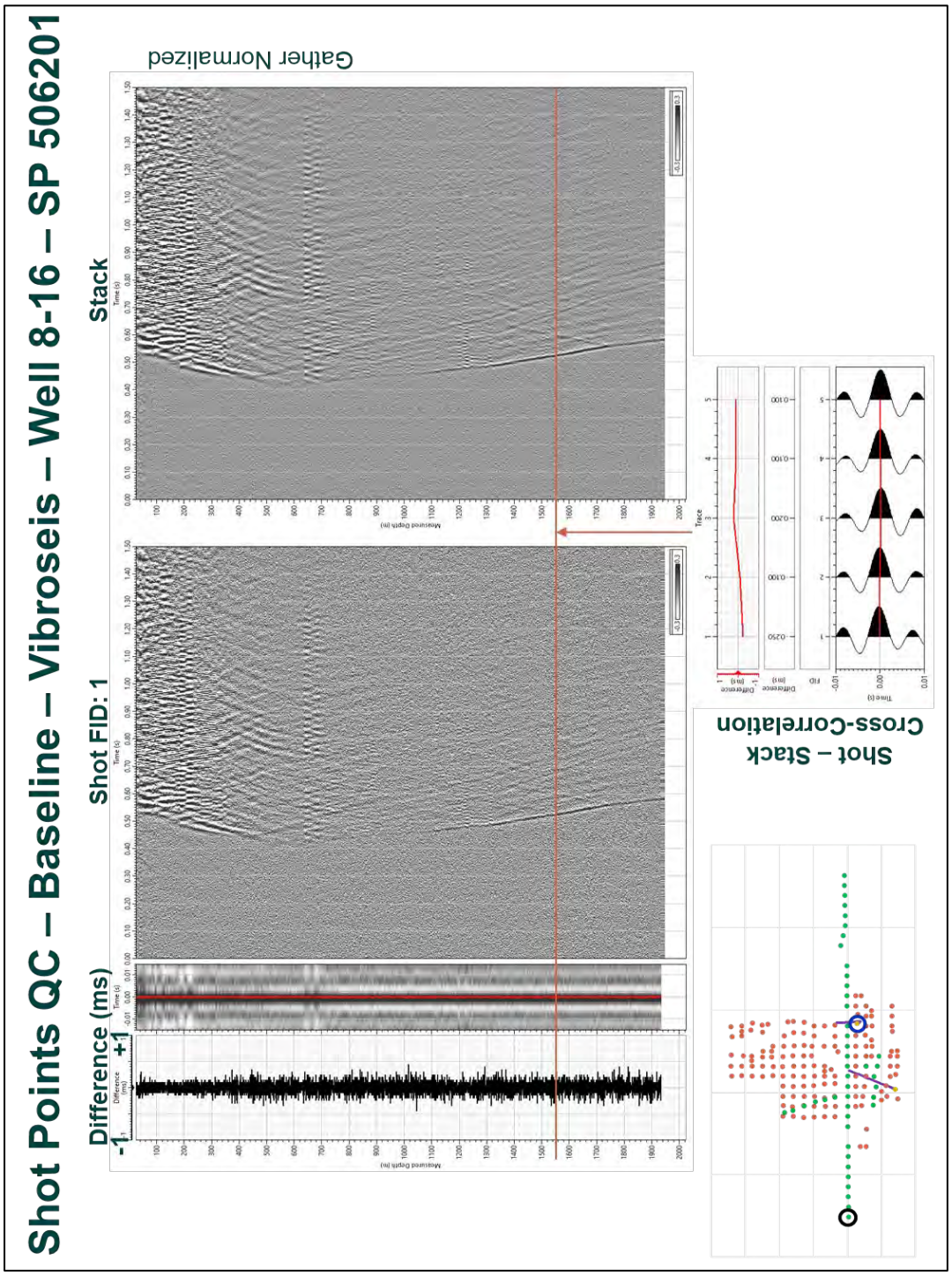


*Figure 6-17. Shot Points QC – Baseline – Vibroseis – Well 8-16 – SP 506201 - Cross-correlation between the shot and stack.*

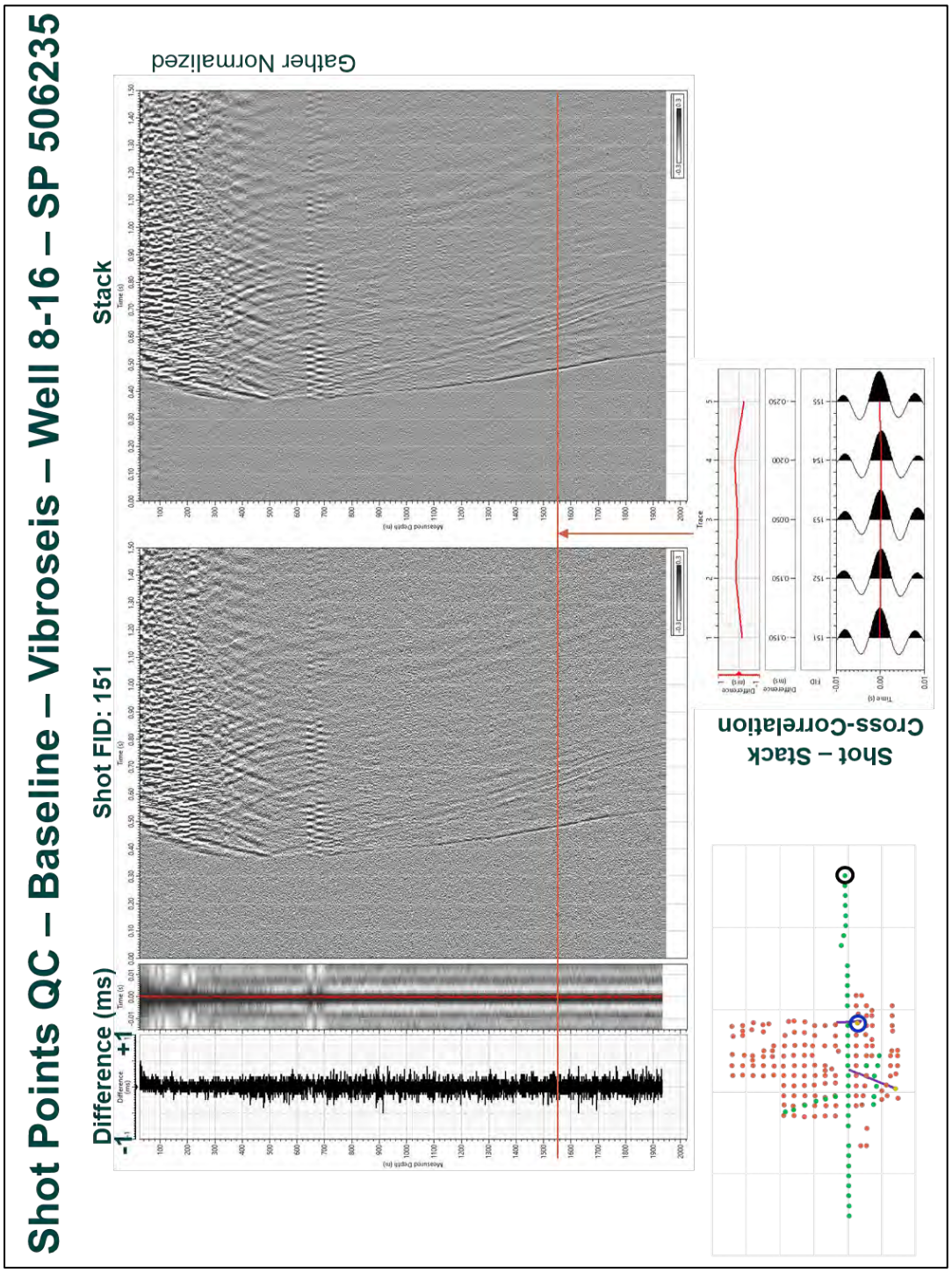


*Figure 6-18. Shot Points QC – Baseline – Vibroseis – Well 8-16 – SP 506235 - Cross-correlation between the shot and stack.*

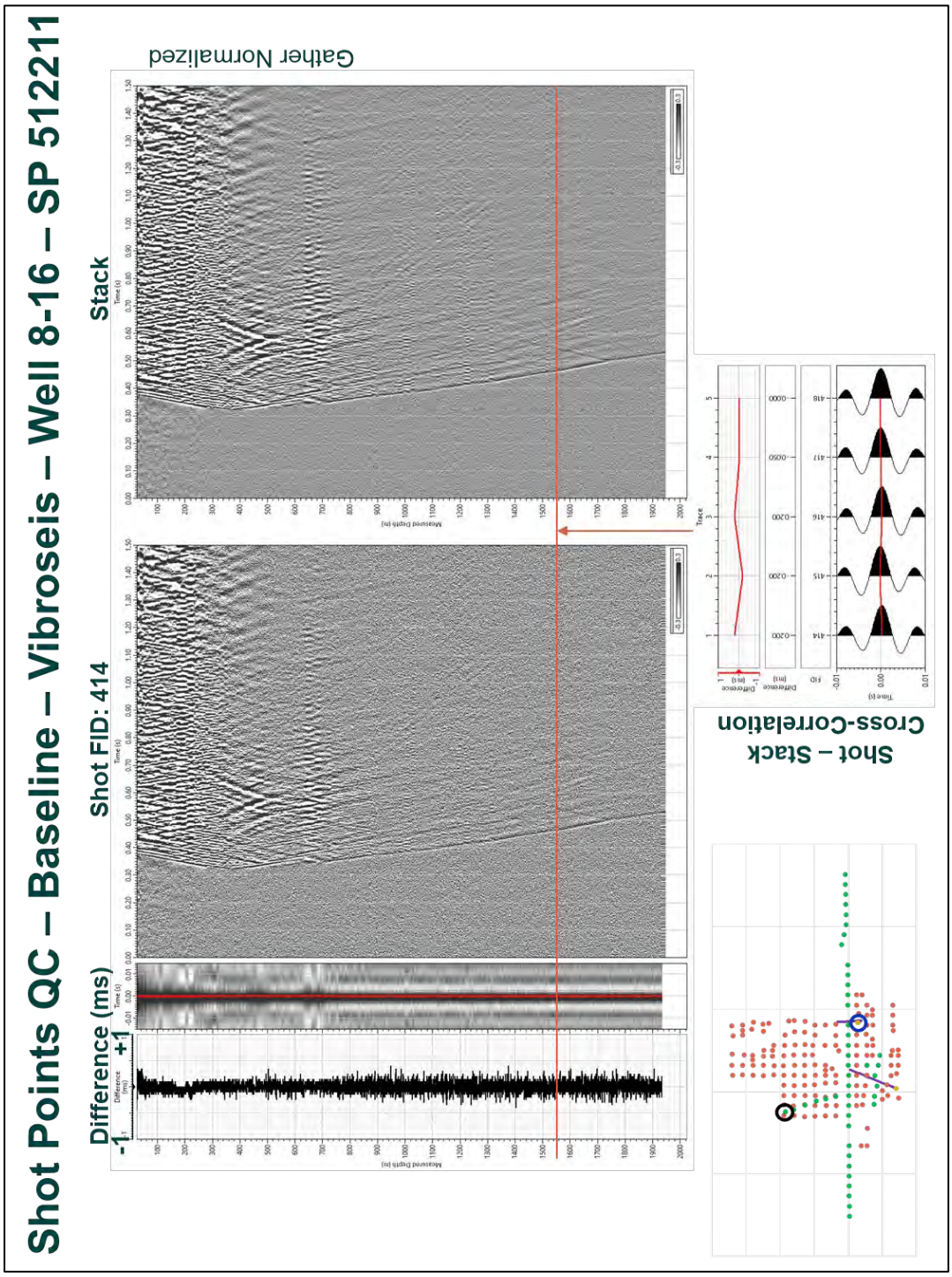


*Figure 6-19. Shot Points QC – Baseline – Vibroseis – Well 8-16 – SP 512211 - Cross-correlation between the shot and stack.*

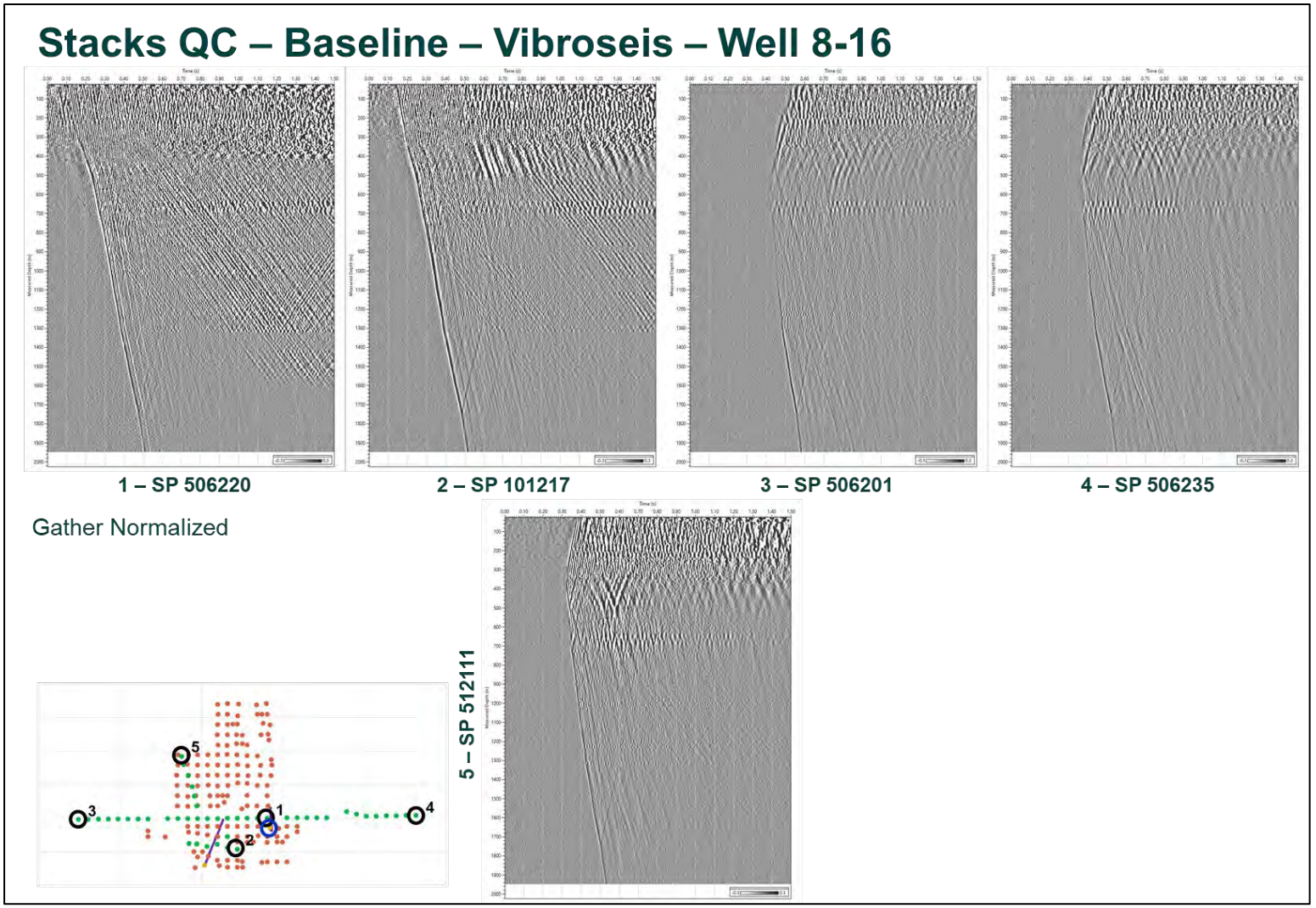


*Figure 6-20. Stacks QC – Baseline – Vibroseis – Well 8-16 - Stack in time domain. It shows a QC of the five stacks.*

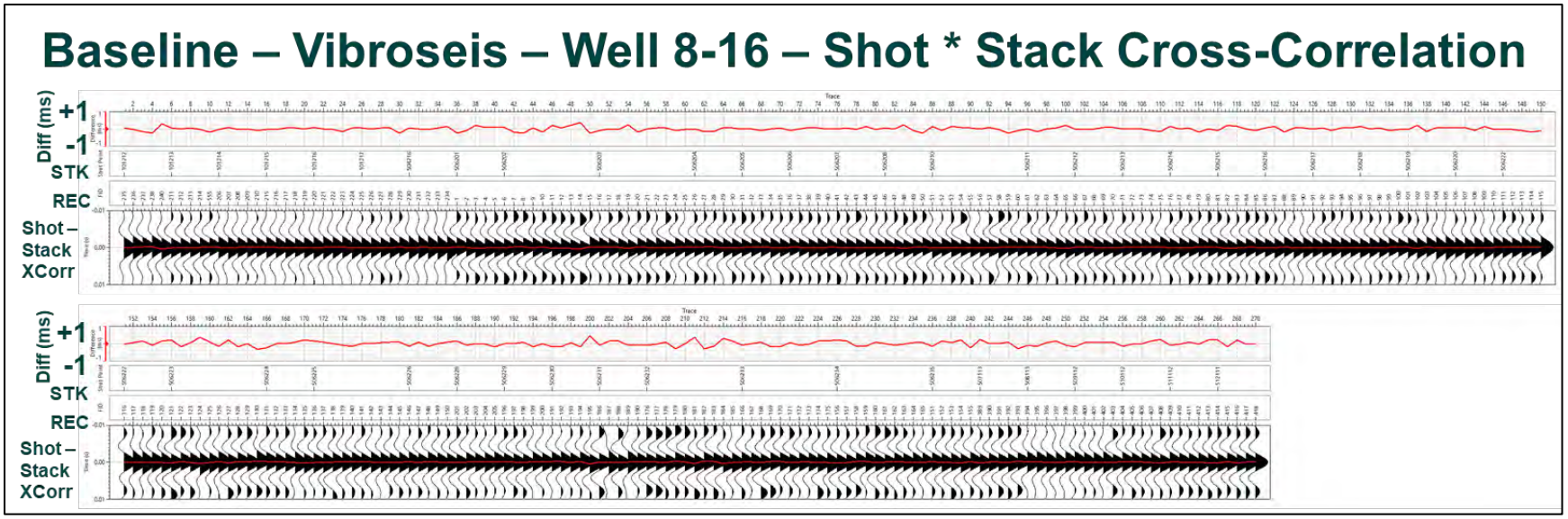


*Figure 6-21. Baseline – Vibroseis – Well 8-16 – Shot * Stack Cross-Correlation - All the shots at 1550 m MD – This figure shows the cross-correlation shot-stack wavelet (bottom row) at 1550 m MD and the time difference (top row) for all the shots of well 8-16, baseline survey. No time shift due to source subsidence was noticed in the data above. The cross-correlation between the shot and stack at well 8-16 is better than at well 6-16 due to a better SNR.*

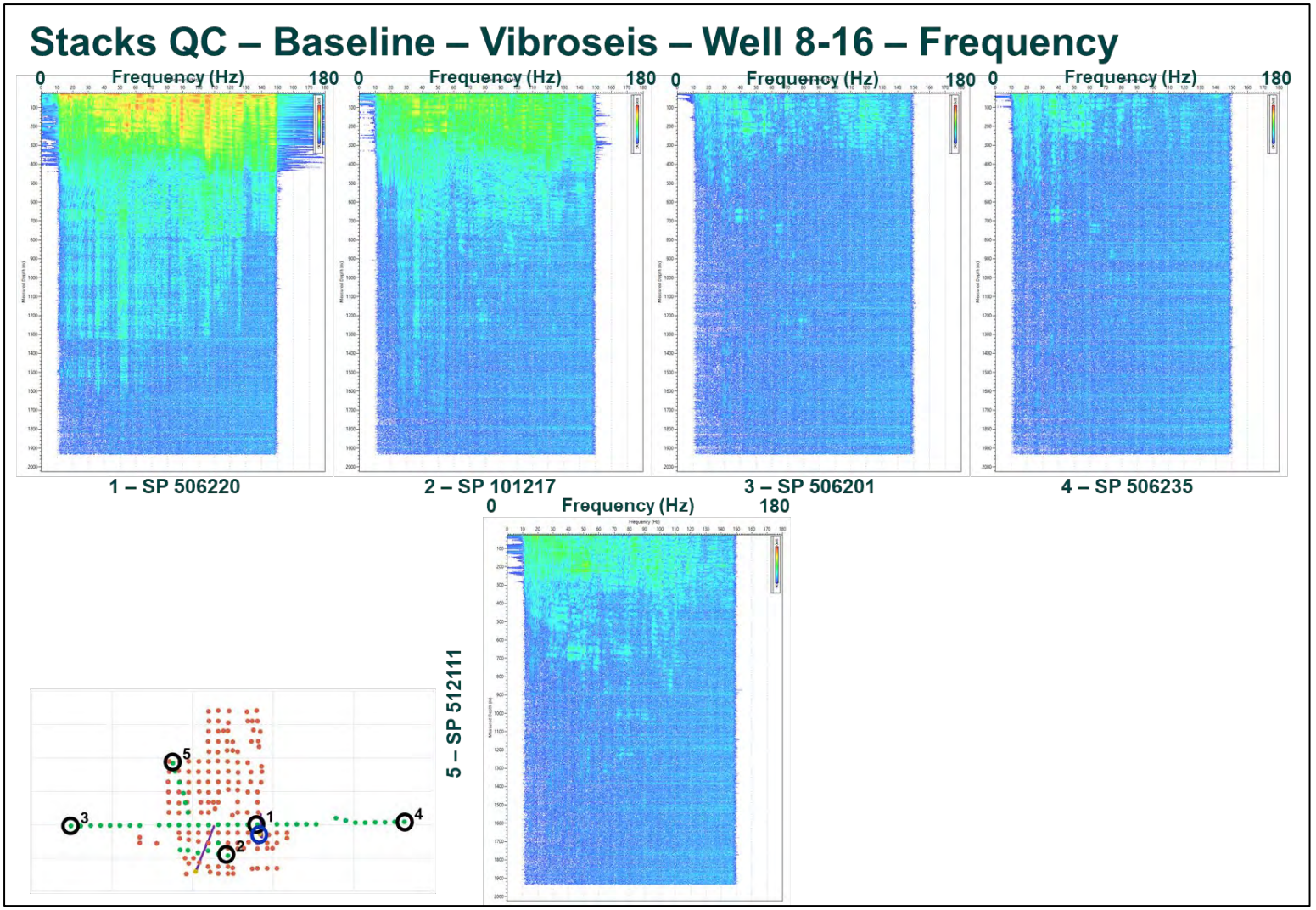


*Figure 6-22. Stacks QC – Baseline – Vibroseis – Well 8-16 – Frequency - Stack in frequency domain. Here we present the same data from figure 6-20 in the frequency domain. The noise level increases with frequency and the main frequency bandwidth is below 110 Hz.*

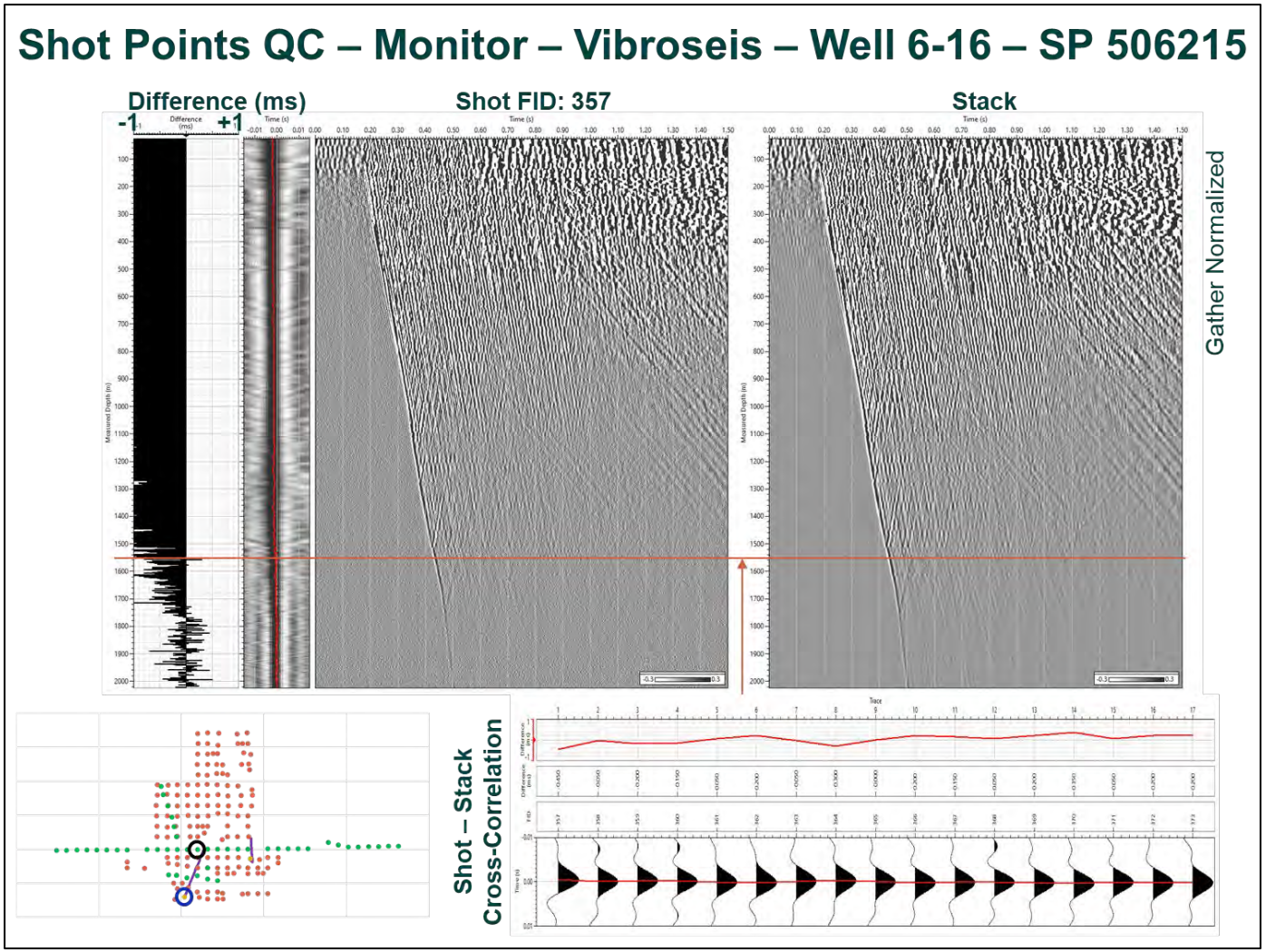


*Figure 6-23. Shot Points QC – Monitor – Vibroseis – Well 6-16 – SP 506215 - Cross-correlation between the shot and stack.*

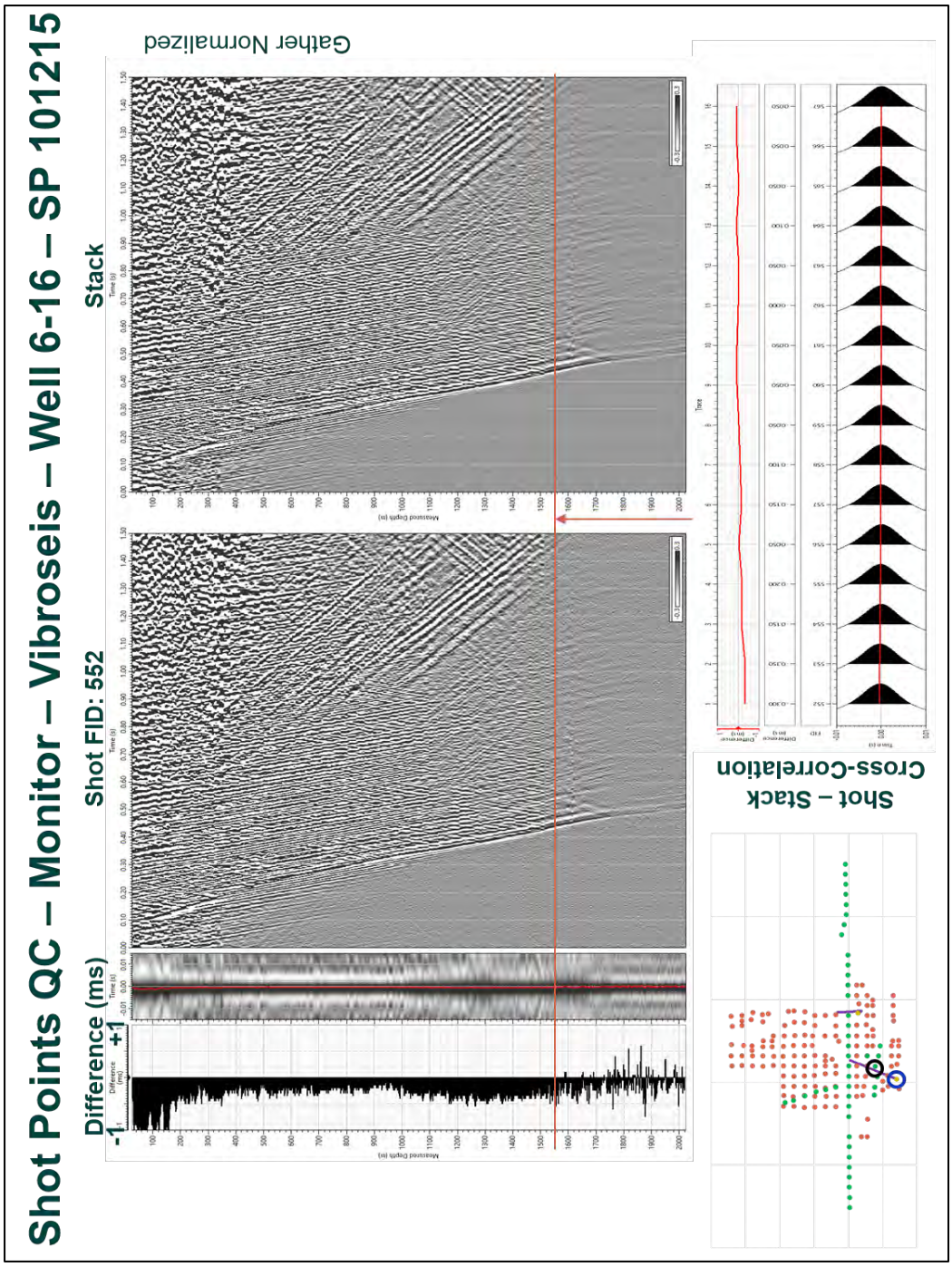


*Figure 6-24. Shot Points QC – Monitor – Vibroseis – Well 6-16 – SP 101215 - Cross-correlation between the shot and stack.*

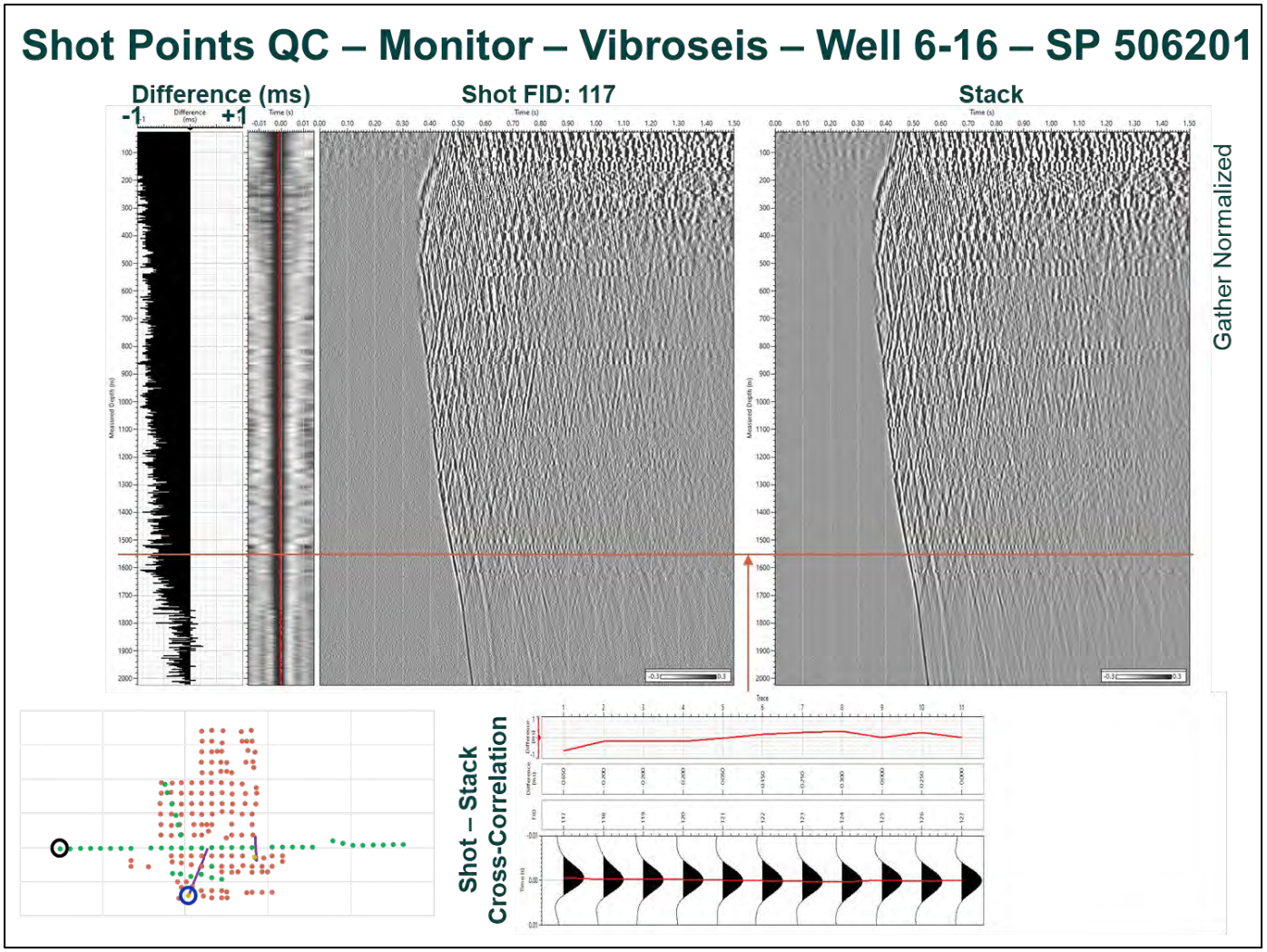


*Figure 6-25. Shot Points QC – Monitor – Vibroseis – Well 6-16 – SP 506201 - Cross-correlation between the shot and stack.*

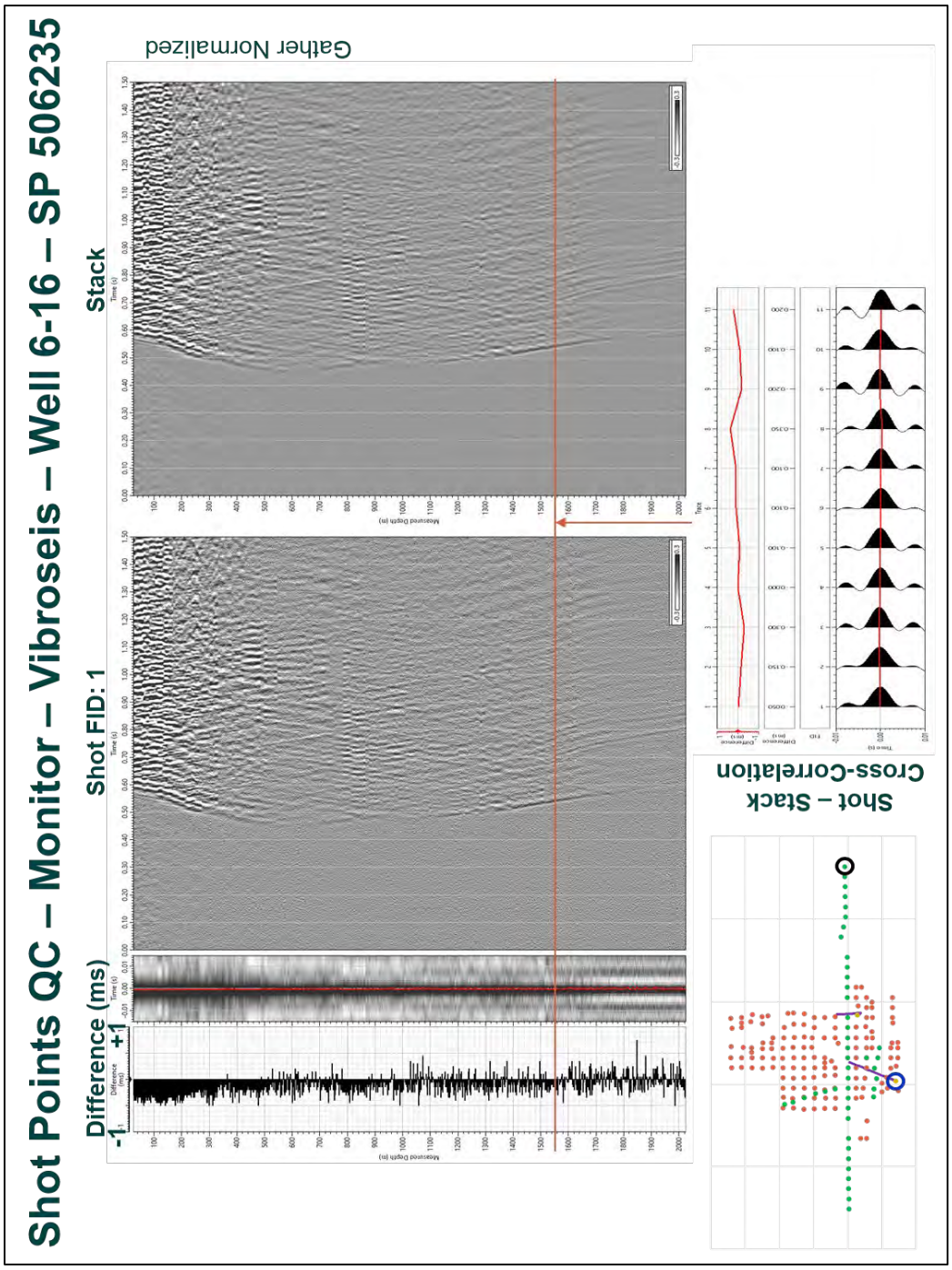


*Figure 6-26. Shot Points QC – Monitor – Vibroseis – Well 6-16 – SP 506235 - Cross-correlation between the shot and stack.*

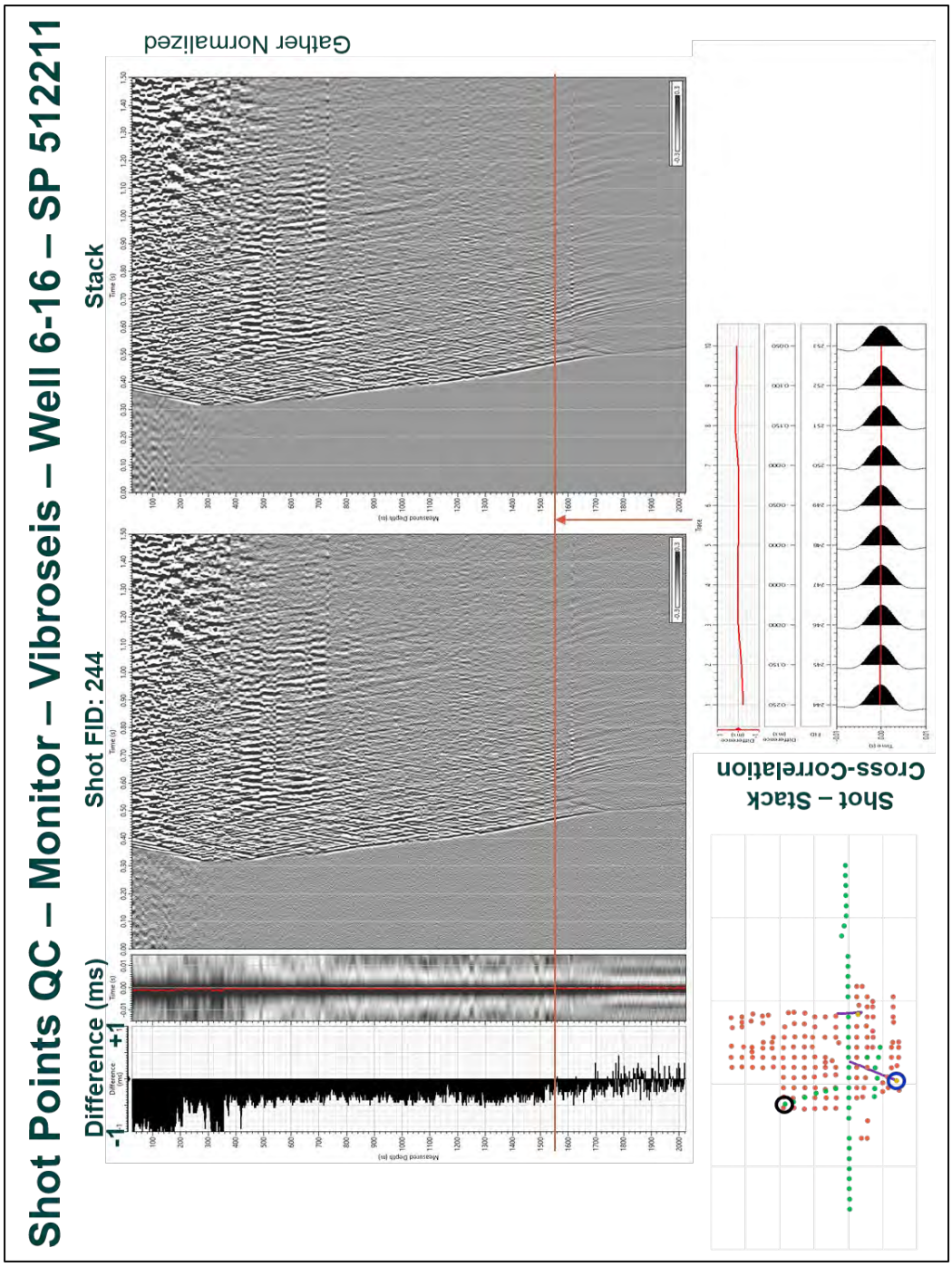


*Figure 6-27. Shot Points QC – Monitor – Vibroseis – Well 6-16 – SP 512211 - Cross-correlation between the shot and stack.*

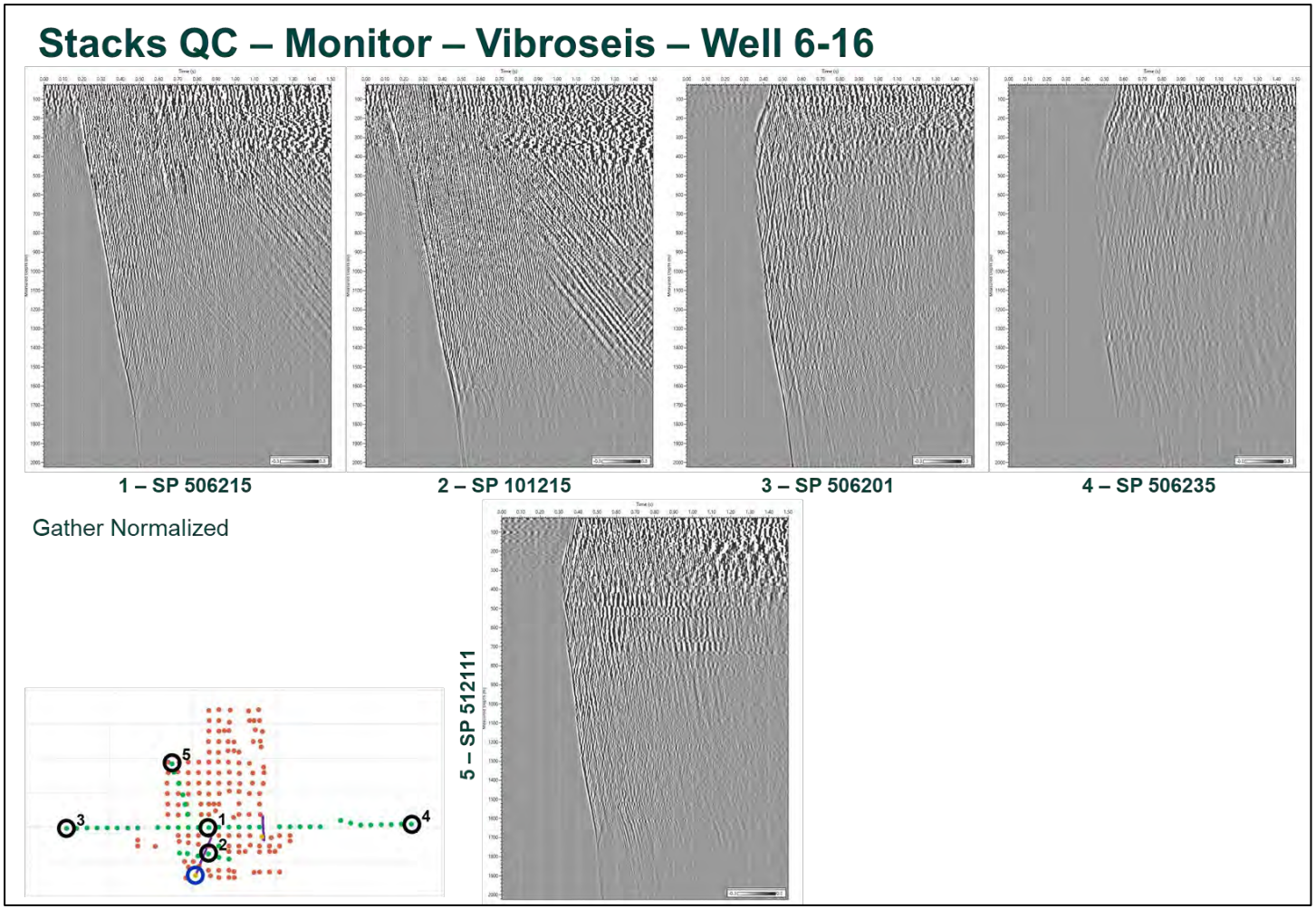


*Figure 6-28. Stacks QC – Monitor – Vibroseis – Well 6-16 - Stack in time domain. It presents the QC of the five stacks. It shows a QC of the five stacks.*

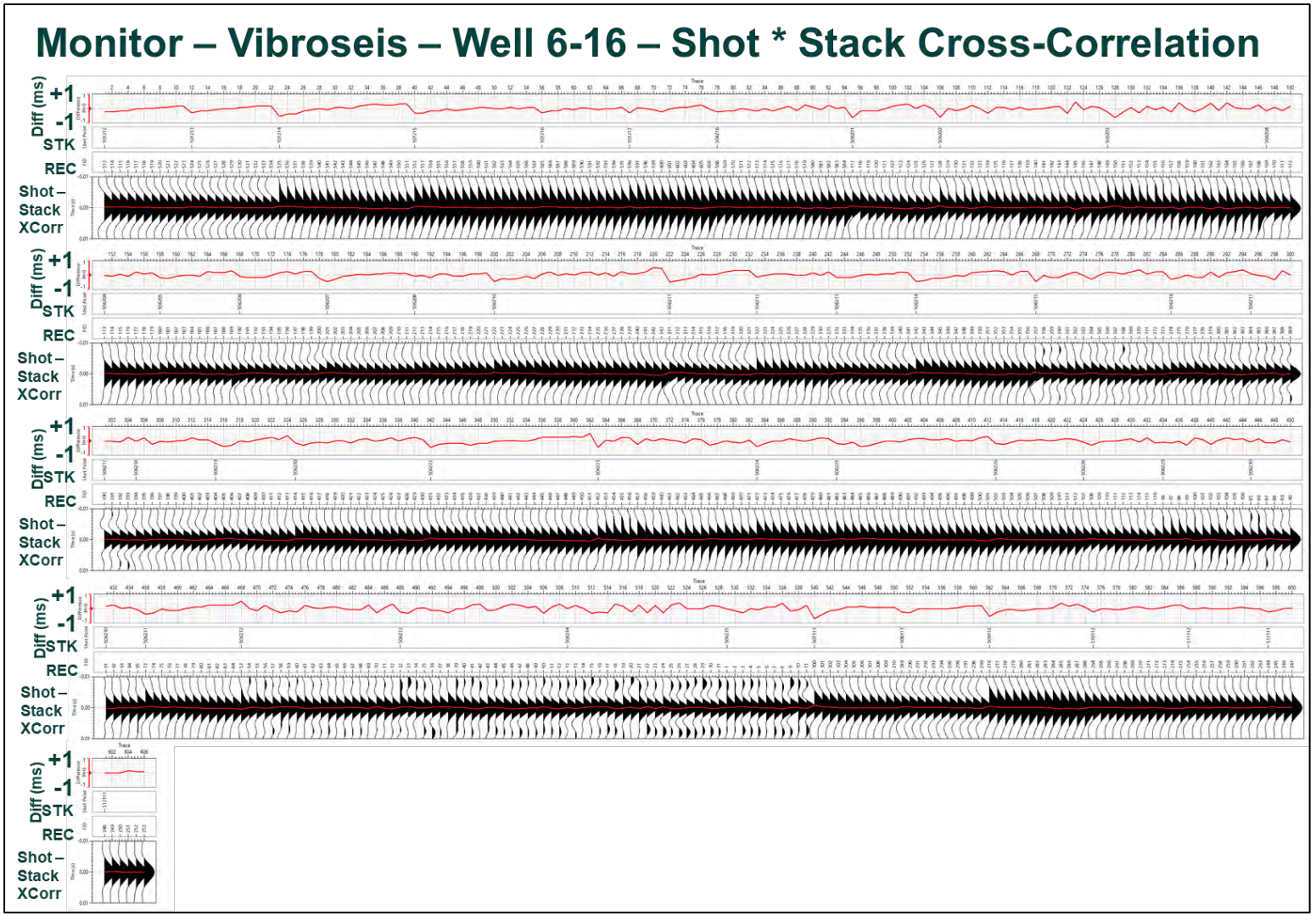


*Figure 6-29. Monitor – Vibroseis – Well 6-16 – Shot * Stack Cross-Correlation - All the shots at 1550 m MD. This figure shows the shot-stack cross-correlation wavelet (bottom row) at 1550 m MD and the time difference (top row) for all the shots of well 8-16, monitor survey. A pattern of small time shifts due to source subsidence was noticed between the shots, more obvious on the western part, but is below 0.5 ms.*

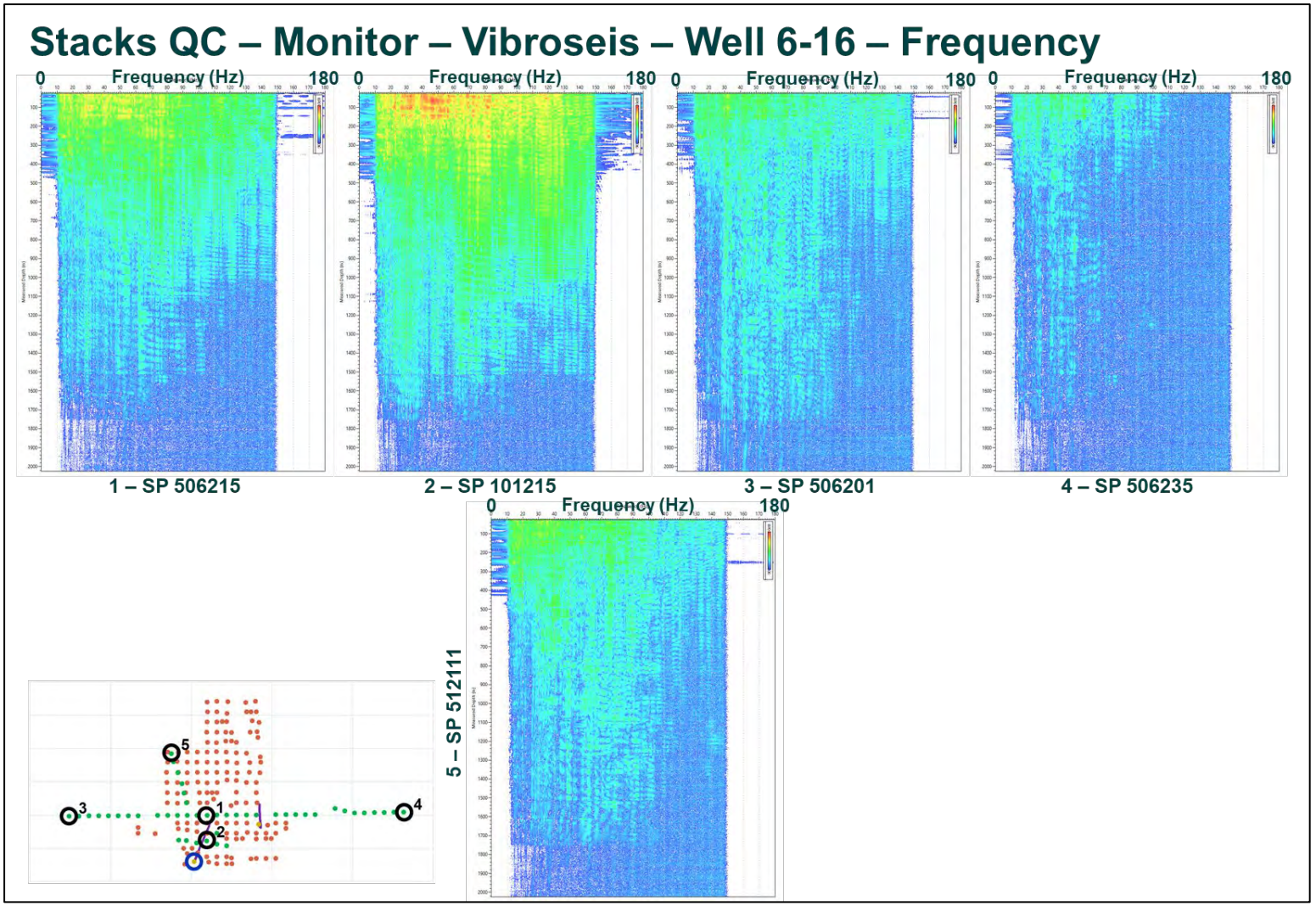


*Figure 6-30. Stacks QC – Monitor – Vibroseis – Well 6-16 – Frequency - Stack in frequency domain. This figure shows the same data from figure 6-28 in the frequency domain. The noise level increases with frequency and the main frequency bandwidth is below 100 Hz. Below the top of the A2 Carbonate is a drop in low frequencies.*

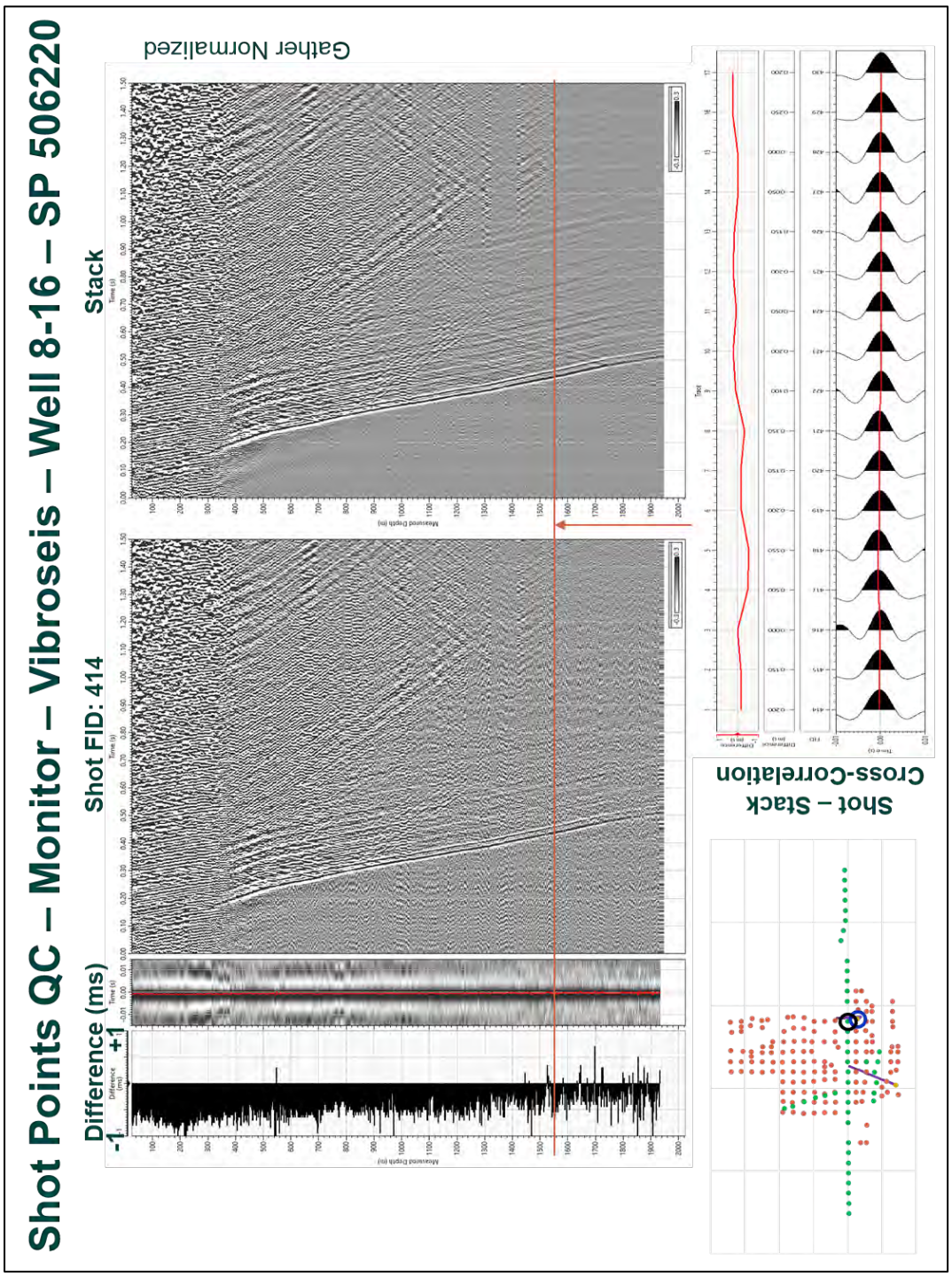


*Figure 6-31. Shot Points QC – Monitor – Vibroseis – Well 8-16 – SP 506220 - Cross-correlation between the shot and stack.*

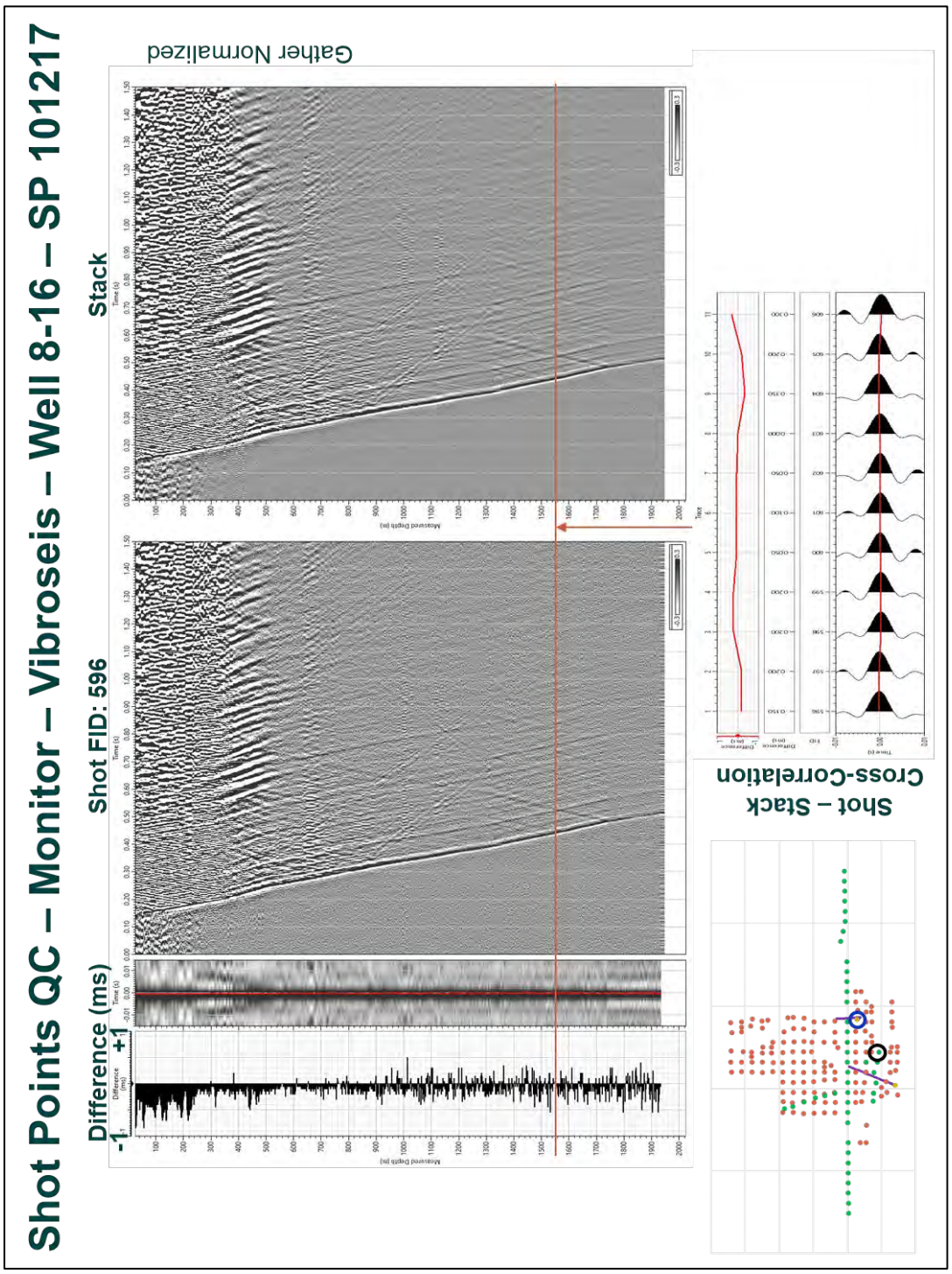


*Figure 6-32. Shot Points QC – Monitor – Vibroseis – Well 8-16 – SP 101217 - Cross-correlation between the shot and stack.*

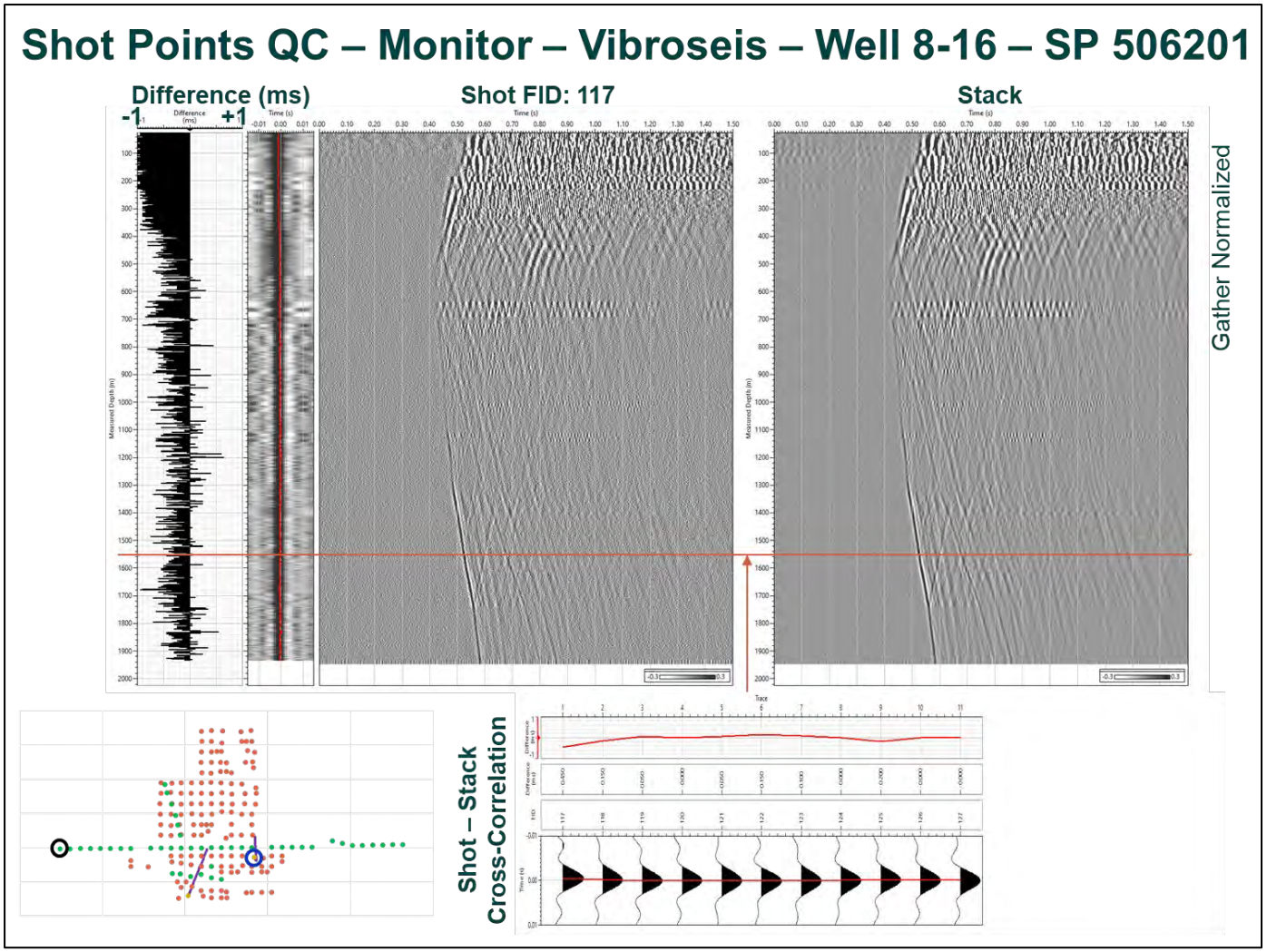


*Figure 6-33. Shot Points QC – Monitor – Vibroseis – Well 8-16 – SP 506201 - Cross-correlation between the shot and stack.*

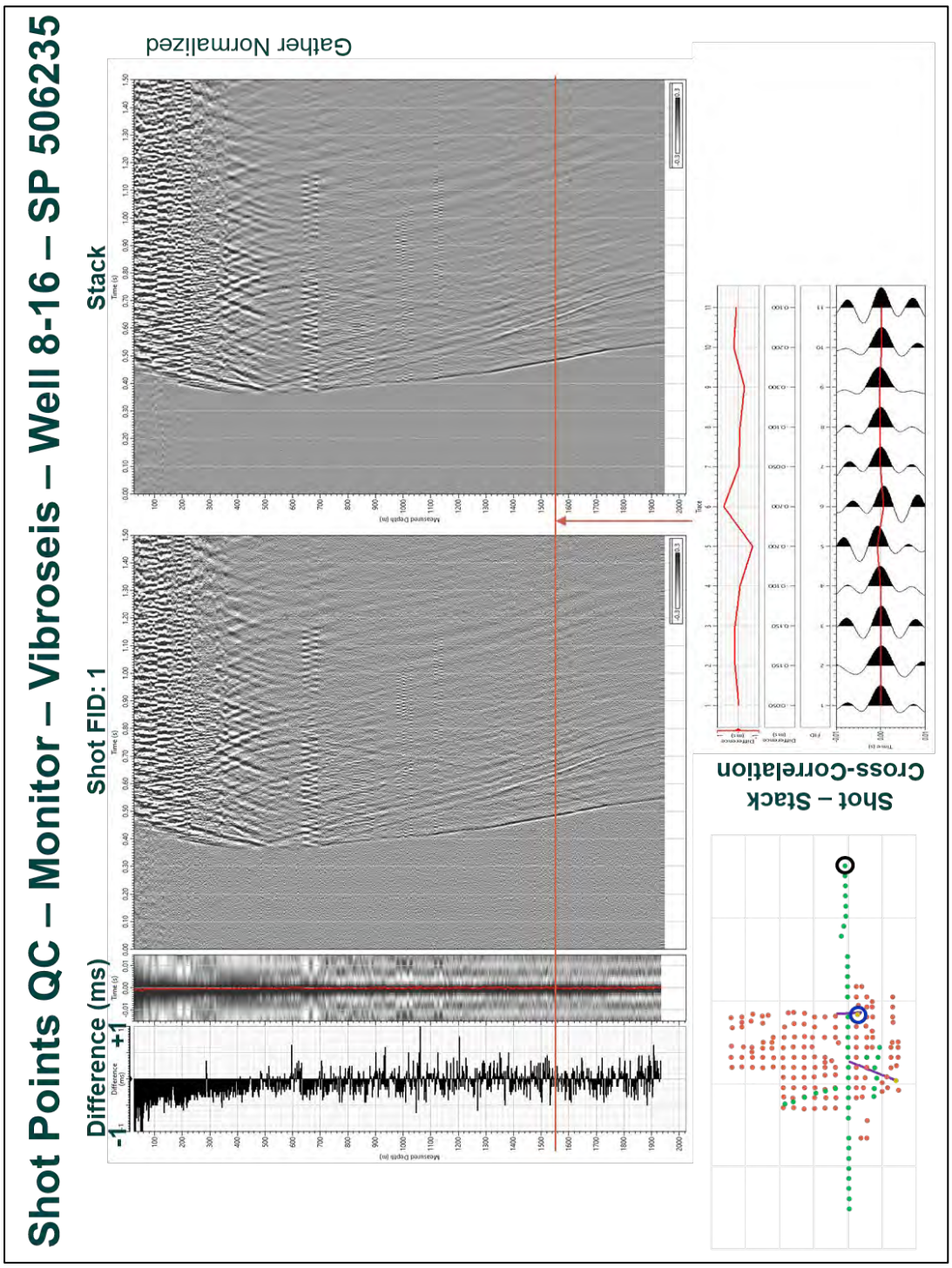


*Figure 6-34. Shot Points QC – Monitor – Vibroseis – Well 8-16 – SP 506235 - Cross-correlation between the shot and stack.*

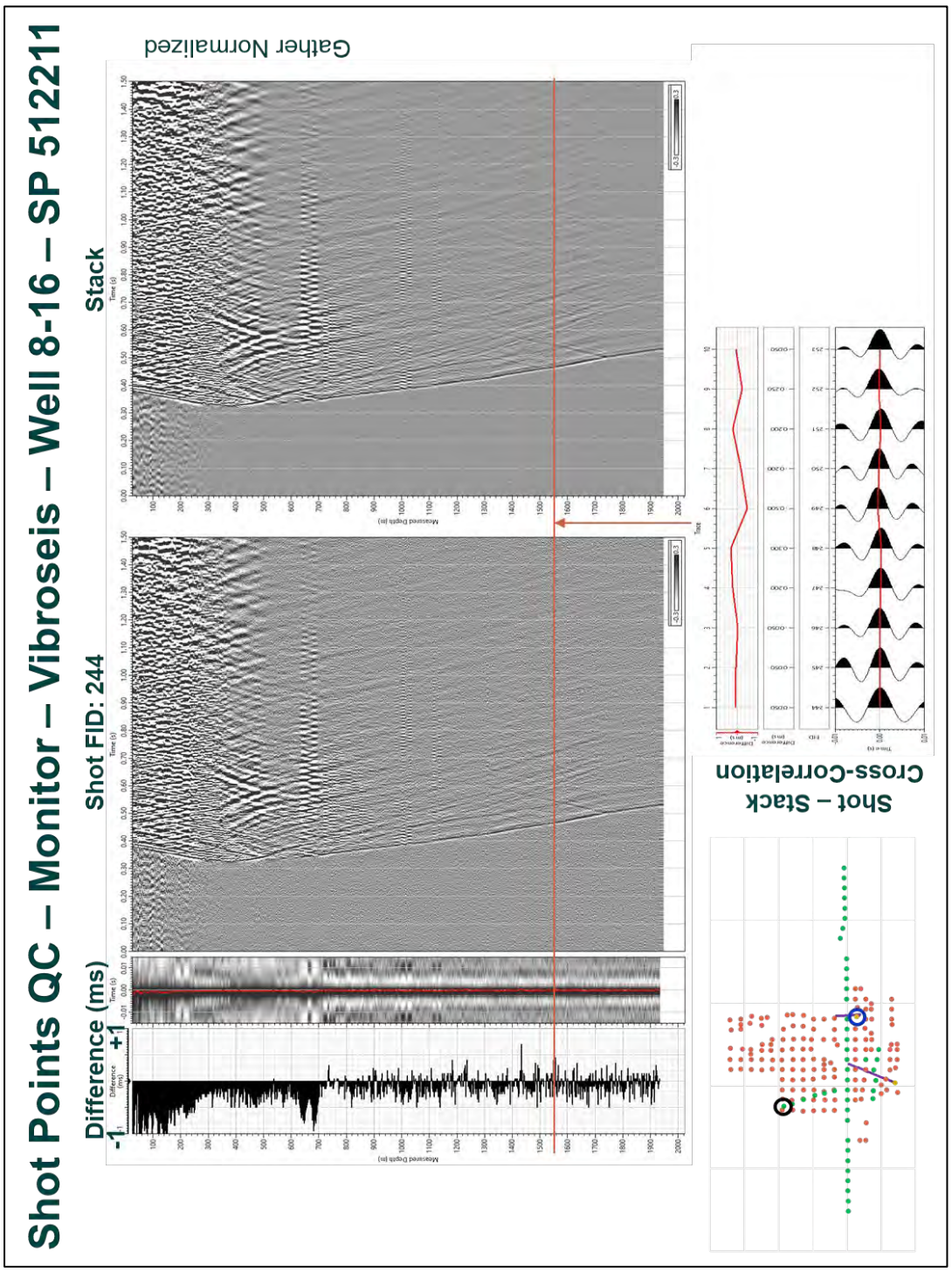


*Figure 6-35. Shot Points QC – Monitor – Vibroseis – Well 8-16 – SP 512211 - Cross-correlation between the shot and stack.*

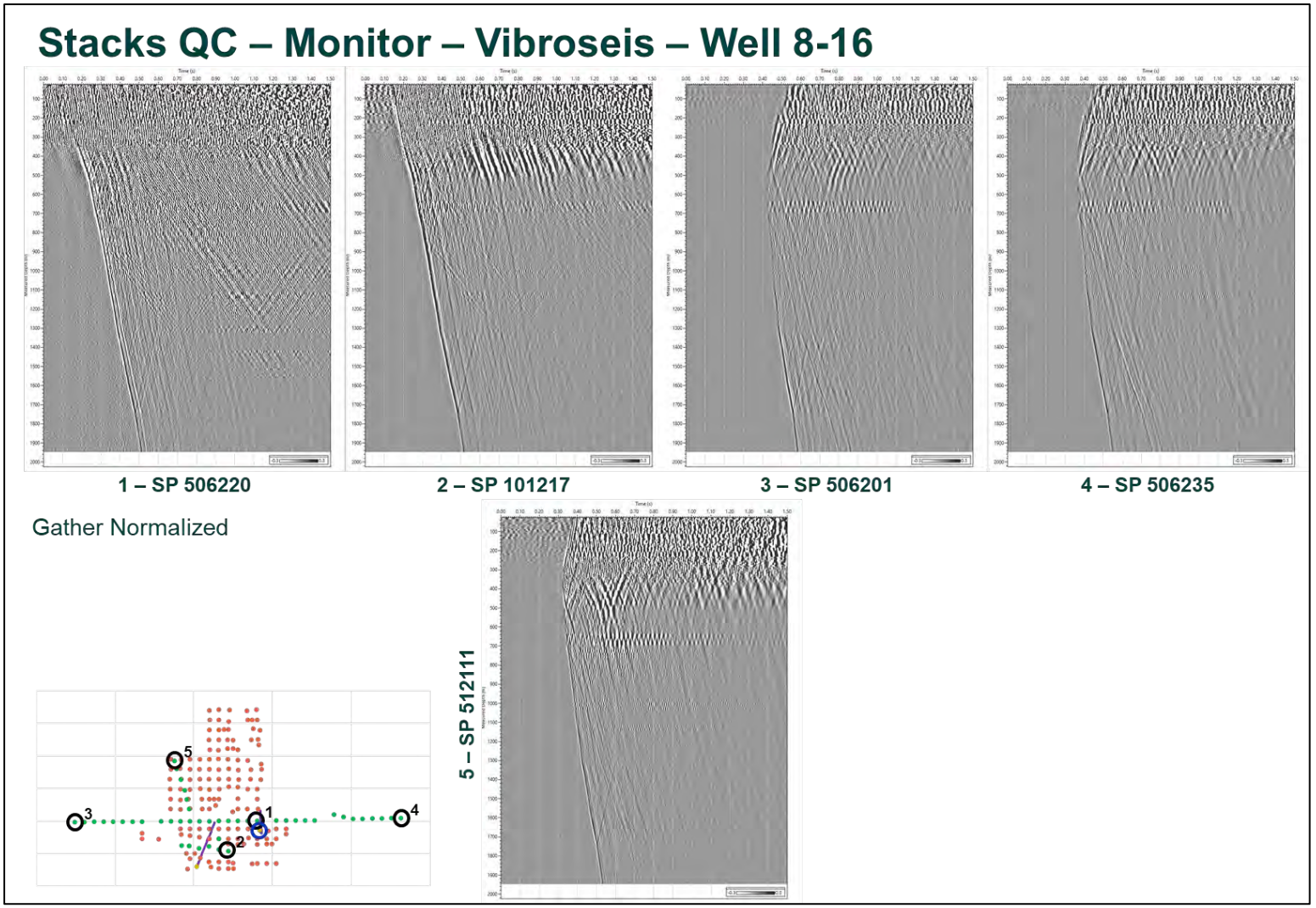


*Figure 6-36. Stacks QC – Monitor – Vibroseis – Well 8-16 - Stack in time domain. It presents a QC of the five stacks.*

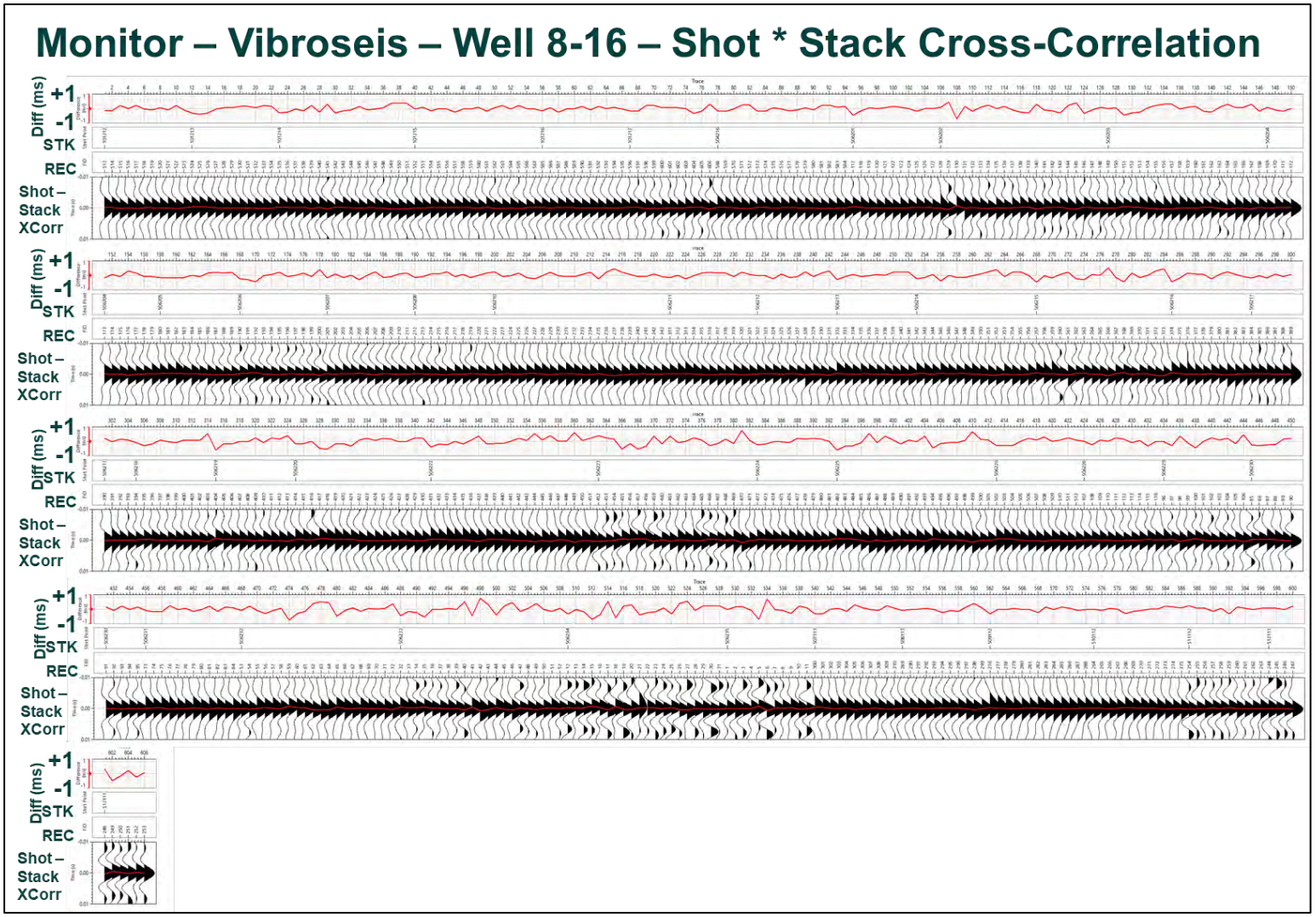


*Figure 6-37. Monitor – Vibroseis – Well 8-16 – Shot * Stack Cross-Correlation - All the shots at 1550 m MD. This shows shot-stack cross-correlation wavelet (bottom row) at 1550 m MD and the time difference (top row) for all the shots of well 8-16, baseline survey. No time shift due to source subsidence was noticed in the well 8-16 data. The cross-correlation between the shot and the stack at well 8-16 is better than at well 6-16 due to a better SNR.*

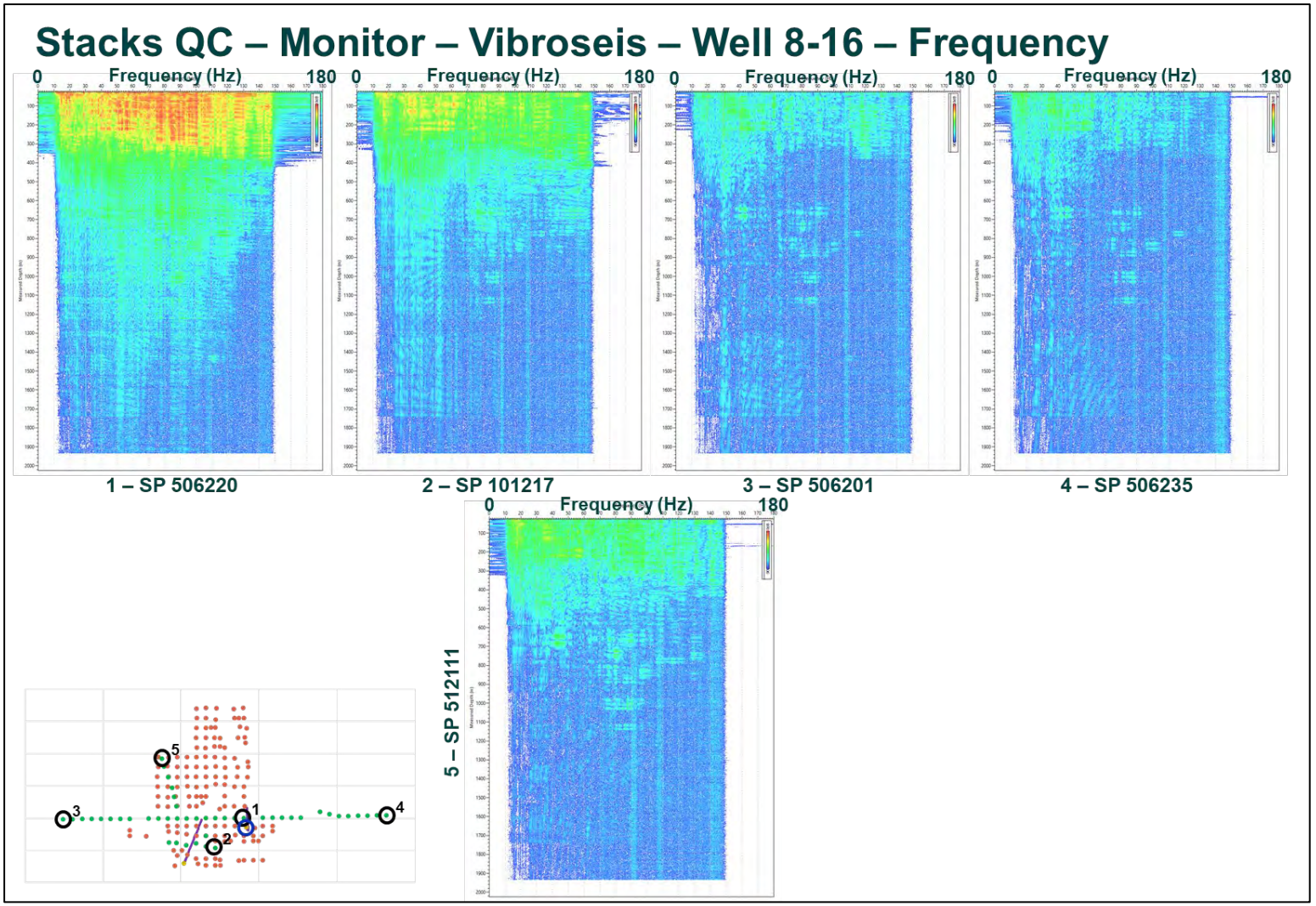


*Figure 6-38. Stacks QC – Monitor – Vibroseis – Well 8-16 – Frequency - Stack in frequency domain. This figure presents the same data from figure 6-36 in the frequency domain. The noise level increases with frequency and the main frequency bandwidth is below 110 Hz. Also, the top of A2 Carbonate can be identified on the frequency displays.*

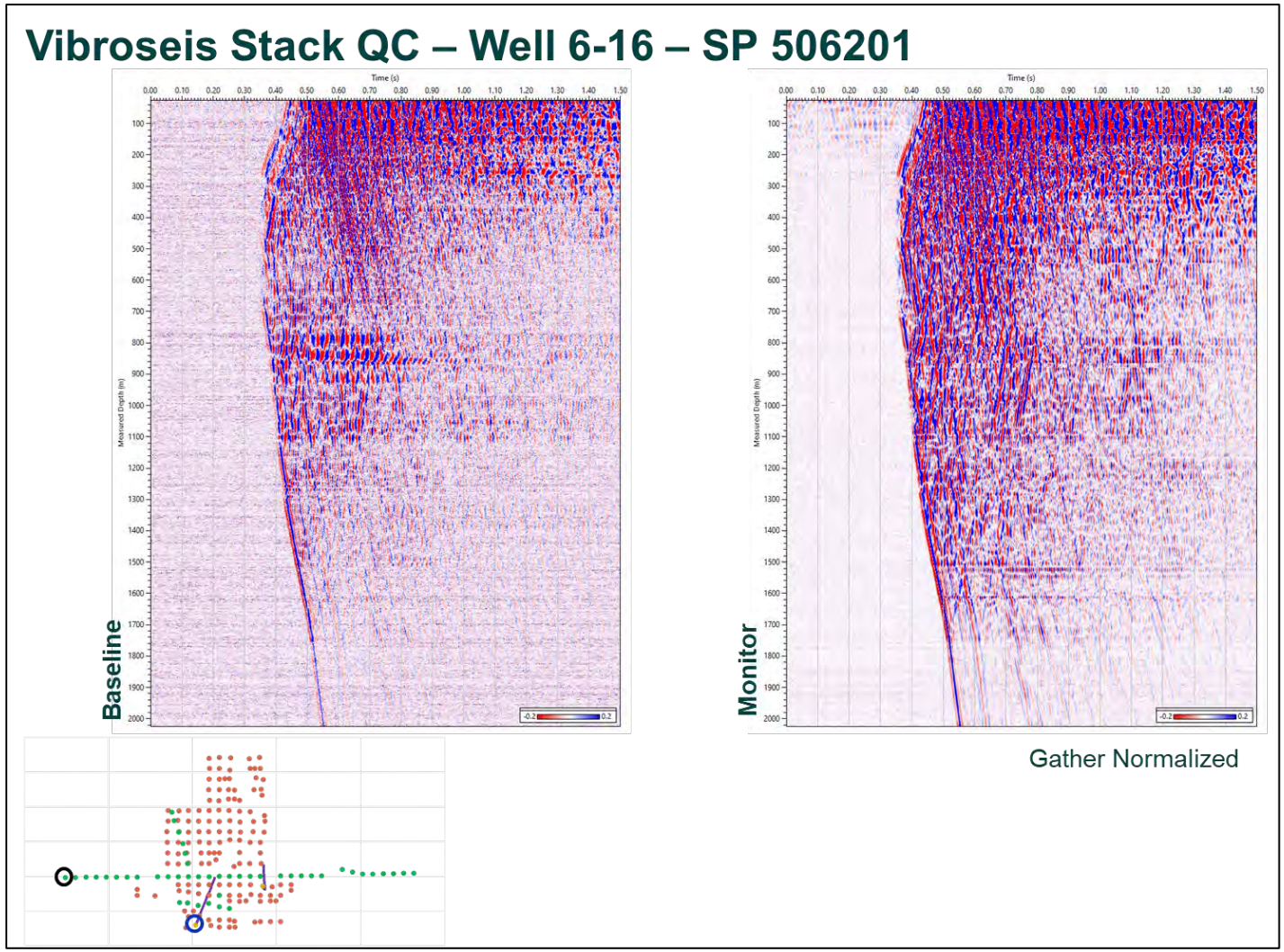


*Figure 6-39. Vibroseis Stack QC – Well 6-16 – SP 506201 - Baseline and monitor survey.*

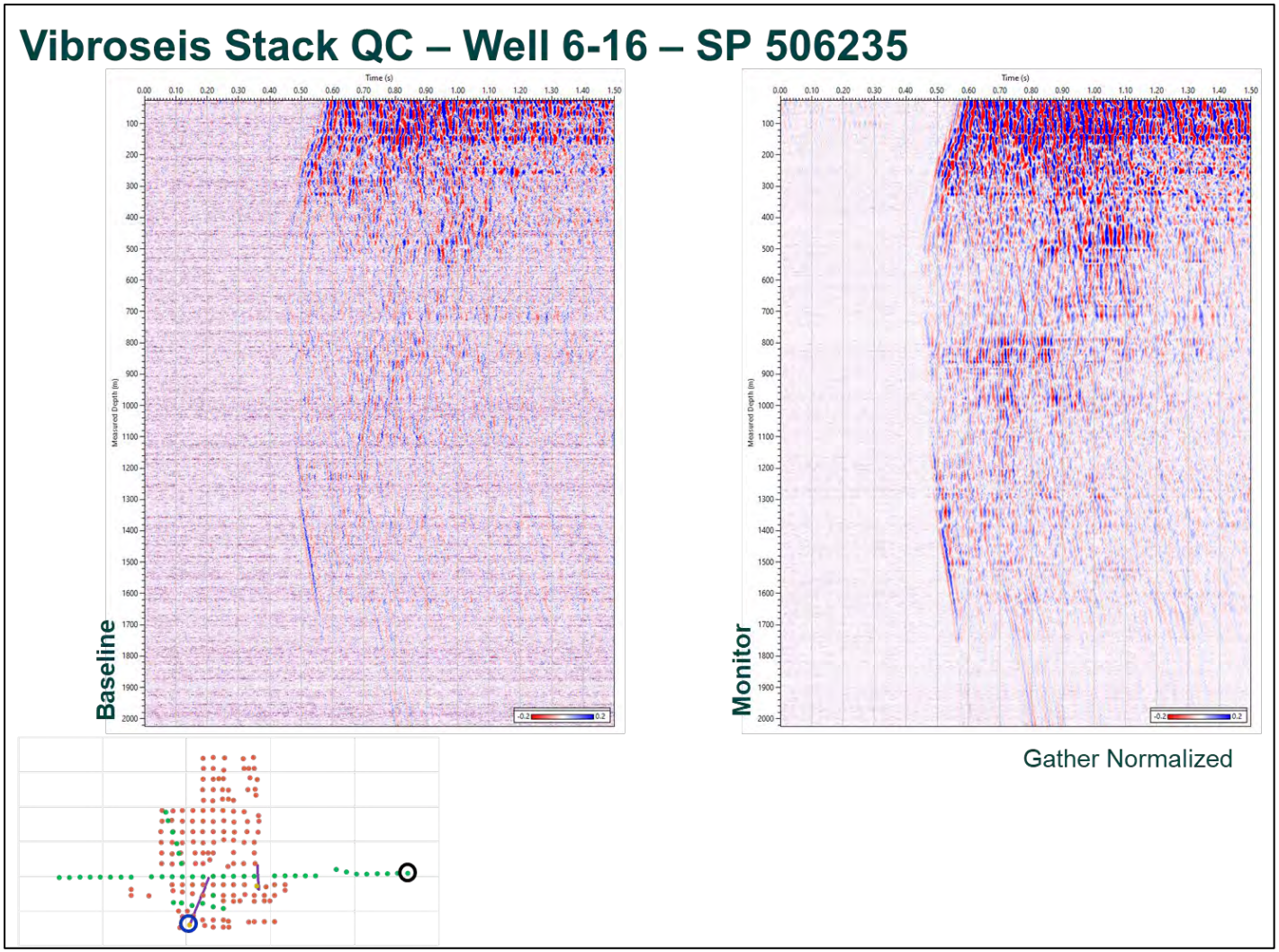


*Figure 6-40. Vibroseis Stack QC – Well 6-16 – SP 506235 - Baseline and monitor survey.*

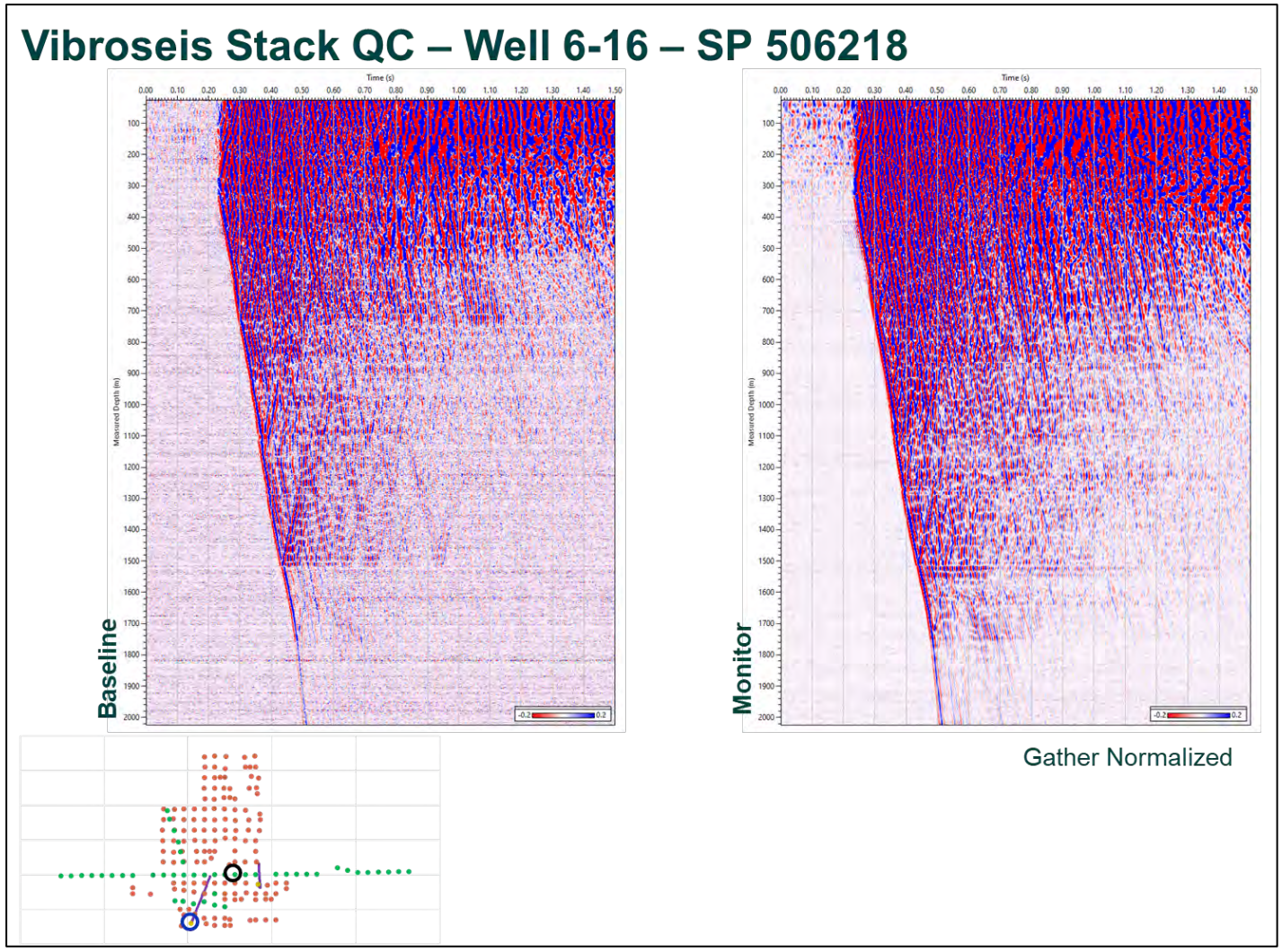


*Figure 6-41. Vibroseis Stack QC – Well 6-16 – SP 506218 - Baseline and monitor survey.*

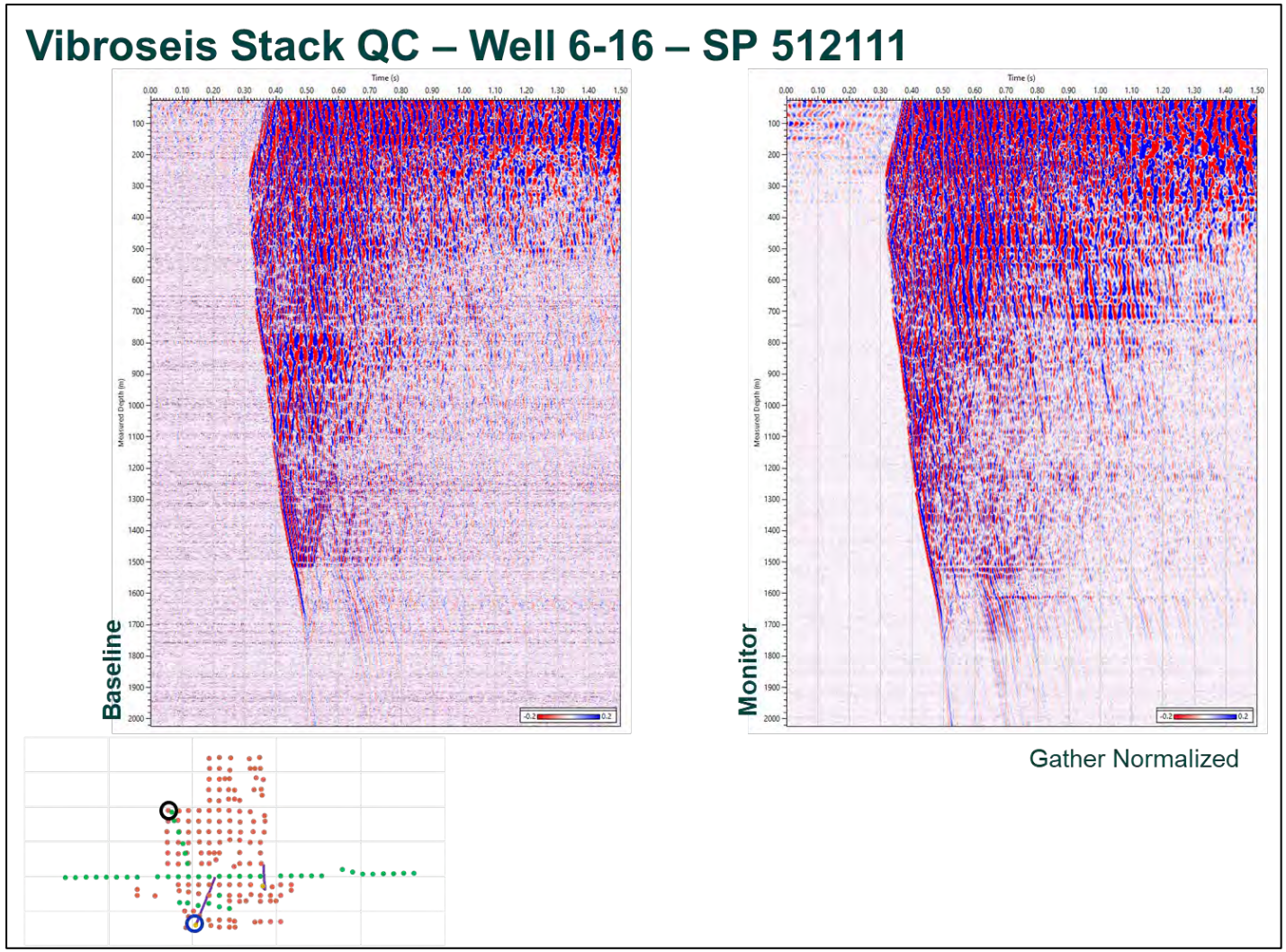


*Figure 6-42. Vibroseis Stack QC – Well 6-16 – SP 512111 - Baseline and monitor survey.*

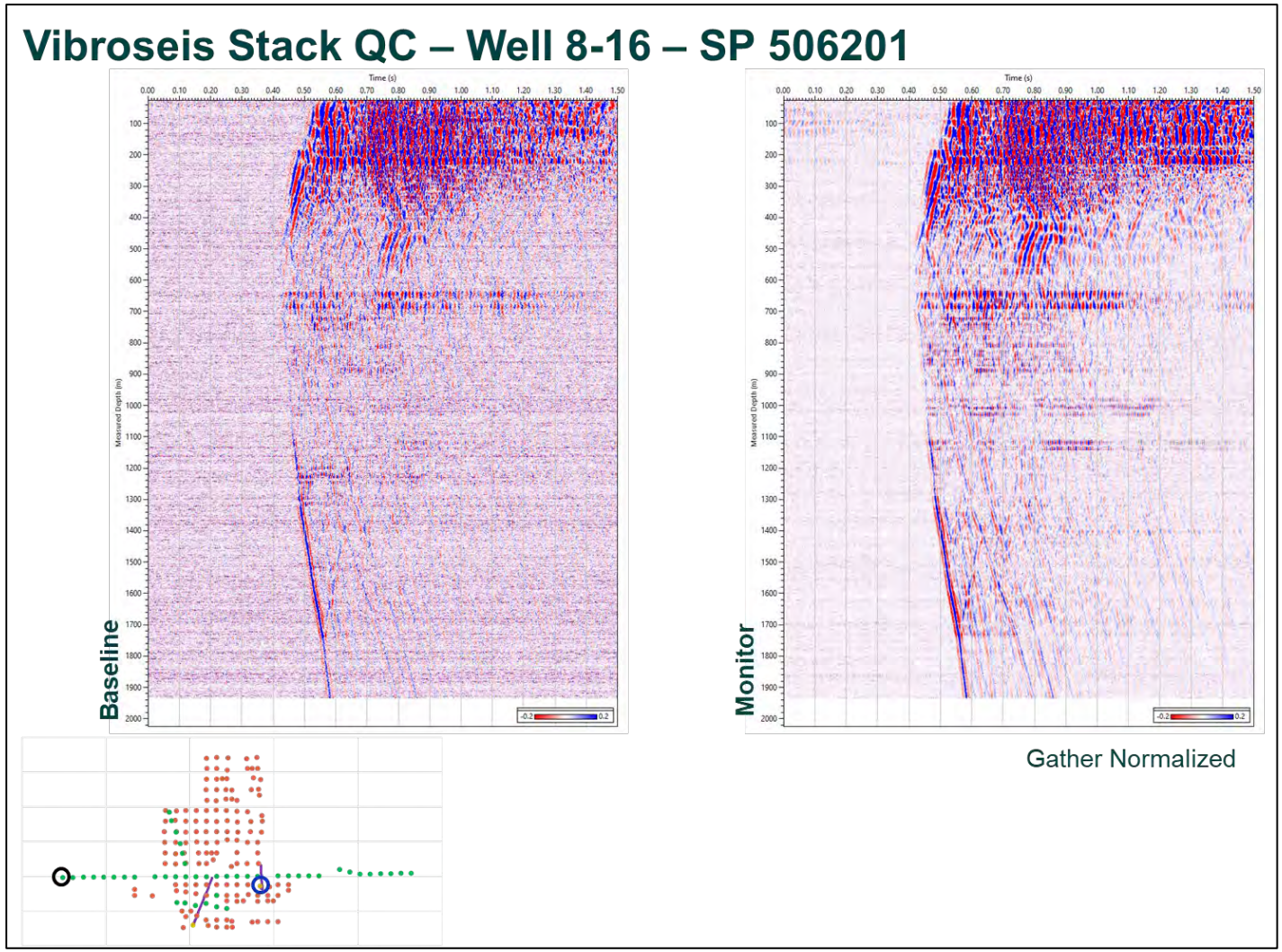


*Figure 6-43. Vibroseis Stack QC – Well 8-16 – SP 506201 - Baseline and monitor survey.*

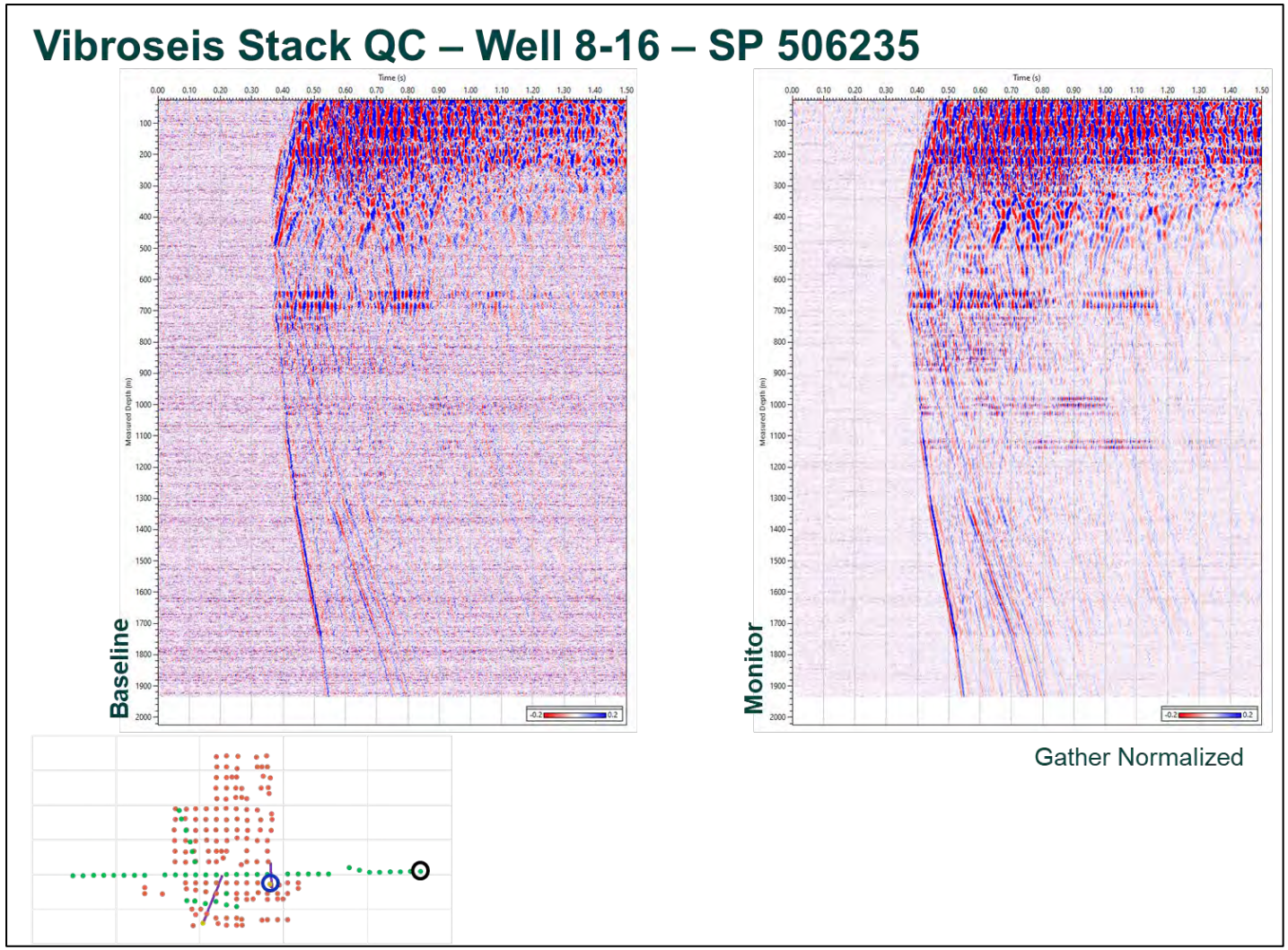


*Figure 6-44. Vibroseis Stack QC – Well 8-16 – SP 506235 - Baseline and monitor survey.*

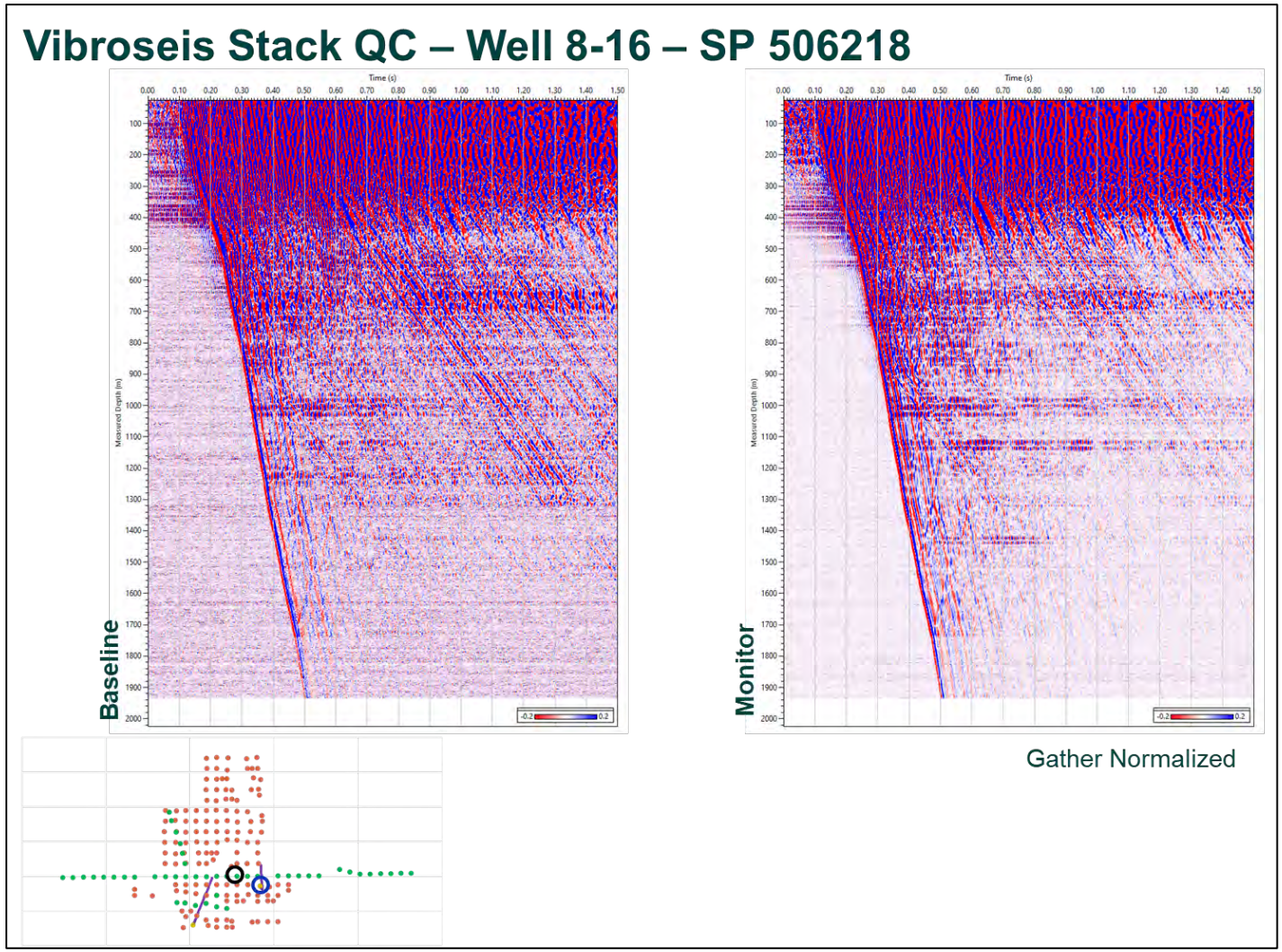


*Figure 6-45. Vibroseis Stack QC – Well 8-16 – SP 506218 - Baseline and monitor survey.*

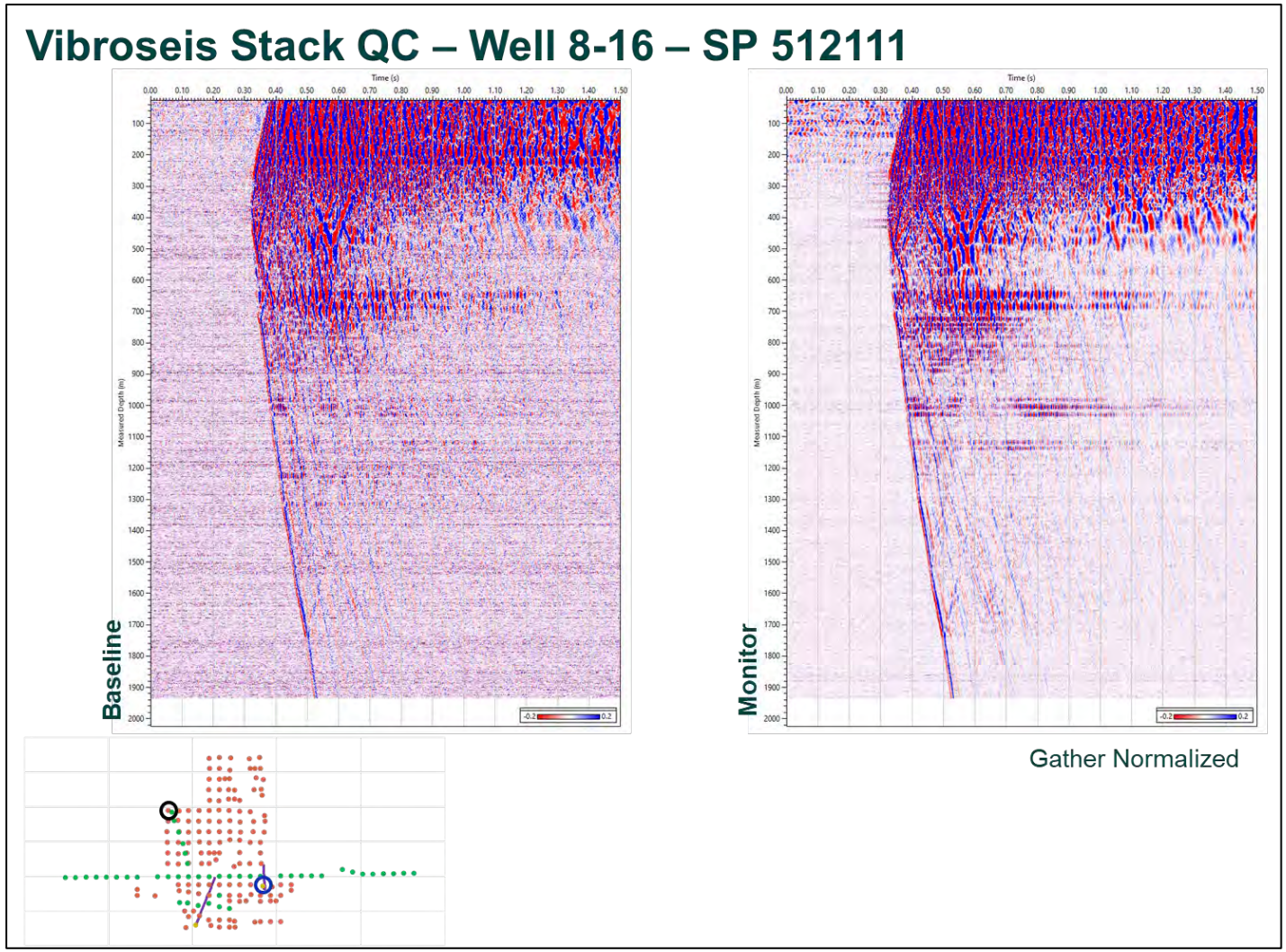


*Figure 6-46. Vibroseis Stack QC – Well 8-16 – SP 512111 - Baseline and monitor survey.*

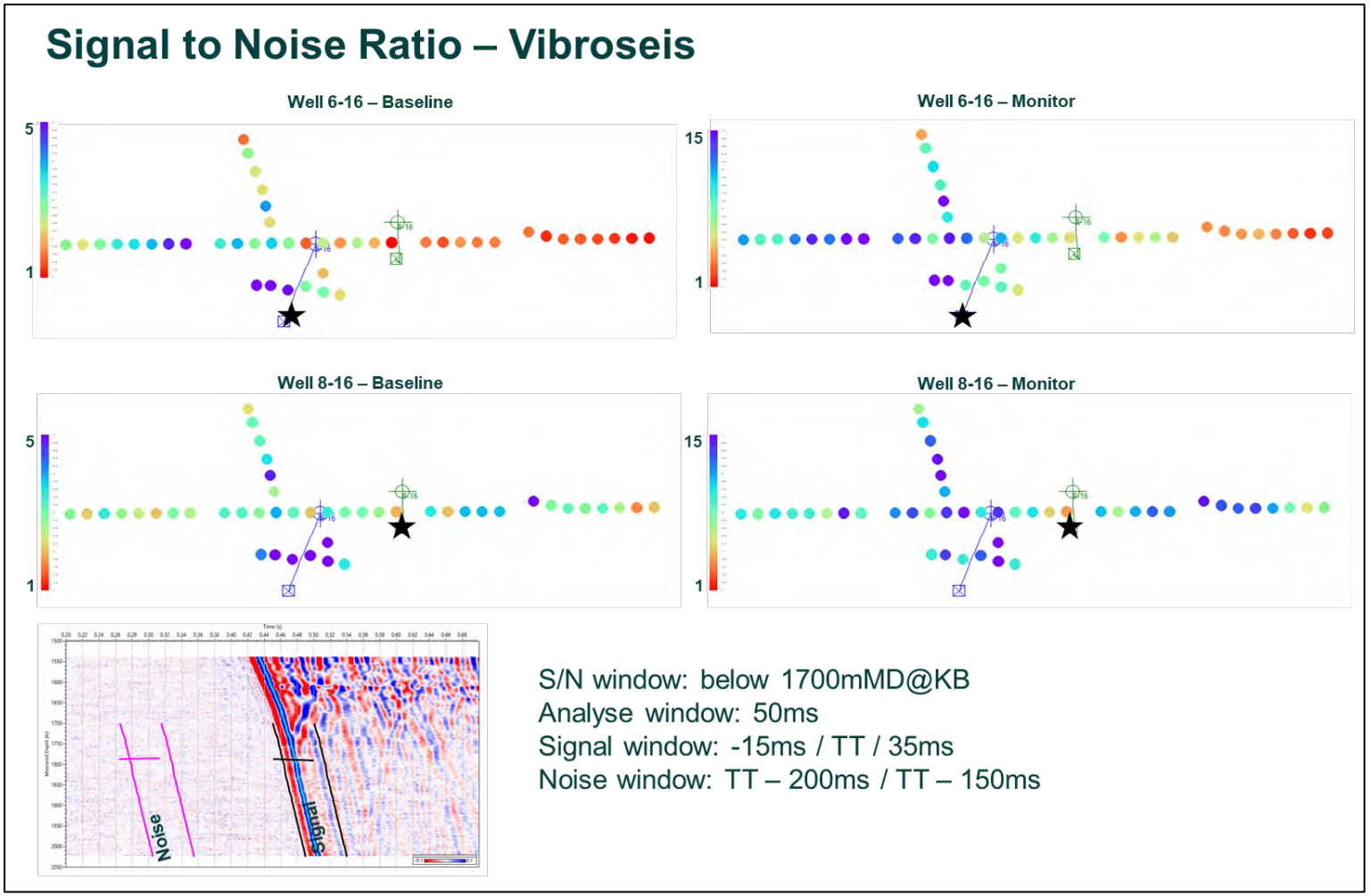


*Figure 6-47. Signal to Noise Ratio – Vibroseis - Computing window below 1700 m MD. This figure presents the average signal to noise ratio at each SP location for: well 6-16 baseline survey (top left), well 8-16 baseline survey (middle left), well 6-16 monitor survey (top right) and well 8-16 monitor survey (middle right). For each stack we defined the signal window from 15 ms before First Break (FB) pick to 35 ms after the FB. The elevated noise window starts at 200 ms before FB and continues for 50 ms. For each channel below 1700 m MD a SNR value is computed as the ratio of the signal window RMS and the noise window RMS (Fig. 6-47 bottom left). Finally, an average value is computed for each SP.*

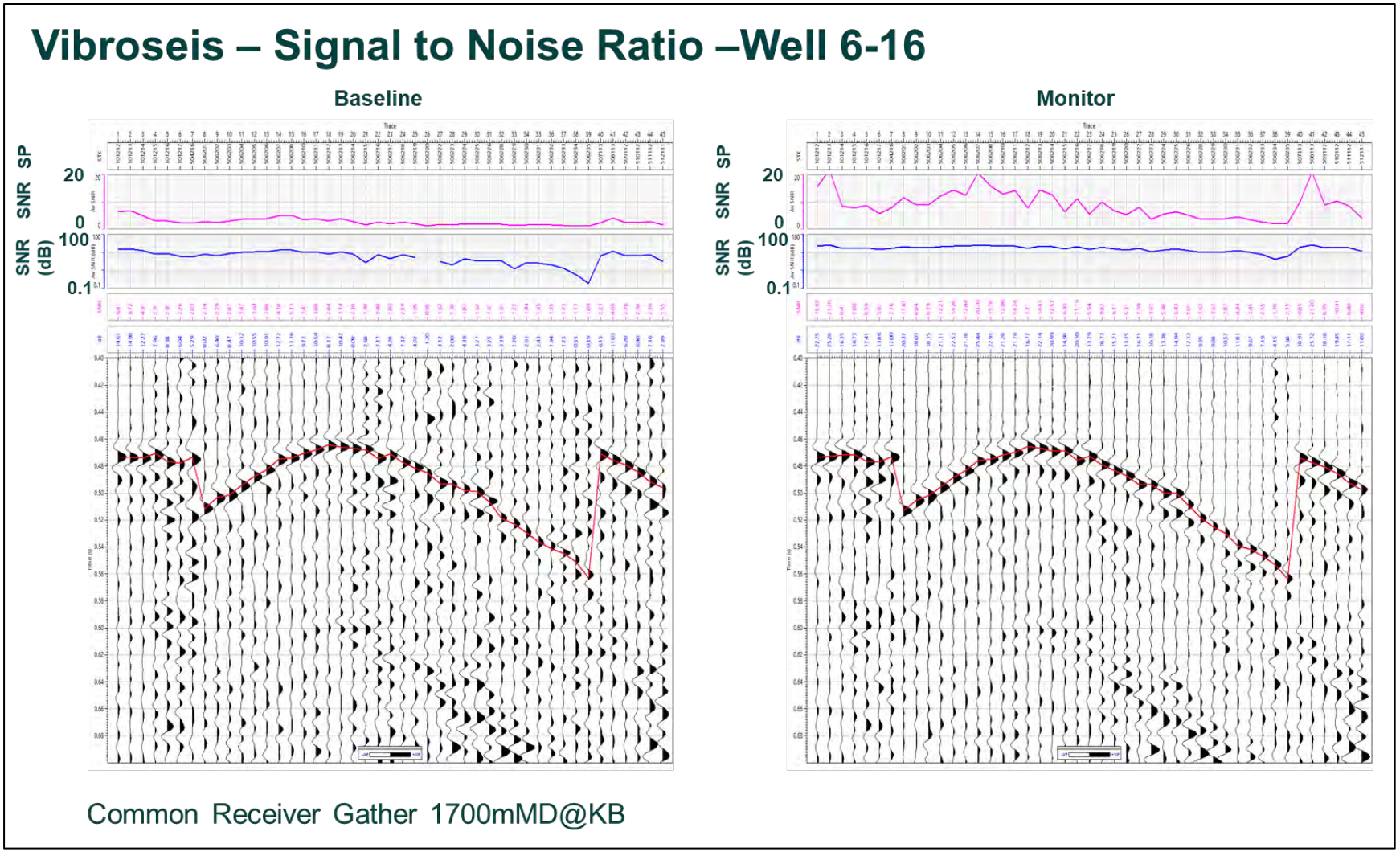


*Figure 6-48. Vibroseis – Signal to Noise Ratio –Well 6-16 - Baseline and monitor survey.*

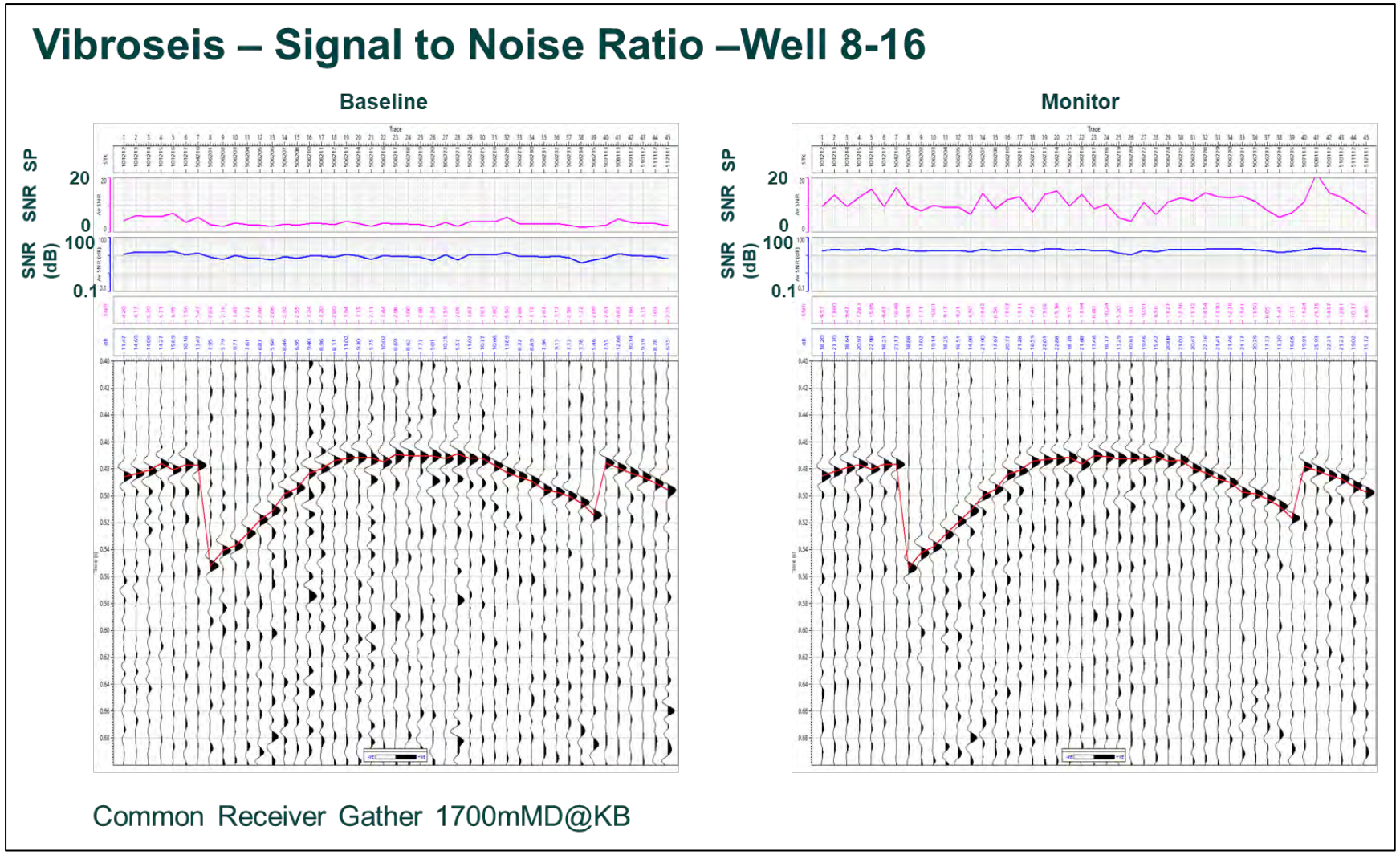


*Figure 6-49. Vibroseis – Signal to Noise Ratio –Well 8-16 - Baseline and monitor survey.*

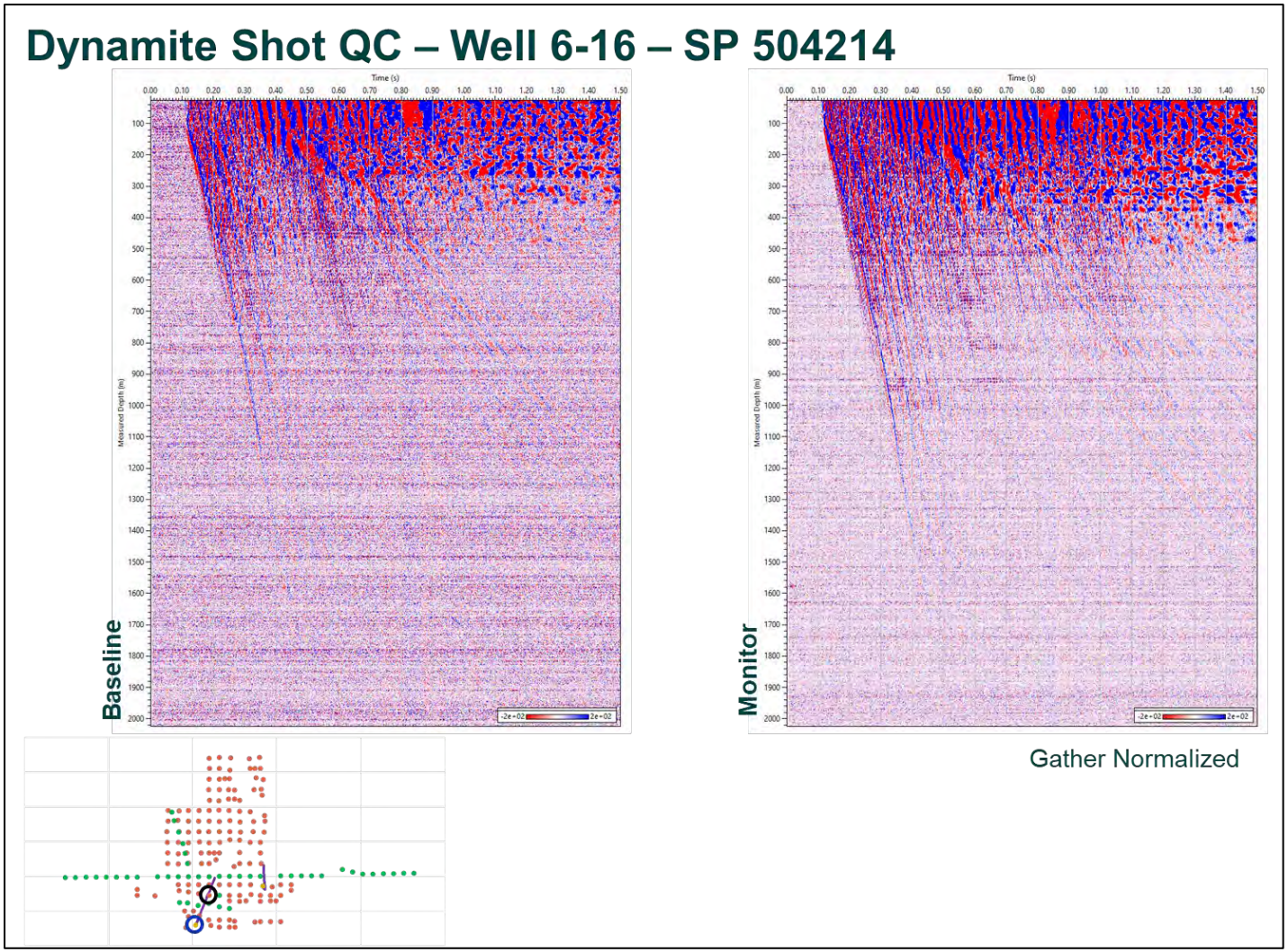


*Figure 6-50. Dynamite Shot QC – Well 6-16 – SP 504214 - Baseline and monitor survey.*

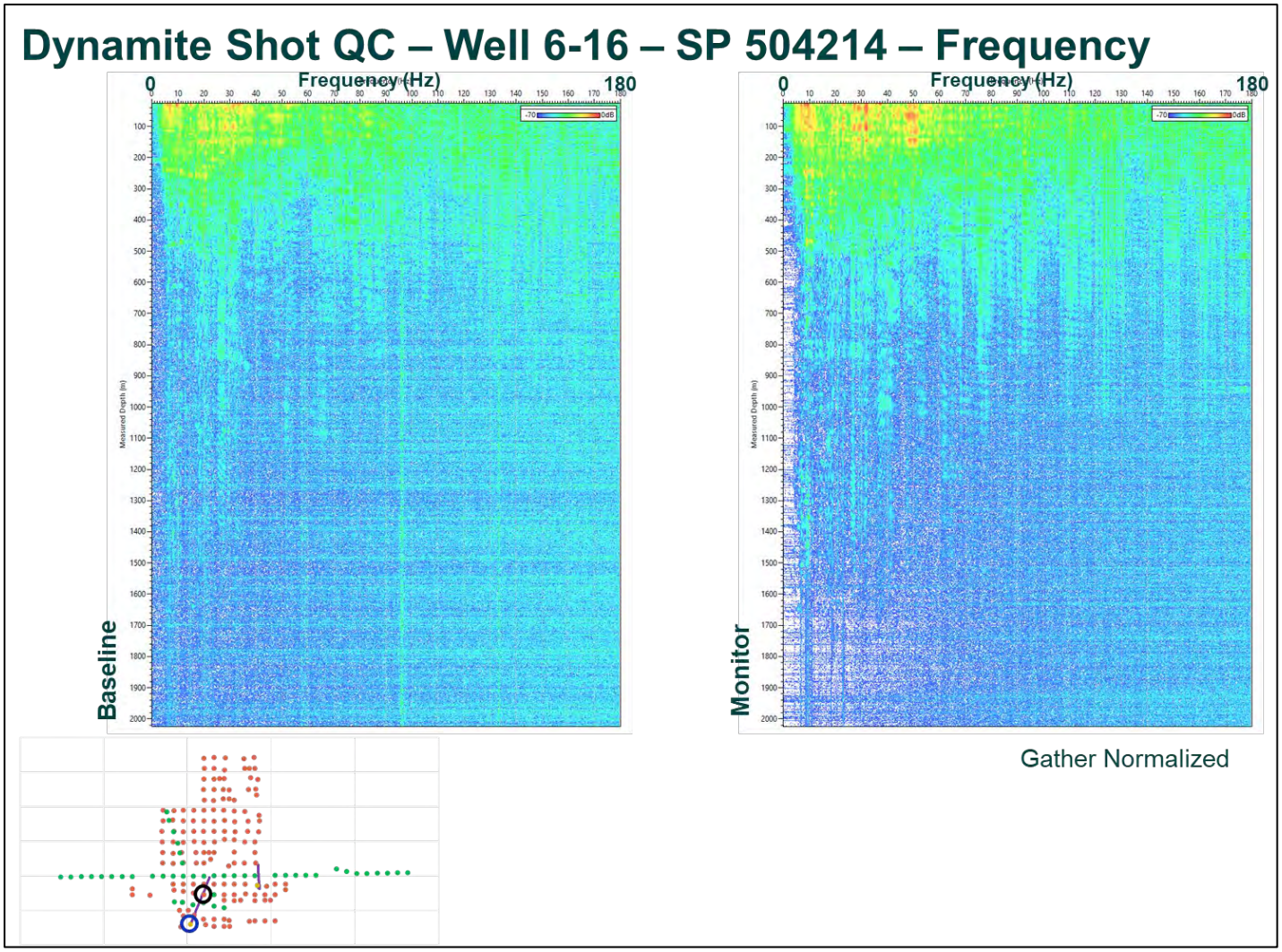


*Figure 6-51. Dynamite Shot QC – Well 6-16 – SP 504214 – Frequency - Baseline and monitor survey.*

.

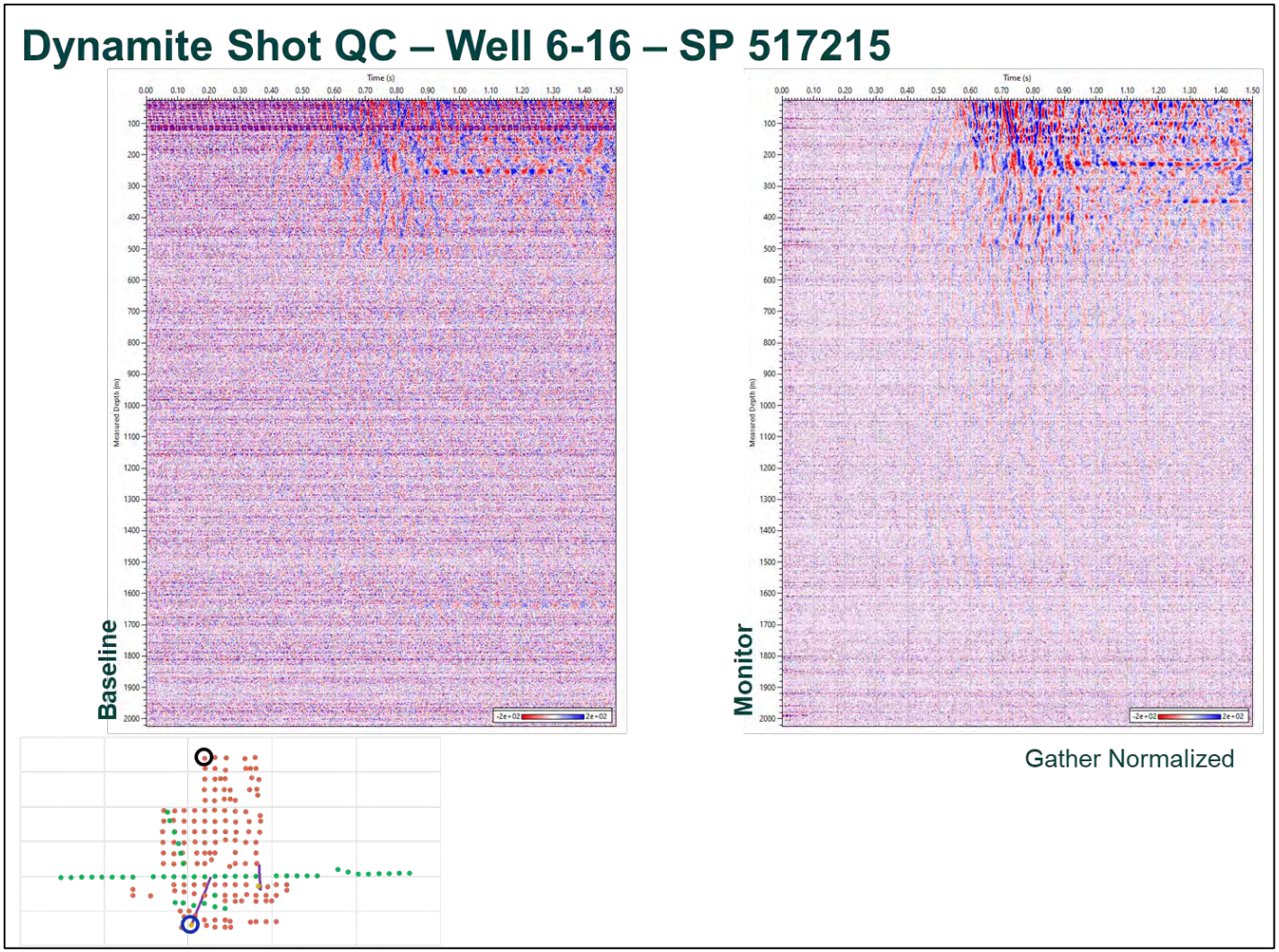


*Figure 6-52. Dynamite Shot QC – Well 6-16 – SP 517215 - Baseline and monitor survey.*

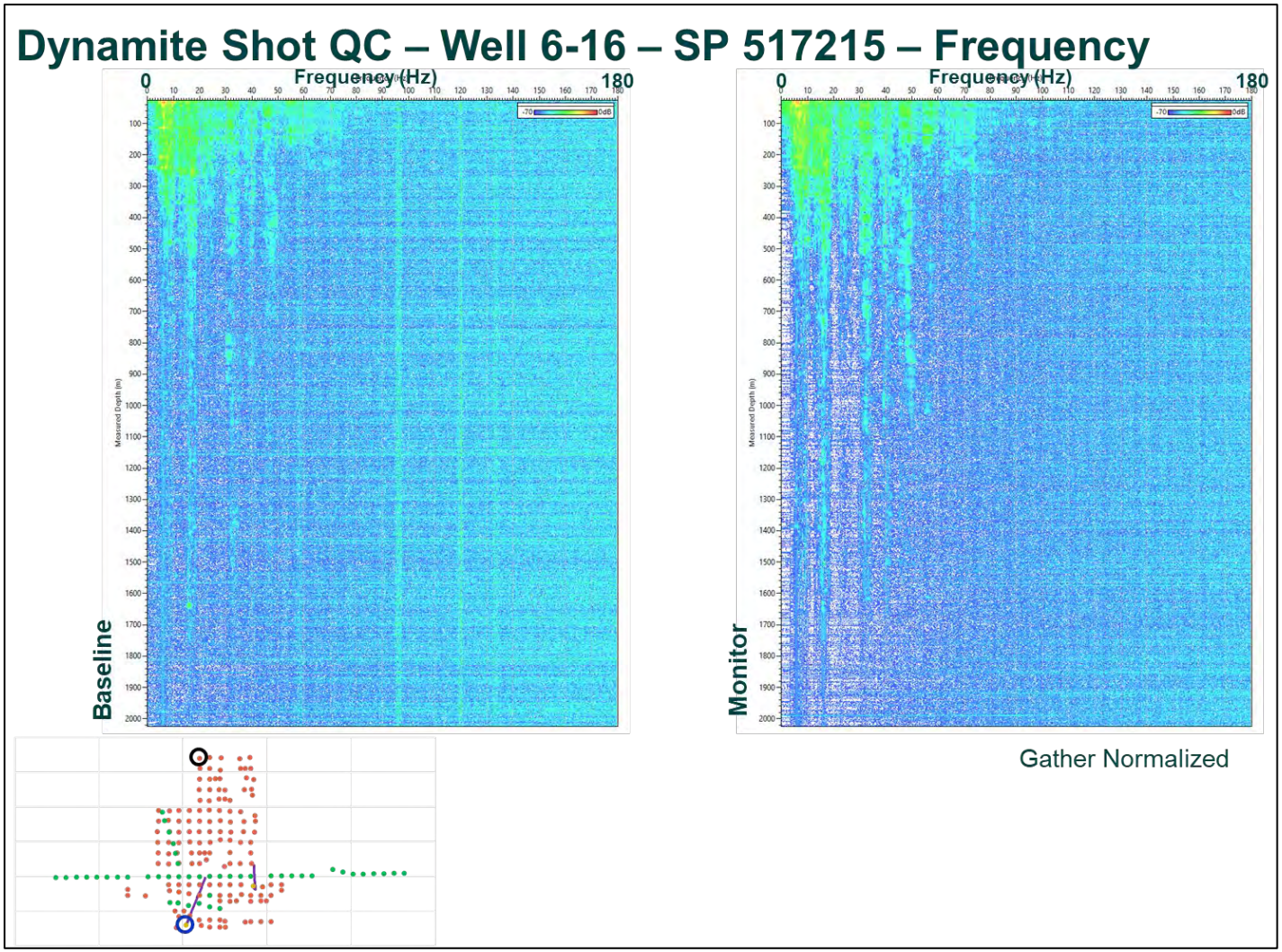


*Figure 6-53. Dynamite Shot QC – Well 6-16 – SP 517215 – Frequency - Baseline and monitor survey.*

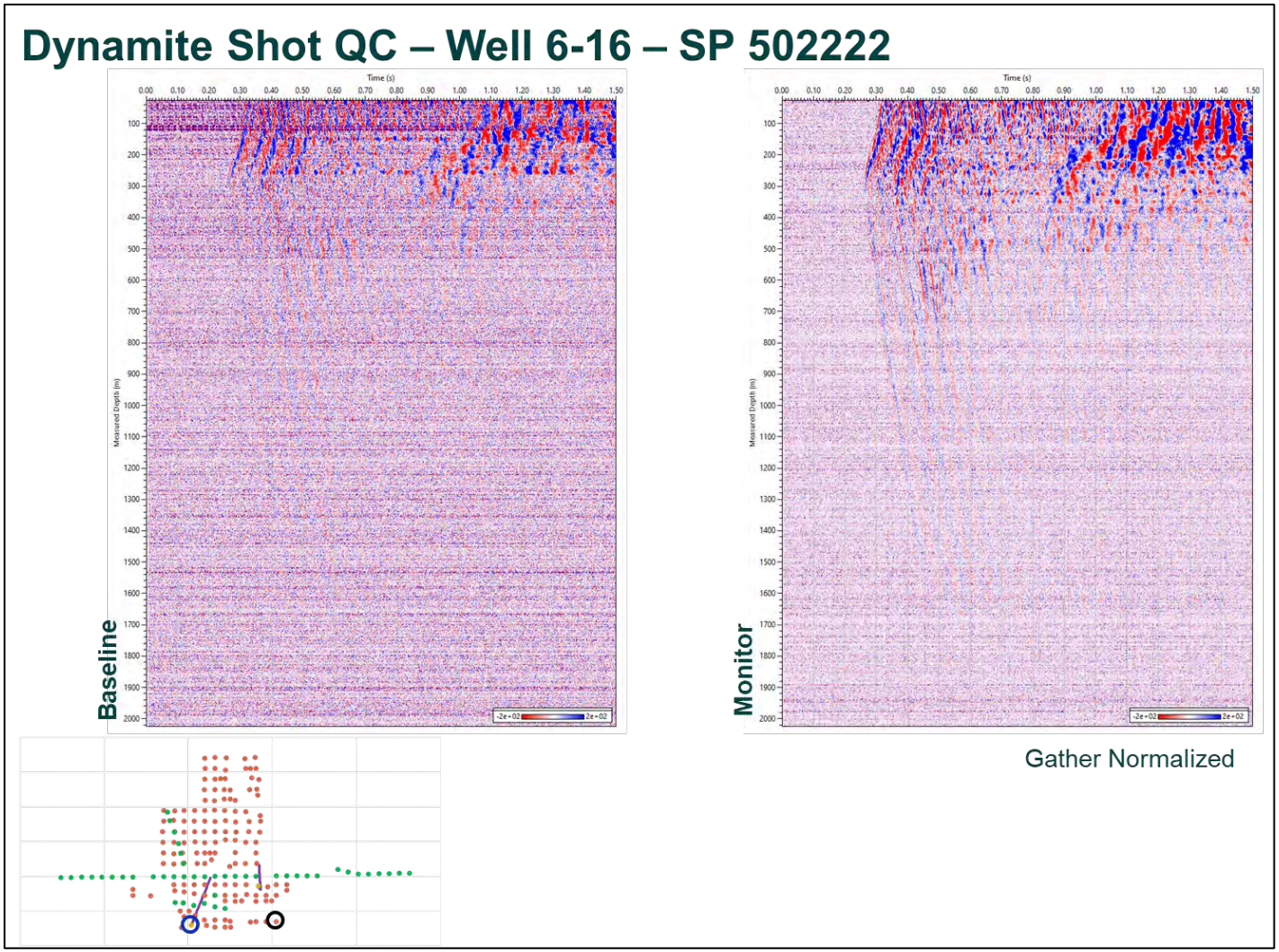


*Figure 6-54. Dynamite Shot QC – Well 6-16 – SP 502222 - Baseline and monitor survey.*

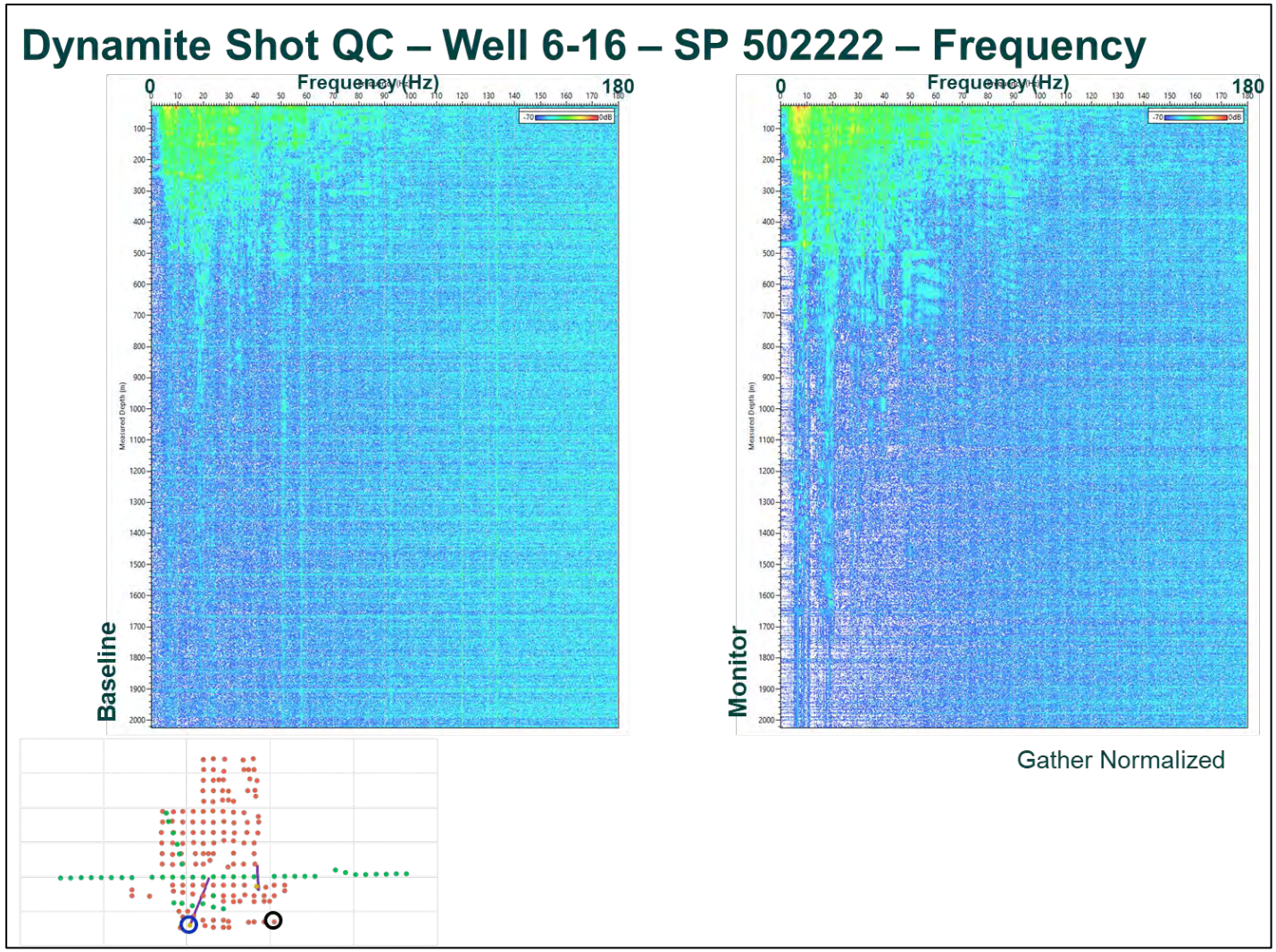


*Figure 6-55. Dynamite Shot QC – Well 6-16 – SP 502222 – Frequency - Baseline and monitor survey.*


*Figure 6-56. Dynamite Shot QC – Well 8-16 – SP 505221 - Baseline and monitor survey.*

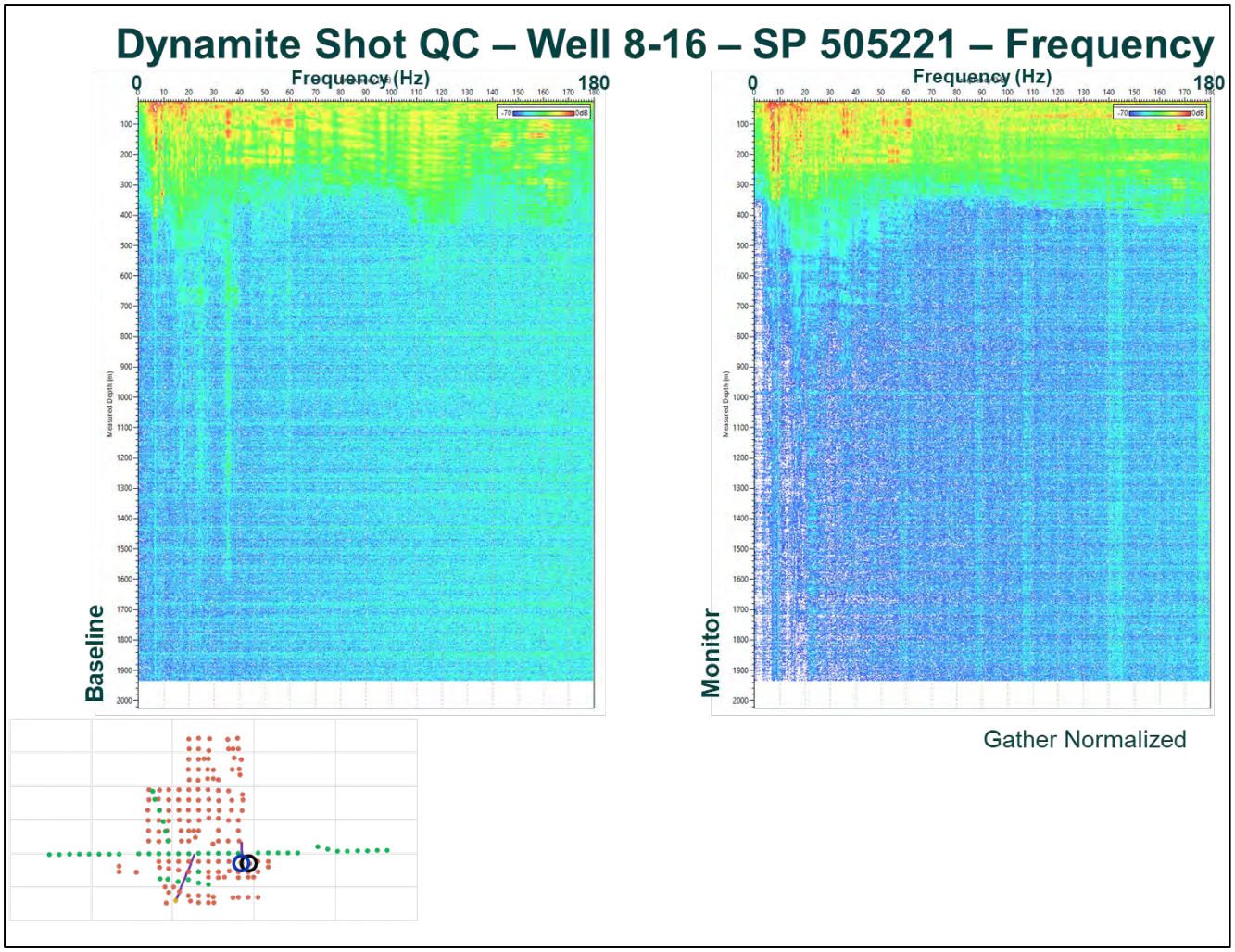


*Figure 6-57. Dynamite Shot QC – Well 8-16 – SP 505221 – Frequency - Baseline and monitor survey.*

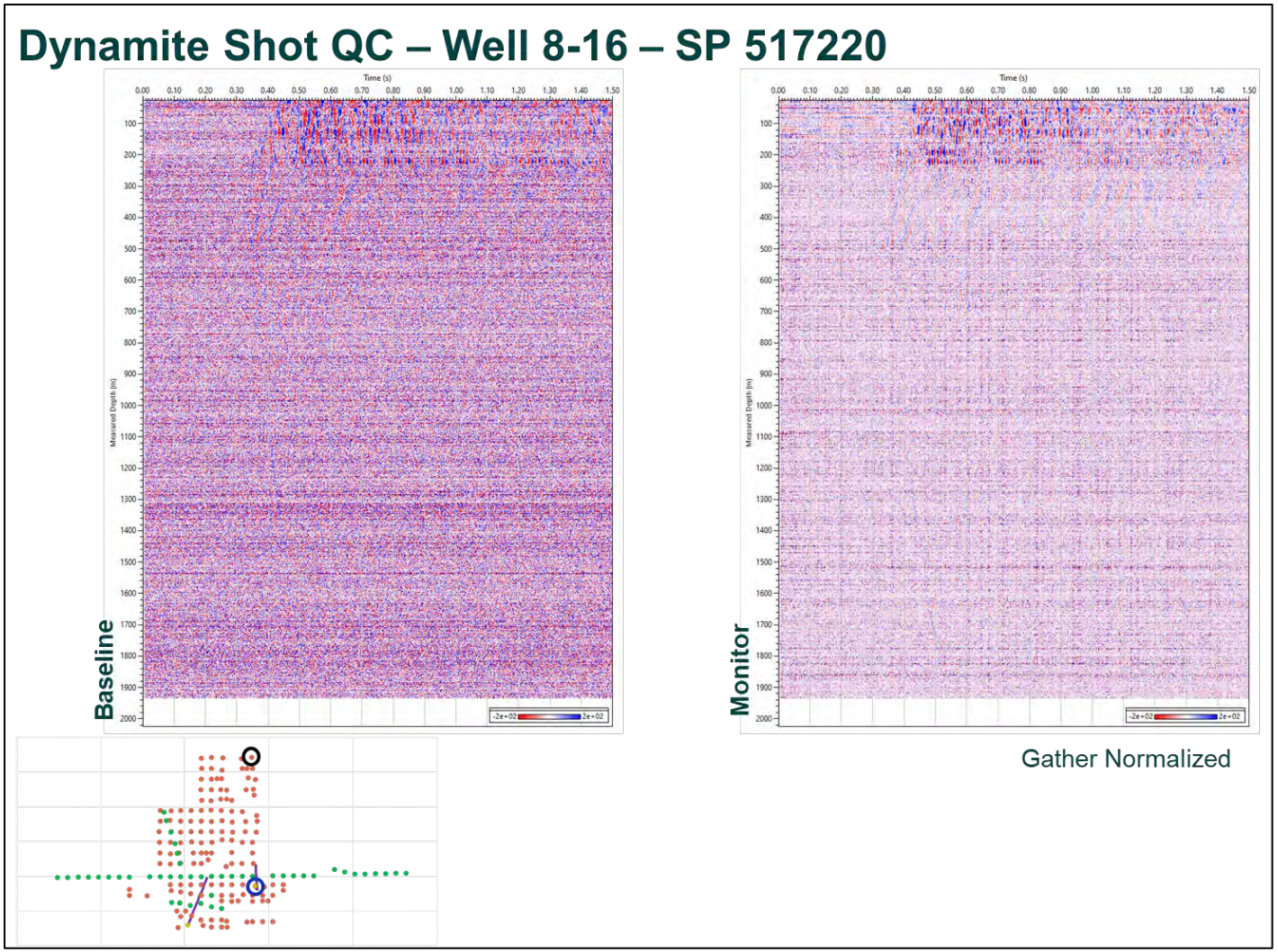


*Figure 6-58. Dynamite Shot QC – Well 8-16 – SP 517220 - Baseline and monitor survey.*

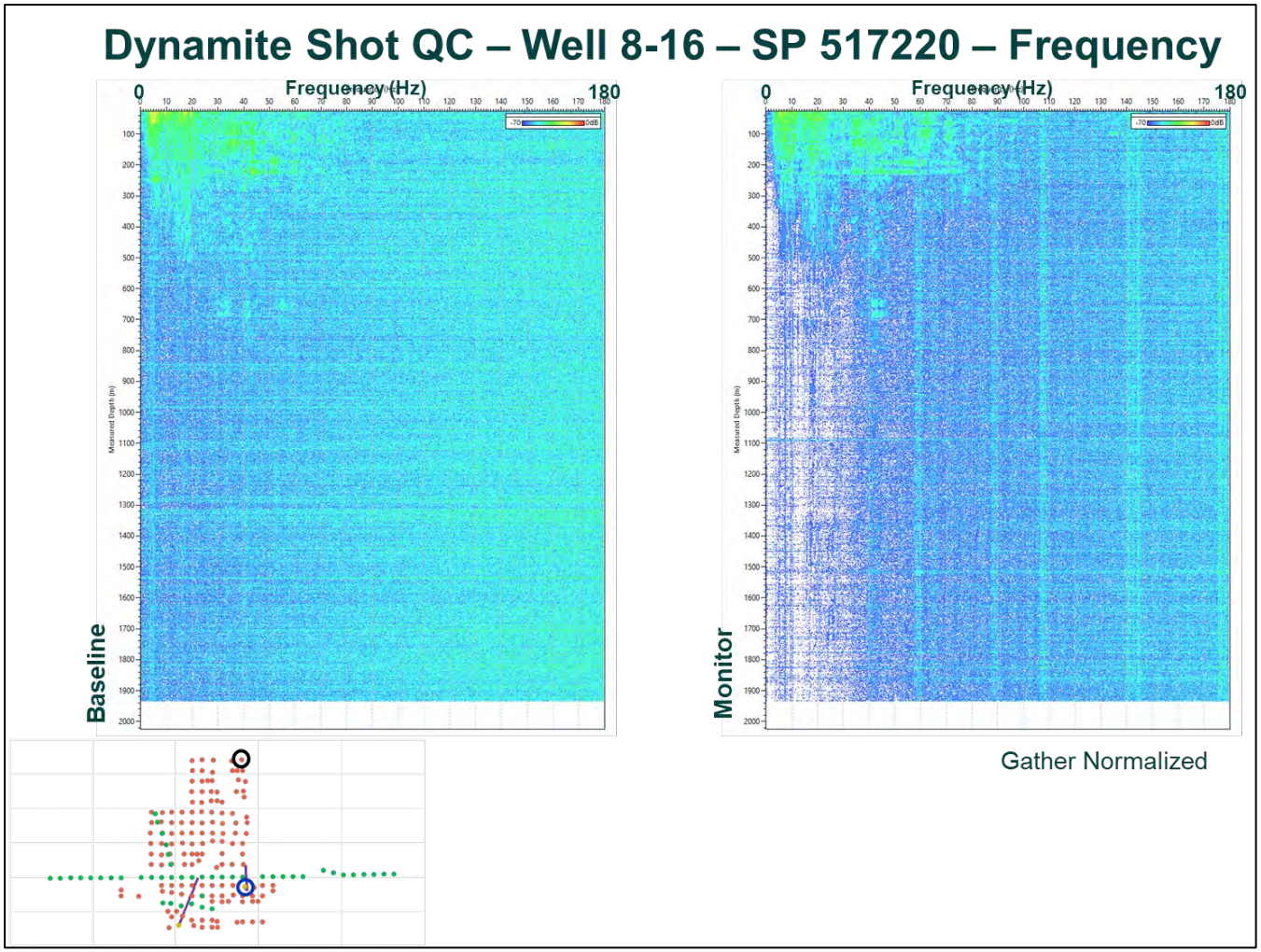


*Figure 6-59. Dynamite Shot QC – Well 8-16 – SP 517220 – Frequency - Baseline and monitor survey.*

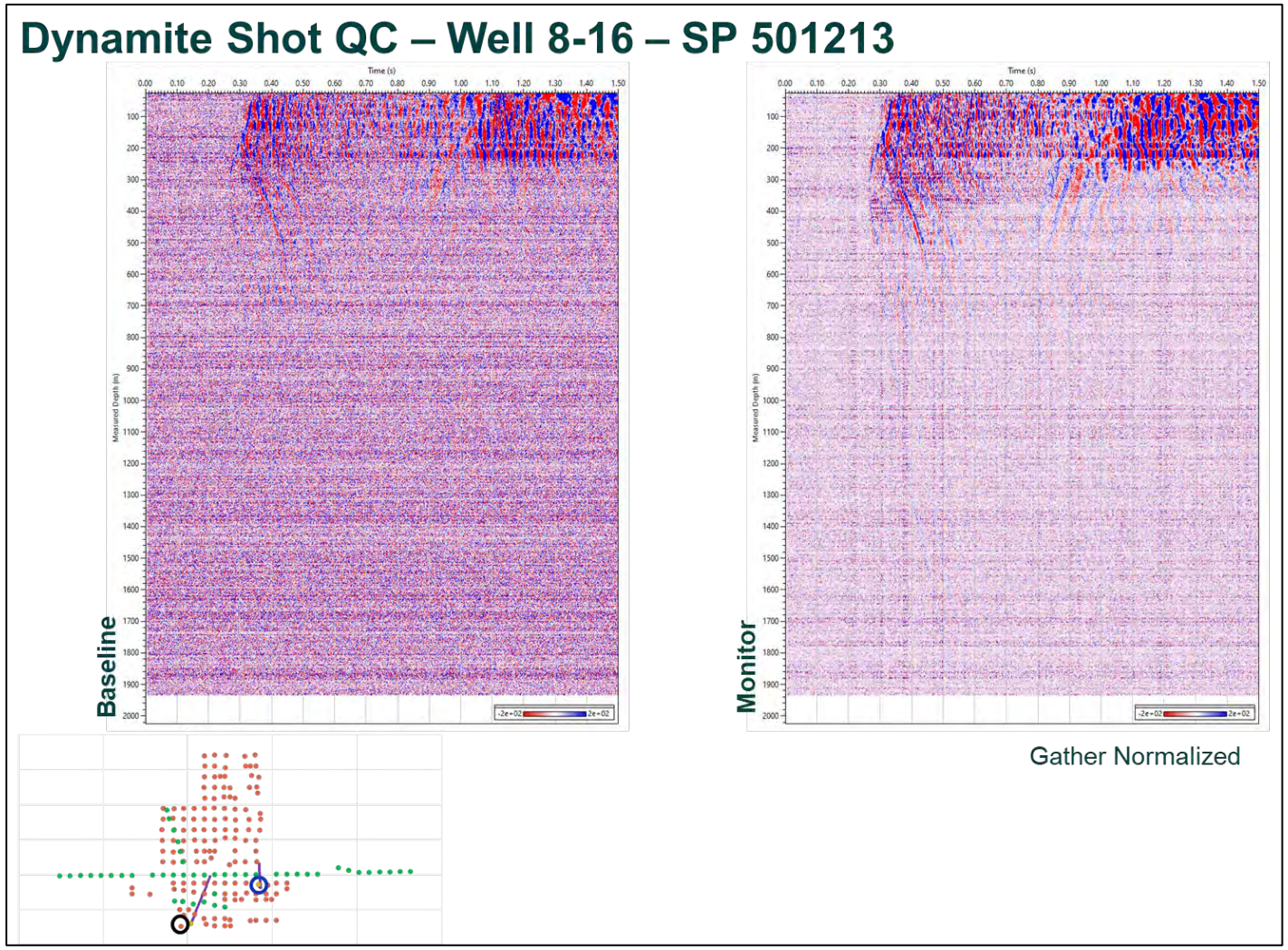


*Figure 6-60. Dynamite Shot QC – Well 8-16 – SP 501213 - Baseline and monitor survey.*

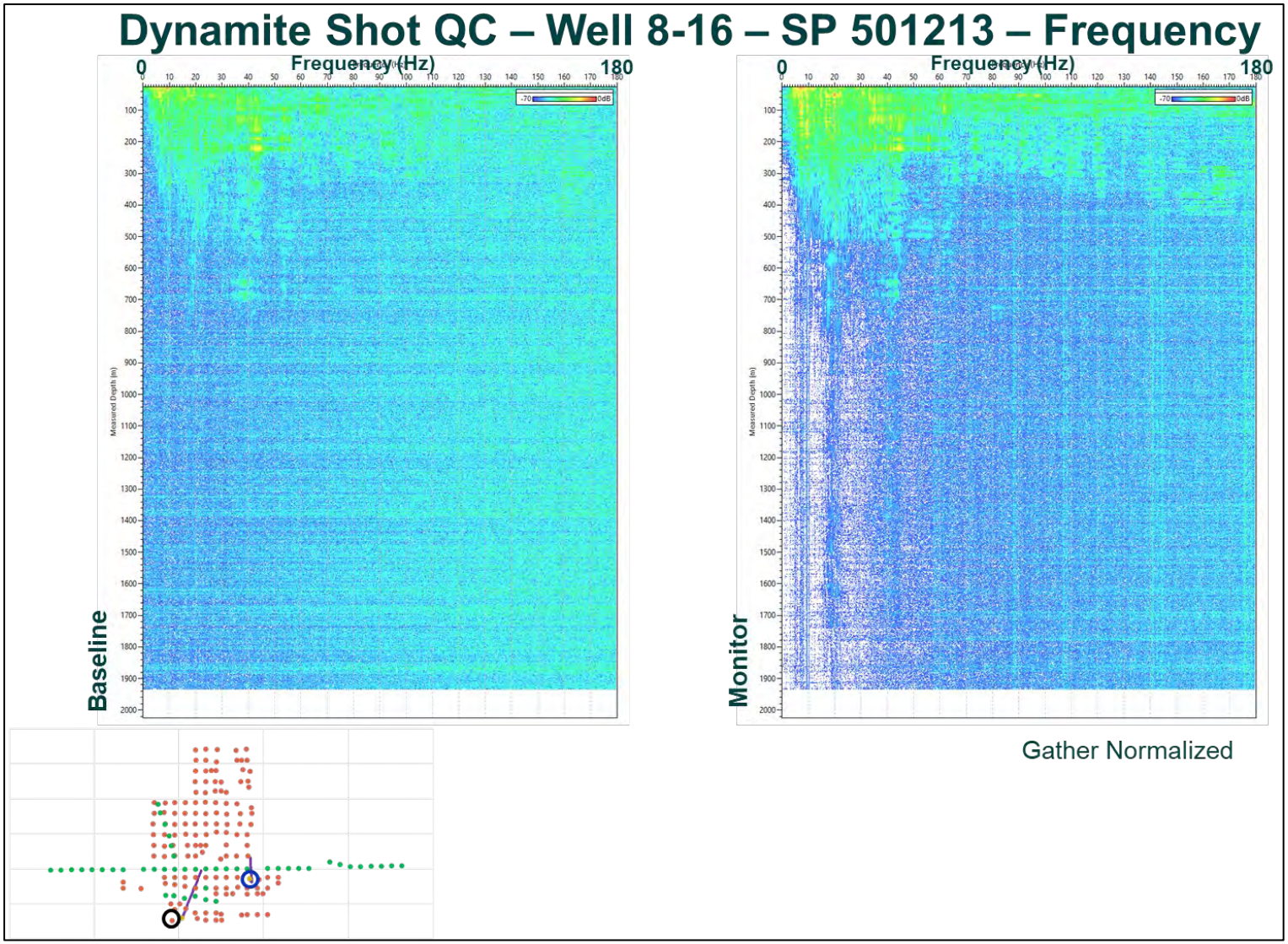


*Figure 6-61. Dynamite Shot QC – Well 8-16 – SP 501213 – Frequency - Baseline and monitor survey.*

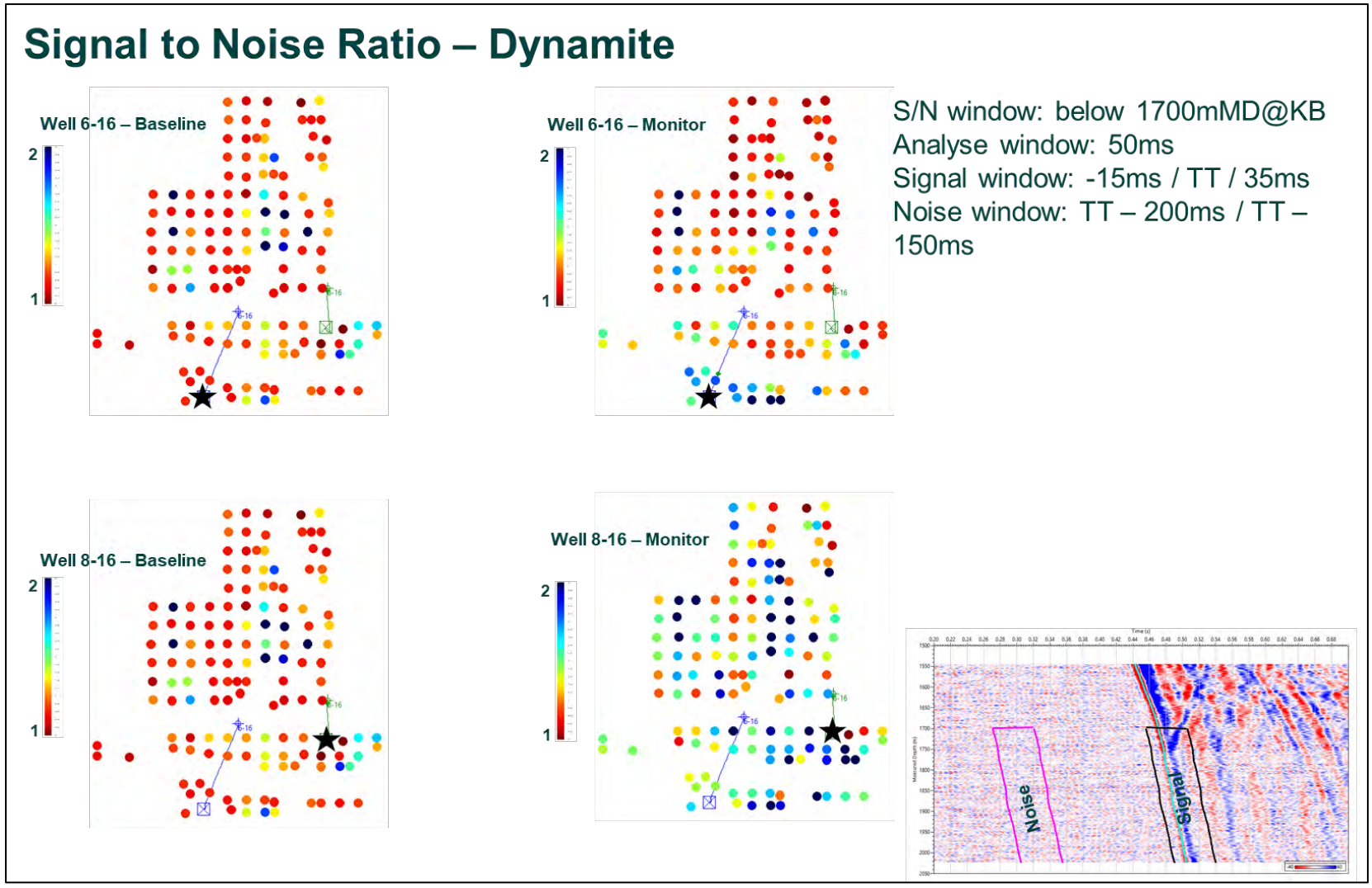


*Figure 6-62. Signal to Noise Ratio – Dynamite - Computing window below 1700 m MD. In this figure we show the average SNR computed in the same window interval as in figure 6-47 for the for well 6-16 baseline survey (top left), well 8-16 baseline survey (middle left), well 6-16 monitor survey (top right) and well 8-16 monitor survey (middle right). We applied a band pass filter (BPF) of 5,10 – 90,110Hz to the input data before the computation.*

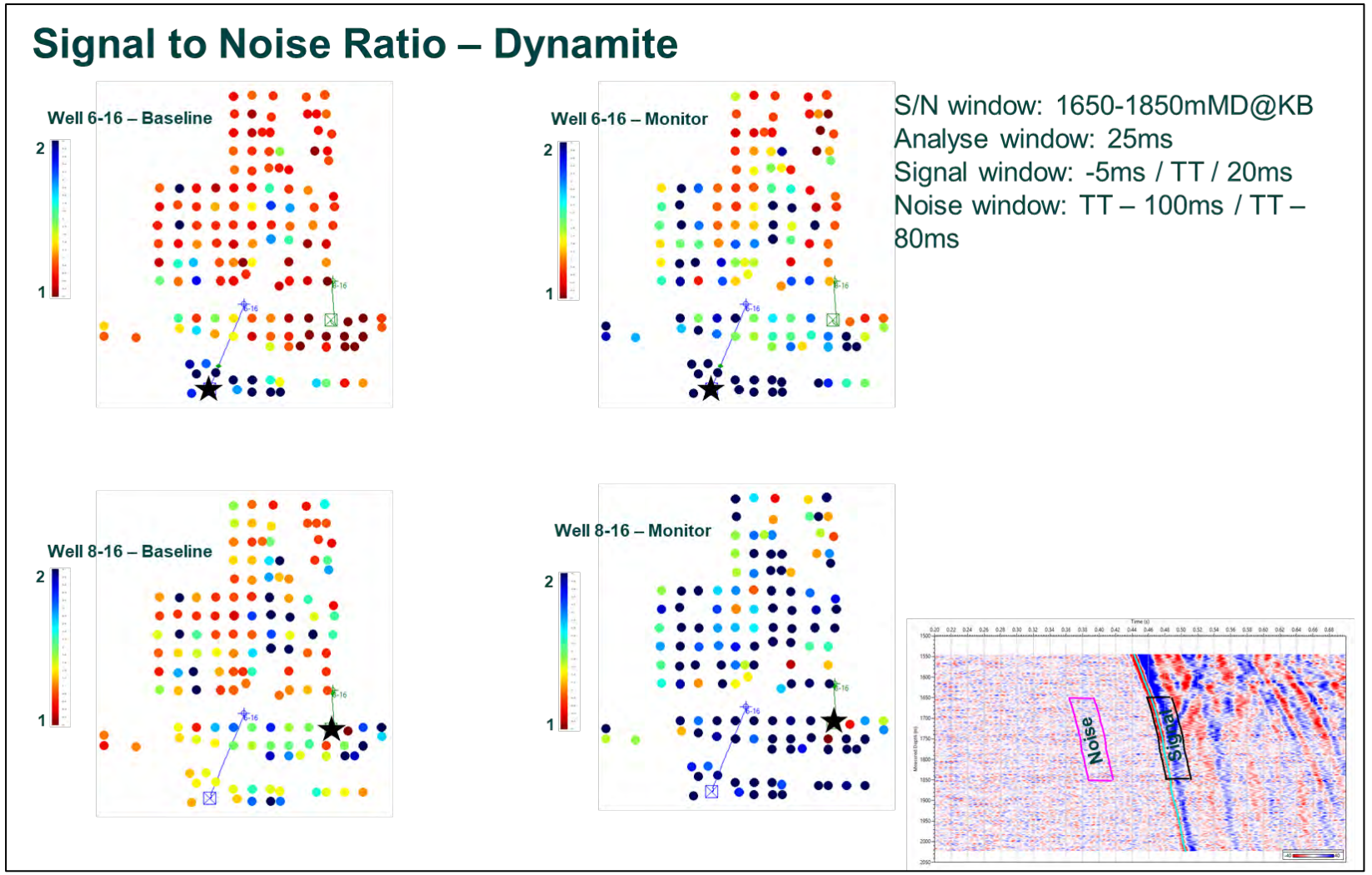


*Figure 6-63. Signal to Noise Ratio – Dynamite - Computing window 1650-1850 m MD. This figure shows also the average SNR per SP but computed in a window from 5 ms before FB to 20 ms after FB for the signal and a 20 ms window starting 100 ms before FB for the noise; the average SNR value is computed using the channels from 1650 m to 1850 m MD. Excepting the close offsets, the signal level is below or very close to the noise level; the monitor survey has a better SNR.*

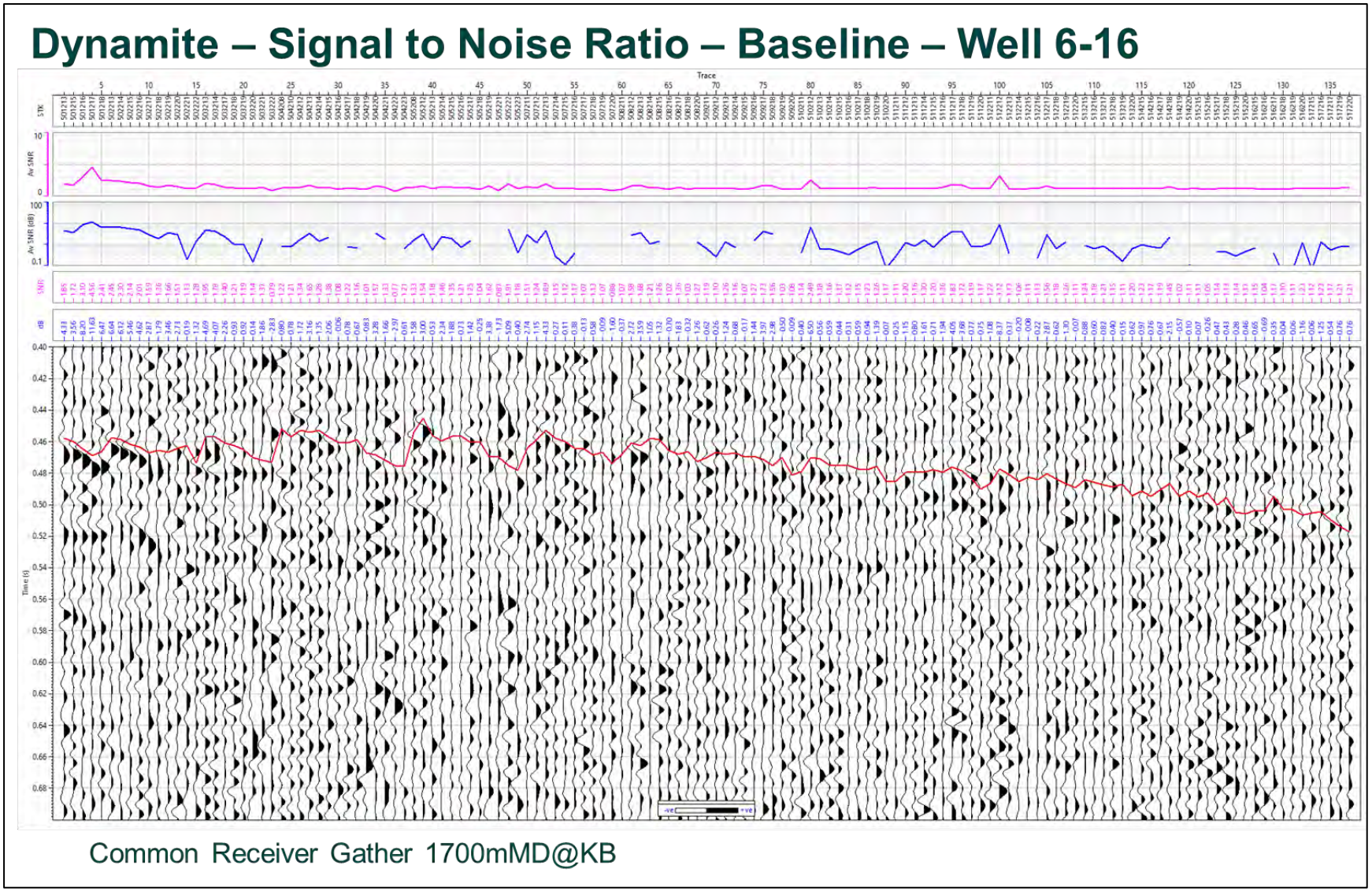


*Figure 6-64. Dynamite – Signal to Noise Ratio – Baseline – Well 6-16 - Common Receiver Gather 1700mMD@KB.*

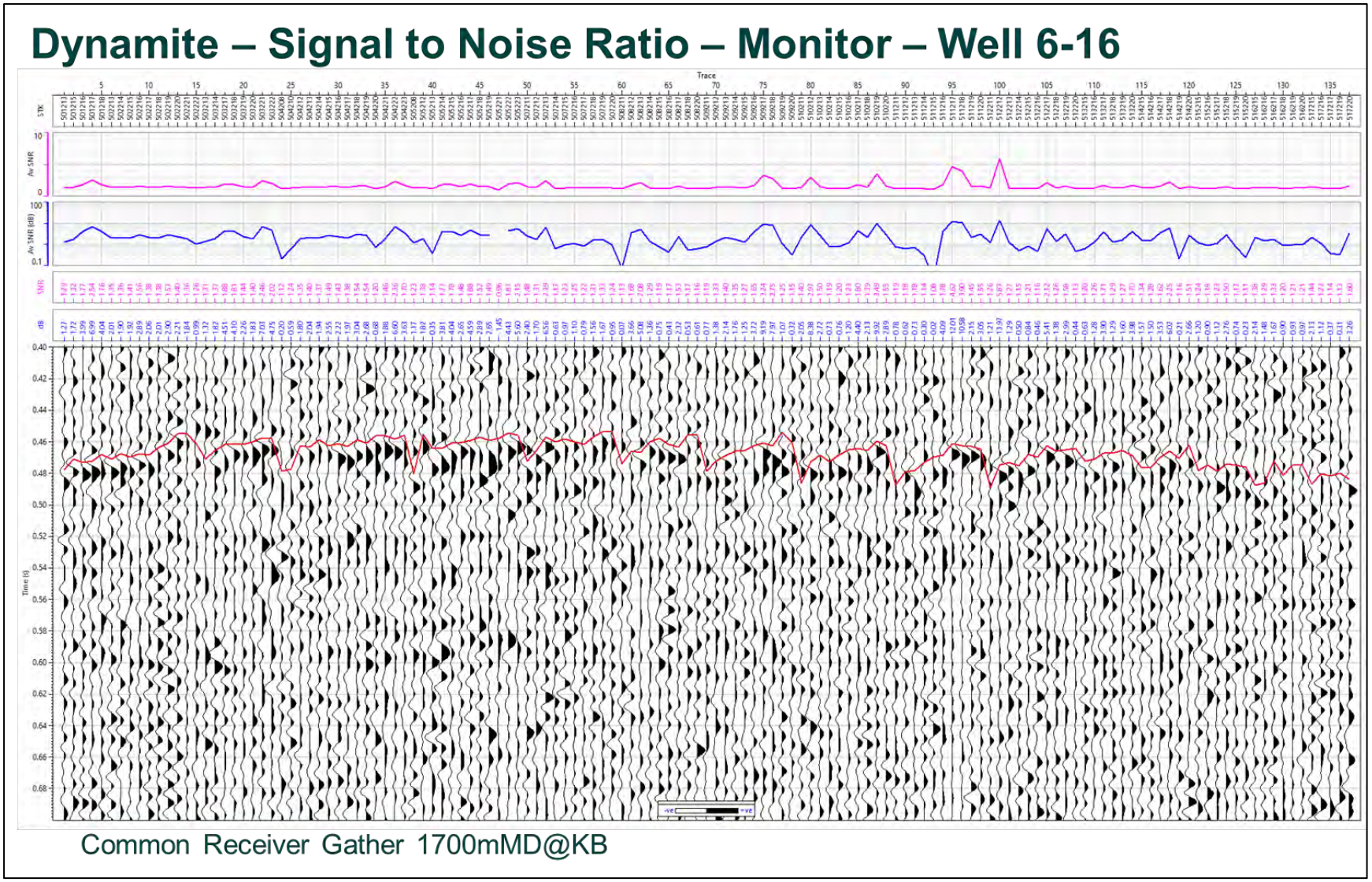


*Figure 6-65. Dynamite – Signal to Noise Ratio – Monitor – Well 6-16 - Common Receiver Gather 1700mMD@KB.*

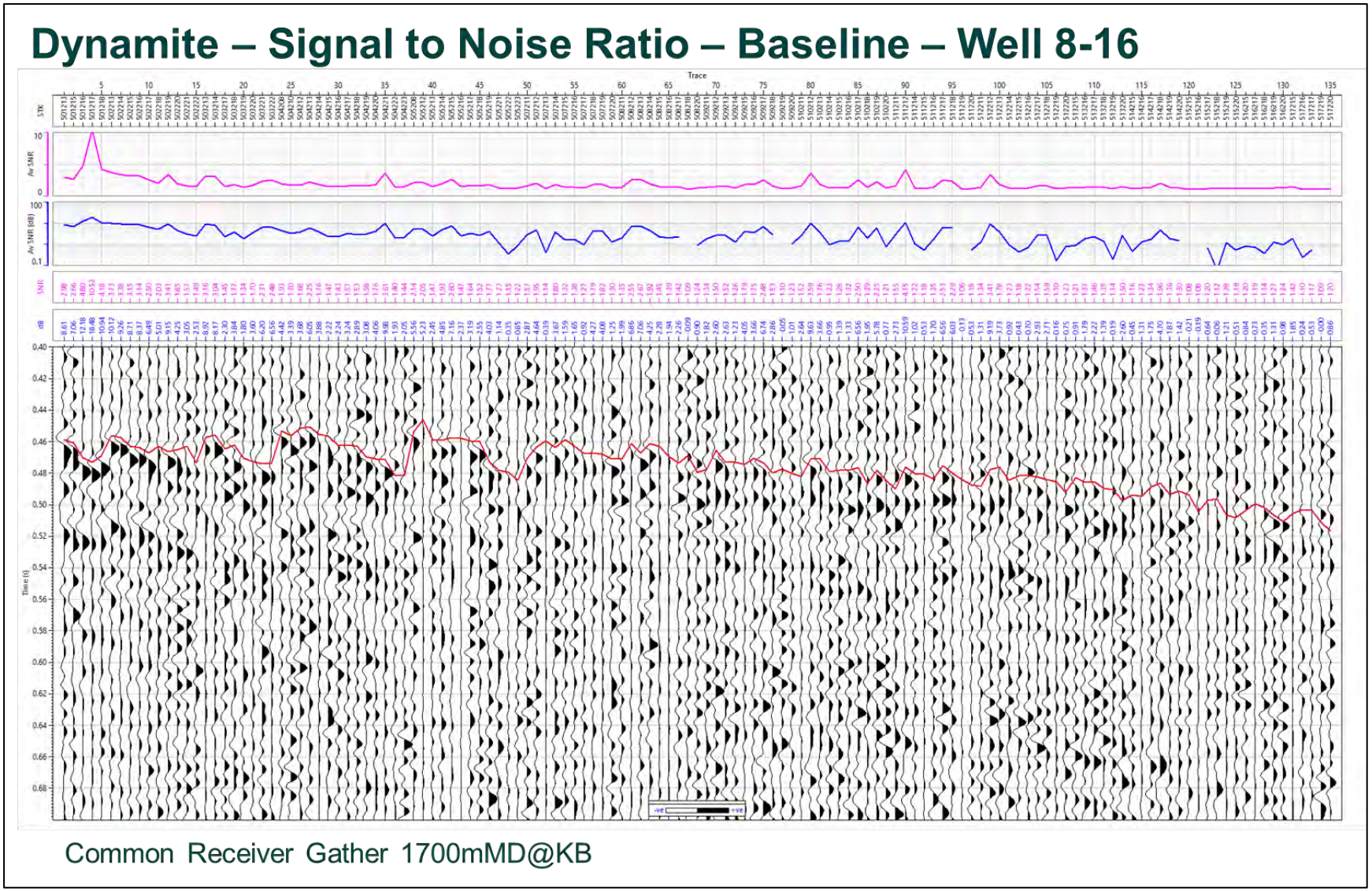


*Figure 6-66. Dynamite – Signal to Noise Ratio – Baseline – Well 8-16 - Common Receiver Gather 1700mMD@KB.*

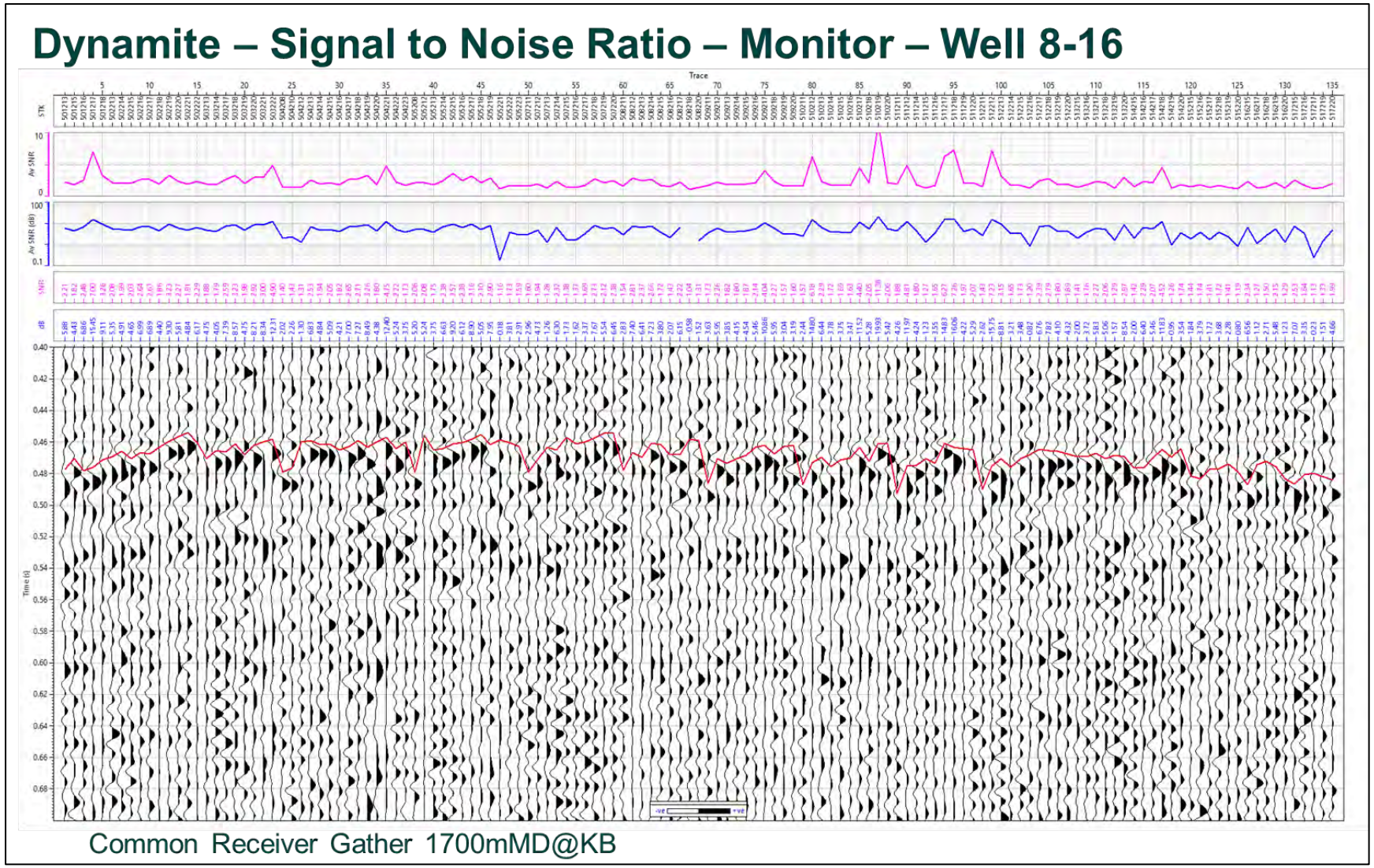


*Figure 6-67. Dynamite – Signal to Noise Ratio – Monitor – Well 8-16 - Common Receiver Gather 1700mMD@KB.*

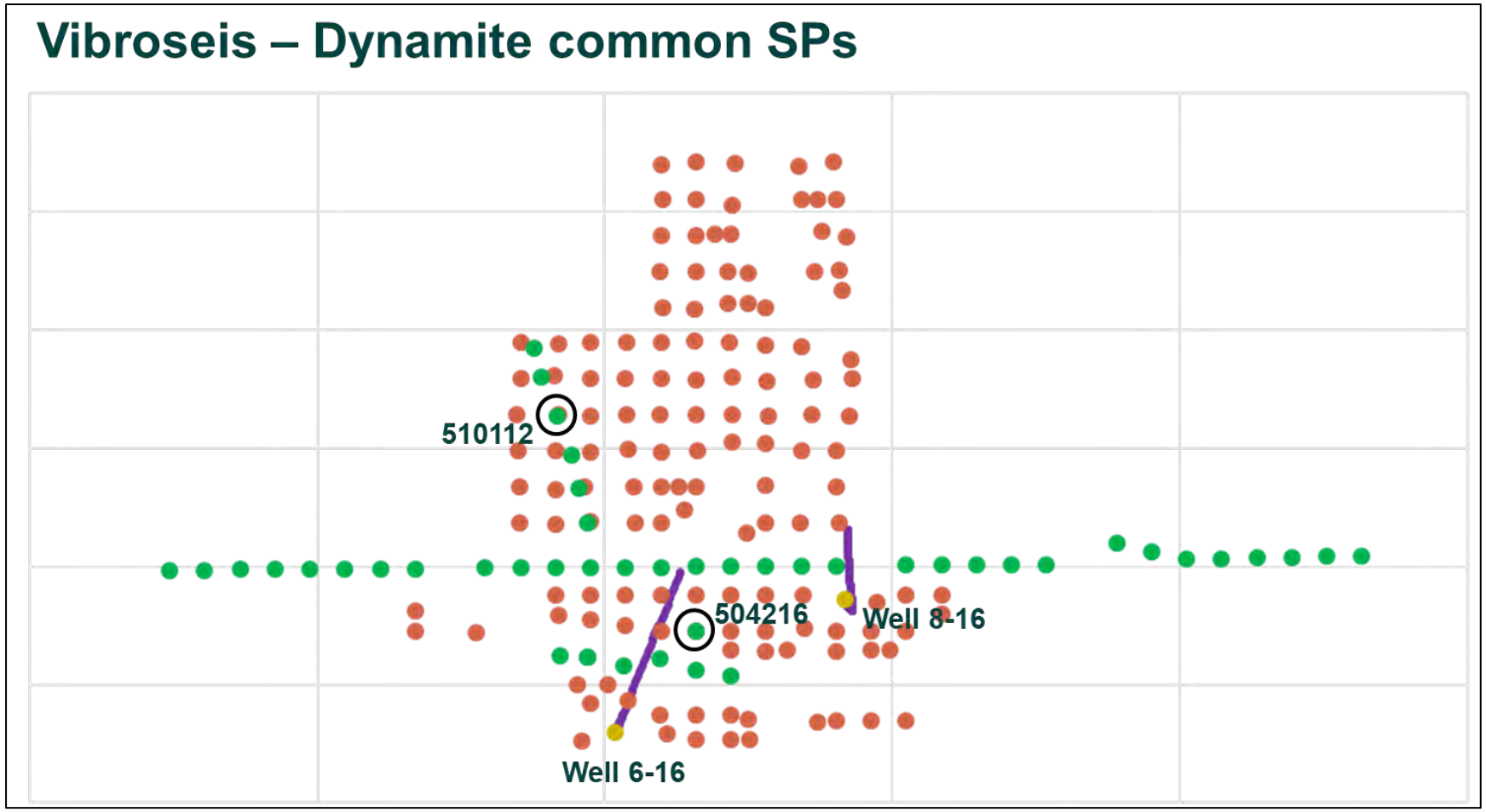


*Figure 6-68. Vibroseis – Dynamite common SPs – Basemap. Two shot point locations have both vibroseis and dynamite data.*

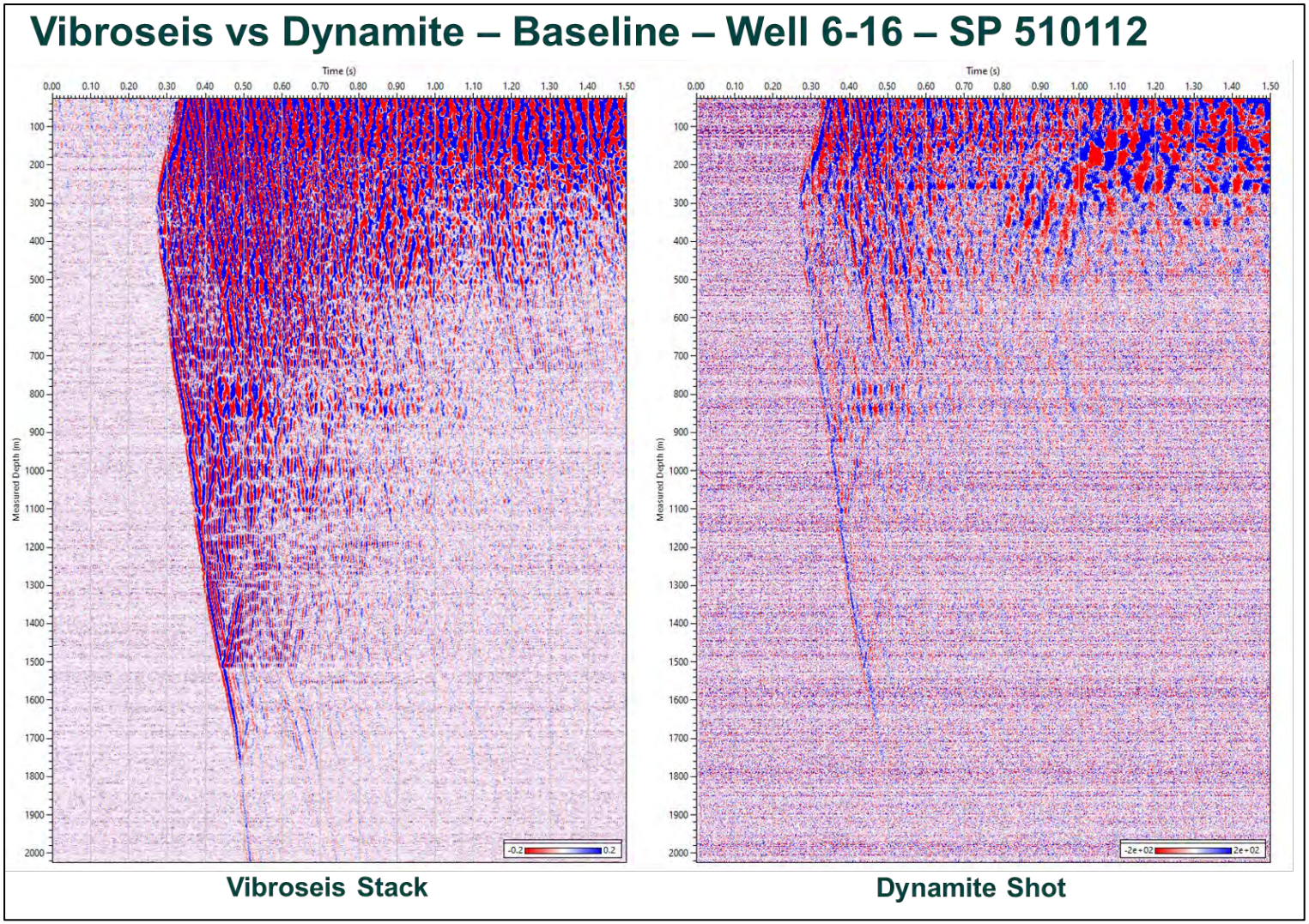


*Figure 6-69. Vibroseis vs Dynamite – Baseline – Well 6-16 – SP 510112 - Total wavefield.*

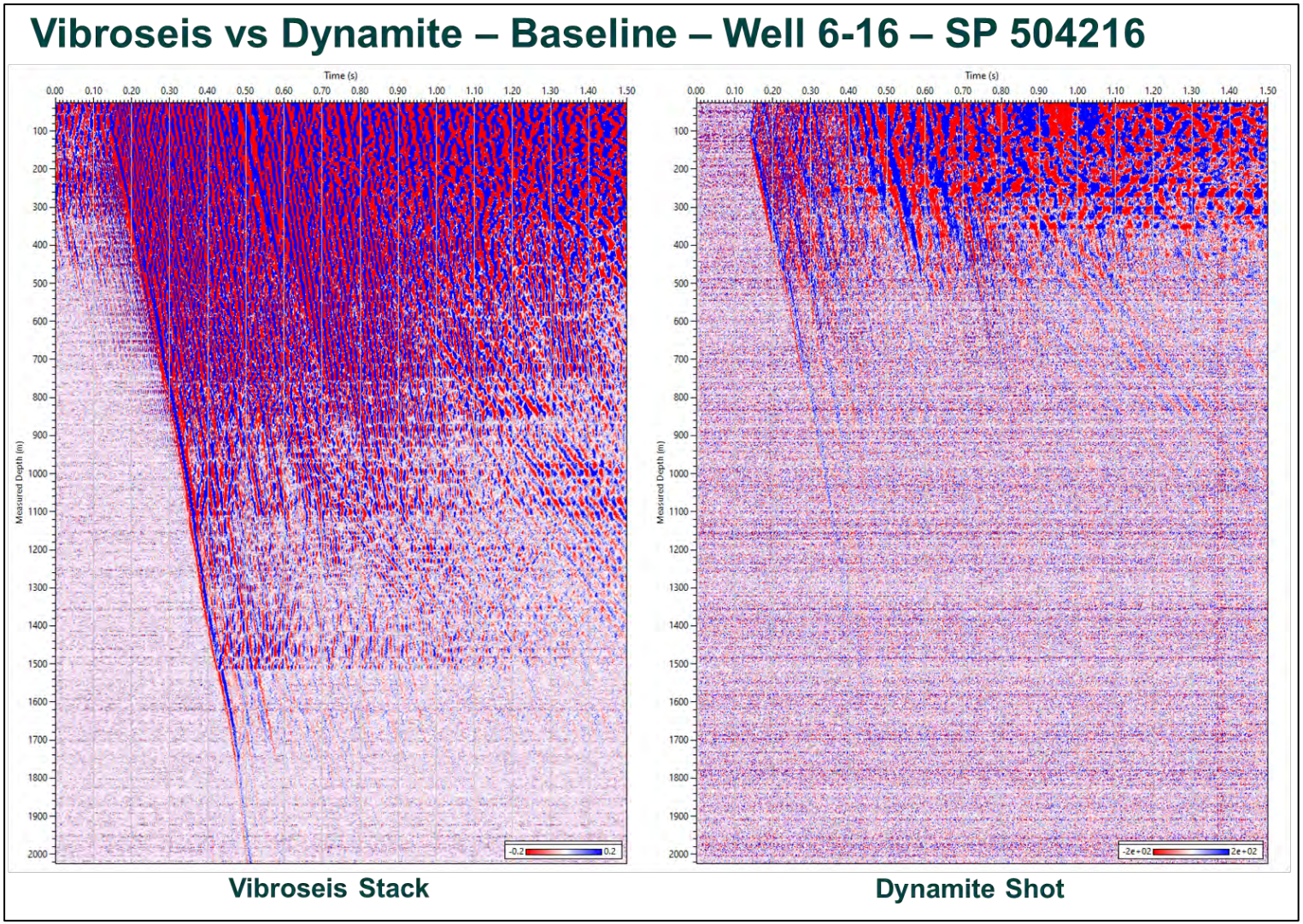


*Figure 6-70. Vibroseis vs Dynamite – Baseline – Well 6-16 – SP 504216 - Total wavefield.*

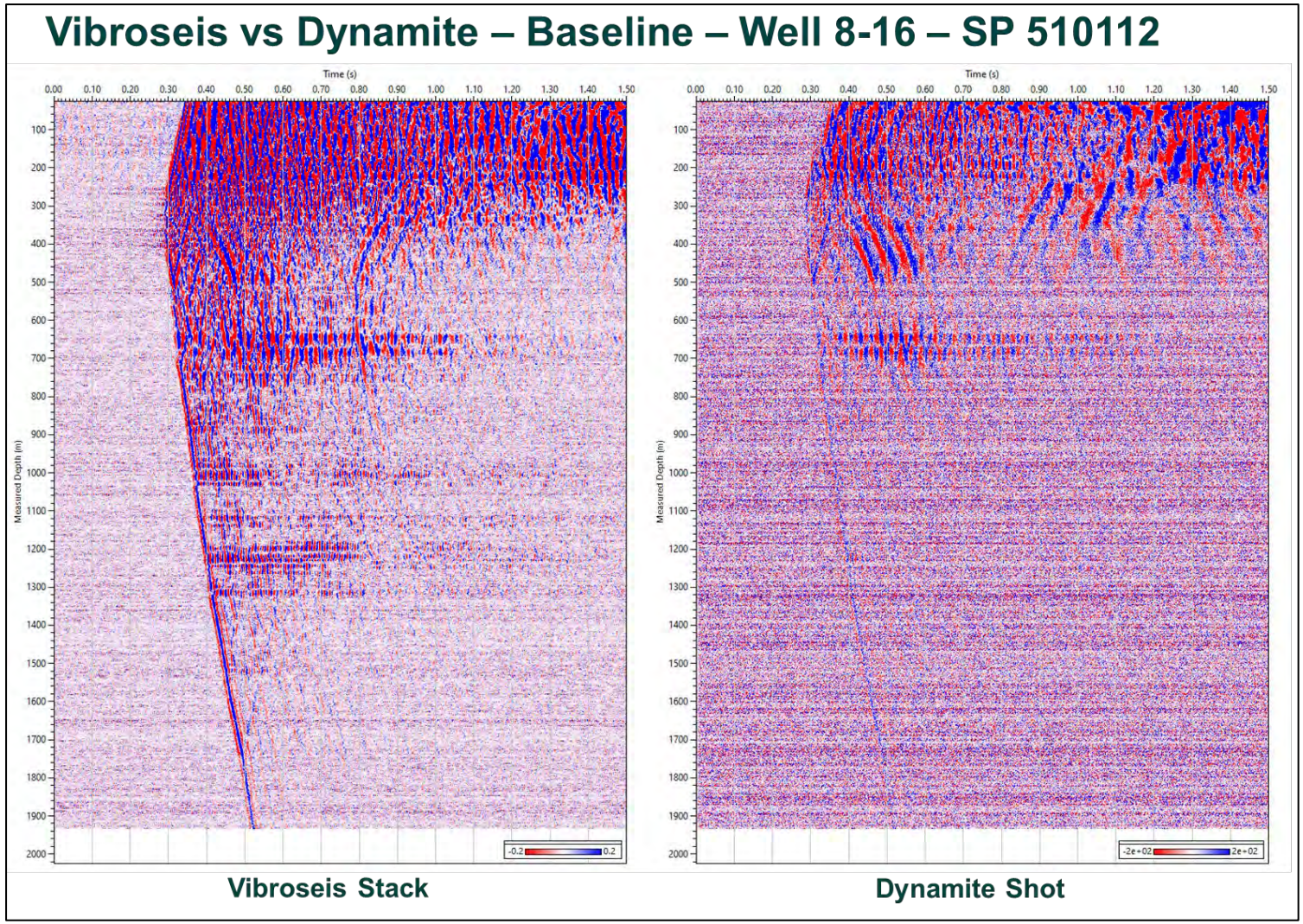


*Figure 6-71. Vibroseis vs Dynamite – Baseline – Well 8-16 – SP 510112 - Total wavefield.*

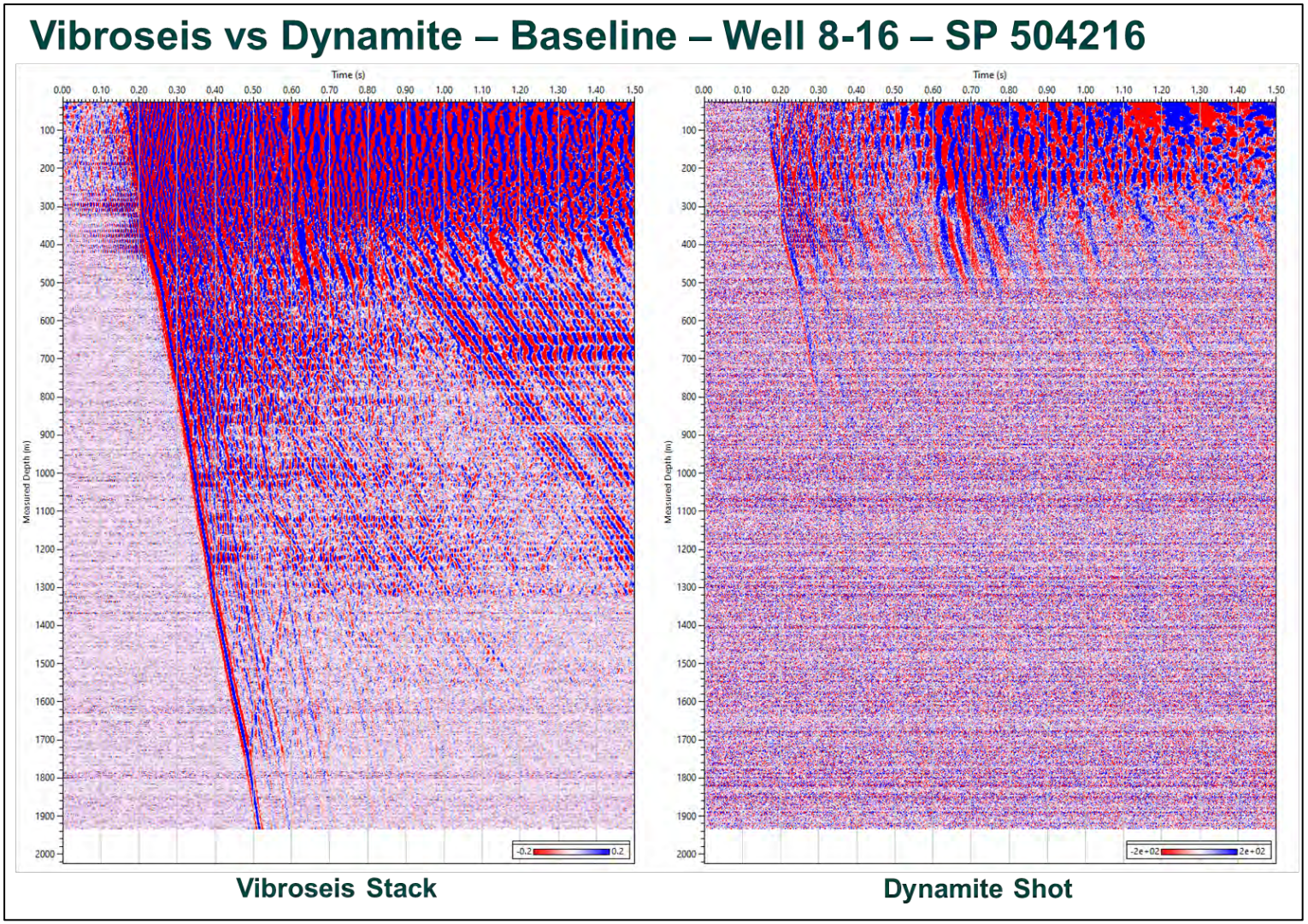


*Figure 6-72. Vibroseis vs Dynamite – Baseline – Well 8-16 – SP 504216 - Total wavefield.*

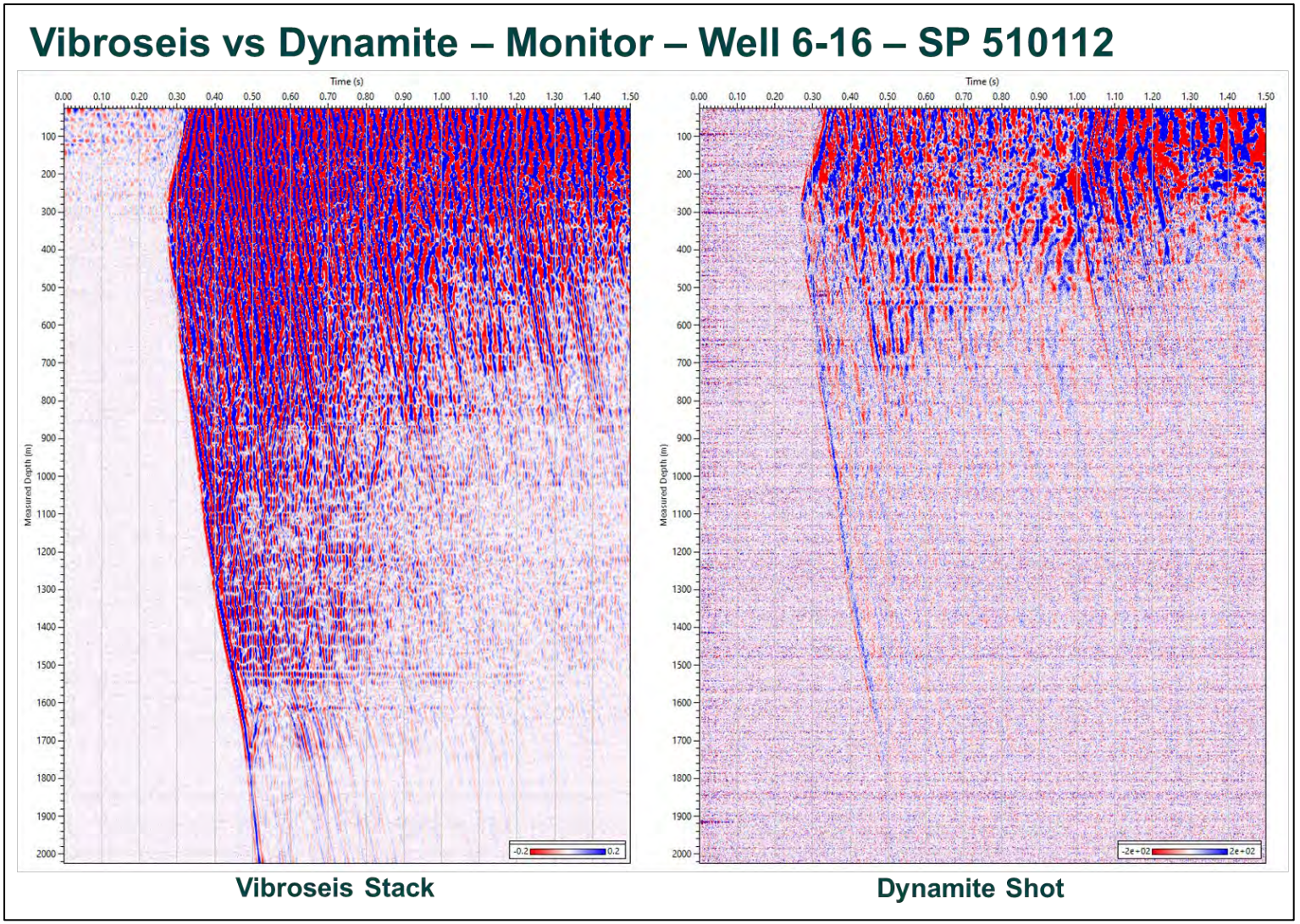


*Figure 6-73. Vibroseis vs Dynamite – Monitor – Well 6-16 – SP 510112 - Total wavefield.*

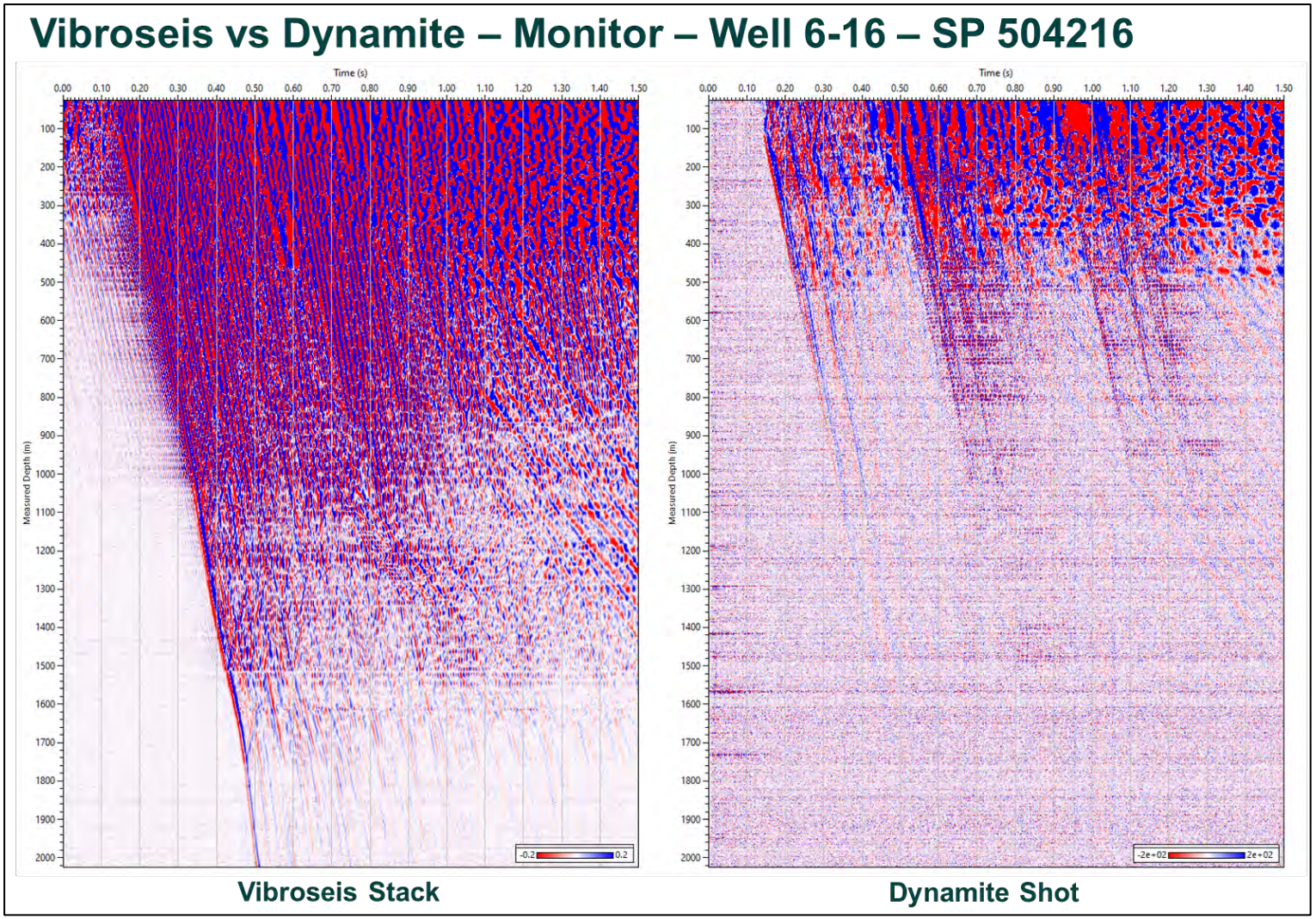


*Figure 6-74. Vibroseis vs Dynamite – Monitor – Well 6-16 – SP 504216 - Total wavefield.*

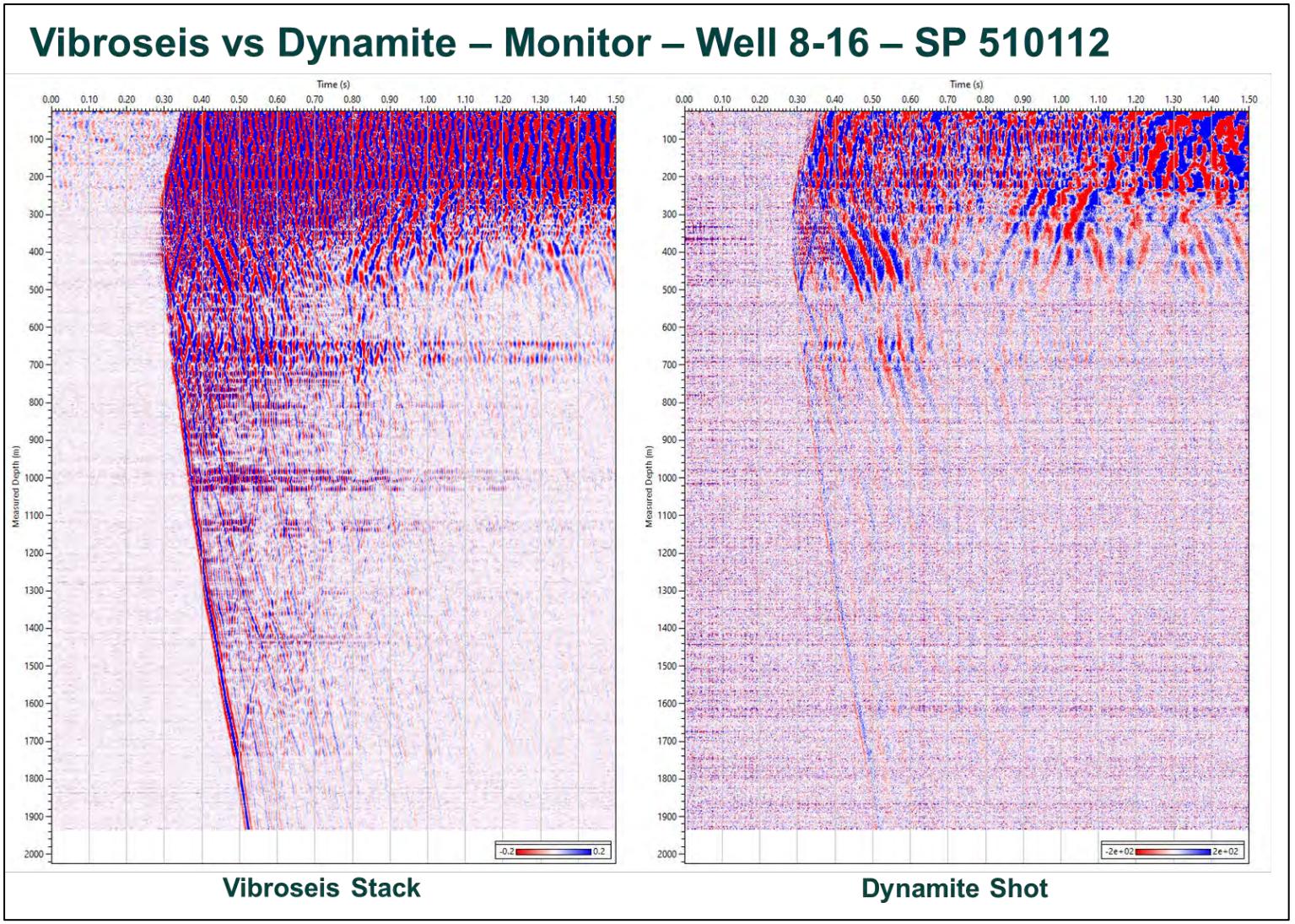


*Figure 6-75. Vibroseis vs Dynamite – Monitor – Well 8-16 – SP 510112 - Total wavefield.*

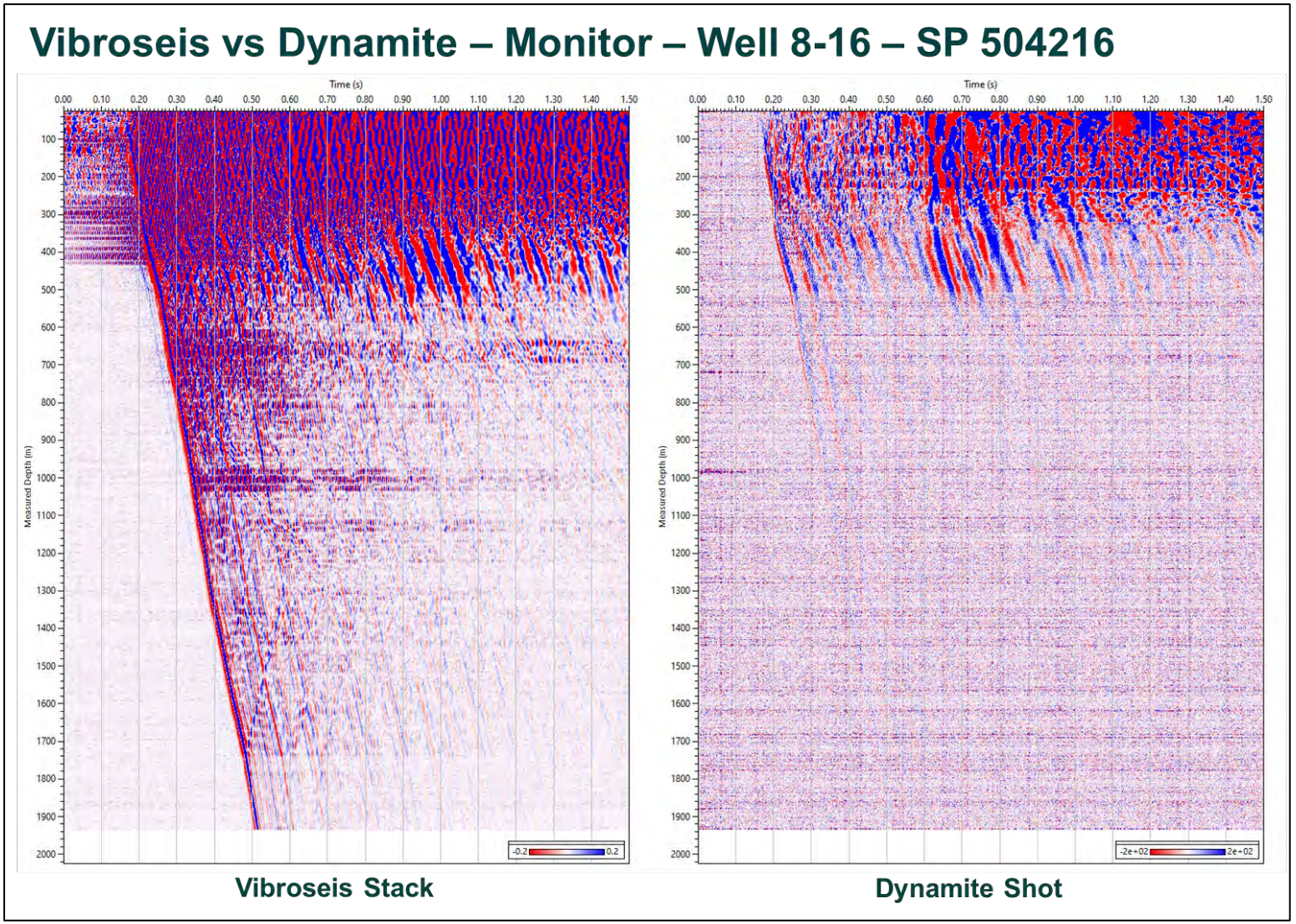


*Figure 6-76. Vibroseis vs Dynamite – Monitor – Well 8-16 – SP 504216 - Total wavefield.*

# 7 ZVSP Processing

During the monitor survey additional zero-offset VSP (ZVSP) source locations were acquired near the well heads. For well 8-16 we used for the ZVSP the data from the closest shot location available. Since well 6-16 is highly deviated and the SP data from the source near the well head is highly affected by tubing ringing, the SP 101215 is a better choice for ZVSP processing.

## 7.1 Well 8-16

The source location was a few meters away from the well head; figure 7-1 shows the acquisition geometry and the survey elevations.

Figure 7-2 presents the well casing (left) and the total wavefield (right). Data are affected by strong casing ringing above 400 m MD where the well deviation is close to vertical (below 3°) and the 5-1/2" casing is not cemented. Moreover, strong tube waves generated at the well head are recorded up to the top of cement behind the 5-1/2" casing.

The frequency spectrum after normalization (Fig. 7-3) shows a downhole recorded bandwidth up to 120Hz. Figure 7-4 presents the FK spectrum. While the tube wave has a strong amplitude in the FK domain and the down P wavefield can be separated up to 70 Hz, the Up P wavefield cannot be isolated. As the depth sampling is very fine, data is not aliased.

Figure 7-5 shows the first arrival amplitude decay. The data was analysed in a window of 15 ms before First Break (FB) to 50 ms after FB. The data follow a typical trend and highlight areas with strong ringing. At the A2 Carbonate level there is a strong drop of the FB amplitude.

### 7.1.1 Picking

A few manually picked points guided the automatic picking which we performed on the enhanced weighted semblance wavefield calculated within the 0.18 – 0.35 ms/m range of slopes, over a 20 m window (Fig. 7-6). We calculated the semblance RMS value for each depth and picks with an RMS semblance value below 0.7 were discarded (Fig 7-7). The picks were interpolated and smoothed over 5 depth levels. Figure 7-8 presents the time to depth curve in the first panel, the average and interval velocity profile in panel 2, semblance RMS near the FB in panel 3 and the picked stack in panel 4.

There is a good match between the interval velocity from the VSP and the acoustic log compressional velocity (Fig. 7-9). This is a good validation of the picking quality.

### 7.1.2 Processing

Figure 7-10 shows the processing input stack data filtered with a BPF: 5,10-90,110 Hz. The amplitudes displayed are cross-normalized. To reduce the casing ringing we applied a 66-92 Hz tracking filter over the following intervals: 628-764 m MD, 995-1037 m MD, 1094-1146 m MD, 1180-1265 m MD, 1265-1326 m MD, 1412-1444 m MD, 1485-1533m MD (Fig. 7-11).

To compensate for absorption and spherical divergence spreading, the amplitude was scaled by the squared sample time. Figure 7-12 shows in panel 1 the RMS amplitude near FB before and after amplitude recovery. After the amplitude recovery the RMS amplitude follows a trend closer to a constant value. In panel 2 is the stack data aligned along the transit time (TT). The stack after amplitude recovery is presented in figure 7-13.

Figure 7-14 shows the stack aligned along the first break in the frequency-slowness domain (FP). To remove noise and tube waves, the slowness outside -1.7 – 0.6 was muted. Figure 7-15 presents the

data after the separation in FP domain. The data from figure 7-15 was muted above the tube wave limit (Fig. 7-13 black).

The Down S wavefield in figure 7-16 was removed using a median filter over 121 traces aligned along the modelled Down S TT (Fig. 7-15 green).

Figure 7-17 shows the Down P wavefield after enhancement using a median filter of 121 traces along the FB. This wavefield will be used later for the deconvolution.

The Up P wavefield was enhanced in the FP domain in a slowness window of -0.15 to 0.15 ms/trace (Fig. 7-18). The input data was aligned along the A2 Carbonate modelled TT (Fig. 7-13 green) before FP transform. Figure 7-19 shows the enhanced Up P along the modelled A2 Carbonate TT over a 10 trace window after the separation in the FP domain.

To reduce the multiples and increase the data frequency, the enhanced Up P was deconvolved (Fig. 7-20). We applied a trace by trace deterministic deconvolution with enhanced Down P (Fig. 7-17) using a 0.15 s operator length and 20% white noise to the enhanced Up P. Finally, the data were filtered with a 5,10-90,110 Hz BPF. The deconvolved Up P wavefield in TWT is presented in figure 7-21.

### 7.1.3 Log calibration and synthetic seismogram

A synthetic seismogram which represents the expected seismic response along the well trajectory was computed using the acoustic and density logs. As the VSP travel path can be different than the acoustic log measuring path, the acoustic log is calibrated with the VSP data.

Figure 7-22 shows the principle of acoustic calibration: the raw acoustic log (graph 1), is extended up to the first VSP receiver (graph 2). The acoustic log is converted from slowness to velocity and is integrated to obtain the transit time (graph 3). The difference (drift log) between the log TT and the VSP TT is computed (graph 5). To reduce the drift, correction values are defined at some points called knee points (graph 6). Between the knee points the correction is interpolated and is added to the acoustic TT (graph 7). The residual drift between the corrected acoustic TT and the VSP TT is computed for QC (graph 8). Finally, the corrected acoustic TT is differentiated to slowness (graph 9). The final graph (graph 10) shows the acoustic log before and after the calibration.

The well 8-16 log calibration is presented in figure 7-23. The first graph shows the acoustic log before calibration in light blue and in blue the acoustic log after calibration. In the second graph is the log-VSP drift before calibration in light blue and the residual drift in blue. The third graph presents the knee points and the correction values and in the right panel is the lithological column. Only three knee points were required to calibrate the acoustic log. The residual drift after acoustic log calibration is below 1 ms.

Figure 7-24 shows the workflow used to compute the synthetic seismogram. The first three graphs show the input logs in depth. The calibrated acoustic log and the density log are used further in the workflow. If the density is not available it can be estimated for example using Gardner's equation or replaced with a constant value. The logs are converted in time (graphs 4 and 5) using the time to depth function computed from the calibrated acoustic log integration. The acoustic log is converted from slowness to velocity (graph 6) and this velocity log is then multiplied with the density log to find the acoustic impedance (graph 7). Graph 8 shows the reflection coefficients computed using the formula written below the graph. The reflection coefficients are convolved with a wavelet (synthetic wavelet or extracted from the seismic data) (panel 9) to produce the synthetic seismogram from panel 10.

Figure 7-25 presents a composite plot with the logs in time, the lithological column, reflection coefficients, the wavelet used to compute the synthetic seismogram on the left side and enhanced Upgoing P wavefield, the corridor and the corridor stack on the right side (from right to left). There is a

good tie at the main reflectors between the synthetic seismogram and the ZVSP corridor stack. The top of the A2 Carbonate is represented by the strong positive reflection at 0.55 s TWT (strong blue reflector) and the top of the A1 Carbonate by the following trough (red reflector).

## 7.2 Well 6-16

The source location is in the middle of the well trajectory projected on a surface, 148 meters away from the well head. Figure 7-26 shows the acquisition geometry and the 6-16 ZVSP survey elevations.

Figure 7-27 shows the well casing (left) and the total wavefield (right). The data above 1520 m MD, where the well deviation is below 3°, is affected by strong tubing and casing ringing. Weak tube waves and the Down S wavefield are also recorded.

The frequency spectrum after normalization (Fig. 7-28) shows that the data recorded in the reservoir area is affected by a high frequency noise. Figure 7-29 presents the FK spectrum. The tube wave has a weak amplitude in the FK domain. The Down and Up waves have strong amplitudes, but are mainly generated by the ringing. As the depth sampling is very fine the data is not aliased.

Figure 7-30 shows the first arrival amplitude decay. The data have been analysed in a window from 15 ms before FB to 50 ms after FB. The data follow a normal trend, the limit of the depth interval with strong ringing is noticeable from the graph shape. At the A2 Carbonate level there is a drop in the FB amplitude.

### 7.2.1 Picking

Few manual points guided the automatic picking which was performed on the enhanced weighted semblance wavefield between 0.18 and 0.35 ms/m over a 20 m window (Fig. 7-31). Above 900 m MD manual editing was required. The semblance RMS value was calculated for each depth and below 0.6 RMS semblance value the picks were discarded (Fig 7-32). The picks were interpolated and smoothed over 5 levels. Figure 7-33 presents the time to depth curve on track 1, the average and interval velocity profile on track 2, the semblance RMS near the FB on track 3 and the picked stack on track 4.

Above 1540 m MD there is a poor match between the interval velocity from the VSP and the acoustic log compressional velocity (Fig. 7-34) as the VSP is recording velocity close to elastic wave in the steel.

### 7.2.2 Processing

Figure 7-35 shows the processing input data, a filtered stack data with a BPF: 5,10-90,110 Hz. The data above 1540 m MD affected by ringing were excluded from the processing. The amplitudes displayed are cross-normalized.

To compensate for the absorption and spherical divergence spreading, the amplitude was scaled by the squared sample time. The stack after amplitude recovery is presented in figure 7-36.

Figure 7-37 shows the stack aligned along the first break in the frequency-slowness domain (FP). To remove noise and tube waves, the data was muted outside the -1.7 – 0.6 slowness interval then the separation was performed in the FP domain (Figure 7-38).

The Down S wavefield shown in figure 7-39 was removed using a median filter over 121 traces aligned along the modelled Down S TT (Fig. 7-38 green).

We enhanced the Down P wavefield using a median filter of 121 traces along the FB (Figure 7-40). This wavefield will be used later in the deconvolution.

The Up P wavefield was enhanced in the FP domain in a slowness window of -0.25 to 0.15 ms/trace (Fig. 7-41). The input data were aligned along the A2 Carbonate modelled TT (Fig. 7-36 green) before FP. Figure 7-42 shows the enhanced Up P along the modelled A2 Carbonate TT over a 10 trace window after the separation in the FP domain.

To reduce the multiples and boost the high frequency data, the enhanced Up P was deconvolved (Fig. 7-43). Trace by trace deterministic deconvolution with enhanced Down P (Fig. 7-40) using a 0.15 s operator length and 20% white noise was applied to the enhanced Up P. Finally, the data were filtered with a 5,10-90,110 Hz BPF. The deconvolved Up P wavefield in TWT is presented in figure 7-44.

### 7.2.3 Log calibration and synthetic seismogram

The log calibration for well 6-16 is presented in figure 7-45. The first panel shows the acoustic log before calibration in light blue and in blue the acoustic log after calibration. In second panel is the log-VSP drift before calibration in light blue and the residual drift in blue. The third panel presents the knee points and the correction values and in the last panel is the lithological column. Only two knee points were required to calibrate the acoustic log located in the same area as the knee points used for well 8-16. The residual drift after acoustic log calibration is below 1.5 ms.

Figure 7-46 presents (from right to left): a composite plot with the logs in time, the lithological column, the reflection coefficients, the wavelet used to compute the synthetic seismogram on the left side and enhanced Upgoing P wavefield, the corridor and the corridor stack on the right side. There is a good tie at the main reflectors between the synthetic seismogram and the ZVSP corridor stack. The top of A2 Carbonate is represented by the strong positive reflection at 0.56 s TWT (strong blue reflector) and the top of A1 Carbonate by the following trough (red reflector).

## 7.3 Strain rate to geophone equivalent

DAS and geophones measure different quantities: the strain of the fibre (output as strain rate) for DAS system and the particle velocity for geophone. A workflow was developed to convert the DAS strain rate to geophone equivalent data. The conversion may introduce artefacts in the data or may increase the noise level. A test of geophone equivalent processing was made using well 8-16 ZVSP data.

The conversion was made by integrating in time the stack data (Fig. 7-2). We used a leaky integration with a 0.96 coefficient followed by a phase rotation of -90°. Then we filtered the data with a 5,1-90,110 Hz BPF. Figure 7-47 shows the well 8-16 ZVSP total wavefield after conversion from strain rate to geophone equivalent.

After conversion, the frequency spectrum is rebalanced by increasing the low frequencies and decreasing the higher ones (Fig. 7-48). The wavefield slopes in the FK domain are not affected by the conversion (Fig. 7-49).

The data was picked using the same workflow presented in section 7.1.1. Figure 7-50 shows the semblance and the geophone equivalent stack after picking. The picked times are less consistent at the well bottom due to the low SNR. The geophone-equivalent data picks follow the same velocity trend as the strain rate stack picks (Fig. 7-51).

The same workflow and parameters used to process the well 8-16 ZVSP strain rate data was used to process the well 8-16 ZVSP geophone-equivalent data.

Figure 7-52 presents the enhanced Down P wavefield used in the deconvolution. Comparing with the strain rate data, the main multiples are similar, but with a lower frequency bandwidth.

The enhanced Up P wavefield (Fig. 7-53) is mapping the same reflections as the strain rate enhanced Up P wavefield. The geophone equivalent deconvolved Up P is presented in figure 7-54.

A BPF 5,10-70,70 Hz was applied to the strain rate deconvolved Up P (Fig. 7-55) and geophone equivalent deconvolved Up P (Fig. 7-56). Both wavefields present the same seismic response and amplitude response.

As the processed strain rate and geophone equivalent data have a similar seismic response, to avoid the additional noise introduced by the conversion artefacts, the time-lapse analysis was made on the strain rate data.

| Title | Description | Figure |
|---|---|---|
| Remove Down-S | Median filter | **7.39** |
| Enhanced Down-P | Median filter | **7.40** |
| FP domain – data aligned along modelled A2 Carbonate TT | Enhance Up P | **7.41** |
| Enhanced Up-P | After FP separation | **7.42** |
| Deconvolved enhanced Up-P | Trace by trace deterministic deconvolution | **7.43** |
| 6-16 ZVSP – Deconvolved Up-P - TWT | | **7.44** |
| Acoustic log calibration | | **7.45** |
| Synthetic seismogram | | **7.46** |
| | | |
| **7.3 Strain rate to geophone equivalent** | | |
| Total wavefield – Geophone Equivalent | Leaky integration in time | **7.47** |
| Frequency spectrum | Stack after normalization | **7.48** |
| FK spectrum | Stack after normalization | **7.49** |
| Picking | Integrated stack | **7.50** |
| Picking – Velocity profile | Log vs VSP | **7.51** |
| Enhanced Down-P | | **7.52** |
| Enhanced Up-P | | **7.53** |
| Deconvolved enhanced Up-P | Trace by trace deterministic deconvolution | **7.54** |
| Deconvolved enhanced Up-P – Strain Rate | BPF: 5,10-70,90 Hz | **7.55** |
| Deconvolved enhanced Up-P – Geophone Equivalent | BPF: 5,10-70,90 Hz | **7.56** |

*Table 7-15 ZVSP Processing figures*

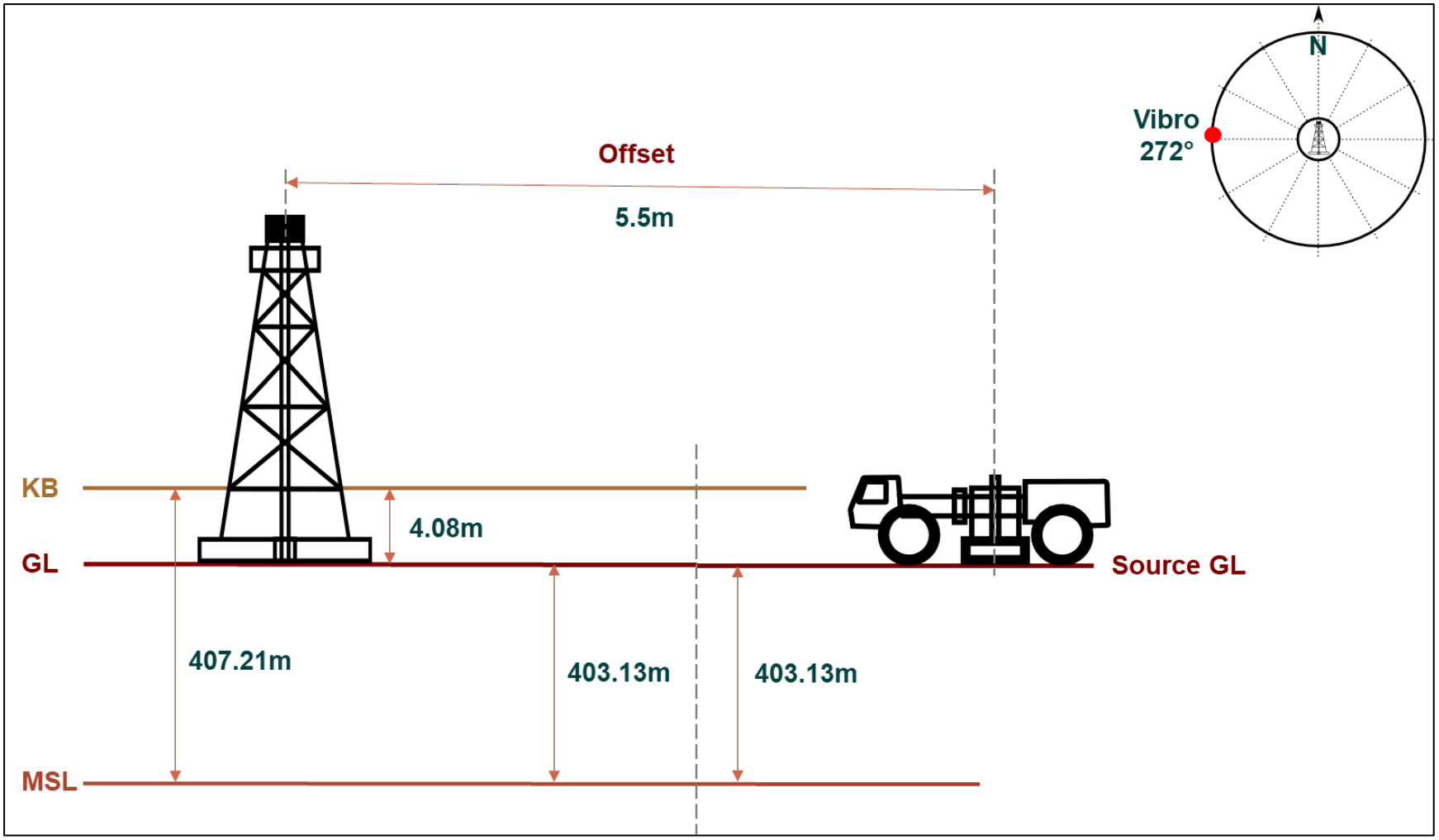


*Figure 7-1. Acquisition Geometry – Well 8-16 - Well and source elevations. The source location was a few meters away from the well head; figure 7-1 shows the acquisition geometry and the survey elevations.*

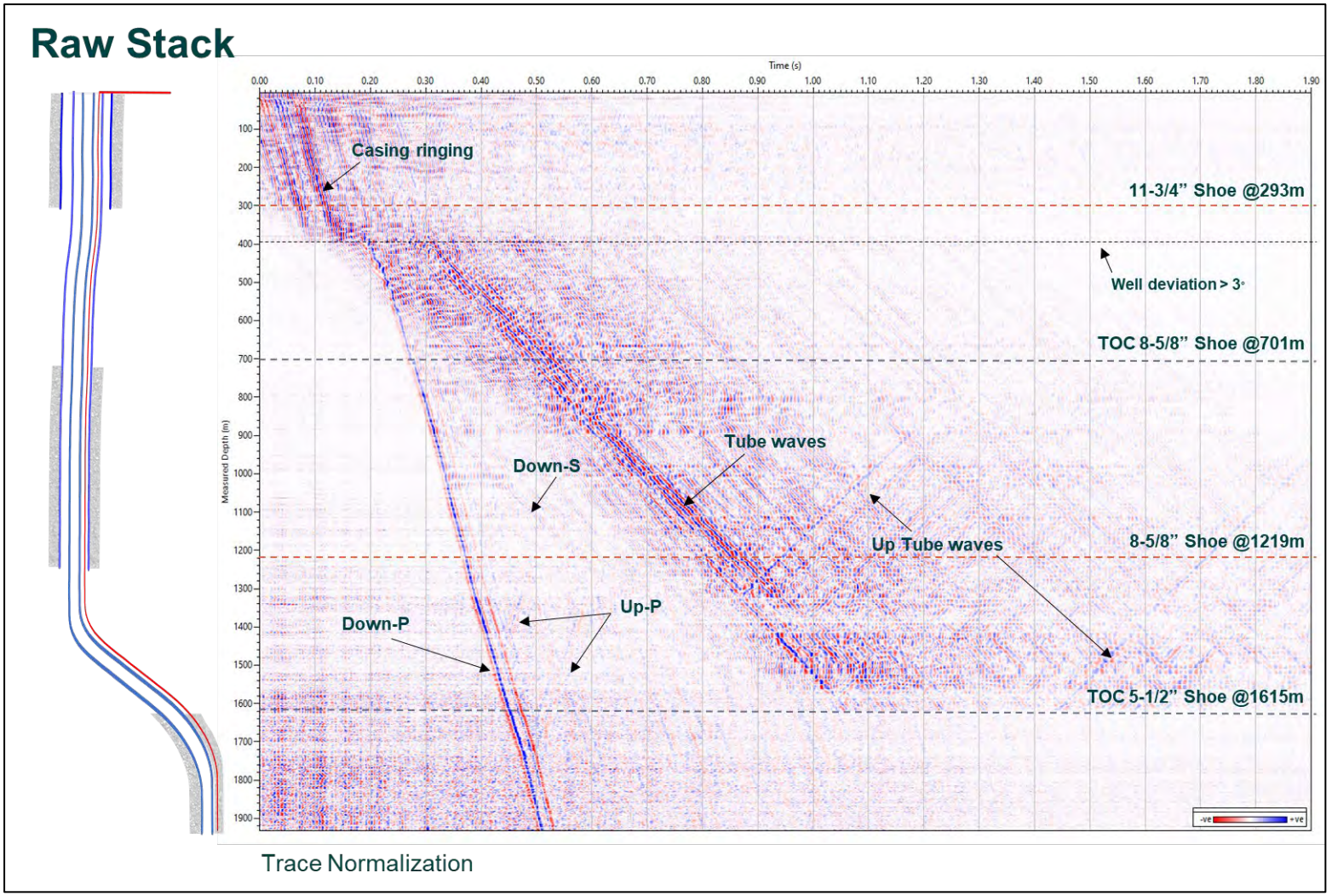


*Figure 7-2. Raw Stack - Total wavefield. It presents the well casing (left) and the total wavefield (right). Data are affected by strong casing ringing above 400 m MD where the well deviation is close to vertical (below 3°) and the 5-1/2" casing is not cemented. Moreover, strong tube waves generated at the well head are recorded up to the top of cement behind the 5-1/2" casing.*

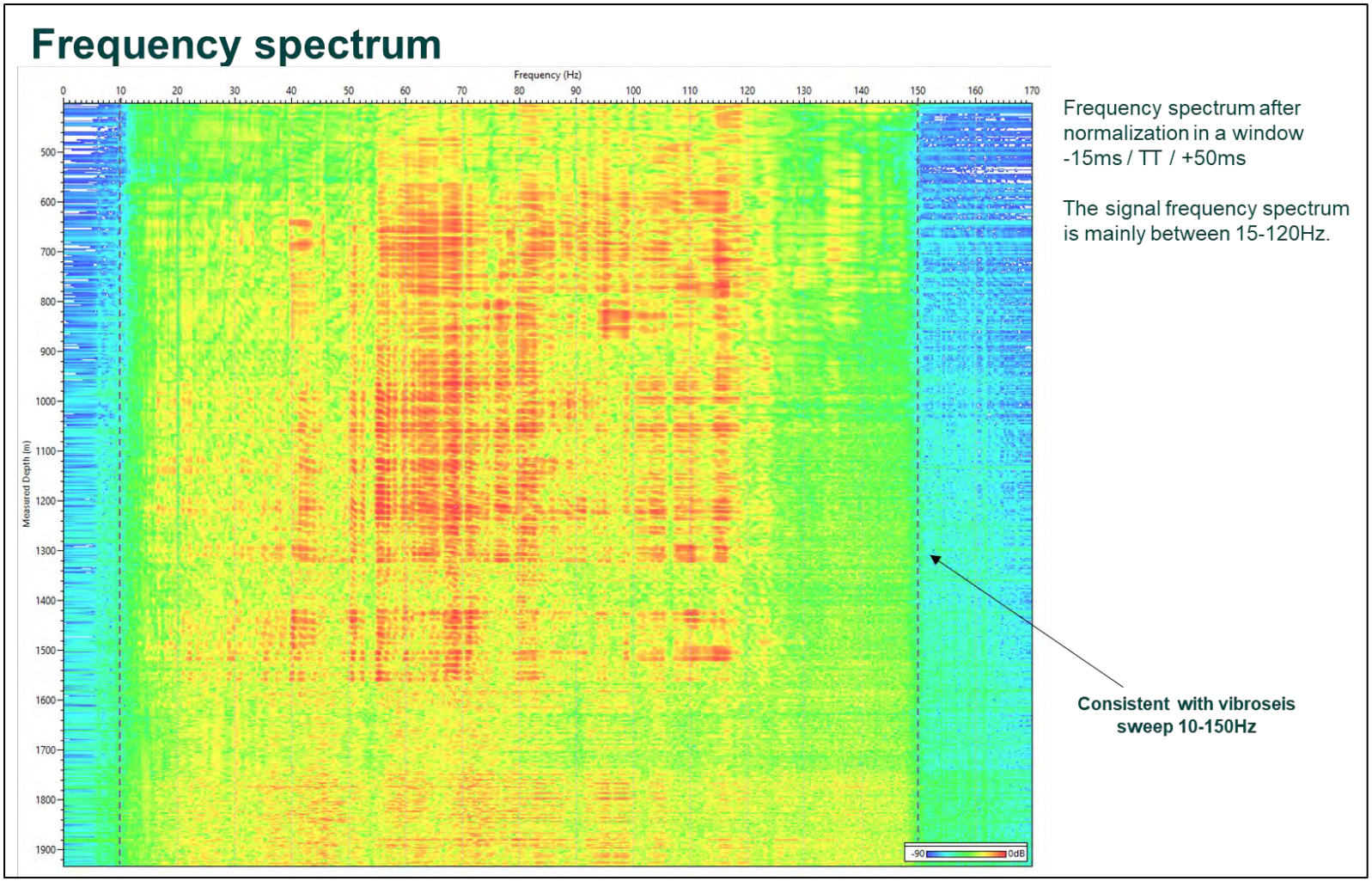


*Figure 7-3. Frequency spectrum - Stack after normalization. The frequency spectrum after normalization (Fig. 7.3) shows a downhole recorded bandwidth up to 120Hz.*

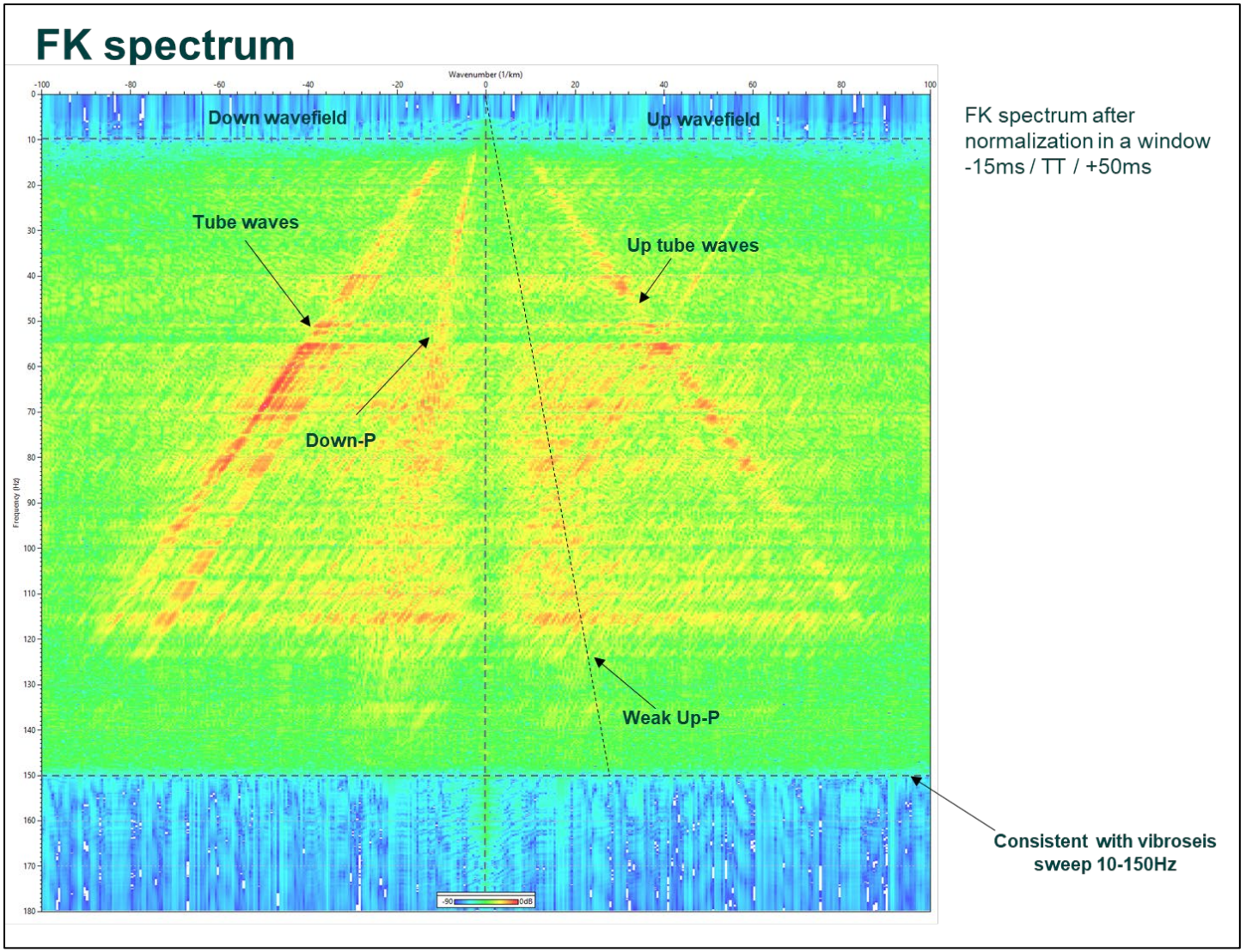


*Figure 7-4. FK spectrum - Stack after normalization. While the tube wave has a strong amplitude in the FK domain and the down P wavefield can be separated up to 70 Hz, the Up P wavefield cannot be isolated. As the depth sampling is very fine, data is not aliased.*

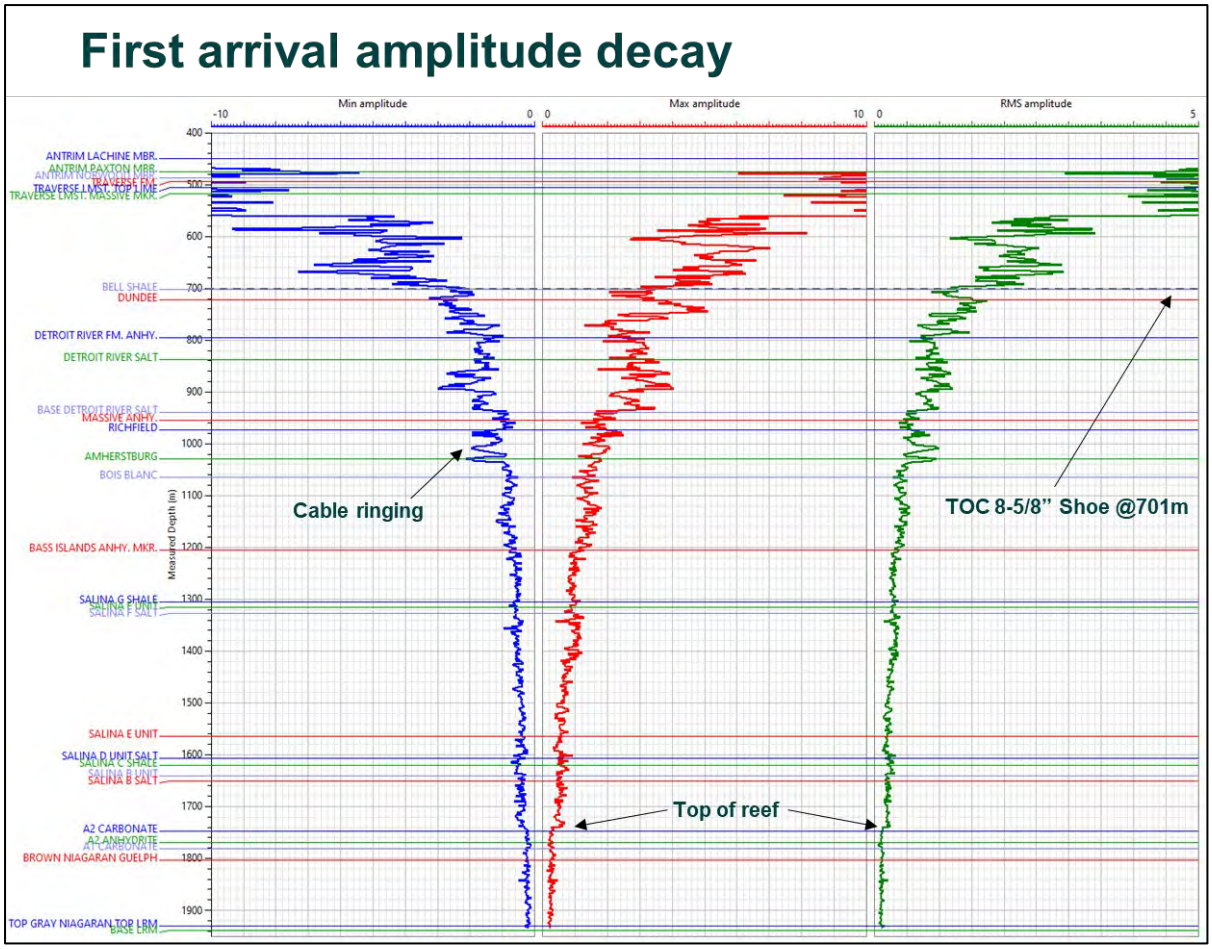


*Figure 7-5. First arrival amplitude decay. The data was analysed in a window of 15 ms before First Break (FB) to 50 ms after FB. The data follows a typical trend and highlight areas with strong ringing. At the A2 Carbonate level there is a strong drop of the FB amplitude.*

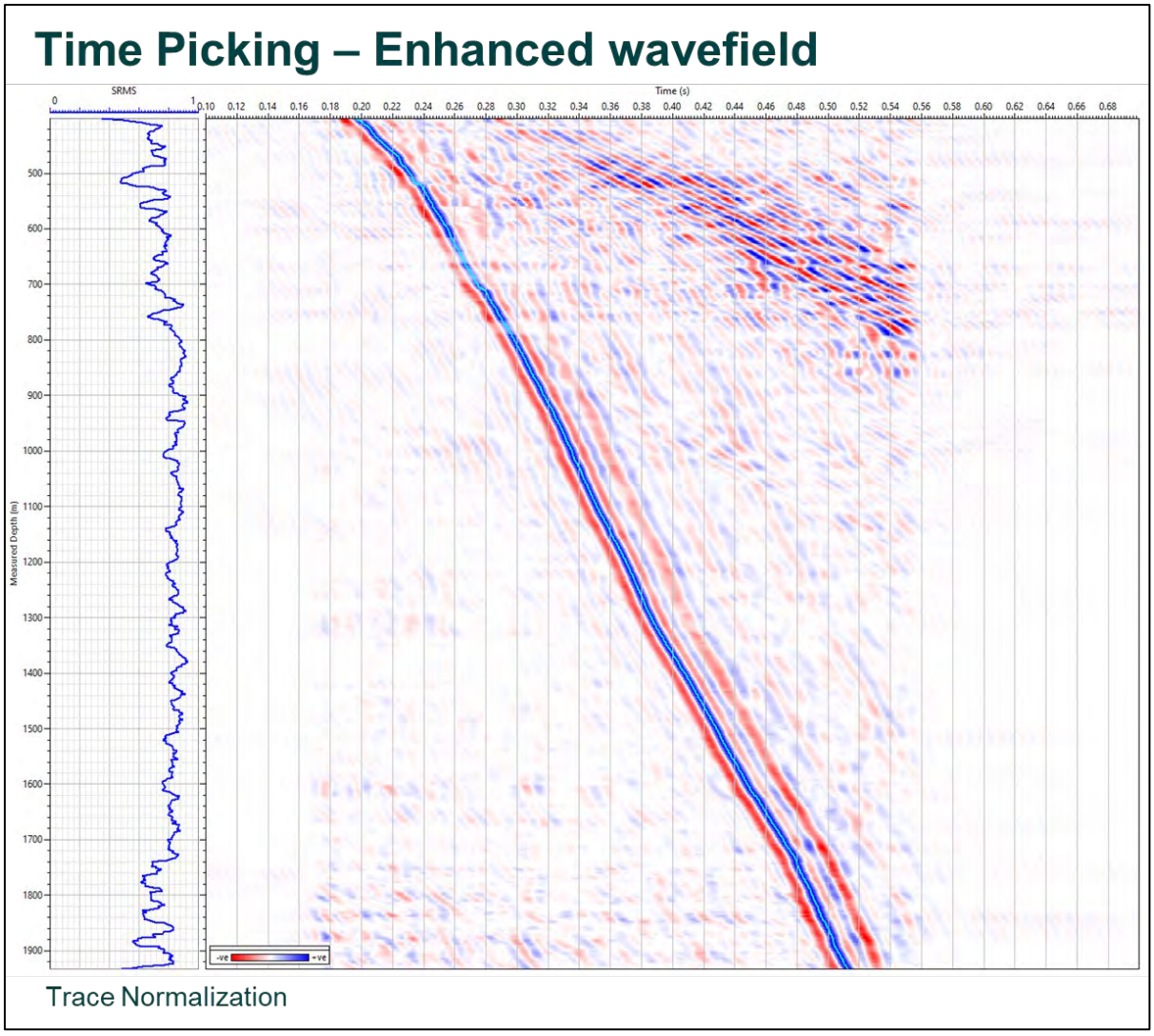


*Figure 7-6. Time Picking – Enhanced wavefield - Slopes enhancement. A few manually picked points guided the automatic picking which we performed on the enhanced weighted semblance wavefield calculated within the 0.18 – 0.35 ms/m range of slopes, over a 20 m window.*

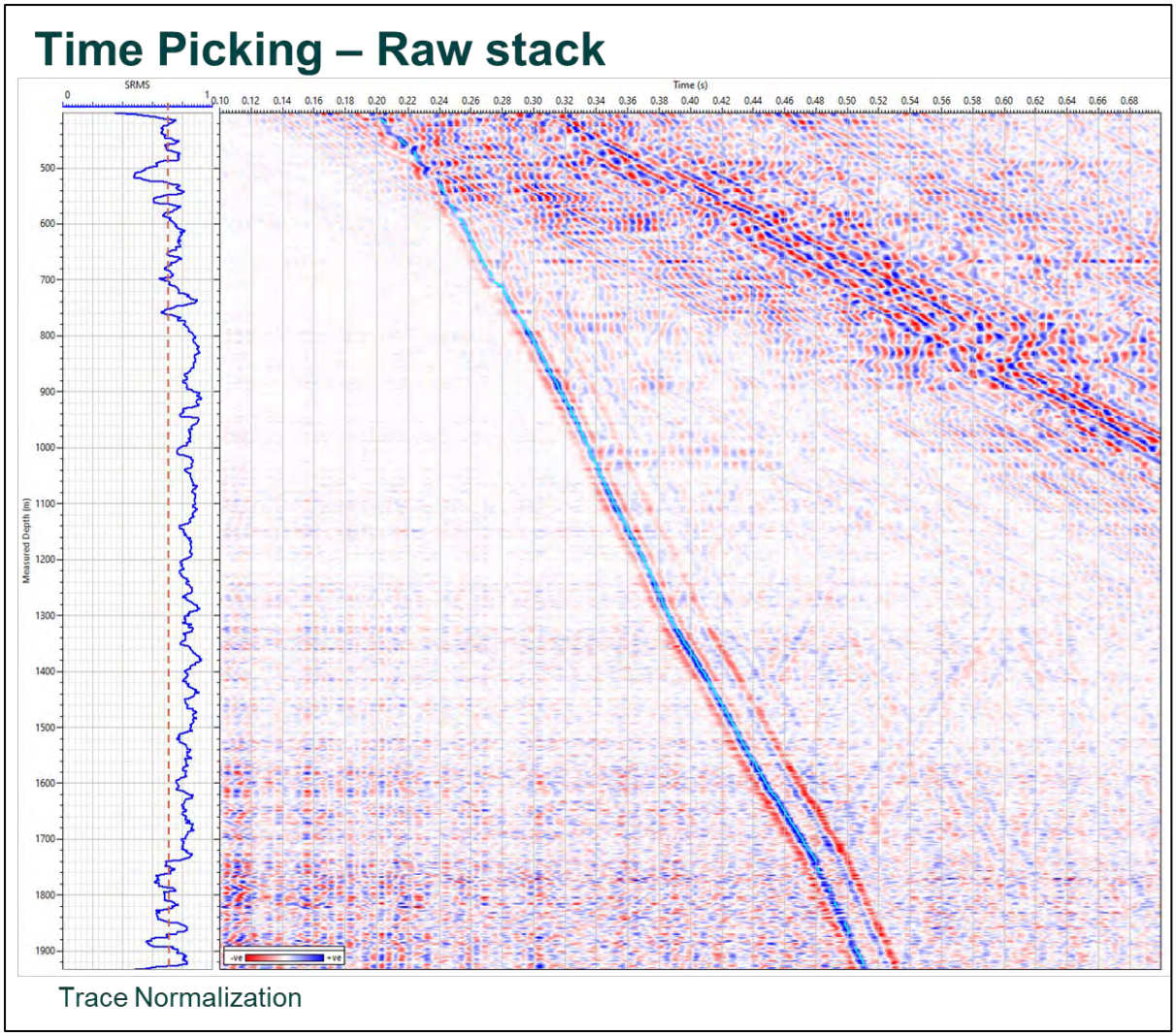


*Figure 7-7. Time Picking – Raw stack. We calculated the semblance RMS value for each depth and picks with an RMS semblance value below 0.7 were discarded. The picks were interpolated and smoothed over 5 depth levels.*

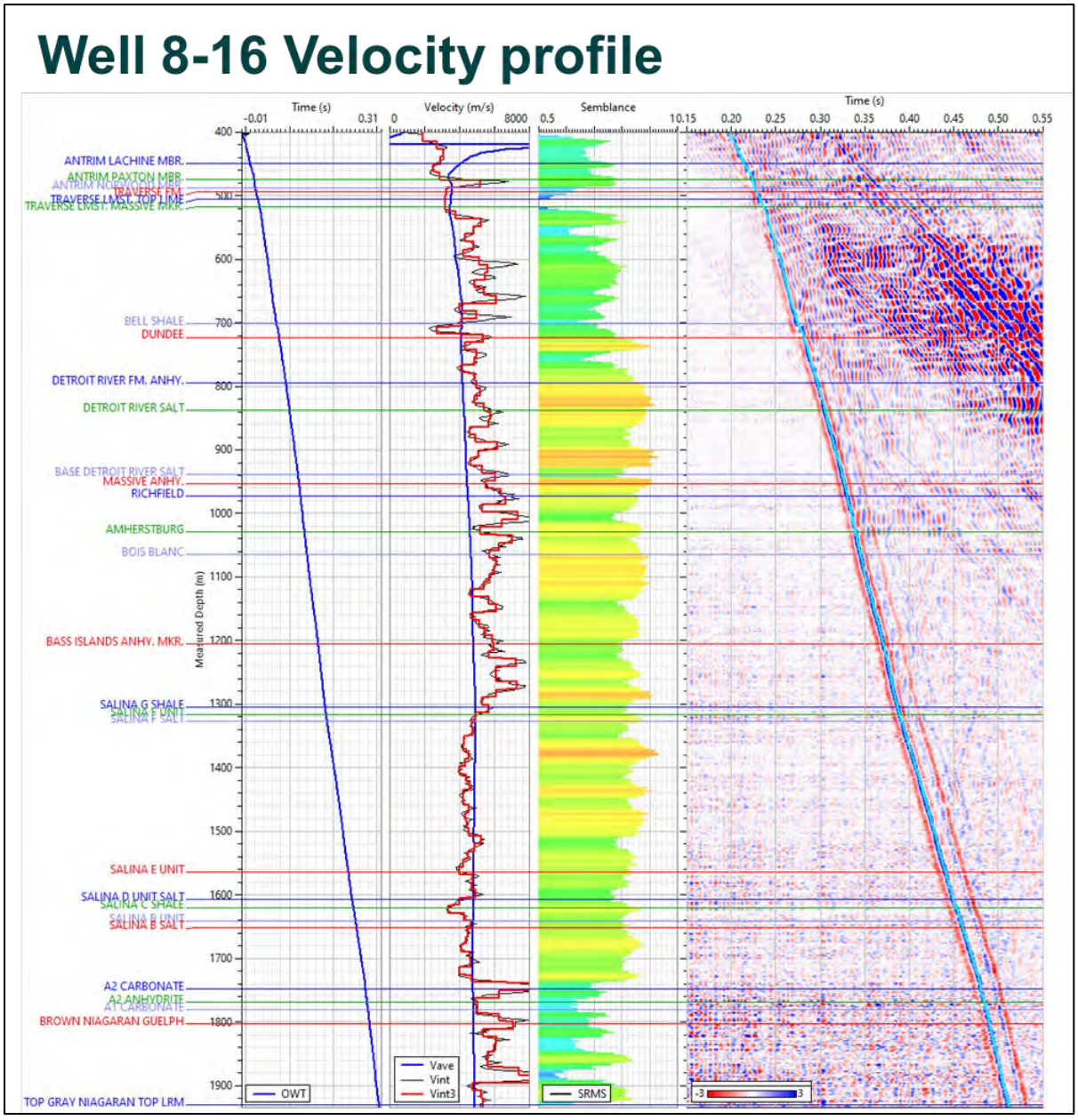


*Figure 7-8. Well 8-16 Velocity profile. This figure presents the time to depth curve in the first panel, the average and interval velocity profile in panel 2, semblance RMS near the FB in panel 3 and the picked stack in panel 4.*

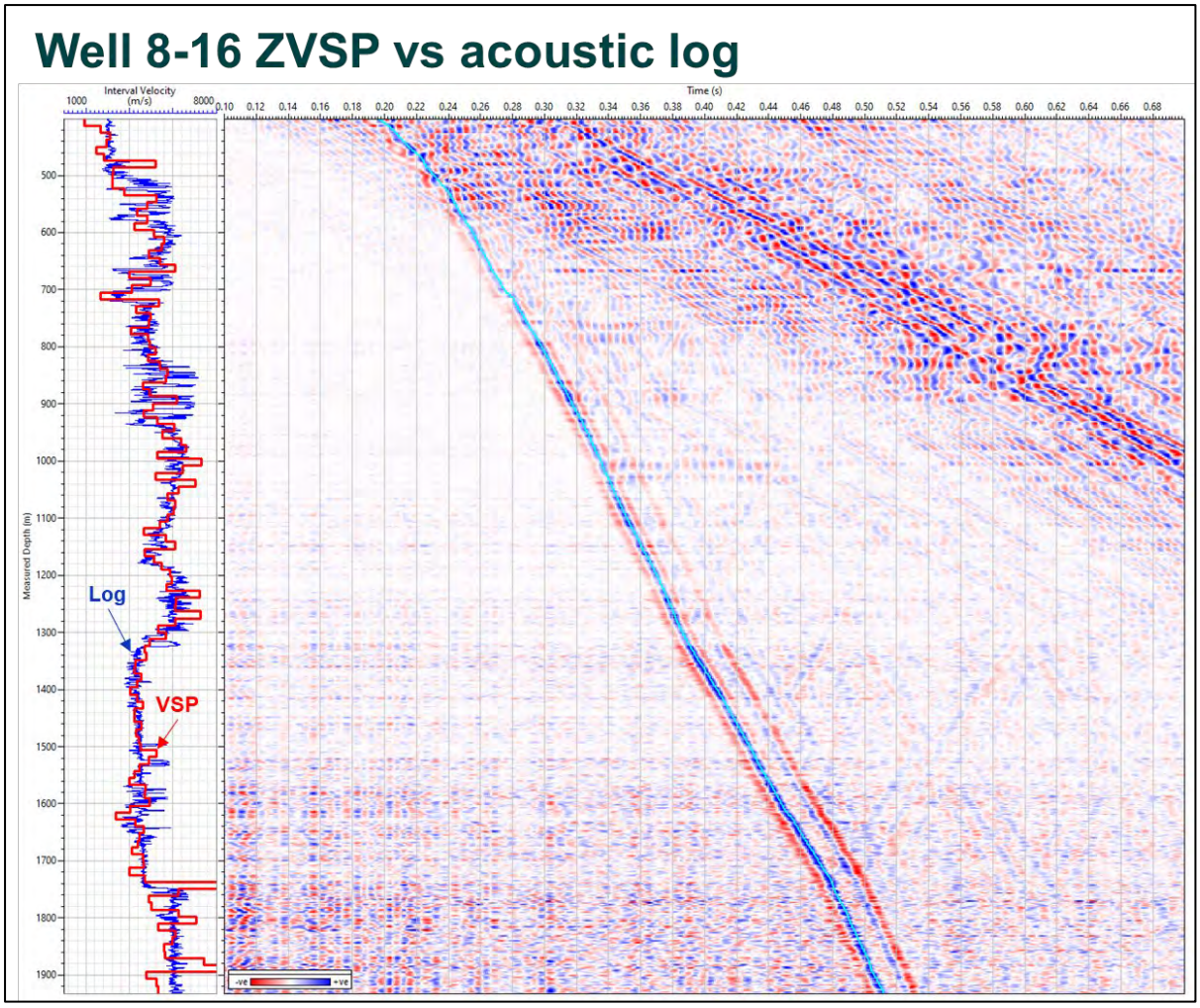


*Figure 7-9. Well 8-16 ZVSP vs acoustic log. We can perceive that there is a good match between the interval velocity from the VSP and the acoustic log compressional velocity.*

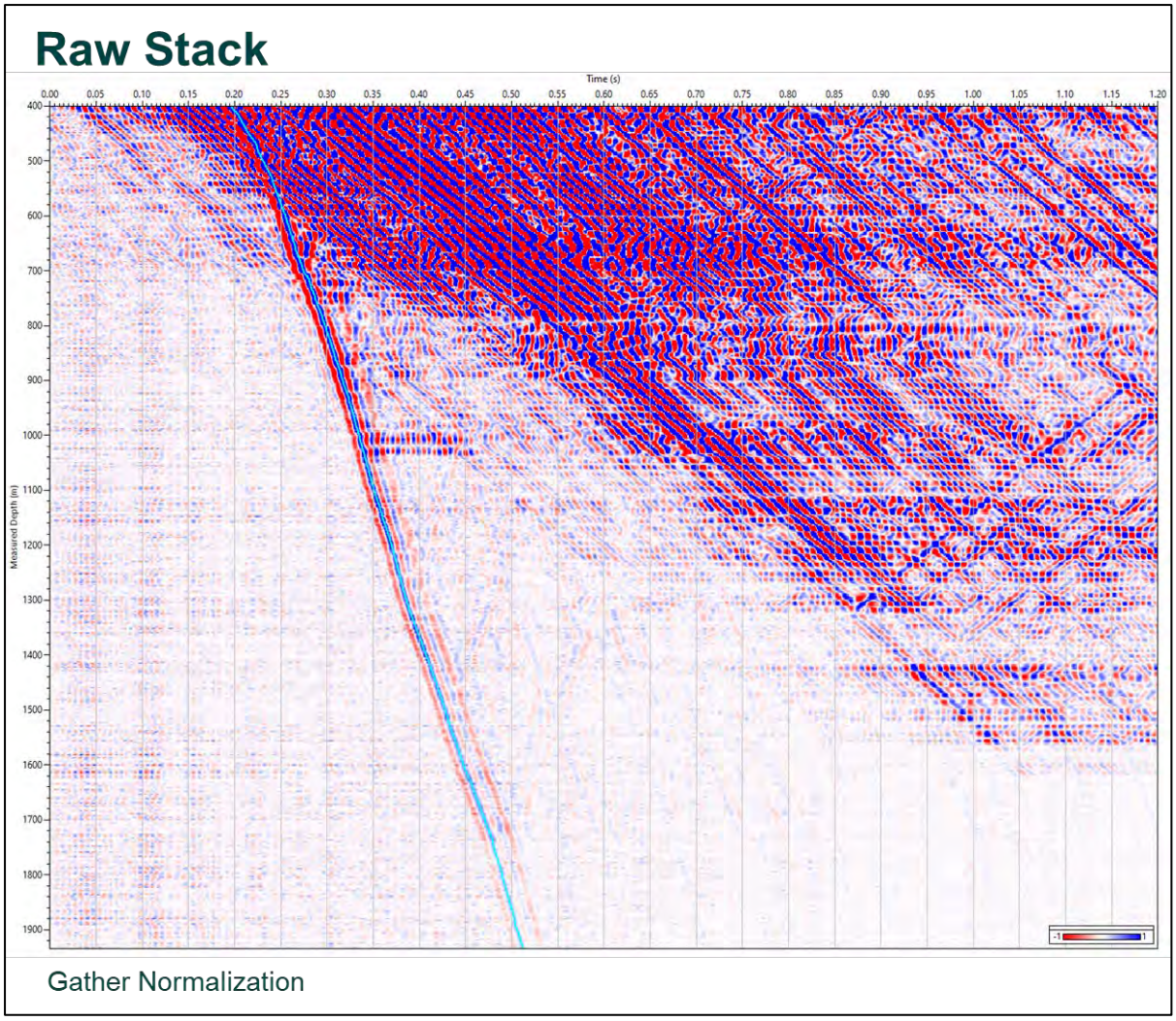


*Figure 7-10. Raw Stack. This figure shows the processing input stack data filtered with a BPF: 5,10-90,110 Hz. The amplitudes displayed are cross-normalized.*

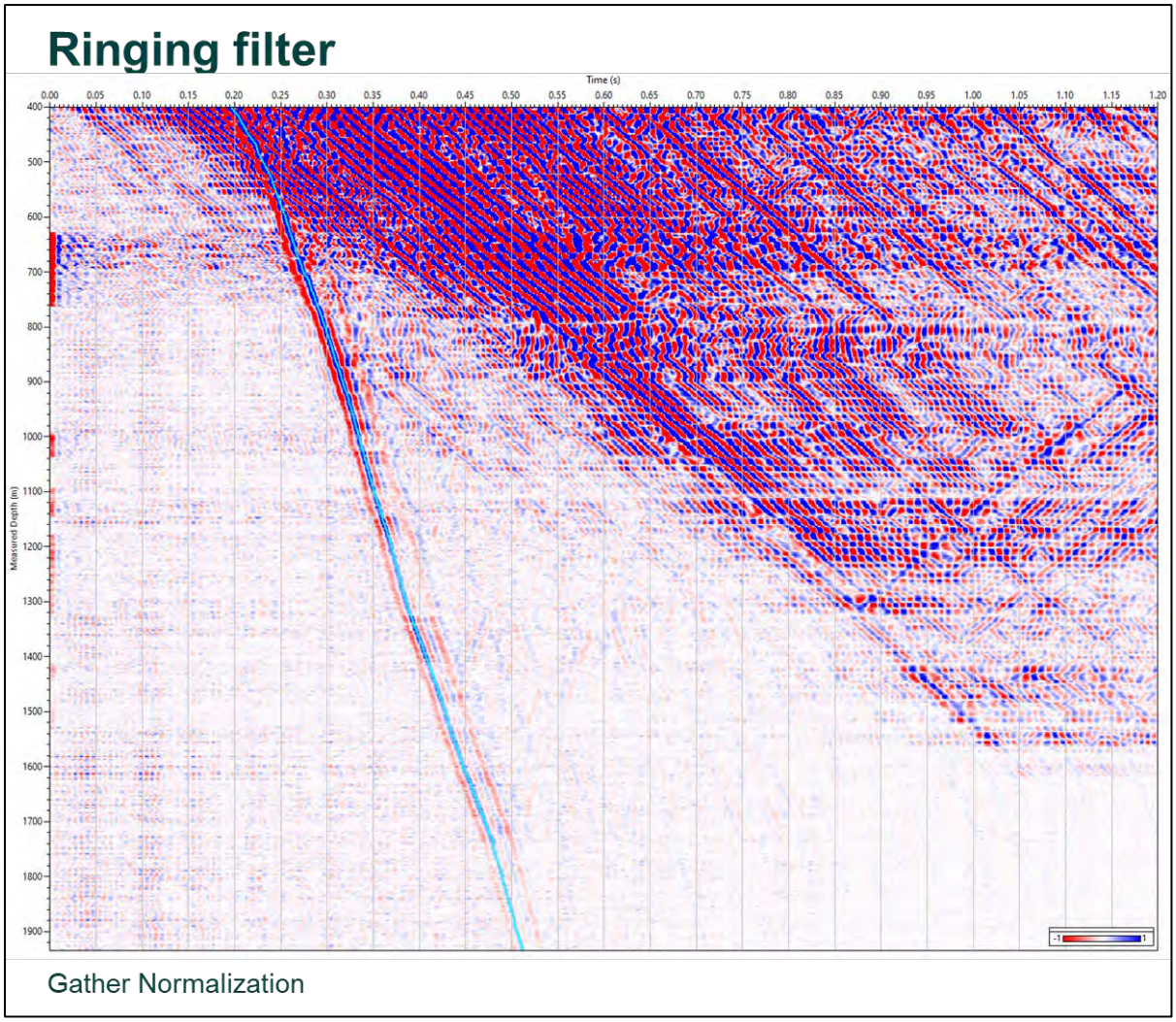


*Figure 7-11. Ringing filter - Attenuate the ringing on affected intervals. To reduce the casing ringing we applied a 66-92 Hz tracking filter over the following intervals: 628-764 m MD, 995-1037 m MD, 1094-1146 m MD, 1180-1265 m MD, 1265-1326 m MD, 1412-1444 m MD, 1485-1533m MD.*

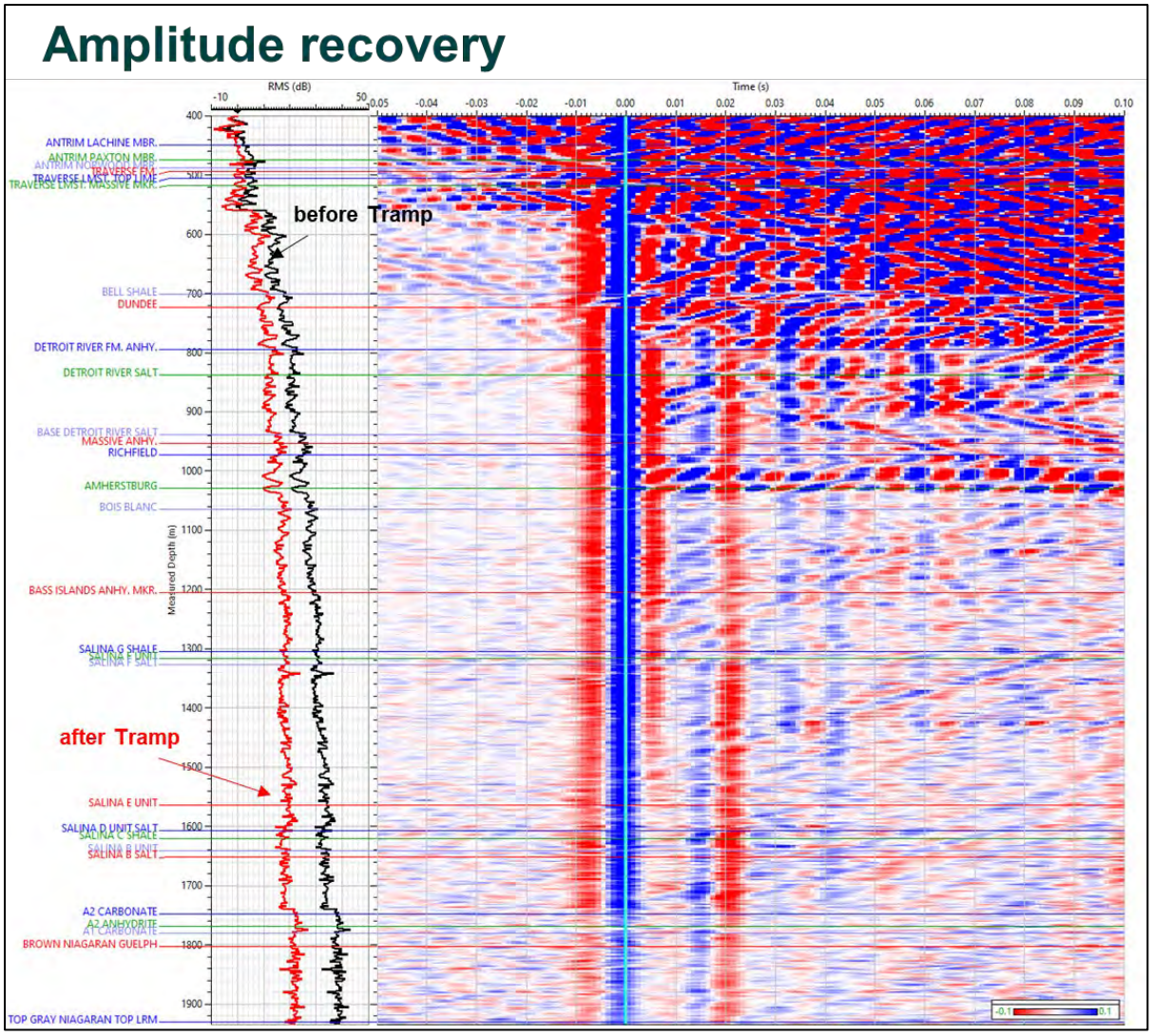


*Figure 7-12. Amplitude recovery - Amplitude recovery QC. To compensate for absorption and spherical divergence spreading, the amplitude was scaled by the squared sample time. Figure 7.12 shows in panel 1 the RMS amplitude near FB before and after amplitude recovery. After the amplitude recovery the RMS amplitude follows a trend closer to a constant value. In panel 2 the stack data is aligned along the transit time (TT).*

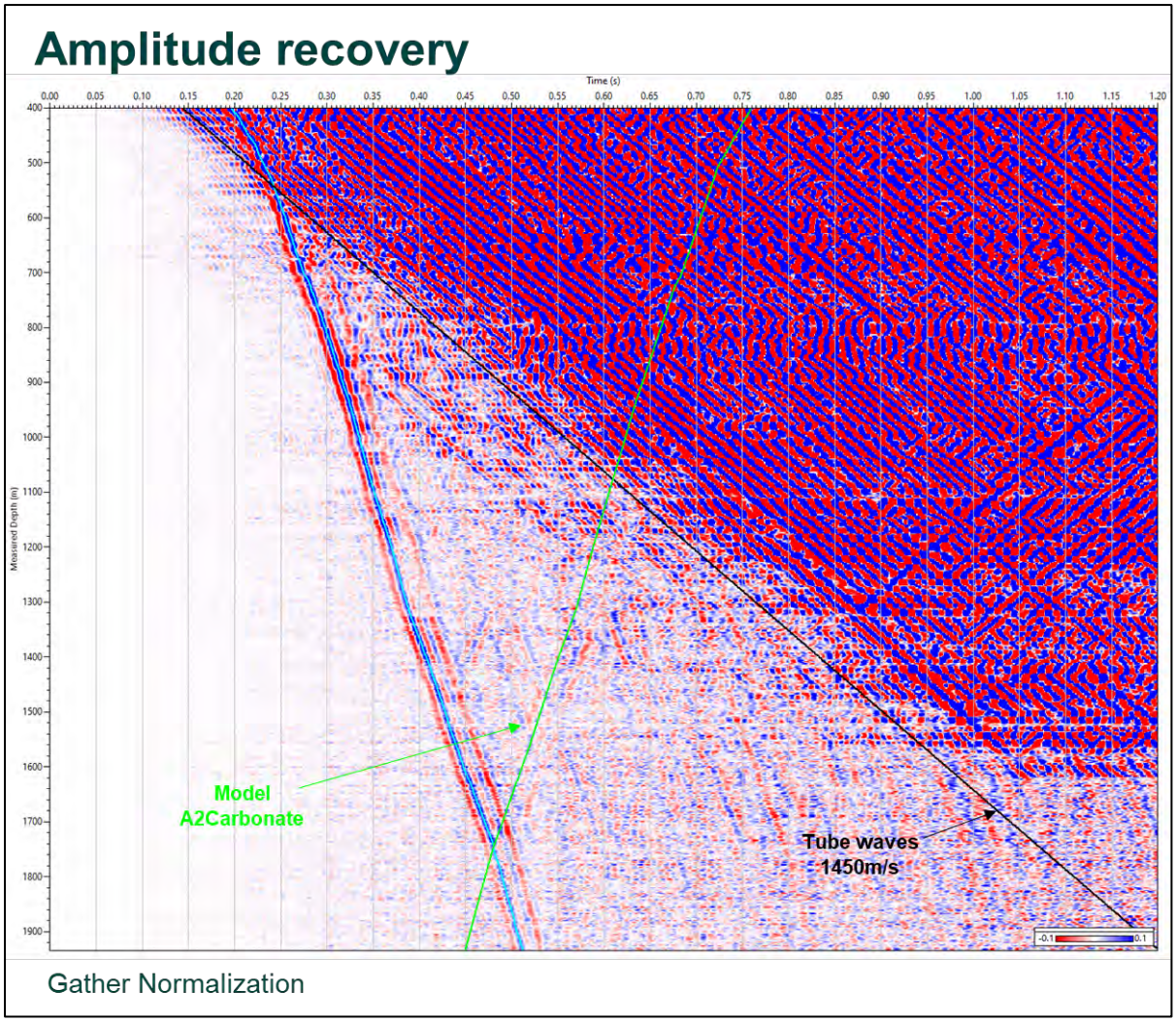


*Figure 7-13. Amplitude recovery - Time power function. The stack after amplitude recovery is presented in figure 7.13.*

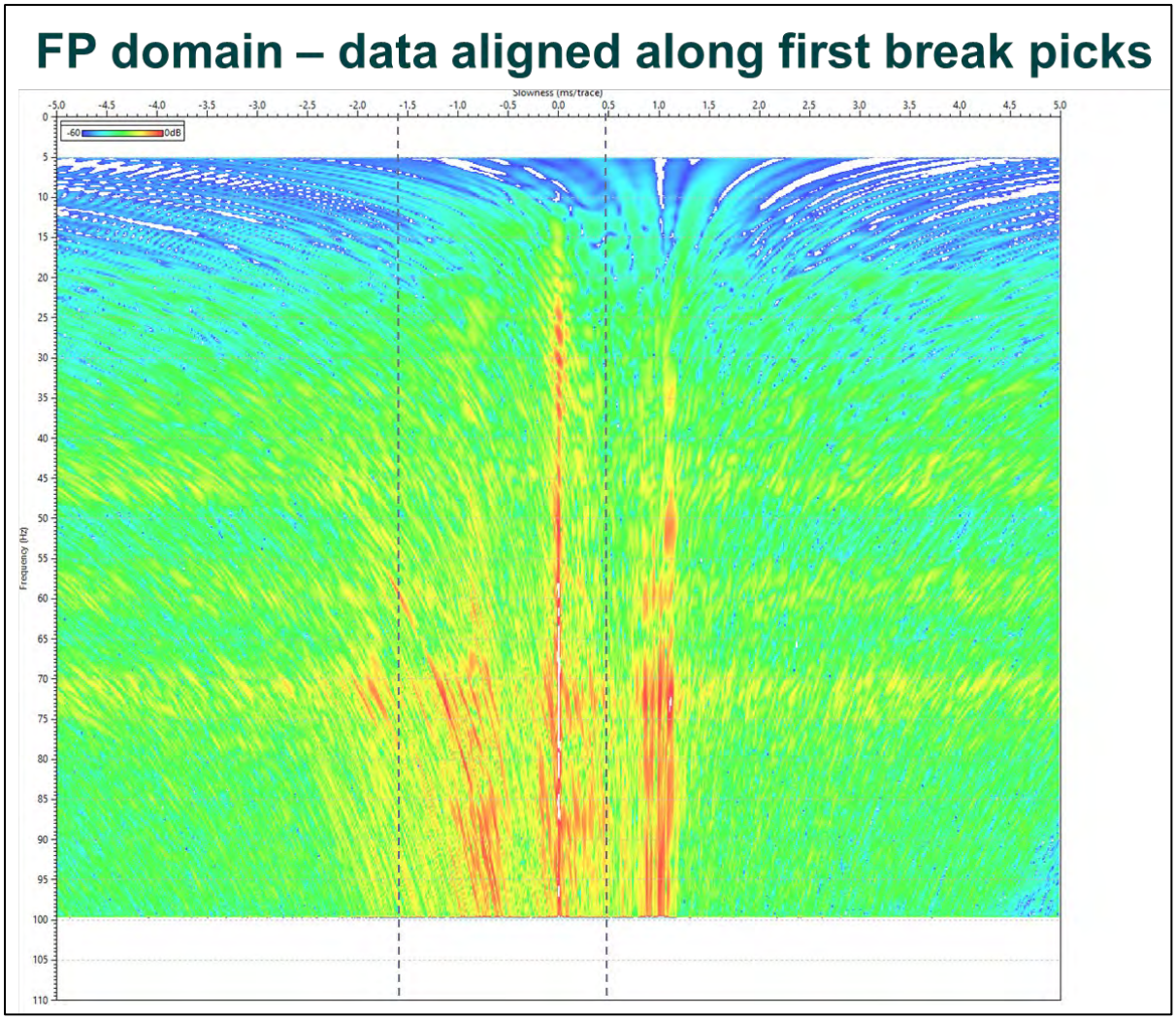


*Figure 7-14. FP domain – data aligned along first break picks - Removed tube waves and noise. This figure shows the stack aligned along the first break in the frequency-slowness domain (FP). To remove noise and tube waves, the slowness outside -1.7 – 0.6 was muted.*

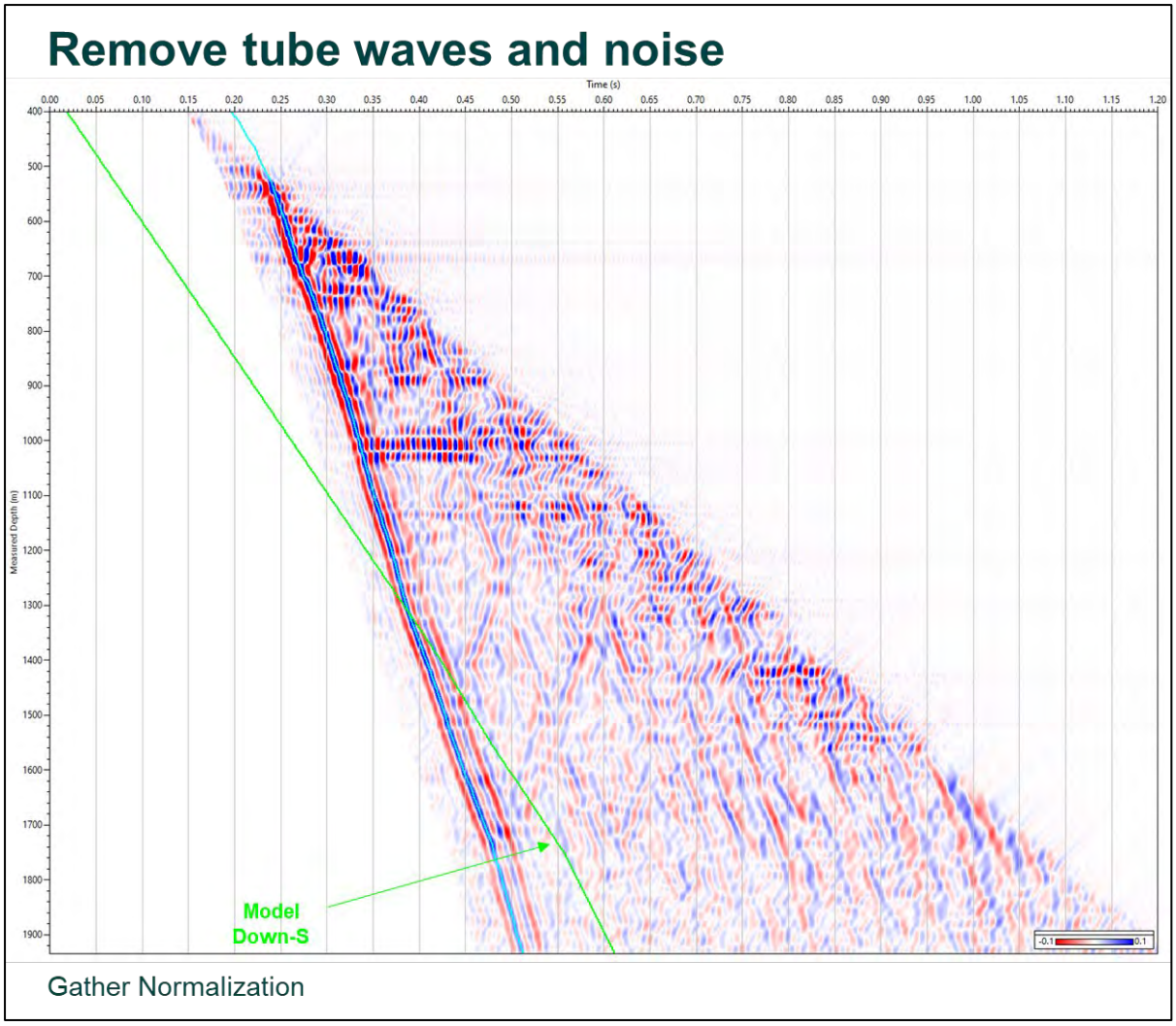


*Figure 7-15. Remove tube waves and noise - After FP separation. The data from figure 7.15 was muted above the tube wave limit.*

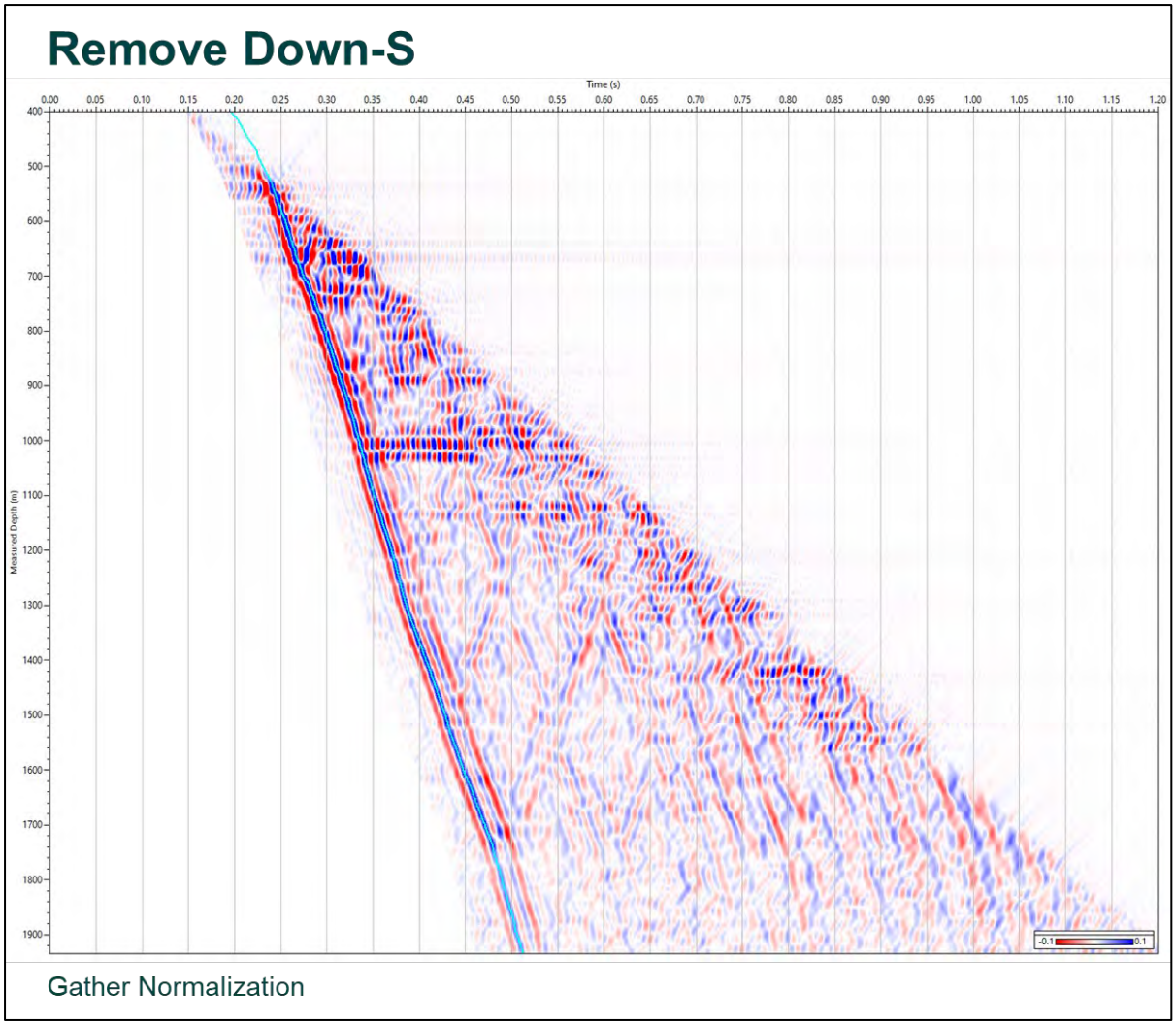


*Figure 7-16. Remove Down-S - Median filter. The Down S wavefield in figure 7.16 was removed using a median filter over 121 traces aligned along the modelled Down S TT (Fig. 7.15 green).*

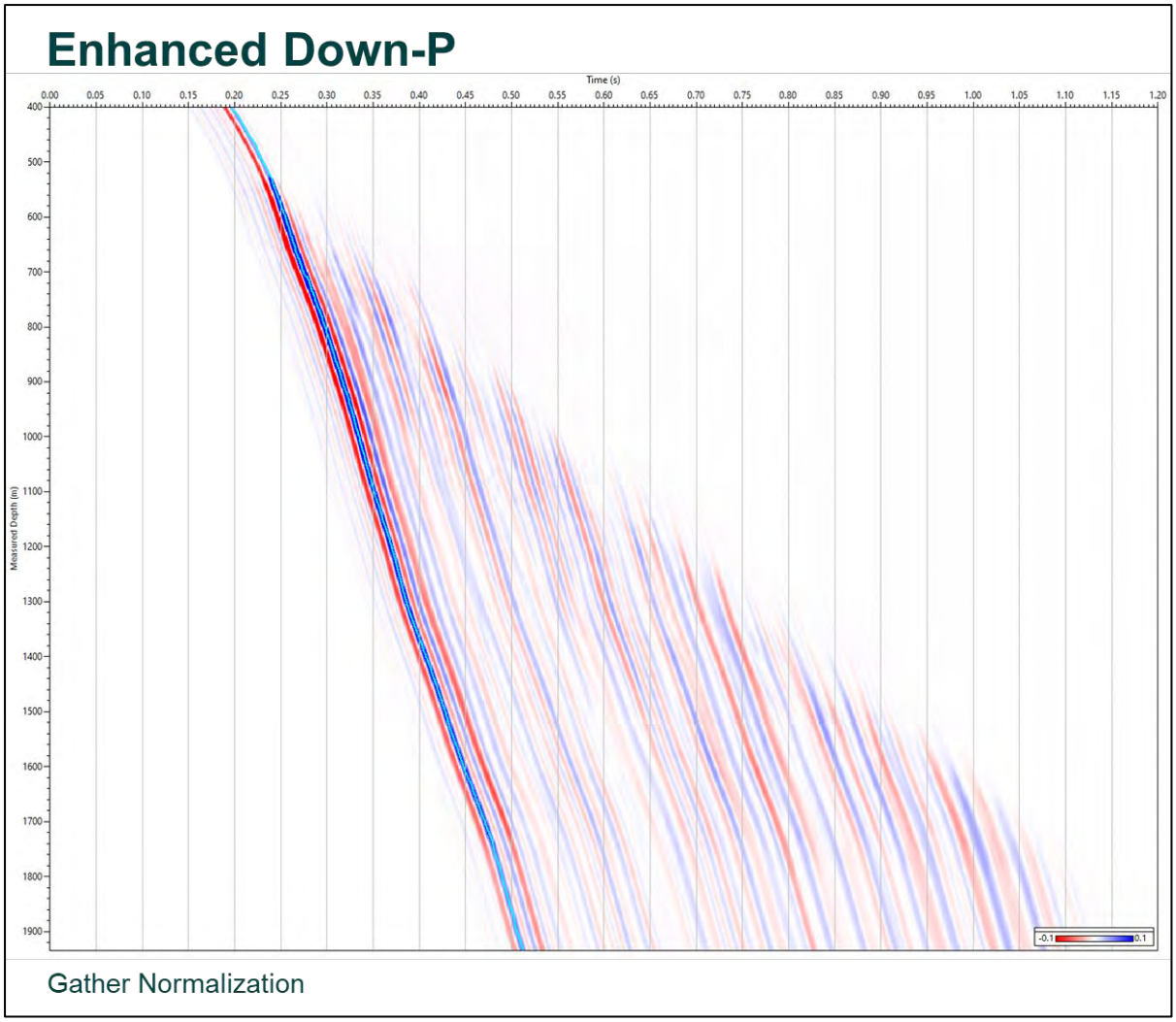


*Figure 7-17. Enhanced Down-P - Median filter. This figure shows the Down P wavefield after enhancement using a median filter of 121 traces along the FB. This wavefield will be used later for the deconvolution.*

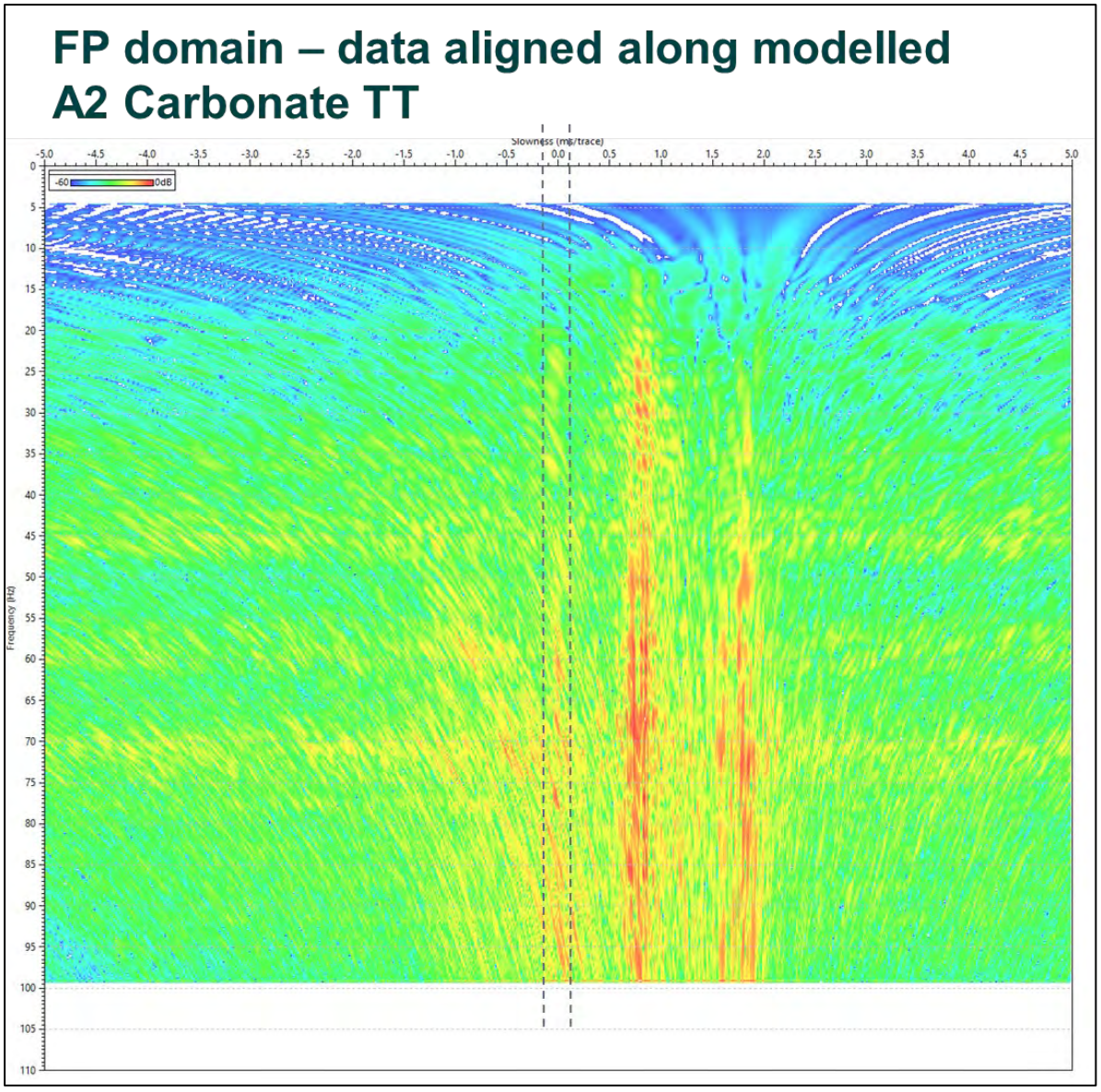


*Figure 7-18. FP domain – data aligned along modelled A2 Carbonate TT - Enhance Up P. The Up P wavefield was enhanced in the FP domain in a slowness window of -0.15 to 0.15 ms/trace.*

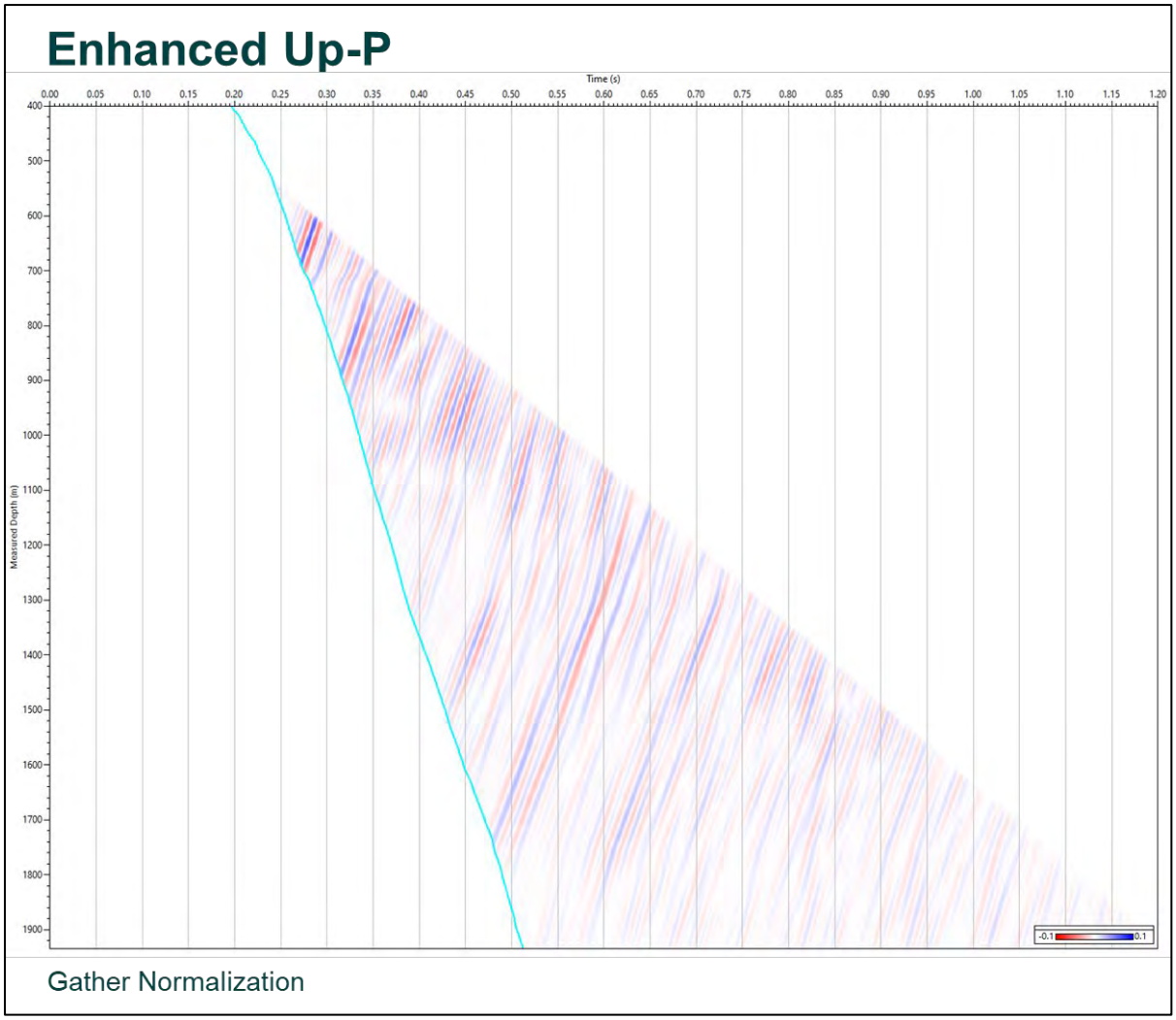


*Figure 7-19. Enhanced Up-P - After FP separation. This shows the enhanced Up P along the modelled A2 Carbonate TT over a 10 trace window after the separation in the FP domain.*

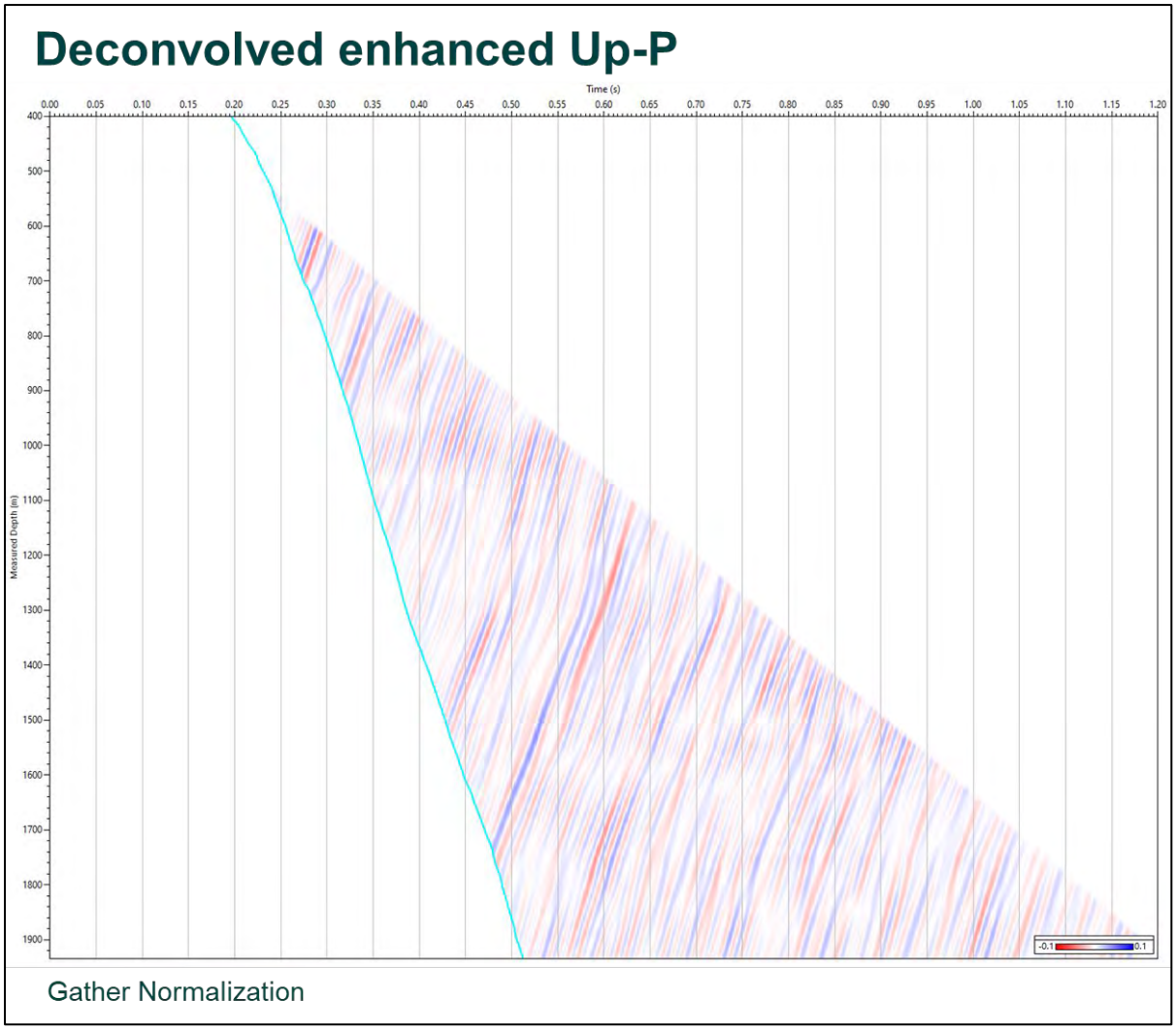


*Figure 7-20. Deconvolved enhanced Up-P - Trace by trace deterministic deconvolution. To reduce the multiples and increase the data frequency, the enhanced Up P was deconvolved. We applied a trace by trace deterministic deconvolution with enhanced Down P (Fig. 7.17) using a 0.15 s operator length and 20% white noise to the enhanced Up P. Finally, the data were filtered with a 5,10-90,110 Hz BPF.*

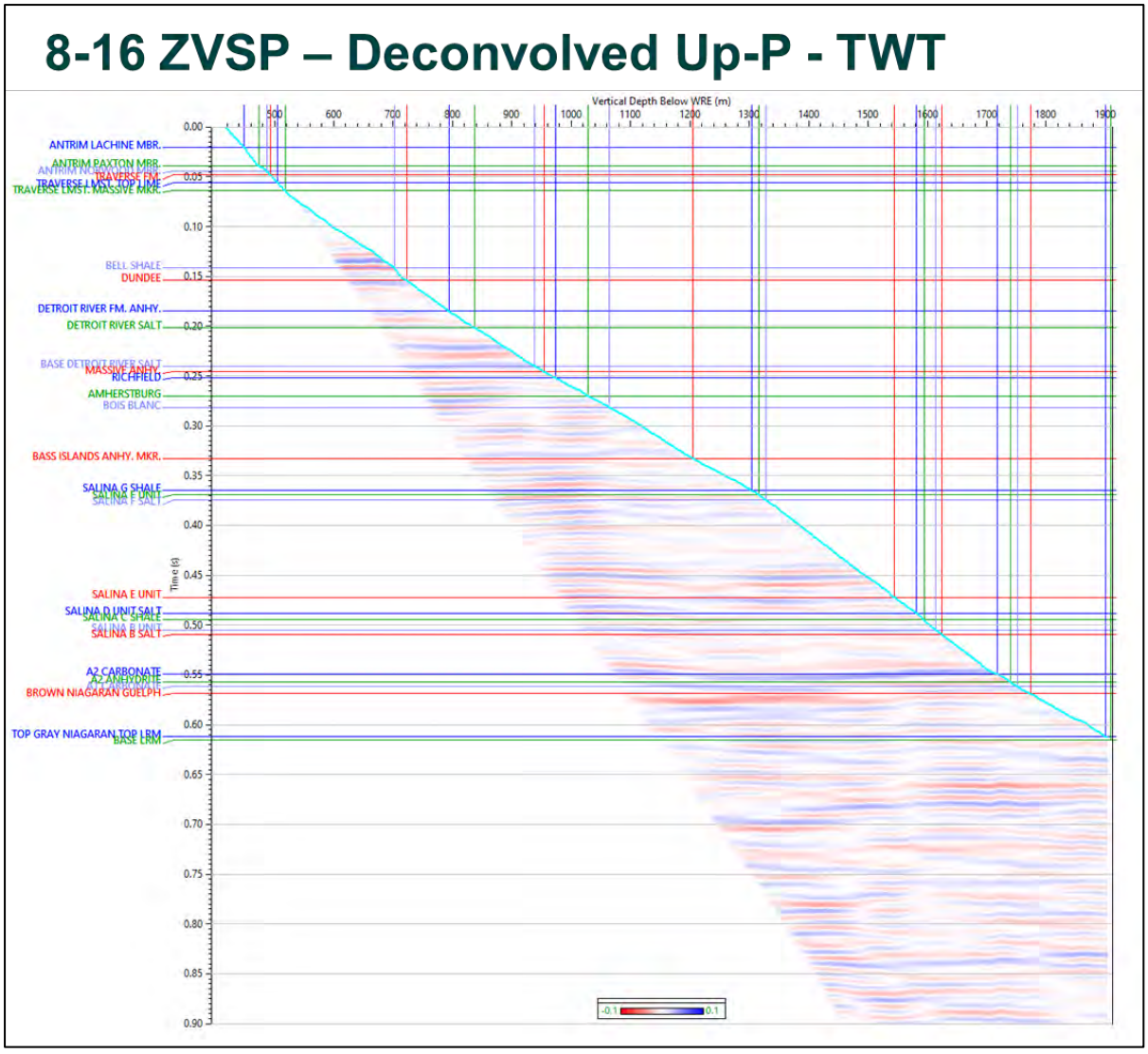


*Figure 7-21. 8-16 ZVSP – Deconvolved Up-P – TWT. Deconvolved Up P wavefield presented in TWT.*

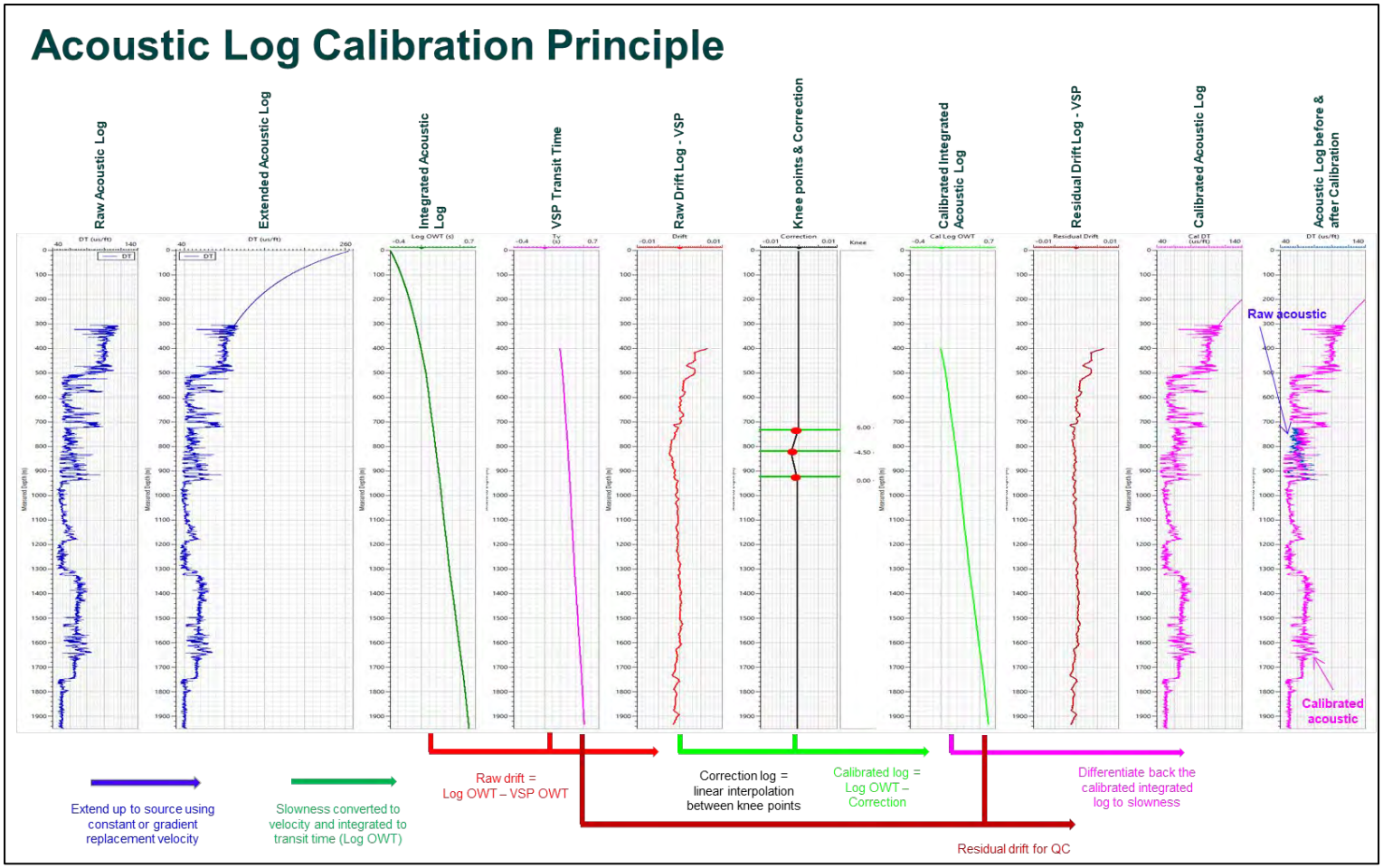


*Figure 7-22. Acoustic Log Calibration Principle – Workflow. This figure shows the principle of acoustic calibration: the raw acoustic log (graph 1), is extended up to the first VSP receiver (graph 2). The acoustic log is converted from slowness to velocity and is integrated to obtain the transit time (graph 3). The difference (drift log) between the log TT and the VSP TT is computed (graph 5). To reduce the drift, correction values are defined at some points called knee points (graph 6). Between the knee points the correction is interpolated and is added to the acoustic TT (graph 7). The residual drift between the corrected acoustic TT and the VSP TT is computed for QC (graph 8). Finally, the corrected acoustic TT is differentiated to slowness (graph 9). The final graph (graph 10) shows the acoustic log before and after the calibration.*

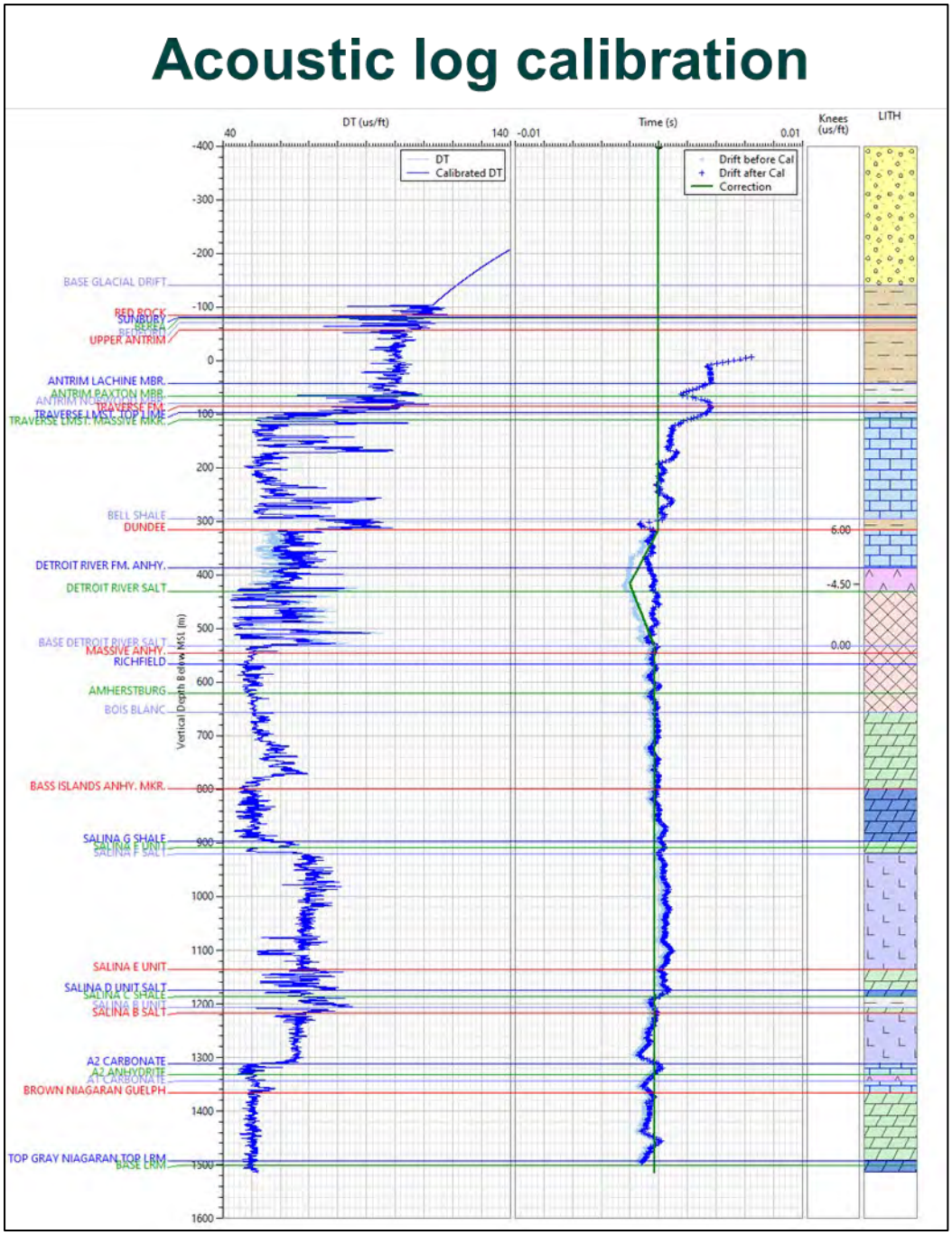


*Figure 7-23. Acoustic log calibration. The first graph shows the acoustic log before calibration in light blue and in blue the acoustic log after calibration. In the second graph is the log-VSP drift before calibration in light blue and the residual drift in blue. The third graph presents the knee points and the correction values and in the right panel is the lithological column. Only three knee points were required to calibrate the acoustic log. The residual drift after acoustic log calibration is below 1 ms.*

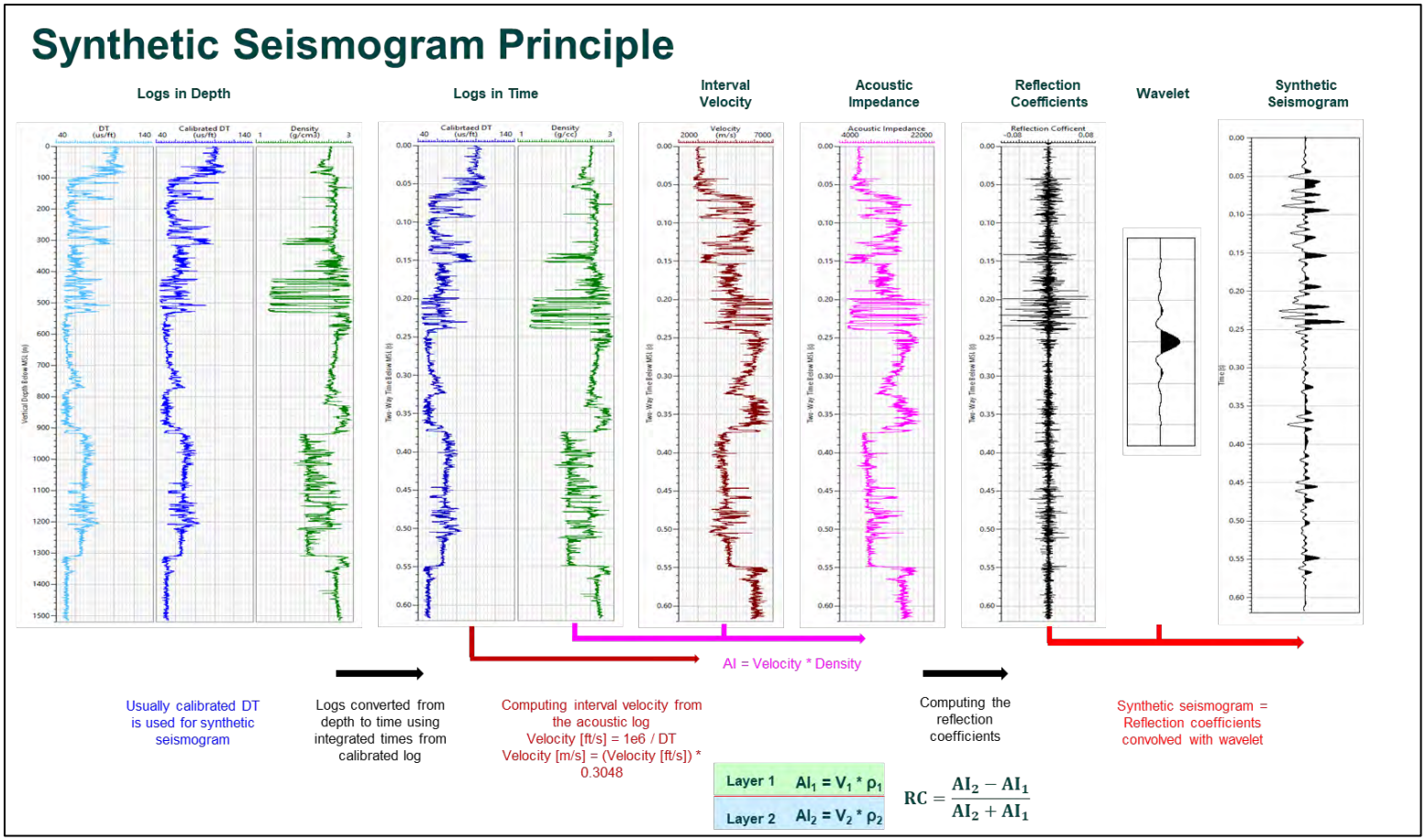


*Figure 7-24. Synthetic Seismogram Principle – Workflow. The first three graphs show the input logs in depth. The calibrated acoustic log and the density log are used further in the workflow. If the density is not available, it can be estimated using Gardner's equation or it can be replaced with a constant value. The logs are converted in time (graphs 4 and 5) using the time to depth function computed from the calibrated acoustic log integration. The acoustic log is converted from slowness to velocity (graph 6) and this velocity log is then multiplied with the density log to find the acoustic impedance (graph 7). Graph 8 shows the reflection coefficients computed using the formula written below the graph. The reflection coefficients are convolved with a wavelet (synthetic wavelet or extracted from the seismic data) (panel 9) to produce the synthetic seismogram from panel 10. Another method to compute synthetic seismogram form reflection coefficients is to filter the reflection coefficient's frequency spectrum (as the reflection coefficients log is spiky, the frequency spectrum is infinite) to the VSP or seismic frequency bandwidth.*

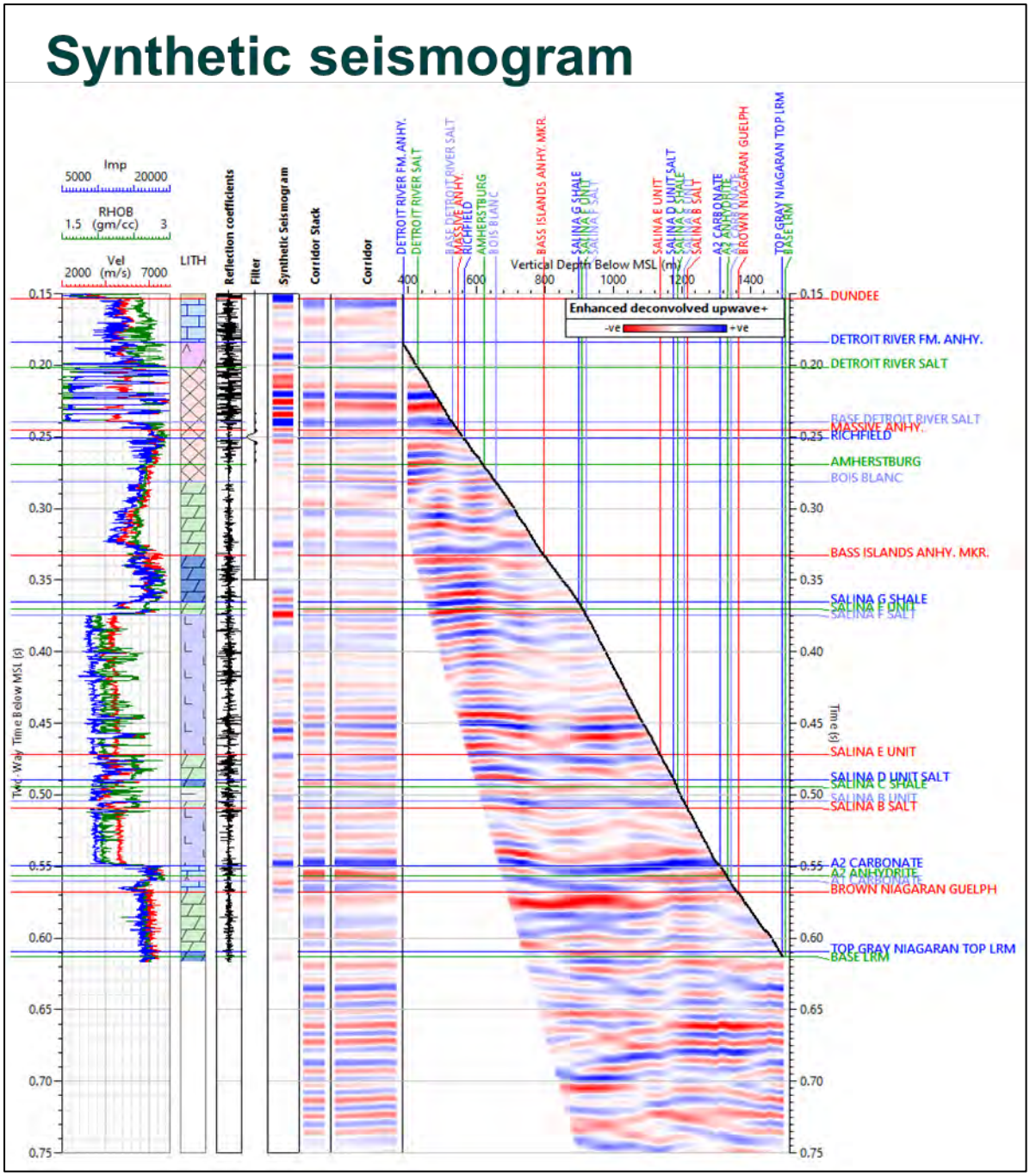


*Figure 7-25. Synthetic seismogram. This figure presents a composite plot with the logs in time, the lithological column, reflection coefficients, the wavelet used to compute the synthetic seismogram on the left side and enhanced Upgoing P wavefield, the corridor and the corridor stack on the right side (from right to left). There is a good tie at the main reflectors between the synthetic seismogram and the ZVSP corridor stack. The top of the A2 Carbonate is represented by the strong positive reflection at 0.55 s TWT (strong blue reflector) and the top of the A1 Carbonate by the following trough (red reflector).*

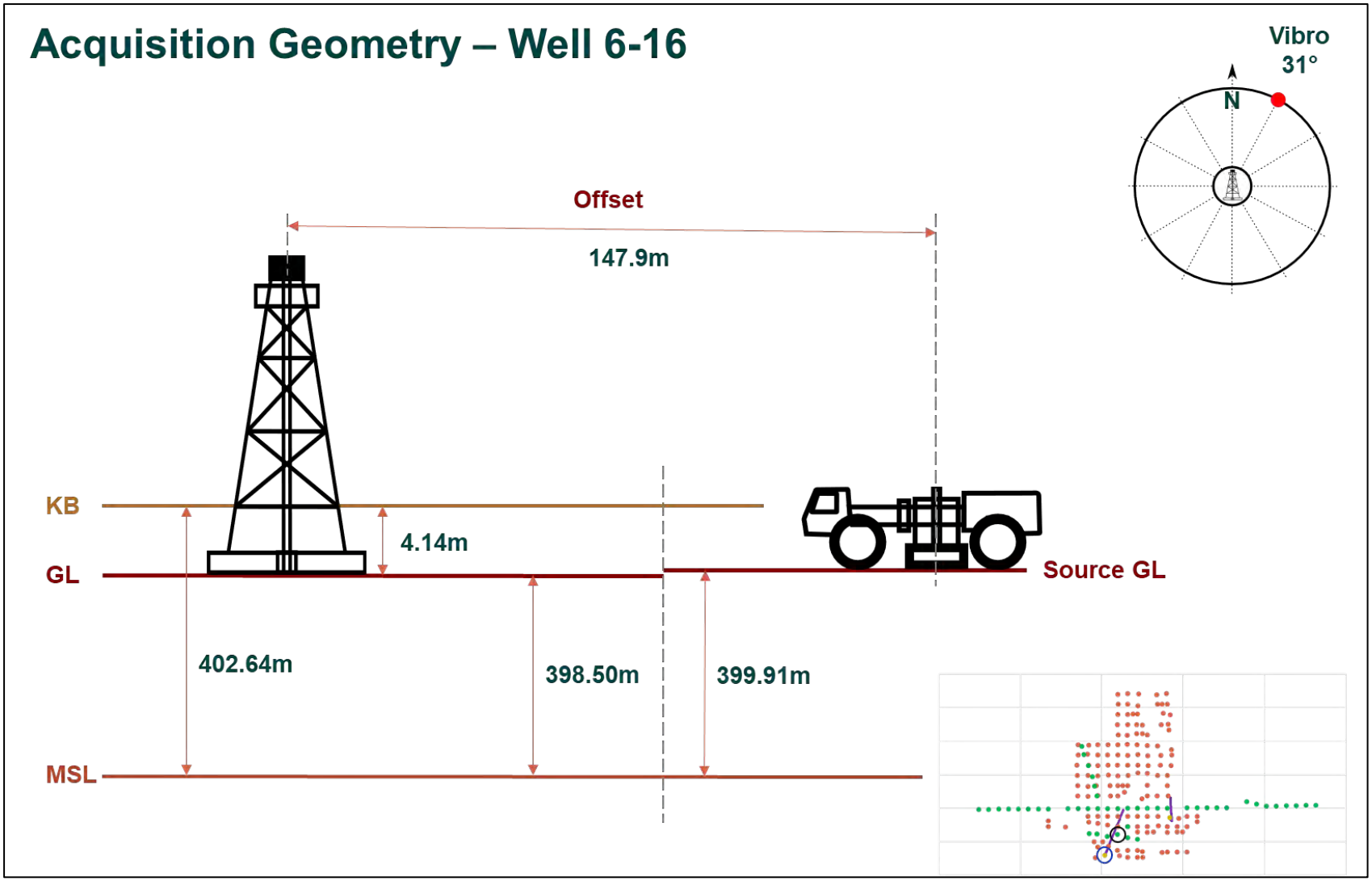


*Figure 7-26. Acquisition Geometry – Well 6-16 - Well and source elevations. The source location is in the middle of the well trajectory projected on a surface, 148 meters away from the well head.*

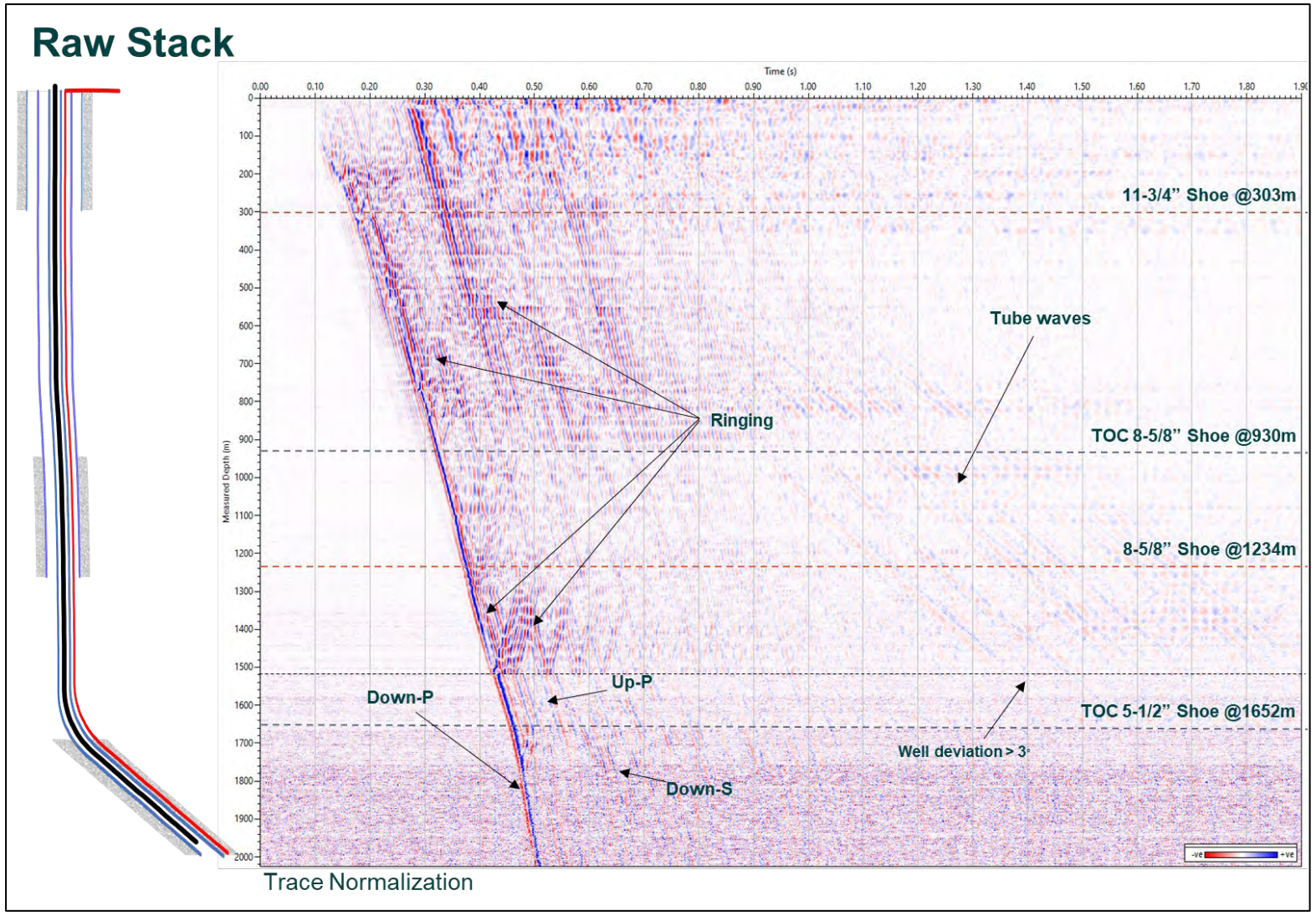


*Figure 7-27. Raw Stack - Total wavefield. This figure shows the well casing (left) and the total wavefield (right). The data above 1520 m MD, where the well deviation is below 3°, is affected by strong tubing and casing ringing. Weak tube waves and the Down S wavefield are also recorded.*

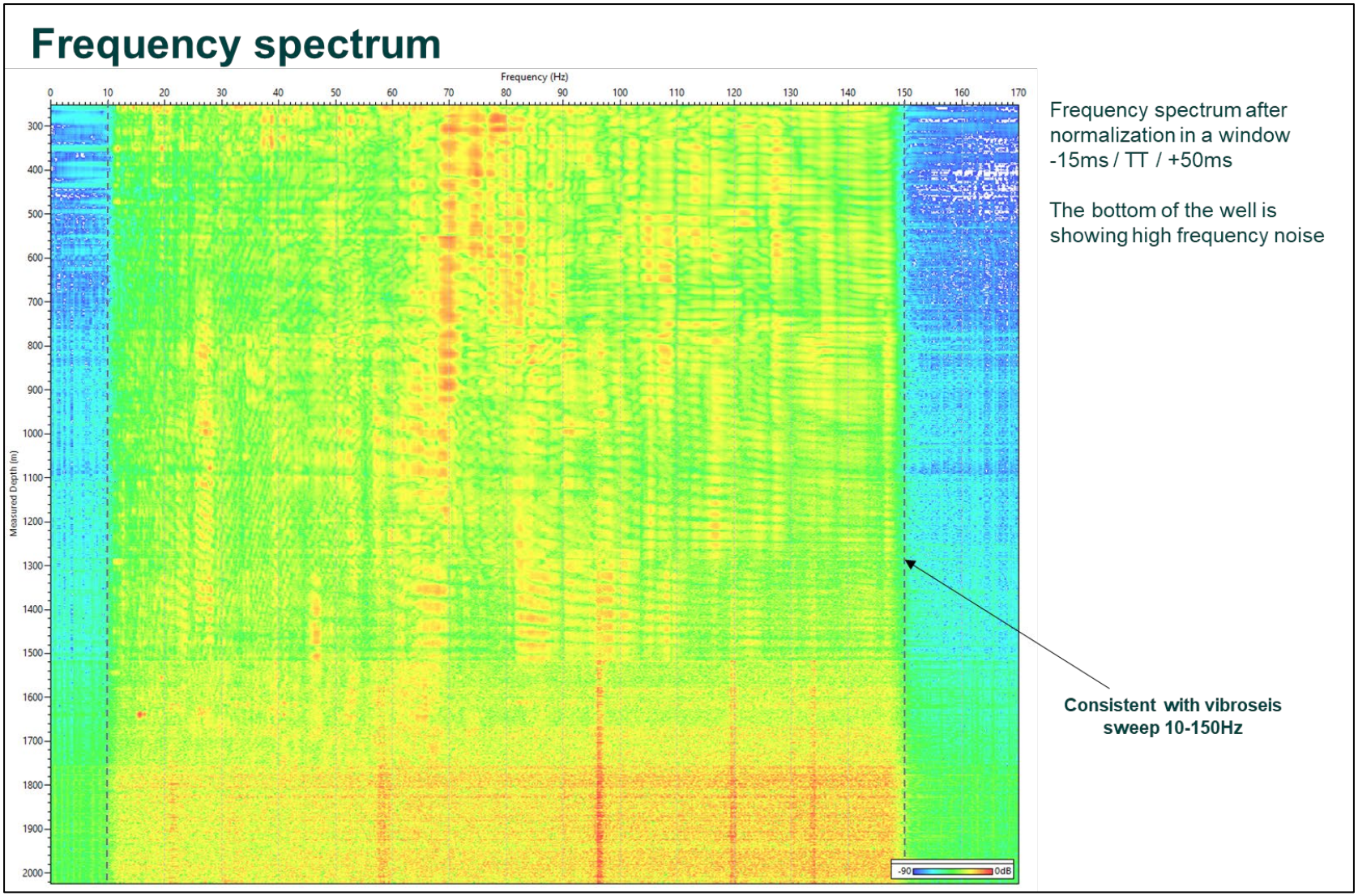


*Figure 7-28. Frequency spectrum - Stack after normalization. The frequency spectrum after normalization shows that the data recorded in the reservoir area is affected by a high frequency noise.*

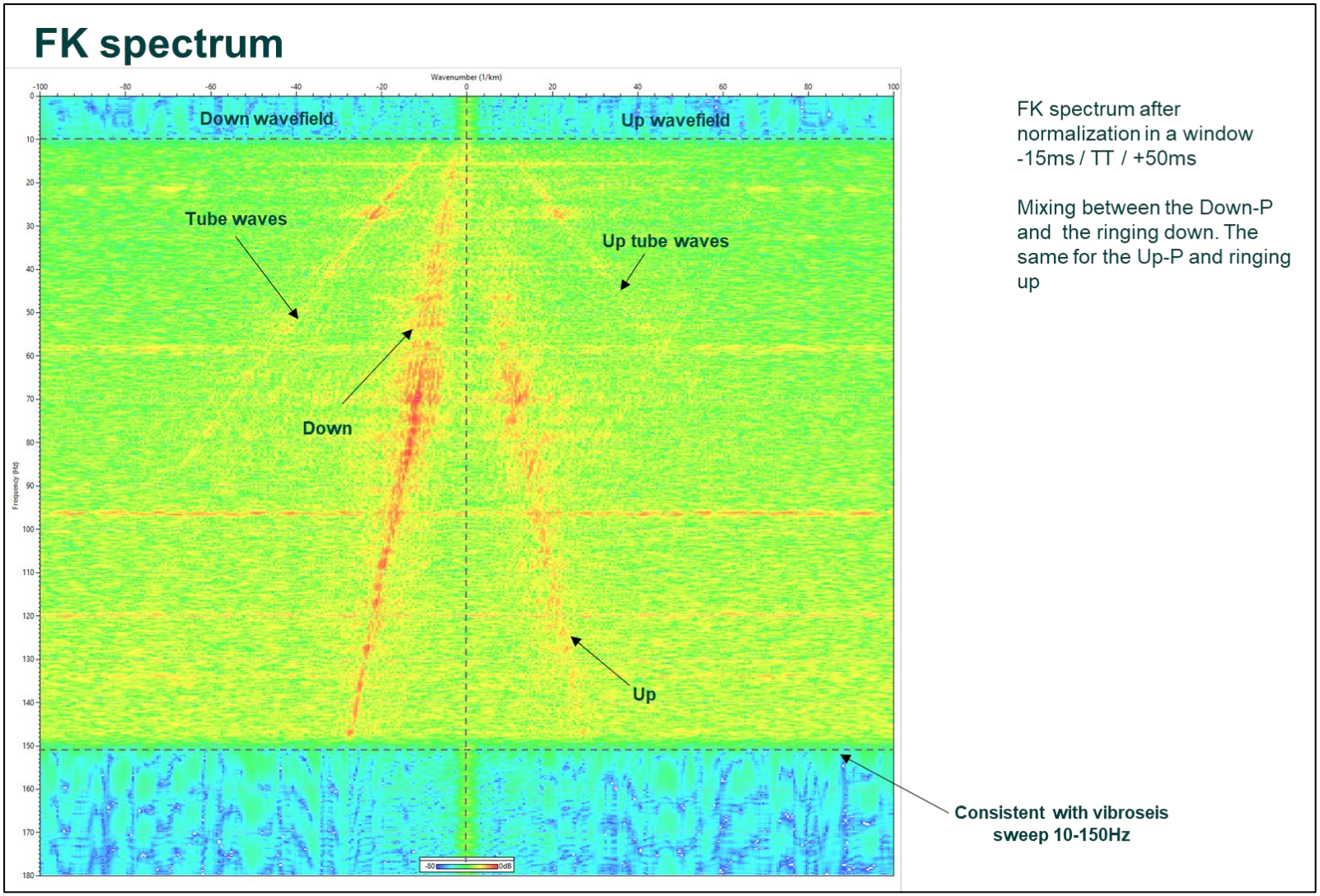


*Figure 7-29. FK spectrum - Stack after normalization. The tube wave has a weak amplitude in the FK domain. The Down and Up waves have strong amplitudes but are mainly generated by the ringing. As the depth sampling is very fine the data is not aliased.*

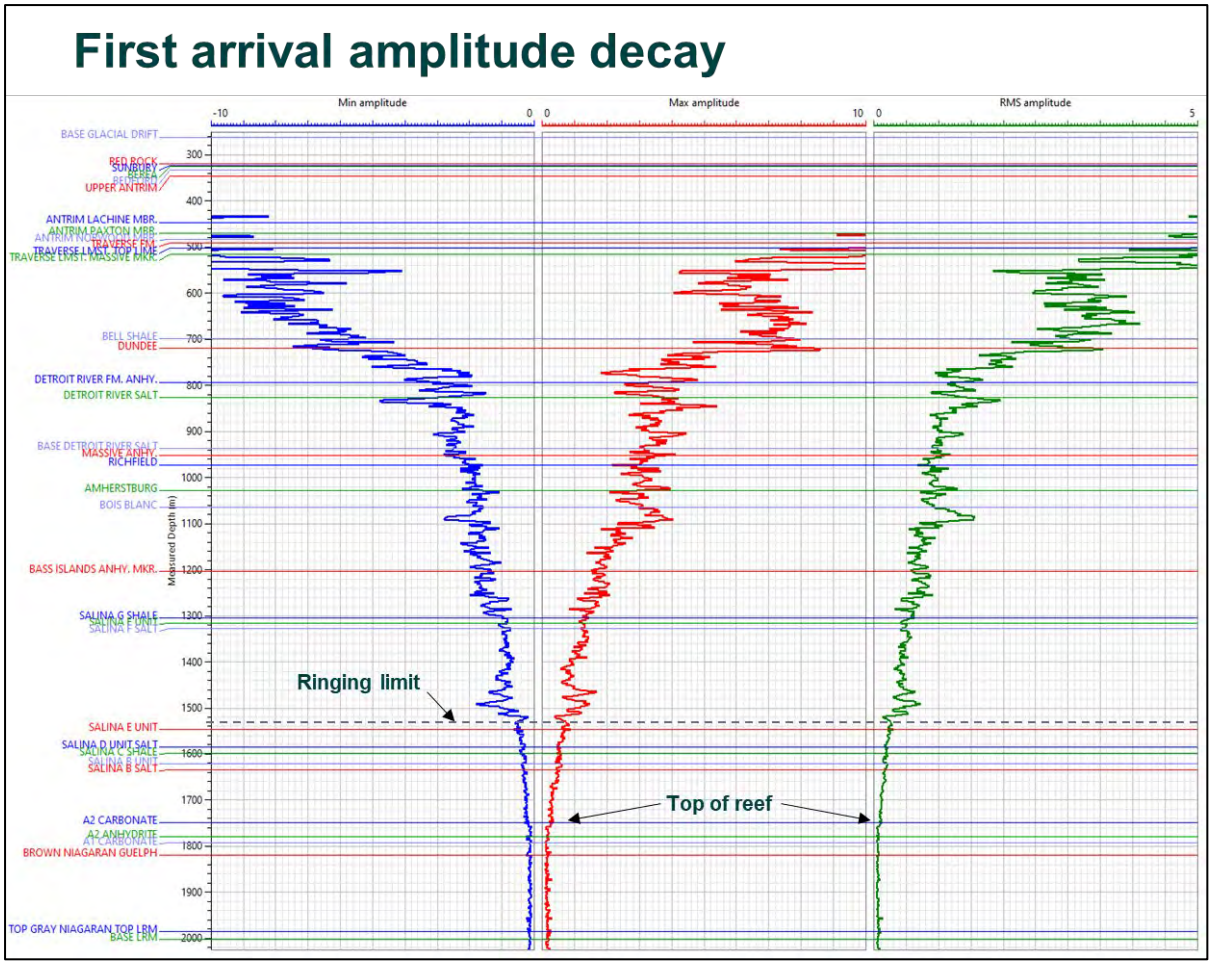


*Figure 7-30. First arrival amplitude decay. The data have been analysed in a window from 15 ms before FB to 50 ms after FB. The data follow a normal trend, the limit of the depth interval with strong ringing is noticeable from the graph shape. At the A2 Carbonate level there is a drop in the FB amplitude.*

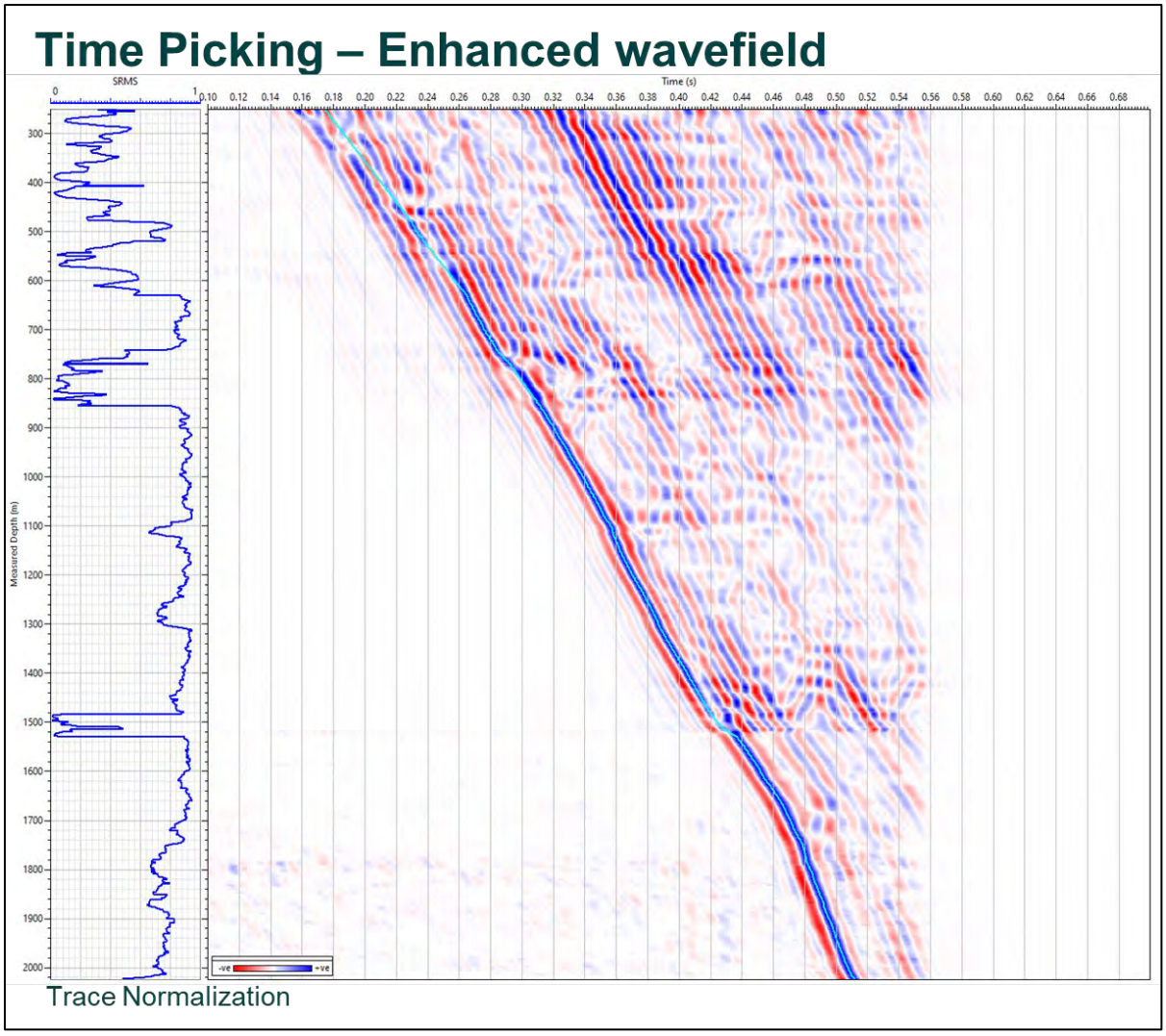


*Figure 7-31. Time Picking – Enhanced wavefield - Slopes enhancement. Few manual points guided the automatic picking which was performed on the enhanced weighted semblance wavefield between 0.18 and 0.35 ms/m over a 20 m window.*

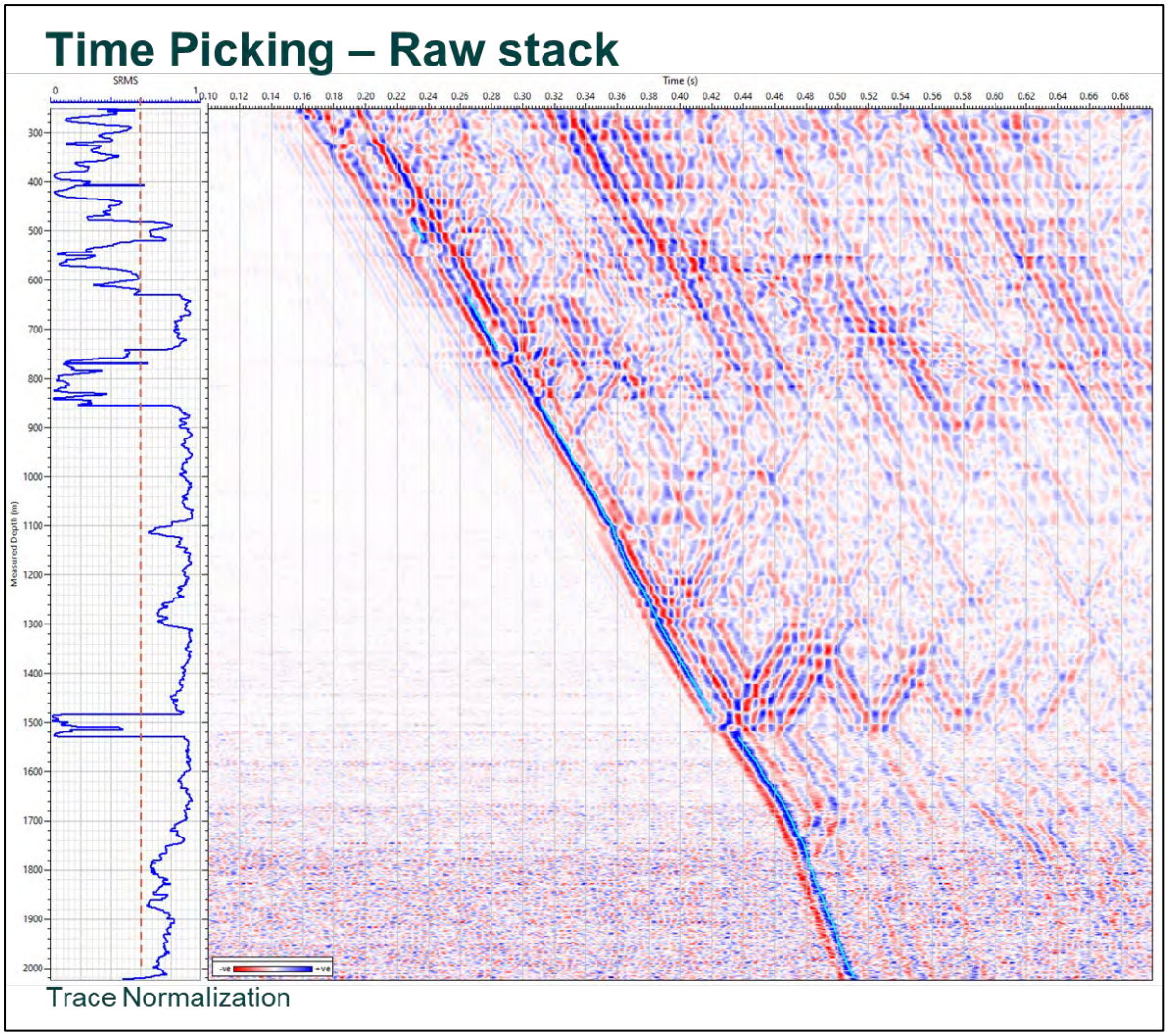


*Figure 7-32. Time Picking – Raw stack. Above 900 m MD manual editing was required. The semblance RMS value was calculated for each depth and below 0.6 RMS semblance value the picks were discarded. The picks were interpolated and smoothed over 5 levels.*

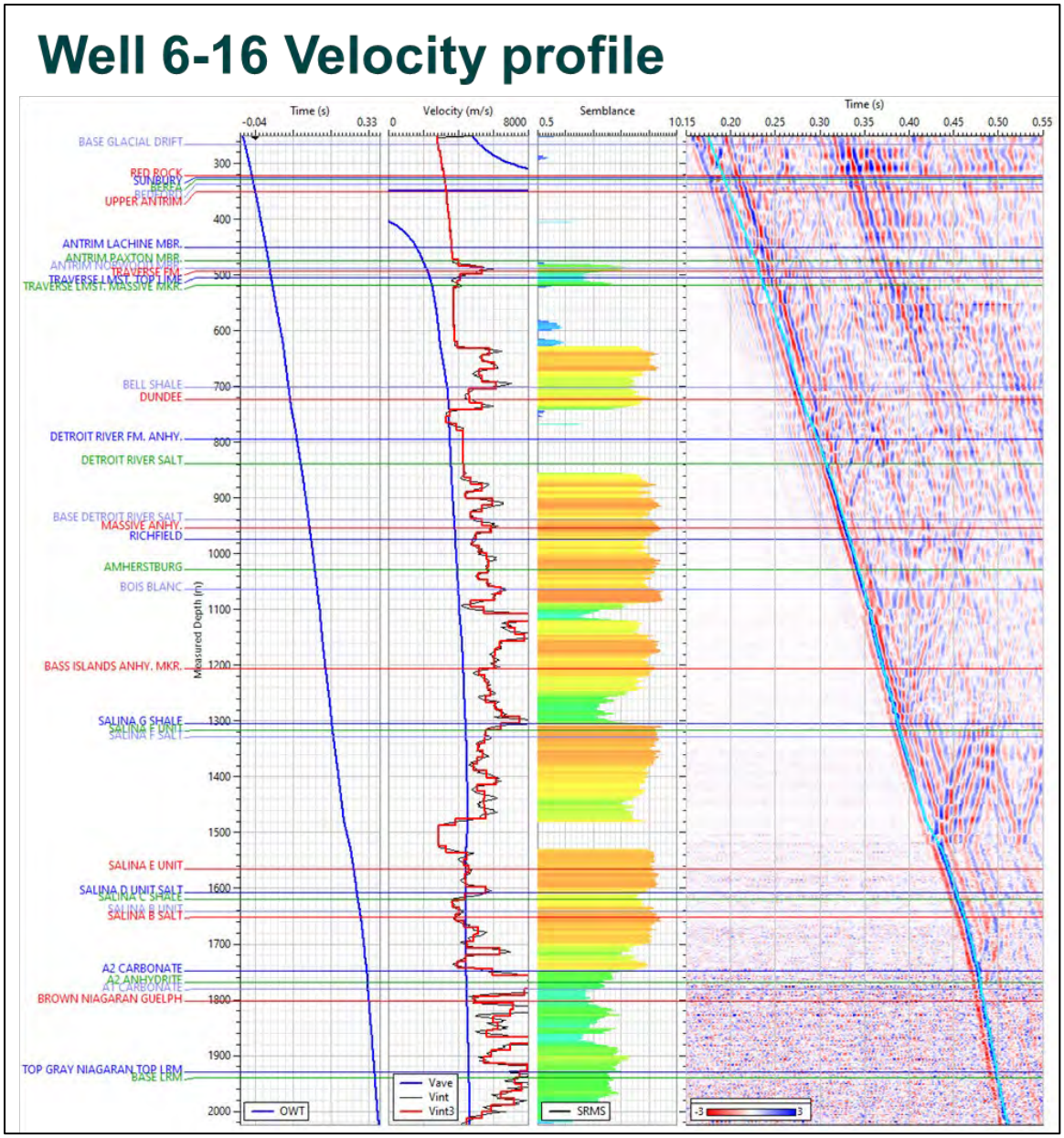


*Figure 7-33. Well 6-16 Velocity profile. This figure presents the time to depth curve on track 1, the average and interval velocity profile on track 2, the semblance RMS near the FB on track 3 and the picked stack on track 4.*

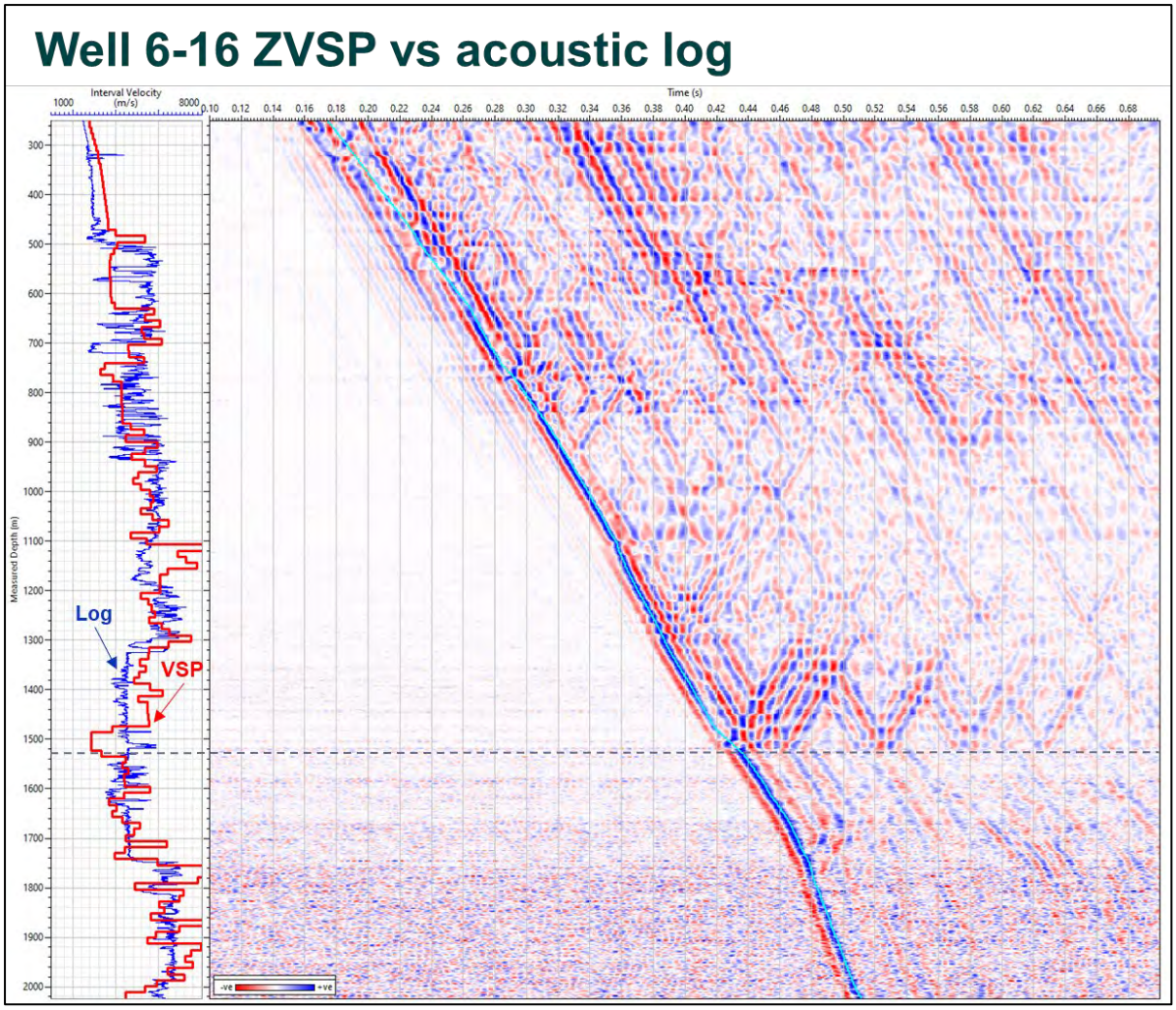


*Figure 7-34. Well 6-16 ZVSP vs acoustic log. Above 1540 m MD there is a poor match between the interval velocity from the VSP and the acoustic log compressional velocity as the VSP is recording velocity close to elastic wave in the steel.*

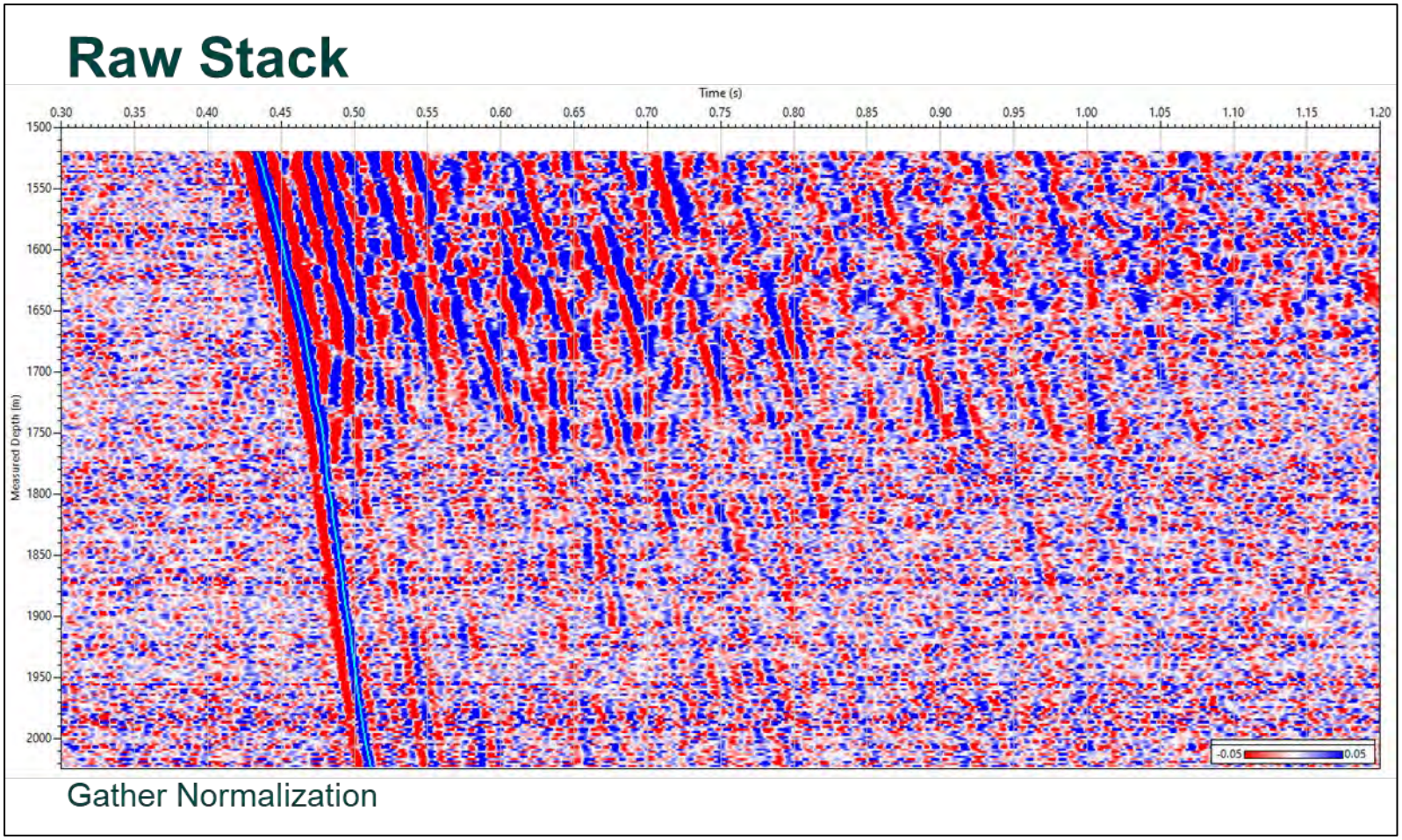


*Figure 7-35. Raw Stack. It shows the processing input data, a filtered stack data with a BPF: 5,10-90,110 Hz. The data above 1540 m MD affected by ringing were excluded from the processing. The amplitudes displayed are cross-normalized.*

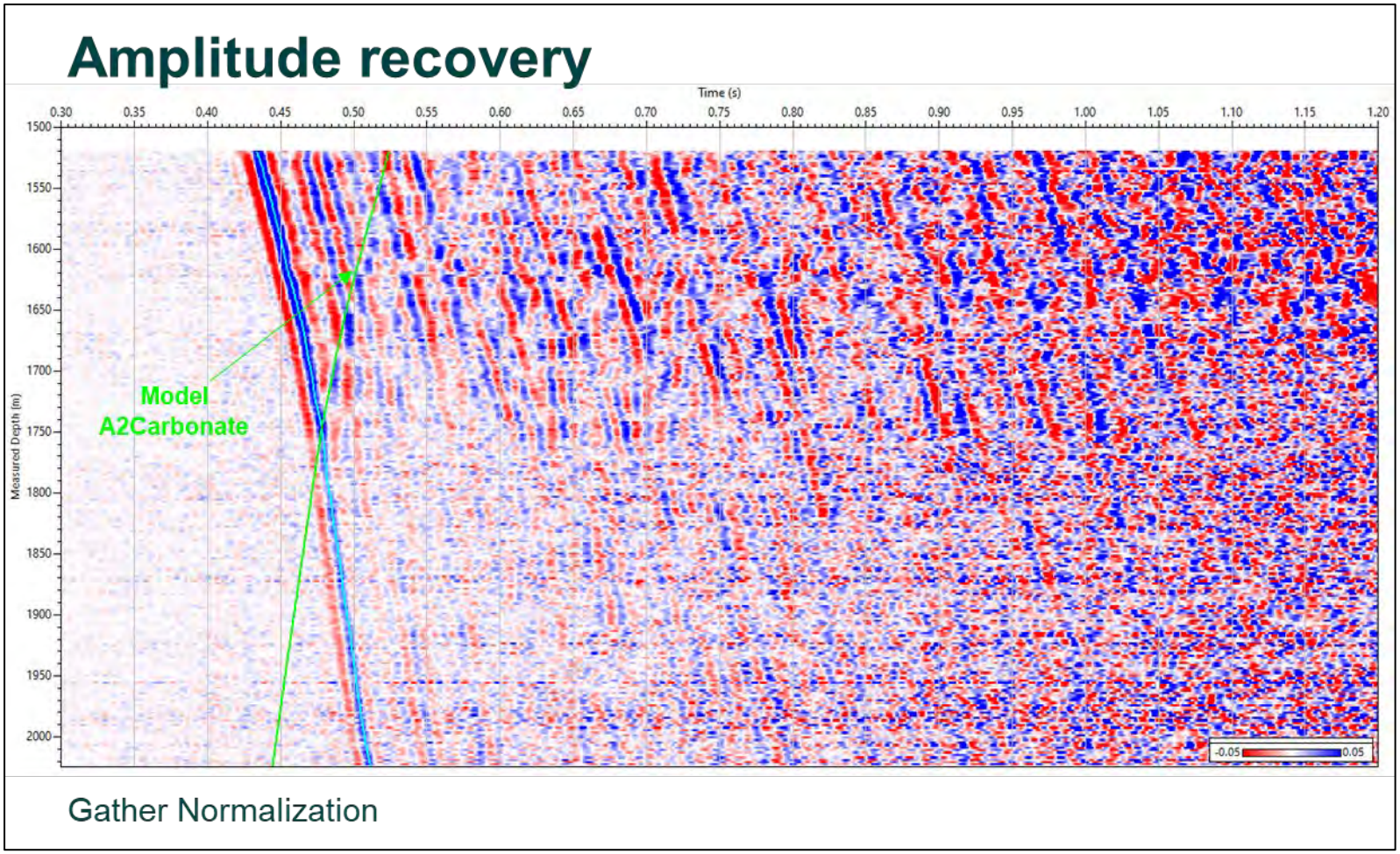


*Figure 7-36. Amplitude recovery - Time power function. To compensate for the absorption and spherical divergence spreading, the amplitude was scaled by the squared sample time. The stack after amplitude recovery is presented here.*

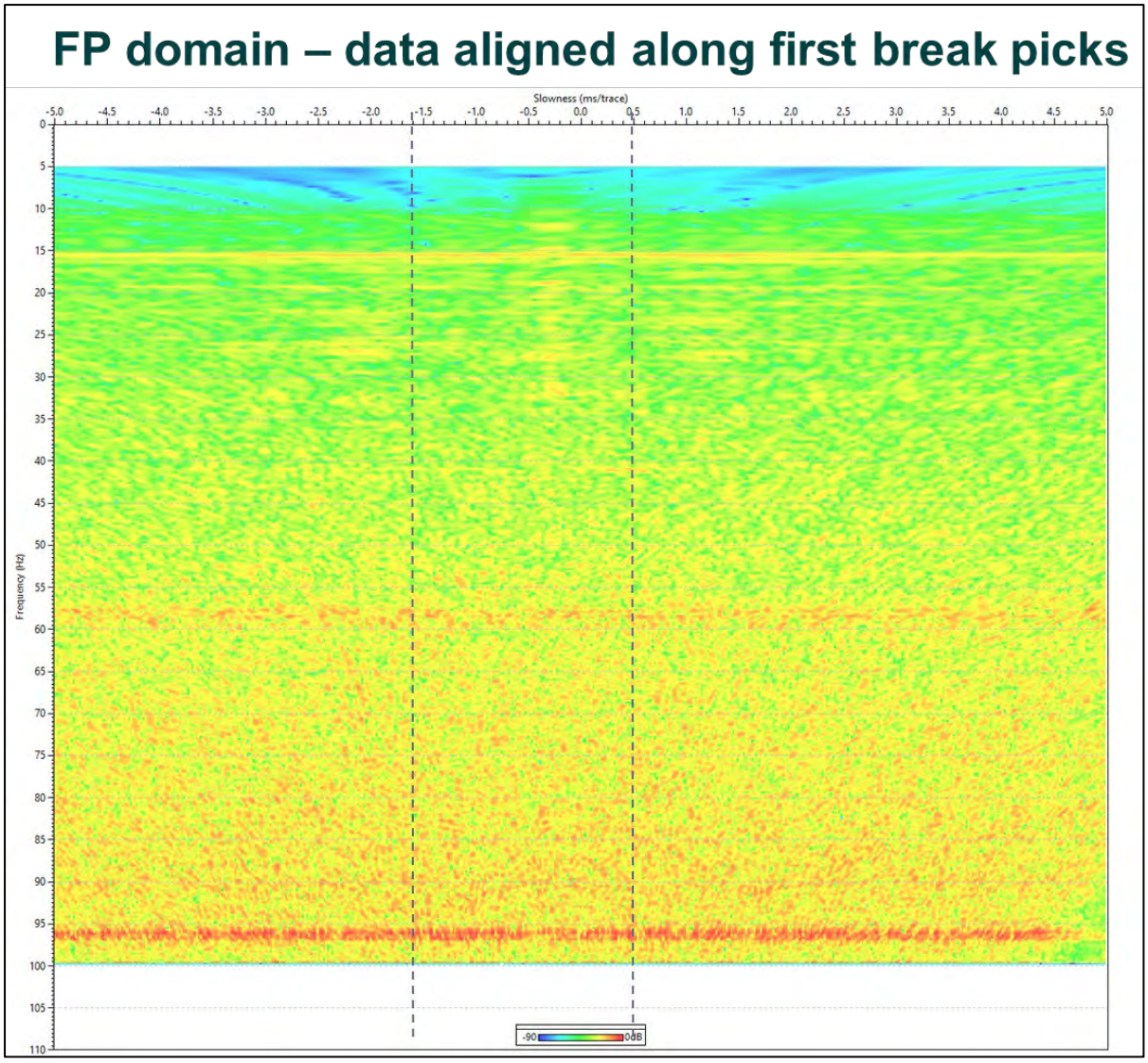


*Figure 7-37. FP domain – data aligned along first break picks - Remove tube waves and noise. This figure shows the stack aligned along the first break in the frequency-slowness domain (FP).*

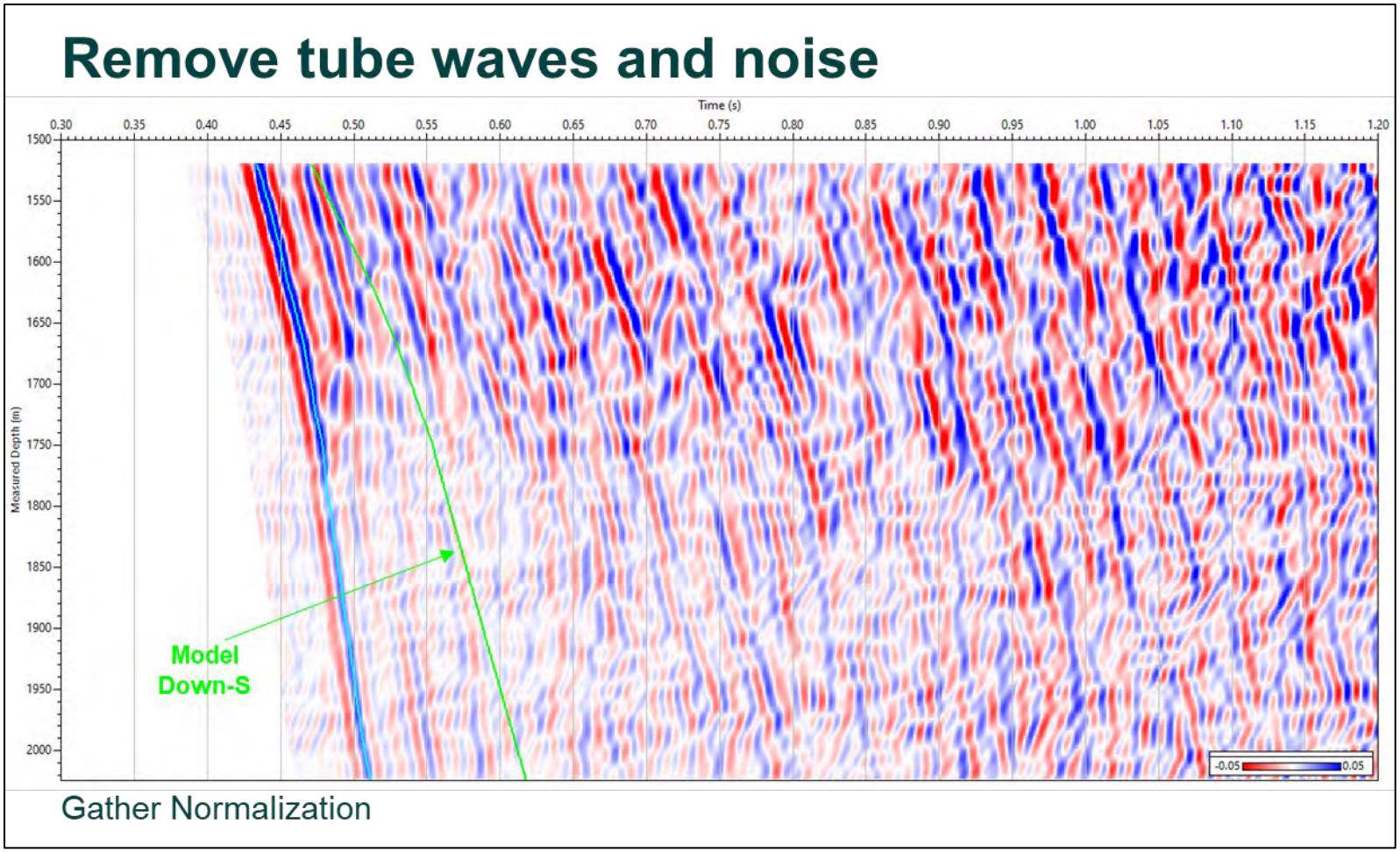


*Figure 7-38. Remove tube waves and noise - After FP separation. To remove noise and tube waves, the data was muted outside the -1.7 – 0.6 slowness interval then the separation was performed in the FP domain.*

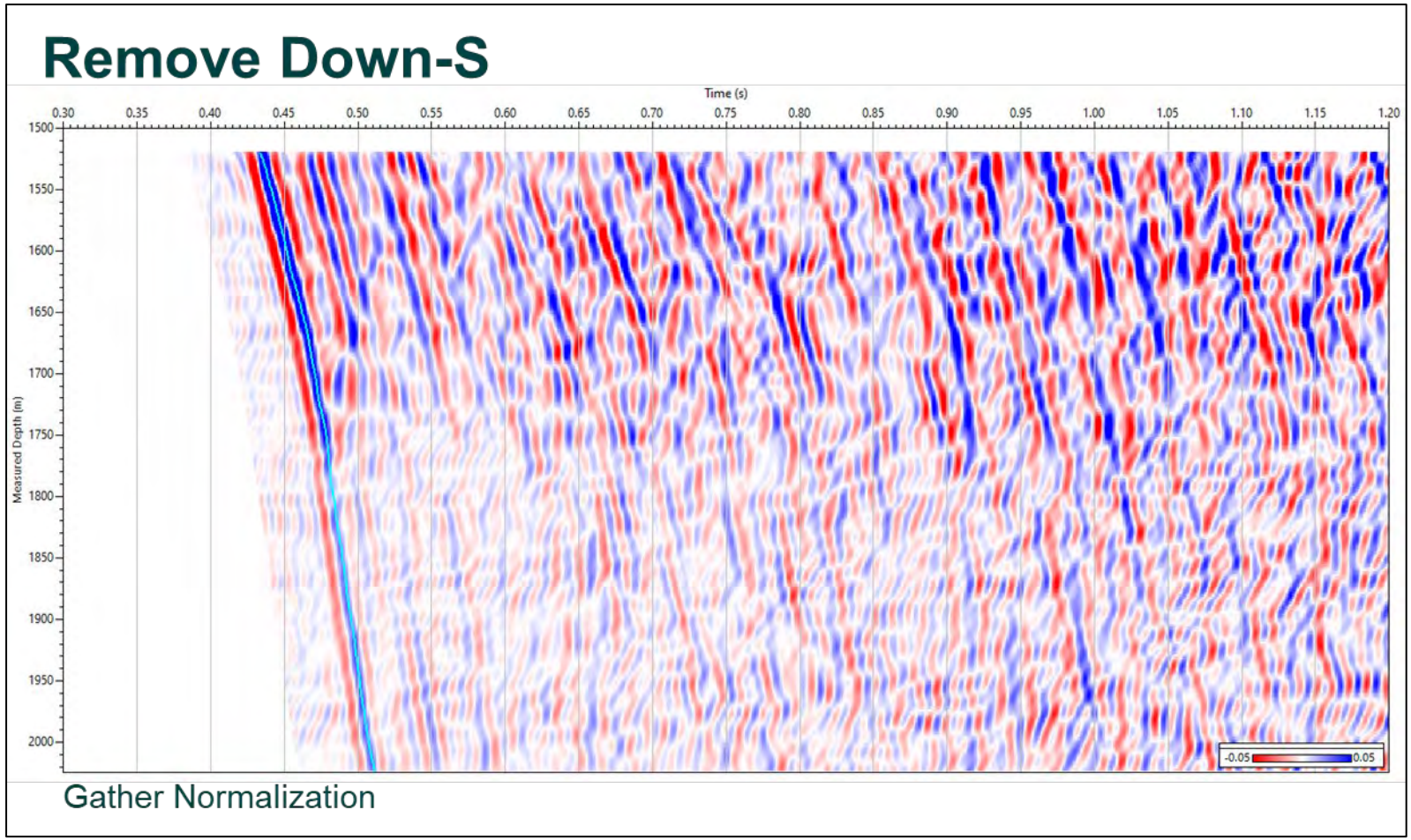


*Figure 7-39. Remove Down-S - Median filter. The Down S wavefield shown in figure 7.39 was removed using a median filter over 121 traces aligned along the modelled Down S TT (Fig. 7.38 green).*

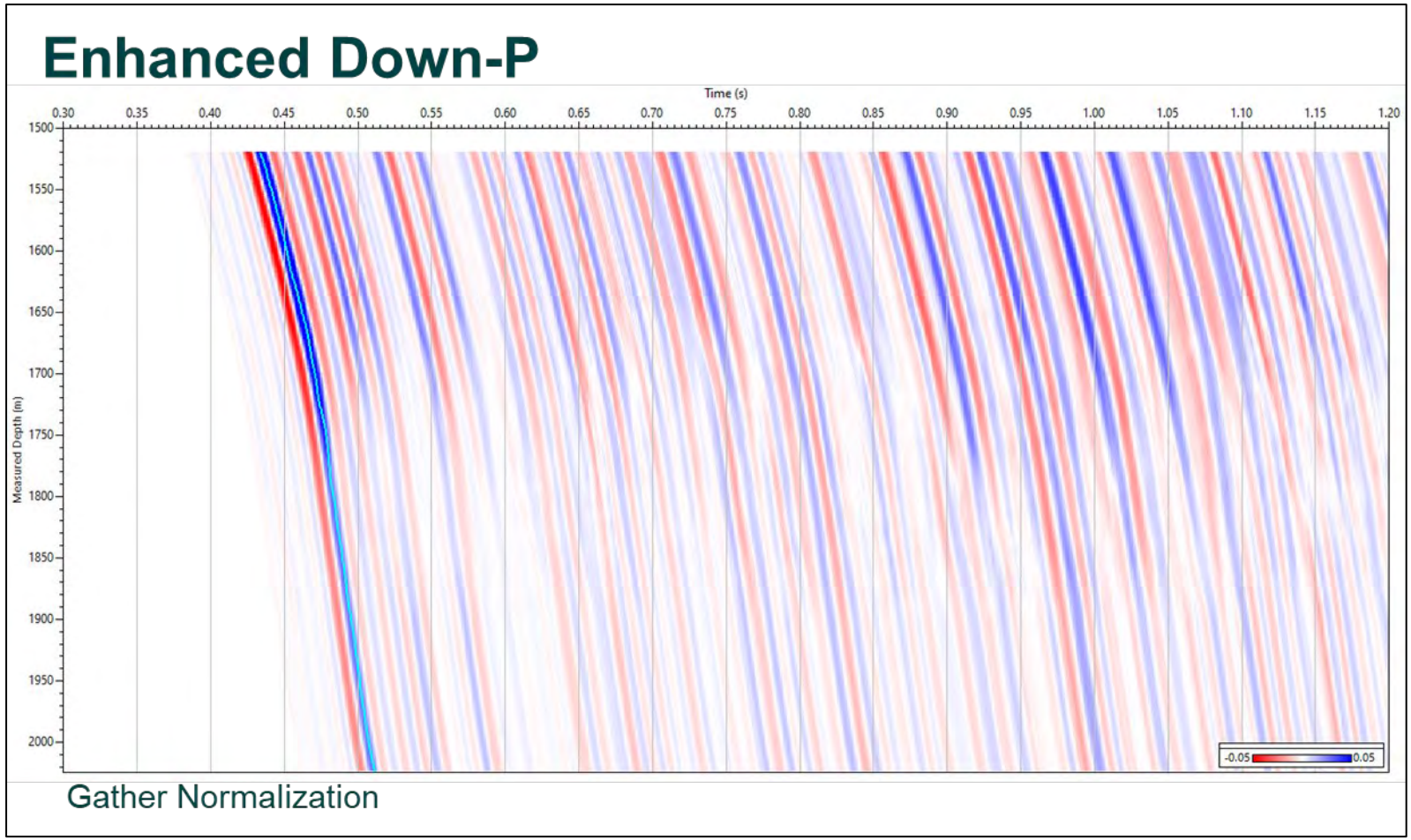


*Figure 7-40. Enhanced Down-P - Median filter. We enhanced the Down P wavefield using a median filter of 121 traces along the FB. This wavefield will be used later in the deconvolution.*

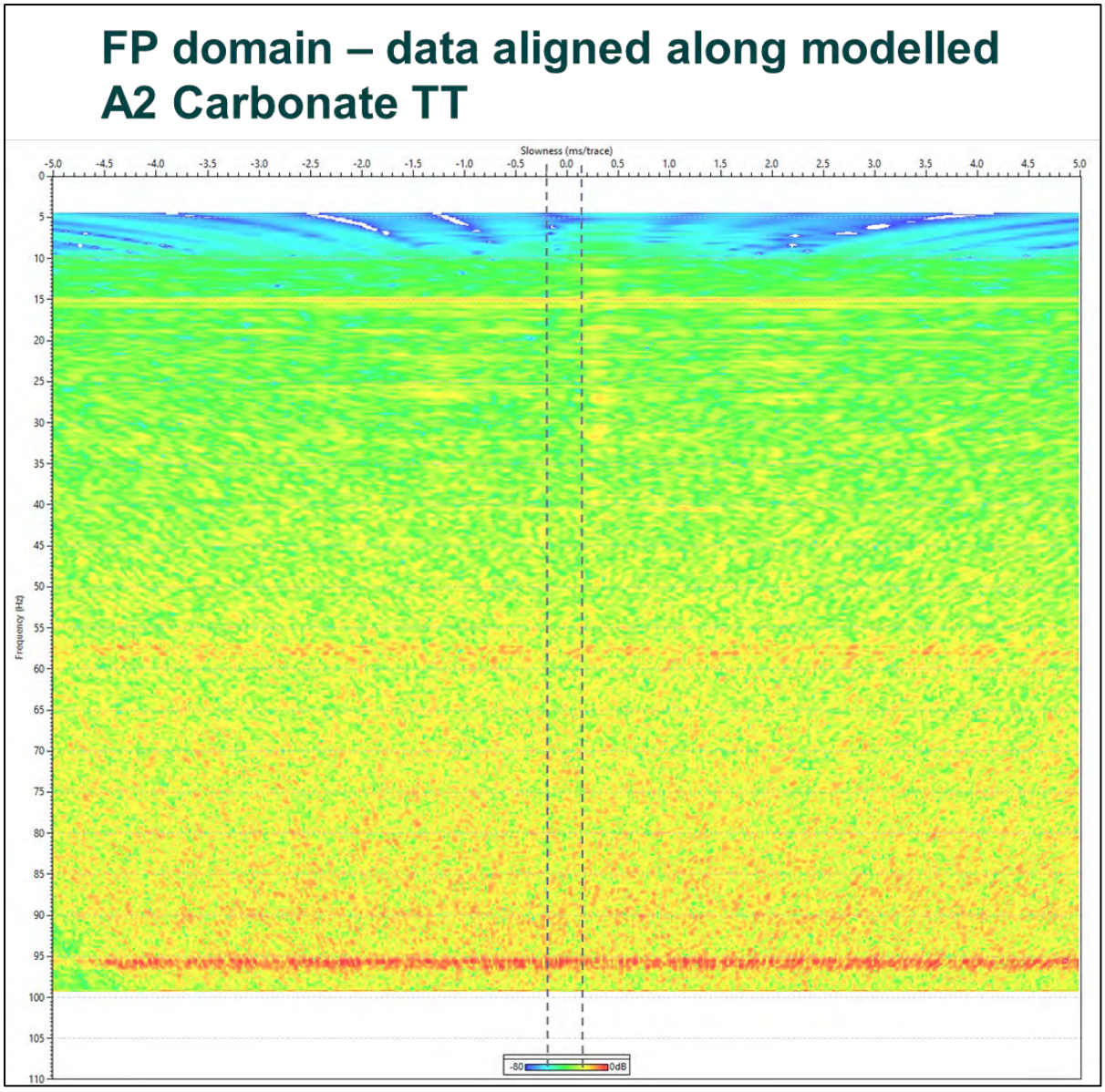


*Figure 7-41. FP domain – data aligned along modelled A2 Carbonate TT - Enhance Up P. The Up P wavefield was enhanced in the FP domain in a slowness window of -0.25 to 0.15 ms/trace.*

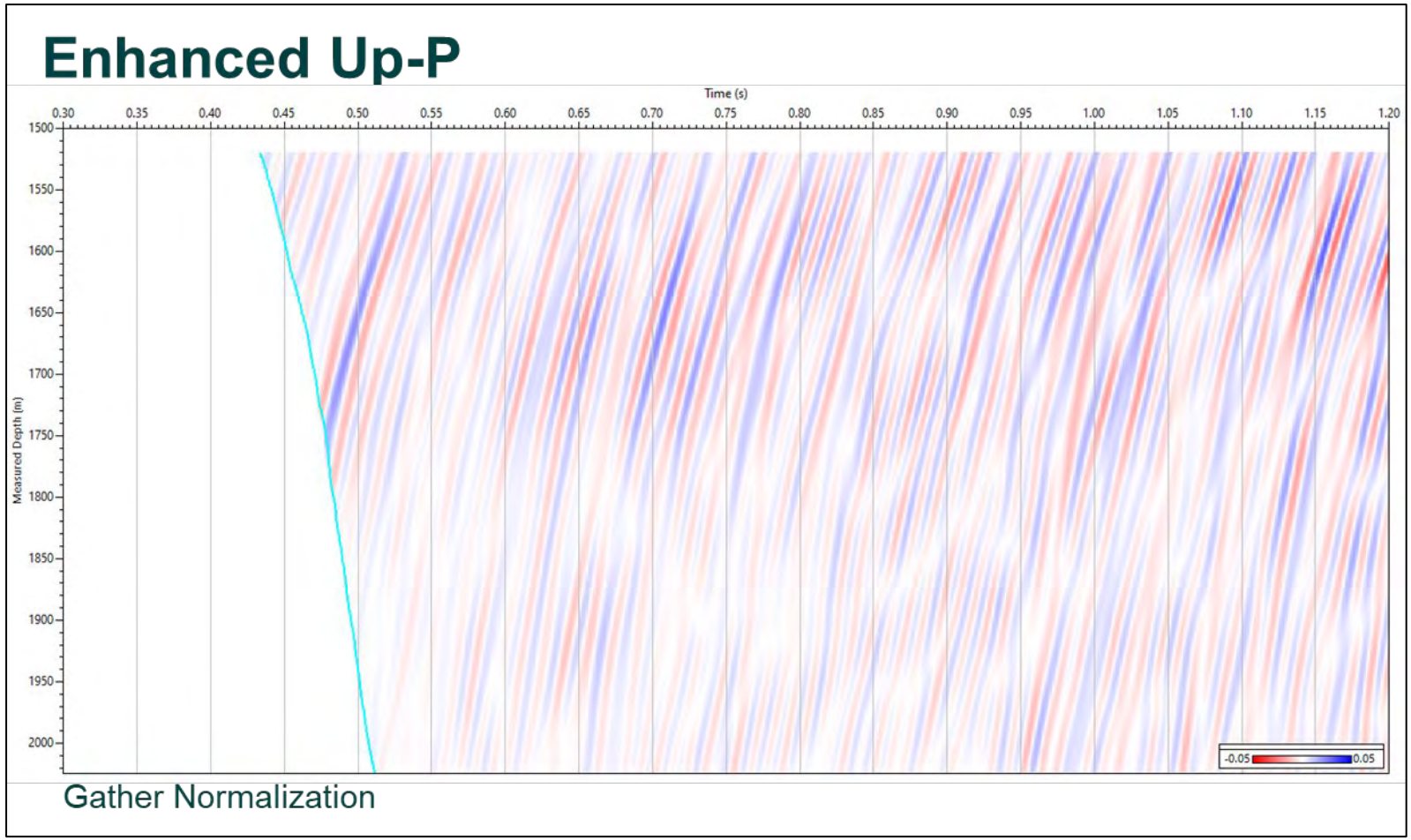


*Figure 7-42. Enhanced Up-P - After FP separation. The input data were aligned along the A2 Carbonate modelled TT (Fig. 7.36 green) before FP. Figure 7.42 shows the enhanced Up P along the modelled A2 Carbonate TT over a 10 trace window after the separation in the FP domain.*

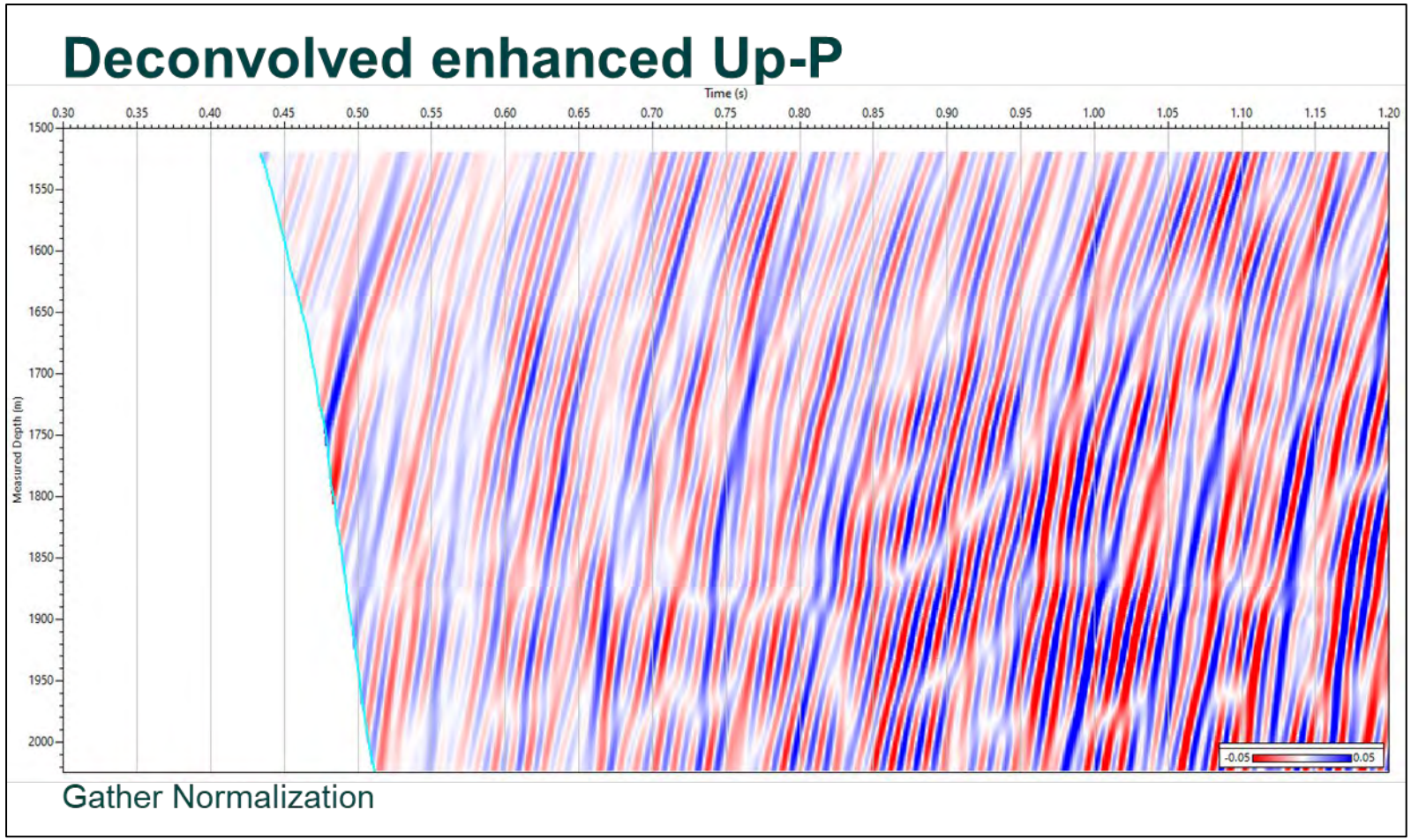


*Figure 7-43. Deconvolved enhanced Up-P - Trace by trace deterministic deconvolution. To reduce the multiples and boost the high frequency data, the enhanced Up P was deconvolved. Trace by trace deterministic deconvolution with enhanced Down P (Fig. 7.40) using a 0.15 s operator length and 20% white noise was applied to the enhanced Up P. Finally, the data were filtered with a 5,10-90,110 Hz BPF.*

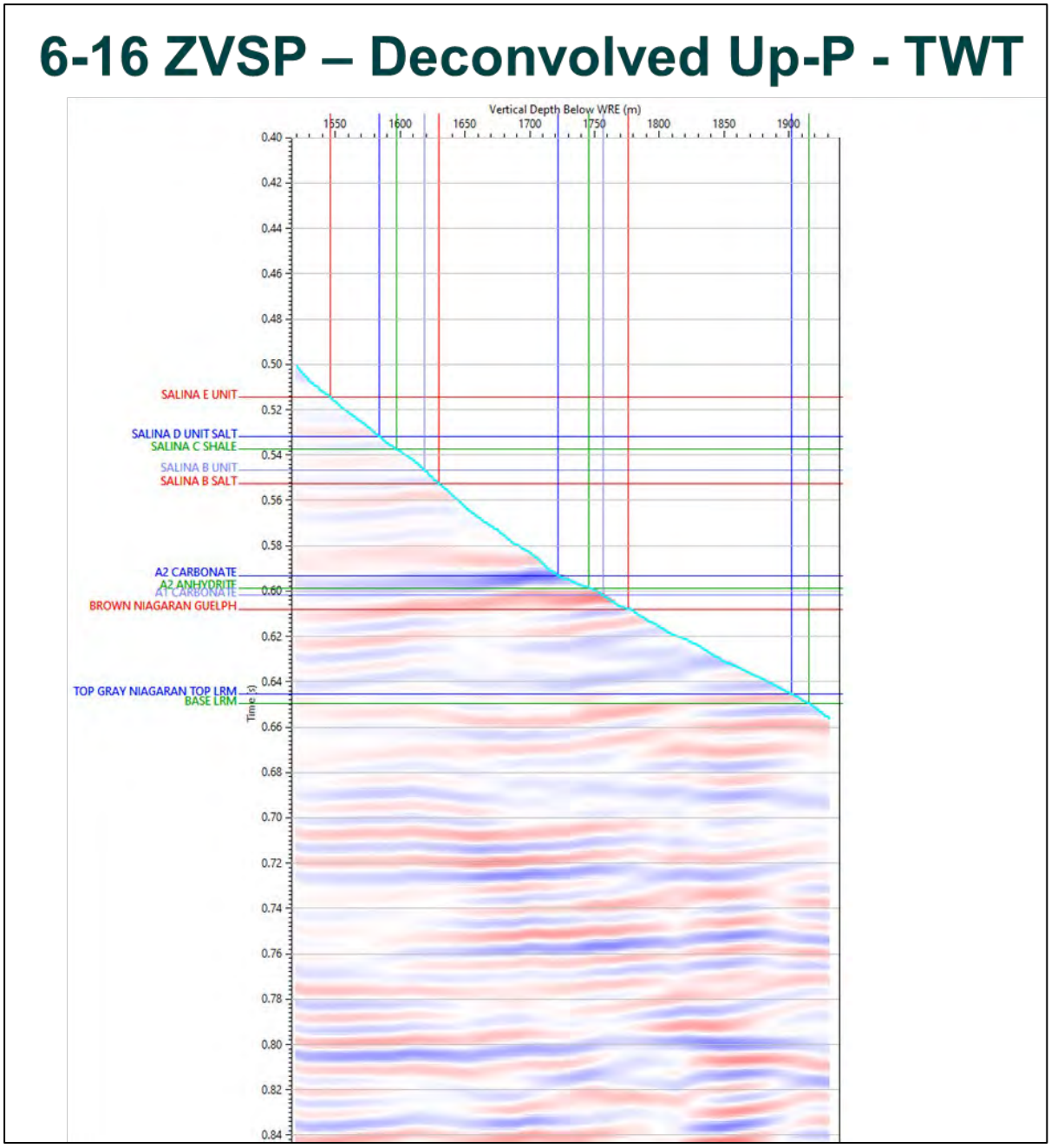


*Figure 7-44. 6-16 ZVSP – Deconvolved Up-P – TWT. Deconvolved Up P wavefield with the index presented in TWT.*

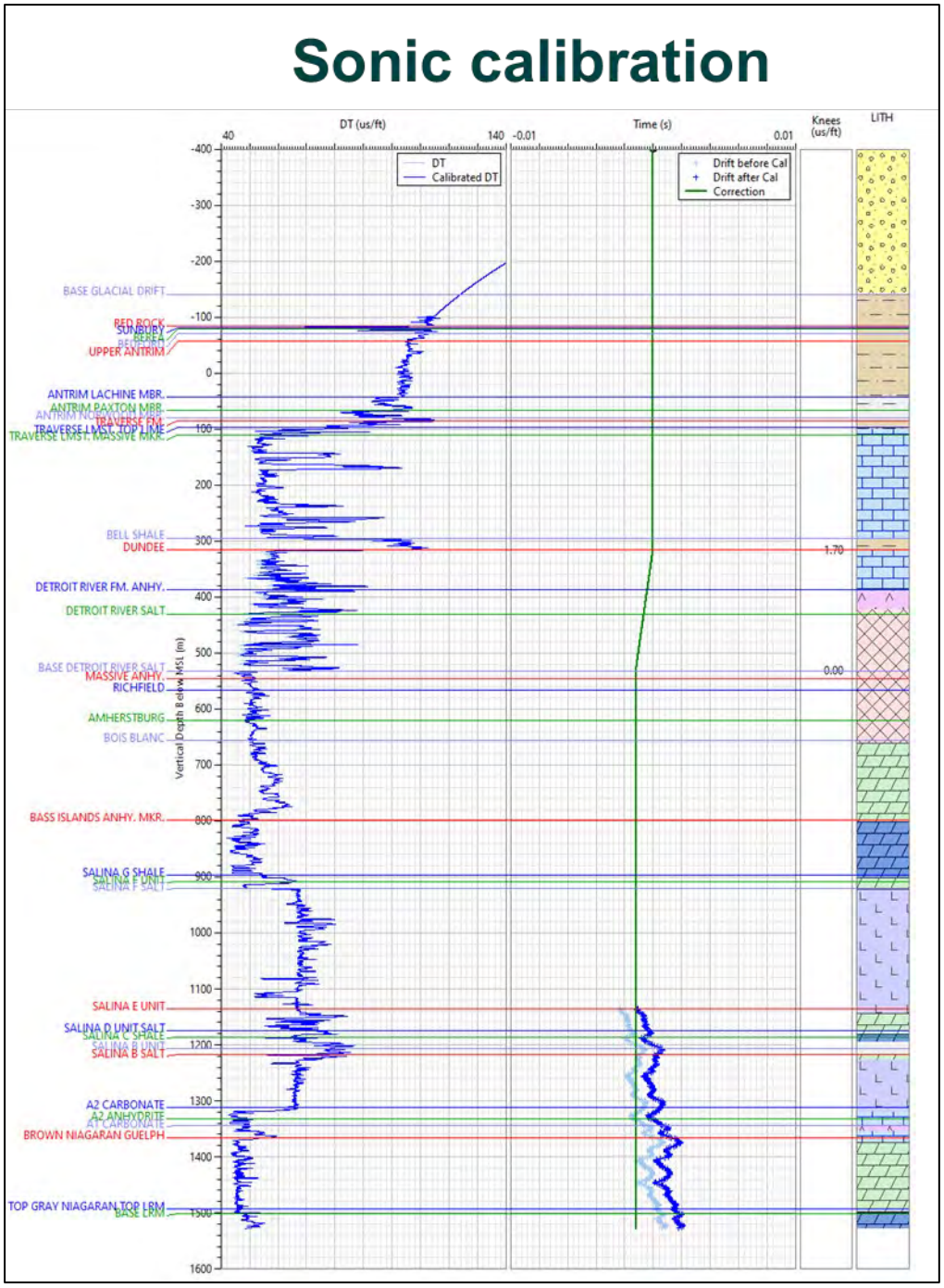


*Figure 7-45. Acoustic log calibration. The log calibration for well 6-16 is presented here. The first panel shows the acoustic log before calibration in light blue and in blue the acoustic log after calibration. In second panel is the log-VSP drift before calibration in light blue and the residual drift in blue. The third panel presents the knee points and the correction values and in the last panel is the lithological column. Only two knee points were required to calibrate the acoustic log located in the same area as the knee points used for well 8-16. The residual drift after acoustic log calibration is below 1.5 ms.*

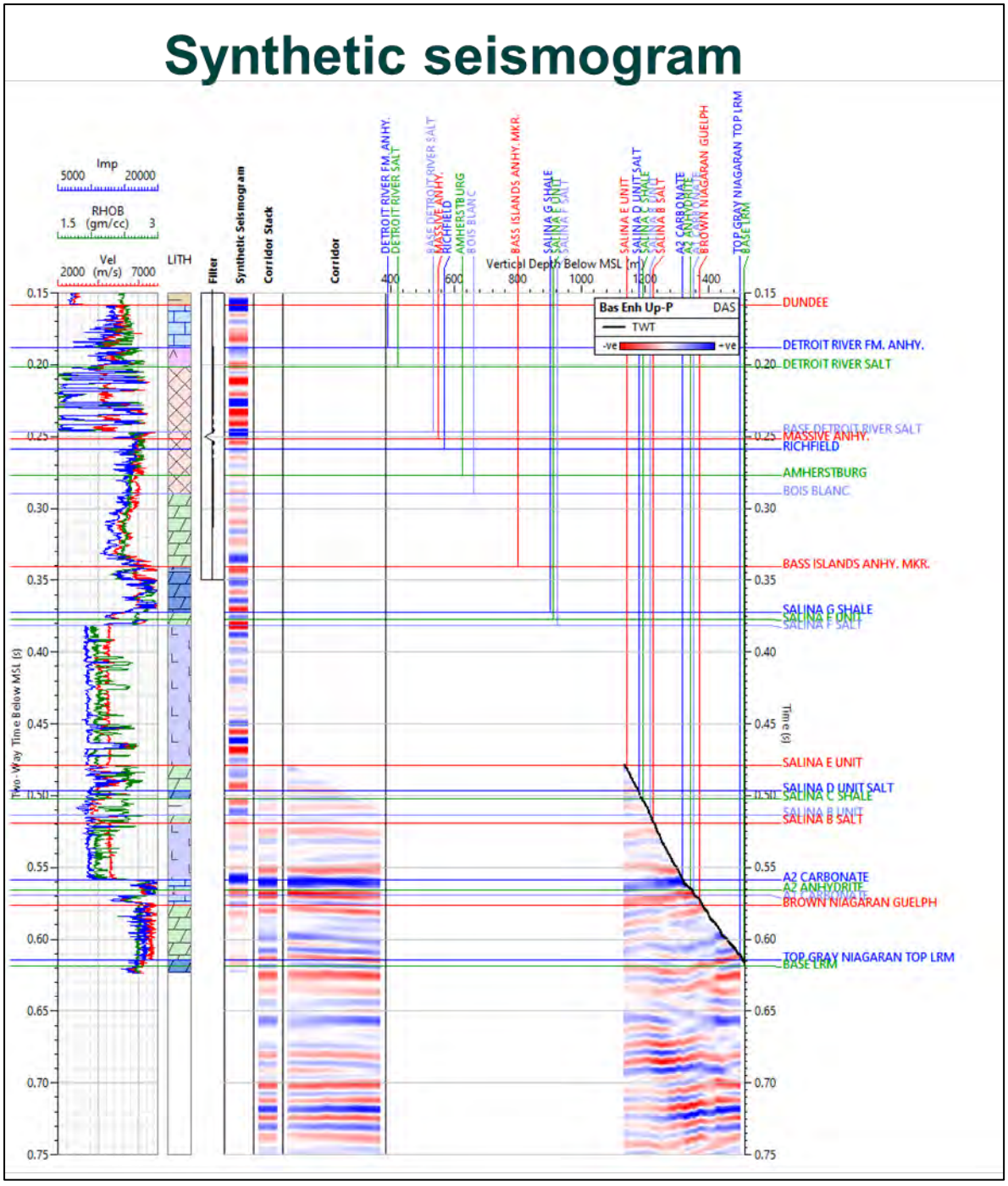


*Figure 7-46. Synthetic seismogram. This figure presents (from right to left): a composite plot with the logs in time, the lithological column, the reflection coefficients, the wavelet used to compute the synthetic seismogram on the left side and enhanced Upgoing P wavefield, the corridor and the corridor stack on the right side. There is a good tie at the main reflectors between the synthetic seismogram and the ZVSP corridor stack. The top of A2 Carbonate is represented by the strong positive reflection at 0.56 s TWT (strong blue reflector) and the top of A1 Carbonate by the following trough (red reflector).*

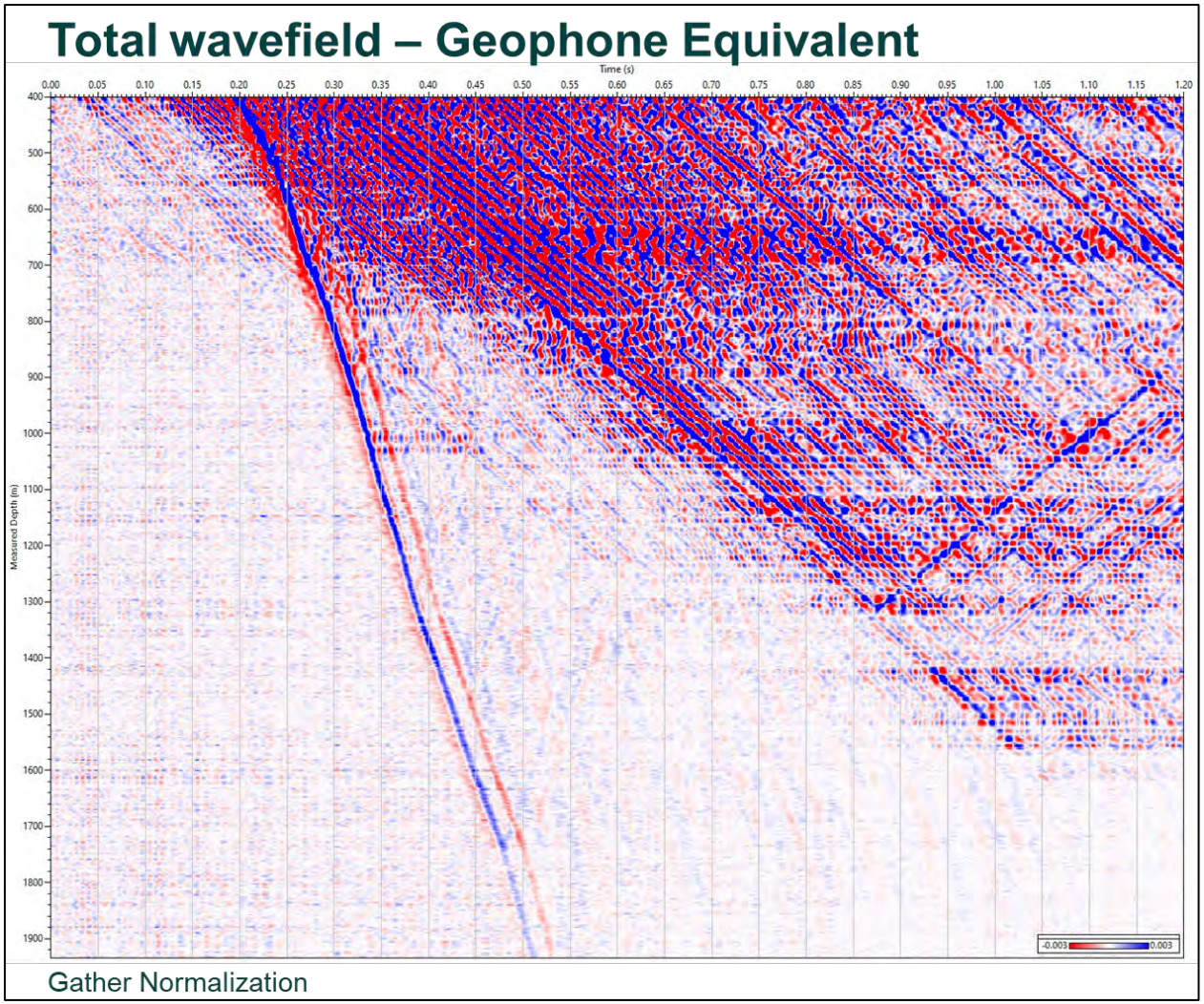


*Figure 7-47. Total wavefiel7d – Geophone Equivalent - Leaky integration in time. This shows the well 8-16 ZVSP total wavefield after conversion from strain rate to geophone equivalent.*

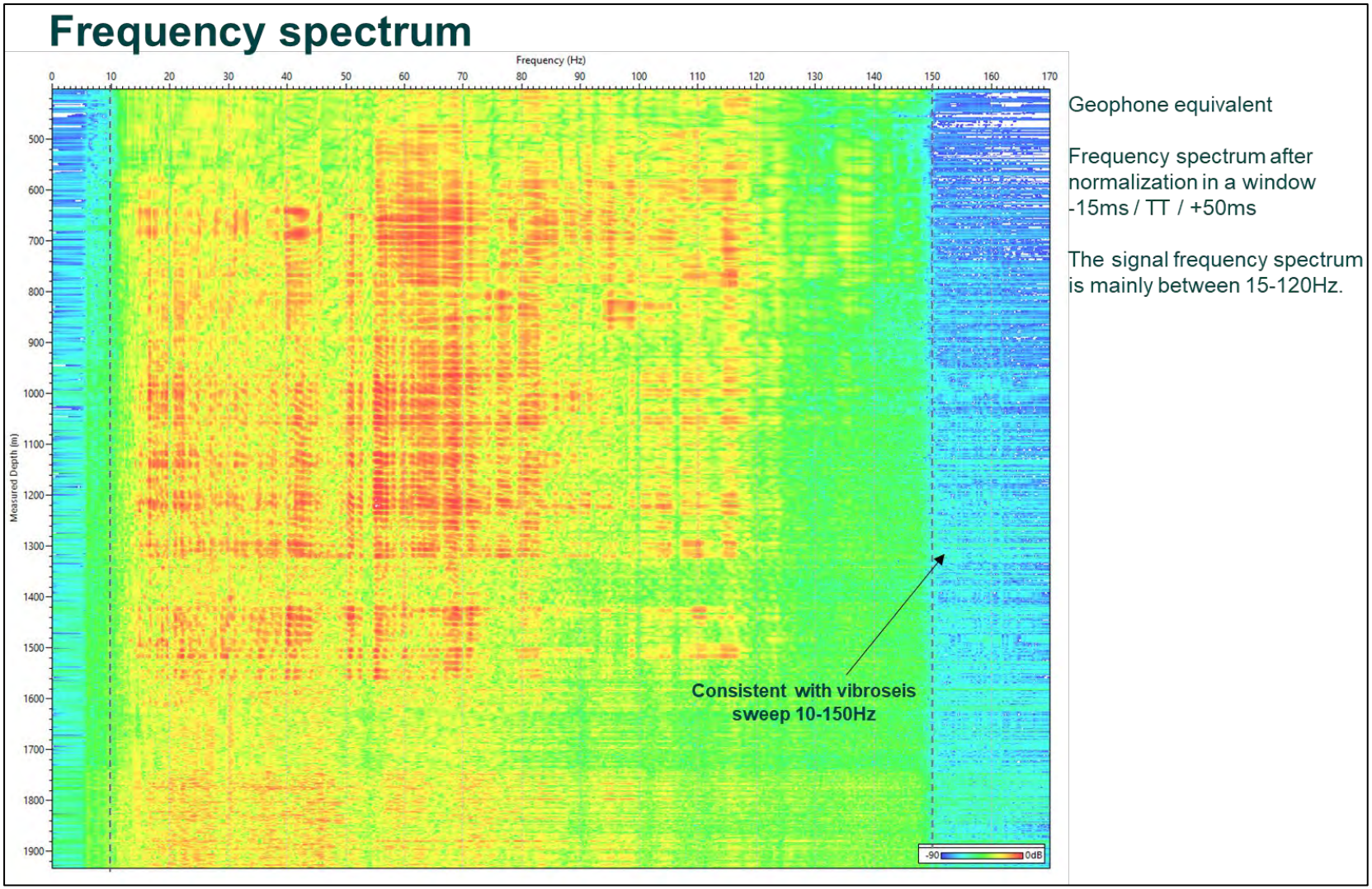


*Figure 7-48. Frequency spectrum - Stack after normalization. After conversion, the frequency spectrum is rebalanced by increasing the low frequencies and decreasing the higher ones.*

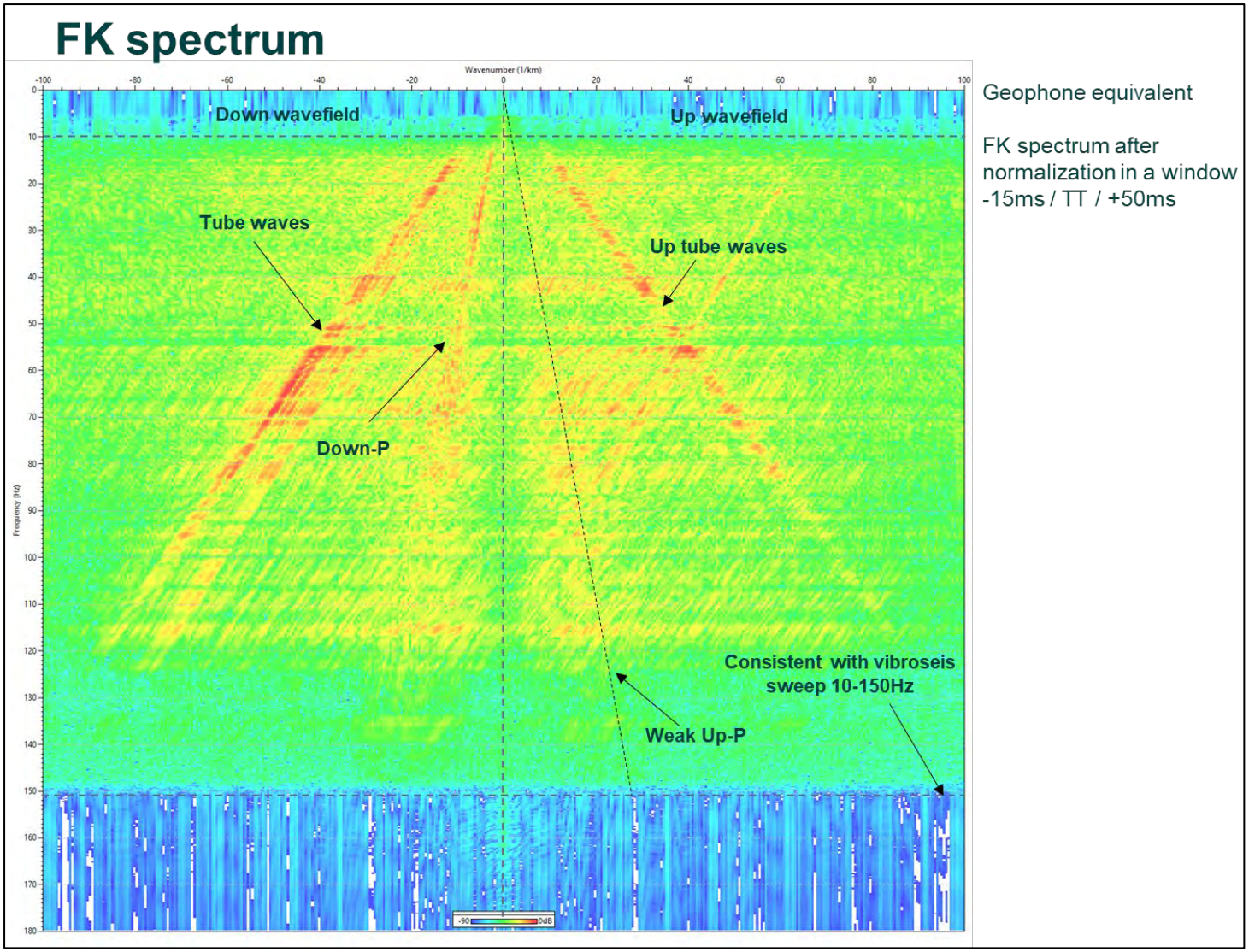


*Figure 7-49. FK spectrum - Stack after normalization. The wavefield slopes in the FK domain are not affected by the conversion.*

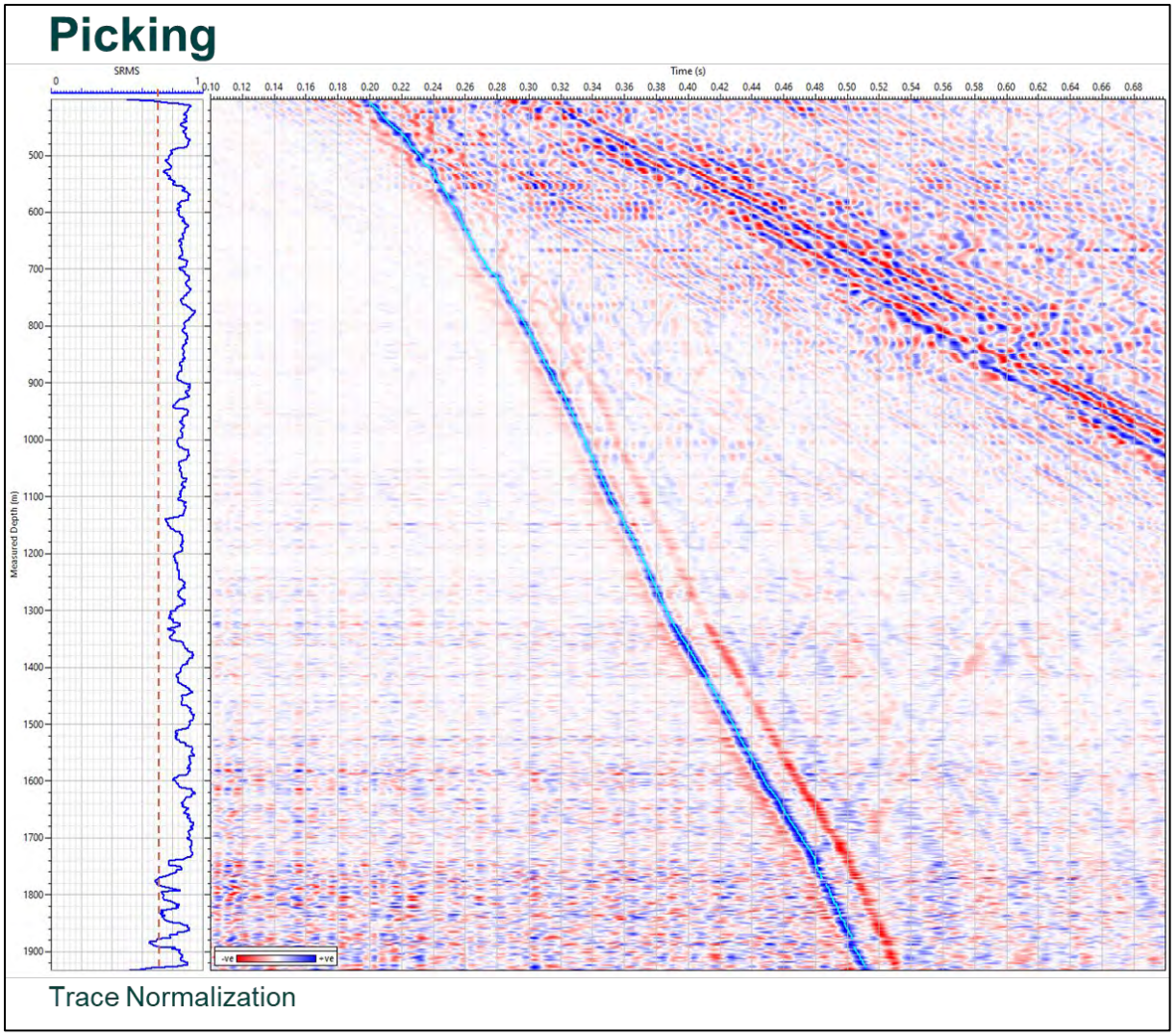


*Figure 7-50. Picking - Integrated stack. The data was picked using the same workflow presented in section 7.1.1. Figure 7.50 shows the semblance and the geophone equivalent stack after picking. The picked times are less consistent at the well bottom due to the low SNR.*

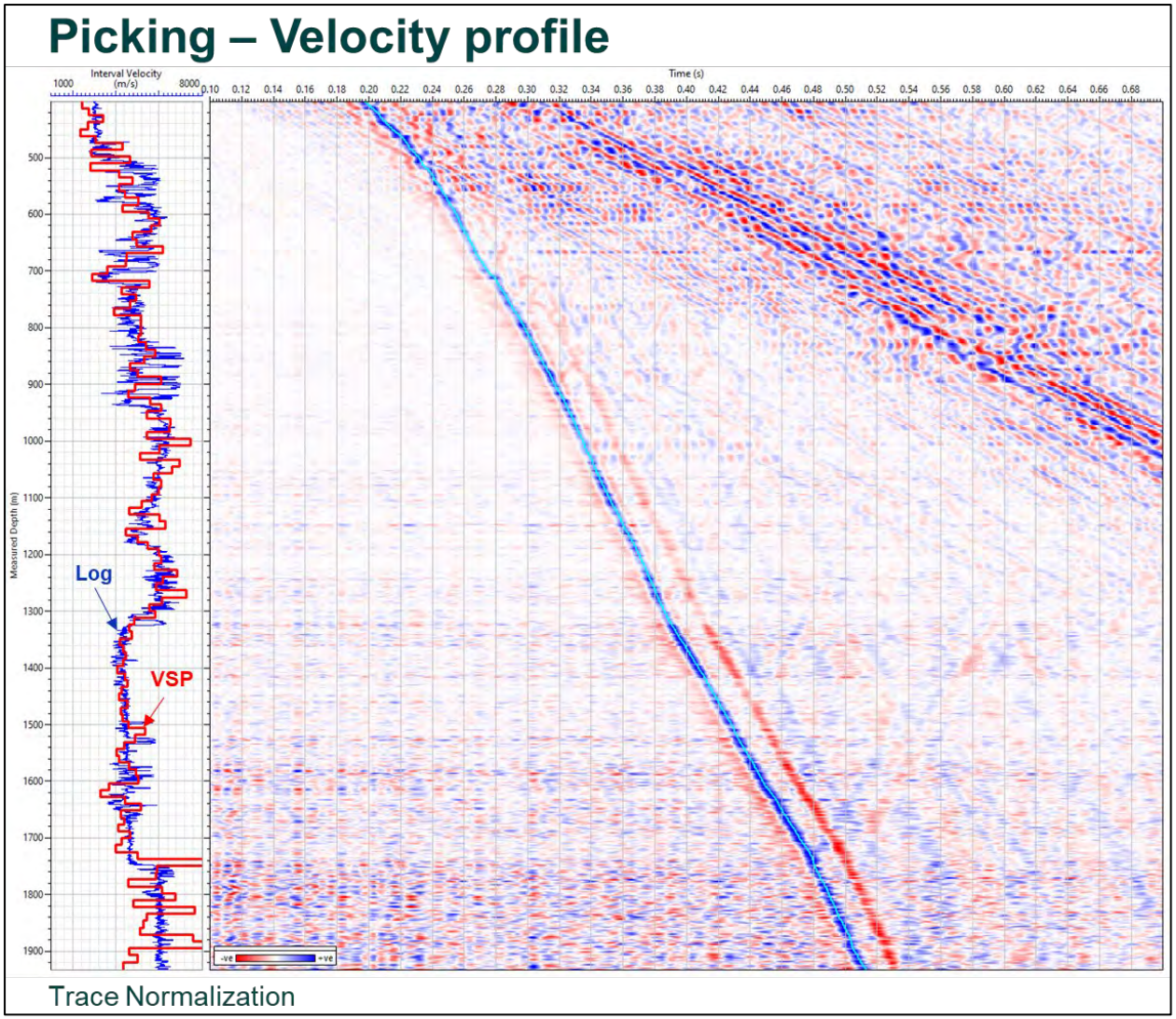


*Figure 7-51. Picking – Velocity profile - Log vs VSP. The geophone-equivalent data picks follow the same velocity trend as the strain rate stack picks. The same workflow and parameters used to process the well 8-16 ZVSP strain rate data was used to process the well 8-16 ZVSP geophone-equivalent data.*

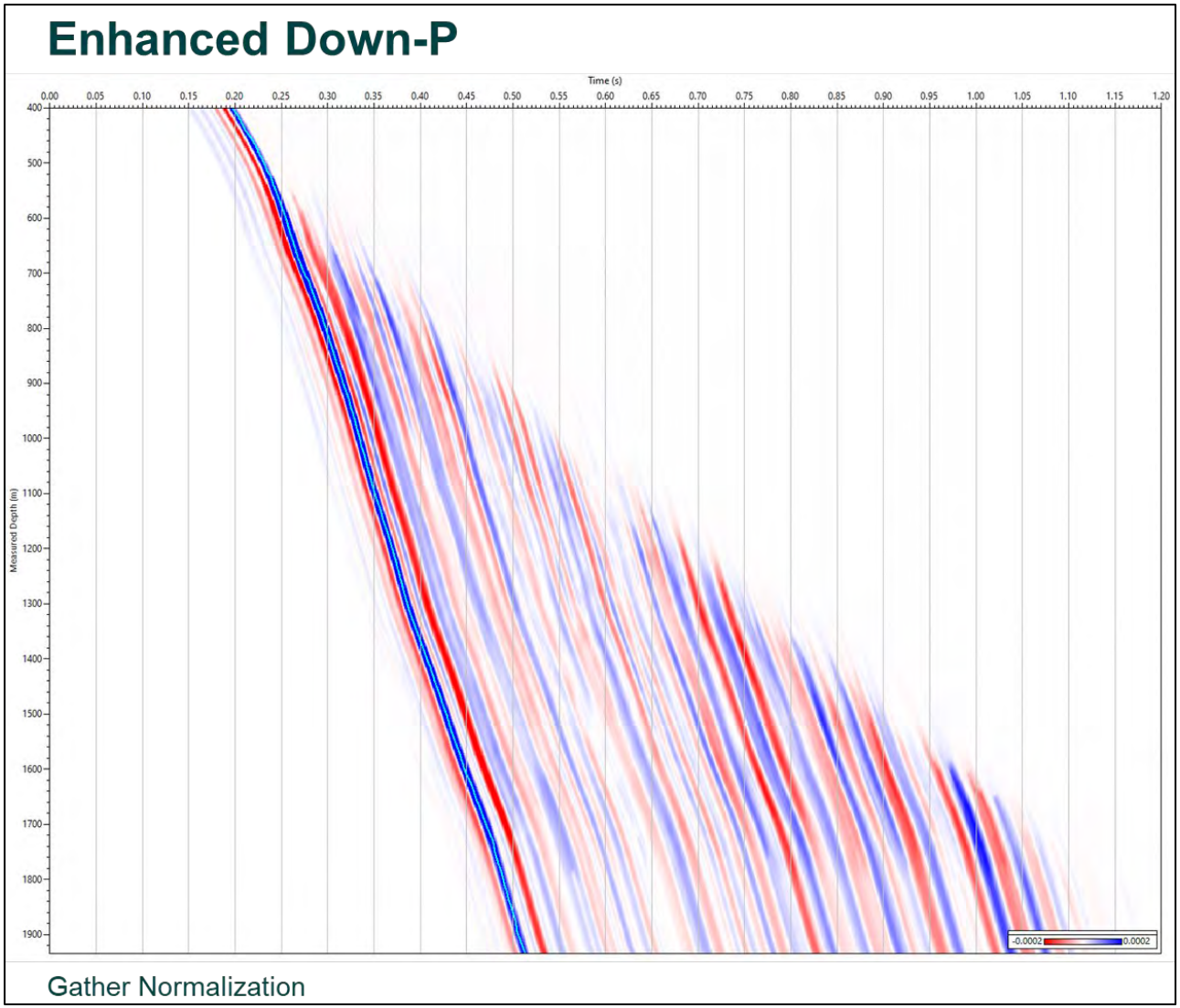


*Figure 7-52. Enhanced Down-P. It presents the enhanced Down P wavefield used in the deconvolution. Comparing with the strain rate data, the main multiples are similar, but with a lower frequency bandwidth.*

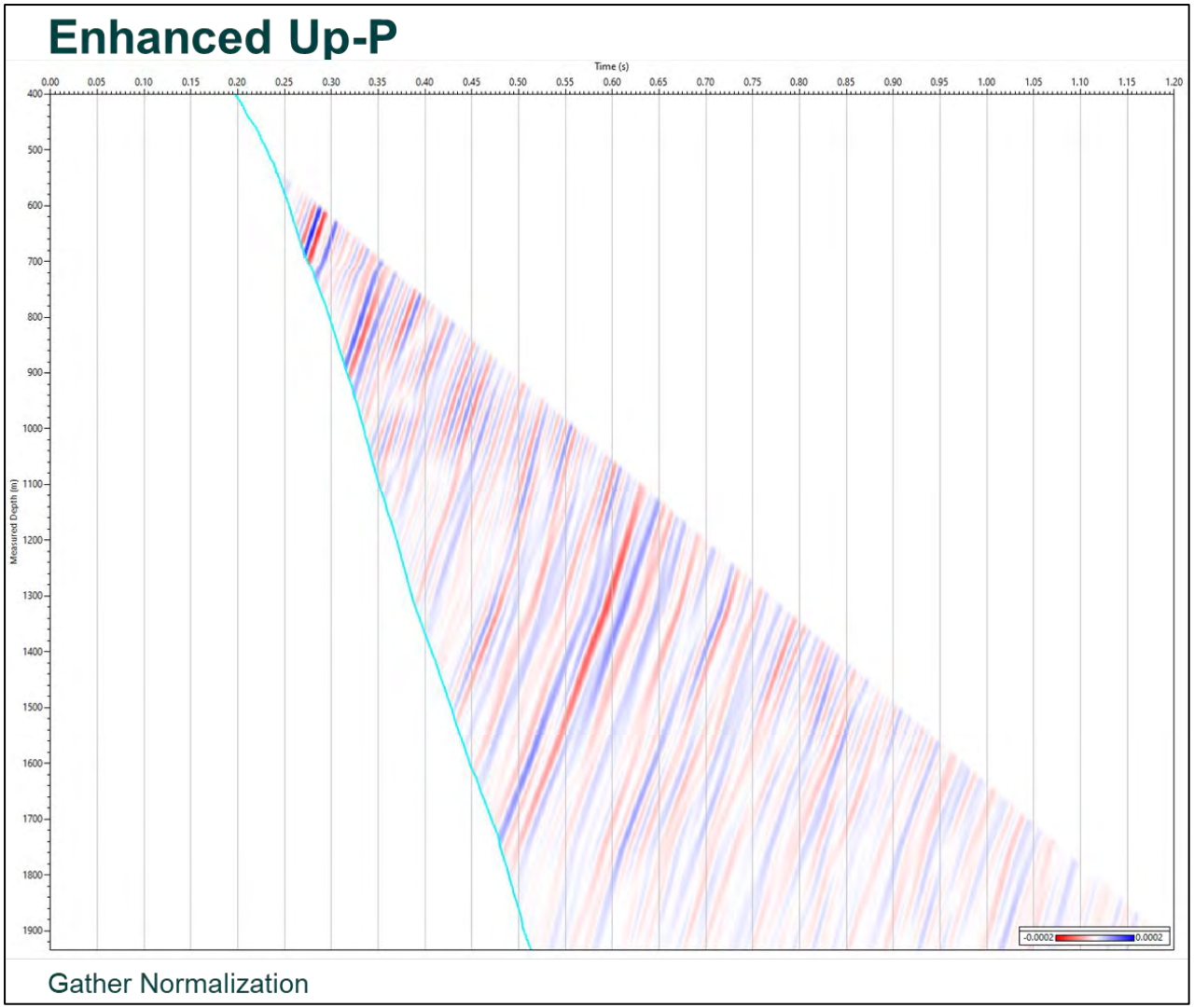


*Figure 7-53. Enhanced Up-P. The enhanced Up P wavefield (Fig. 7.53) is mapping the same reflections as the strain rate enhanced Up P wavefield.*

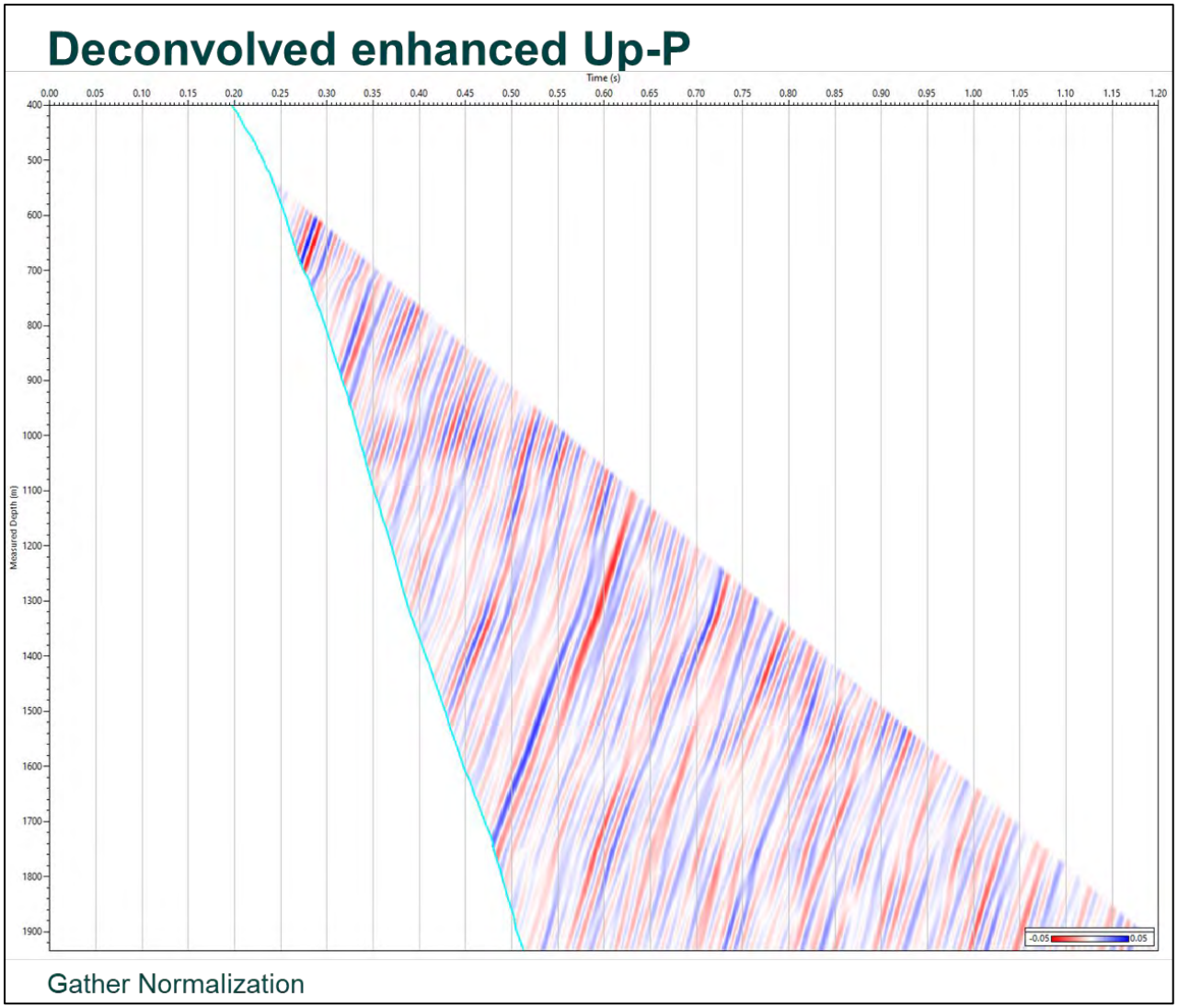


*Figure 7-54. Deconvolved enhanced Up-P - Trace by trace deterministic deconvolution. The geophone equivalent deconvolved Up P is presented in figure 7.54.*

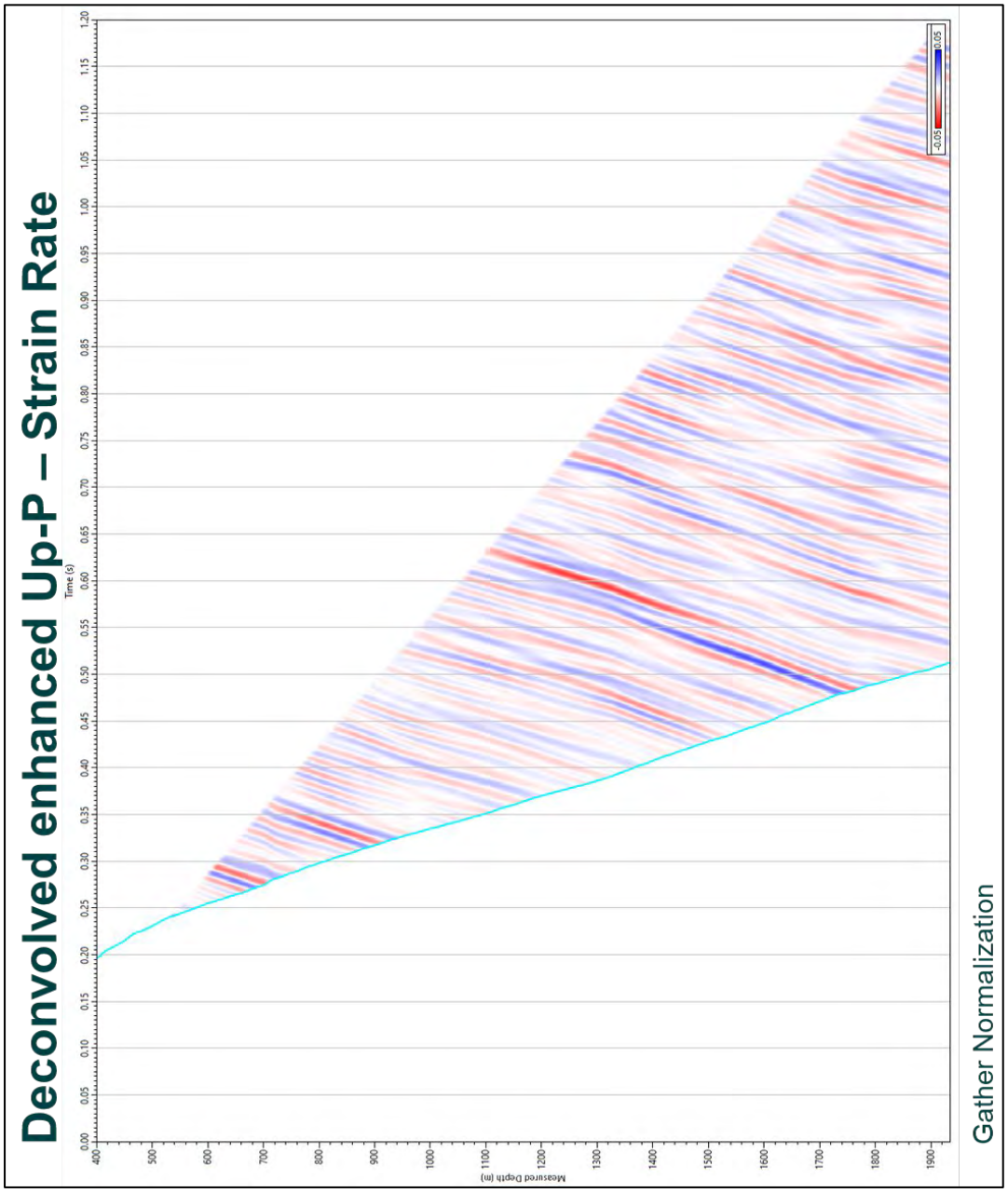


*Figure 7-55. Deconvolved enhanced Up-P. A BPF 5,10-70,90 Hz was applied to the strain rate deconvolved Up P.*

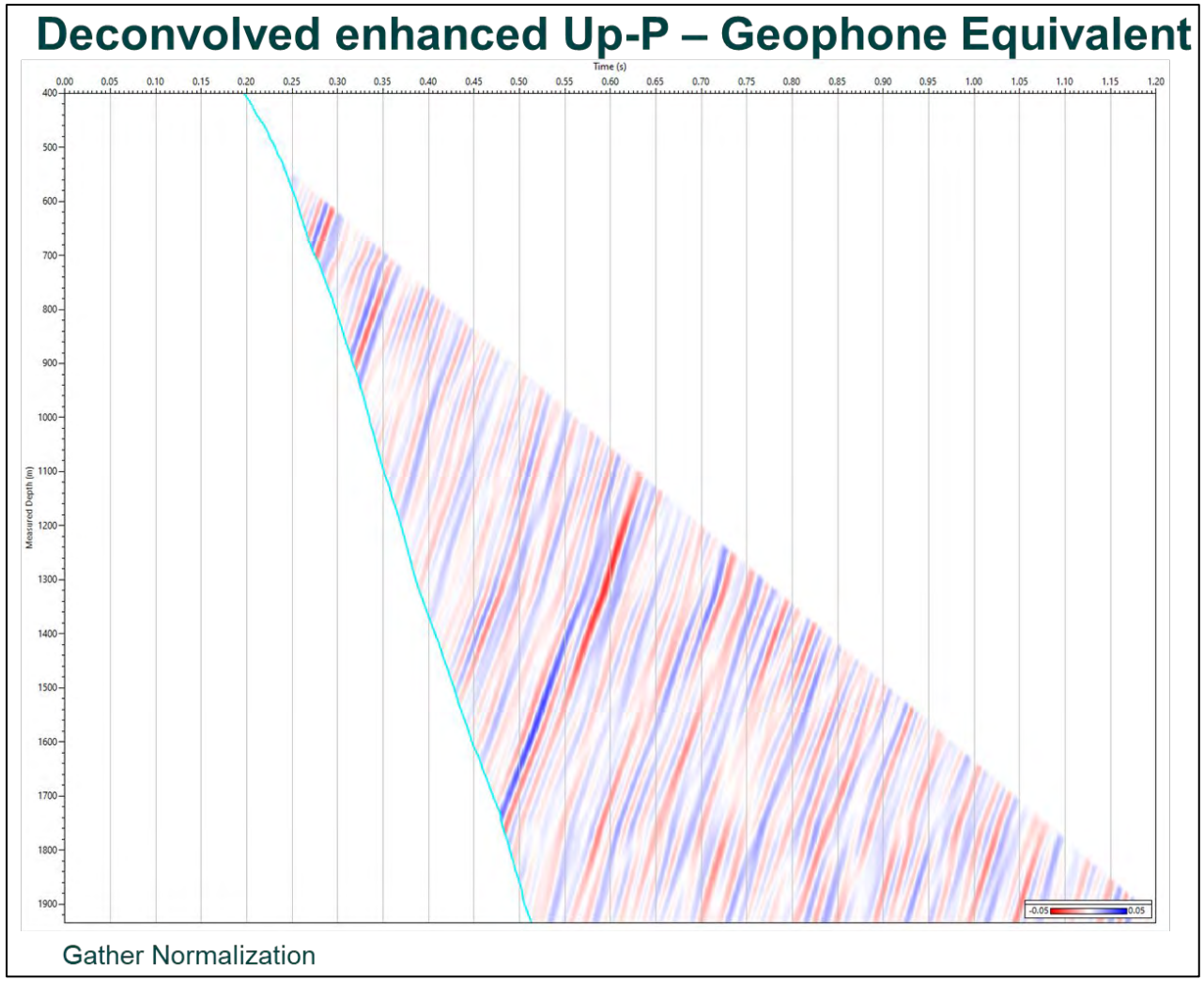


*Figure 7-56. Deconvolved enhanced Up-P – Geophone Equivalent - BPF: 5,10-70,90 Hz. Both wavefields present the same seismic response and amplitude response. As the processed strain rate and geophone equivalent data have a similar seismic response, to avoid the additional noise introduced by the conversion artefacts, the time-lapse analysis was made on the strain rate data.*

# 8 Vibroseis Data Processing

Two separate workflows were designed for the two wells because they are affected by different noise levels (Fig. 8-1). For each well the same workflow with the same parameters was applied to the baseline and monitor survey.

The shallowest layers of the Earth have, in general, poor compaction due to: the absence of the weight above, biosphere activity and weather influence. Very often the shallow layer is referred to as the weathering zone. The shallow layers are highly laterally inhomogeneous (regarding structure, mineral content and inter particle content such as water).

To compensate for lateral velocity changes in the near surface layers, we applied static corrections to the data before imaging. Physical properties of the weathering zone (the layers down to few meters below the surface) are influence by the temperature and the water content. The baseline was acquired during the winter when the soil was covered with snow and the monitor survey during the summer. The weathering zone velocity profile was different between the baseline and the monitor survey, for this reason the static correction values change from the baseline to the monitor survey. The statics workflow is presented in figure 8-2.

## 8.1 Well 8-16

### 8.1.1 Data selection and de-noising

Figures 8-3 and 8-4 present the baseline and the monitor raw stacks respectively, for SP 506203 (far offset to west), SP 506210 (mid offset to the west) and SP 506220 (close to the well trajectory). The baseline survey noise level is higher compared with the monitor survey. The data above 1050 m MD is more affected by the ringing noise. Additionally, the far offset direct arrival is not recorded at shallow depth because the arriving incidence angle on the fibre is close to 90°. As the area of interest is below 1700 m MD, only the data below 850 m MD will be used for picking Down P arrival times and the data below 1050 m MD will be used for processing.

### 8.1.2 Picking

The modelled Down P transit time was used to guide the automatic picking which was performed on the enhanced weighted semblance wavefield in the 0.15 – 0.35 ms/m slowness range over an 11 trace window. The semblance RMS value was calculated for each depth and picks were discarded for traces with an RMS semblance value below 0.5. The picked times were interpolated and smoothed over 5 levels.

Figure 8-5 shows the results of picking the baseline enhanced wavefield for SP 506203 (far west) and SP 506222 (near well). In figure 8-6 are the picked stacks for the same SP. Figures 8-7 and 8-8 show the same data as figures 8-5 and 8-6 for the monitor survey.

### 8.1.3 Down-waves

Figure 8-9 shows the processing input data, a filtered stack data (SP 506222) with a BPF: 5,10-90,110 Hz applied. The amplitudes displayed are cross-normalized.

To reduce the casing ringing a 66-92 Hz tracking filter was applied over the following intervals: 1094-1146 m MD, 1180-1265 m MD, 1265-1326 m MD, 1412-1444 m MD, and 1485-1533m MD (Fig. 8-10). A BPF: 5,10-90,110 Hz was also applied.

To compensate for the absorption and spherical divergence spreading, the amplitude was scaled by the squared sample time. Figure 8-11 shows the stack after amplitude recovery.

Figure 8-12 shows the stack aligned along the first break in the frequency-slowness domain (FP). To remove noise and tube waves only the data inside the -1.7 – 0.6 slowness window were retained. Figure 8-13 presents the data after the separation in the FP domain. The data from figure 7-15 have been muted above the tube wave limit (Fig. 8-11 black).

The Down S wavefield was removed from the data (Fig. 8-14) using a median filter over 121 traces aligned along the modelled Down S TT (Fig. 8-13 green).

Figure 8-15 shows the Down P wavefield after enhancement with a median filter of 121 traces along the FB. This wavefield will be used later in the deconvolution.

### 8.1.4 Reflections

The Up P wavefield was separated in the FP domain in a slowness window of -0.15 to 0.15 ms/trace (Fig. 8-16). The input data was aligned along the A2 Carbonate modelled TT (Fig. 8-11 green) before FP. Figure 8-17 shows the enhanced Up P along the modelled A2 Carbonate TT over a 10 trace window after the separation in the FP domain.

To reduce the multiples and increase the high frequency data content, the enhanced Up P was deconvolved (Fig. 8-18). Trace by trace deterministic deconvolution with enhanced Down P (Fig. 8-15) using a 0.15 s operator length and 20% white noise was applied to the enhanced Up P. Finally, the data have been filtered with a 5,10-90,110 Hz BPF.

Figures 8-19 and 8-20 present the baseline and the monitor Up P wavefield after deconvolution for SP 506203 (far offset to west), SP 506210 (mid offset to the west) and SP 506220 (close to the well trajectory). The reef reflectors are visible on all the offsets. Notice that the baseline data present a slightly higher noise level boosted by the deconvolution.

### 8.1.5 Statics

There are different methods to map the velocity profile of the shallow zone. We used the method that is computing a static time shift for each source point. The static shift was computed as the average difference between the travel time of the calibrated model and the picked travel time. This assumes that ray travel paths are near-vertical in the shallow layers.

In figure 8-21 is presented the drift between the ray-tracing modelled TT (bottom left picture in blue) and the picked TT (bottom left picture in green) for the baseline and monitor survey. In the top pictures are the differences between the model TT and the picked TT all along the available data intervals for each SP. On the horizontal axis is the Shot Point number, on the vertical axis is the Measured Depth (MD from KB) while the difference value is colour coded. The SP numbers are in increasing order: the first six traces are SPs from the line near the injection well (6-16), followed, from trace 8 to 39, by the walkaway line recorded on the paved road (including the interstate road 32 on the far right) and from trace 40 are the SPs along the SN dirt road. The vertically striped appearance suggests that the difference is mainly a static shift between the modelled times and the picked times. As the model was calibrated for minimal difference at the well 8-18 ZVSP location, the static shift is due to the lateral variation in the weathering zone. Between nearby shots there is a gradual increase or decrease in difference, confirming that the shift is due to the weathering zone (the change in the acoustic properties of the shallow layer is not random). Between the baseline and repeat survey, the drift values are different due to seasonal differences and variations in water content at shallow levels. Nevertheless, they follow the same pattern confirming that the shift is mainly due to lateral velocity changes in the weathering zone. Above 1250 m MD the difference increases and is partially due to higher picking uncertainly (due to the ringing) and partially to some unaccounted velocity anisotropy. This is more evident at far offsets.

We calculated a static shift for each SP by averaging the errors in the 1600m-1700m MD interval located above the reservoir (Fig. 8-21 bottom left). Static shift values were calculated separately for the baseline and the monitor survey (Fig. 8-24).

Figures 8-22 and 8-23 show the residual drift after the statics were applied to the data. Figure 8-23 presents the data below 1500 m MD with a -5/+5 ms scale. The residual drift after the statics is close to zero.

The Up P common receiver gathers at 1700 m MD before and after statics correction are presented in figure 8-25 and 8-26, respectively. After the correction data fit better an expected hyperbolic shape.

## 8.2 Well 6-16

### 8.2.1 Data selection and de-noising

Figures 8-27 and 8-28 present the baseline and the monitor raw stacks for SP 506216 (near well TD), SP 506224 (mid offset to east) and SP 506230 (far offset to east). The baseline survey noise level is higher compared to the monitor survey; this is more visible at far offsets where the SNR is lower. All the SPs are affected by strong ringing above 1520 m MD (where the well deviation is below 3°) with stronger impact on the close offsets. The time-lapse analysis is looking for small changes in the seismic response, for this reason the area affected by the ringing above 1540 m MD was excluded from the processing.

### 8.2.2 Picking

The automatic picking was performed on the enhanced weighted semblance wavefield in a 0.15 – 0.35 ms/m slowness range over an 11 trace window and was guided by the modelled Down P transit time. The semblance RMS value was calculated for each depth and picks for traces with an RMS semblance value below 0.5 were discarded. The picks were interpolated and smoothed over 5 levels.

Figure 8-29 shows the baseline enhanced wavefield time picks for SP 506216 (near well TD) and SP 506232 (far east). Figure 8-30 presents the stacks after picking for the same SP. Figures 8-31 and 8-32 show the same data as figures 8-29 and 8-30 for the monitor survey. Far offset pick times have a high uncertainty, especially for the baseline survey.

### 8.2.3 Down-waves

Figure 8-33 shows the data used as input for the down-wave processing for SP 506216 stack data with a BPF: 5,10-90,110 Hz applied. The amplitudes displayed are cross-normalized.

To compensate for the absorption and spherical divergence spreading, the amplitude was scaled by the squared sample time. Figure 8-34 shows the stack after amplitude recovery.

Figure 8-35 shows the stack aligned along the first break in the frequency-slowness domain (FP). We selected the data inside the -0.3 – 0.6 slowness window and performed the Down wavefield separation in the FP domain (figure 8-36). The Down S wavefield was removed from the data (Fig. 8-37) with a median filter over 121 traces aligned along the modelled Down S TT (Fig. 8-36 green).

Figure 8-38 shows the Down P wavefield after enhancement with a median filter of 121 traces along the FB. This wavefield will be used later for the deconvolution.

### 8.2.4 Reflections

The Up P wavefield was separated in the FP domain in a slowness window of -0.15 to 0.15 ms/traces (Fig. 8-39). The input data have been aligned along the A2 Carbonate modelled TT (Fig. 8-34 green) before FP. Figure 8-40 shows the enhanced Up P along the modelled A2 Carbonate TT over a 10 trace window after the separation in FP domain.

To reduce the multiples and increase the data high frequency bandwidth, the enhanced Up P was deconvolved (Fig. 8-41). Trace by trace deterministic deconvolution with enhanced Down P (Fig. 8-38) using a 0.15 s operator length and 20% white noise was applied to the enhanced Up P. Finally, the data have been filtered with a 5,10-90,110 Hz BPF.

Figures 8-42 and 8-43 present the baseline and the monitor Up P wavefield after deconvolution for SP 506216 (close to well TD), SP 506224 (mid offset to the east) and SP 506230 (far offset to east). The reef reflectors are visible at all offsets. The far offsets have a higher noise level boosted by the deconvolution, especially for the baseline survey.

### 8.2.5 Statics

We computed the statics for each SP using only the well 8-16 data because well 8-16 has a longer data interval above the area of interest. We applied these statics to well 6-16 SPs. As ray travel paths in well 6-16 are different from those in well 8-16 a residual static shift was calculated for well 6-16 (separately for the baseline and the monitor survey).

In figure 8-44 is presented the drift between the ray tracing-modelled TT (in the bottom left picture in blue) and the picked TT (in the bottom left picture in green) for the baseline and monitor survey. In the top pictures for each SP are the differences between the model TT and the picked TT all along the available data interval. On the horizontal axis is the Shot Point number, on the vertical axis is the Measured Depth (MD from KB) and the difference is colour coded. The SP numbers are in increasing order, the first six traces are SPs from the line near the injection well (6-16), followed, from trace 8 to 39, by the walkaway line recorded on the paved road (including the interstate road 32 on the far right) and from trace 40 are the SPs along the SN dirt road. The difference plot shows vertical stripes suggesting there is mainly a static shift between the model and the picks. Between nearby shots there is a gradual increase or decrease in drift, confirming that the shift is due to the weathering zone (the change in the acoustic properties of the shallow layer is not random). Between the baseline and the monitor survey, the errors have different values due to different season and water content in the shallow layer but follow the same pattern confirming that the shift is mainly due to lateral velocity changes in the weathering zone.

Figures 8-45 and 8-46 show the drift after the statics were applied to the data. Figure 8-46 presents the drift with a -5/+5 ms scale.

Using the statics computed based on the well 8-16 data the remaining error is still significant. Residual statics were computed by averaging the error over the 1650 m – 1700 m MD interval (Fig. 8-46 bottom left). Residual static shift values were calculated separately for the baseline and the monitor survey (Fig. 8-48).

In figure 8-47 is the residual drift after the residual statics were applied. For the offsets close to the well the residual drift is close to zero, but for the far offsets there is still some residual drift due to the high FB picking uncertainly (Fig. 8-47 mid bottom).

The Up P common receiver gather at 1700 m MD before and after statics correction is presented in figures 8-49 and 8-50 respectively. Figure 8-51 shows the Up P common receiver gather at 1700 m MD after residual statics correction. After the correction the data fit better an expected hyperbolic shape.

| Title | Description | Figure |
|---|---|---|
| Deconvolved enhanced Up-P | Trace by trace deterministic deconvolution | **8.41** |
| Well 6-16 – Baseline – Deconvolved Up-P | Far, mid and near offsets | **8.42** |
| Well 6-16 – Monitor – Deconvolved Up-P | Far, mid and near offsets | **8.43** |
| Drift between modelled and picked TT before statics | | **8.44** |
| Drift between modelled and picked TT after statics | Data and picks shifted with 8-16 statics | **8.45** |
| Drift between modelled and picked TT after statics | Data and picks shifted with 8-16 statics | **8.46** |
| Drift between modelled and picked TT after residual statics | Data and picks shifted | **8.47** |
| Residual statics | Plane view with residual statics for each SP | **8.48** |
| Up-P before statics | Common receiver gather | **8.49** |
| Up-P after statics | Common receiver gather | **8.50** |
| Up-P after residual statics | Common receiver gather | **8.51** |

*Table 8-16 Vibroseis Data Processing figures*

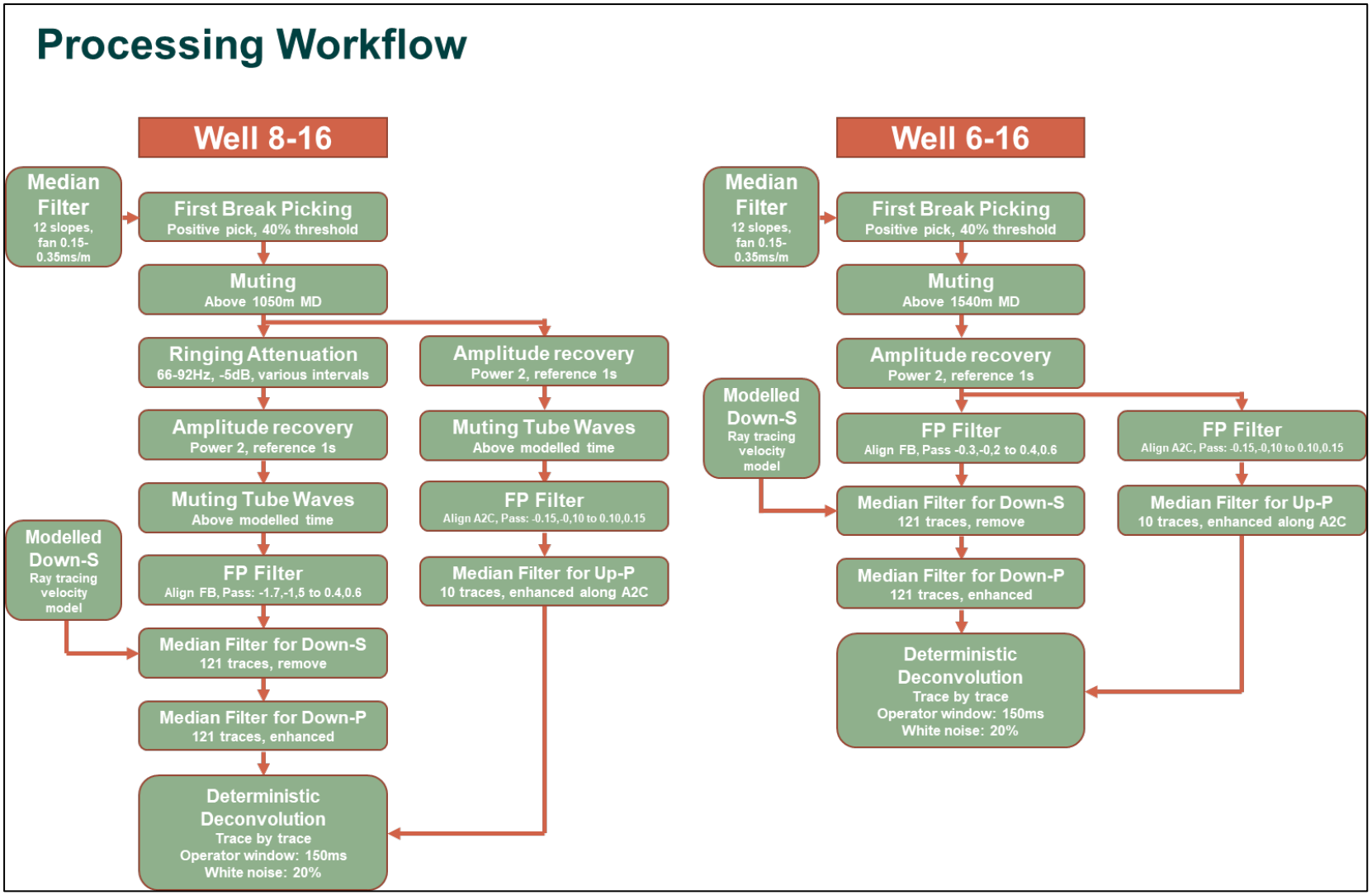


*Figure 8-1. Processing Workflow. Two separate workflows were designed for the two wells because they are affected by different noise levels. For each well the same workflow with the same parameters was applied to the baseline and monitor survey.*

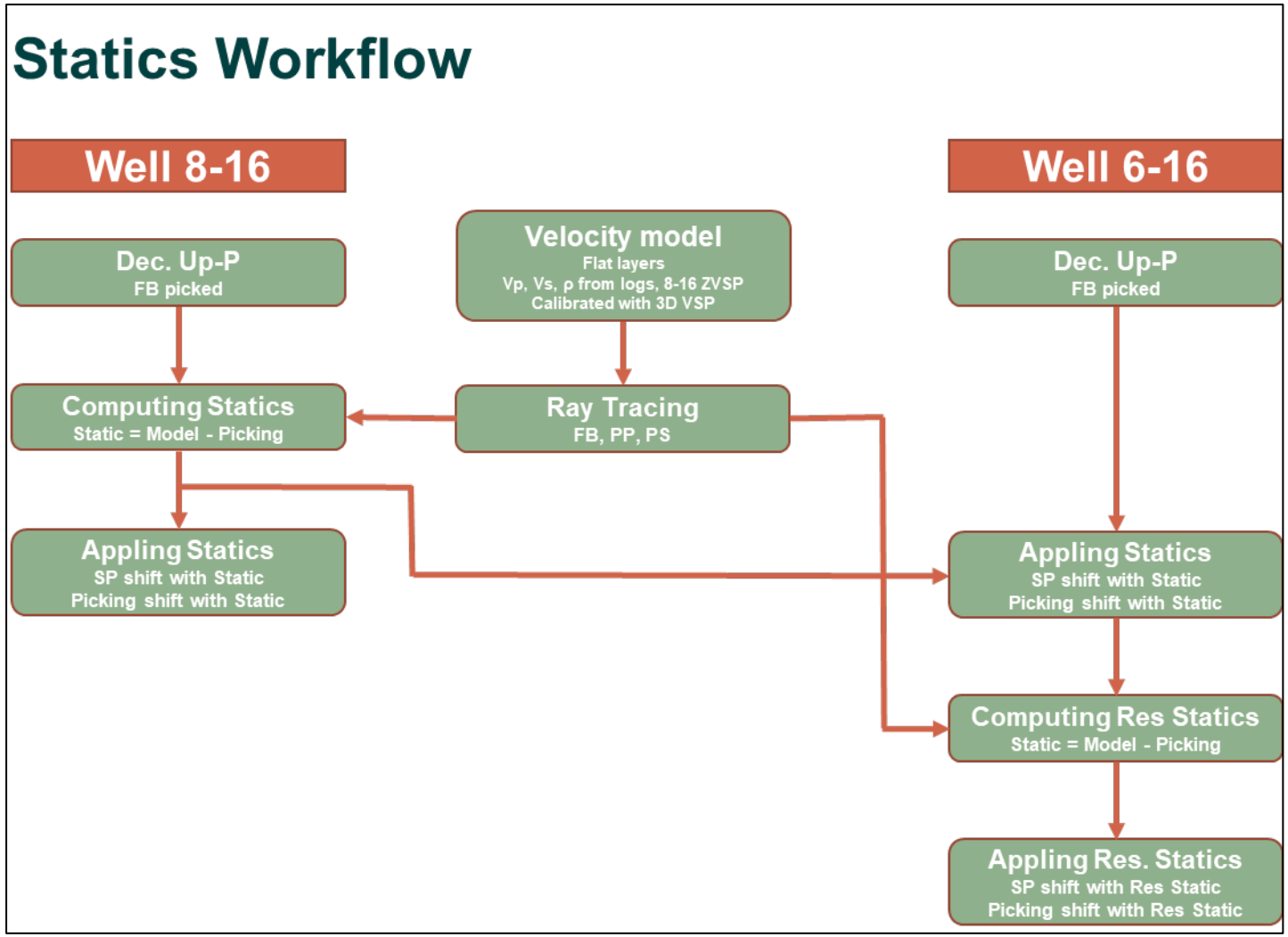


*Figure 8-2. Statics Workflow. To compensate for lateral velocity changes in the near surface layers, we applied static corrections to the data before imaging. Physical properties of the weathering zone (the layers down to few meters below the surface) are influenced by the temperature and the water content. The baseline was acquired during the winter when the soil was covered with snow and the monitor survey during the summer. The weathering zone velocity profile was different between the baseline and the monitor survey, for this reason the static correction values change from the baseline to the monitor survey.*

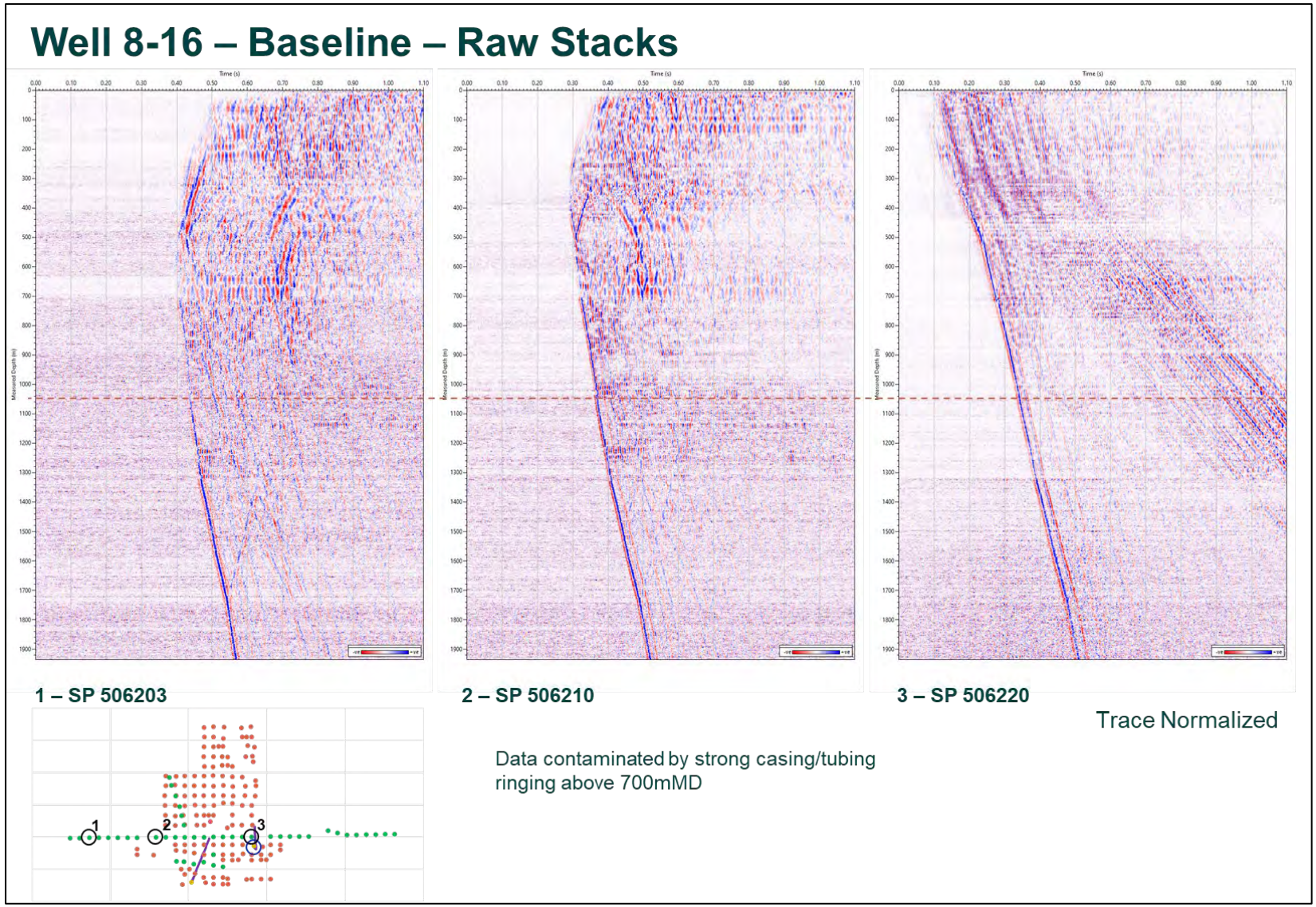


*Figure 8-3. Well 8-16 – Baseline – Raw Stacks - Far, mid and near offset total wavefield.*

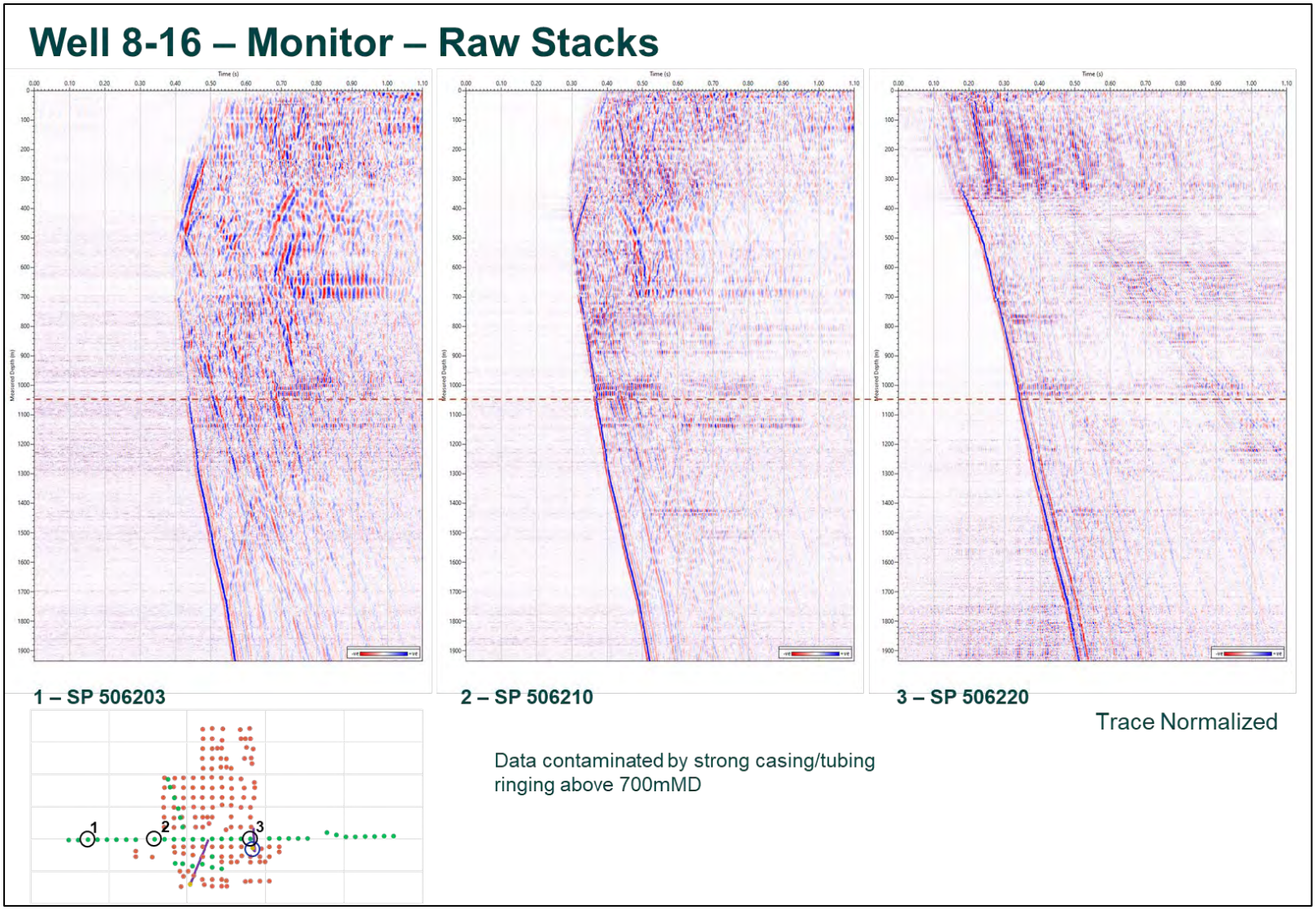


*Figure 8-4. Well 8-16 – Monitor – Raw Stacks - Far, mid and near offset total wavefield.*

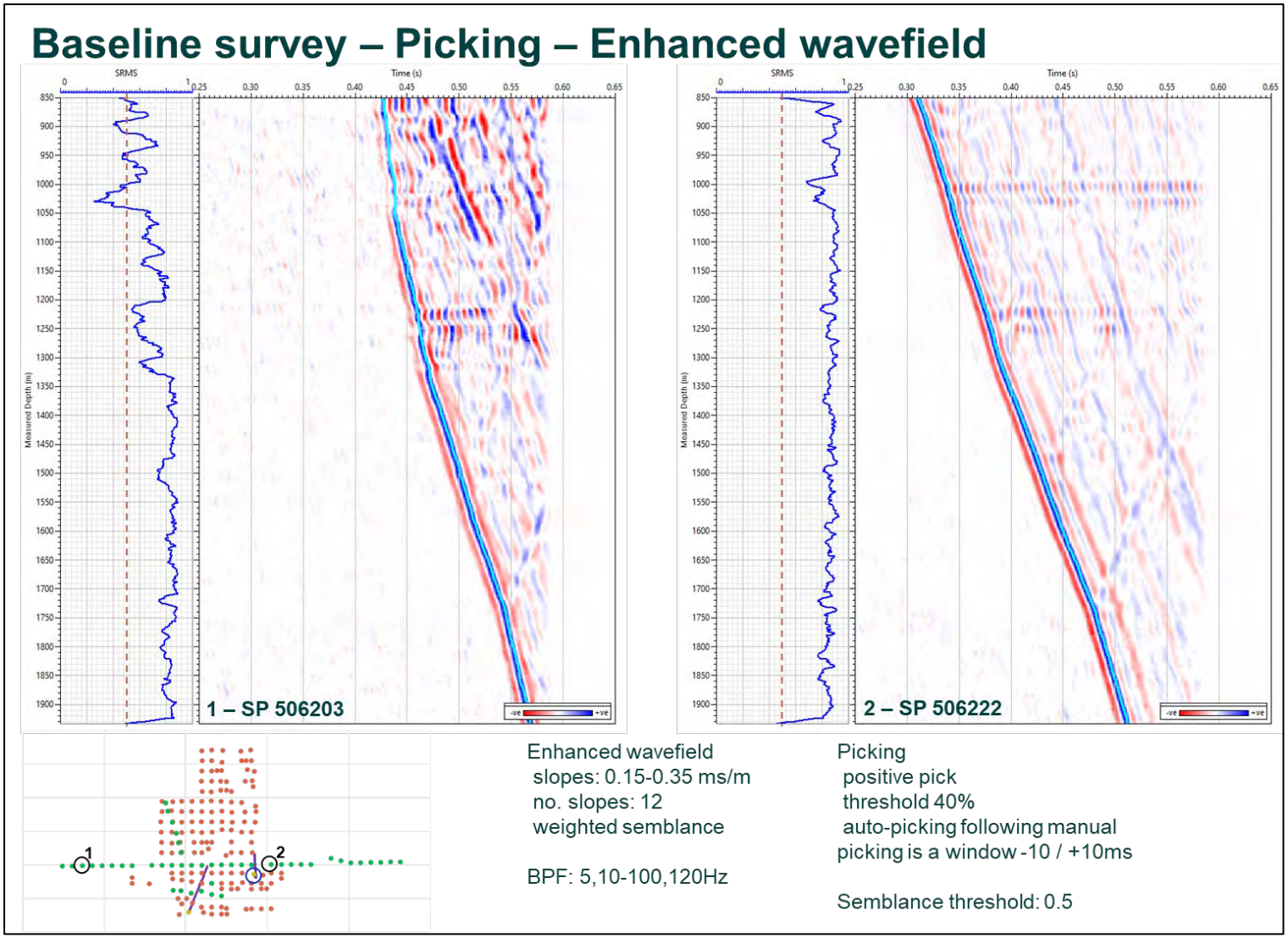


*Figure 8-5. Baseline survey – Picking – Enhanced wavefield – To help the picking, the slopes along Down P wavefield were enhanced. This figure shows the results of picking the baseline enhanced wavefield for SP 506203 (far west) and SP 506222 (near well).*

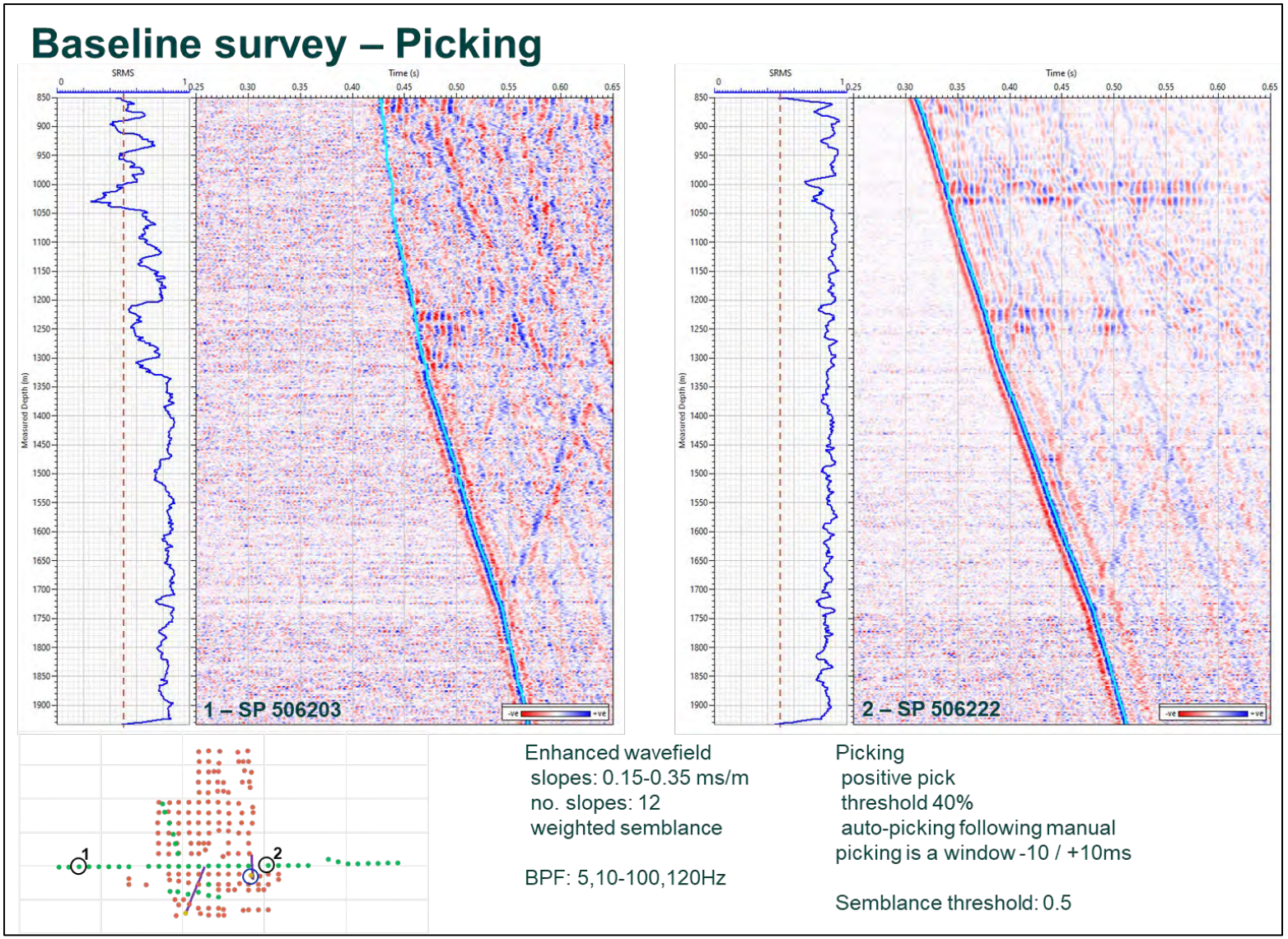


*Figure 8-6. Baseline survey – Picking. Here are presented the picked stacks for the same SP.*

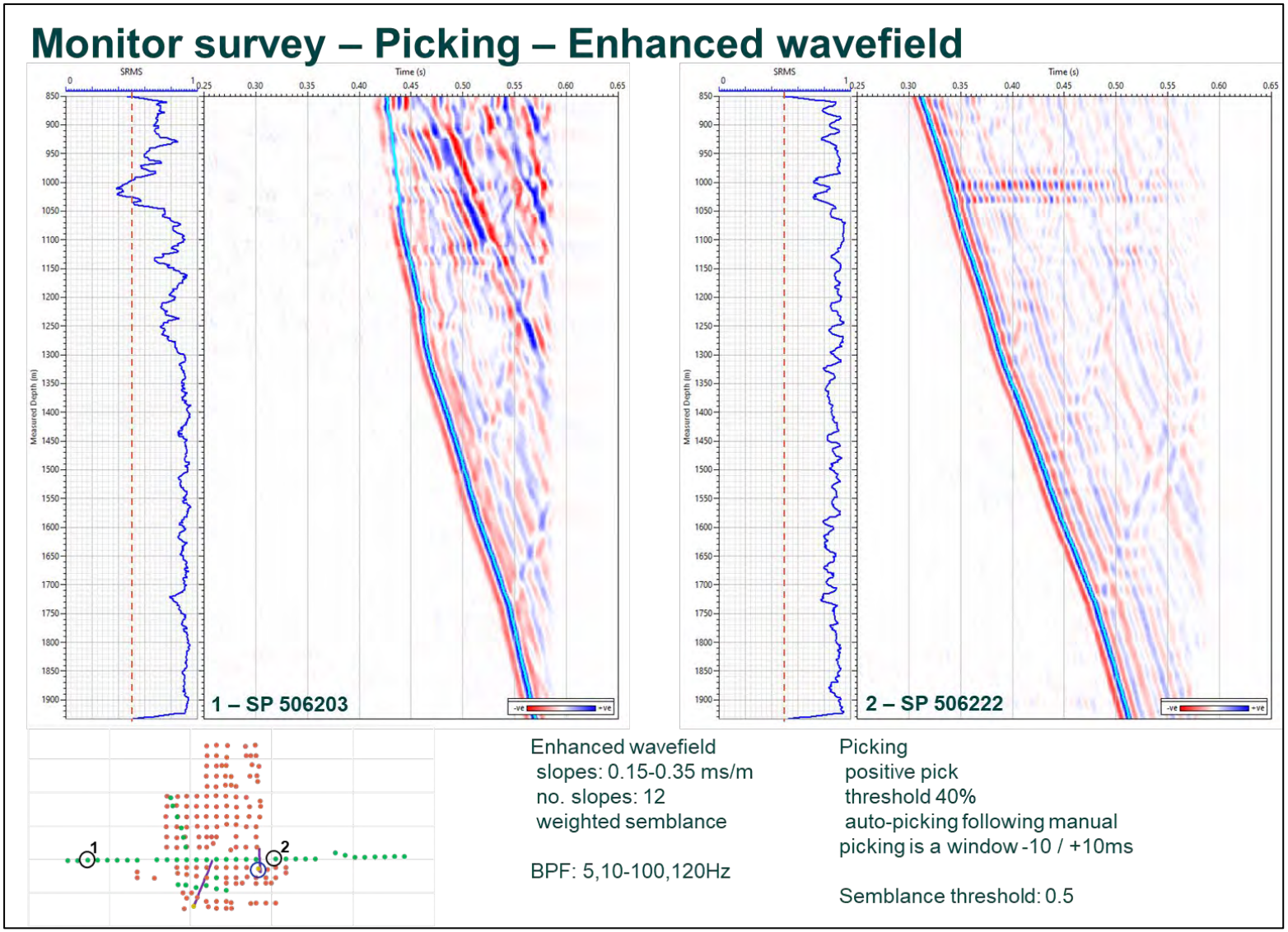


*Figure 8-7. Monitor survey – Picking – Enhanced wavefield - Slopes enhancement.*

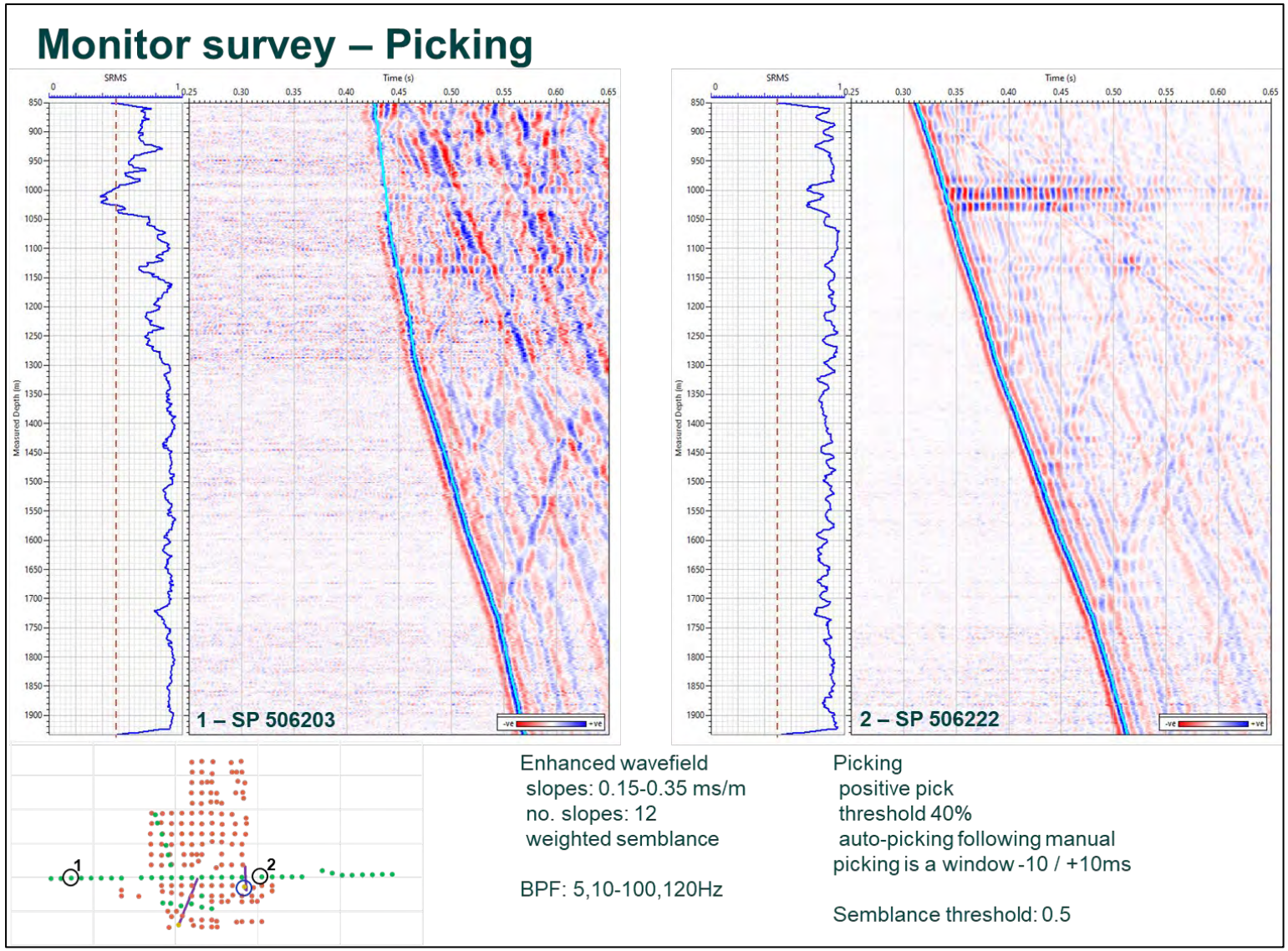


*Figure 8-8. Monitor survey – Picking.*

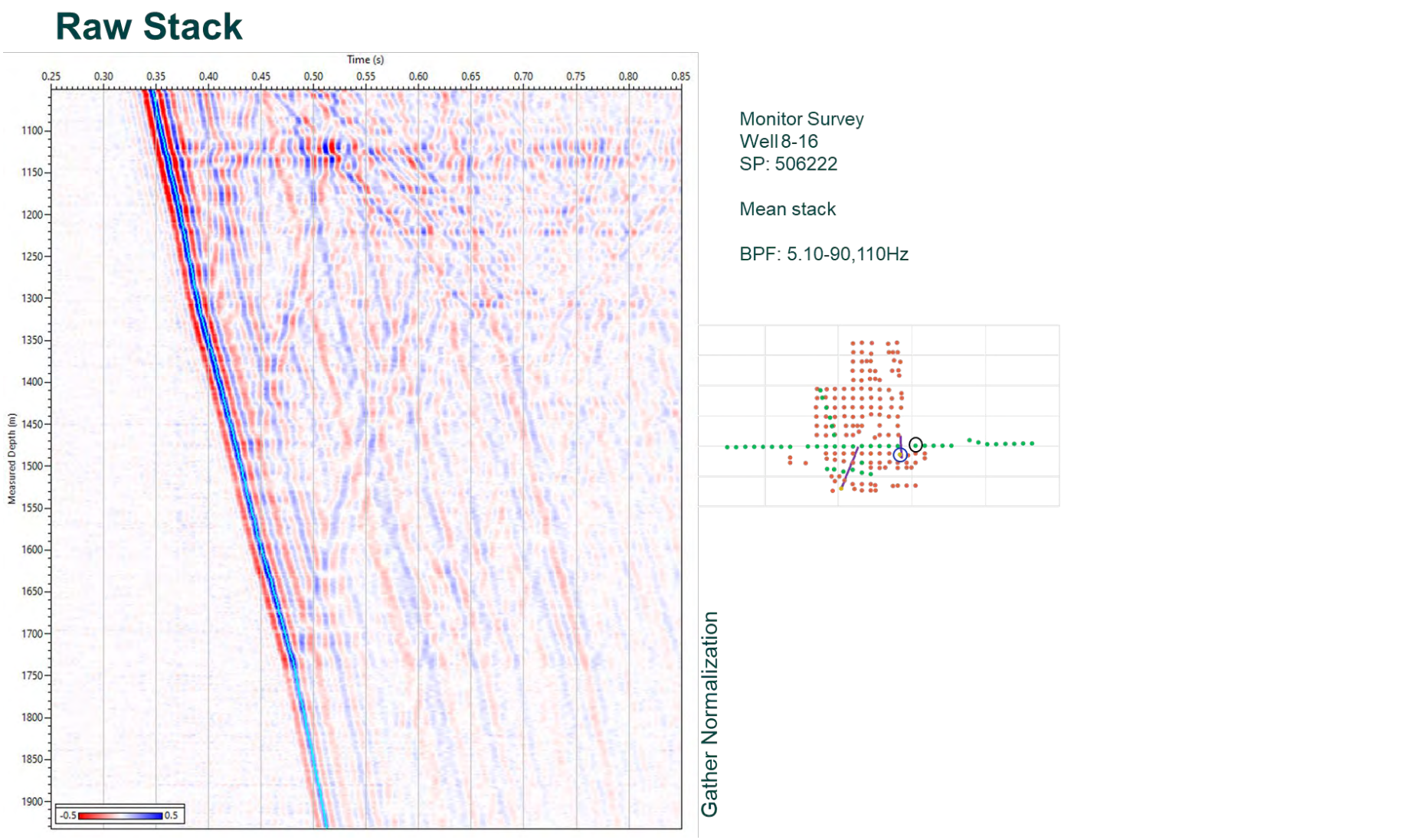


*Figure 8-9. Raw Stack. This figure shows the processing input data, a filtered stack data (SP 506222) with a BPF: 5,10-90,110 Hz applied. The amplitudes displayed are cross-normalized.*

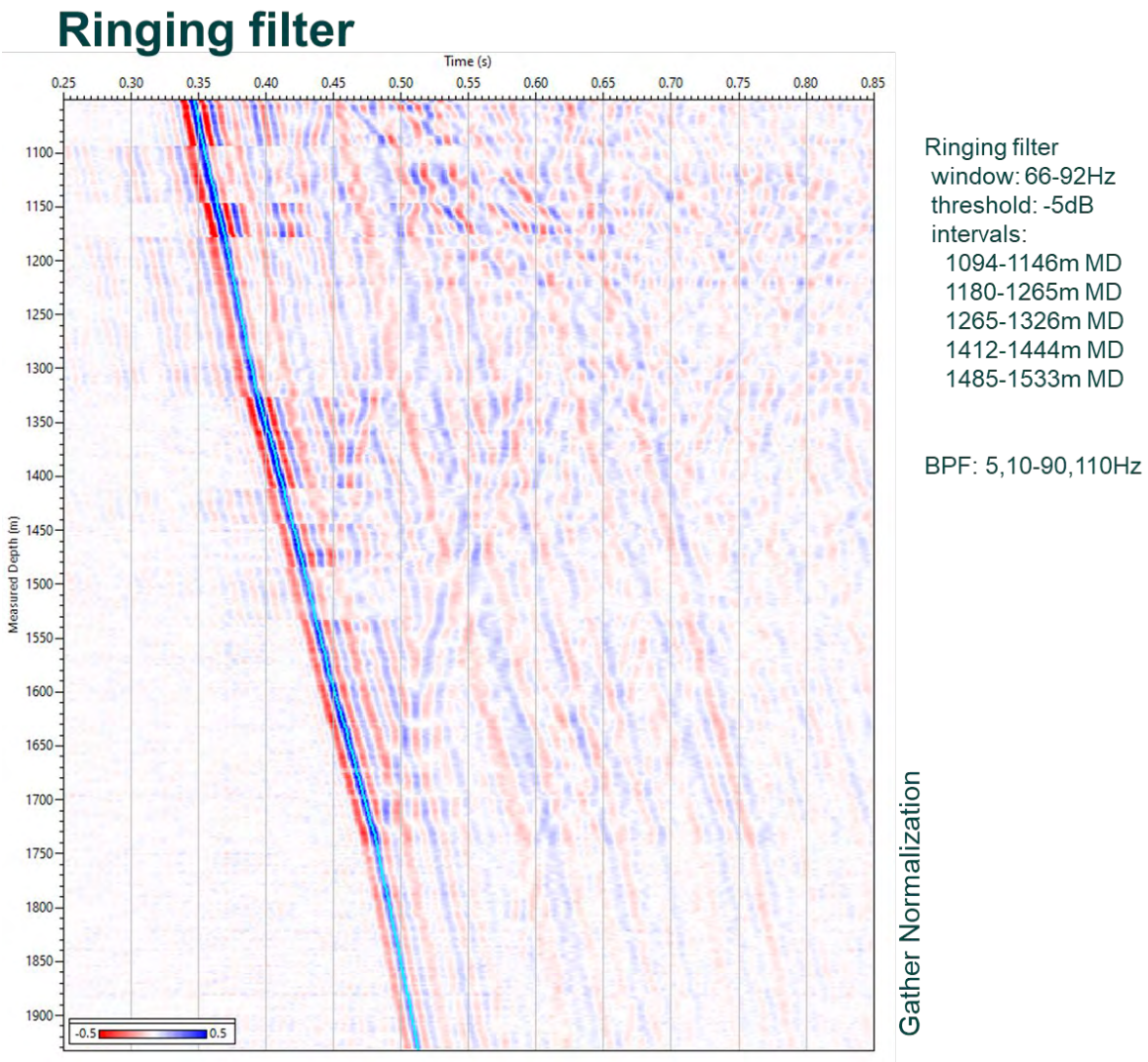


*Figure 8-10. Ringing filter - Attenuate the ringing in affected intervals. To reduce the casing ringing a 66-92 Hz tracking filter was applied over the following intervals: 1094-1146 m MD, 1180-1265 m MD, 1265-1326 m MD, 1412-1444 m MD, and 1485-1533m MD. A BPF: 5,10-90,110 Hz was also applied. The ringing filter introduces energy before the first arrival but improves the upgoing wavefield.*

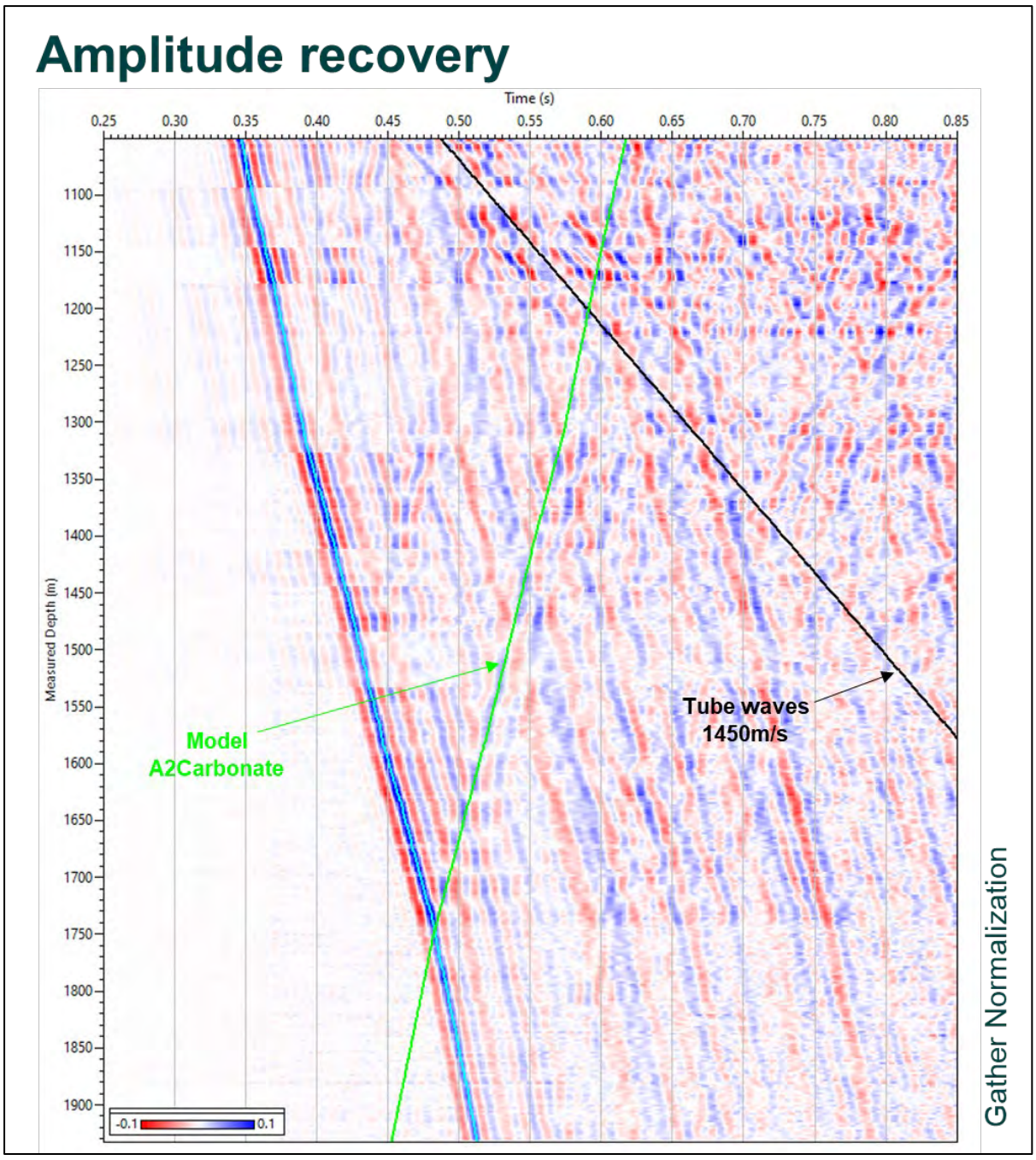


*Figure 8-11. Amplitude recovery - Time power function. To compensate for the absorption and spherical divergence spreading, the amplitude was scaled by the squared sample time. Figure 8.11 shows the stack after amplitude recovery.*

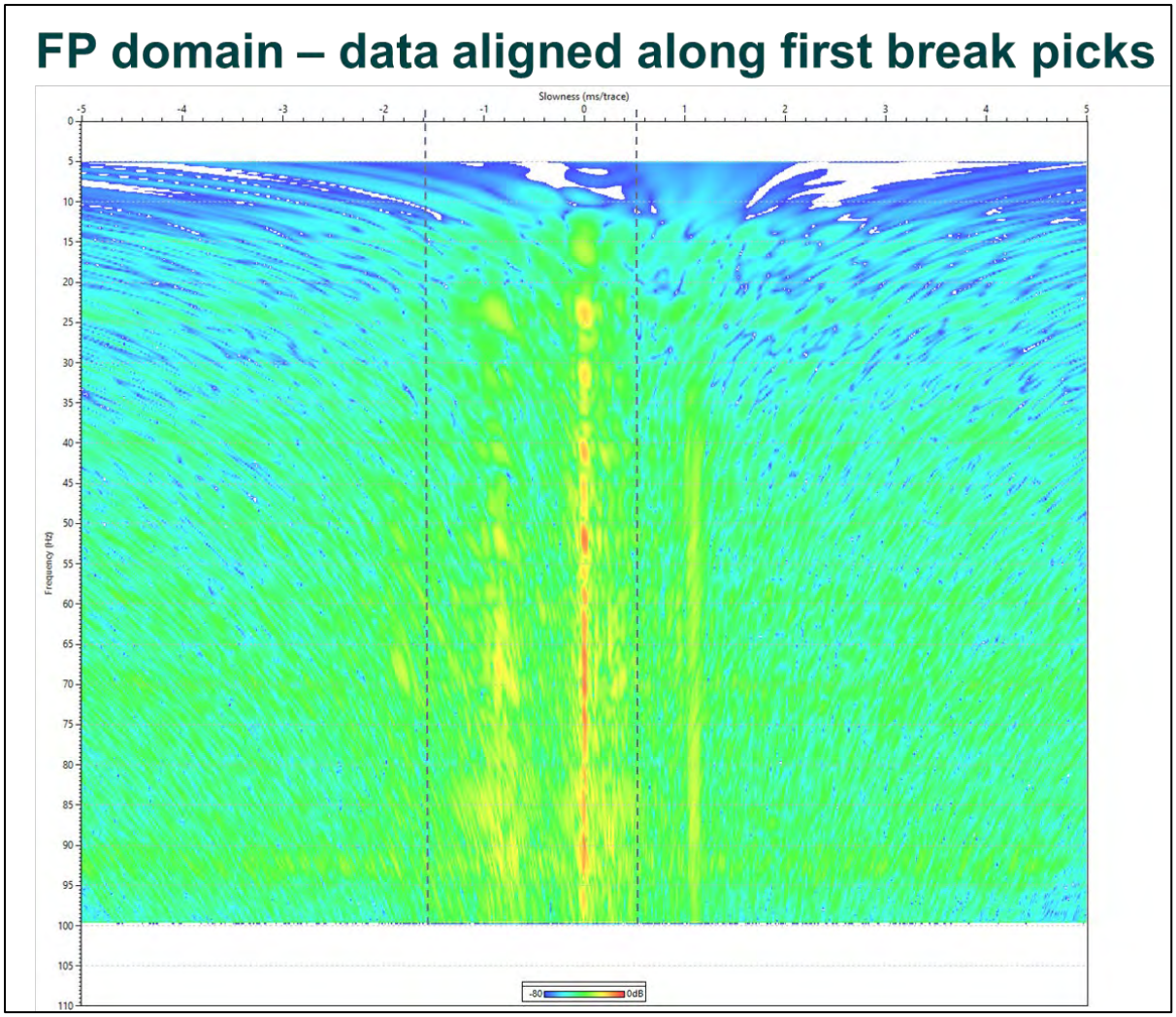


*Figure 8-12. FP domain – data aligned along first break picks - Remove tube waves and noise. This figure shows the stack aligned along the first break in the frequency-slowness domain (FP). To remove noise and tube waves only the data inside the -1.7 – 0.6 slowness window were retained.*

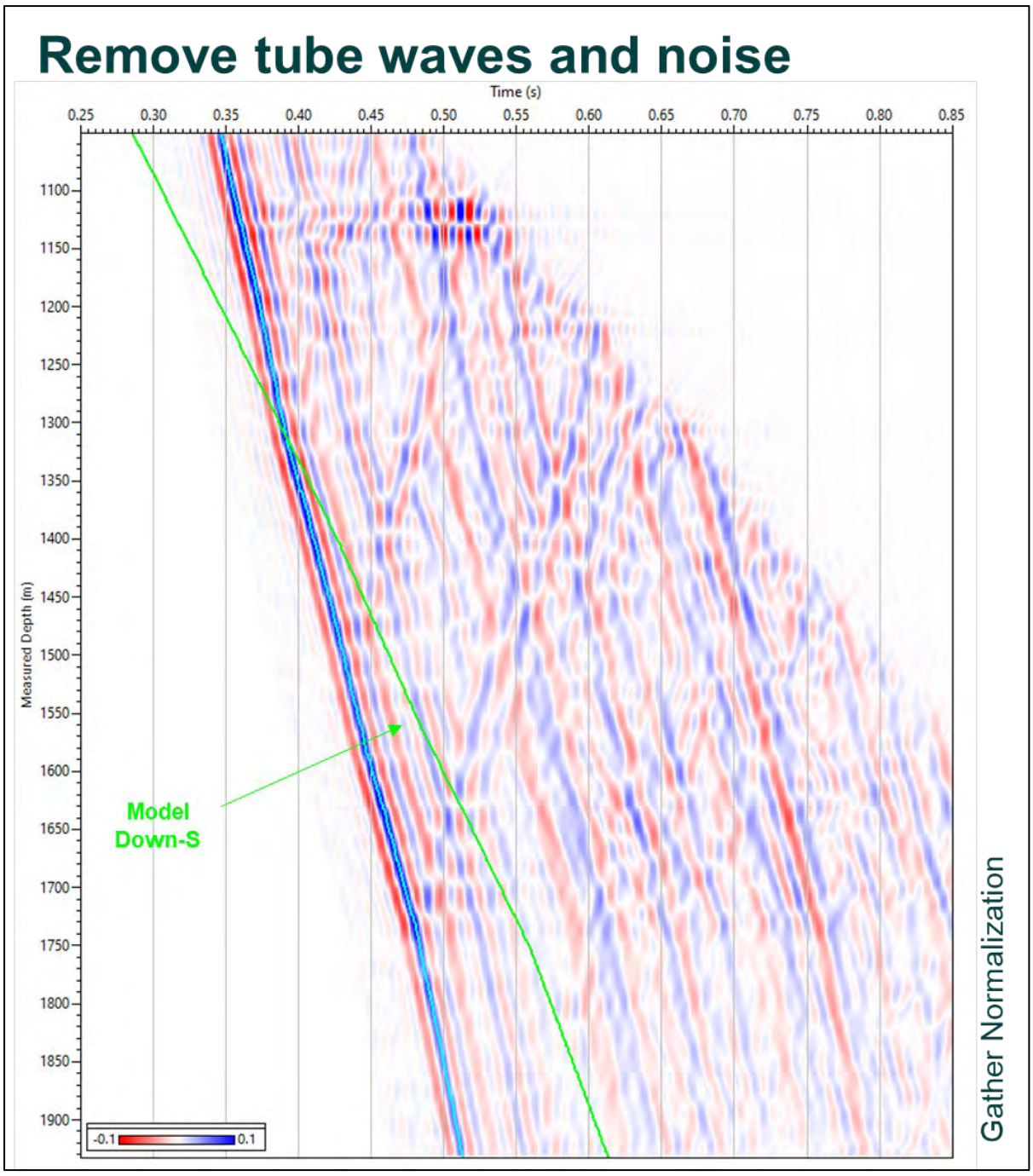


*Figure 8-13. Remove tube waves and noise - After FP separation.*

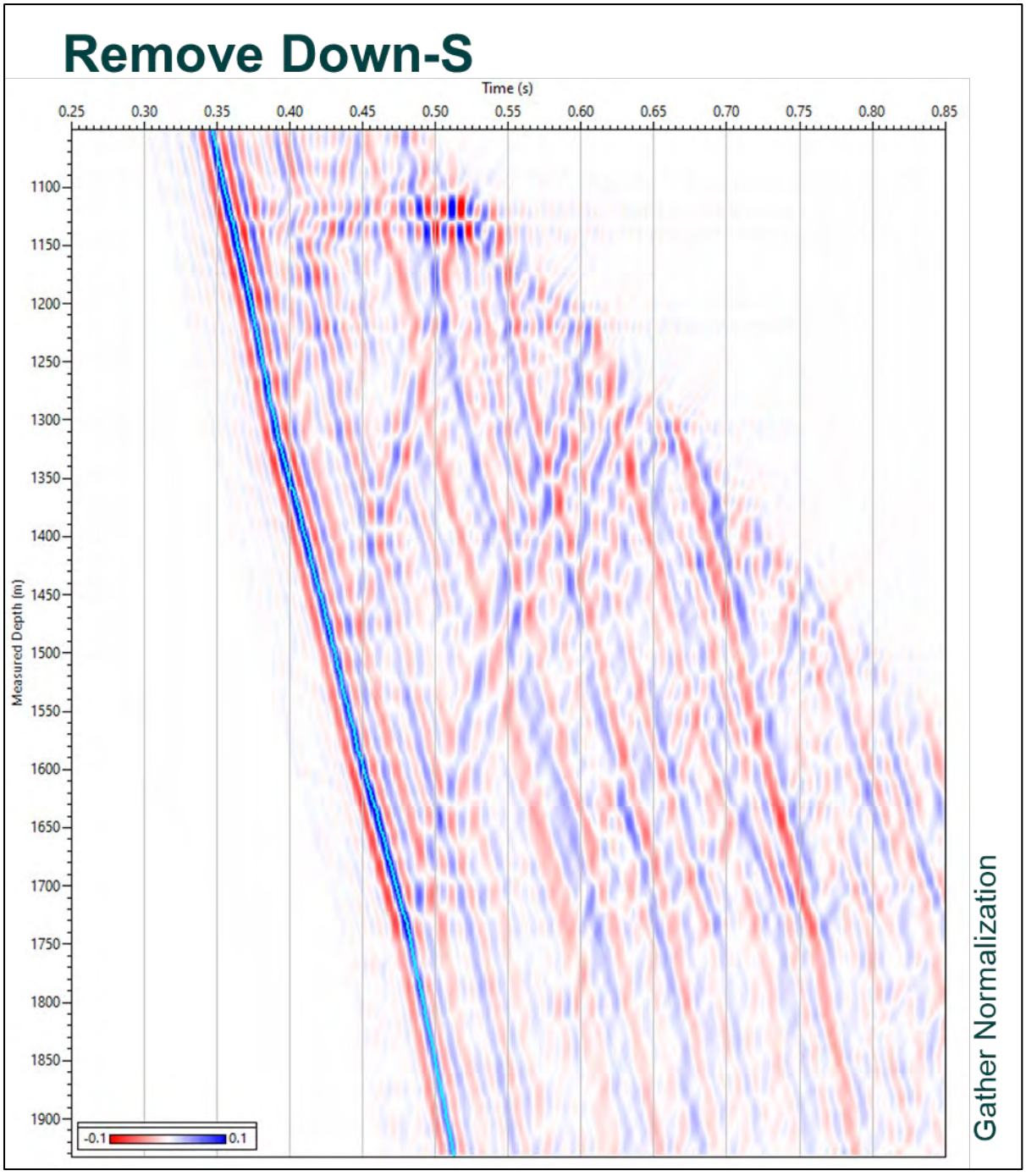


*Figure 8-14. Remove Down-S - Median filter. The Down S wavefield was removed from the data (Fig. 8.14) using a median filter over 121 traces aligned along the modelled Down S TT (Fig. 8.13 green).*

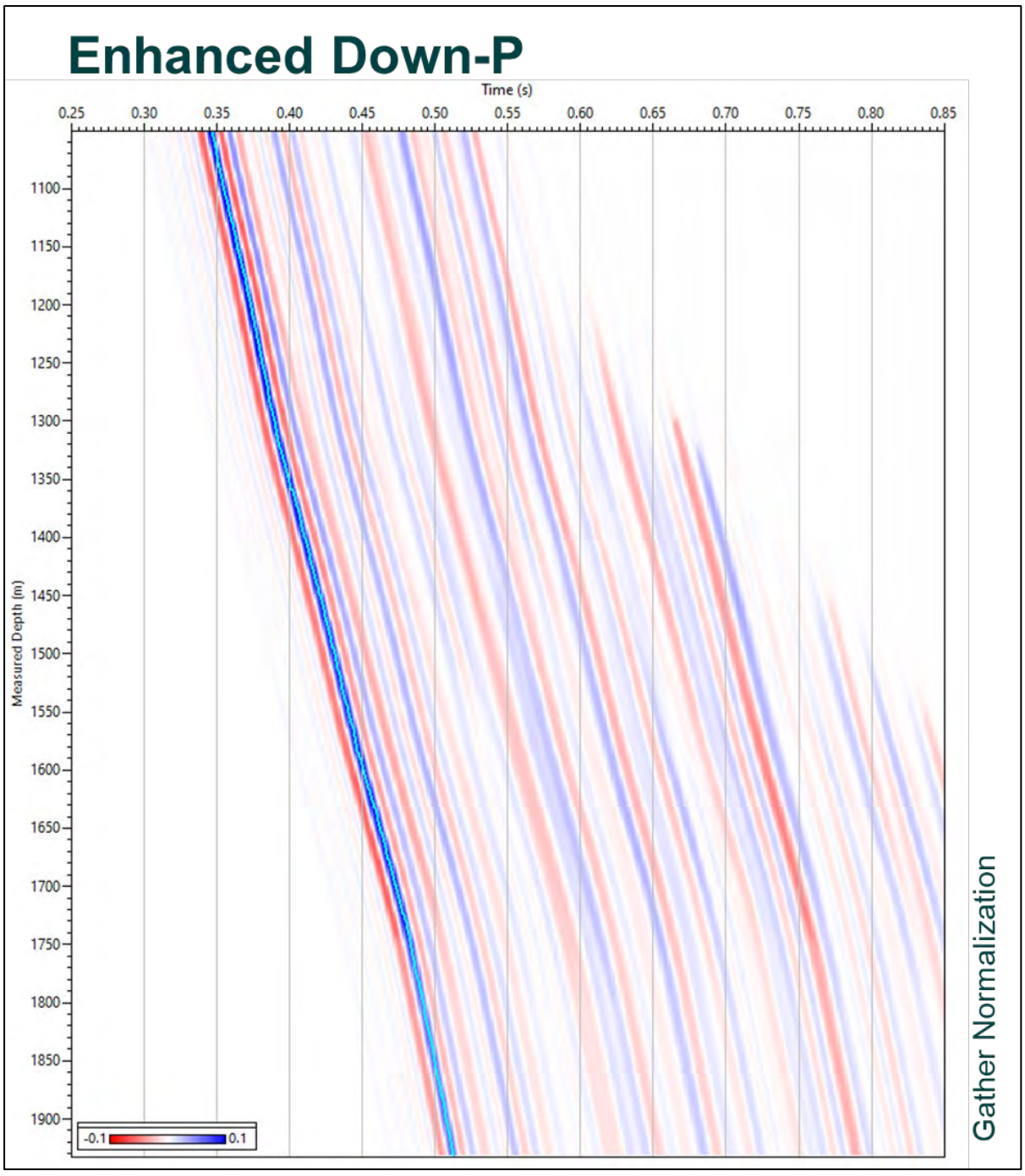


*Figure 8-15. Enhanced Down-P - Median filter. This figure shows the Down P wavefield after enhancement with a median filter of 121 traces along the FB. This wavefield will be used later in the deconvolution.*

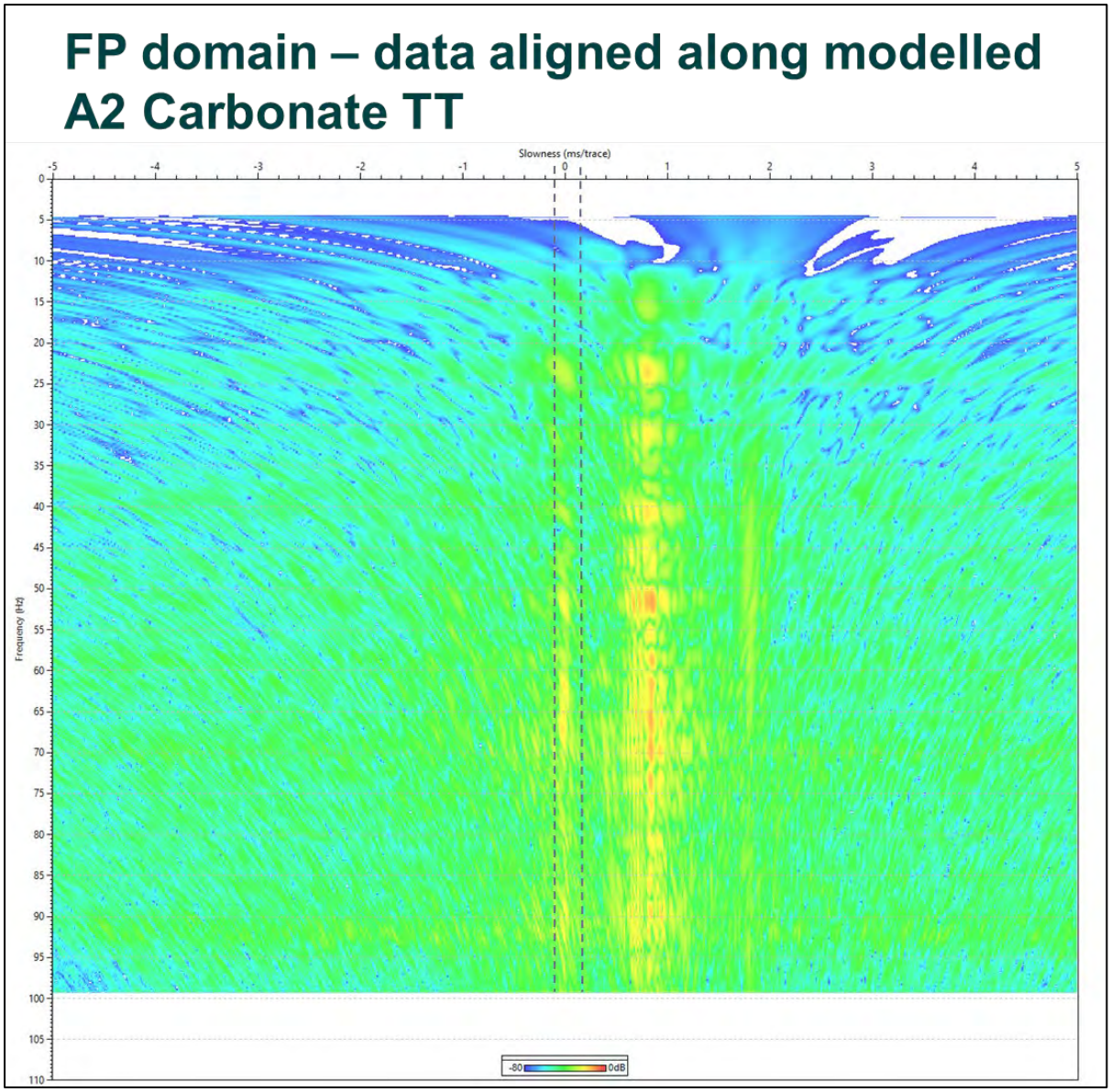


*Figure 8-16. FP domain – data aligned along modelled A2 Carbonate TT - Enhance Up P. The Up P wavefield was separated in the FP domain in a slowness window of -0.15 to 0.15 ms/trace.*

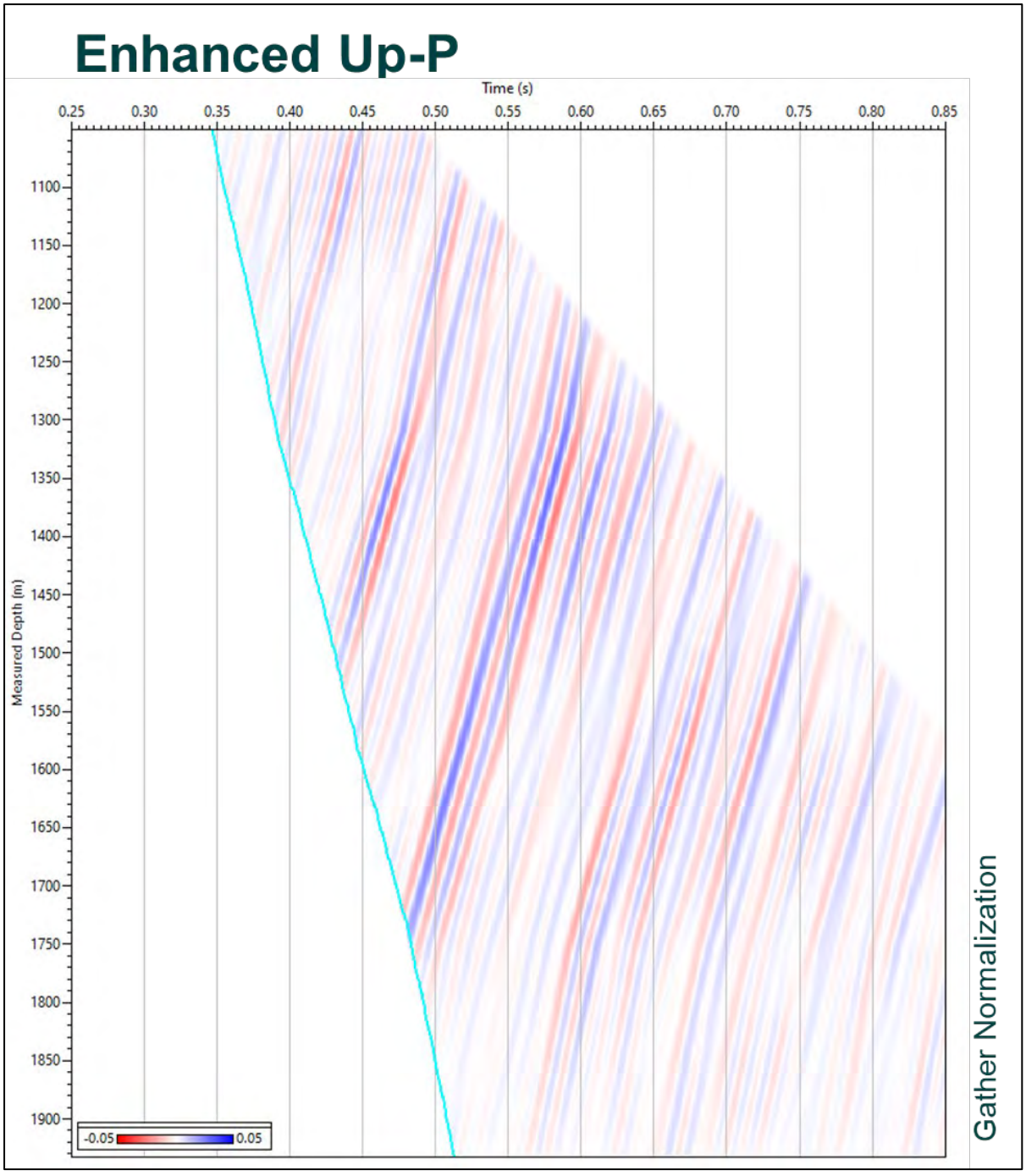


*Figure 8-17. Enhanced Up-P - After FP separation. The input data was aligned along the A2 Carbonate modelled TT (Fig. 8.11 green) before FP. Figure 8.17 shows the enhanced Up P along the modelled A2 Carbonate TT over a 10 trace window after the separation in the FP domain.*

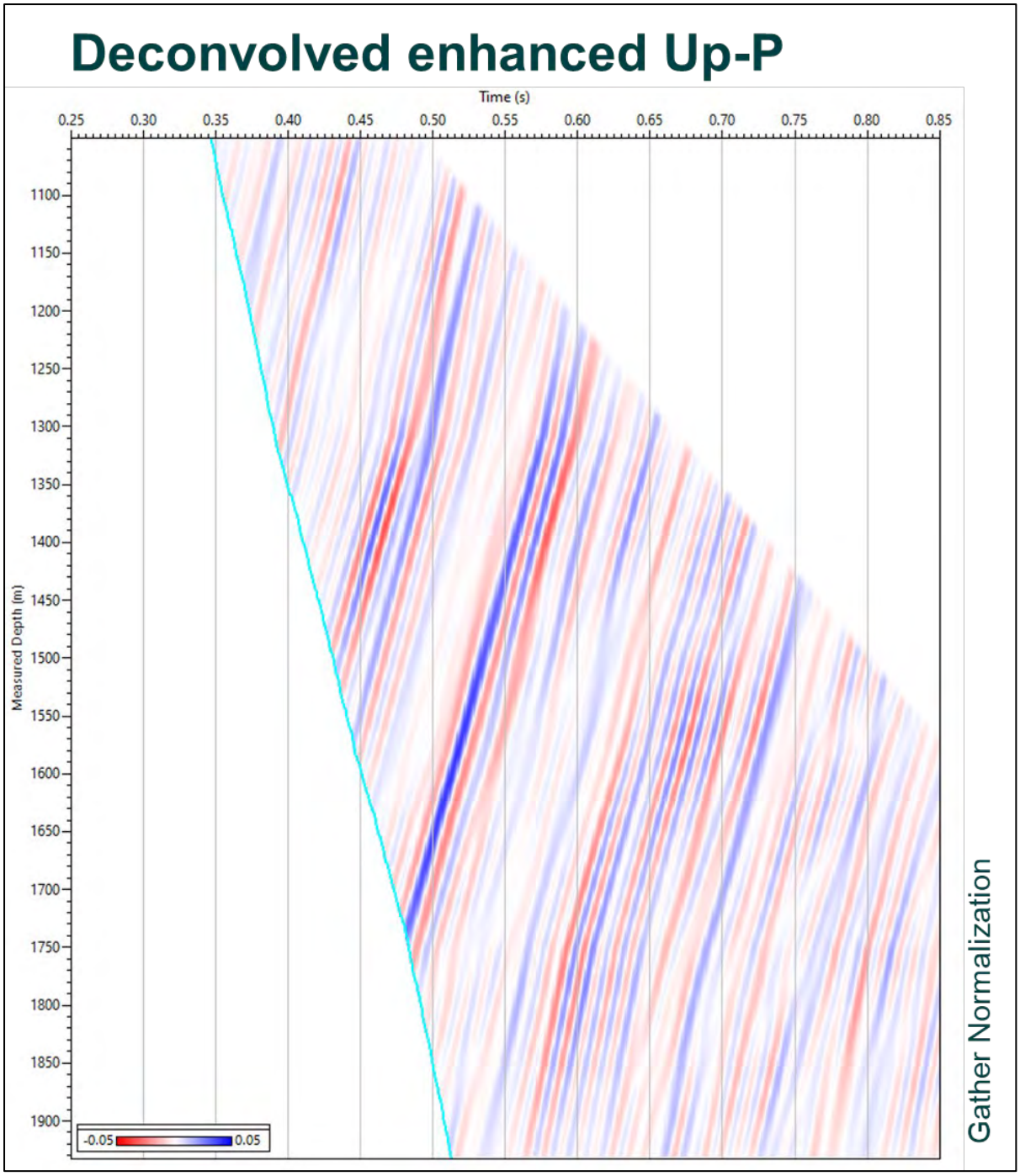


*Figure 8-18. Deconvolved enhanced Up-P - Trace by trace deterministic deconvolution. To reduce the multiples and increase the high frequency data content, the enhanced Up P was deconvolved. Trace by trace deterministic deconvolution with enhanced Down P (Fig. 8.15) using a 0.15 s operator length and 20% white noise was applied to the enhanced Up P. Finally, the data have been filtered with a 5,10-90,110 Hz BPF.*

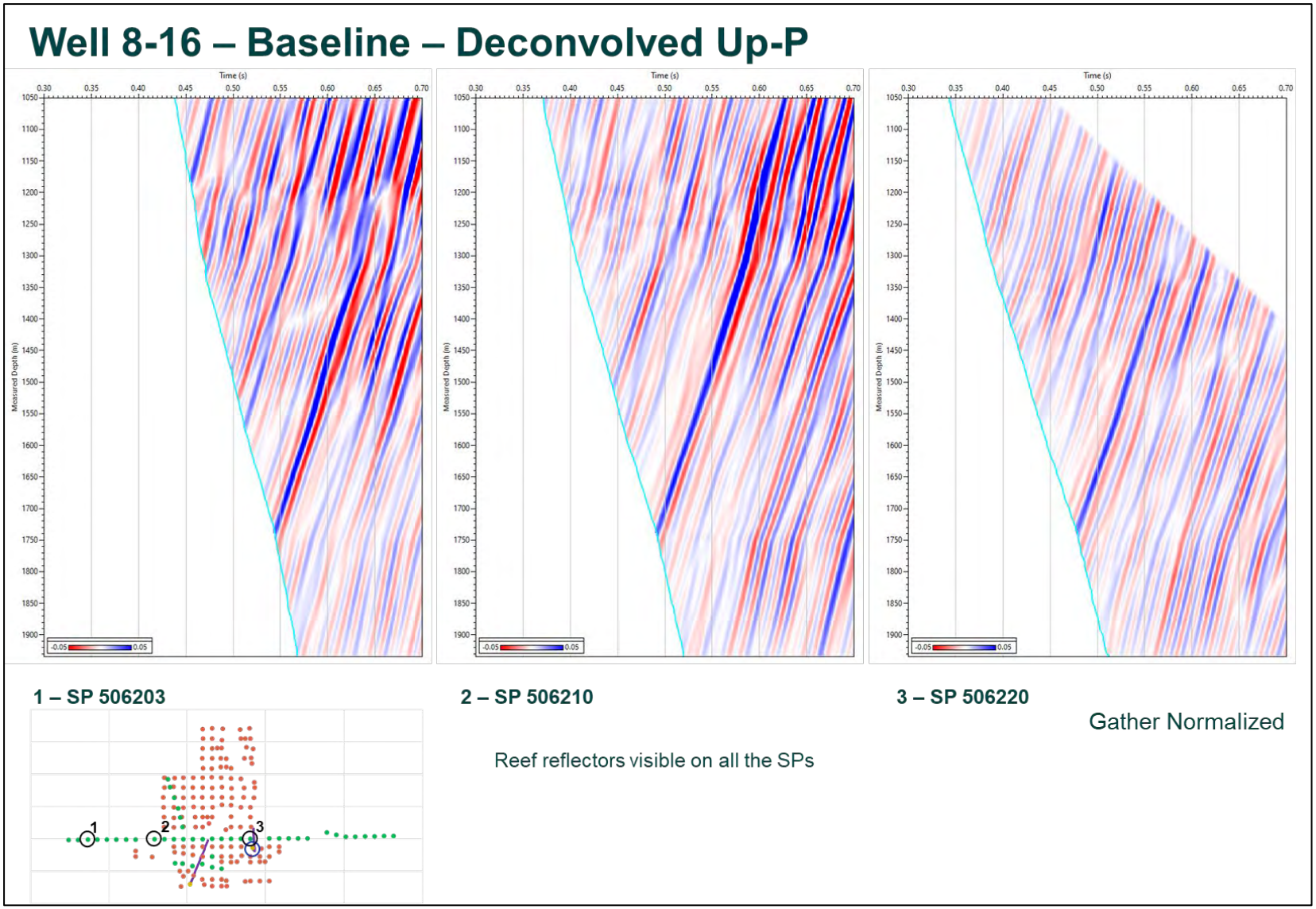


*Figure 8-19. Well 8-16 – Baseline – Deconvolved Up-P - Far, mid and near offsets.*

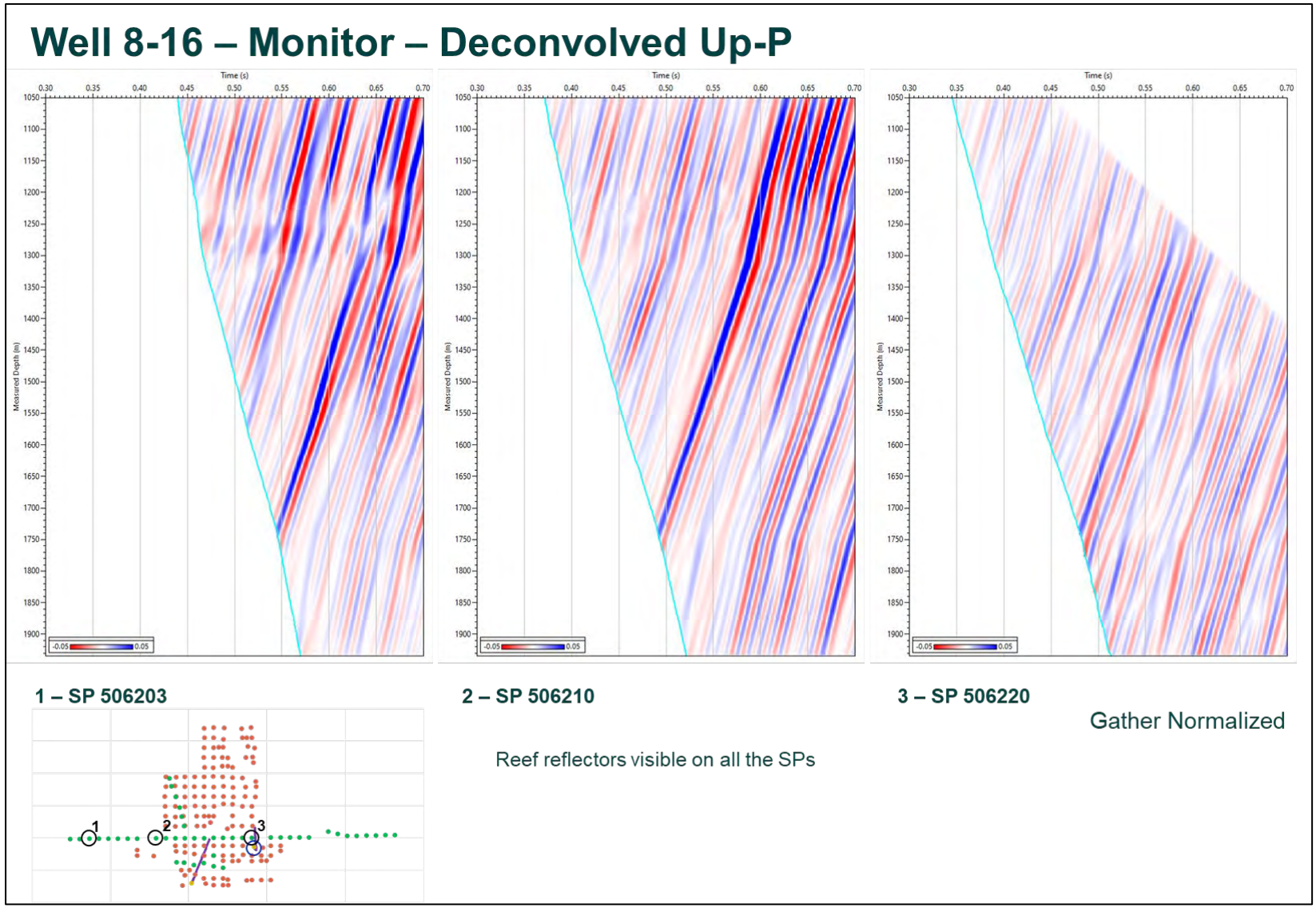


*Figure 8-20. Well 8-16 – Monitor – Deconvolved Up-P - Far, mid and near offsets.*

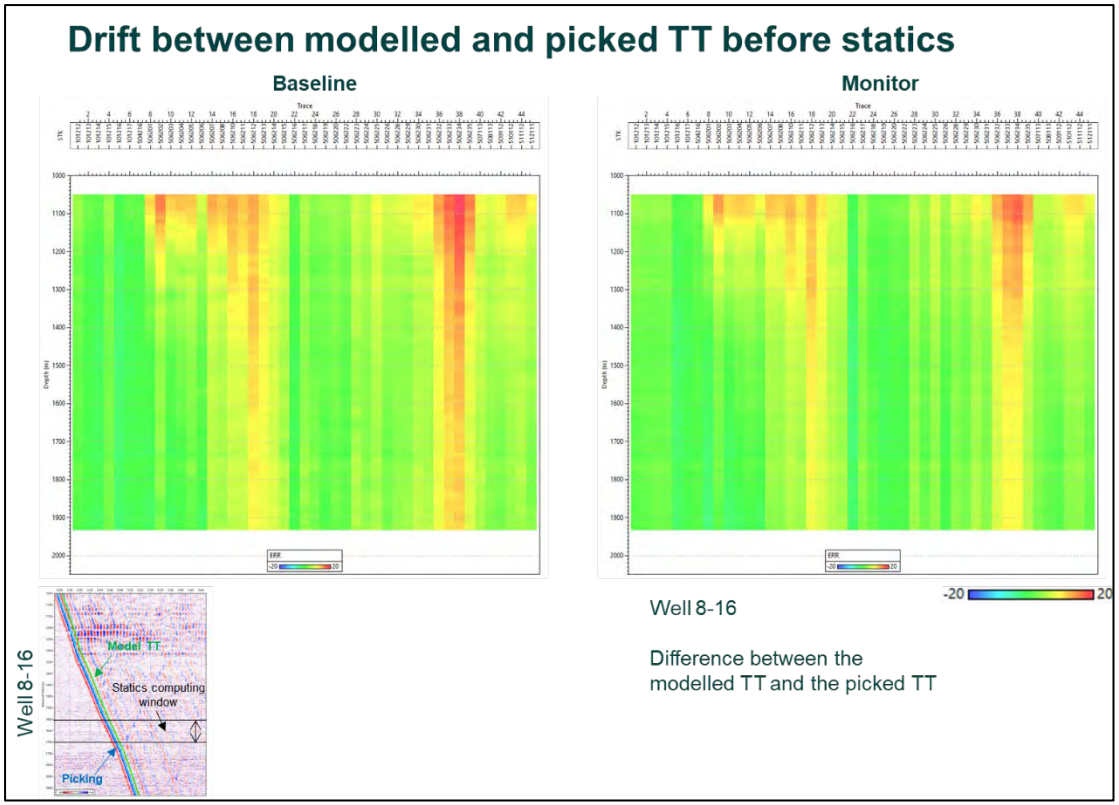


*Figure 8-21. Drift between modelled and picked TT before statics. In this figure is presented the drift between the ray-tracing modelled TT (bottom left picture in blue) and the picked TT (bottom left picture in green) for the baseline and monitor survey. In the top pictures are the differences between the model TT and the picked TT all along the available data intervals for each SP. On the horizontal axis is the Shot Point number, on the vertical axis is the Measured Depth (MD from KB) while the difference value is colour coded. The SP numbers are in increasing order: the first six traces are SPs from the line near the injection well (6-16), followed, from trace 8 to 39, by the walkaway line recorded on the paved road (including the interstate road 32 on the far right) and from trace 40 are the SPs along the SN dirt road. The vertically striped appearance suggests that the difference is mainly a static shift between the modelled times and the picked times. As the model was calibrated for minimal difference at the well 8-18 ZVSP location, the static shift is due to the lateral variation in the weathering zone. Between nearby shots there is a gradual increase or decrease in difference, confirming that the shift is due to the weathering zone (the change in the acoustic properties of the shallow layer is not random). Between the baseline and repeat survey, the drift values are different due to seasonal differences and variations in water content at shallow levels. Nevertheless, they follow the same pattern confirming that the shift is mainly due to lateral velocity changes in the weathering zone. Above 1250 m MD the difference increases and is partially due to higher picking uncertainly (due to the ringing) and partially to some unaccounted velocity anisotropy. This is more evident at far offsets.*

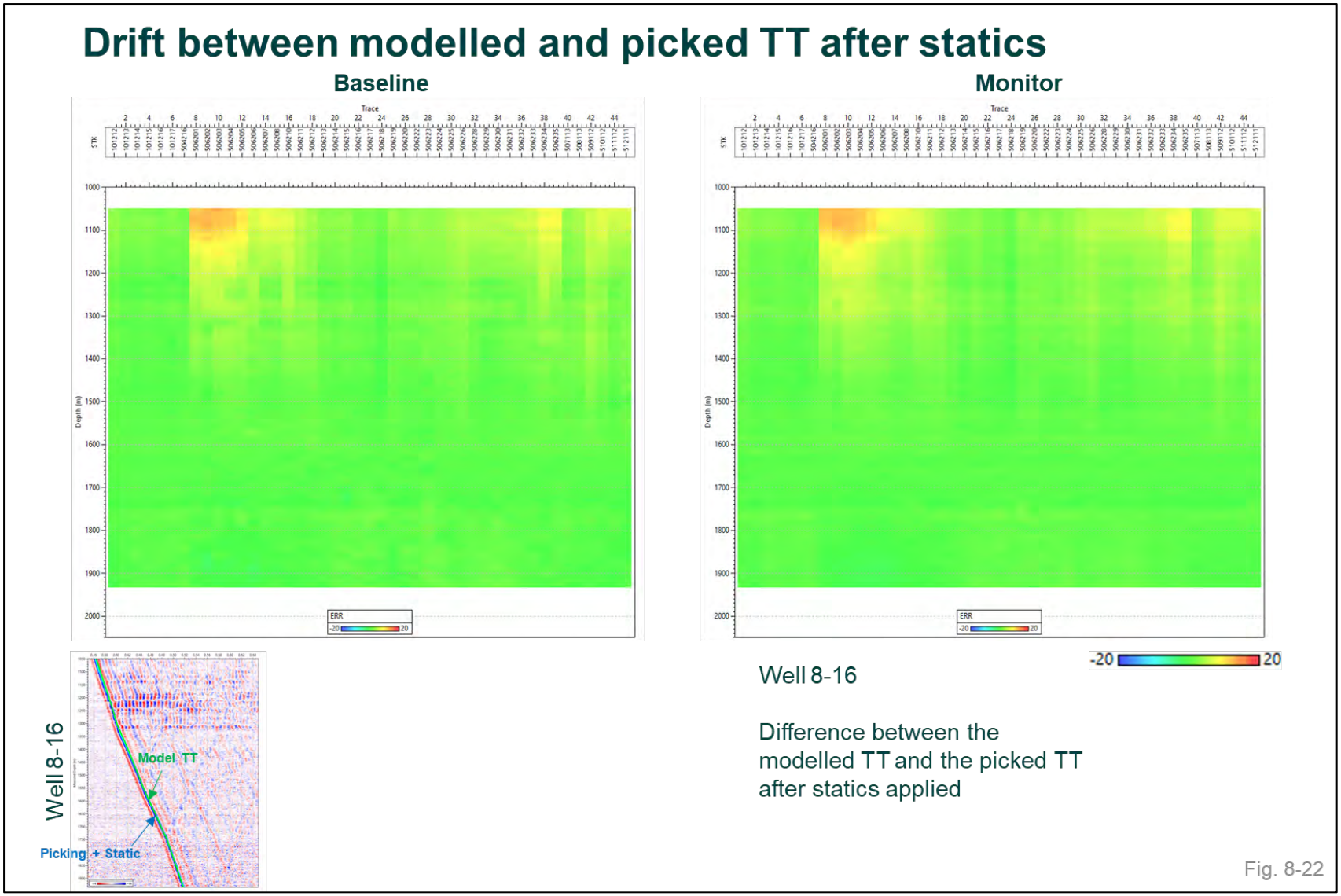


*Figure 8-22. Drift between modelled and picked TT after statics - Data and picks shifted.*

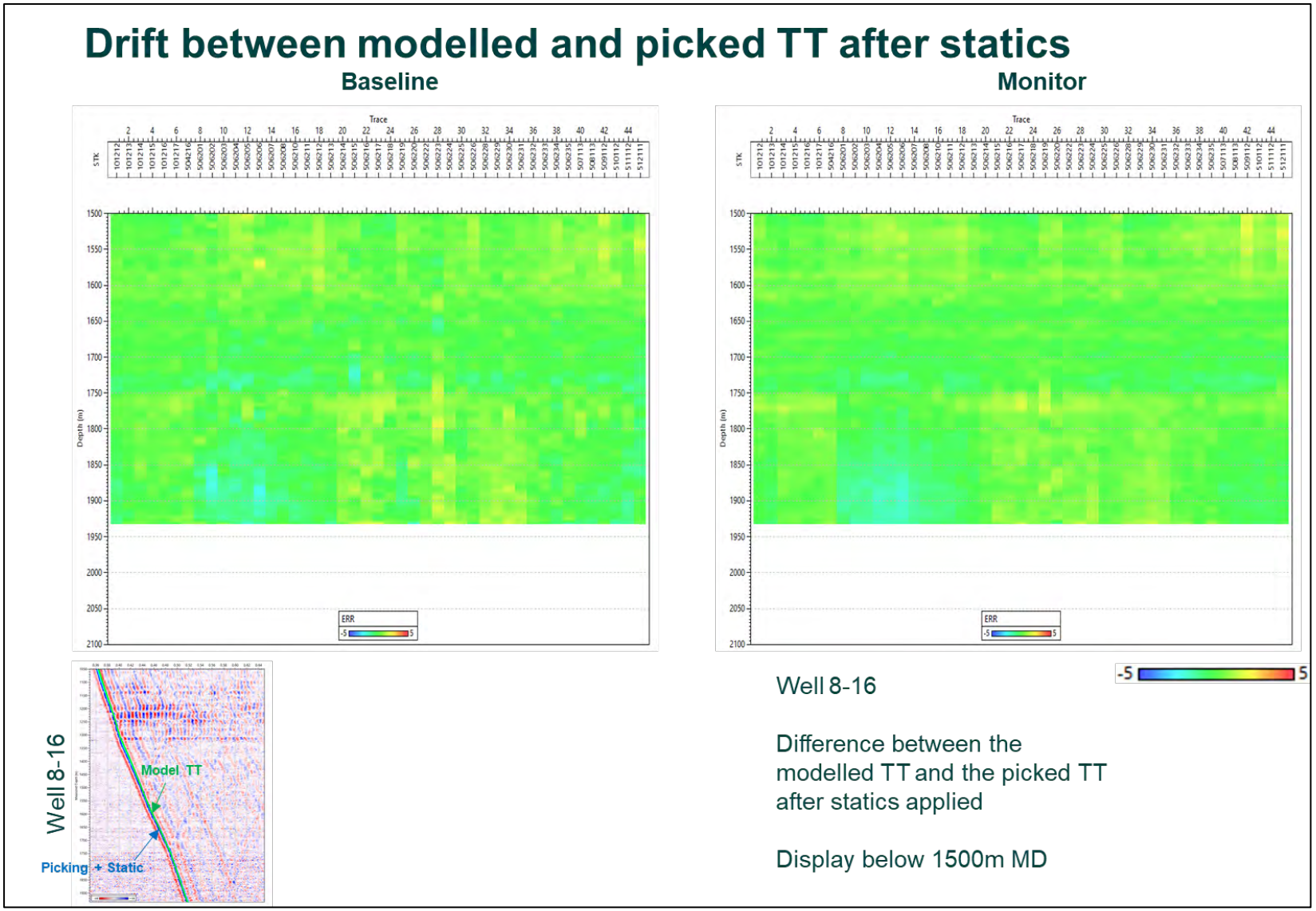


*Figure 8-23. Drift between modelled and picked TT after statics data below 1500 m MD - Data and picks shifted.*

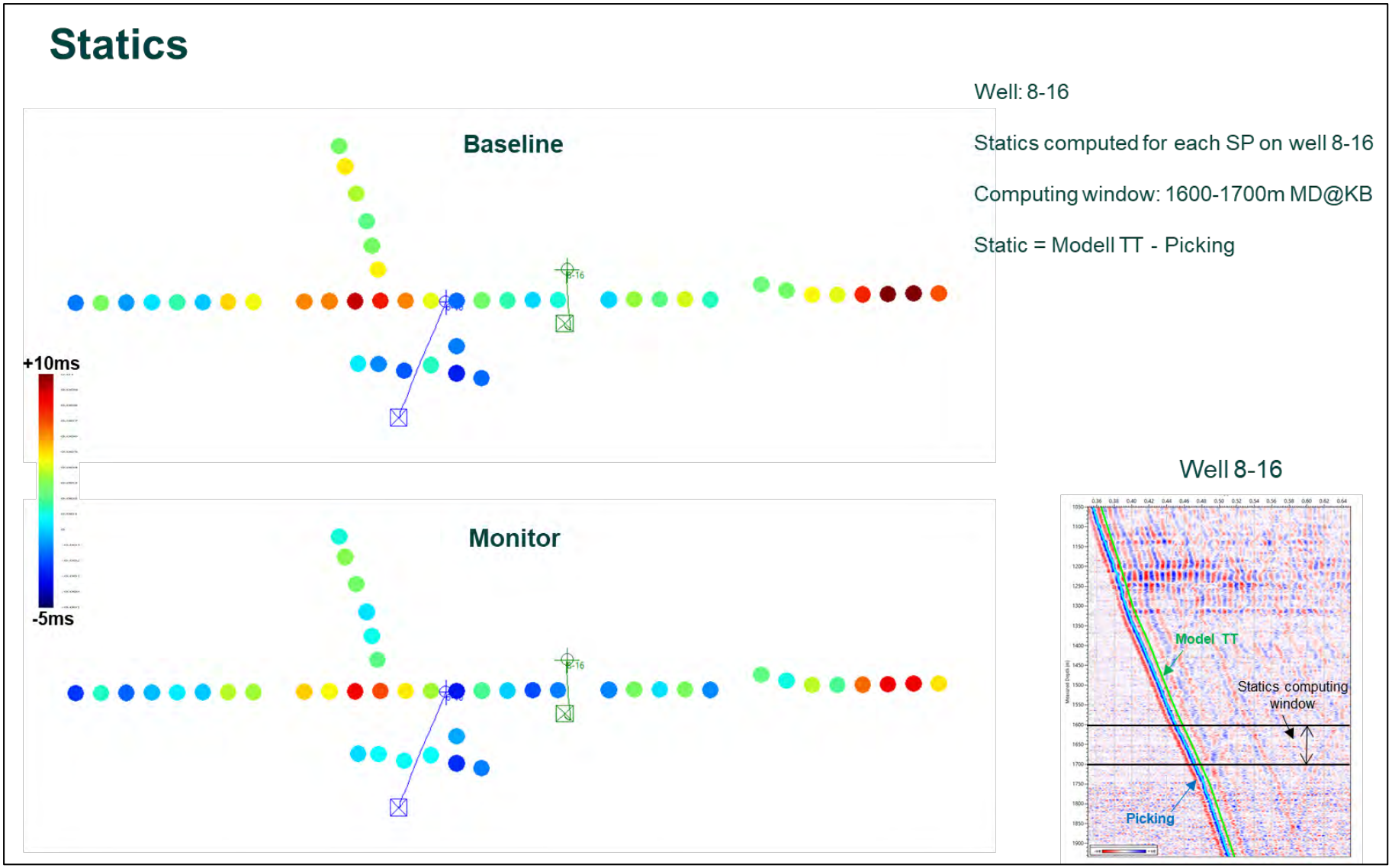


*Figure 8-24. Statics - Plane view with statics for each SP. Static shift values were calculated separately for the baseline and the monitor survey.*

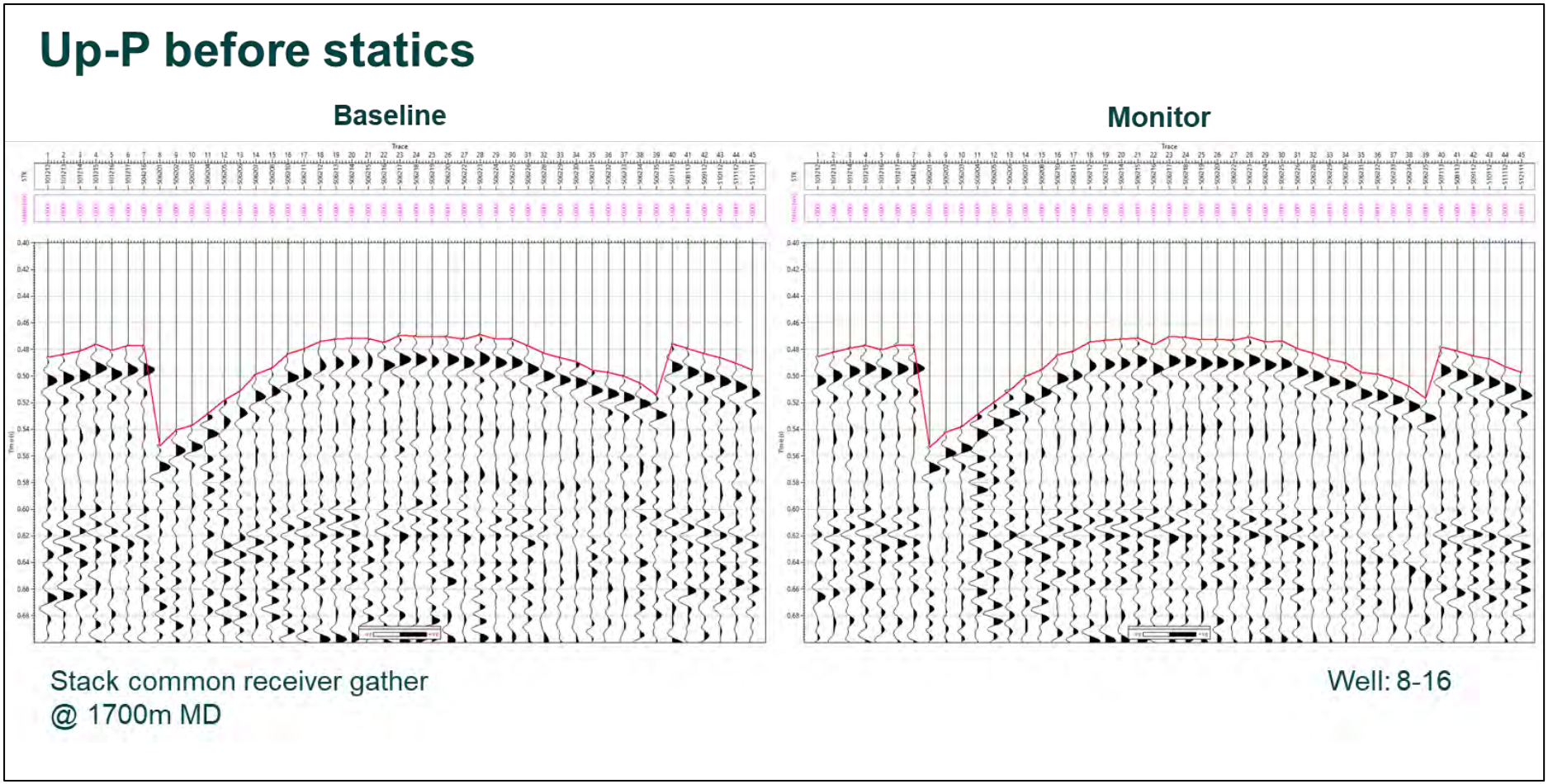


*Figure 8-25. Up-P before statics - Common receiver gather.*

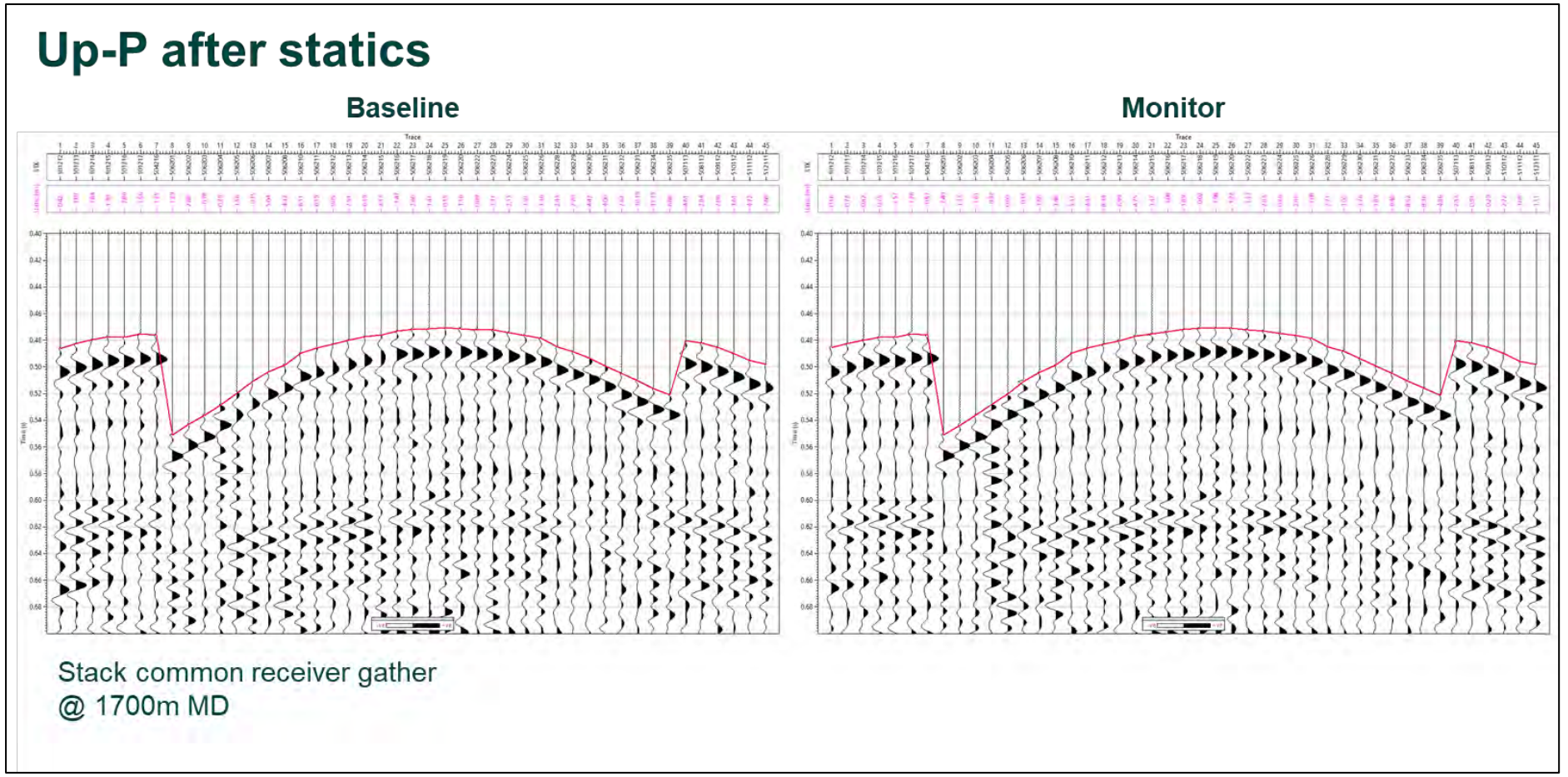


*Figure 8-26. Up-P after statics - Common receiver gather.*

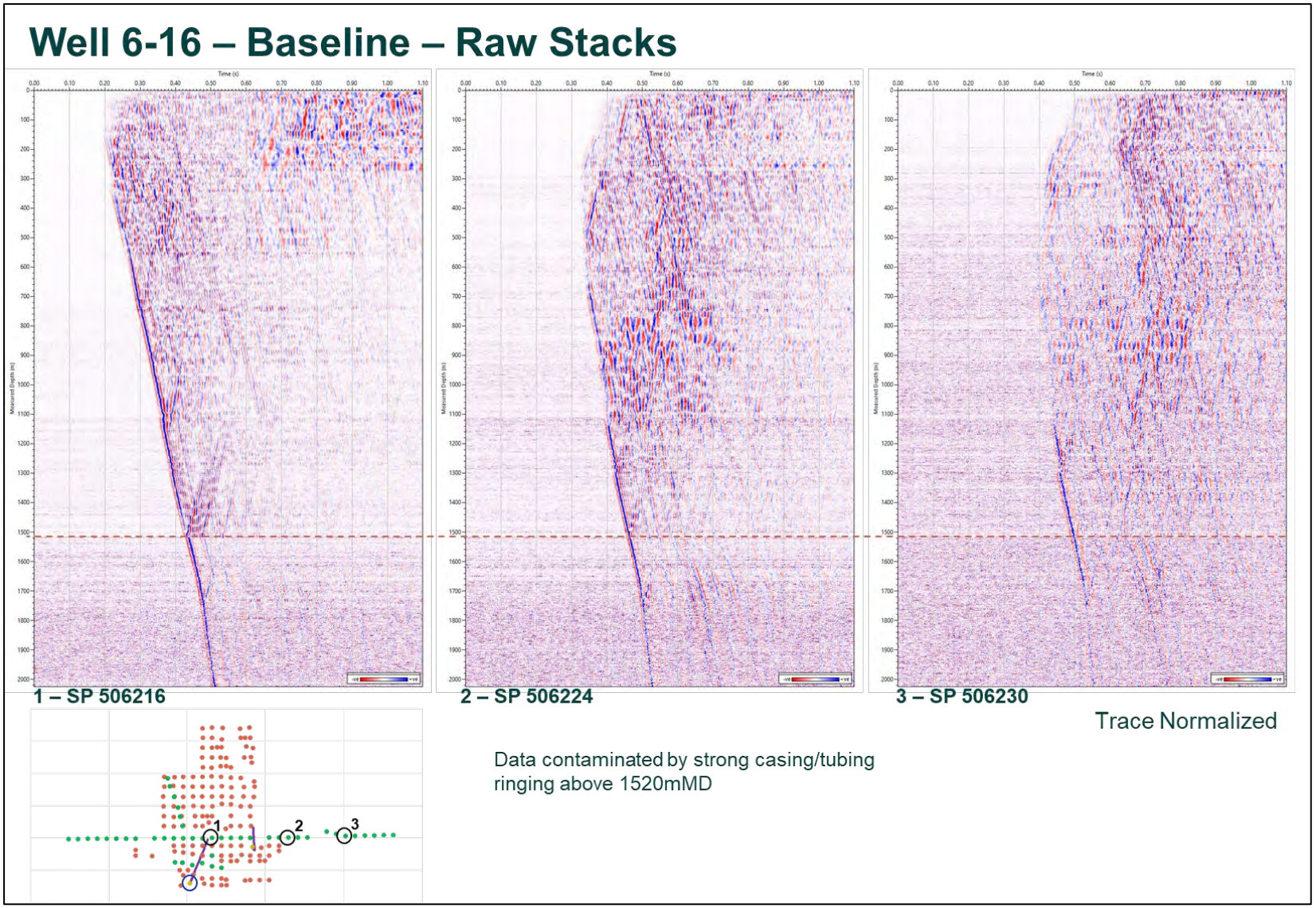


*Figure 8-27. Well 6-16 – Baseline – Raw Stacks - Far, mid and near offset total wavefield.*

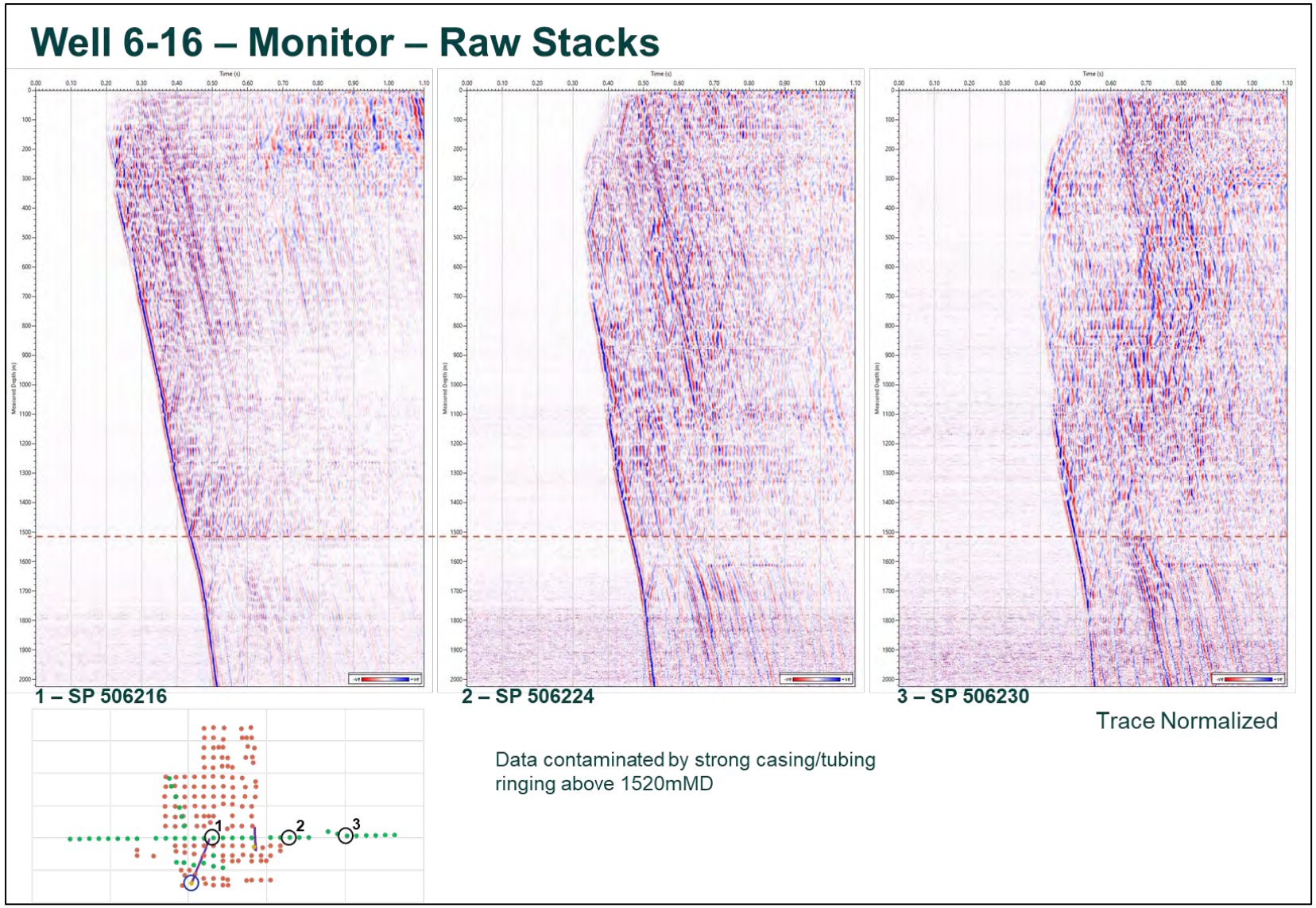


*Figure 8-28. Well 6-16 – Monitor – Raw Stacks - Far, mid and near offset total wavefield.*

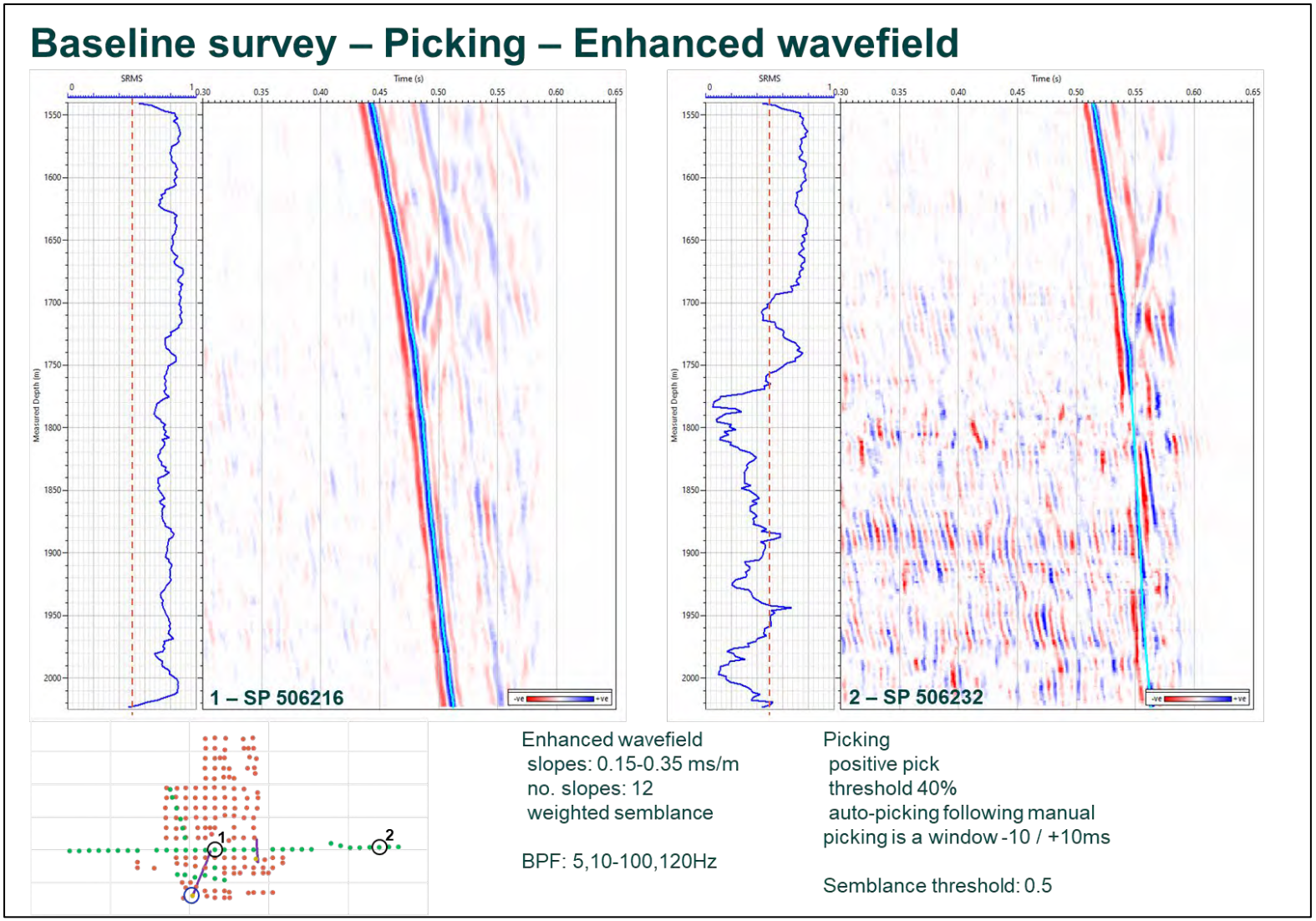


*Figure 8-29. Baseline survey – Picking – Enhanced wavefield - Slopes enhancement. This figure shows the baseline enhanced wavefield time picks for SP 506216 (near well TD) and SP 506232 (far east).*

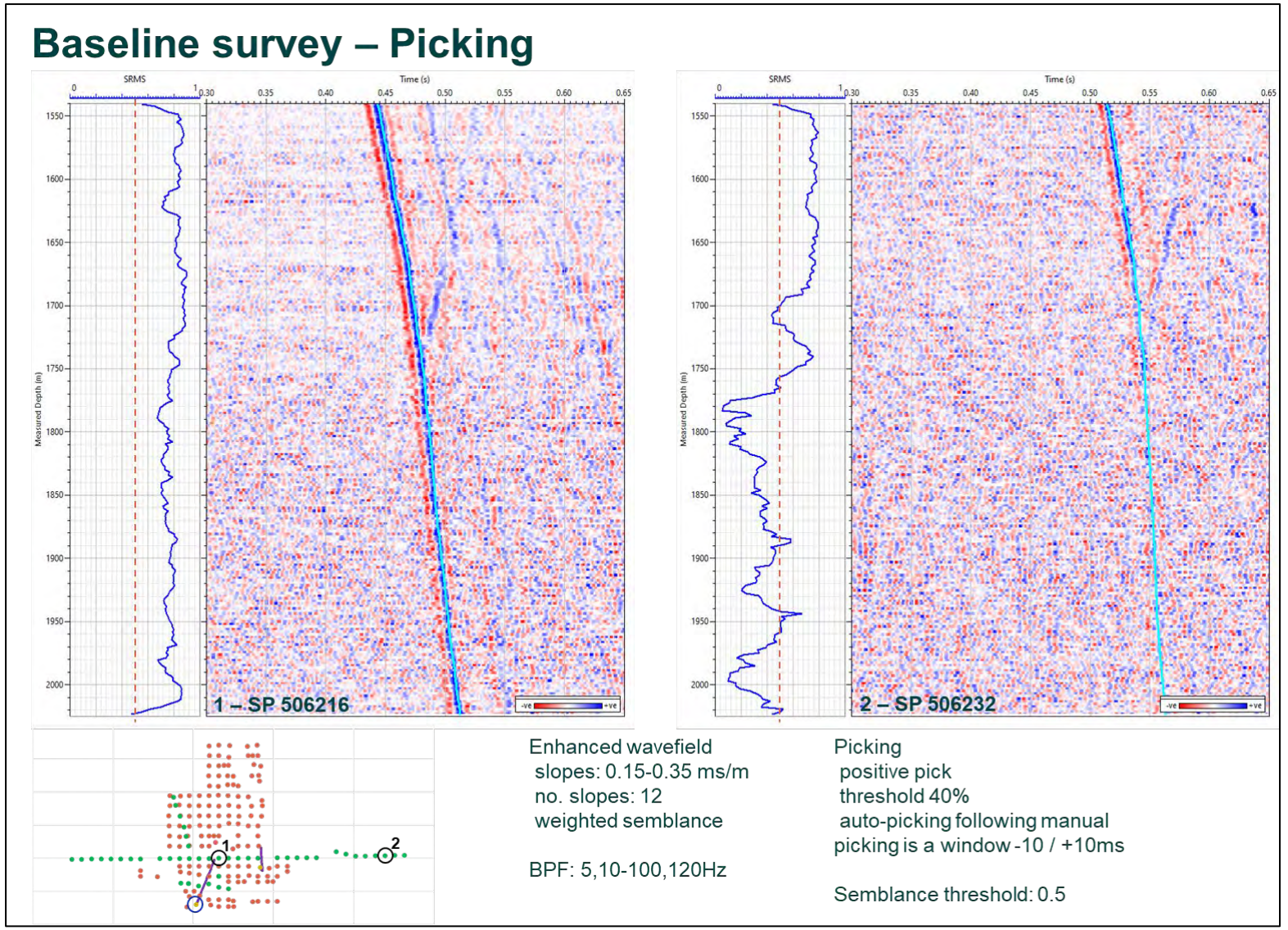


*Figure 8-30. Baseline survey – Picking. It presents the stacks after picking for the same SP.*

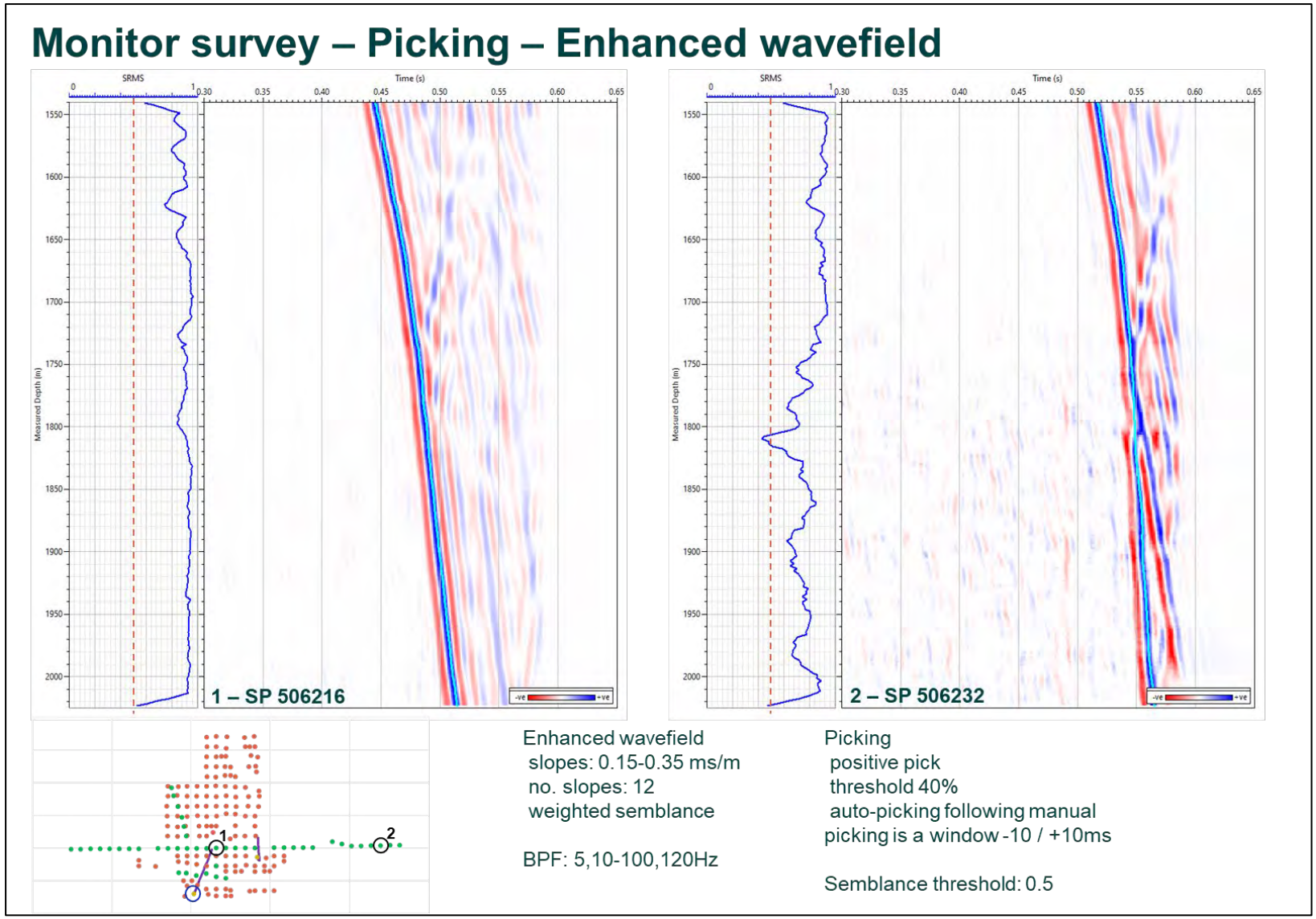


*Figure 8-31. Monitor survey – Picking – Enhanced wavefield - Slopes enhancement.*

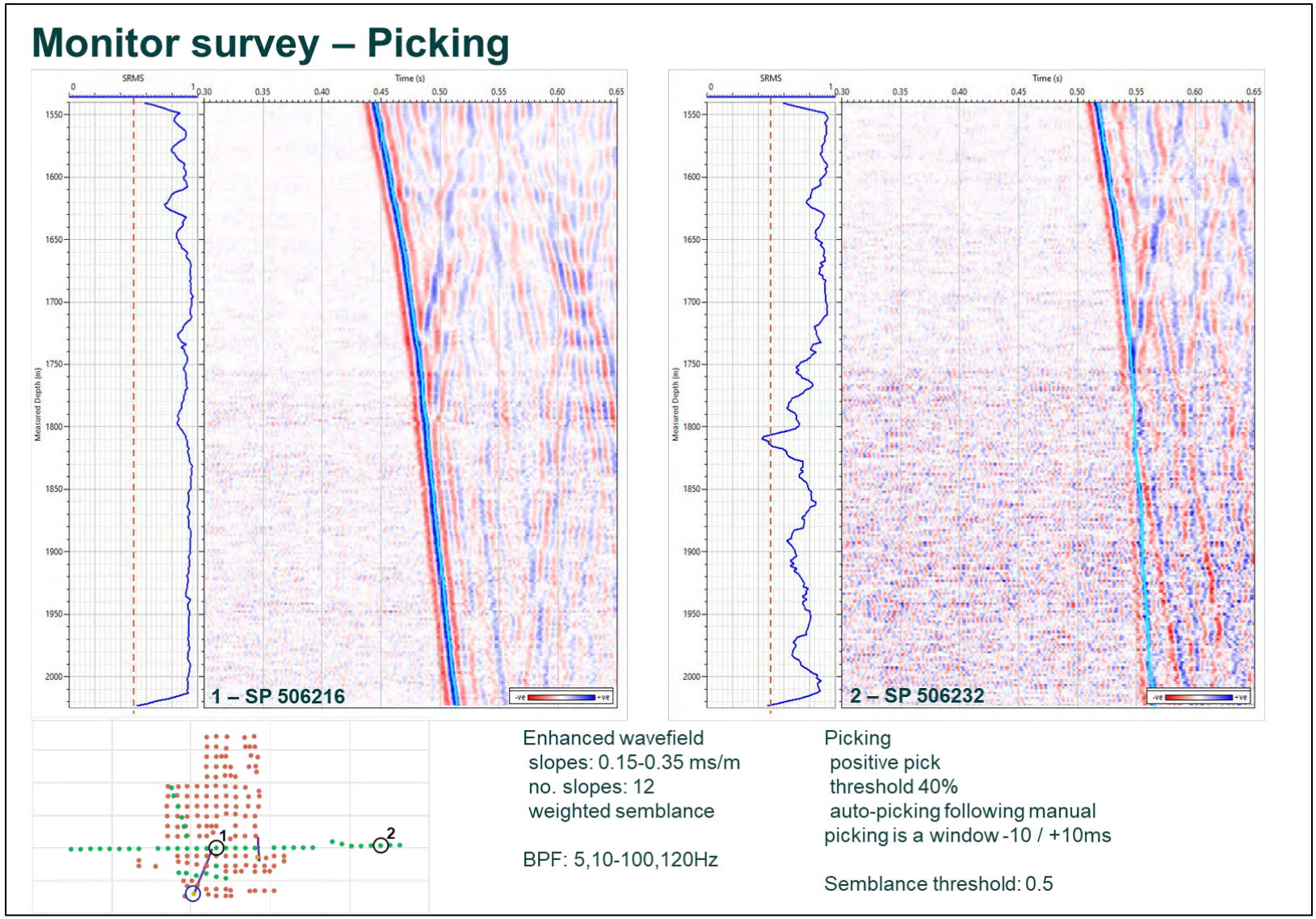


*Figure 8-32. Monitor survey – Picking.*

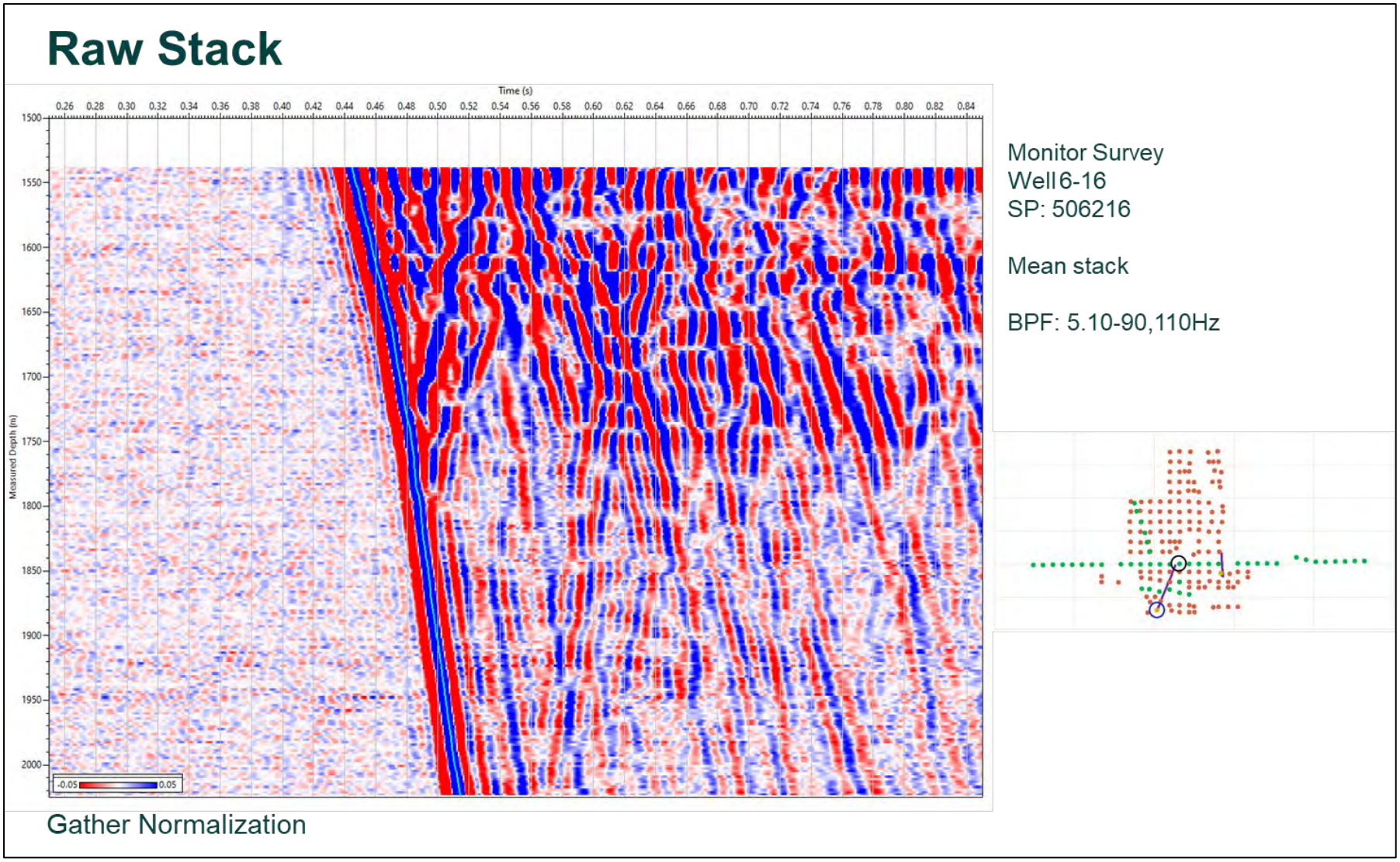


*Figure 8-33. Raw Stack. It shows the data used as input for the down-wave processing for SP 506216 stack data with a BPF: 5,10-90,110 Hz applied. The amplitudes displayed are cross-normalized.*

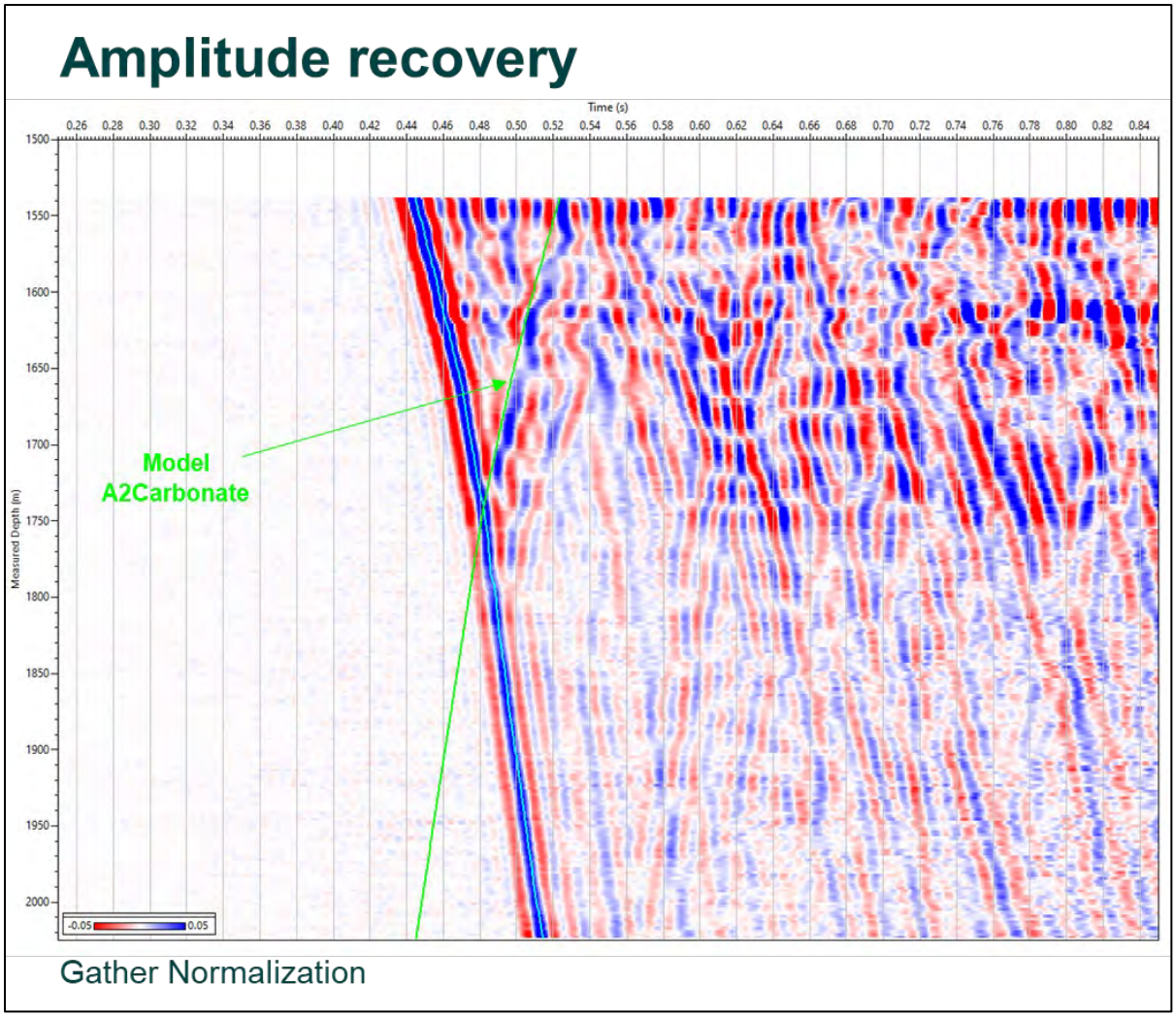


*Figure 8-34. Amplitude recovery - Time power function. To compensate for the absorption and spherical divergence spreading, the amplitude was scaled by the squared sample time. Figure 8.34 shows the stack after amplitude recovery.*

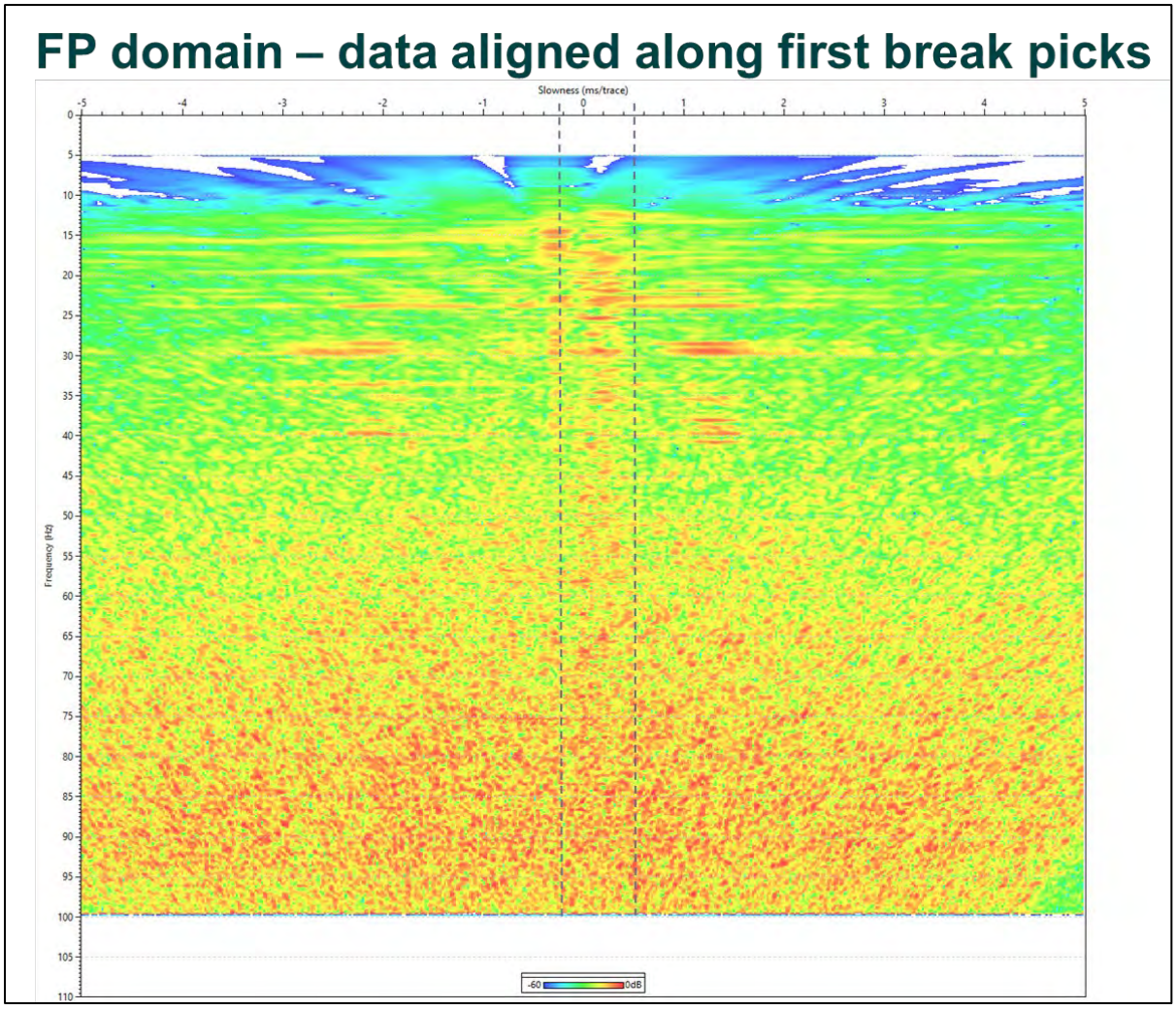


*Figure 8-35. FP domain – data aligned along first break picks - Remove tube waves and noise. This figure shows the stack aligned along the first break in the frequency-slowness domain (FP).*

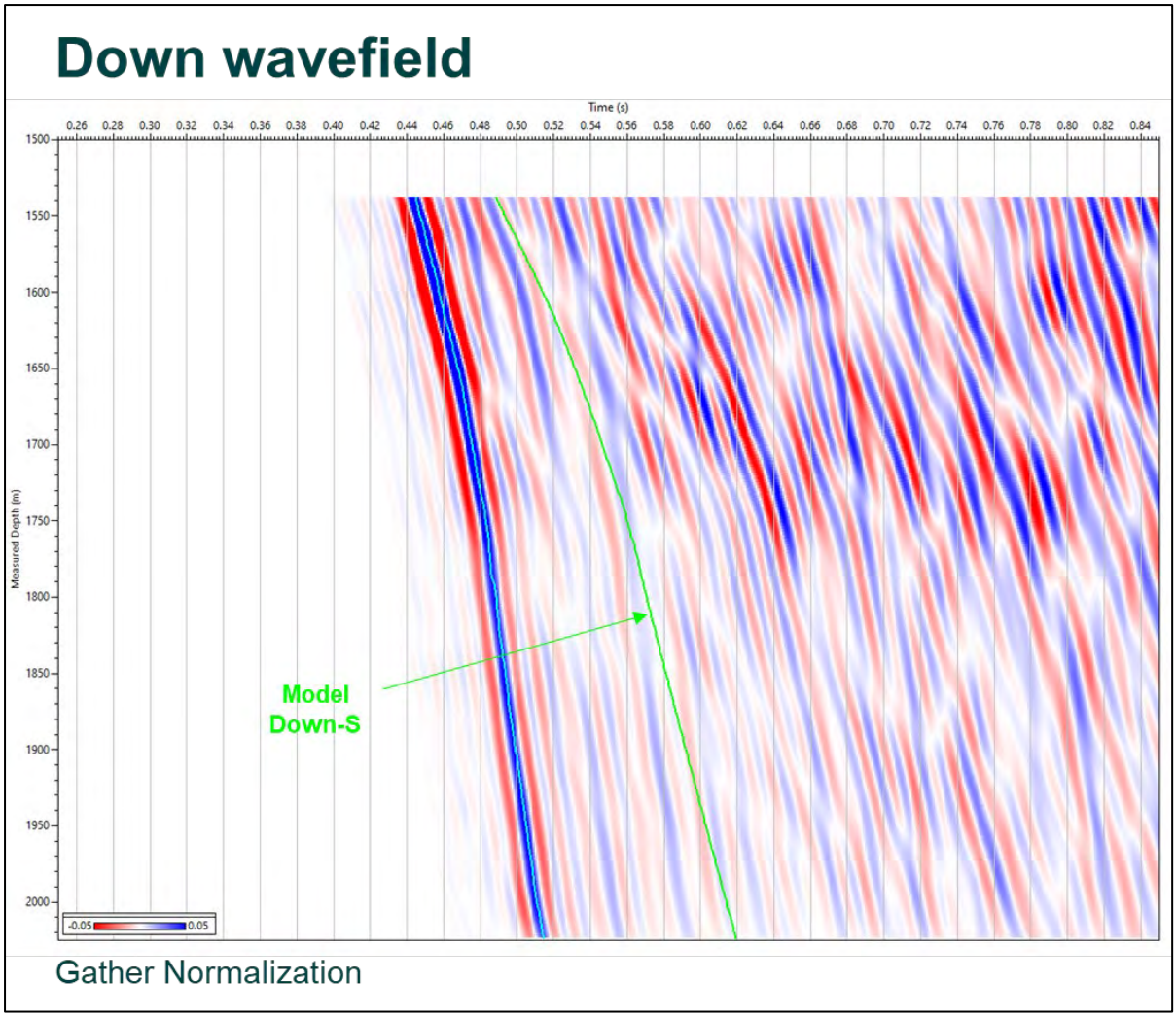


*Figure 8-36. Down wavefield - After FP separation. We selected the data inside the -0.3 – 0.6 slowness window and performed the Down wavefield separation in the FP domain.*

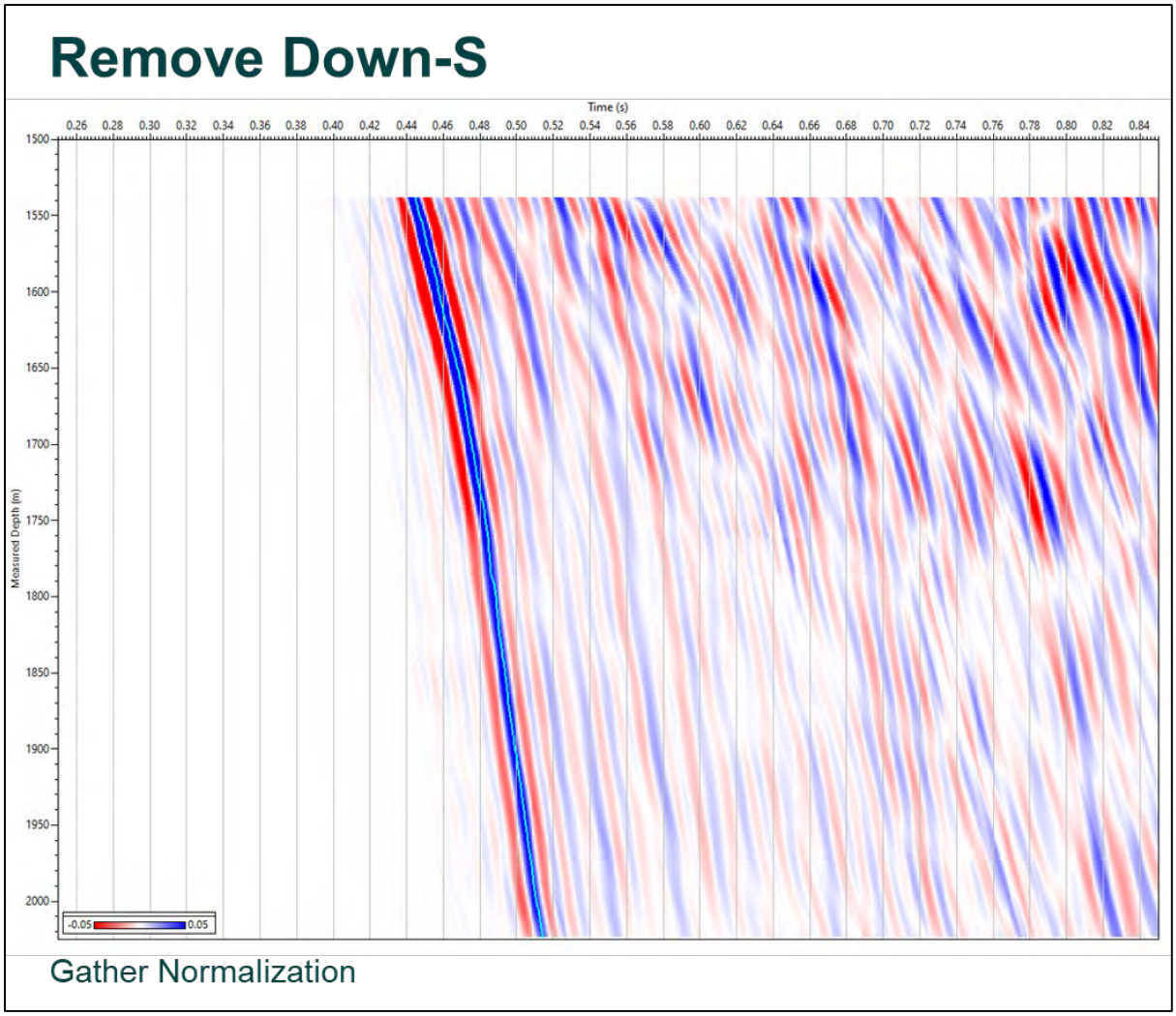


*Figure 8-37. Remove Down-S - Median filter. The Down S wavefield was removed from the data.*

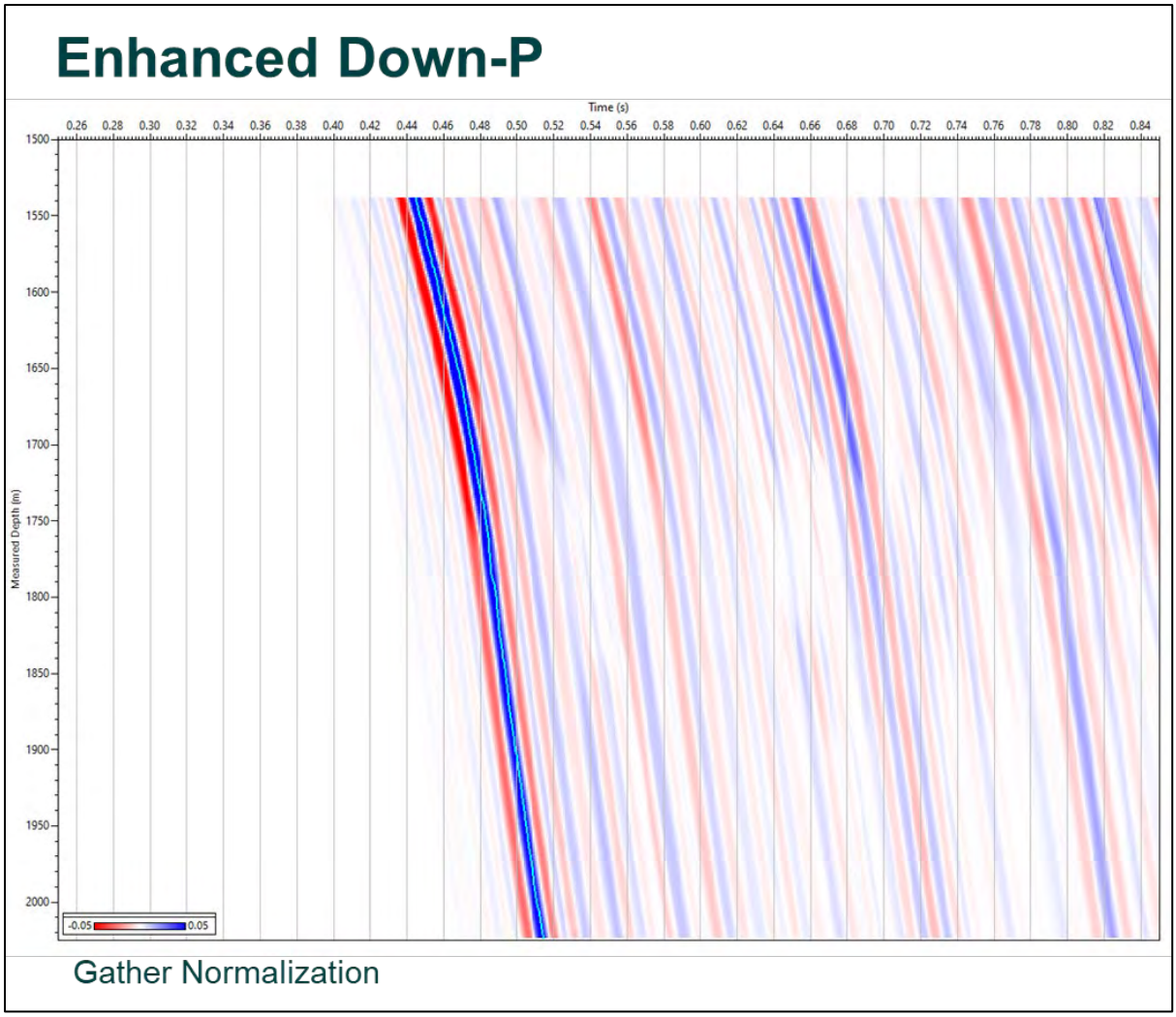


*Figure 8-38. Enhanced Down-P - Median filter. This figure shows the Down P wavefield after enhancement with a median filter of 121 traces along the FB. This wavefield will be used later for the deconvolution. Trace by trace deterministic deconvolution with enhanced Down P using a 0.15 s operator length and 20% white noise was applied to the enhanced Up P. Finally, the data have been filtered with a 5,10-90,110 Hz BPF.*

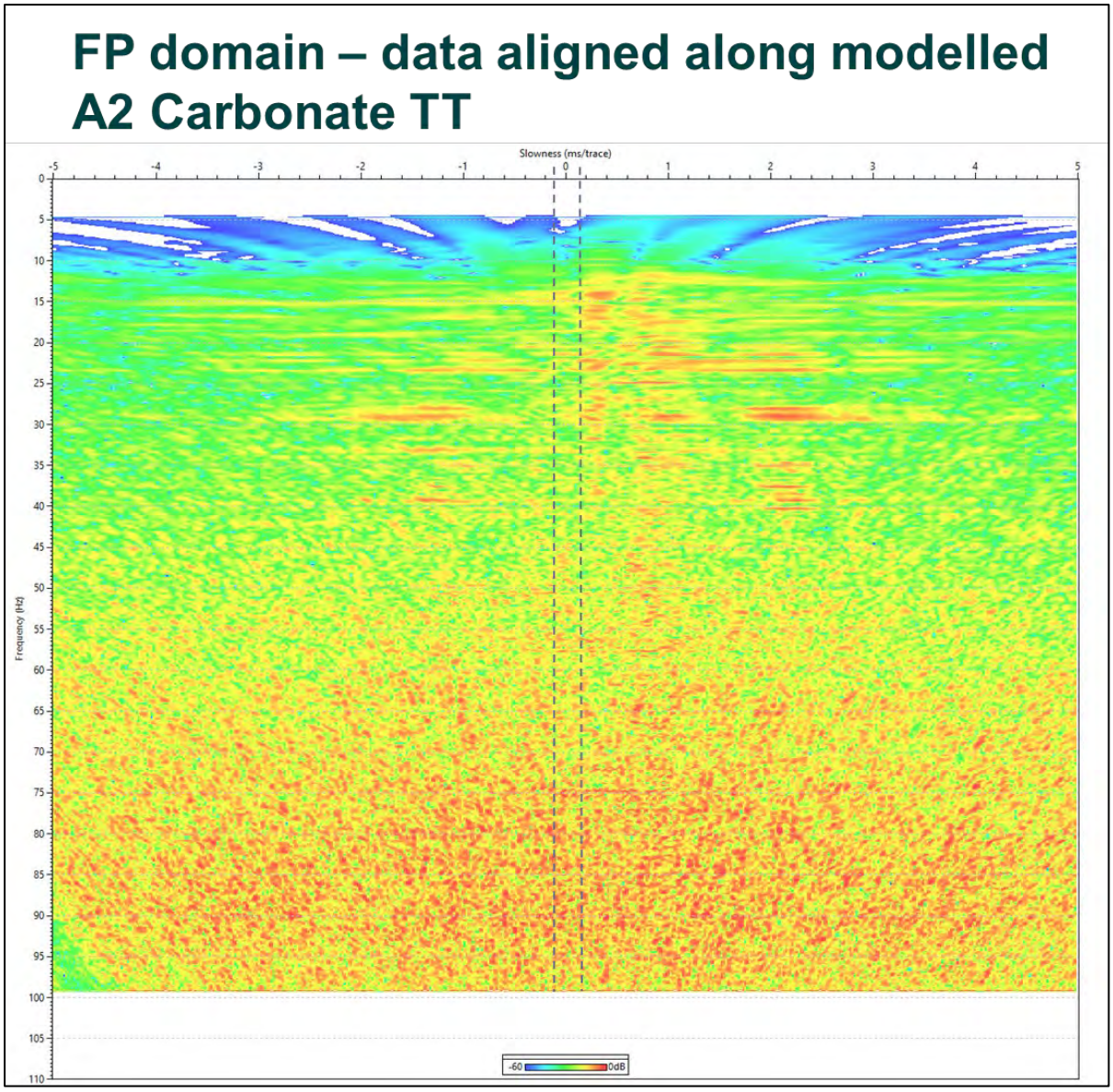


*Figure 8-39. FP domain – data aligned along modelled A2 Carbonate TT - Enhance Up P. The Up P wavefield was separated in the FP domain in a slowness window of -0.15 to 0.15 ms/traces.*

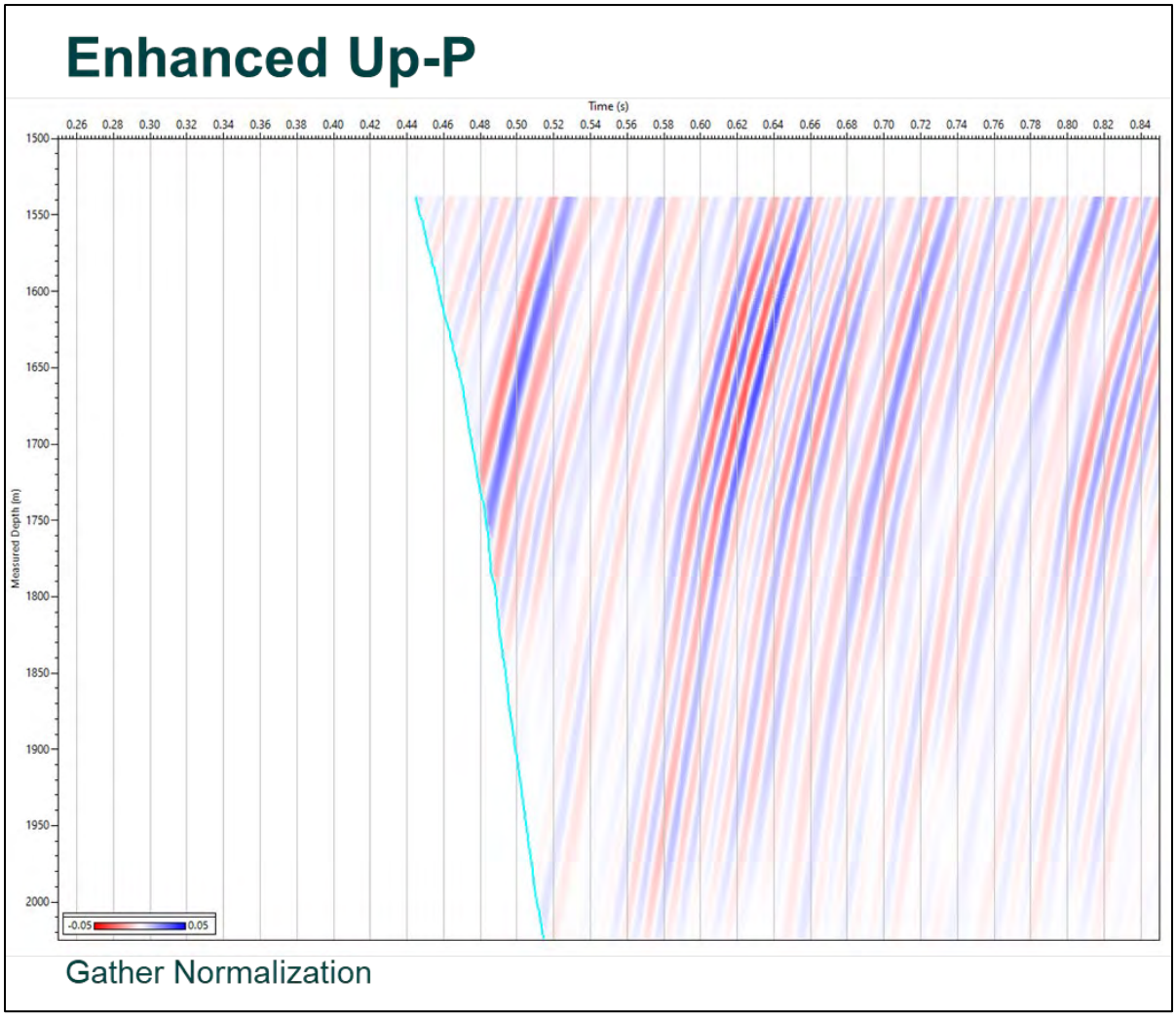


*Figure 8-40. Enhanced Up-P - After FP separation. The input data have been aligned along the A2 Carbonate modelled TT (Fig. 8.34 green) before FP. Figure 8.40 shows the enhanced Up P along the modelled A2 Carbonate TT over a 10 trace window after the separation in FP domain.*

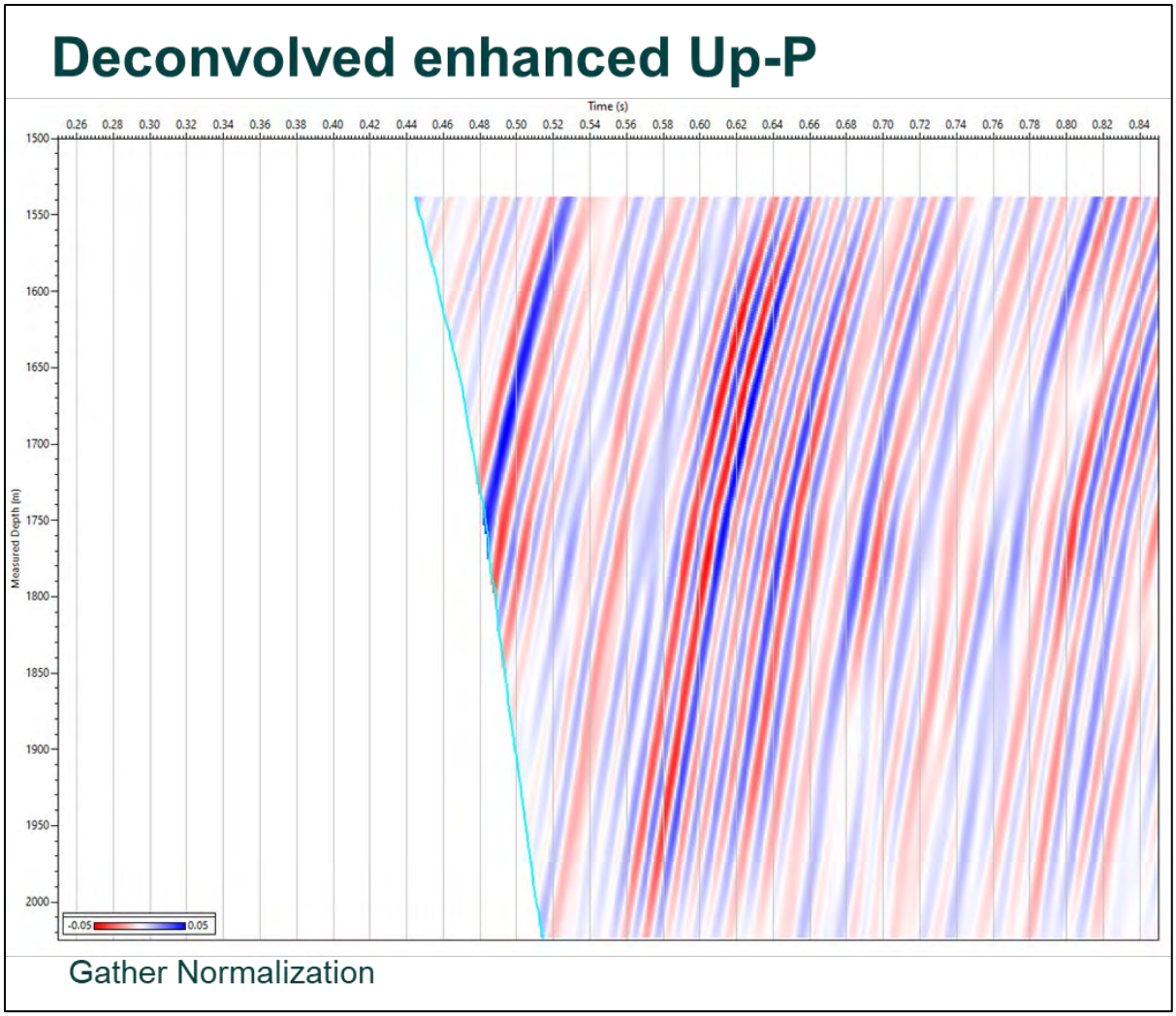


*Figure 8-41. Deconvolved enhanced Up-P - Trace by trace deterministic deconvolution. To reduce the multiples and increase the data high frequency bandwidth, the enhanced Up P was deconvolved.*

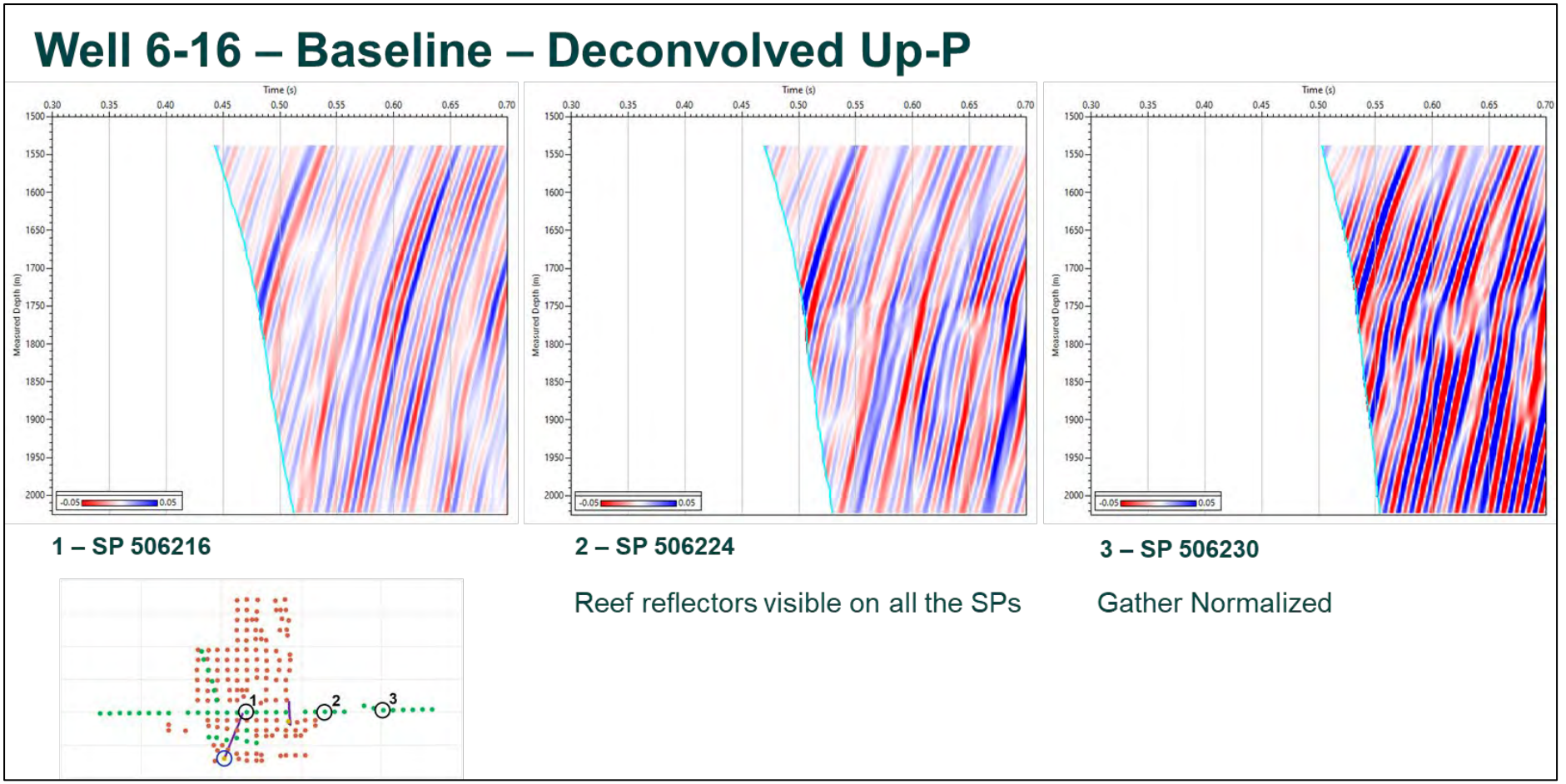


*Figure 8-42. Well 6-16 – Baseline – Deconvolved Up-P - Far, mid and near offsets.*

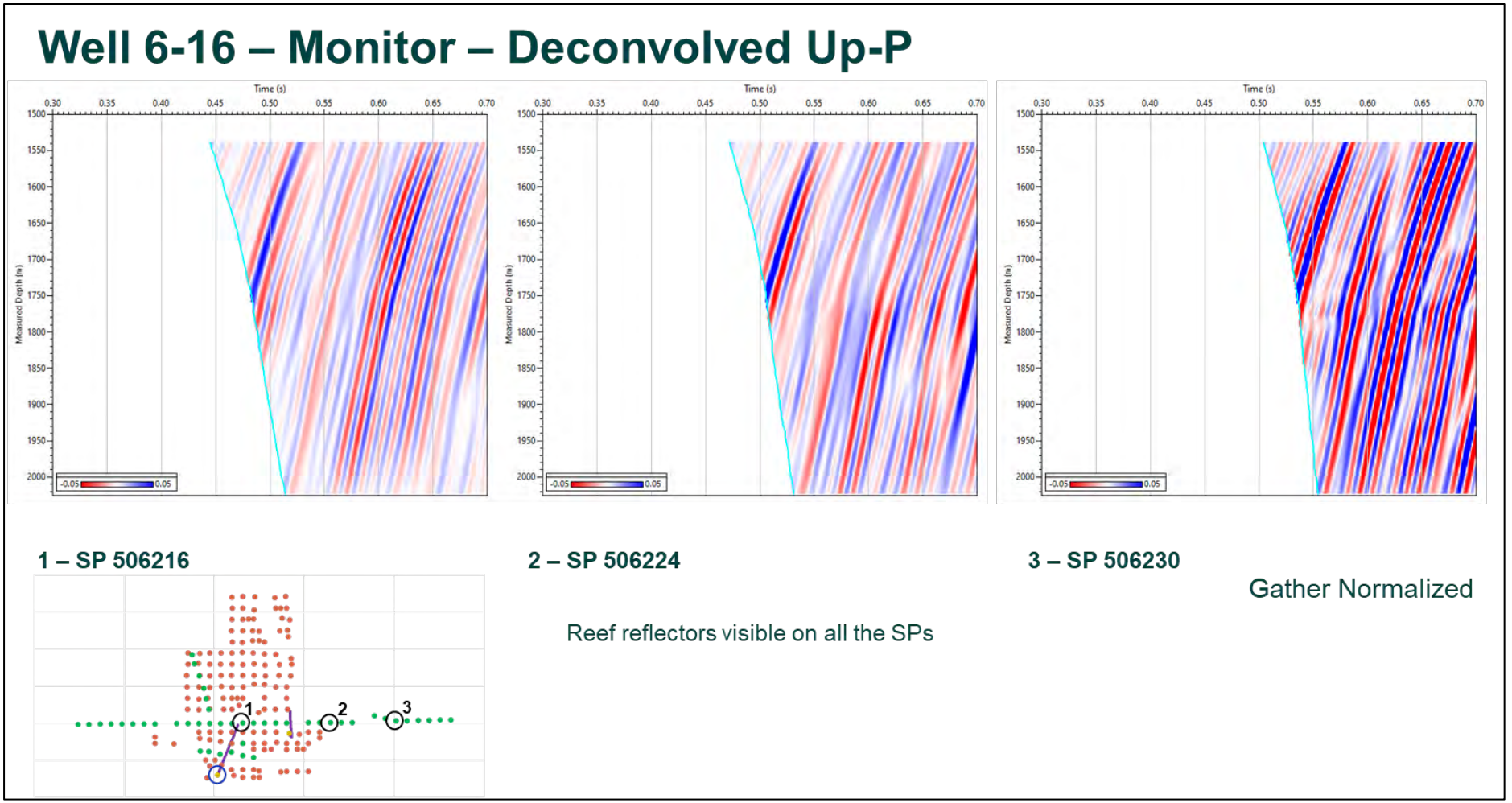


*Figure 8-43. Well 6-16 – Monitor – Deconvolved Up-P - Far, mid and near offsets.*

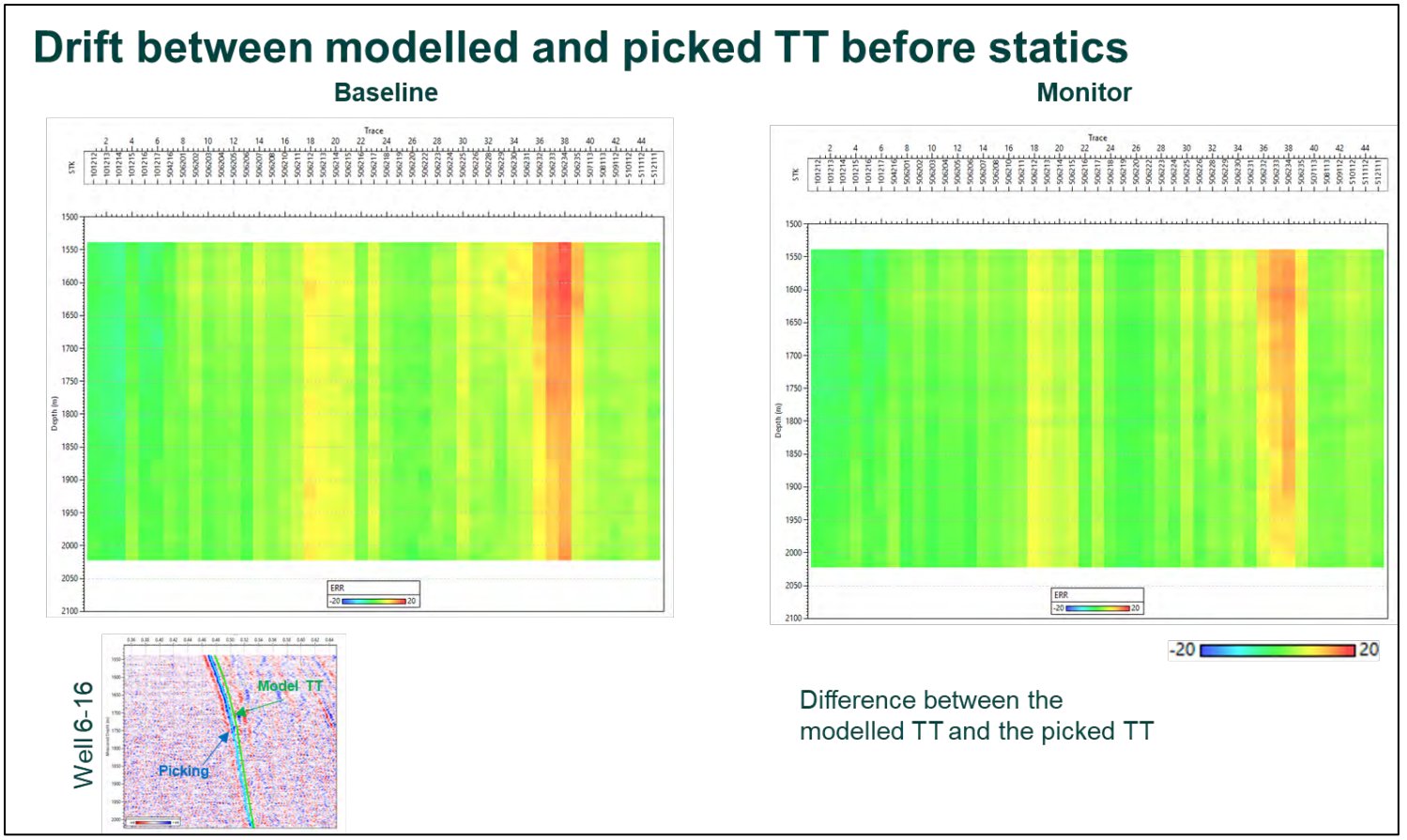


*Figure 8-44. In this figure is presented the drift between the ray tracing-modelled TT (in the bottom left picture in blue) and the picked TT (in the bottom left picture in green) for the baseline and monitor survey. In the top pictures for each SP are the differences between the model TT and the picked TT all along the available data interval. On the horizontal axis is the Shot Point number, on the vertical axis is the Measured Depth (MD from KB) and the difference is colour coded. The SP numbers are in increasing order, the first six traces are SPs from the line near the injection well (6-16), followed, from trace 8 to 39, by the walkaway line recorded on the paved road (including the interstate road 32 on the far right) and from trace 40 are the SPs along the SN dirt road. The difference plot shows vertical stripes suggesting there is mainly a static shift between the model and the picks. Between nearby shots there is a gradual increase or decrease in drift, confirming that the shift is due to the weathering zone (the change in the acoustic properties of the shallow layer is not random). Between the baseline and the monitor survey, the errors have different values due to different season and water content in the shallow layer but follow the same pattern confirming that the shift is mainly due to lateral velocity changes in the weathering zone.*

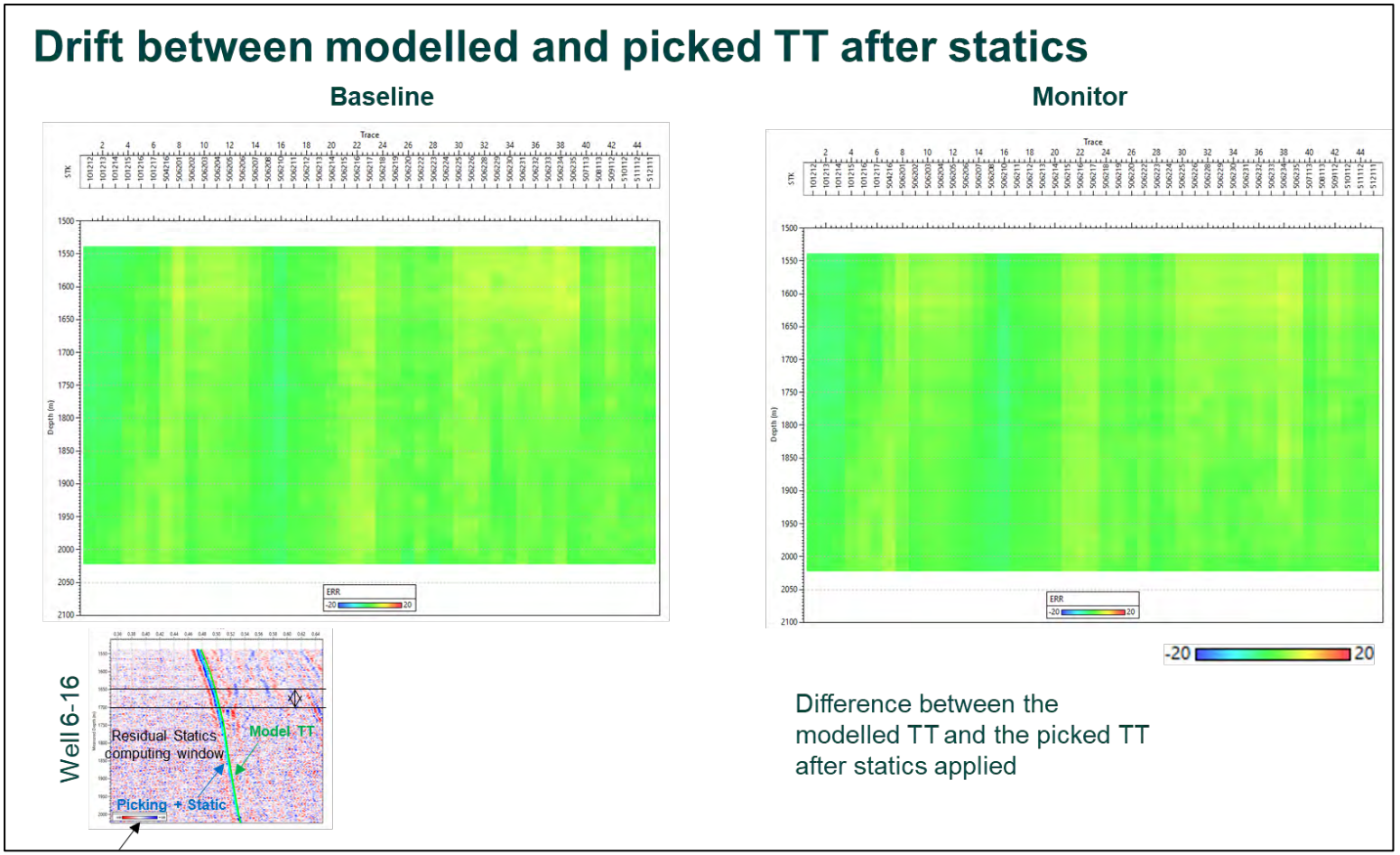


*Figure 8-45. Drift between modelled and picked TT after statics - Data and picks shifted with 8-16 statics.*

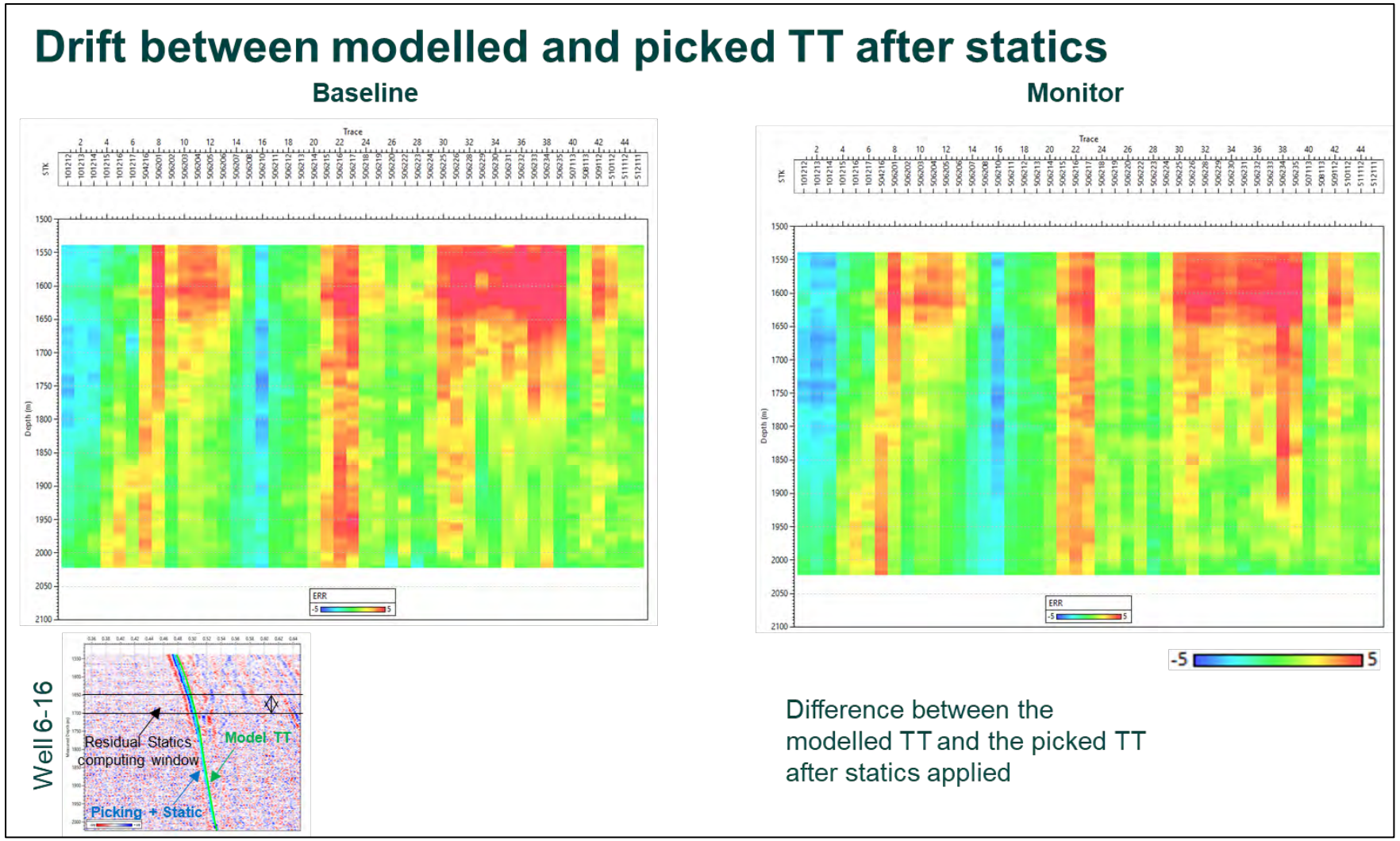


*Figure 8-46. Drift between modelled and picked TT after statics - Data and picks shifted with 8-16 statics. This figure presents the drift with a -5/+5 ms scale. Using the statics computed based on the well 8-16 data the remaining error is still significant. Residual statics were computed by averaging the error over the 1650 m – 1700 m MD interval (Fig. 8.46 bottom left).*

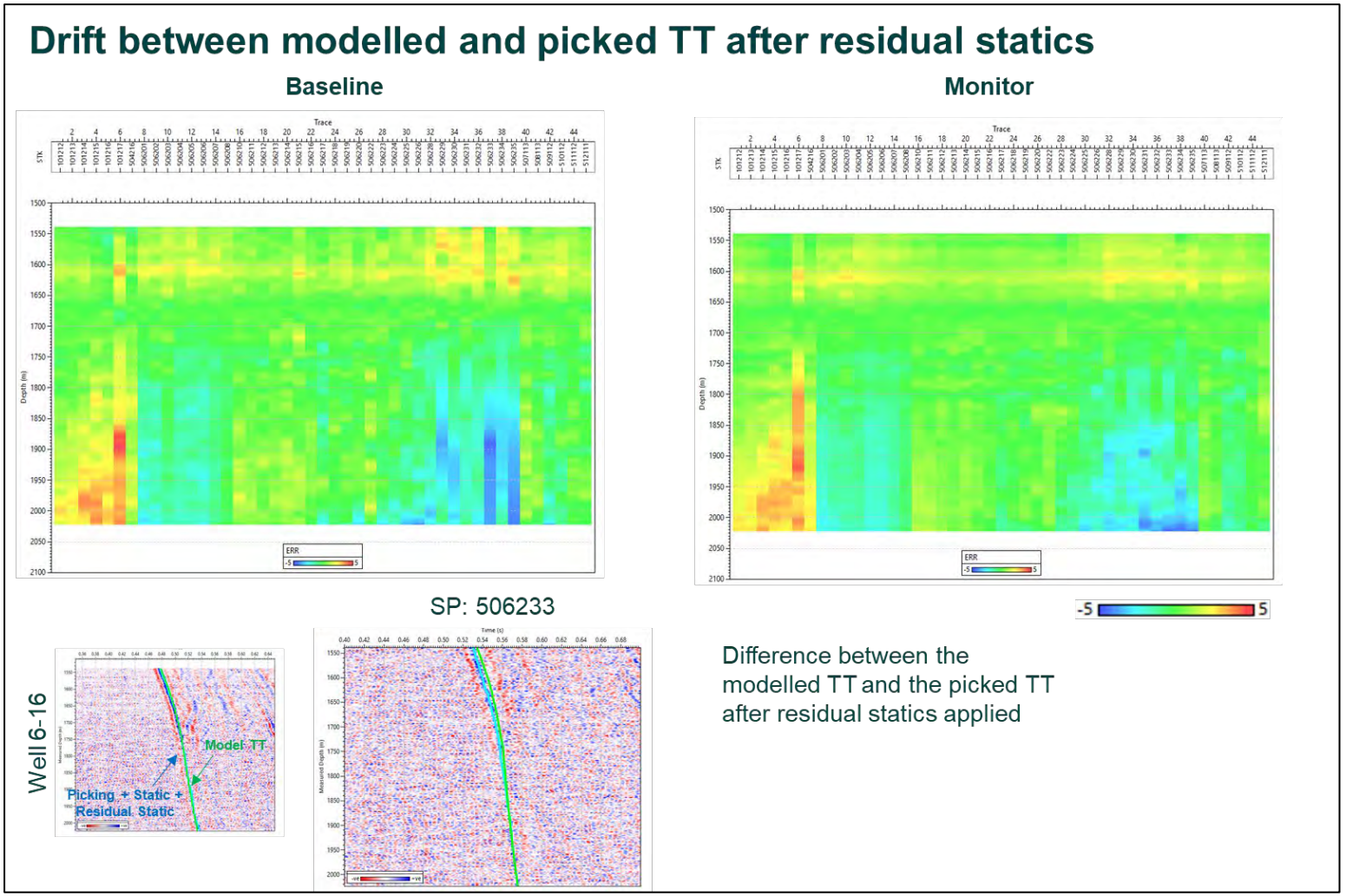


*Figure 8-47. Drift between modelled and picked TT after residual statics - Data and picks shifted. In this figure is the residual drift after the residual statics were applied. For the offsets close to the well the residual drift is close to zero, but for the far offsets there is still some residual drift due to the high FB picking uncertainly (Fig. 8.47 mid bottom).*

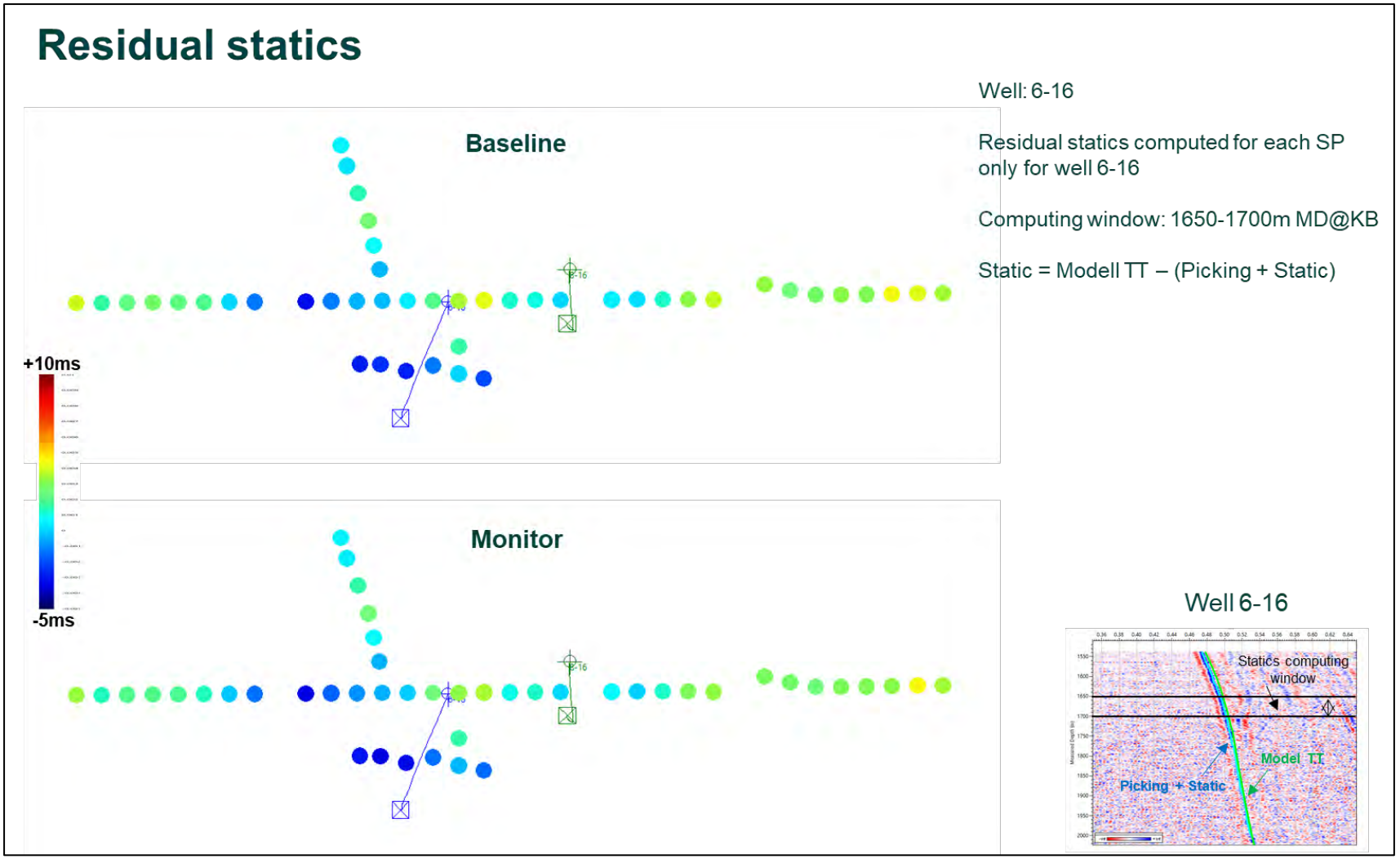


*Figure 8-48. Residual statics - Plane view with residual statics for each SP. Residual static shift values were calculated separately for the baseline and the monitor survey.*

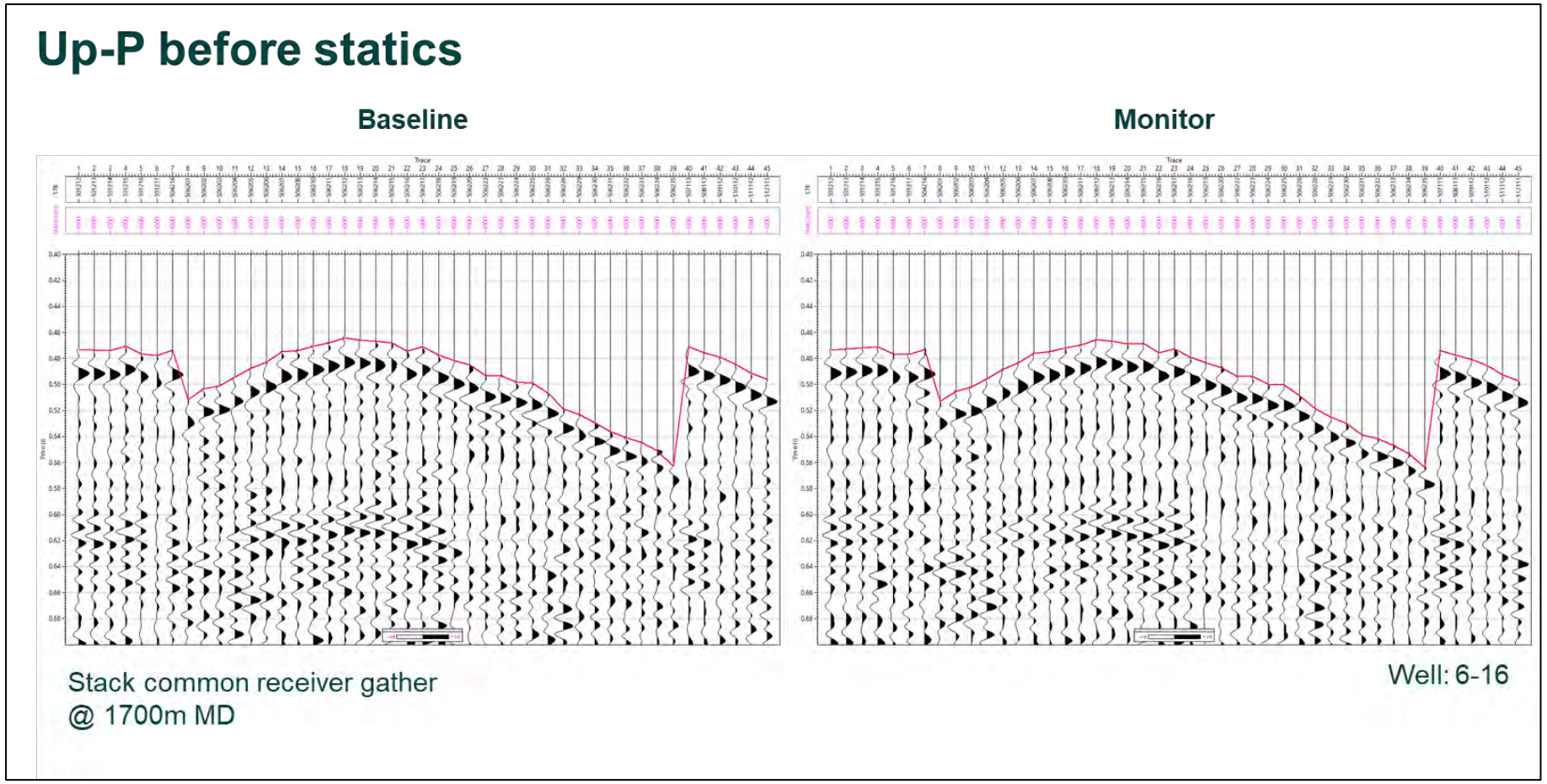


*Figure 8-49. Up-P before statics - Common receiver gather.*

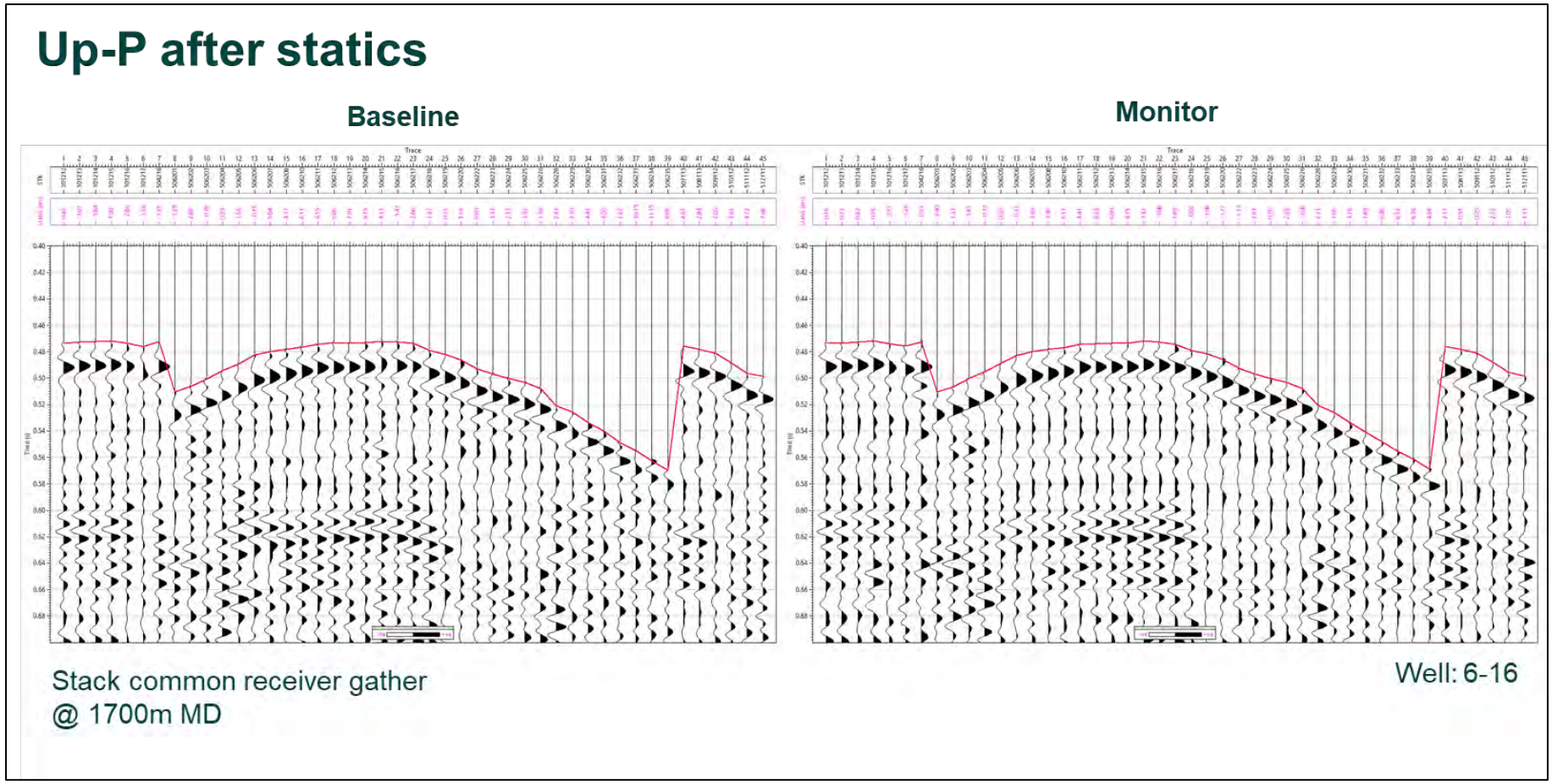


*Figure 8-50. Up-P after statics - Common receiver gather.*

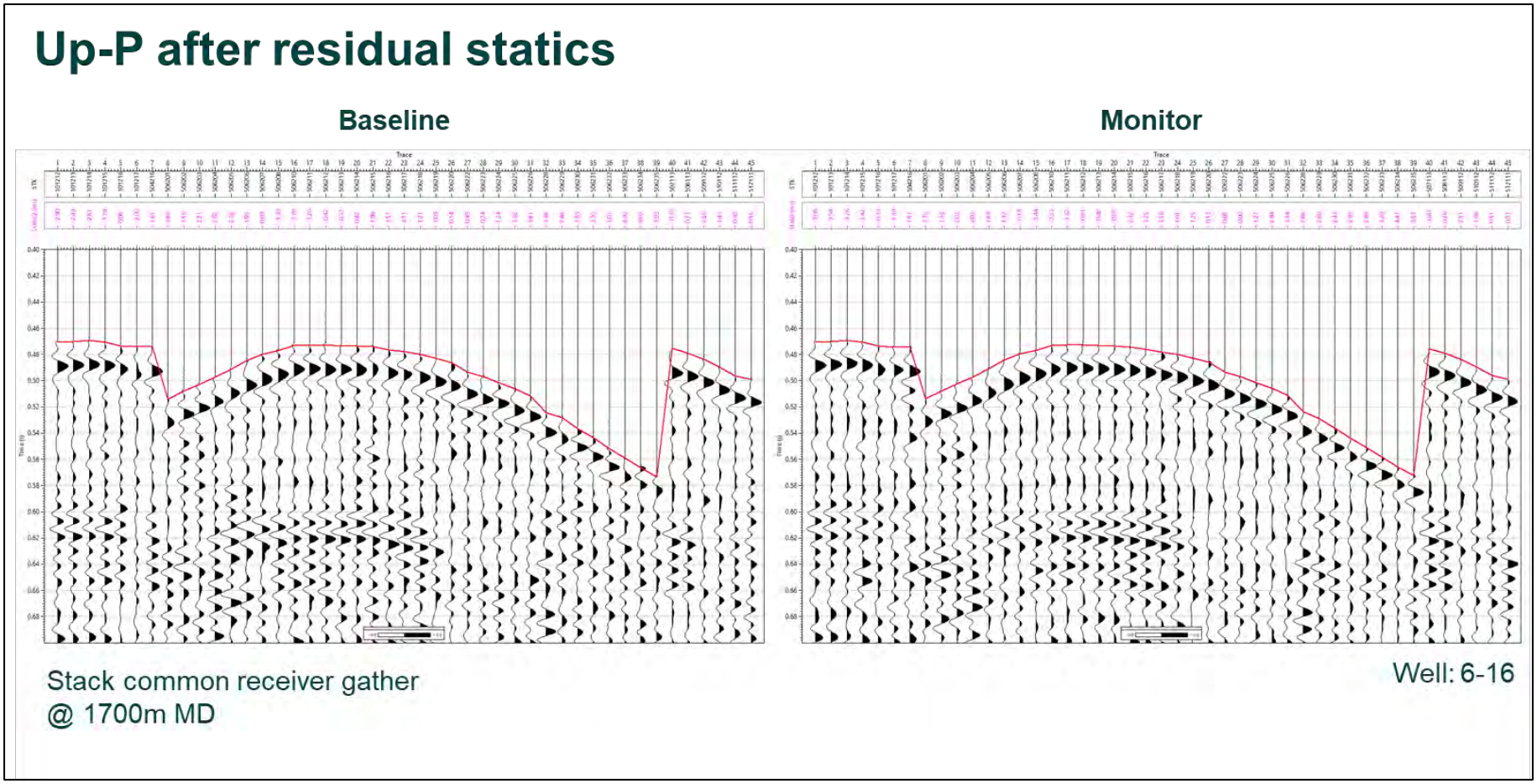


*Figure 8-51. Up-P after residual statics - Common receiver gather. This figure shows the Up P common receiver gather at 1700 m MD after residual statics correction. After the correction the data fit better an expected hyperbolic shape.*

# 9 Dynamite Data Processing

The dynamite sources have a single shot per location. A different processing workflow was built for dynamite data. The processing of the baseline and monitor data for the same well are identical. Figure 9-1 shows the dynamite data processing workflow and figure 9-2 shows the applied statics workflow.

## 9.1 Well 8-16

### 9.1.1 Data selection and de-noising

Figures 9-3 and 9-4 present the baseline and the monitor raw stacks for SP 503222 (close to the well), SP 508214 (mid offset to the north) and SP 515215 (far offset to the north). The baseline survey noise level is higher compared to the monitor survey. We used the same data interval, below 1050 m MD, for well 8-16 dynamite shots as for well 8-16 vibroseis shots.

### 9.1.2 Picking

We conditioned the data before picking: the wavefield was filtered with a low pass filter with 90 Hz cut-off frequency, enhanced along the modelled FB with a 17 trace window, filtered again with an BPF 5,10-100,120Hz and enhanced again along the modelled FB over 13 traces (Fig. 9-5). The modelled Down P transit time was used to guide the automatic picking which was performed on enhanced data on the first peak. The picking on the peak was used to guide the picking on the first trough. The picks were interpolated and smoothed over 5 levels. In figure 9-6 are the picked stacks for the same SP. Figures 9-7 and 9-8 show the same data as figures 9-5 and 9-6 for the monitor survey.

### 9.1.3 Down-waves

Figure 9-9 shows the data used as input for processing: a filtered stack data from the SP 503222. The amplitudes displayed are cross-normalized.

To reduce the noise due to the box vibration, in the FK domain the amplitudes were attenuated in the wavenumber window -1.7 to 1.7 (Fig. 9-10). The result is presented in figure 9-11. A 5,10-90,110Hz band pass filter was then applied (Fig. 9-12).

To reduce the casing ringing a 66-92 Hz tracking filter was applied over the following intervals: 1094-1146 m MD, 1180-1265 m MD, 1265-1326 m MD, 1412-1444 m MD, 1485-1533m MD followed by a BPF: 5,10-90,110 Hz (Fig. 9-13).

To compensate for the absorption and spherical divergence spreading, the amplitude was scaled by the squared sample time. Figure 9-14 shows the stack after amplitude recovery.

Figure 9-15 shows the stack aligned along the first break in the frequency-slowness domain (FP). The Down wavefield was separated inside the -1.7 – 0.6 slowness window. Figure 9-16 presents the data after the separation in the FP domain. The data from figure 9-16 was muted above the tube wave limit (Fig. 9-14 black).

Figure 9-17 shows the Down P wavefield after enhancement with a median filter of 121 traces along the FB. This wavefield will be used later in the deconvolution.

### 9.1.4 Reflections

The Up P wavefield was separated in the FP domain in a slowness window of -0.10 to 0.10 ms/trace (Fig. 9-18). The input data was aligned along the A2 Carbonate modelled TT (Fig. 9-14 green) before FP. Figure 9-19 shows the enhanced Up P along the modelled A2 Carbonate TT over a 10 trace window after the separation in the FP domain.

To reduce the multiples and increase the data high frequency bandwidth, the enhanced Up P were deconvolved (Fig. 9-20). Trace by trace deterministic deconvolution with the enhanced Down P (Fig. 8-17) using a 0.15 s operator length and 20% white noise was applied to the enhanced Up P. Finally, the data were filtered with a 5,10-90,110 Hz BPF.

Figures 9-21 and 9-22 present the baseline and the monitor Up P wavefield after deconvolution for SP 503222 (south of the well head), SP 508214 (mid offset to the north-west) and SP 515215 (far offset to north). The reef reflectors are only visible at the near offsets, at the same level with the noise at mid offsets and below the noise level at the far offsets. Notice that the baseline data present a slightly higher noise level. The noise level is boosted by the deconvolution.

### 9.1.5 Statics

In land seismic surveys, most of the energy is absorbed in the weathering zone. For this reason, the dynamite charges are located in shallow wells preferably drilled below the weathering zone in more compact formations.

Dynamite data went through the same static workflow as the vibroseis data (Fig. 9-2).

In figure 9-23 is presented the drift between the modelled TT after the ray tracing and the picked TT for the baseline survey. The difference between the model TT and the picked TT was computed for each SP all along the available data interval. On the horizontal axis is the Shot Point number, on the vertical axis is the Measured Depth (MD from KB) and the difference is colour coded. The error mainly looks like vertical stripes suggesting that is mainly a static shift between the model and the picks. Between nearby shots is a gradual increase or decrease in error. Between the baseline (Fig 9-23) and monitor survey (Fig. 9-24), the errors are different due to different season but also due to the picking uncertainty, however they follow the same pattern confirming that the shift is mainly due to the lateral velocity changes in the weathering zone.

Figures 9-25 and 9-26 show the residual drift after the statics were applied to the data. Figures 9-27 and 9-28 present the data below 1500 m MD with a -5/+5 ms scale. The residual drift after the statics is close to zero on the near and mid offsets and higher on the far offsets due to picking uncertainly.

For each SP a static shift was calculated by averaging the drift between the model and the picks in the 1200m-1600mMD interval located above the reservoir (Fig. 9-29 bottom left). Static shift values were calculated separately for the baseline and the monitor surveys (Fig. 9-29).

Up P common receiver gather at 1700 m MD before and after statics correction for the baseline survey is presented in figures 9-30, respectively 9-31 and for the monitor survey in figures 9-32 and 9-33. After the correction, data fit better an expected hyperbolic shape.

## 9.2 Well 6-16

### 9.2.1 Data selection and de-noising

The baseline and monitor raw stacks for SP 502213 (close to the well head), SP 507216 (close to the well TD) and SP 515220 (far offset to the north) are presented in figure 9-34 and respectively 9-35. The baseline survey noise level is higher compare with the monitor survey. Data above 1540 m MD is affected by ringing, more visible at near offsets. Only data below this level was used for processing. The signal level is slightly above the noise only at the shot point close to the well head.

### 9.2.2 Picking

Before picking the wavefield was filtered using a low pass filter up to 90 Hz, enhanced along the modelled FB using a 17 trace window, filtered with an BPF 5,10-100,120Hz and enhanced again along the modelled FB over 13 traces (Fig. 9-36). The modelled Down P transit time was used to guide the automatic picking which was performed on enhanced data on the first peak. The picking on

the peak was used to guide the picking on the first trough. The picks were interpolated and smoothed over 5 levels. In figure 9-37 are presented the stacks after picking for the same SP. Figures 9-38 and 9-39 show the same data as figures 9-36 and 9-37 for the monitor survey. Only the data near to the well have a visible first arrival, on the rest of the data the picks follow the model TT.

### 9.2.3 Down-waves

Figure 9-40 shows the processing input data, a filtered stack data from the SP 502213. The amplitudes displayed are cross-normalized.

To reduce the noise due to the box vibration, in the FK domain the values in the -1.7 to 1.7 wavenumber window were attenuated (Fig. 9-41). The shot after this attenuation is presented in figure 9-42. A band pass filter in the range 5, 10 - 90, 110Hz was then applied (Fig. 9-43).

To compensate for the absorption and spherical divergence spreading, the amplitude was scaled by the squared sample time. Figure 9-44 shows the stack after amplitude recovery.

Figure 9-45 shows the stack aligned along the first break in the frequency-slowness domain (FP). The Down wavefield was separated by retaining the data inside the -0.3 – 0.6 slowness window. Figure 9-46 presents the data after the separation in the FP domain.

Figure 9-47 shows the Down P wavefield after enhancement using a median filter of 121 traces along the FB. This wavefield will be used later in the deconvolution.

### 9.2.4 Reflections

The Up P wavefield was separated in the FP domain in a slowness window of -0.10 to 0.10 ms/traces (Fig. 9-48). The input data was aligned along the A2 Carbonate modelled TT (Fig. 9-44 green) before FP. Figure 9-49 shows the enhanced Up P along the modelled A2 Carbonate TT over a 10 trace window after the separation in the FP domain.

To reduce the multiples and increase the data high frequency, the enhanced Up P was deconvolved (Fig. 9-50). Trace by trace deterministic deconvolution with enhanced Down P (Fig. 8-47) using a 0.15 s operator length and 20% white noise was applied to the enhanced Up P. Finally, the data were filtered with a 5,10-90,110 Hz BPF.

Figures 9-51 and 9-52 present the baseline and respectively the monitor Up P wavefield after deconvolution for SP 502213 (close to the well head), SP 507216 (close to the well TD) and SP 515220 (far offset to the north)). The reef reflectors are visible only at near offsets, at the same level with the noise at mid offsets and below the noise level at the far offsets. Notice that the baseline data present a slightly higher noise level. The noise level is boosted by the deconvolution.

### 9.2.5 Statics

Since well 8-16 has a longer data interval above the area of interest, the statics were computed for each SP using only the well 8-16 data and applied to well 6-16 SPs. As ray travel paths in well 6-16 are different from those in well 8-16 a residual static shift was calculated only for well 6-16 (separately for the baseline and monitor surveys).

Figure 9-53 presents the drift between the modelled TT and the picked TT for the baseline survey. The difference between the model TT and the picked TT was computed for each SP all along the available data interval. On the horizontal axis is the Shot Point number, on the vertical axis is the Measured Depth (MD from KB) and the difference is colour coded. The difference mainly appears as vertical stripes suggesting there is mainly a static shift between the model and the picks. Between nearby shots there is a gradual increase or decrease in difference. Between the baseline (Fig 9-53) and monitor survey (Fig. 9-54), the errors have different values due to different weathering zone properties as well as the picking uncertainty. Nevertheless, both follow the same pattern confirming that the shift is mainly due to the lateral velocity changes in the weathering zone.

Figures 9-55 and 9-56 show the residual drift after the statics were applied to the data. Figures 9-57 and 9-58 present the data with a -5/+5 ms scale.

In figures 9-59 and 9-60 is the residual drift after the residual statics were applied. For the near offsets with a visible FB the residual drift is close to zero, but for the far offsets there is still some residual drift due to the high FB picking uncertainly.

Using the statics computed based on the well 8-16 data, the remaining error is still significant. Residual statics were computed by averaging the error over the 1540 m – 1600 m MD interval (Fig. 9-61 bottom left). Residual static shift values were calculated separately for the baseline and monitor surveys (Fig. 9-61).

The baseline Up P common receiver gather at 1700 m MD before and after statics correction is presented in figure 9-62, respectively 9-63. Figure 9-64 shows the baseline Up P common receiver gather at 1700 m MD after the residual statics correction. Figures 9-65 to 9-67 show the same data as figures 9-62 to 9-64 but for the monitor survey. After the correction data fit better an expected hyperbolic shape. We note that in the baseline survey the reflection at top A2 Carbonate is visible only at close offsets and some mid offsets.

| Title | Description | Figure |
|---|---|---|
| | | |
| **9 Dynamite Data Processing** | | |
| Processing Workflow | | **9.1** |
| Statics Workflow | | **9.2** |
| | | |
| **9.1 Well 8-16** | | |
| Well 8-16 – Baseline – Raw Stacks | Far, mid and near offset total wavefield | **9.3** |
| Well 8-16 – Monitor – Raw Stacks | Far, mid and near offset total wavefield | **9.4** |
| Baseline survey – Picking – Enhanced wavefield | Down P enhancement | **9.5** |
| Baseline survey – Picking | | **9.6** |
| Monitor survey – Picking – Enhanced wavefield | Down P enhancement | **9.7** |
| Monitor survey – Picking | | **9.8** |
| Raw Stack | | **9.9** |
| FK domain | CMN attenuation | **9.10** |
| Attenuate box vibrations | CMN attenuation | **9.11** |
| Band pass filter | | **9.12** |
| Ringing filter | Attenuate the ringing in affected intervals | **9.13** |
| Amplitude recovery | Time power function | **9.14** |
| FP domain – data aligned along first break picks | Down separation | **9.15** |
| Down wavefield | Down separation | **9.16** |
| Enhanced Down-P | Median filter | **9.17** |
| FP domain – data aligned along modelled A2 Carbonate TT | Enhance Up P | **9.18** |
| Enhanced Up-P | After FP separation | **9.19** |
| Deconvolved enhanced Up-P | Trace by trace deterministic deconvolution | **9.20** |
| Well 8-16 – Baseline – Deconvolved Up-P | Far, mid and near offsets | **9.21** |
| Well 8-16 – Baseline – Deconvolved Up-P | Far, mid and near offsets | **9.22** |
| Drift between modelled and picked TT before statics | Baseline | **9.23** |
| Drift between modelled and picked TT before statics | Monitor | **9.24** |
| Drift between modelled and picked TT after statics | Baseline | **9.25** |

| Title | Description | Figure |
|---|---|---|
| Drift between modelled and picked TT after statics | Monitor | **9.26** |
| Drift between modelled and picked TT after statics | Baseline | **9.27** |
| Drift between modelled and picked TT after statics | Monitor | **9.28** |
| Statics | Plane view with statics for each SP | **9.29** |
| Up-P before statics | Common receiver gather – Baseline | **9.30** |
| Up-P after statics | Common receiver gather – Baseline | **9.31** |
| Up-P before statics | Common receiver gather – Monitor | **9.32** |
| Up-P after statics | Common receiver gather – Monitor | **9.33** |
| | | |
| **9.2 Well 6-16** | | |
| Well 6-16 – Baseline – Raw Stacks | Far, mid and near offset total wavefield | **9.34** |
| Well 6-16 – Monitor – Raw Stacks | Far, mid and near offset total wavefield | **9.35** |
| Baseline survey – Picking – Enhanced wavefield | Down P enhancement | **9.36** |
| Baseline survey – Picking | | **9.37** |
| Monitor survey – Picking – Enhanced wavefield | Down P enhancement | **9.38** |
| Monitor survey – Picking | | **9.39** |
| Raw Stack | | **9.40** |
| FK domain | CMN attenuation | **9.41** |
| Attenuate box vibrations | CMN attenuation | **9.42** |
| Band pass filter | | **9.43** |
| Amplitude recovery | Time power function | **9.44** |
| FP domain – data aligned along first break picks | Down separation | **9.45** |
| Down wavefield | Down separation | **9.46** |
| Enhanced Down-P | Median filter | **9.47** |
| FP domain – data aligned along modelled A2 Carbonate TT | Enhance Up P | **9.48** |
| Enhanced Up-P | After FP separation | **9.49** |
| Deconvolved enhanced Up-P | Trace by trace deterministic deconvolution | **9.50** |
| Well 6-16 – Baseline – Deconvolved Up-P | Far, mid and near offsets | **9.51** |
| Well 6-16 – Baseline – Deconvolved Up-P | Far, mid and near offsets | **9.52** |
| Drift between modelled and picked TT before statics | Baseline | **9.53** |
| Drift between modelled and picked TT before statics | Monitor | **9.54** |
| Drift between modelled and picked TT after statics | Baseline | **9.55** |
| Drift between modelled and picked TT after statics | Monitor | **9.56** |
| Drift between modelled and picked TT after statics | Baseline | **9.57** |
| Drift between modelled and picked TT after statics | Monitor | **9.58** |
| Drift between modelled and picked TT after residual statics | Baseline | **9.59** |
| Drift between modelled and picked TT after residual statics | Monitor | **9.60** |
| Statics | Plane view with statics for each SP | **9.61** |
| Up-P before statics | Common receiver gather – Baseline | **9.62** |
| Up-P after statics | Common receiver gather – Baseline | **9.63** |
| Up-P after residual statics | Common receiver gather – Baseline | **9.64** |
| Up-P before statics | Common receiver gather – Monitor | **9.65** |
| Up-P after statics | Common receiver gather – Monitor | **9.66** |
| Up-P after residual statics | Common receiver gather – Monitor | **9.67** |

*Table 9-17 Dynamite Data Processing figures*

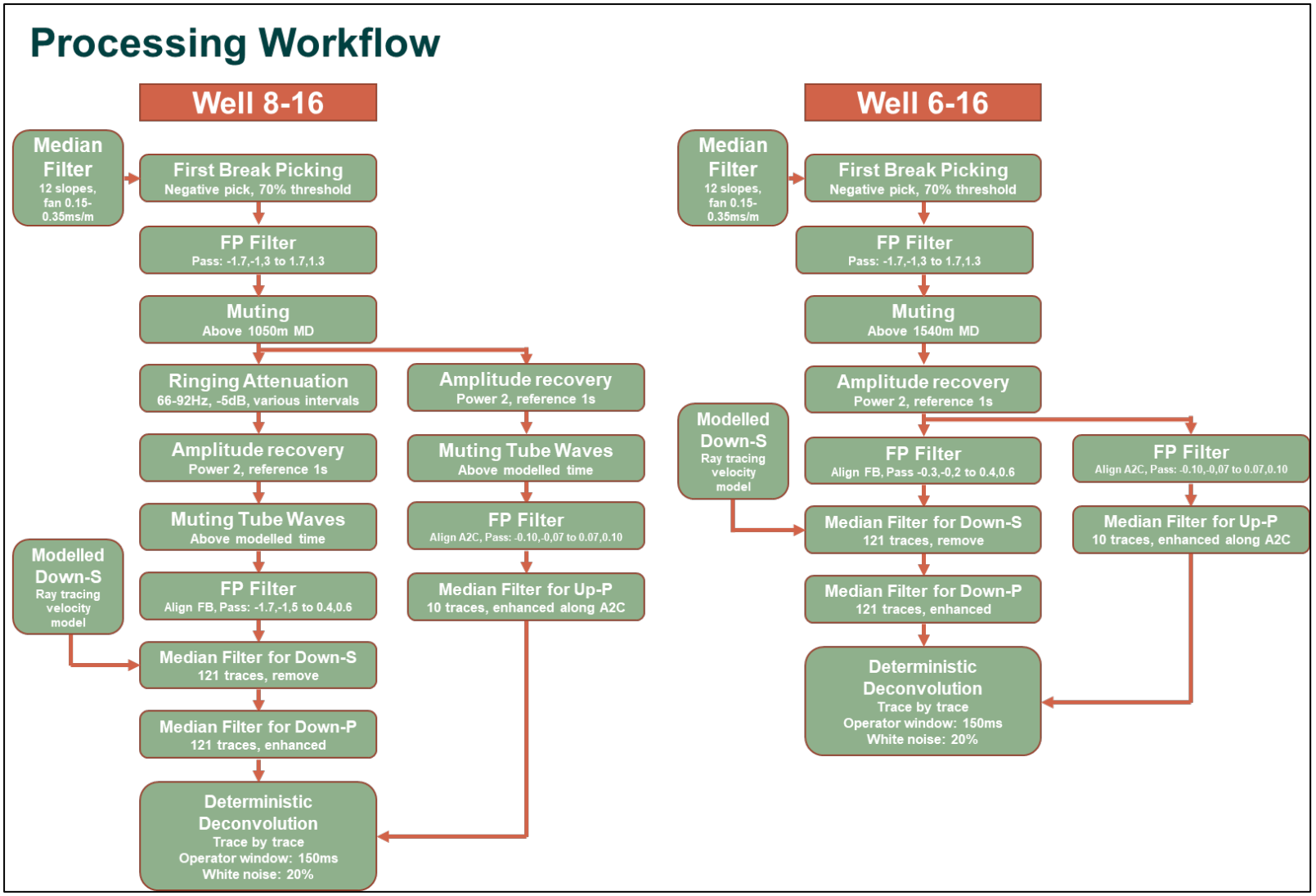


*Figure 9-1. Processing Workflow.*

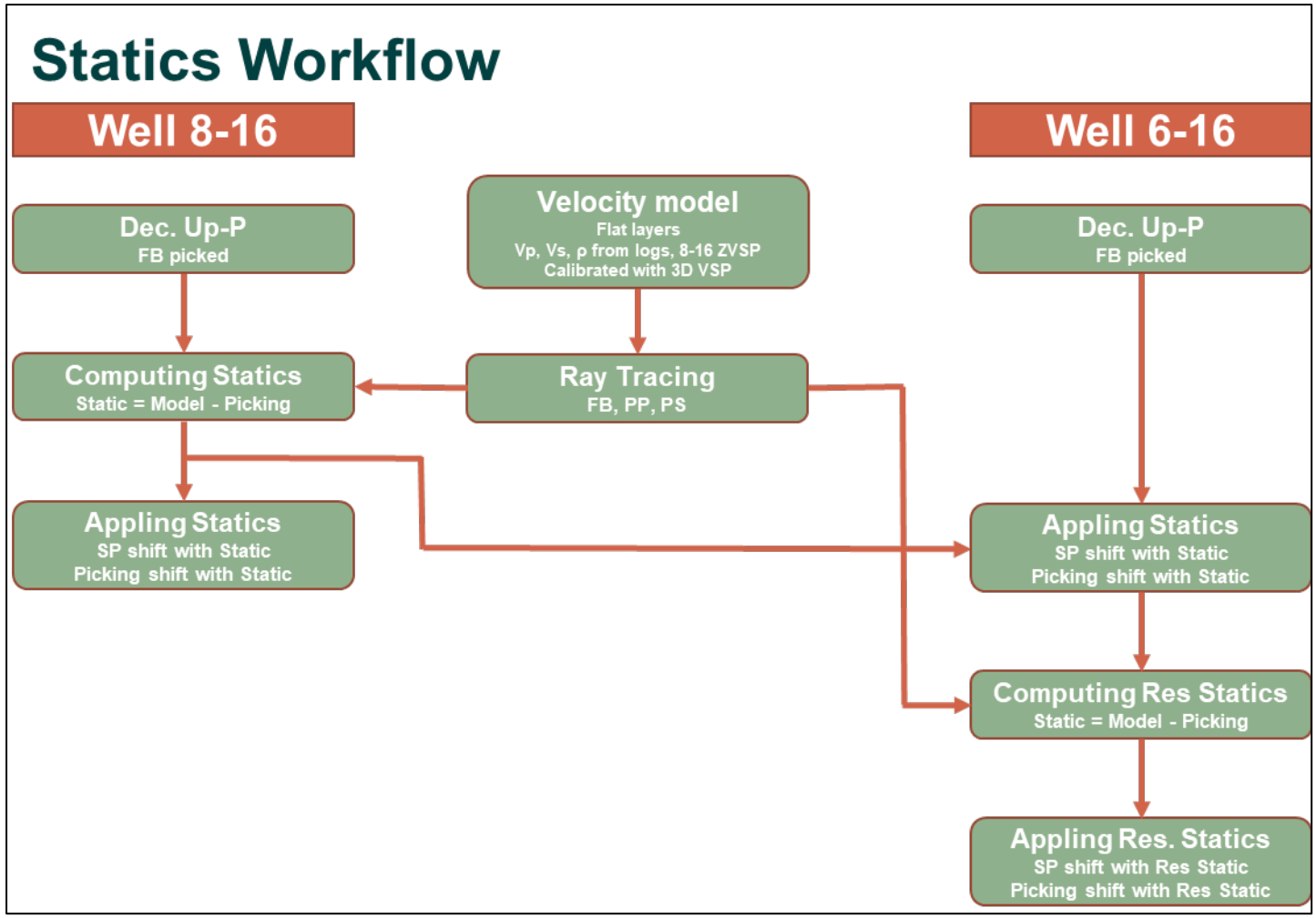


*Figure 9-2. Statics Workflow.*

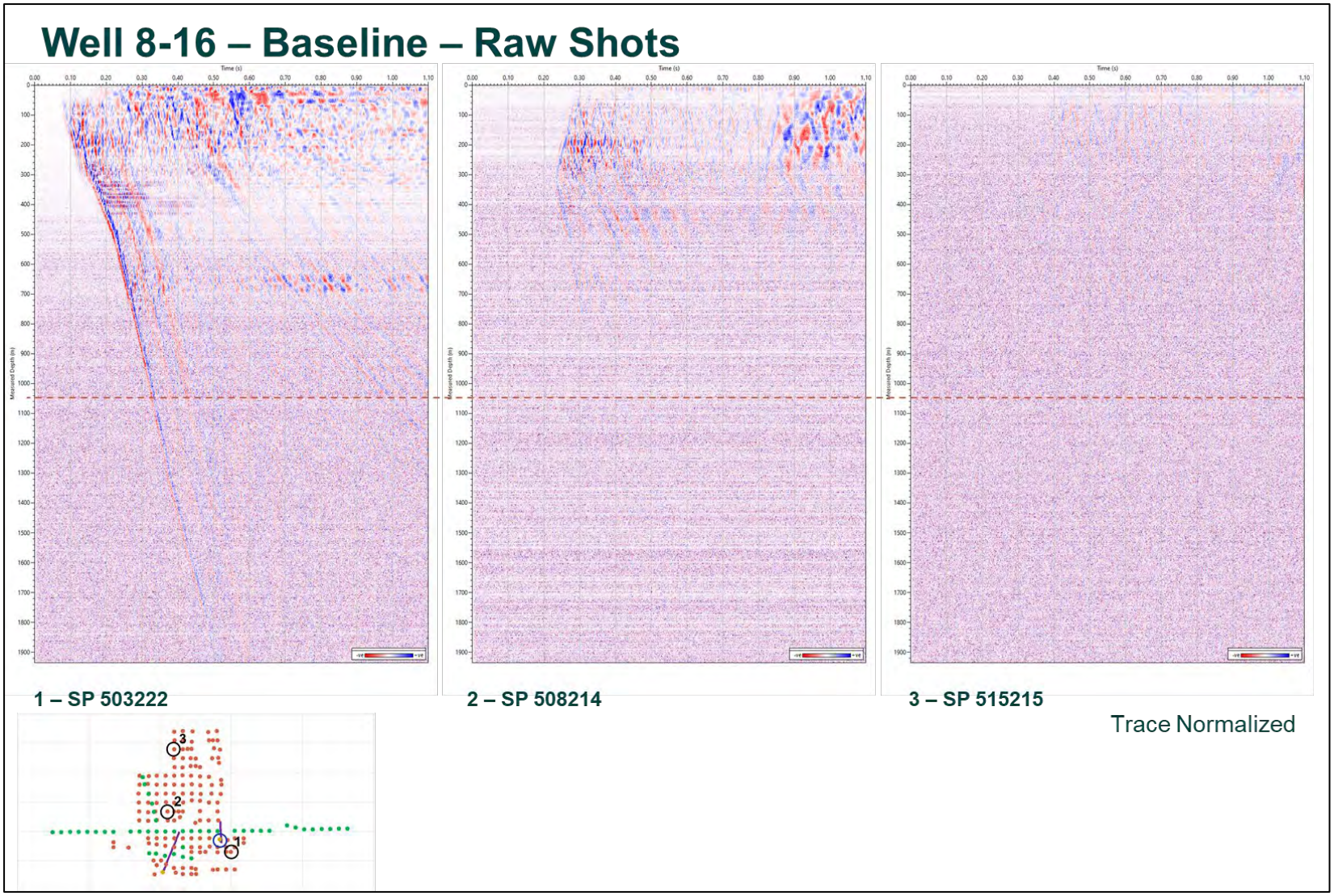


*Figure 9-3. Well 8-16 – Baseline – Raw Stacks - Far, mid and near offset total wavefield.*

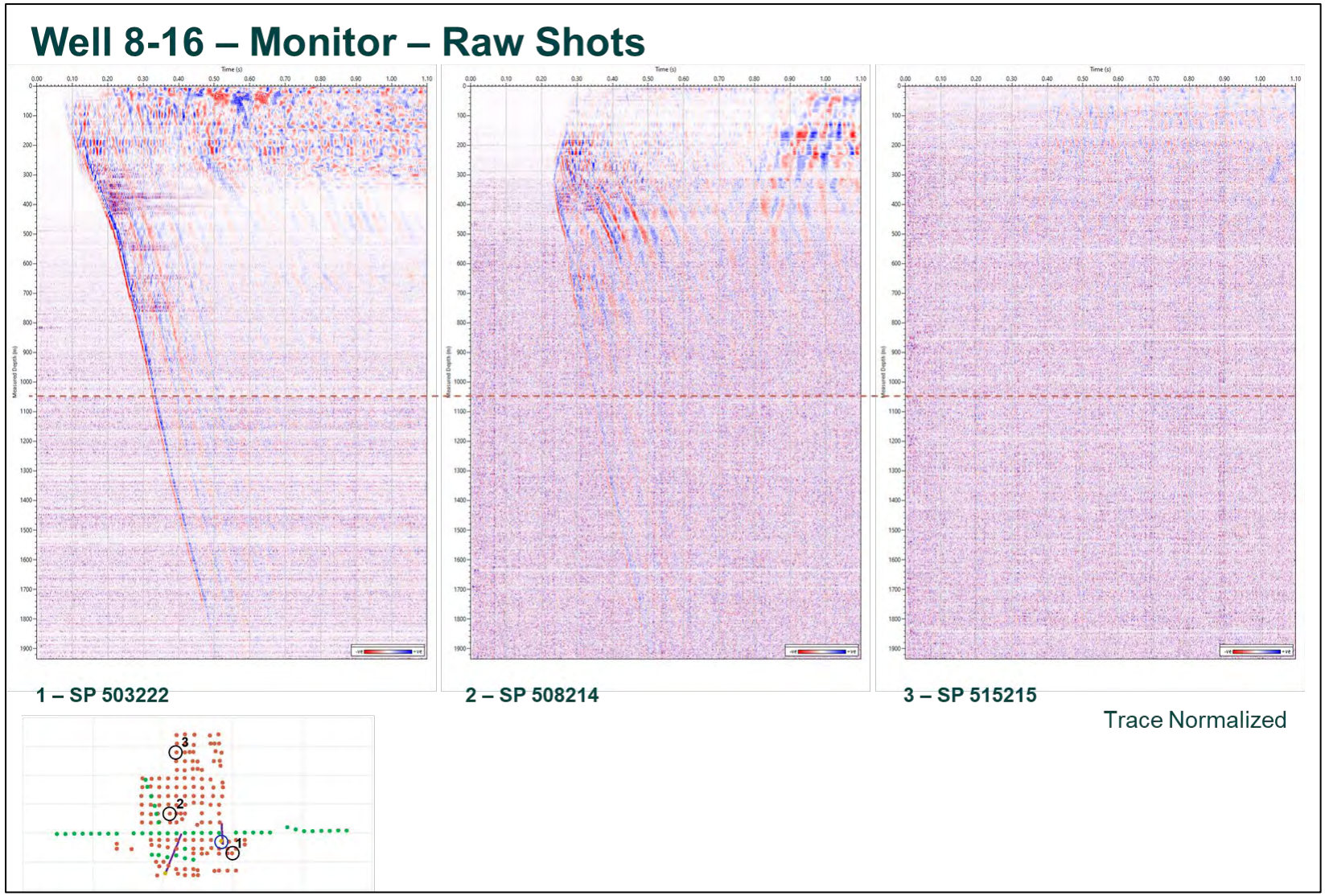


*Figure 9-4. Well 8-16 – Monitor – Raw Stacks - Far, mid and near offset total wavefield.*

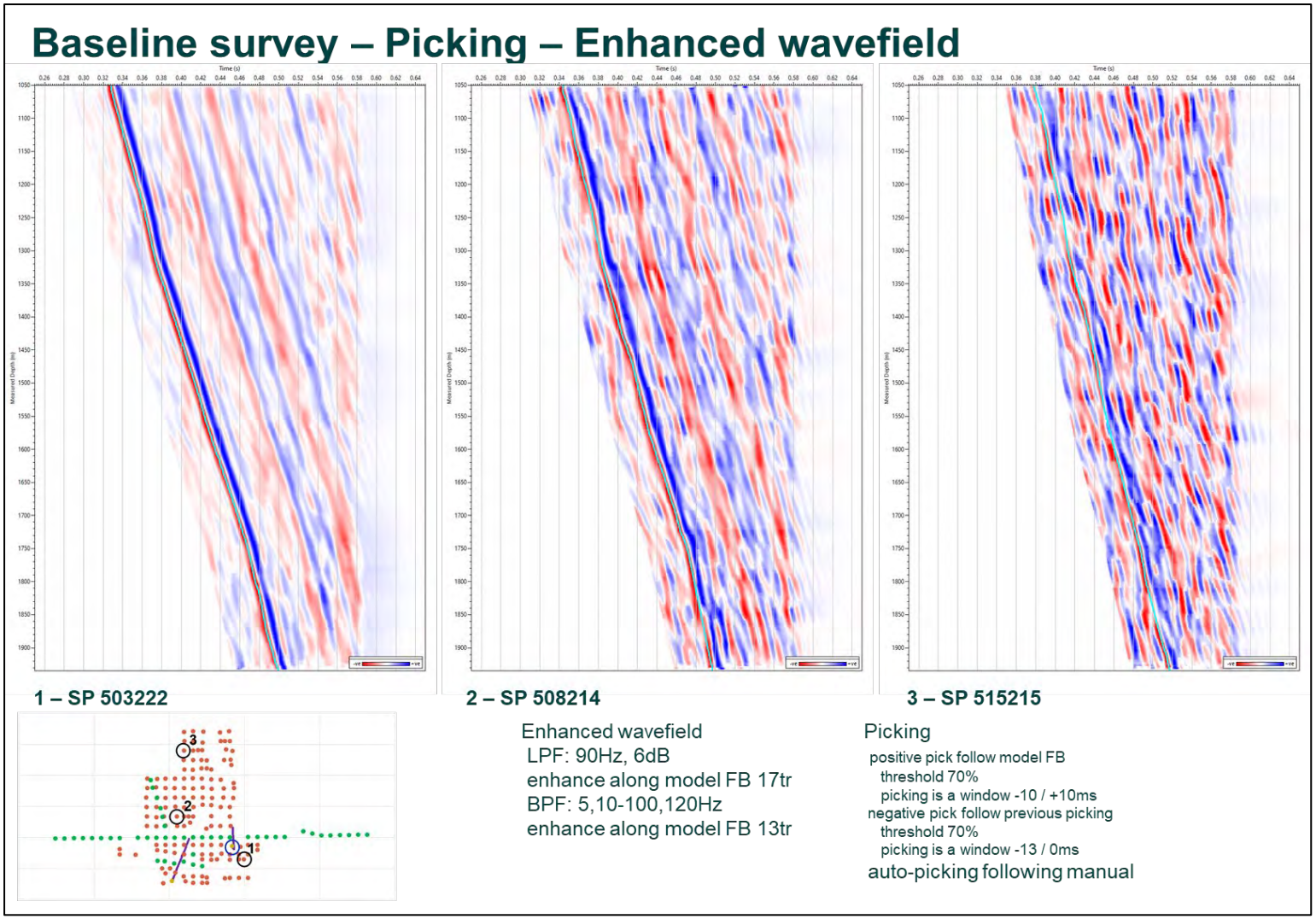


*Figure 9-5. Baseline survey – Picking – Enhanced wavefield - Down P enhancement. We conditioned the data before picking: the wavefield was filtered with a low pass filter with 90 Hz cut-off frequency, enhanced along the modelled FB with a 17 trace window, filtered again with an BPF 5,10-100,120Hz and enhanced again along the modelled FB over 13 traces.*

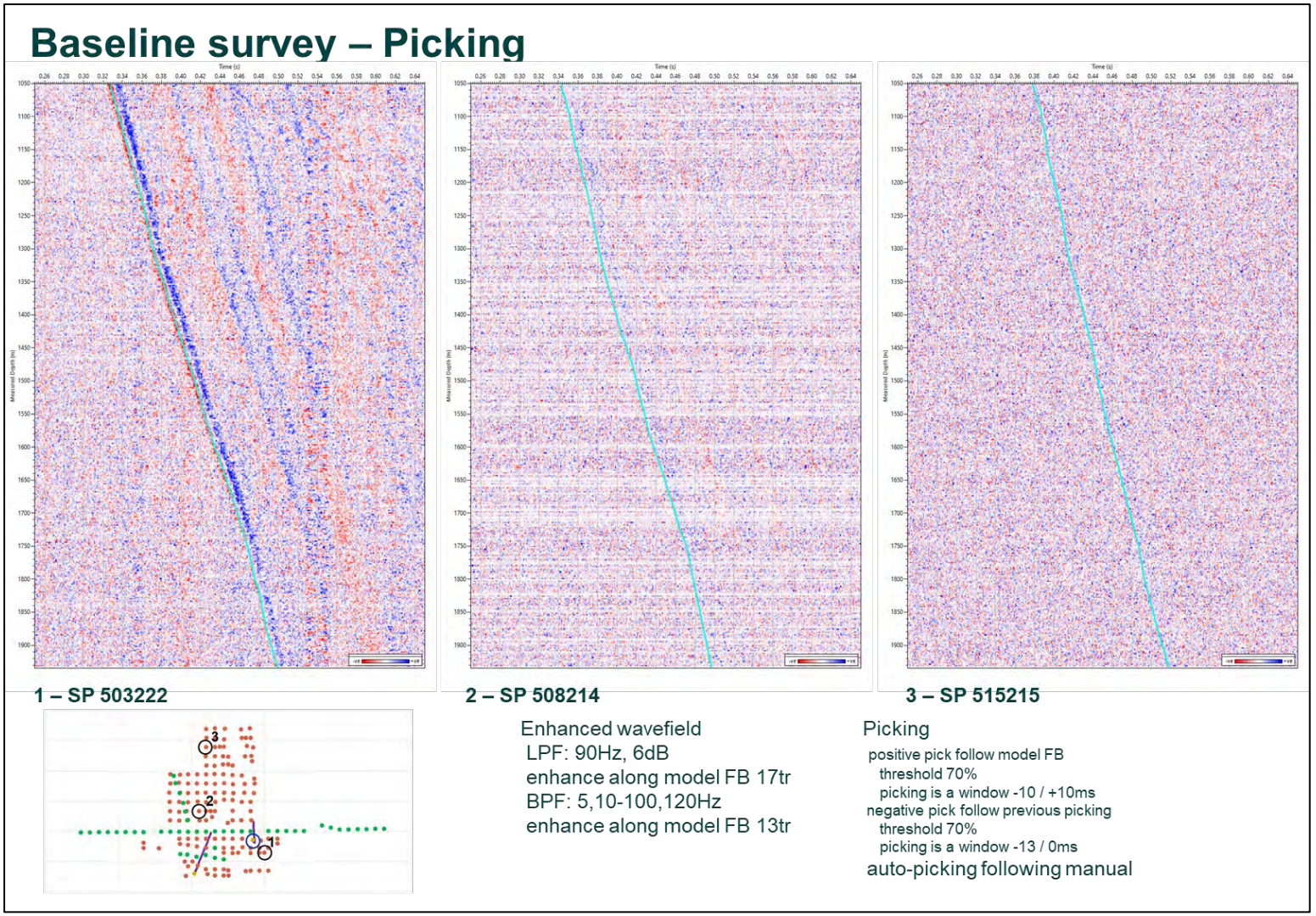


*Figure 9-6. Baseline survey – Picking. The modelled Down P transit time was used to guide the automatic picking which was performed on enhanced data on the first peak. The picking on the peak was used to guide the picking on the first trough. The picks were interpolated and smoothed over 5 levels. In figure 9.6 the picked stacks are for the same SP.*

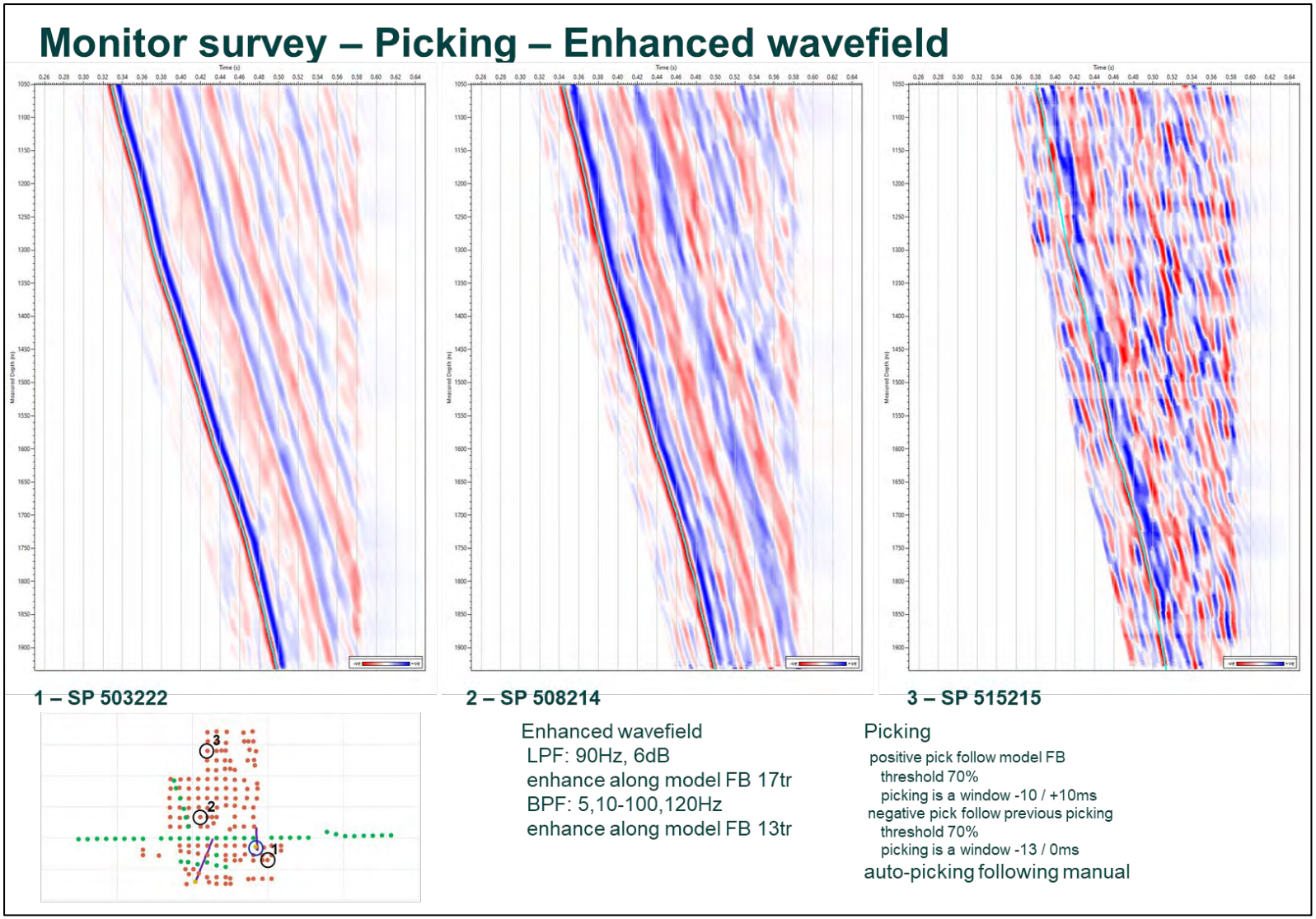


*Figure 9-7. Monitor survey – Picking – Enhanced wavefield - Down P enhancement.*

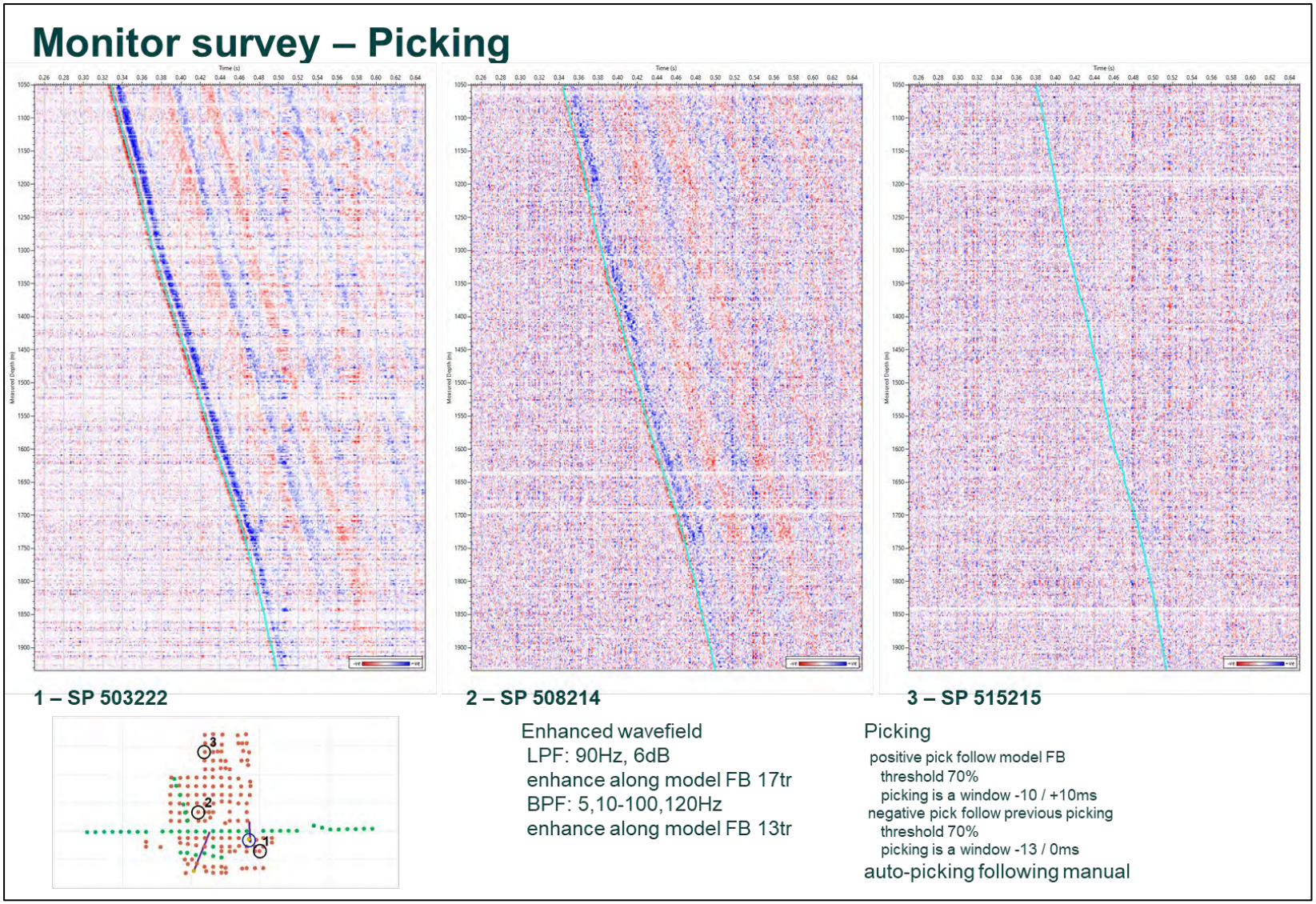


*Figure 9-8. Monitor survey – Picking.*

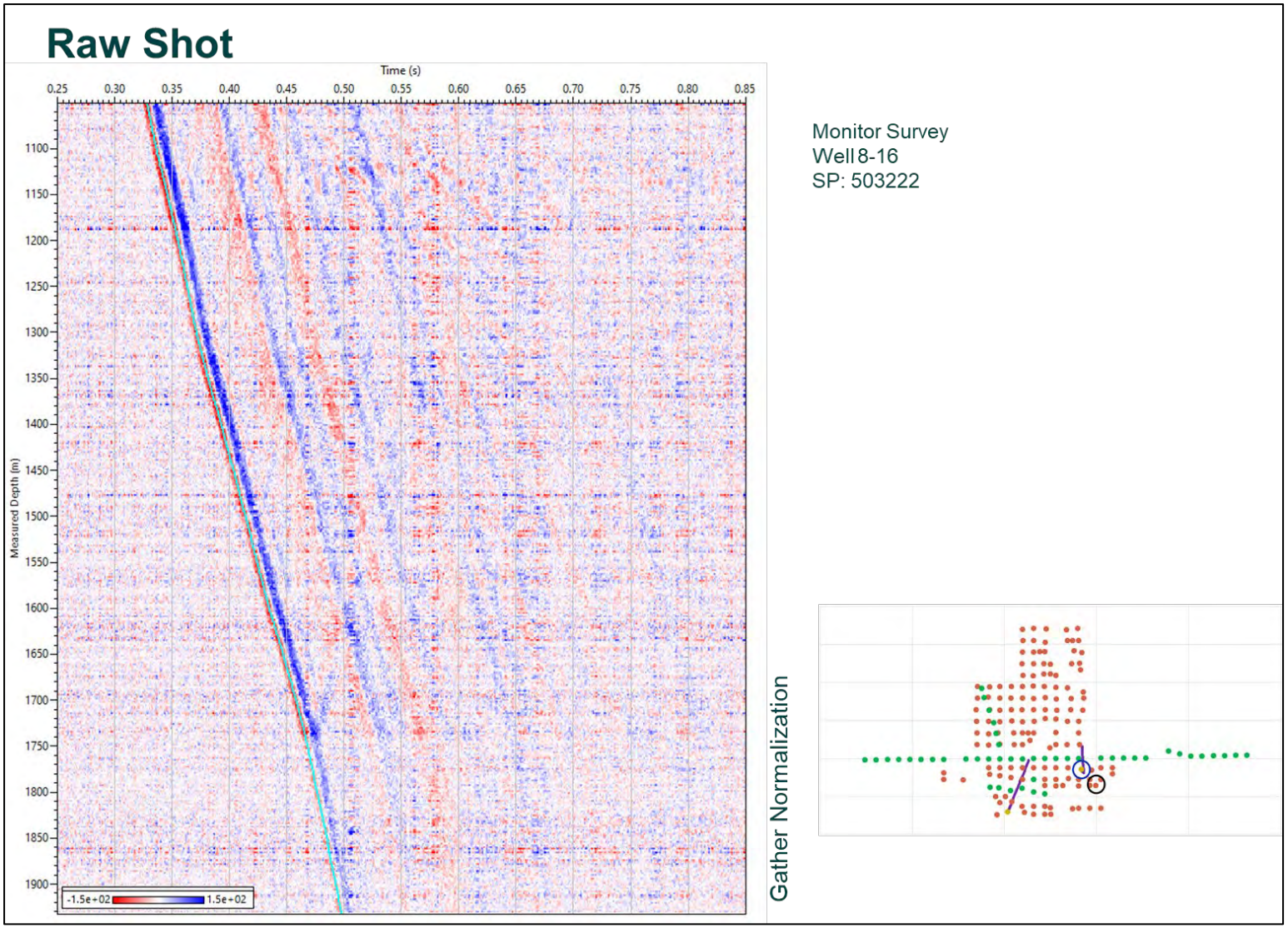


*Figure 9-9. Raw Stack. This figure shows the data used as input for processing: a filtered stack data from the SP 503222. The amplitudes displayed are cross-normalized.*

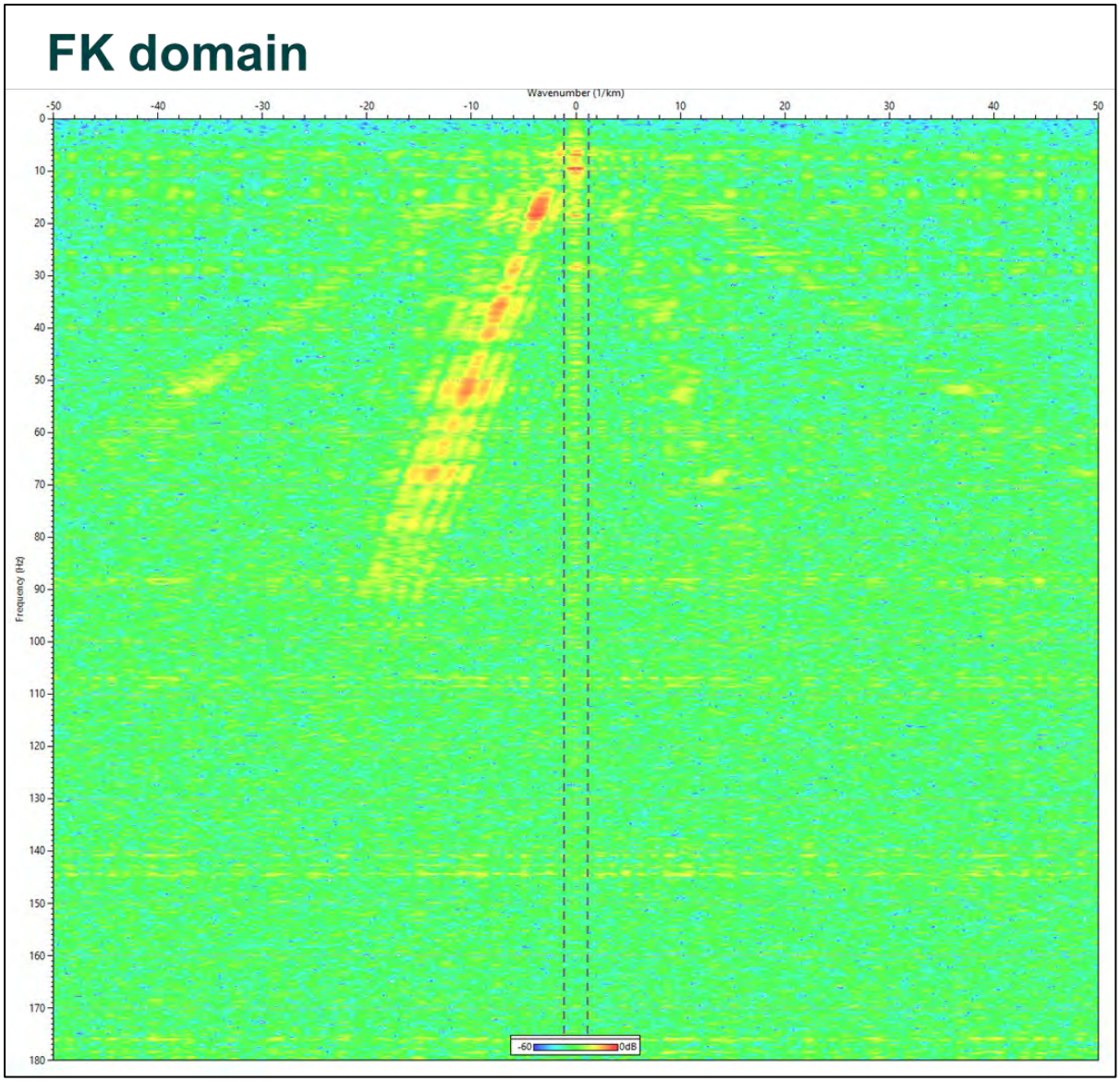


*Figure 9-10. FK domain - CMN attenuation. To reduce the noise due to the box vibration, in the FK domain the amplitudes were attenuated in the wavenumber window -1.7 to 1.7. The result is presented in Figure 9-11.*

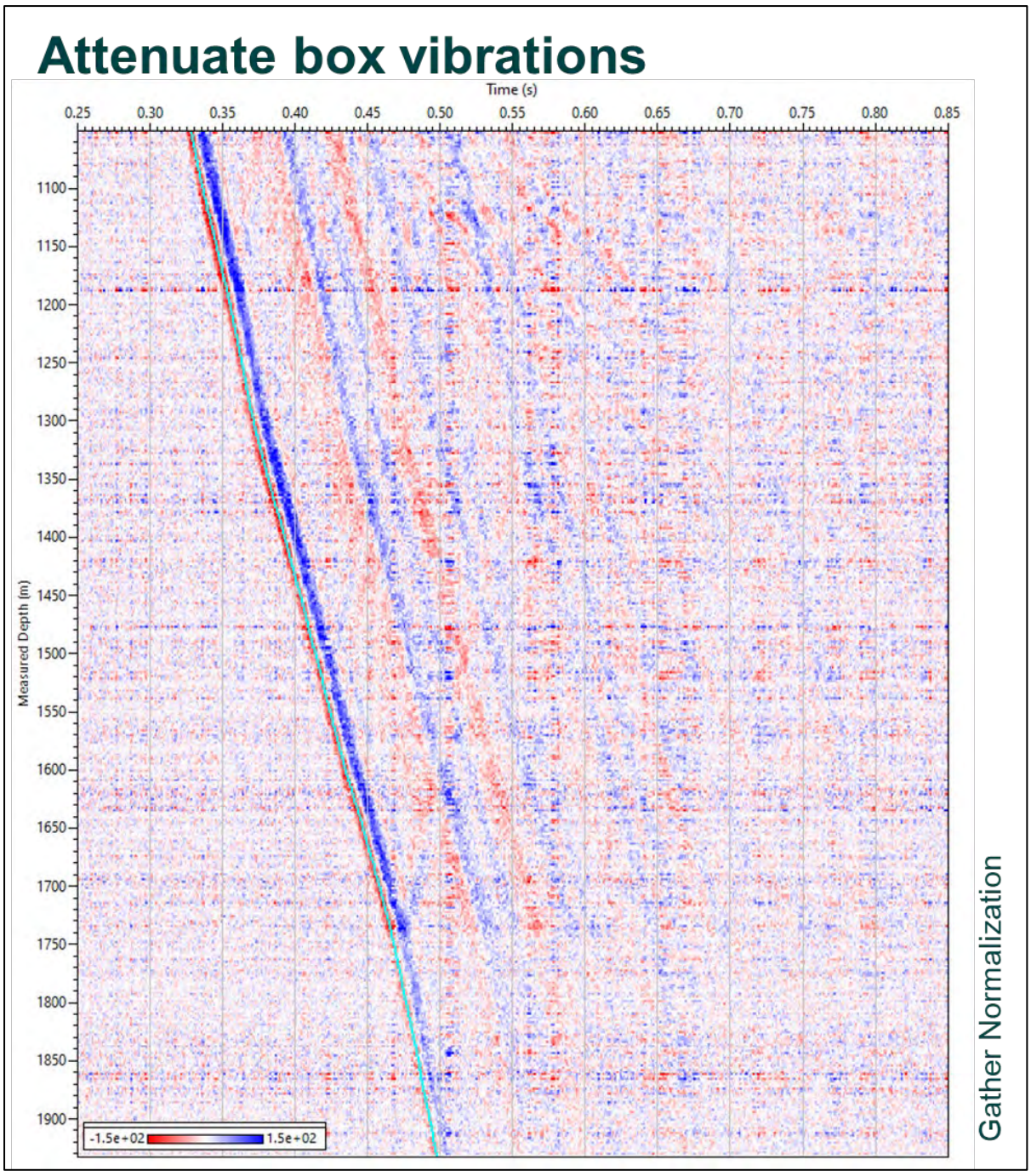


*Figure 9-11. Attenuate box vibrations - CMN attenuation.*

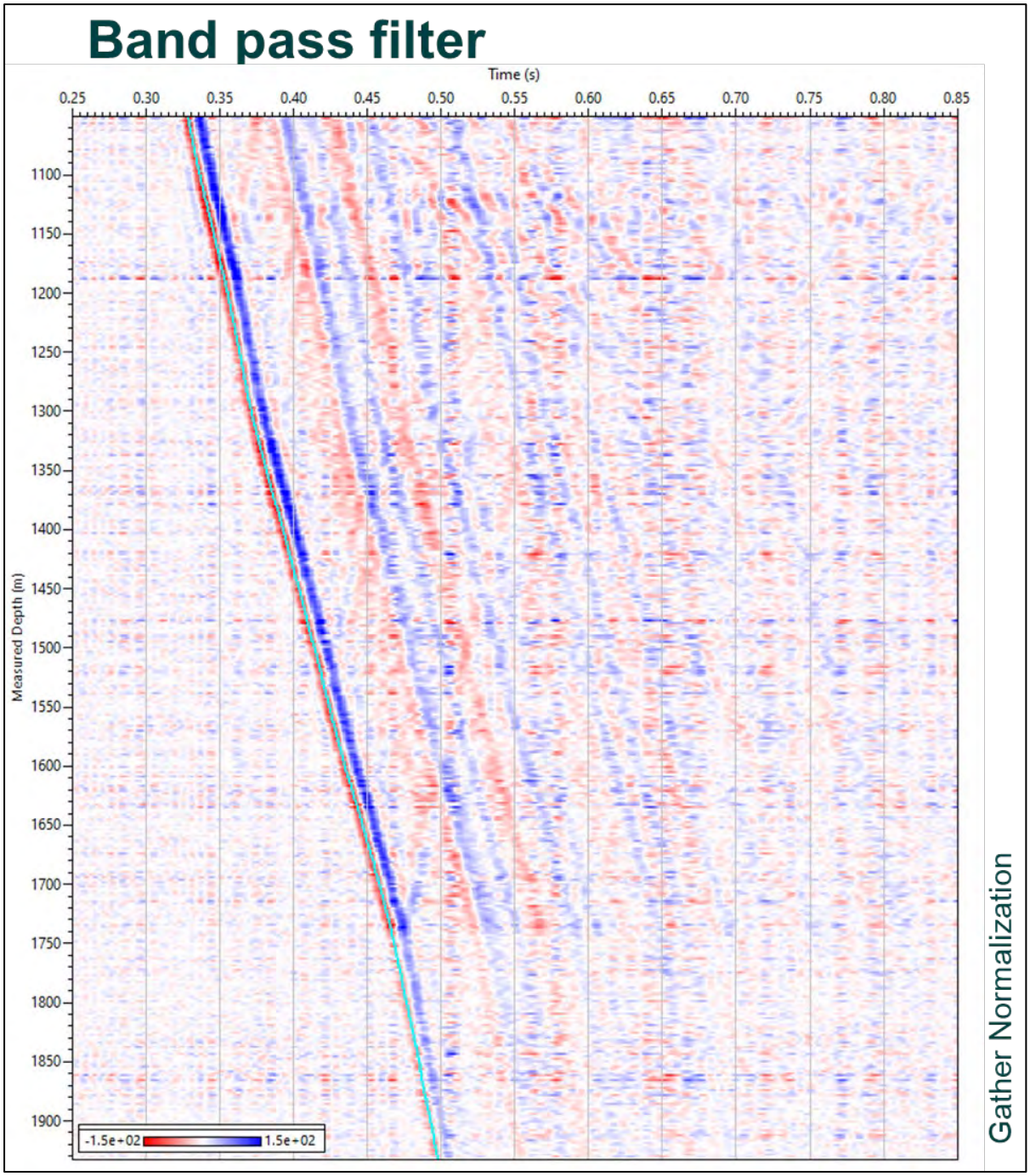


*Figure 9-12. Band pass filter. A 5,10-90,110Hz band pass filter was then applied.*

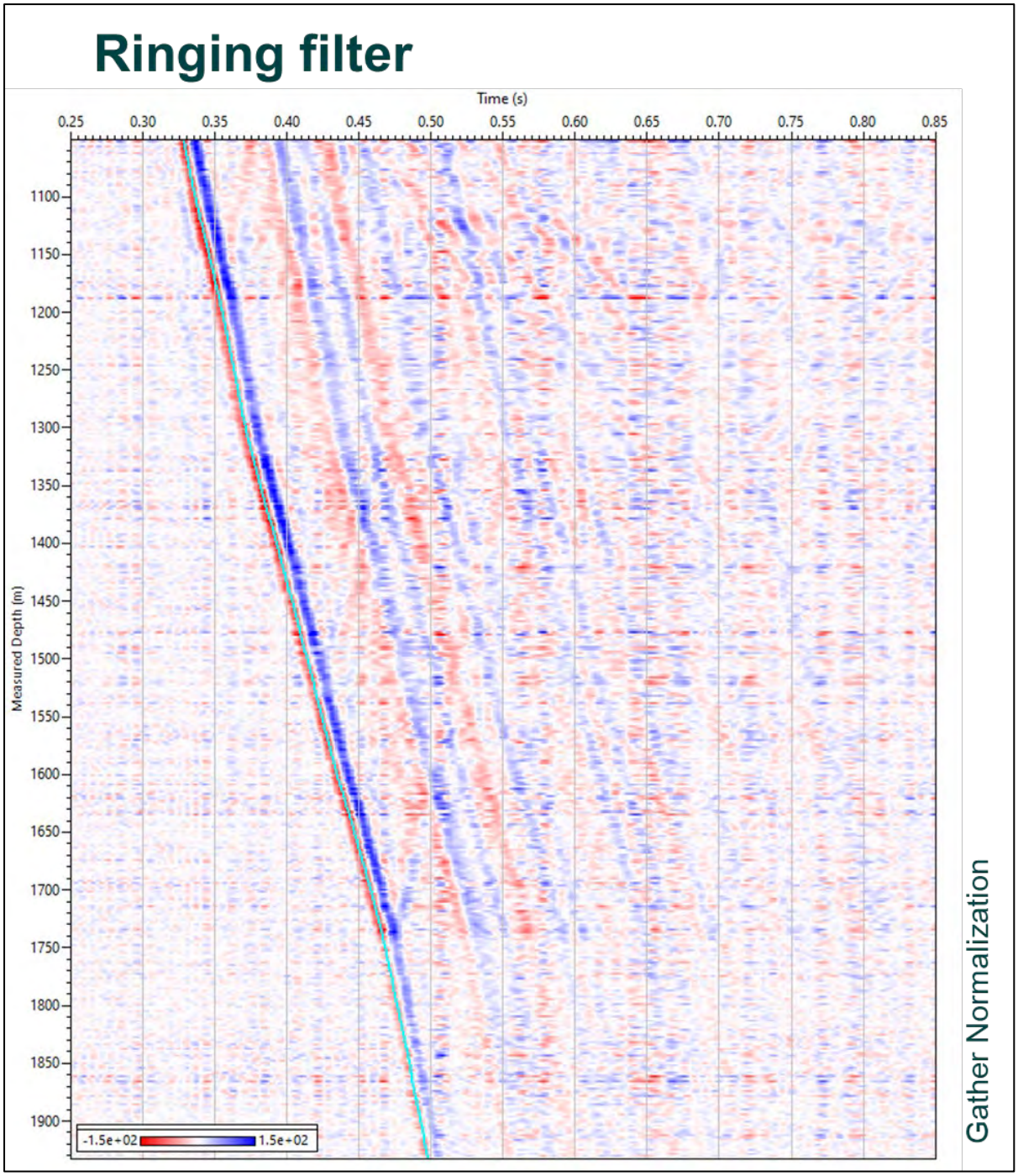


*Figure 9-13. Ringing filter - Attenuate the ringing in affected intervals. To reduce the casing ringing a 66-92 Hz tracking filter was applied over the following intervals: 1094-1146 m MD, 1180-1265 m MD, 1265-1326 m MD, 1412-1444 m MD, 1485-1533m MD followed by a BPF: 5,10-90,110 Hz.*

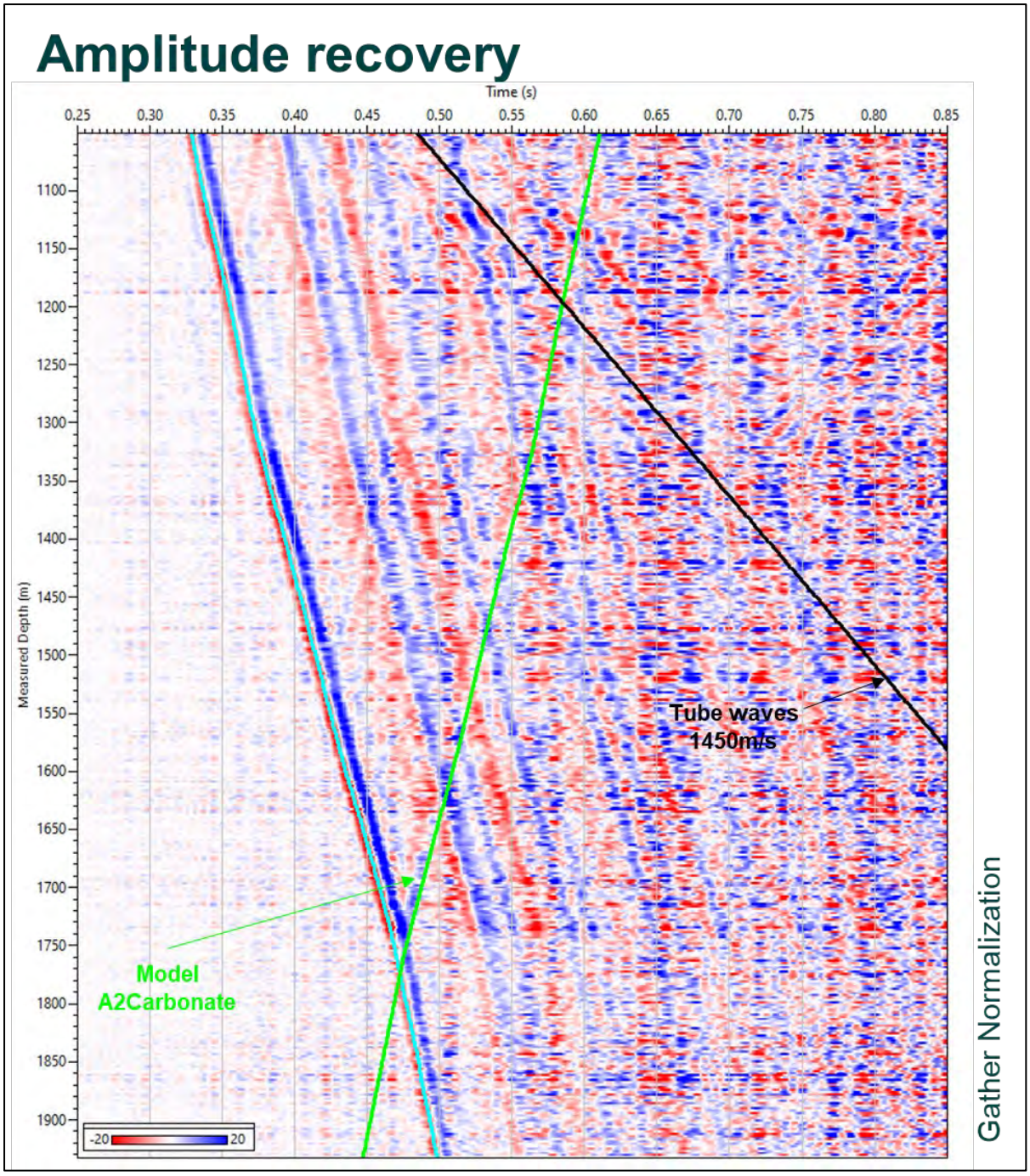


*Figure 9-14. Amplitude recovery - Time power function. To compensate for the absorption and spherical divergence spreading, the amplitude was scaled by the squared sample time. Figure 9.14 shows the stack after amplitude recovery.*

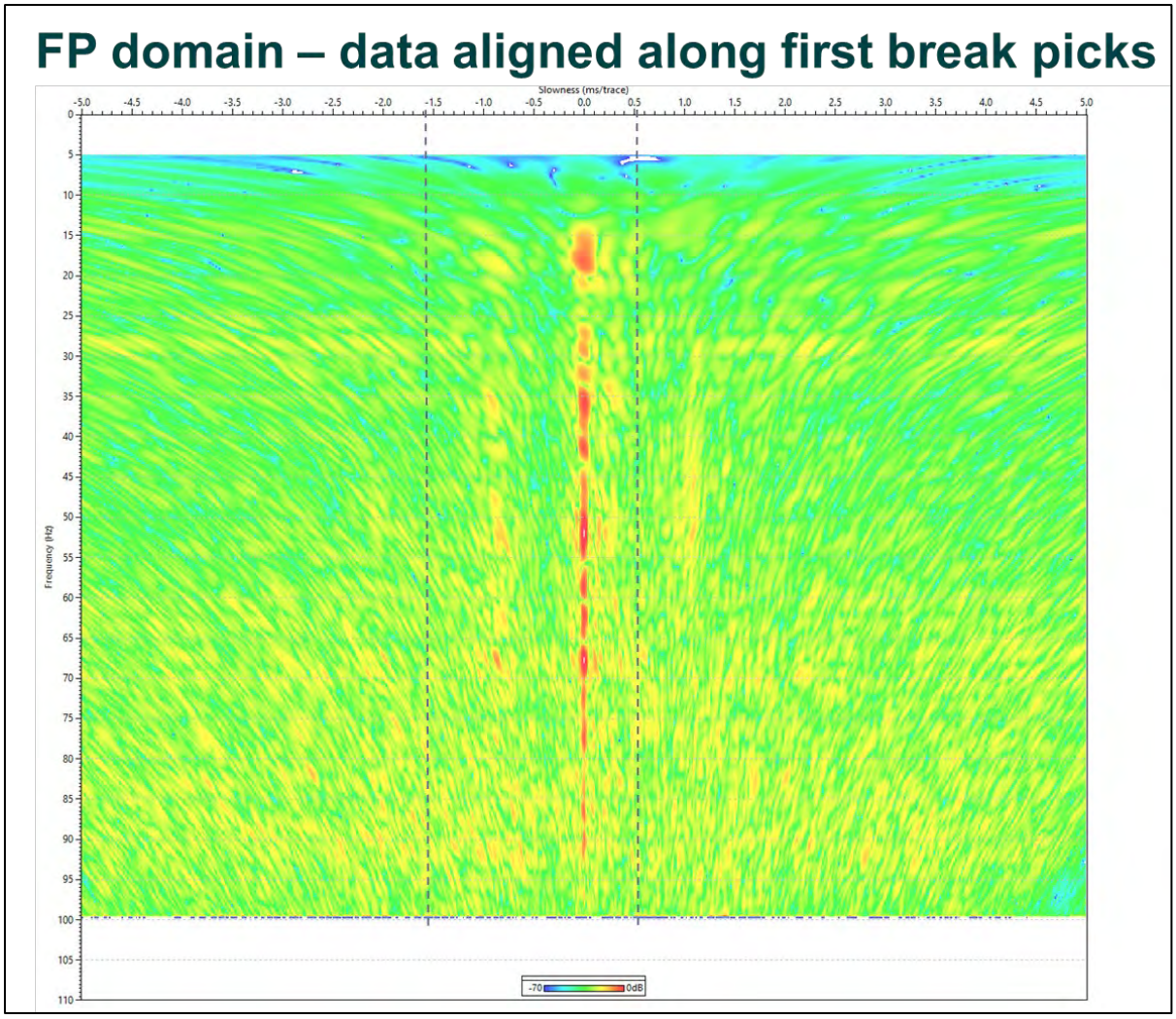


*Figure 9-15. FP domain – data aligned along first break picks - Down separation. This figure shows the stack aligned along the first break in the frequency-slowness domain (FP). The Down wavefield was separated inside the -1.7 – 0.6 slowness window.*

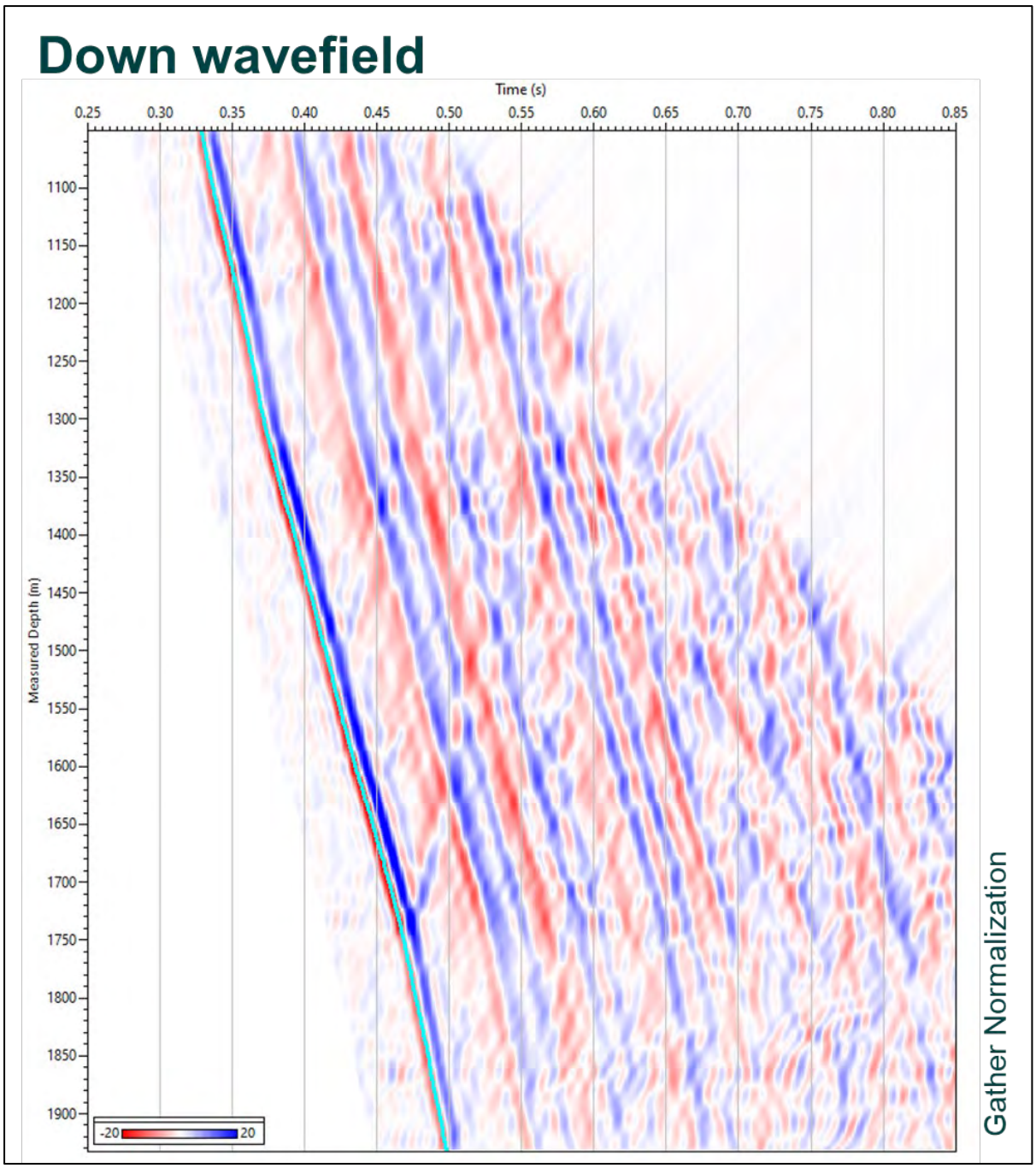


*Figure 9-16. Down wavefield - Down separation. It presents the data after the separation in the FP domain.*

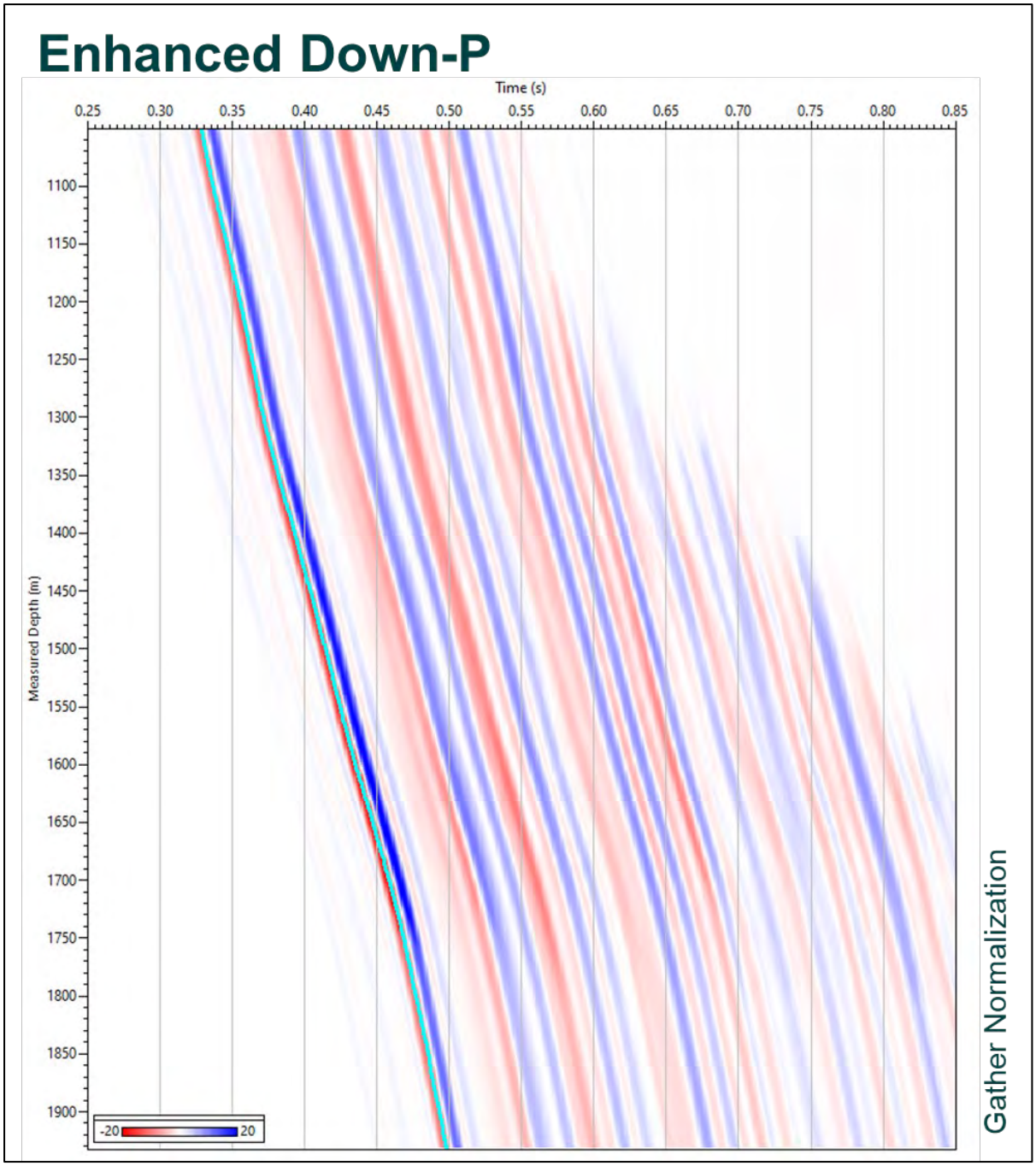


*Figure 9-17. Enhanced Down-P - Median filter. This figure shows the Down P wavefield after enhancement with a median filter of 121 traces along the FB. This wavefield will be used later in the deconvolution.*

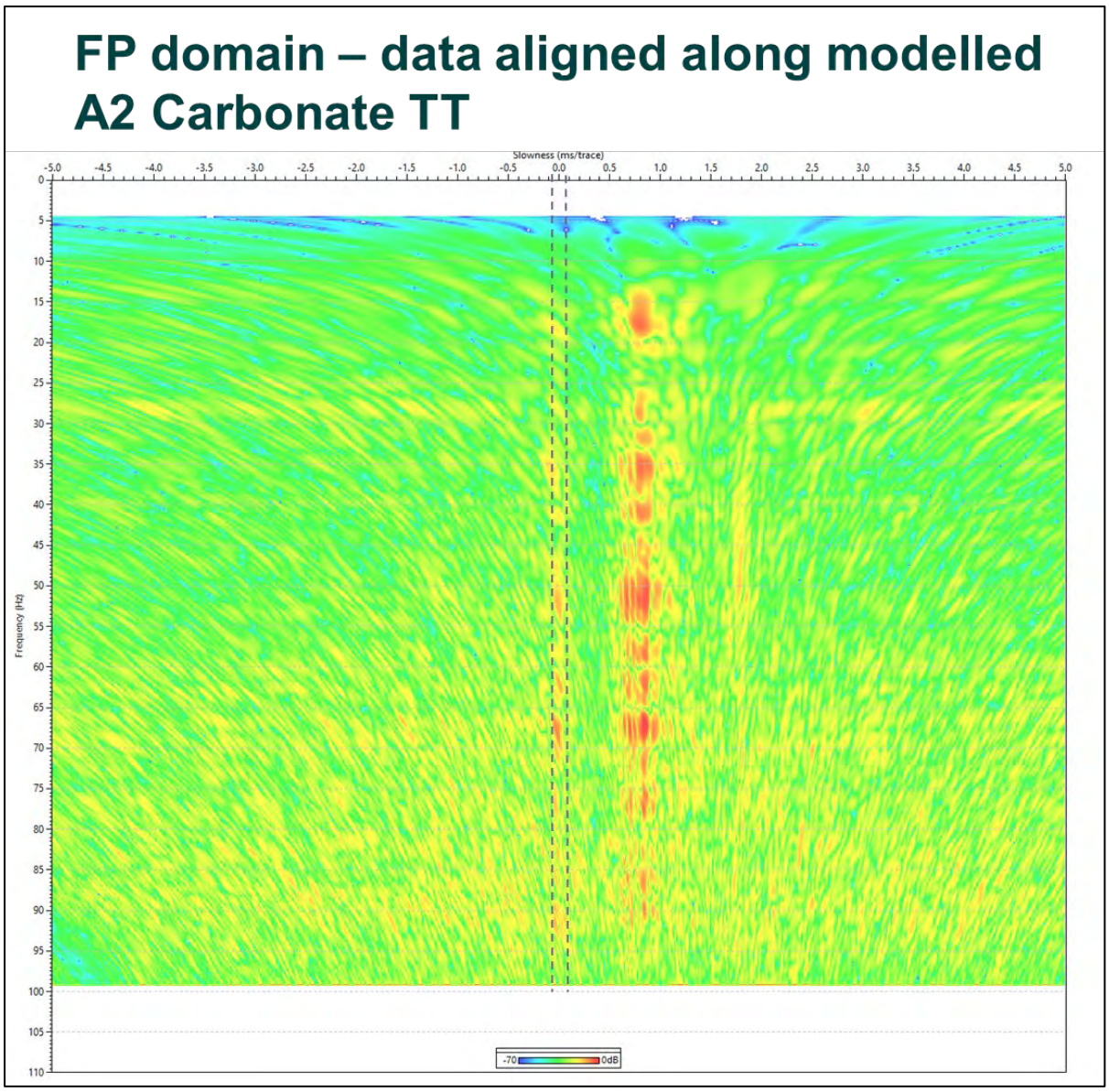


*Figure 9-18. FP domain – data aligned along modelled A2 Carbonate TT - Enhance Up P. The Up P wavefield was separated in the FP domain in a slowness window of -0.10 to 0.10 ms/trace.*

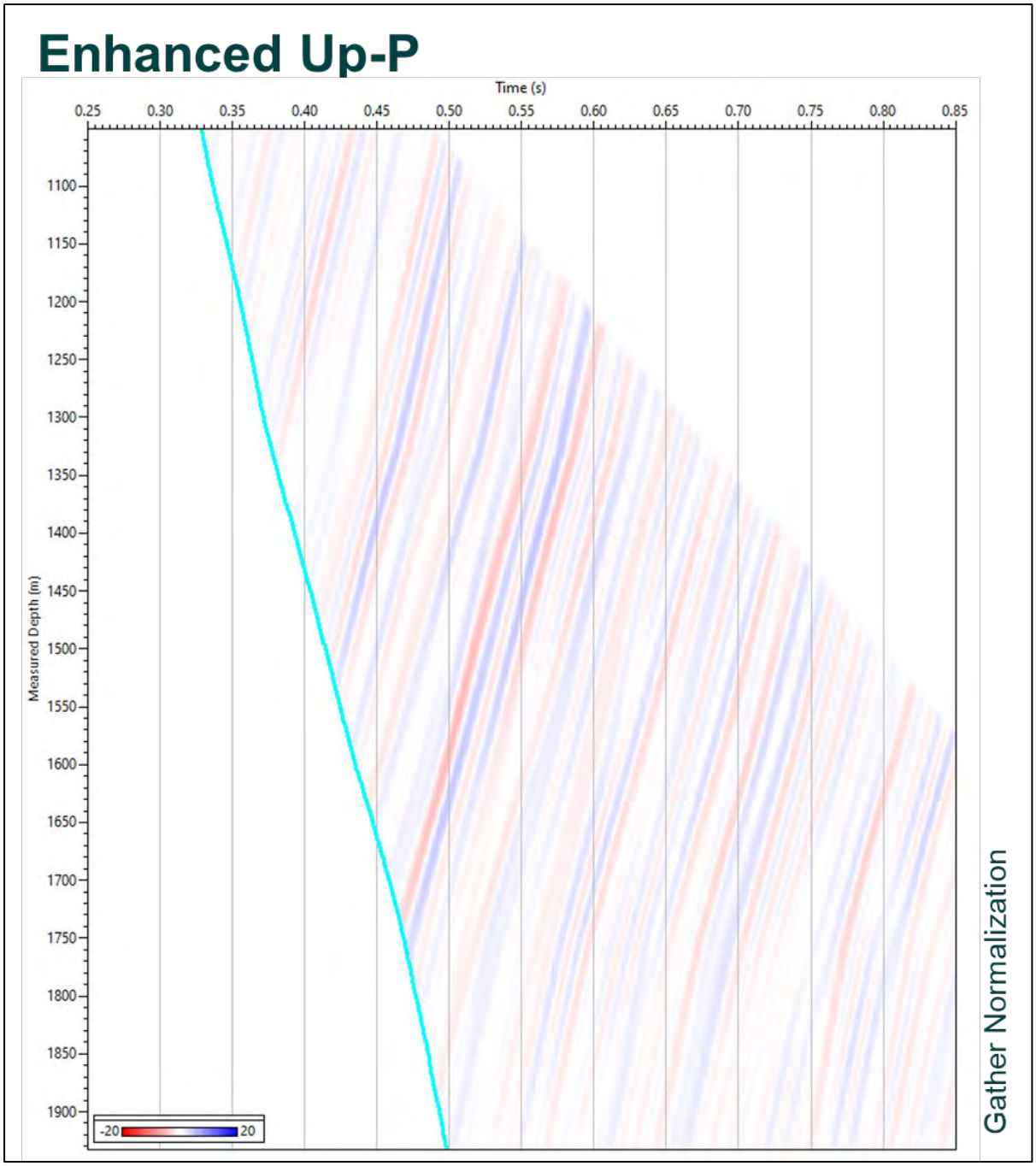


*Figure 9-19. Enhanced Up-P - After FP separation. The input data was aligned along the A2 Carbonate modelled TT (Fig. 9.14 green) before FP. Figure 9.19 shows the enhanced Up P along the modelled A2 Carbonate TT over a 10 trace window after the separation in the FP domain.*

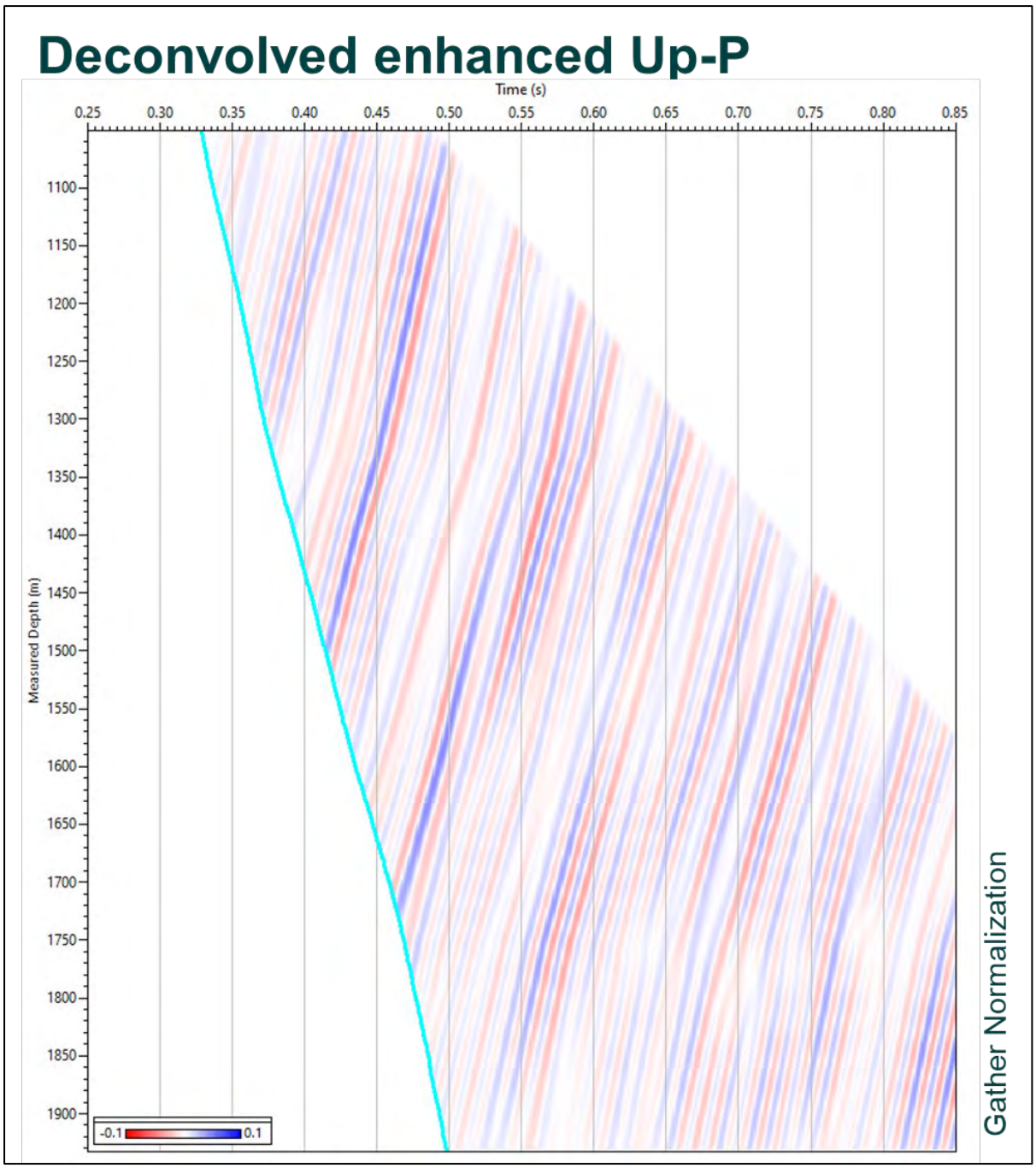


*Figure 9-20. Deconvolved enhanced Up-P - Trace by trace deterministic deconvolution. To reduce the multiples and increase the data high frequency bandwidth, the enhanced Up P were deconvolved. Trace by trace deterministic deconvolution with the enhanced Down P (Fig. 9.17) using a 0.15 s operator length and 20% white noise was applied to the enhanced Up P. Finally, the data were filtered with a 5,10-90,110 Hz BPF.*

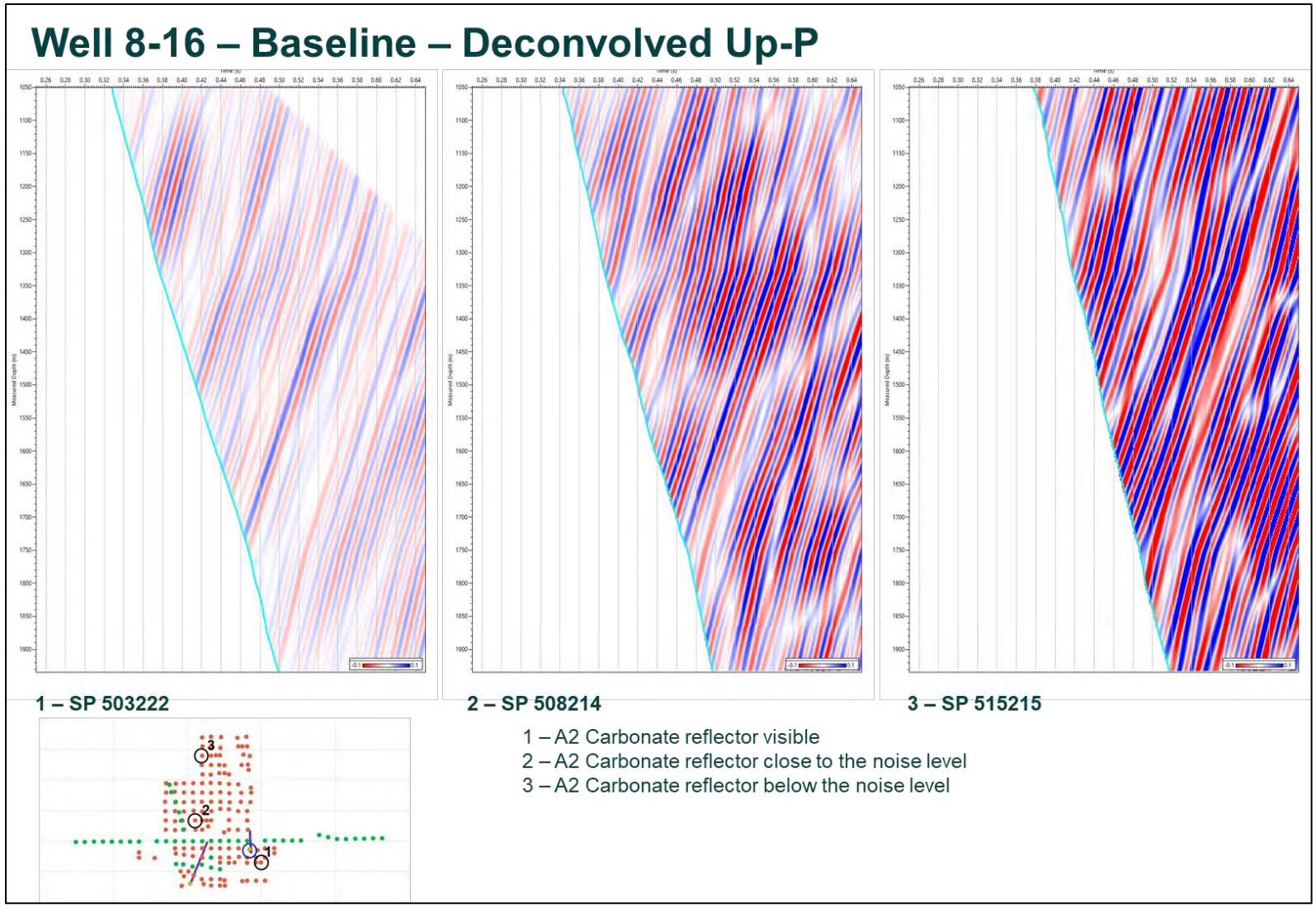


*Figure 9-21. Well 8-16 – Baseline – Deconvolved Up-P - Far, mid and near offsets.*

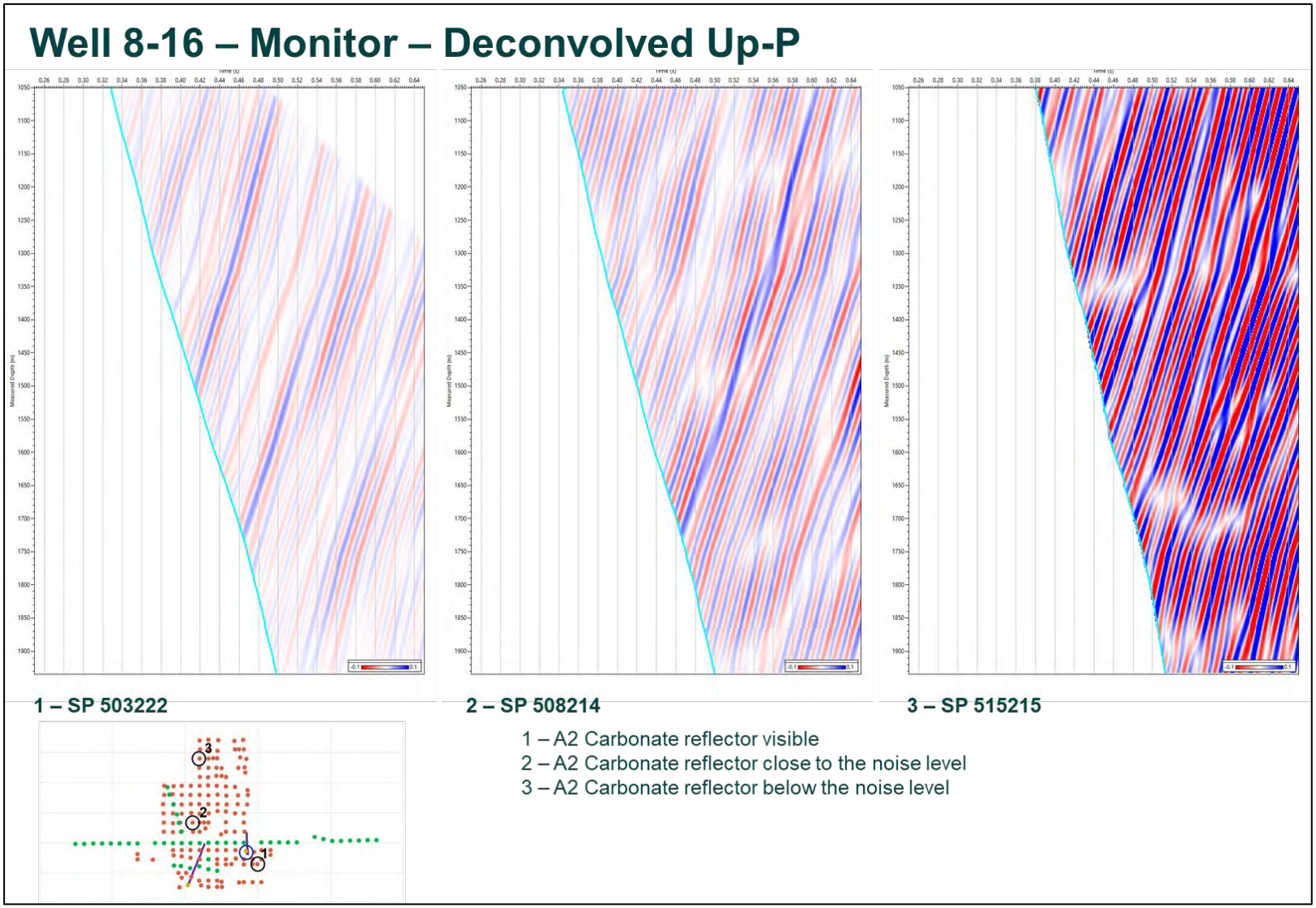


*Figure 9-22. Well 8-16 – Monitor – Deconvolved Up-P - Far, mid and near offsets.*


*Figure 9-23. Drift between modelled and picked TT before statics – Baseline.*

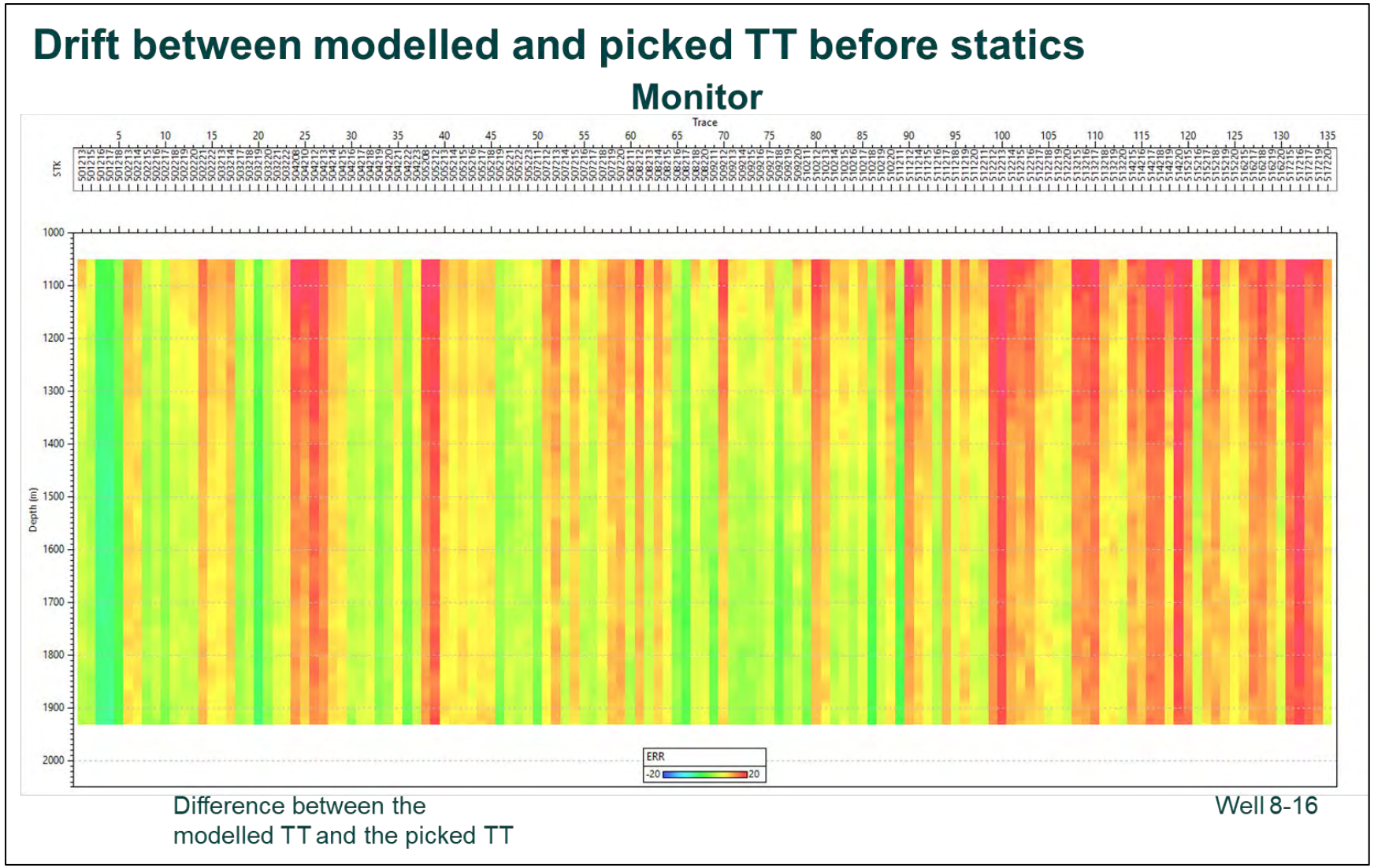


*Figure 9-24. Drift between modelled and picked TT before statics – Monitor.*

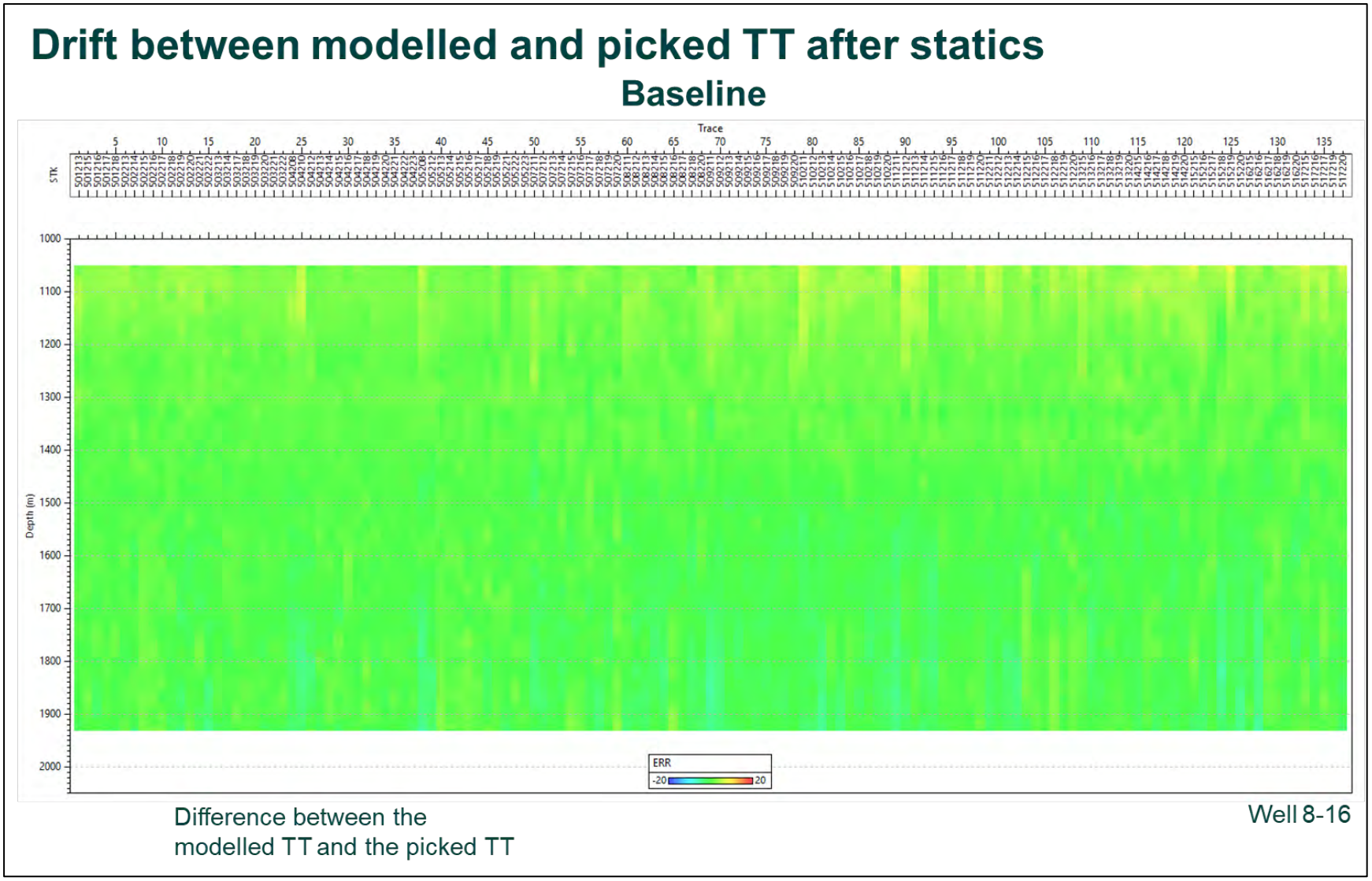


*Figure 9-25. Drift between modelled and picked TT after statics – Baseline.*

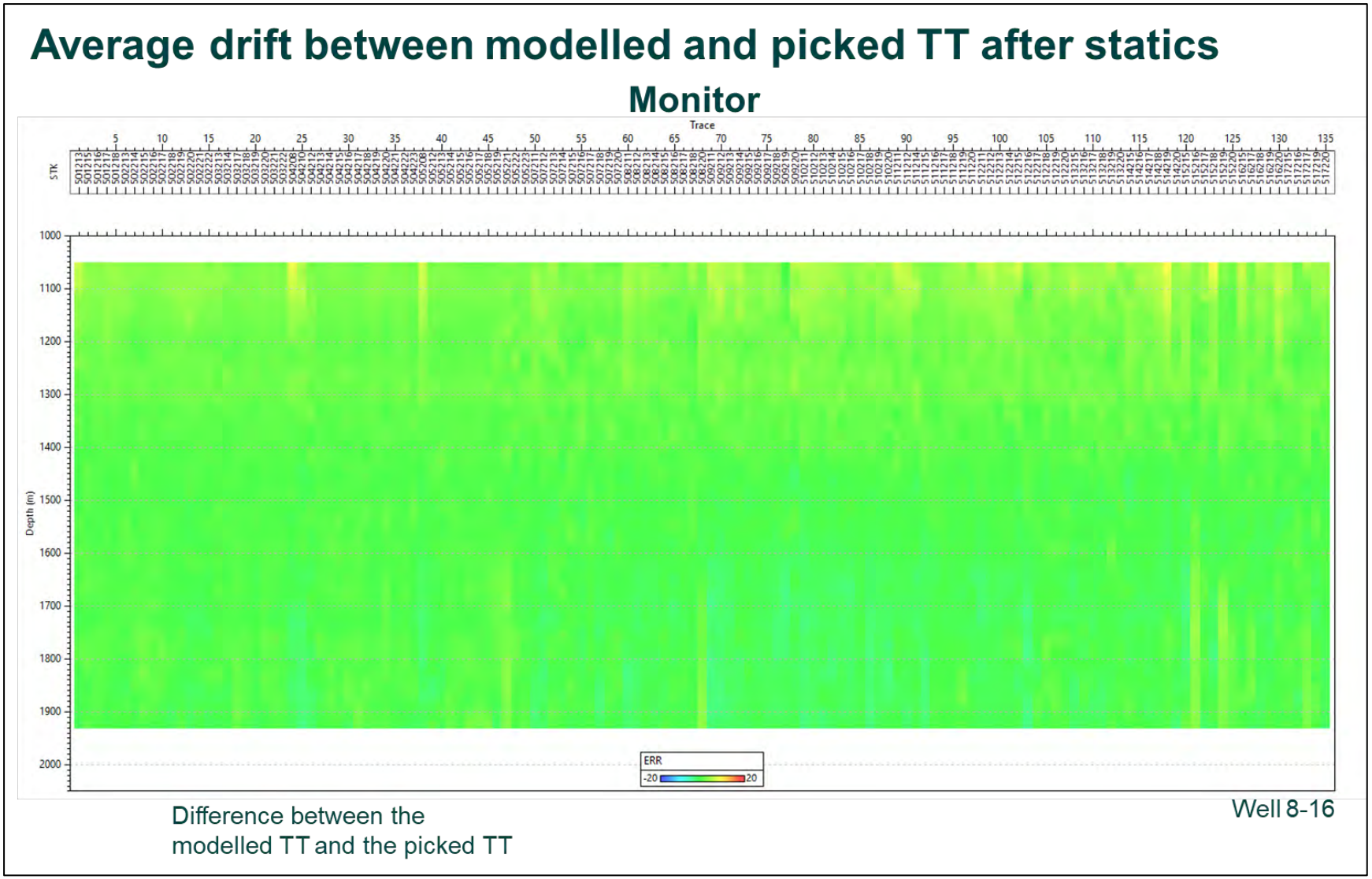


*Figure 9-26. Drift between modelled and picked TT after statics – Monitor.*

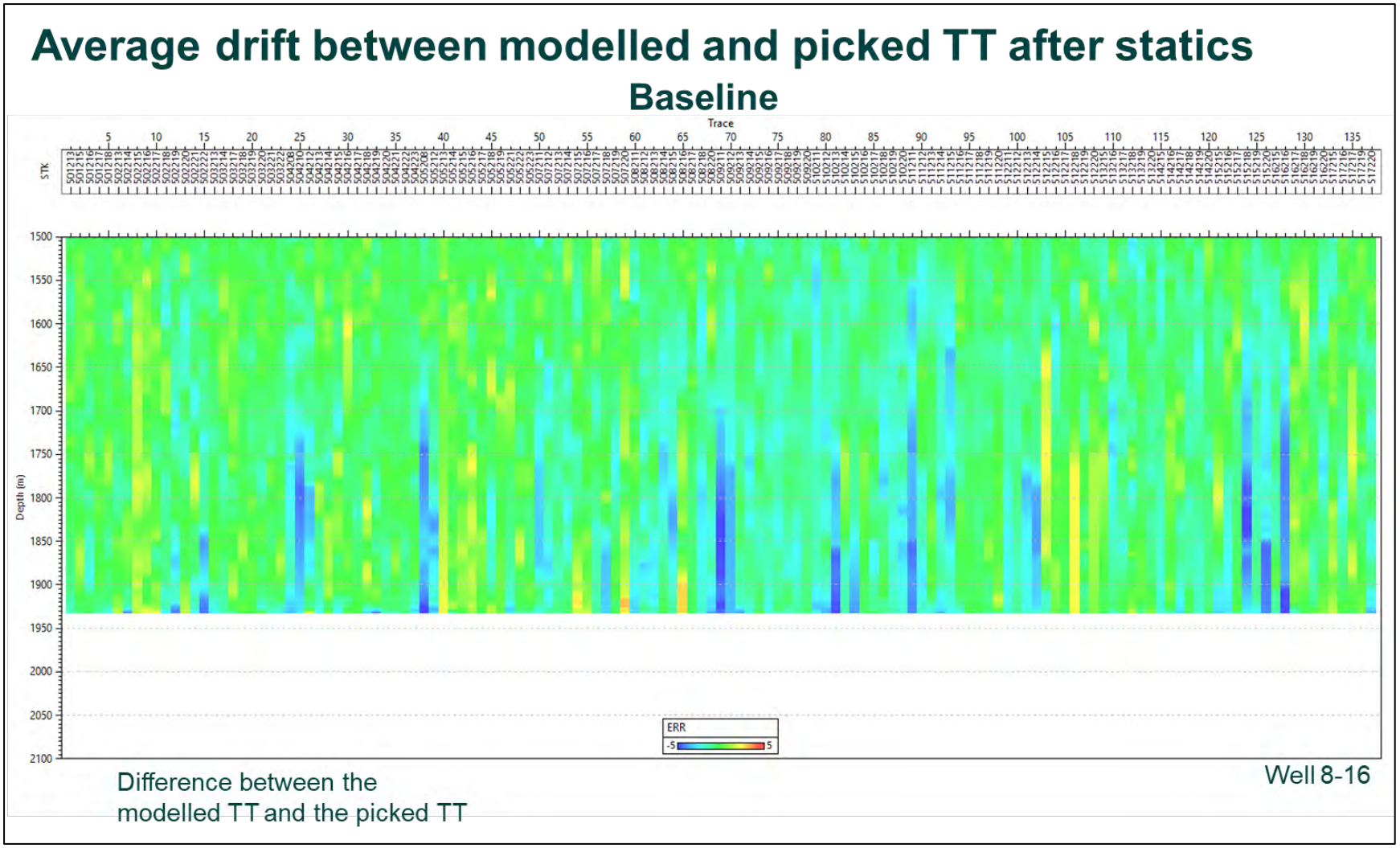


*Figure 9-27. Drift between modelled and picked TT after statics – Baseline.*

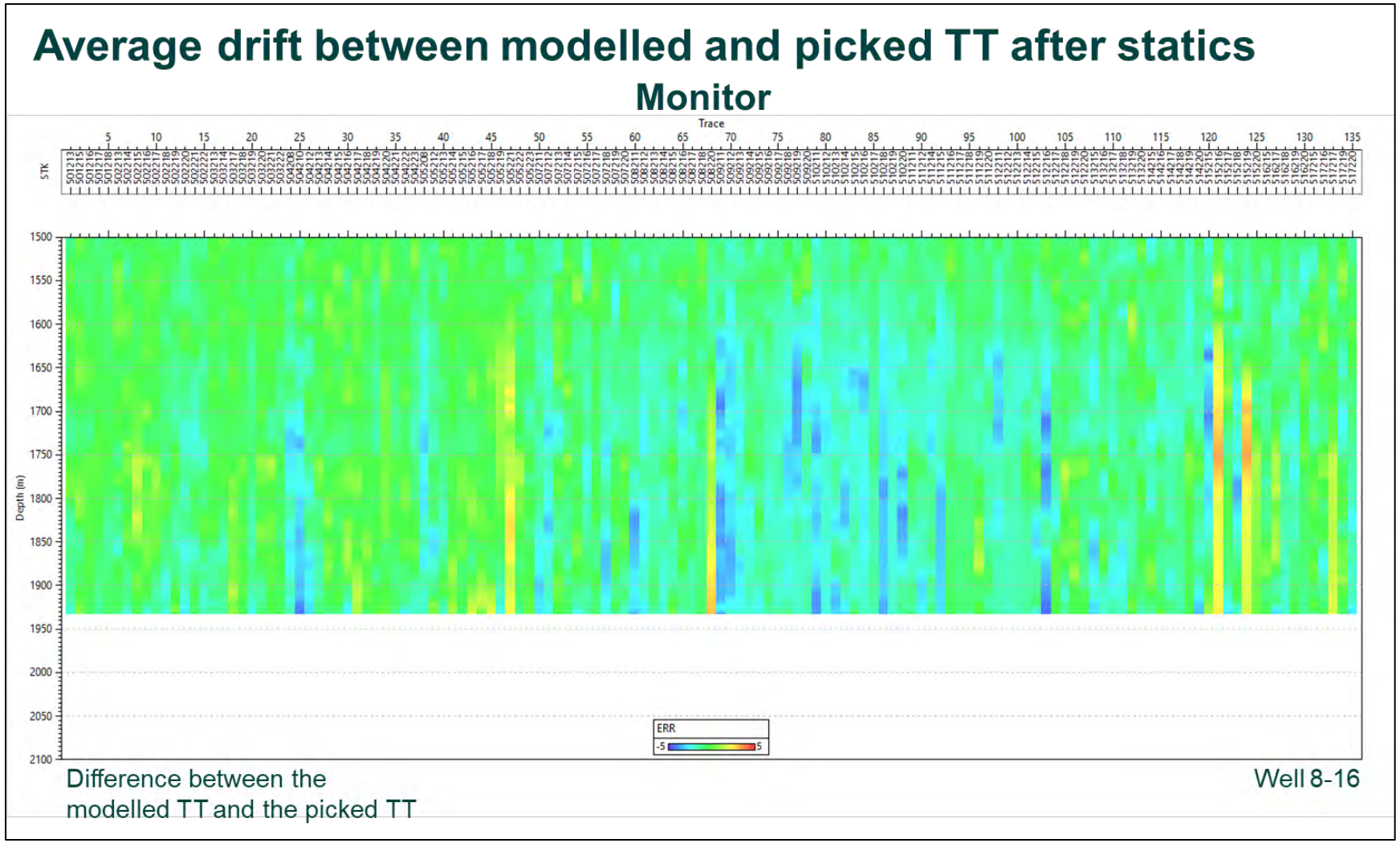


*Figure 9-28. Drift between modelled and picked TT after statics – Monitor.*

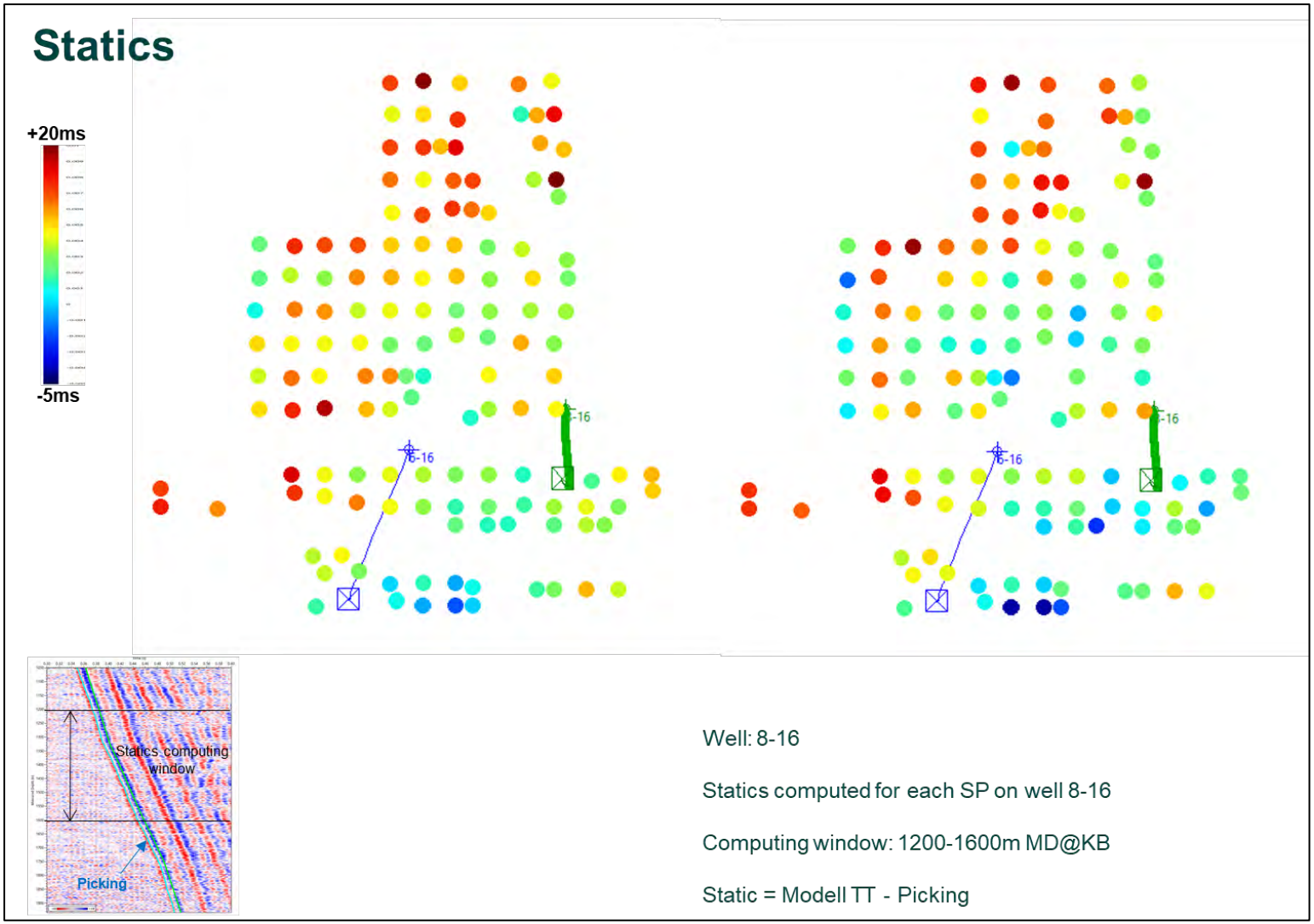


*Figure 9-29. Statics - Plane view with statics for each SP. For each SP a static shift was calculated by averaging the drift between the model and the picks in the 1200m-1600mMD interval located above the reservoir (Fig. 9.29 bottom left). Static shift values were calculated separately for the baseline and the monitor surveys (Fig. 9.29).*

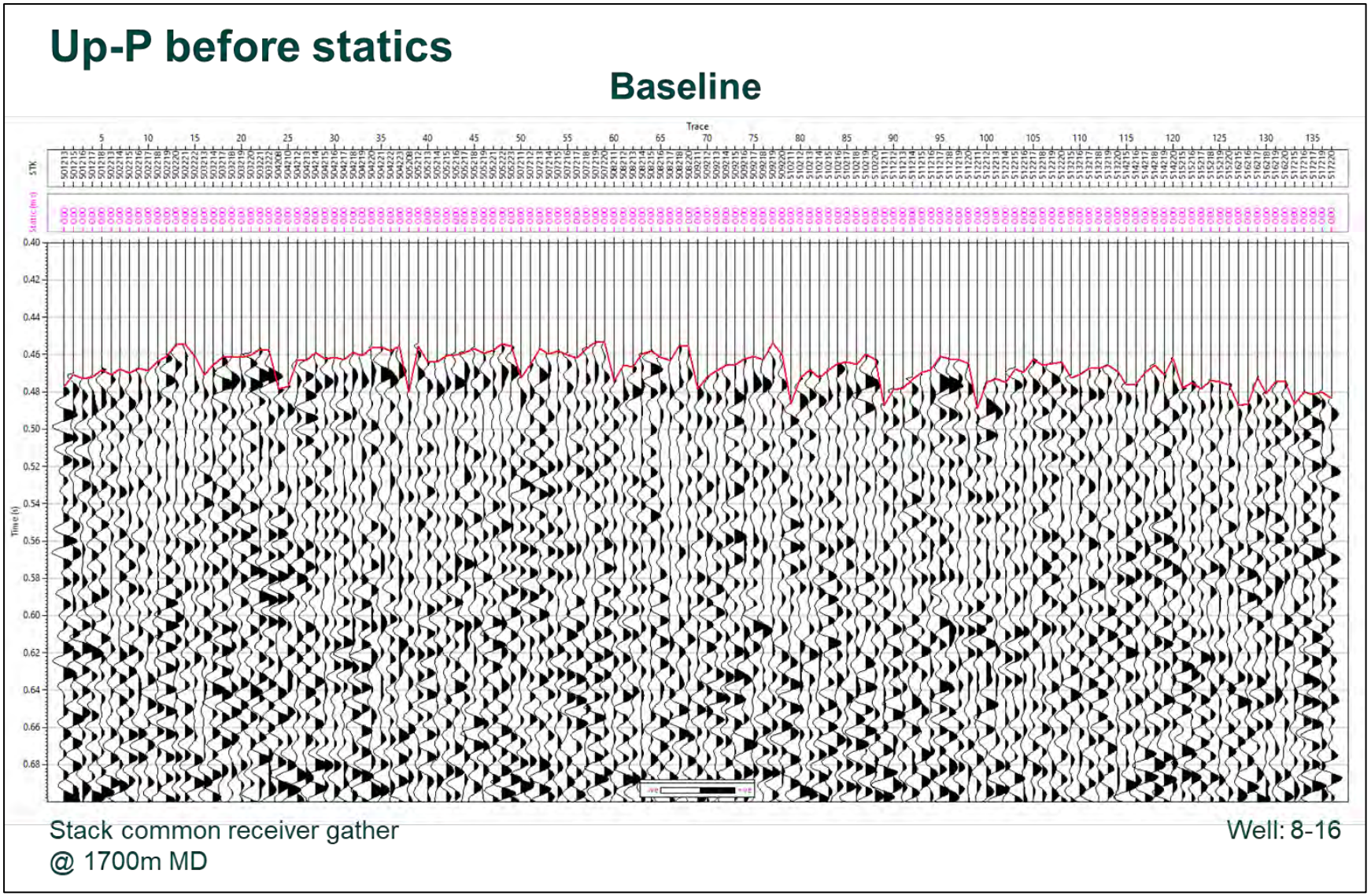


*Figure 9-30. Up-P before statics - Common receiver gather – Baseline.*

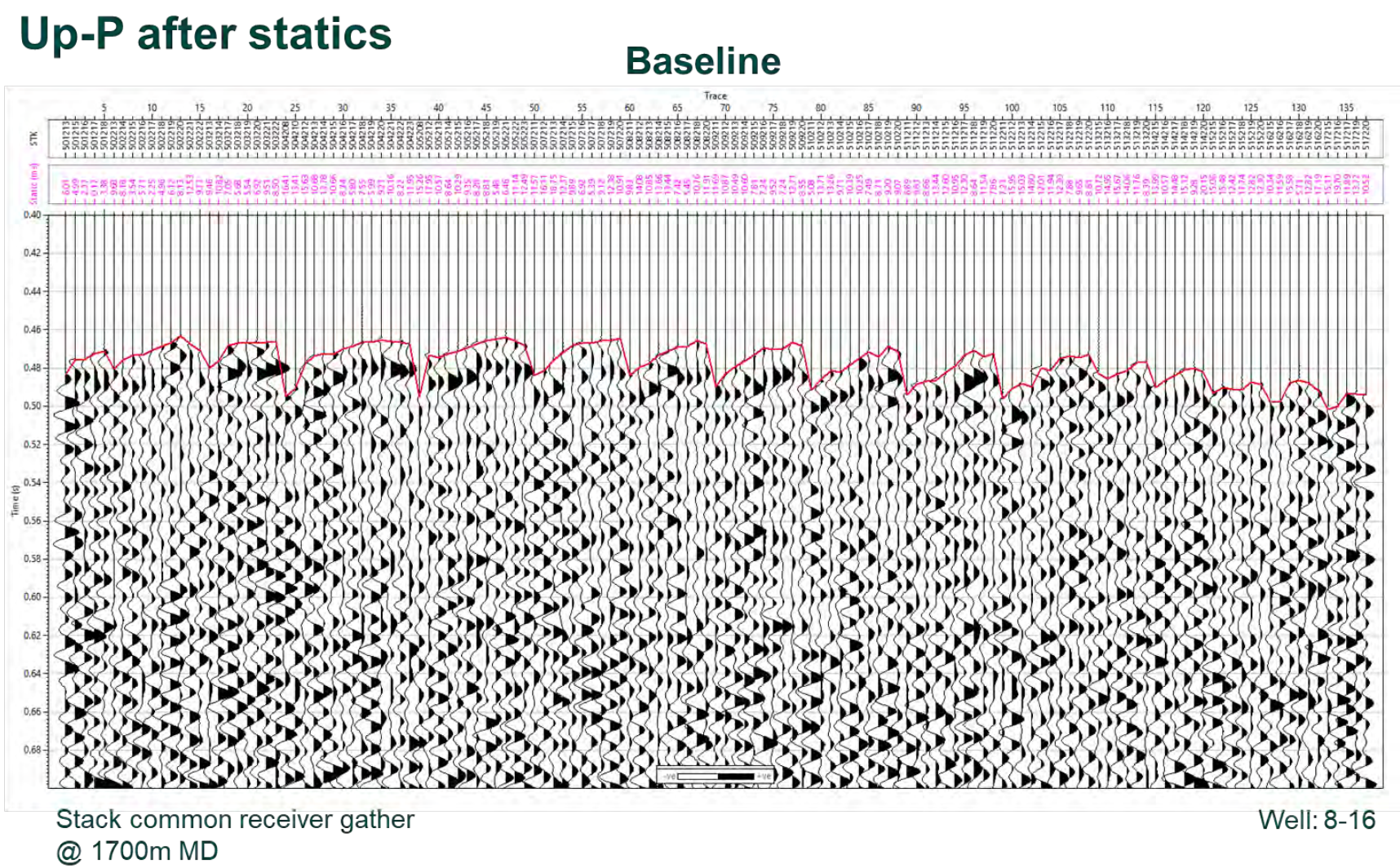


*Figure 9-31. Up-P after statics - Common receiver gather – Baseline.*

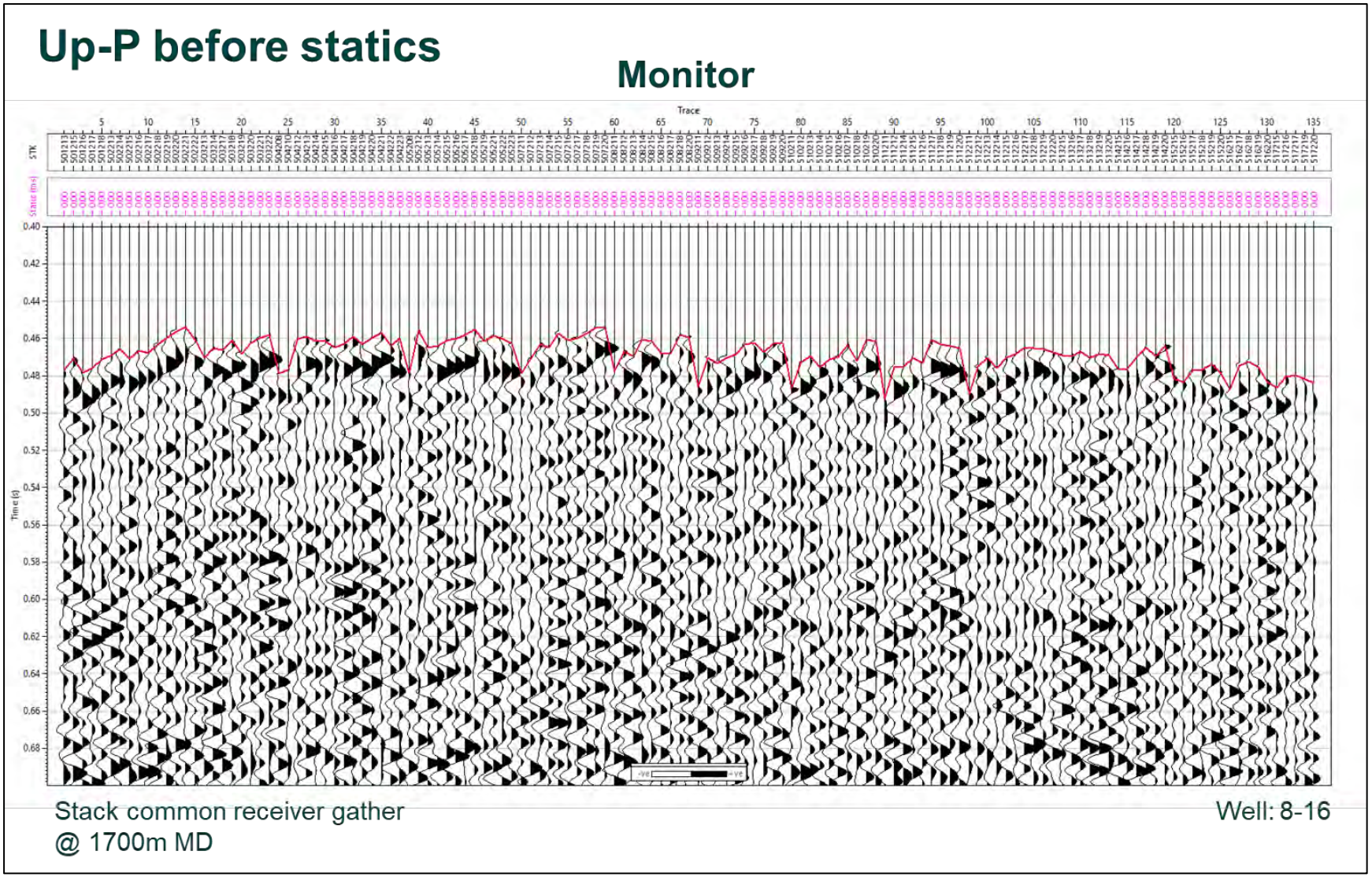


*Figure 9-32. Up-P before statics - Common receiver gather – Monitor.*

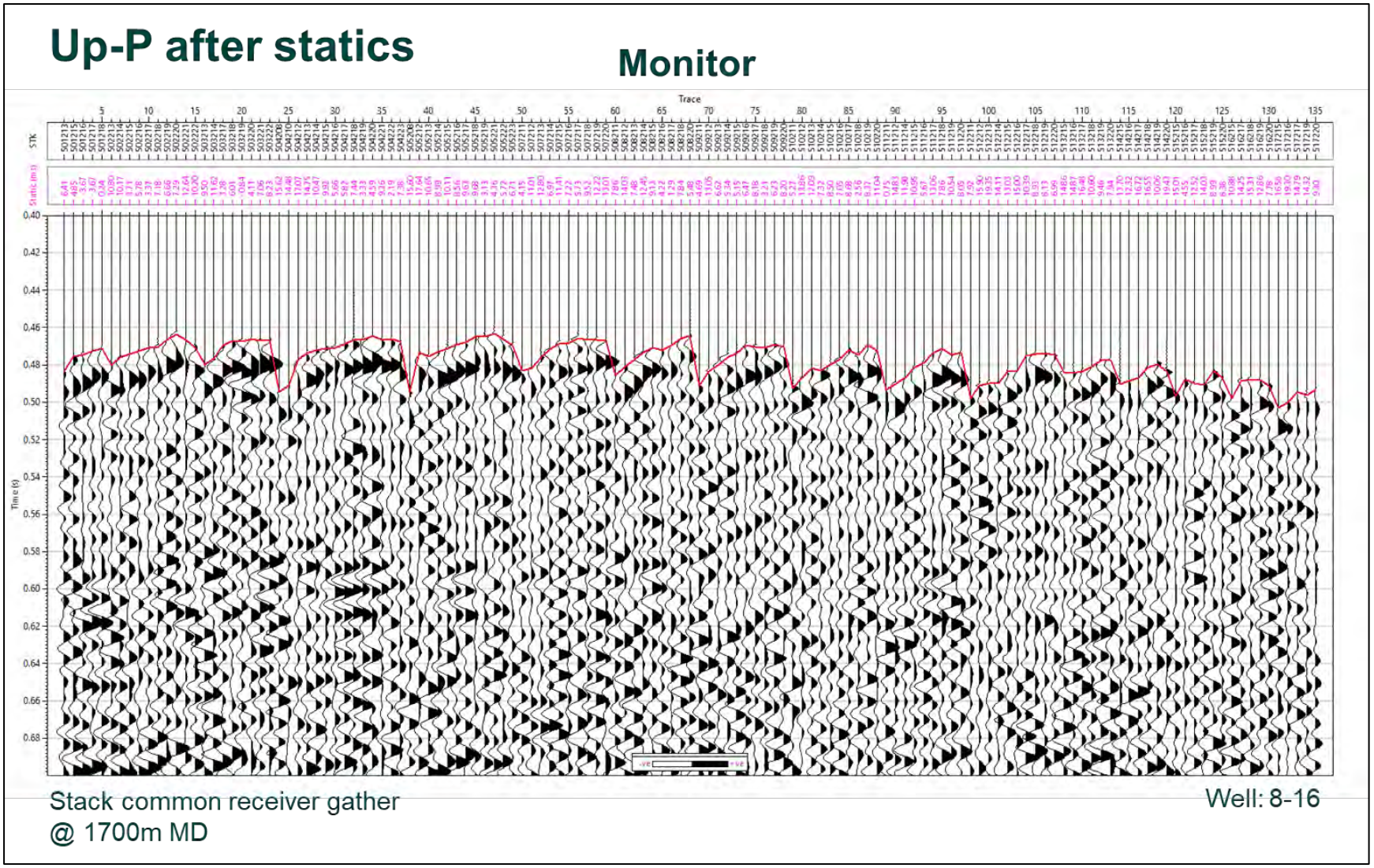


*Figure 9-33. Up-P after statics - Common receiver gather – Monitor.*

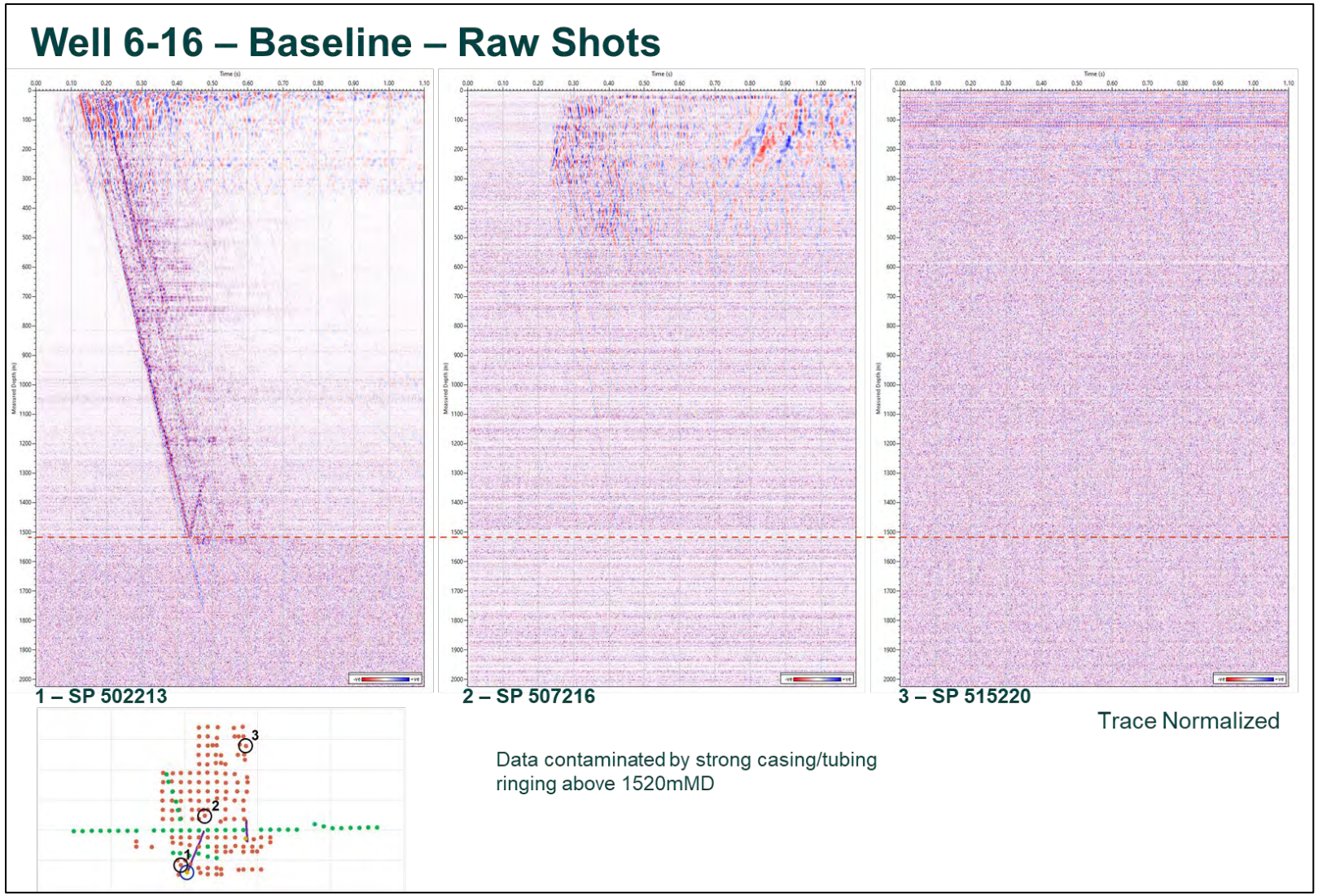


*Figure 9-34. Well 6-16 – Baseline – Raw Stacks - Far, mid and near offset total wavefield.*

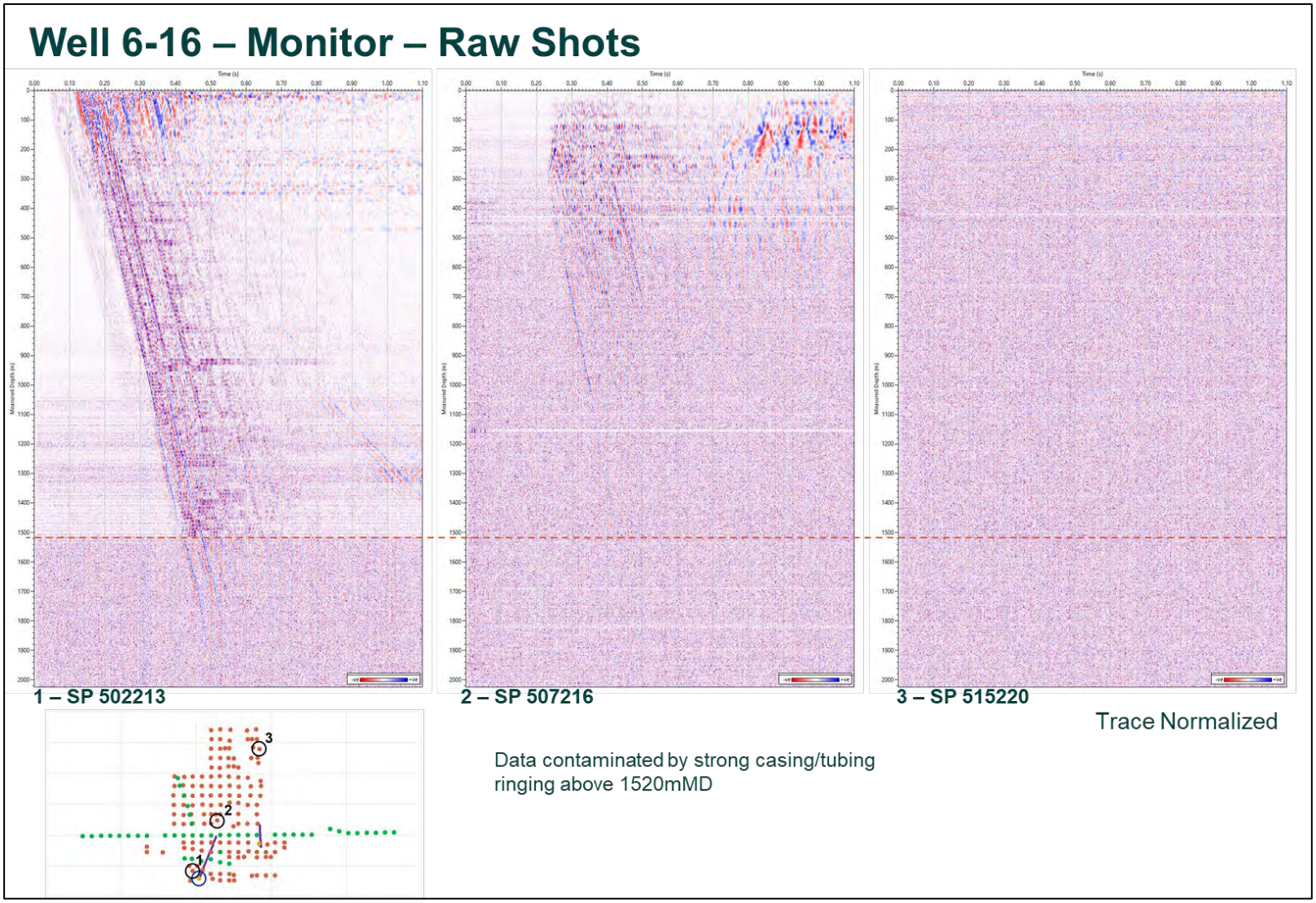


*Figure 9-35. Well 6-16 – Monitor – Raw Stacks - Far, mid, and near offset total wavefield.*

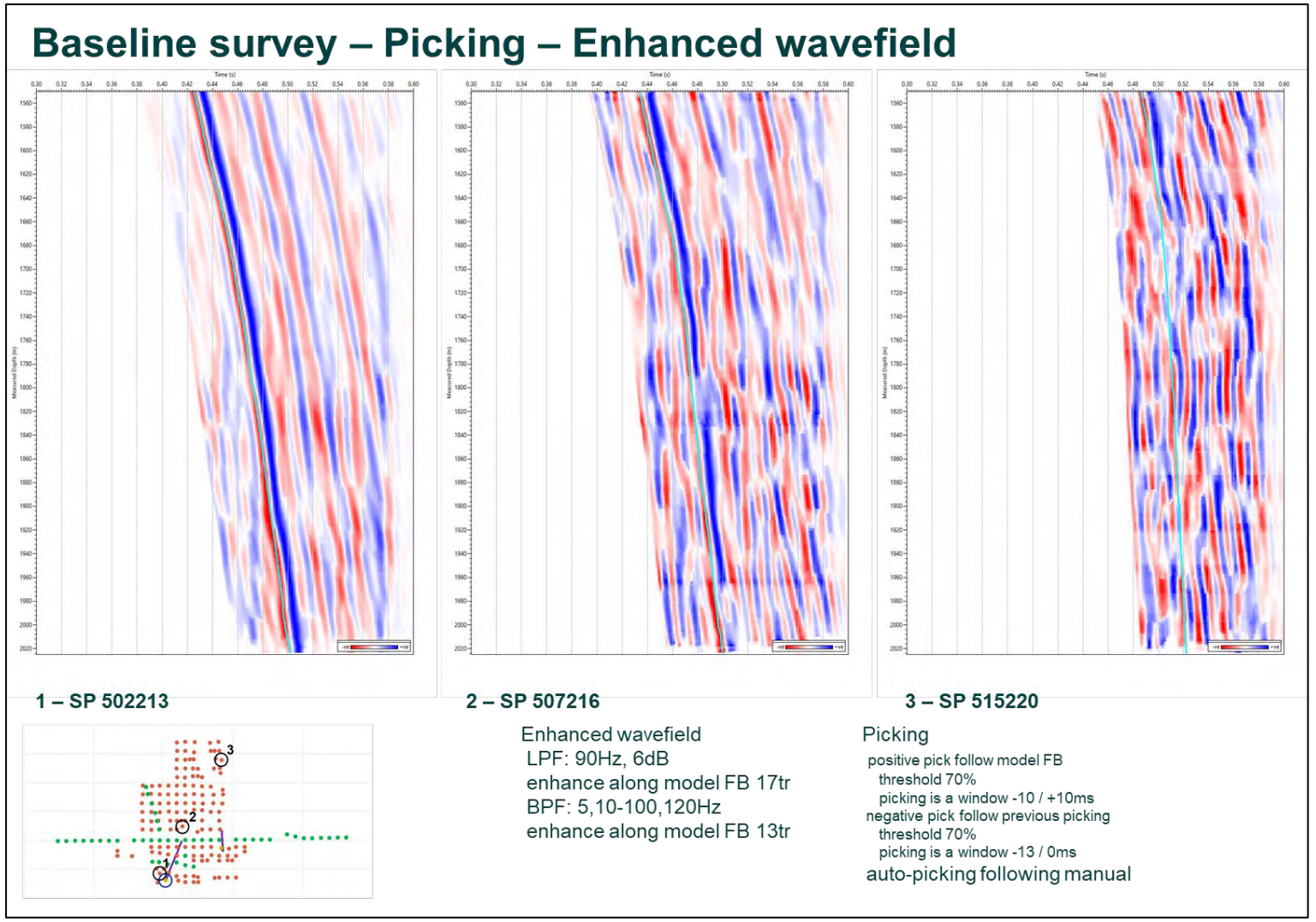


*Figure 9-36. Baseline survey – Picking – Enhanced wavefield - Down P enhancement. Before picking the wavefield was filtered using a low pass filter up to 90 Hz, enhanced along the modelled FB using a 17 trace window, filtered with an BPF 5,10-100,120Hz and enhanced again along the modelled FB over 13 traces.*

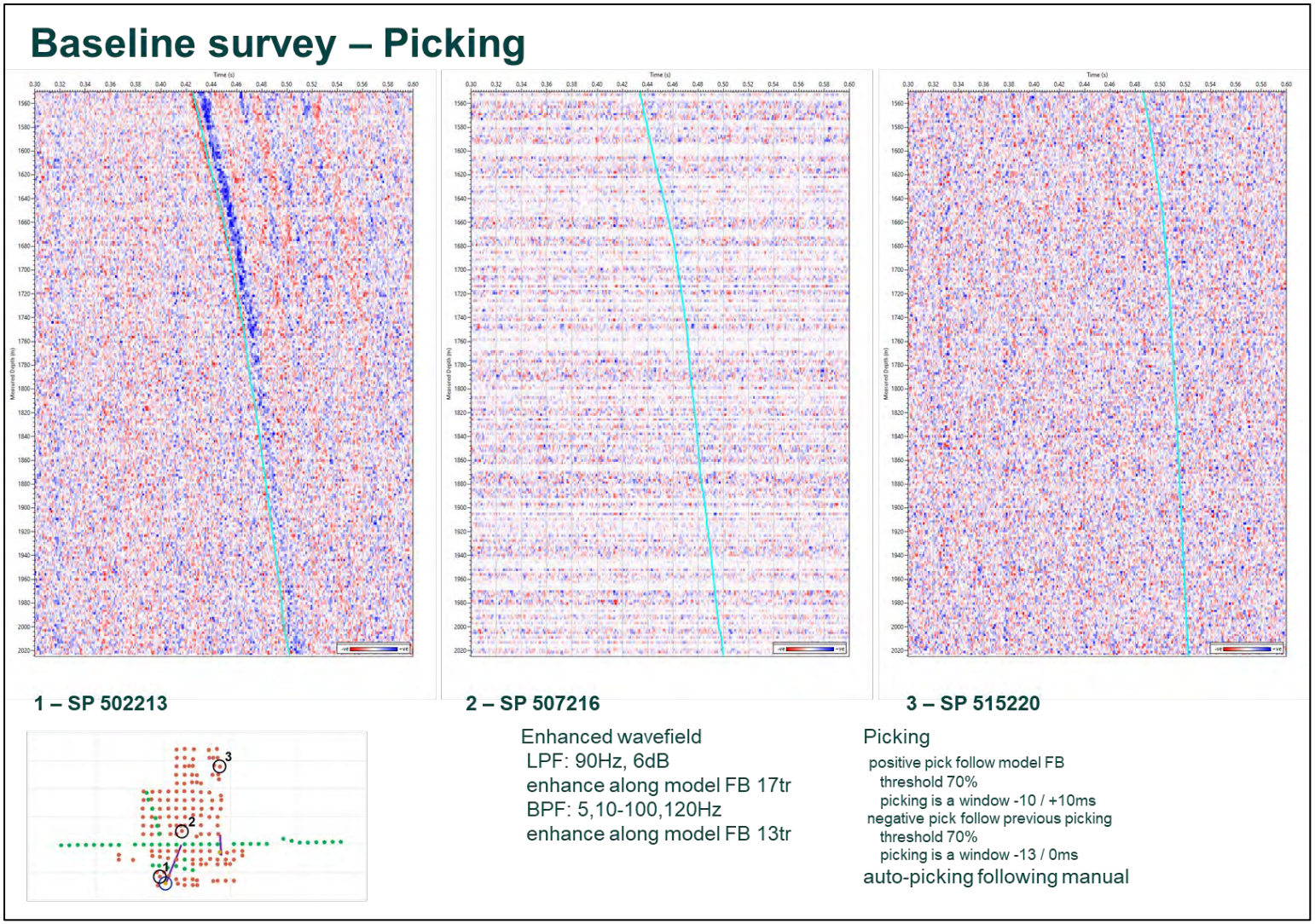


*Figure 9-37. Baseline survey – Picking. The modelled Down P transit time was used to guide the automatic picking which was performed on enhanced data on the first peak. The picking on the peak was used to guide the picking on the first trough. The picks were interpolated and smoothed over 5 levels. In figure 9.37 are presented the stacks after picking for the same SP.*

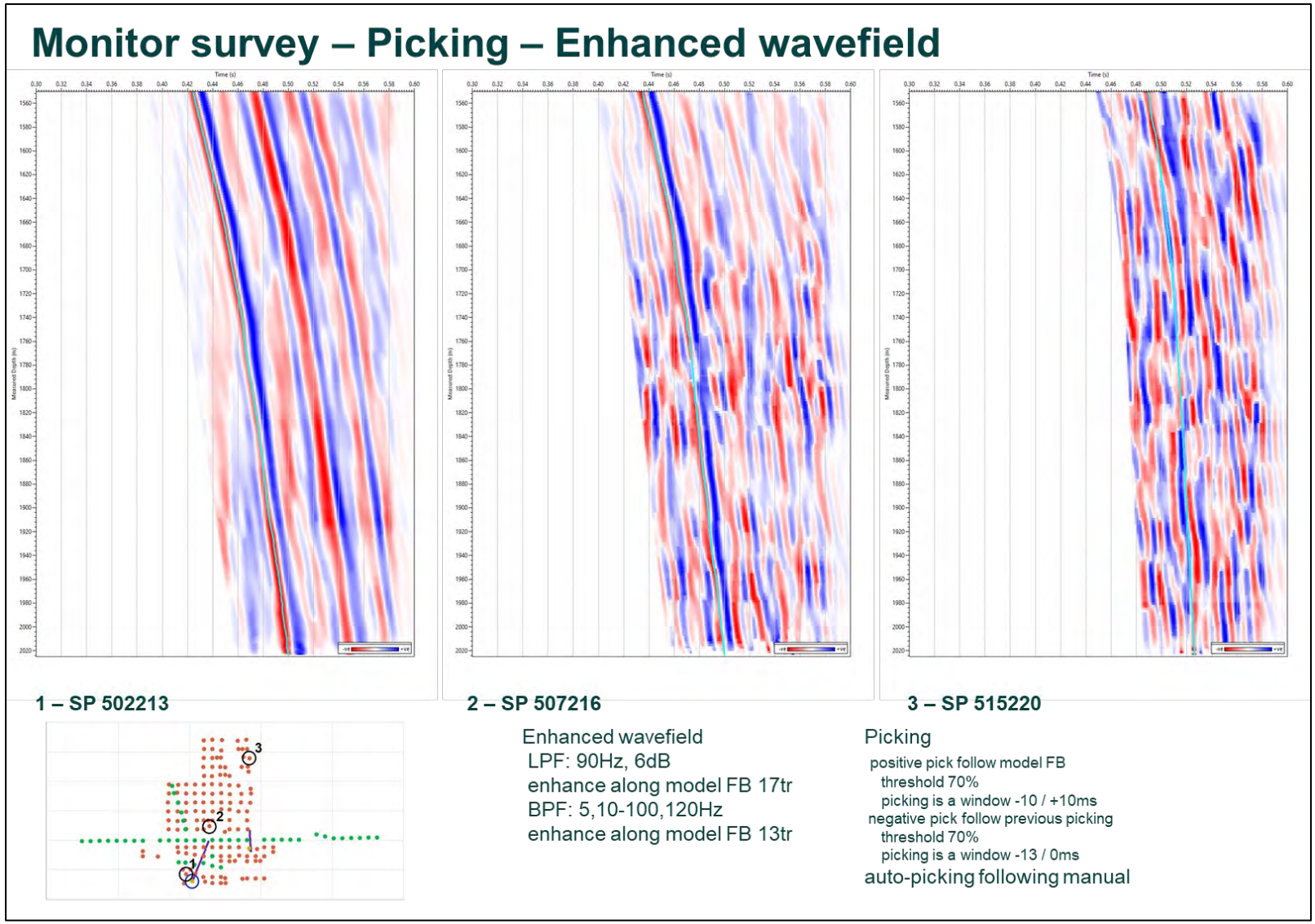


*Figure 9-38. Monitor survey – Picking – Enhanced wavefield - Down P enhancement.*

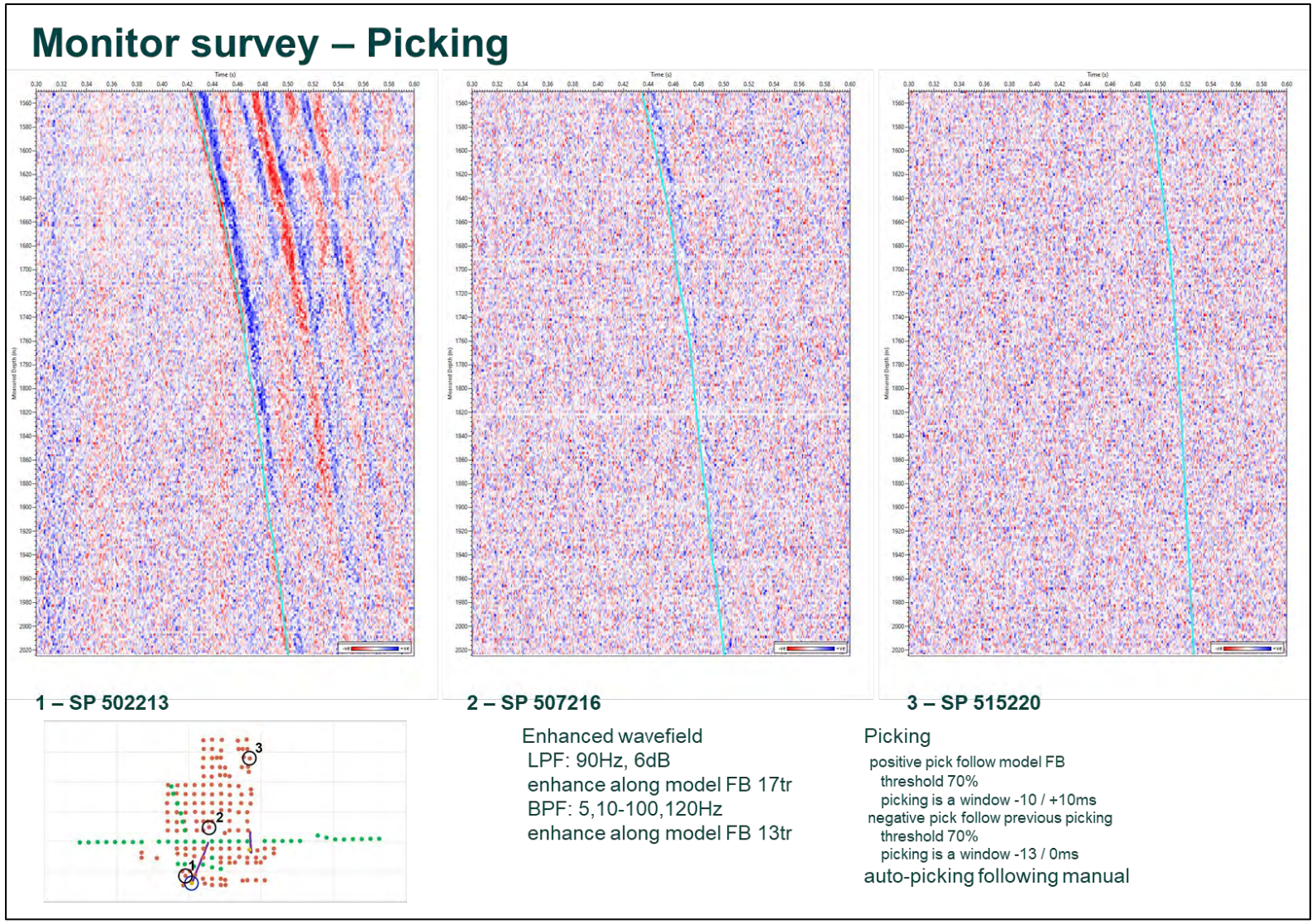


*Figure 9-39. Monitor survey – Picking.*

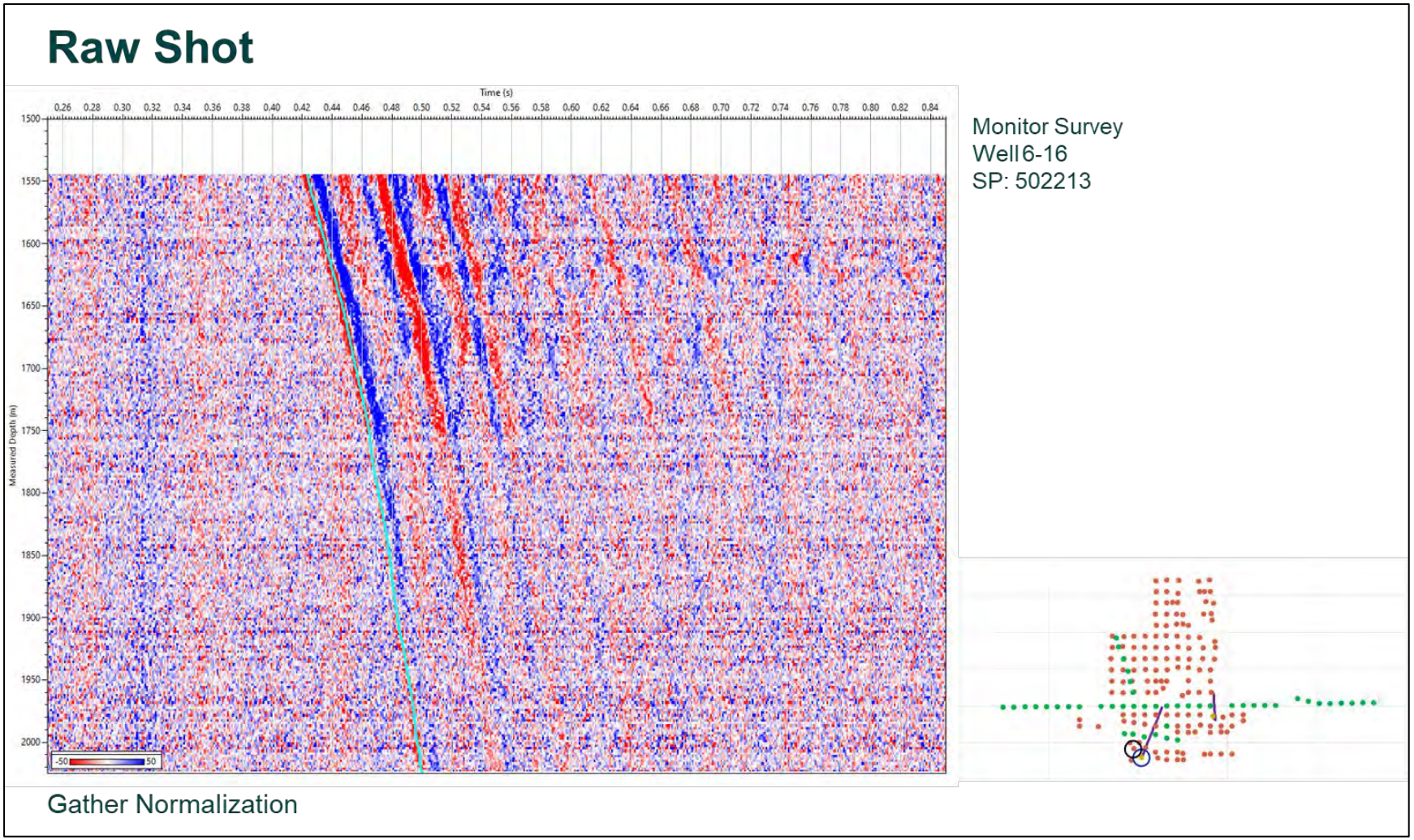


*Figure 9-40. Raw Stack. Figure 9.40 shows the processing input data, a filtered stack data from the SP 502213. The amplitudes displayed are cross-normalized.*

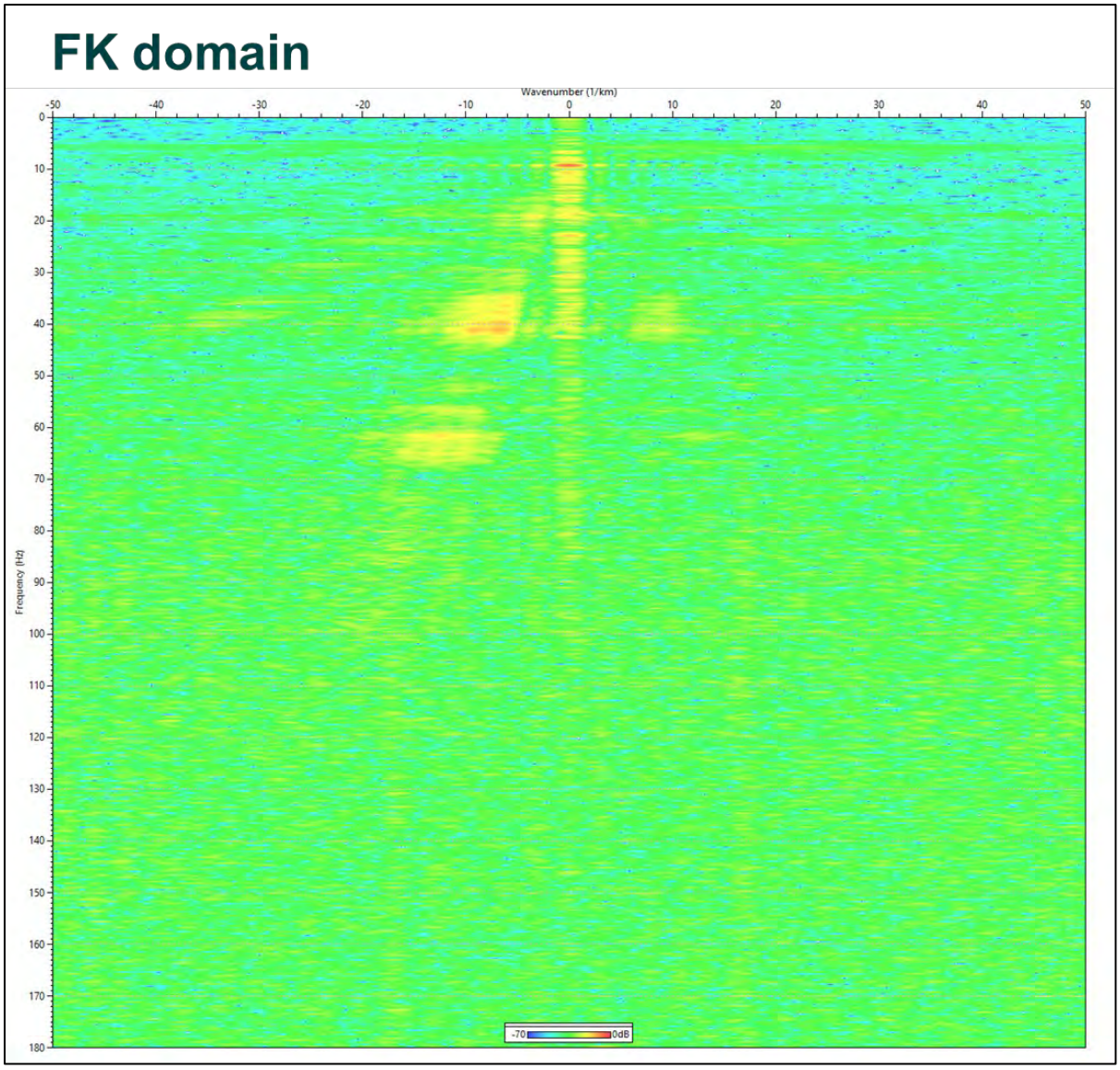


*Figure 9-41. FK domain - CMN attenuation. To reduce the noise due to the box vibration, in the FK domain the values in the -1.7 to 1.7 wave number window were attenuated.*

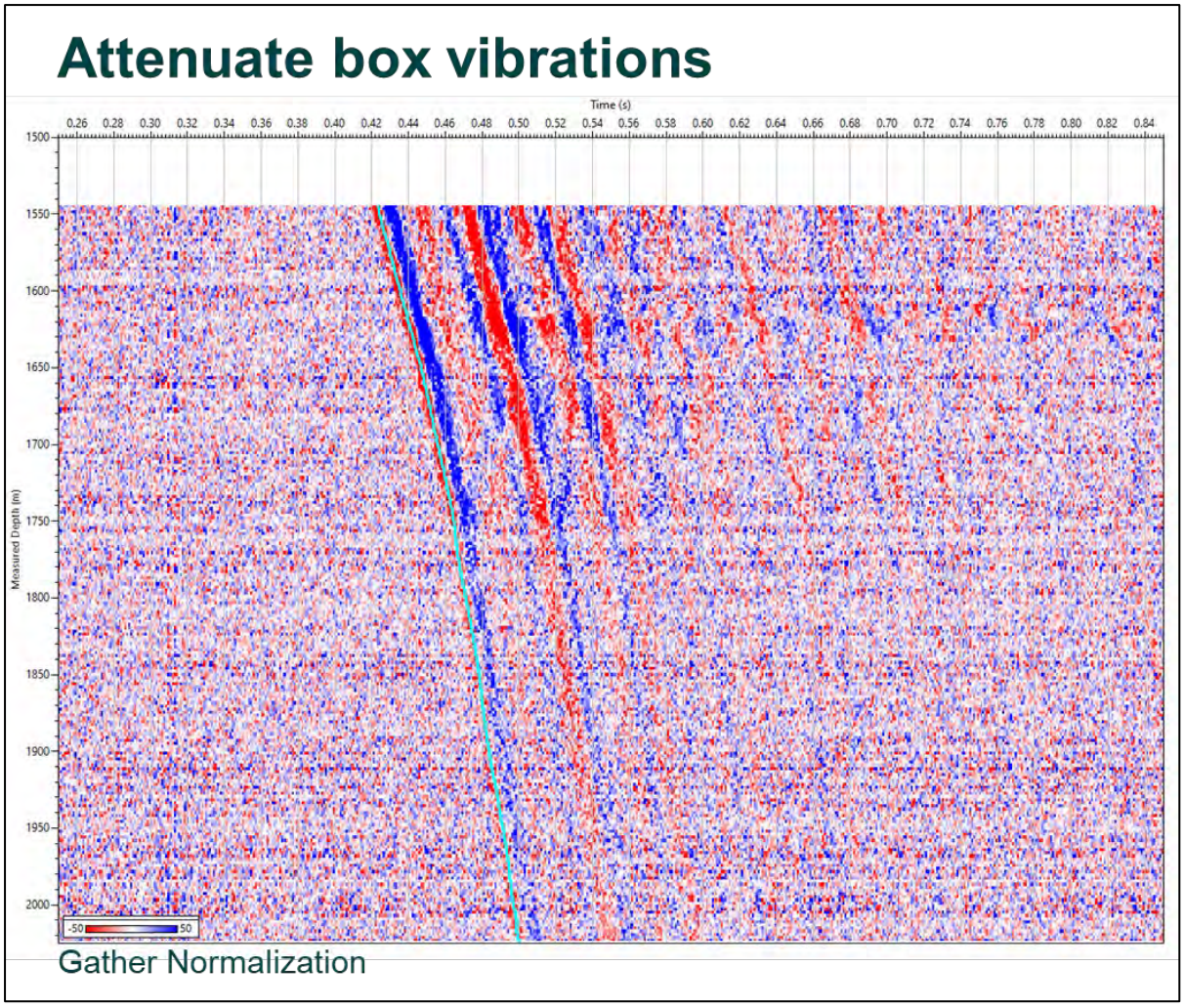


*Figure 9-42. Attenuate box vibrations - CMN attenuation. The shot after this attenuation is presented in this figure.*

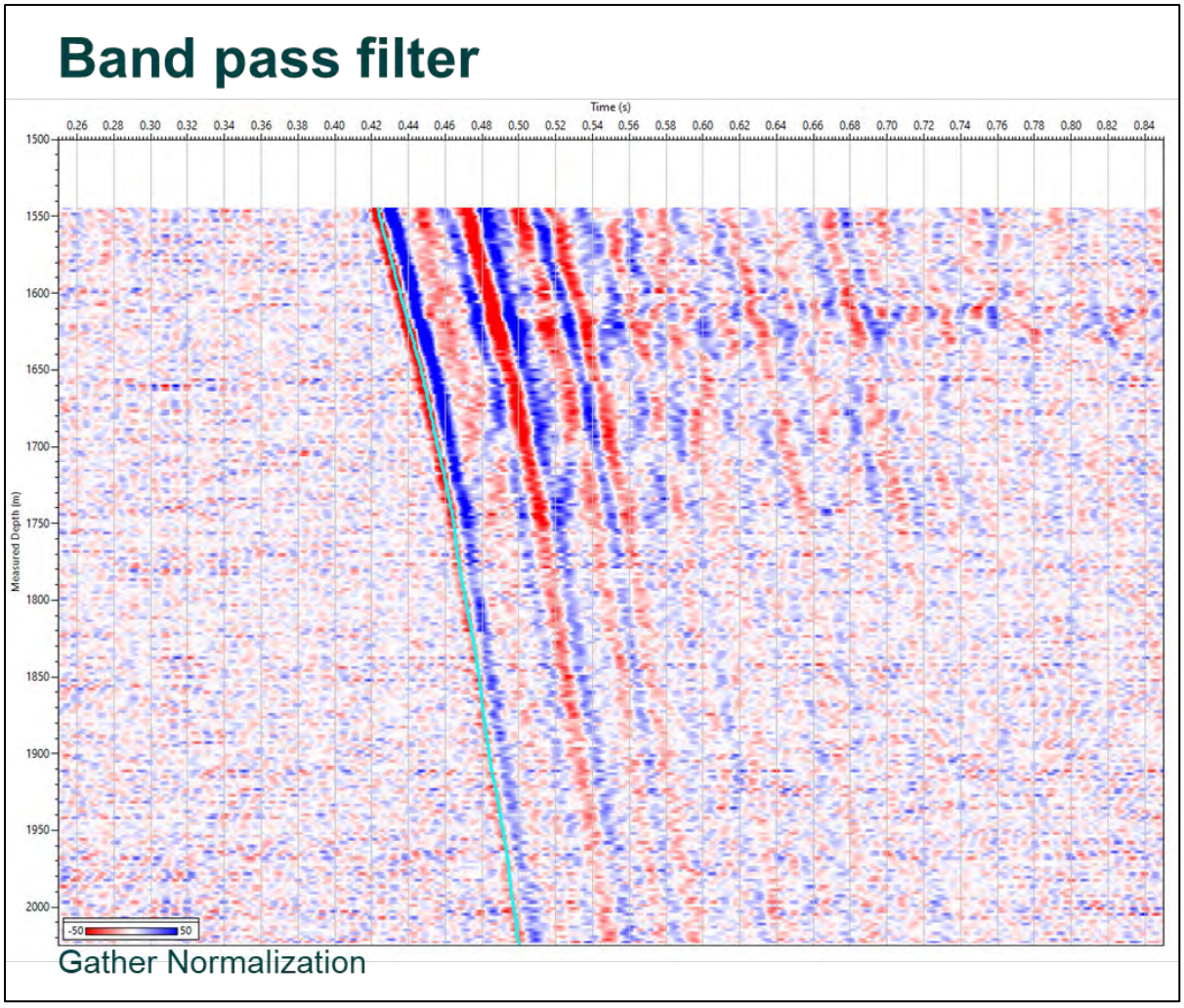


*Figure 9-43. Band pass filter. A band pass filter in the range 5, 10 - 90, 110Hz was then applied.*

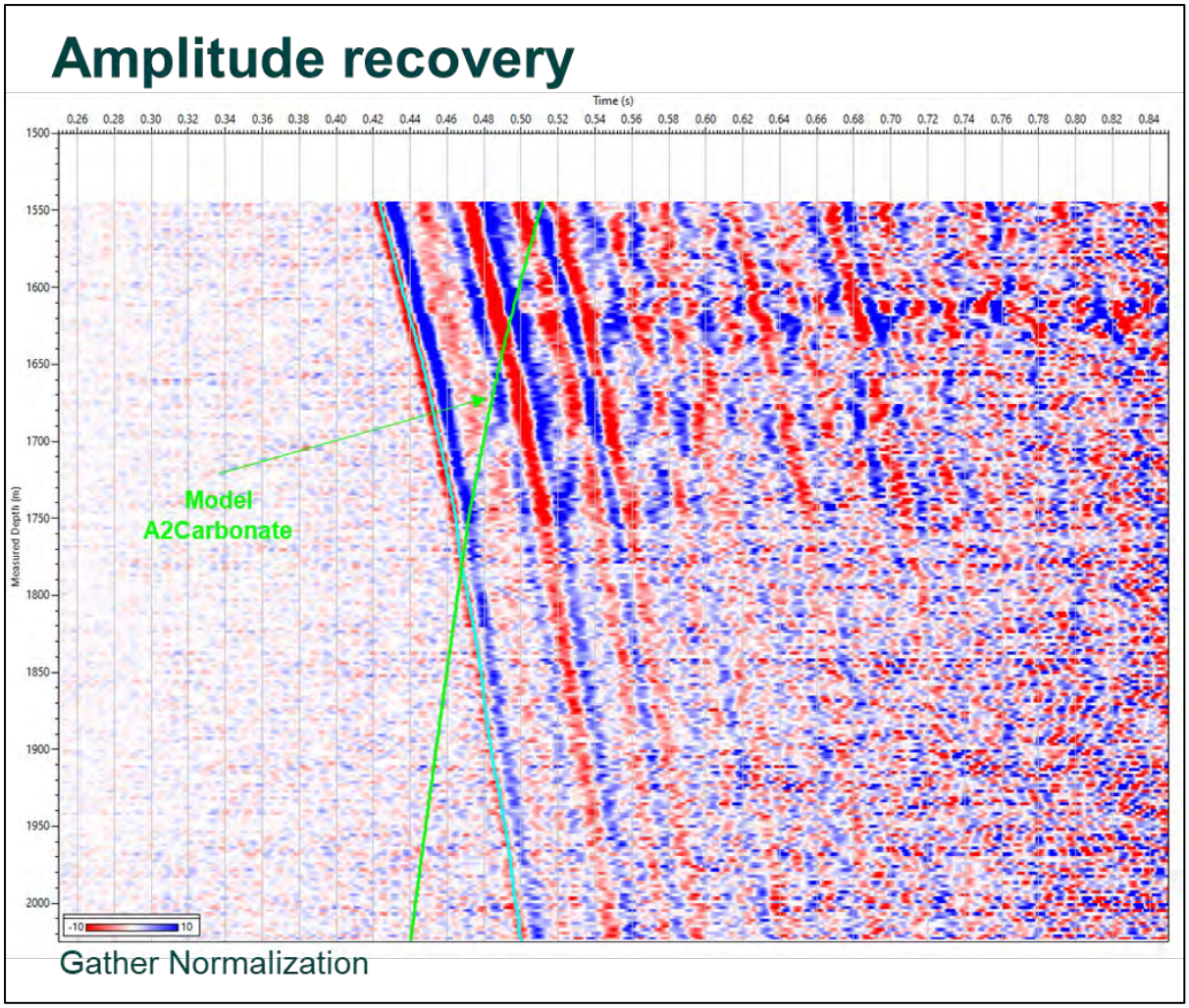


*Figure 9-44. Amplitude recovery - Time power function. To compensate for the absorption and spherical divergence spreading, the amplitude was scaled by the squared sample time. Figure 9.44 shows the stack after amplitude recovery.*

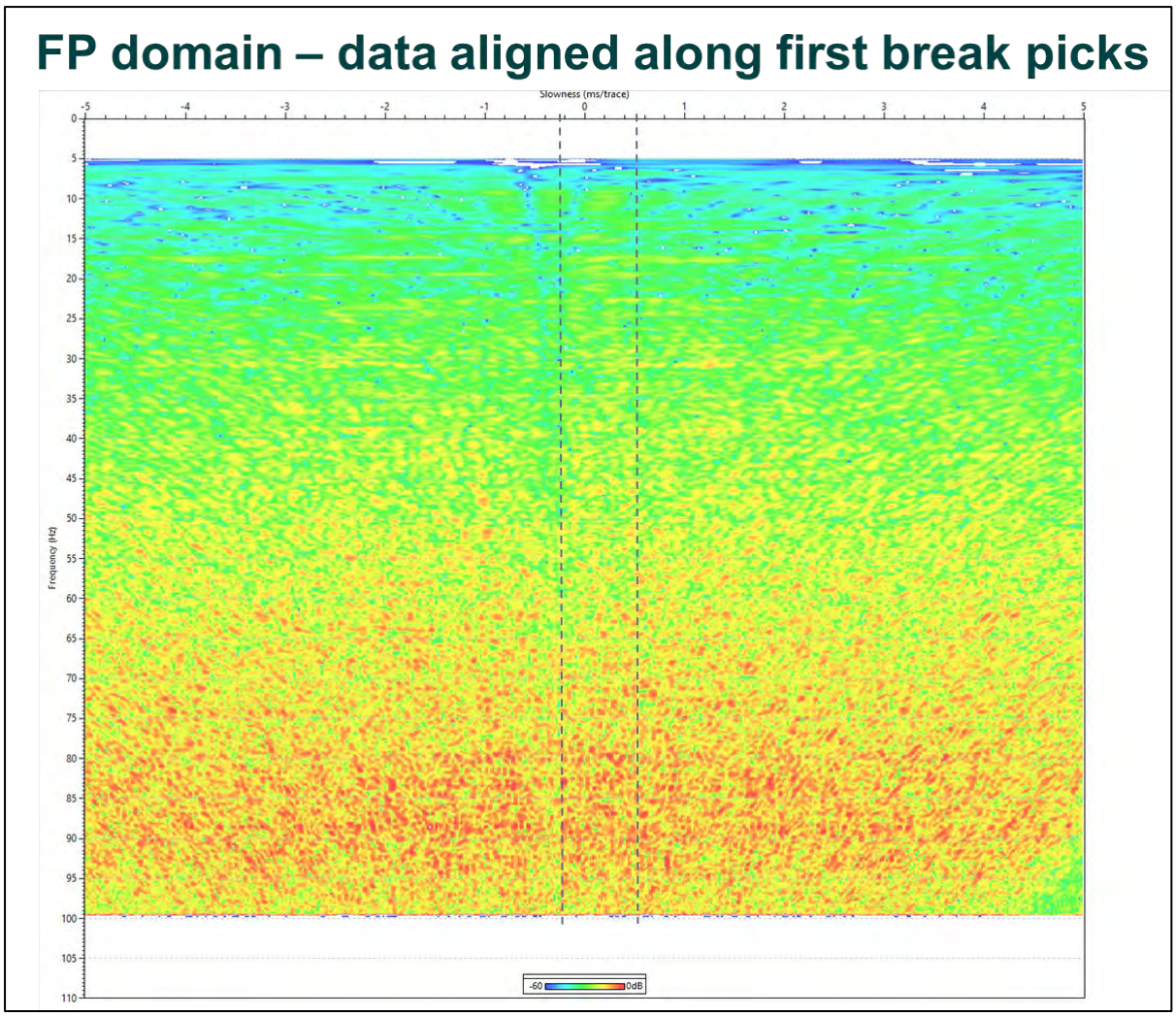


*Figure 9-45. FP domain – data aligned along first break picks - Down separation. Figure 9.45 shows the stack aligned along the first break in the frequency-slowness domain (FP).*

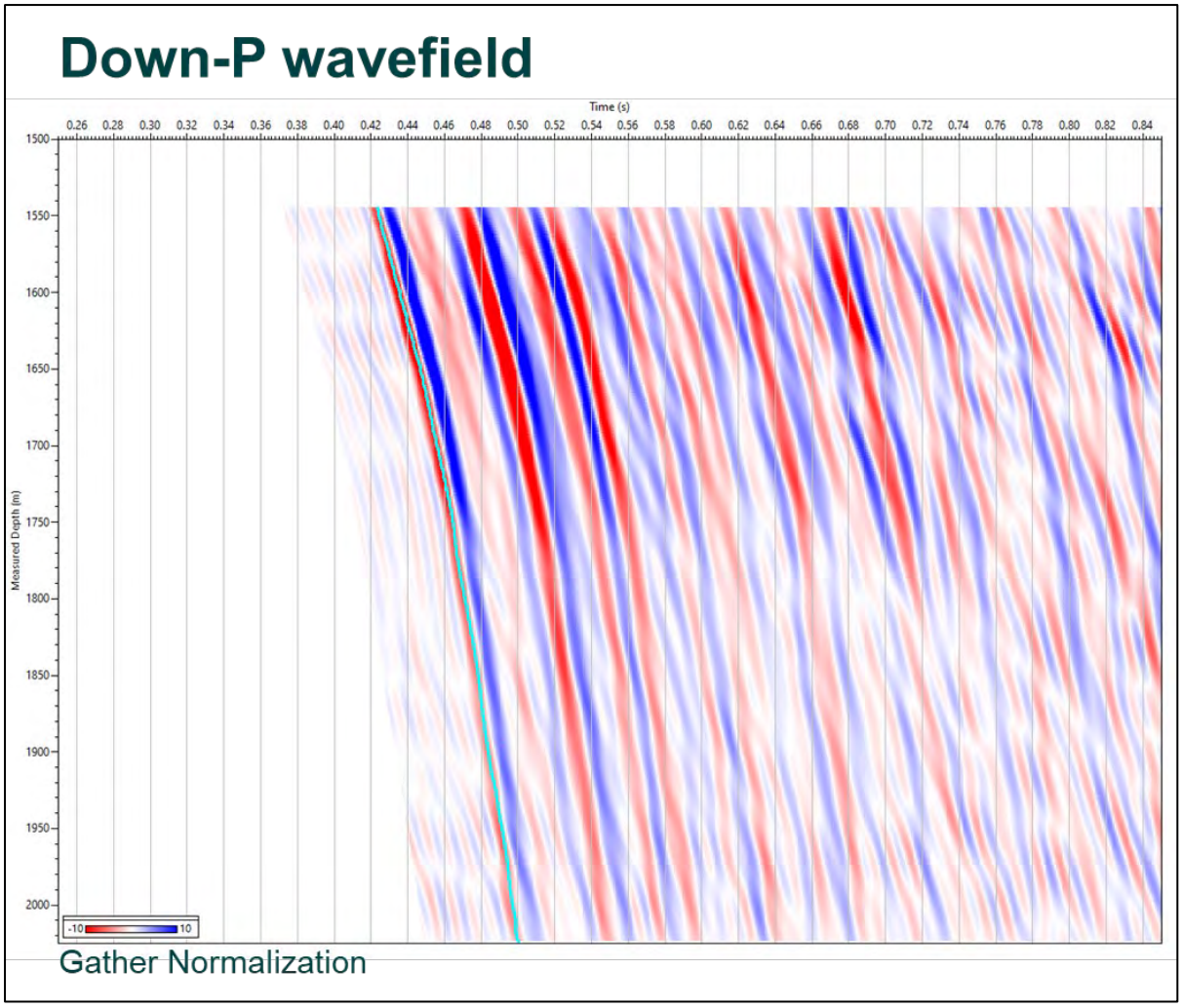


*Figure 9-46. Down wavefield - Down separation. The Down wavefield was separated by retaining the data inside the -0.3 – 0.6 slowness window. Figure 9.46 presents the data after the separation in the FP domain.*

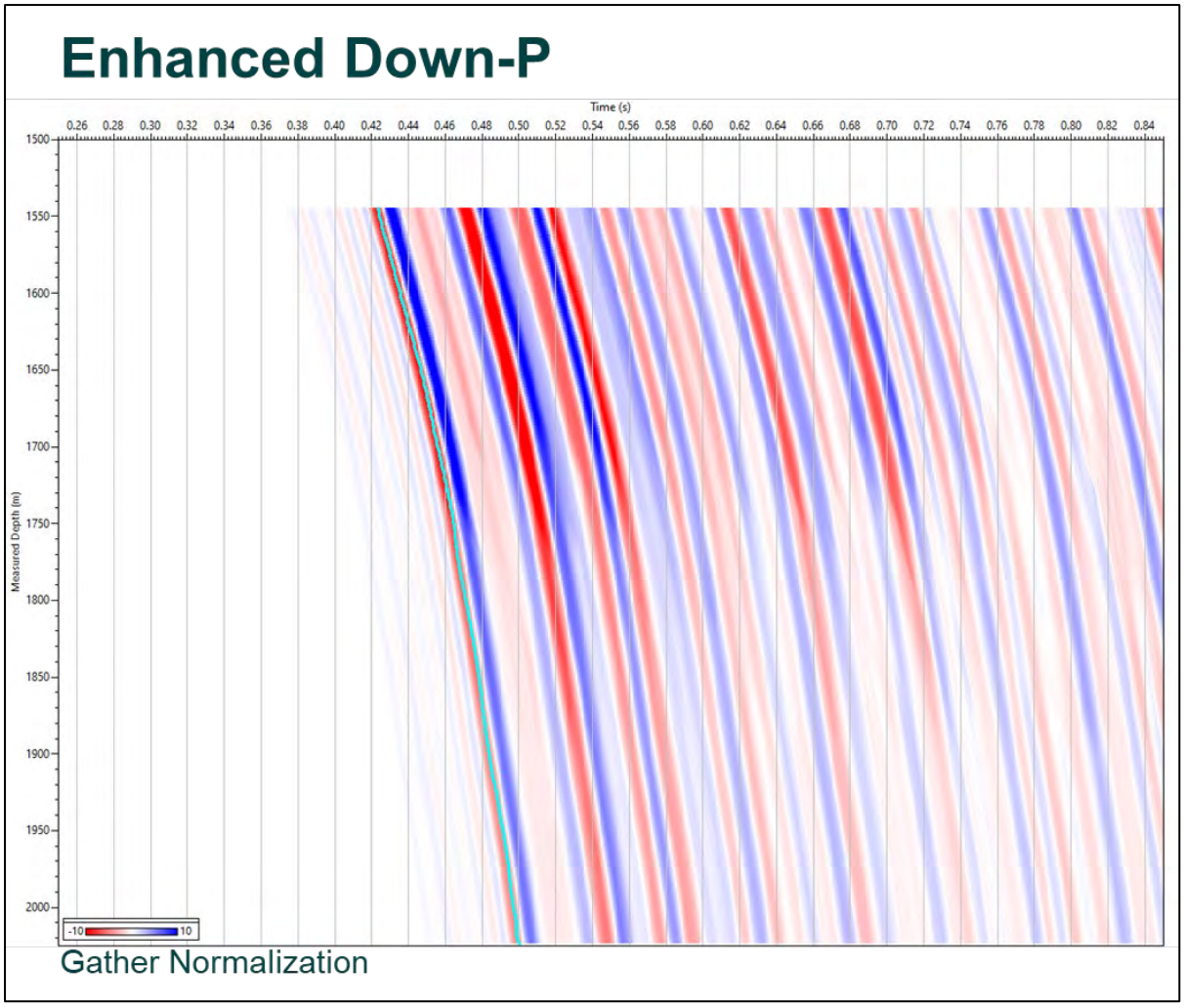


*Figure 9-47. Enhanced Down-P - Median filter. This figure shows the Down P wavefield after enhancement using a median filter of 121 traces along the FB. This wavefield will be used later in the deconvolution.*

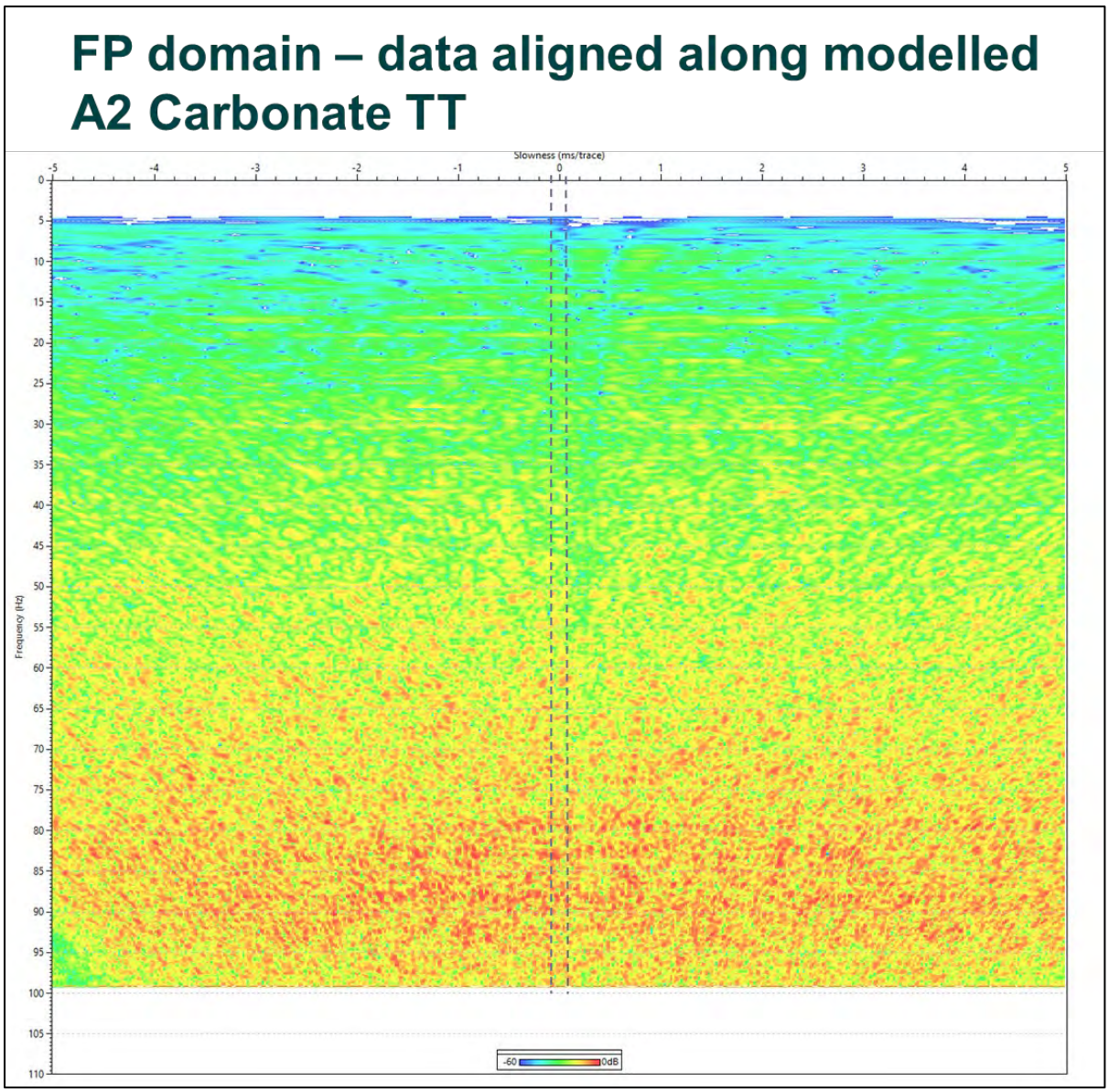


*Figure 9-48. FP domain – data aligned along modelled A2 Carbonate TT - Enhance Up P. The Up P wavefield was separated in the FP domain in a slowness window of -0.10 to 0.10 ms/traces.*

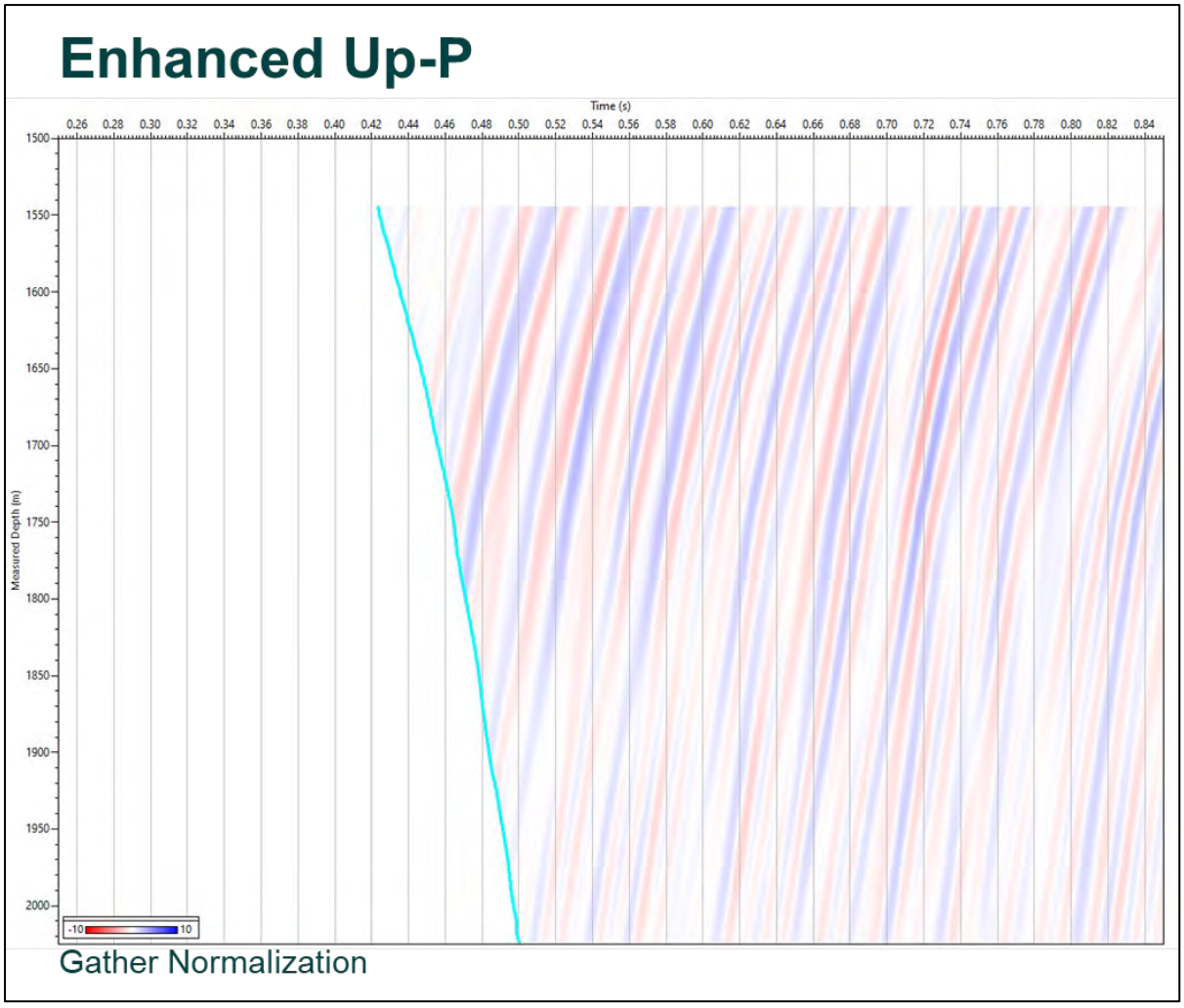


*Figure 9-49. Enhanced Up-P - After FP separation. The input data was aligned along the A2 Carbonate modelled TT (Fig. 9.44 green) before FP. Figure 9.49 shows the enhanced Up P along the modelled A2 Carbonate TT over a 10 trace window after the separation in the FP domain.*

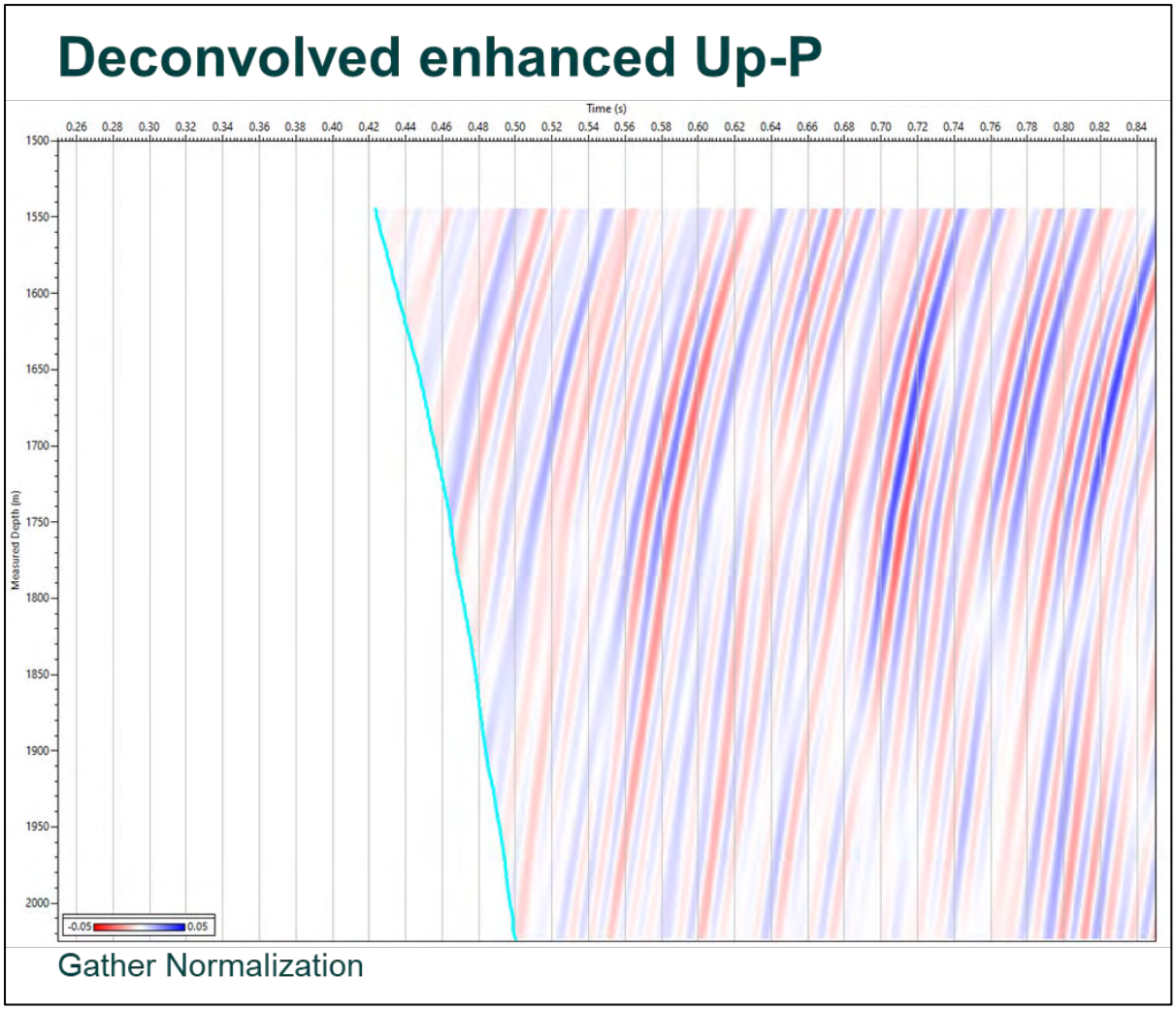


*Figure 9-50. Deconvolved enhanced Up-P - Trace by trace deterministic deconvolution. To reduce the multiples and increase the data high frequency, the enhanced Up P was deconvolved. Trace by trace deterministic deconvolution with enhanced Down P (Fig. 9.47) using a 0.15 s operator length and 20% white noise was applied to the enhanced Up P. Finally, the data were filtered with a 5,10-90,110 Hz BPF.*

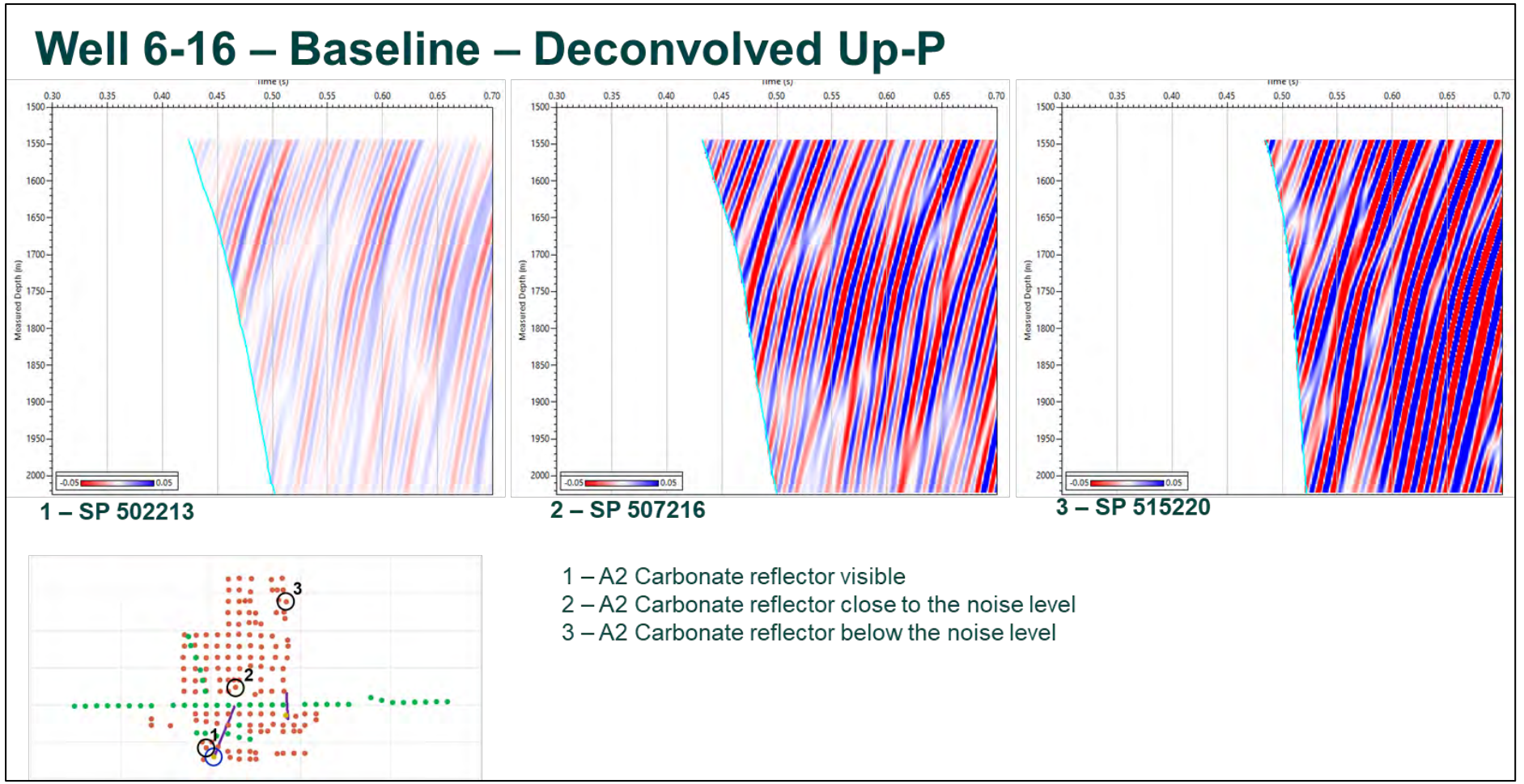


*Figure 9-51. Well 6-16 – Baseline – Deconvolved Up-P - Far, mid and near offsets.*

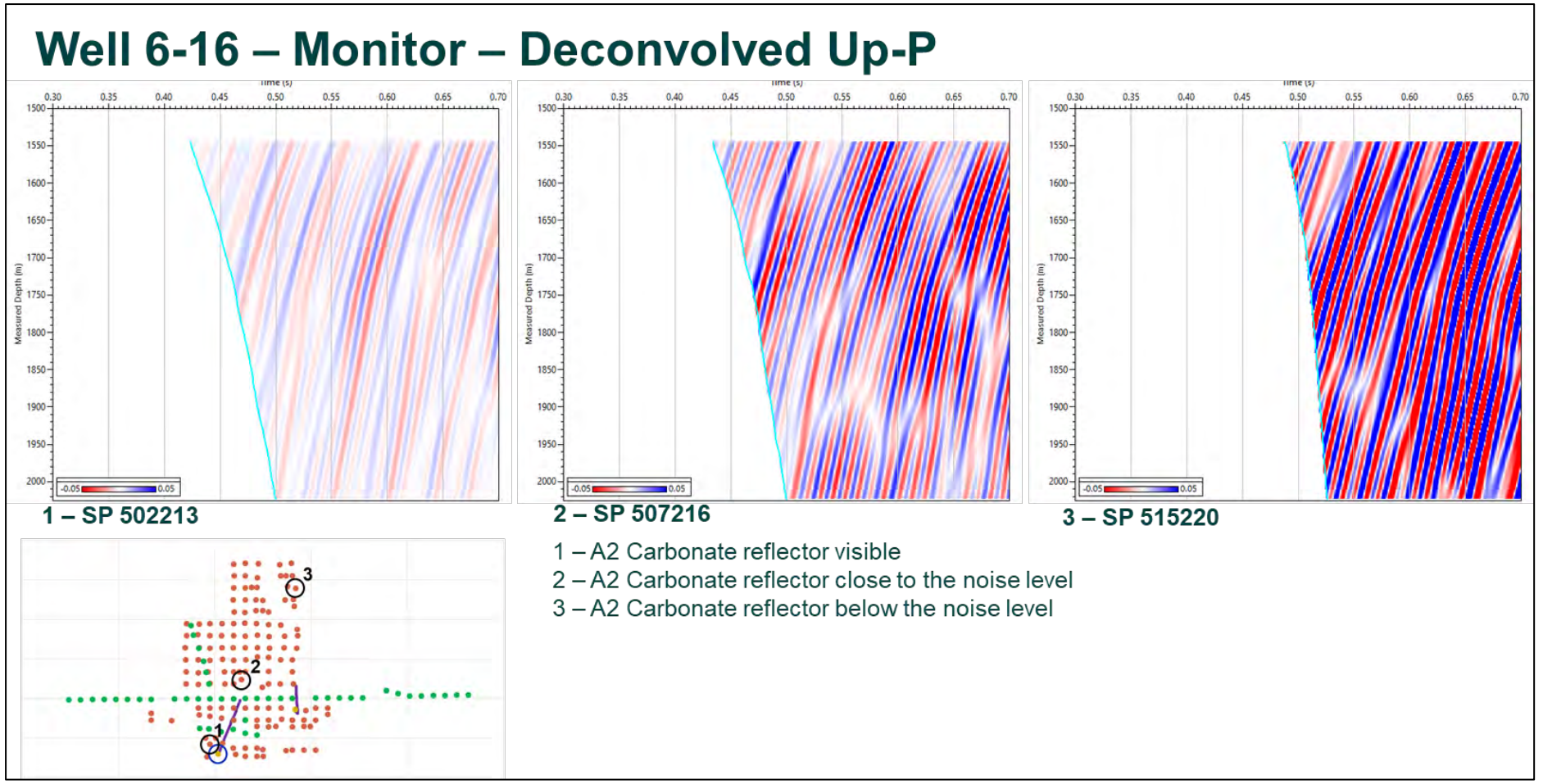


*Figure 9-52. Well 6-16 – Monitor – Deconvolved Up-P - Far, mid and near offsets.*

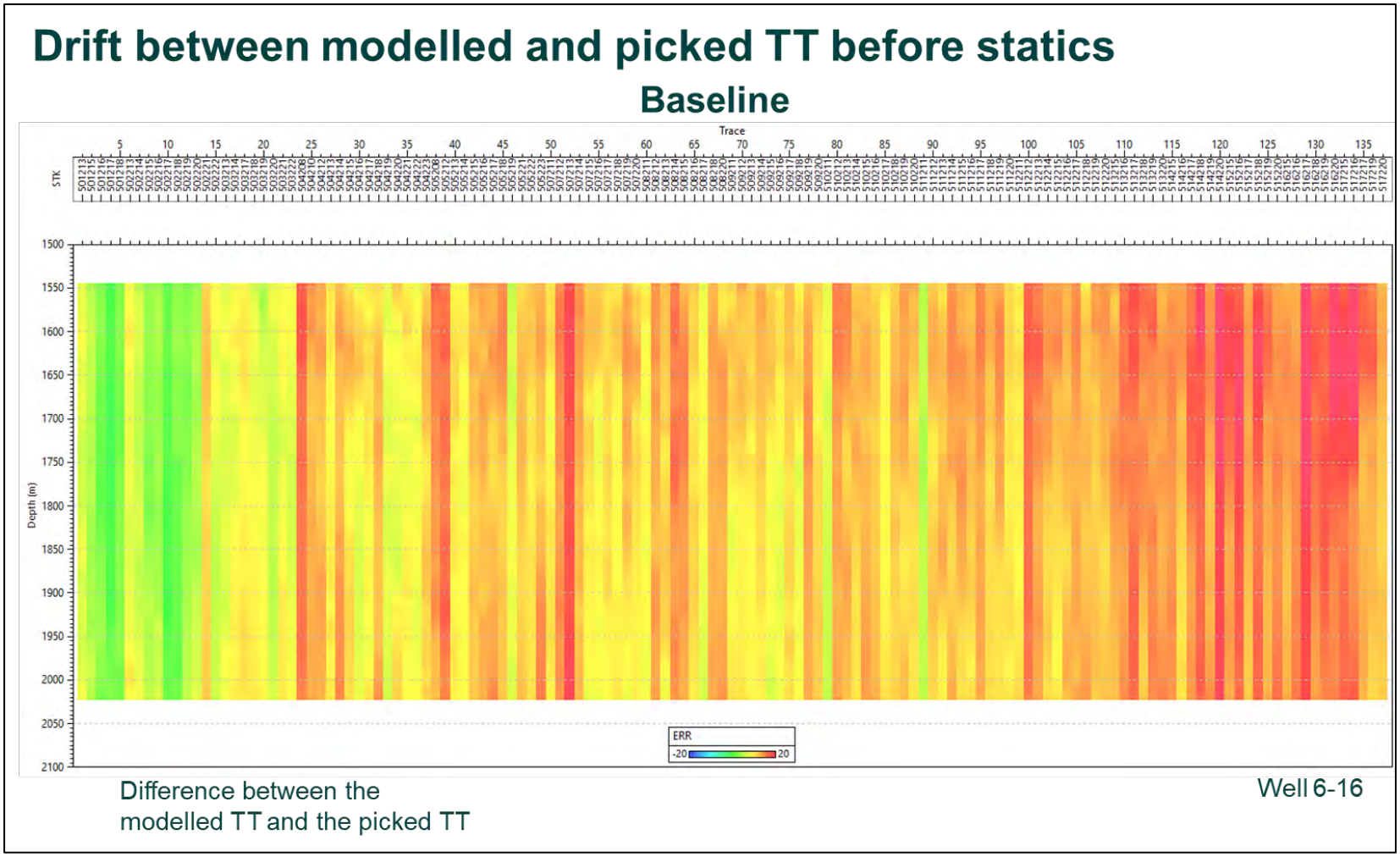


*Figure 9-53. Drift between modelled and picked TT before statics – Baseline. Figure 9.53 presents the drift between the modelled TT and the picked TT for the baseline survey. The difference between the model TT and the picked TT was computed for each SP all along the available data interval. On the horizontal axis is the Shot Point number, on the vertical axis is the Measured Depth (MD from KB) and the difference is colour coded. The difference mainly appears as vertical stripes suggesting there is mainly a static shift between the model and the picks. Between nearby shots there is a gradual increase or decrease in difference.*

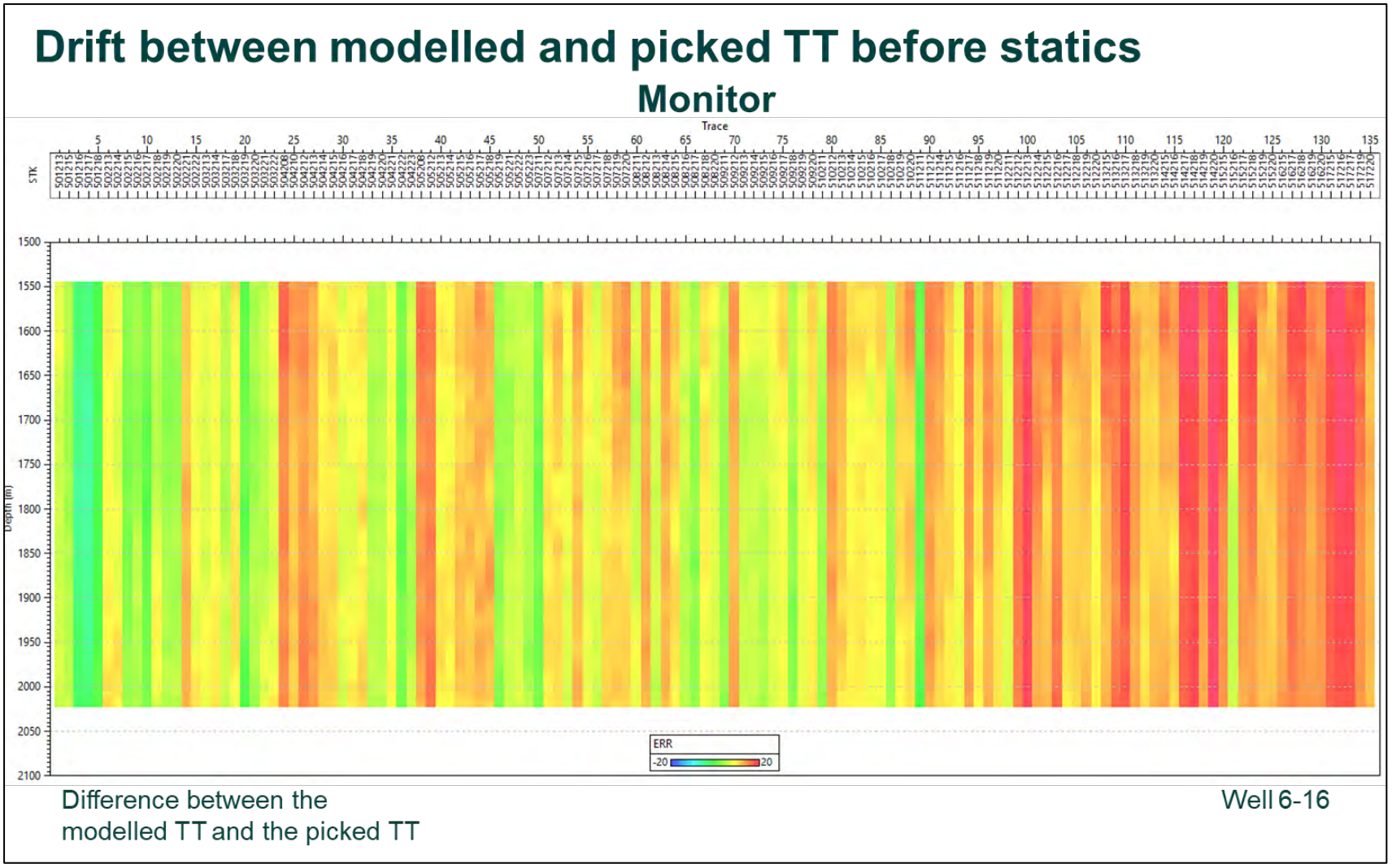


*Figure 9-54. Drift between modelled and picked TT before statics – Monitor. Between the baseline (Fig 9.53) and monitor survey (Fig. 9.54), the errors have different values due to different weathering zone properties as well as the picking uncertainty. Nevertheless, both follow the same pattern confirming that the shift is mainly due to the lateral velocity changes in the weathering zone.*

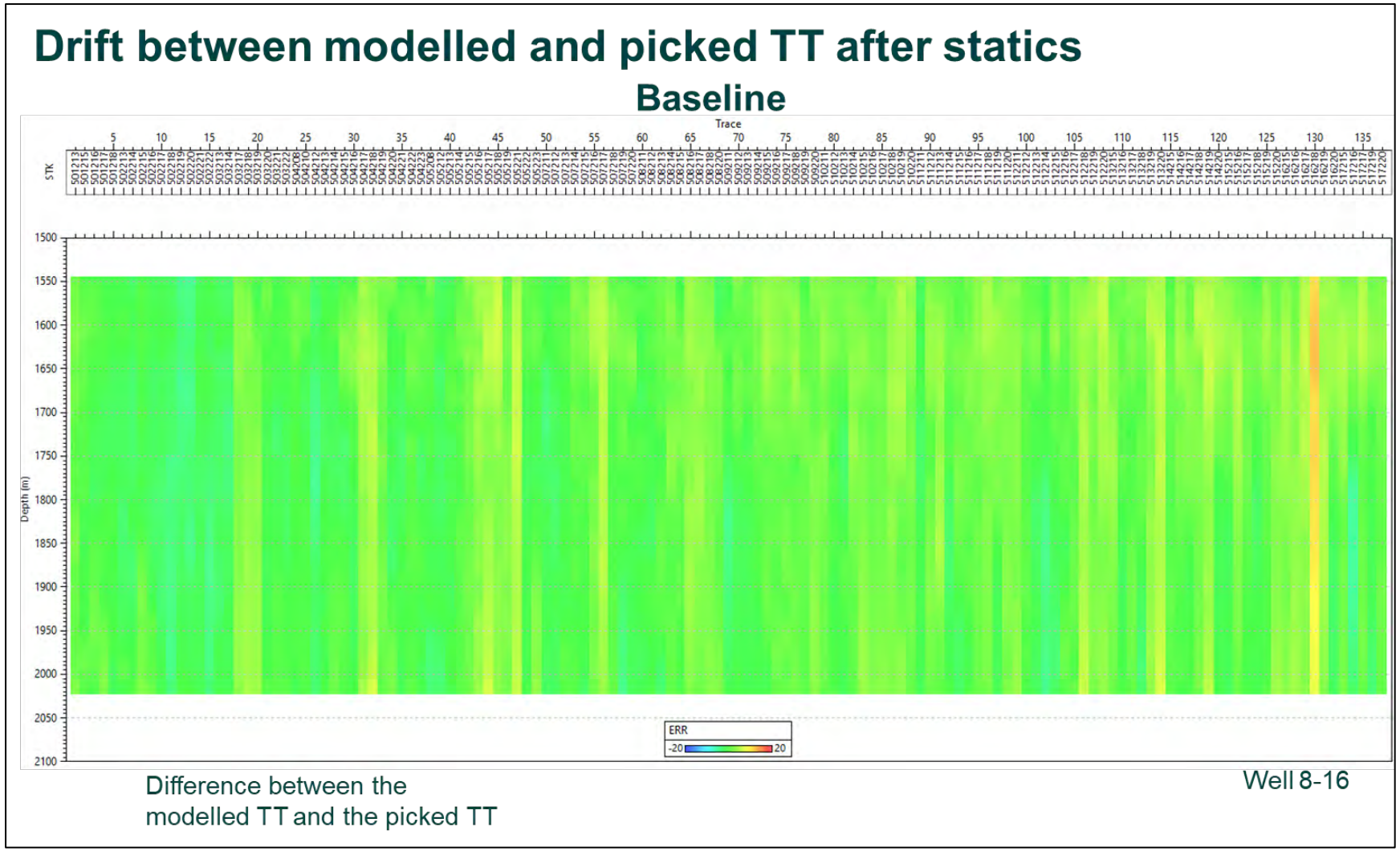


*Figure 9-55. Drift between modelled and picked TT after statics – Baseline.*

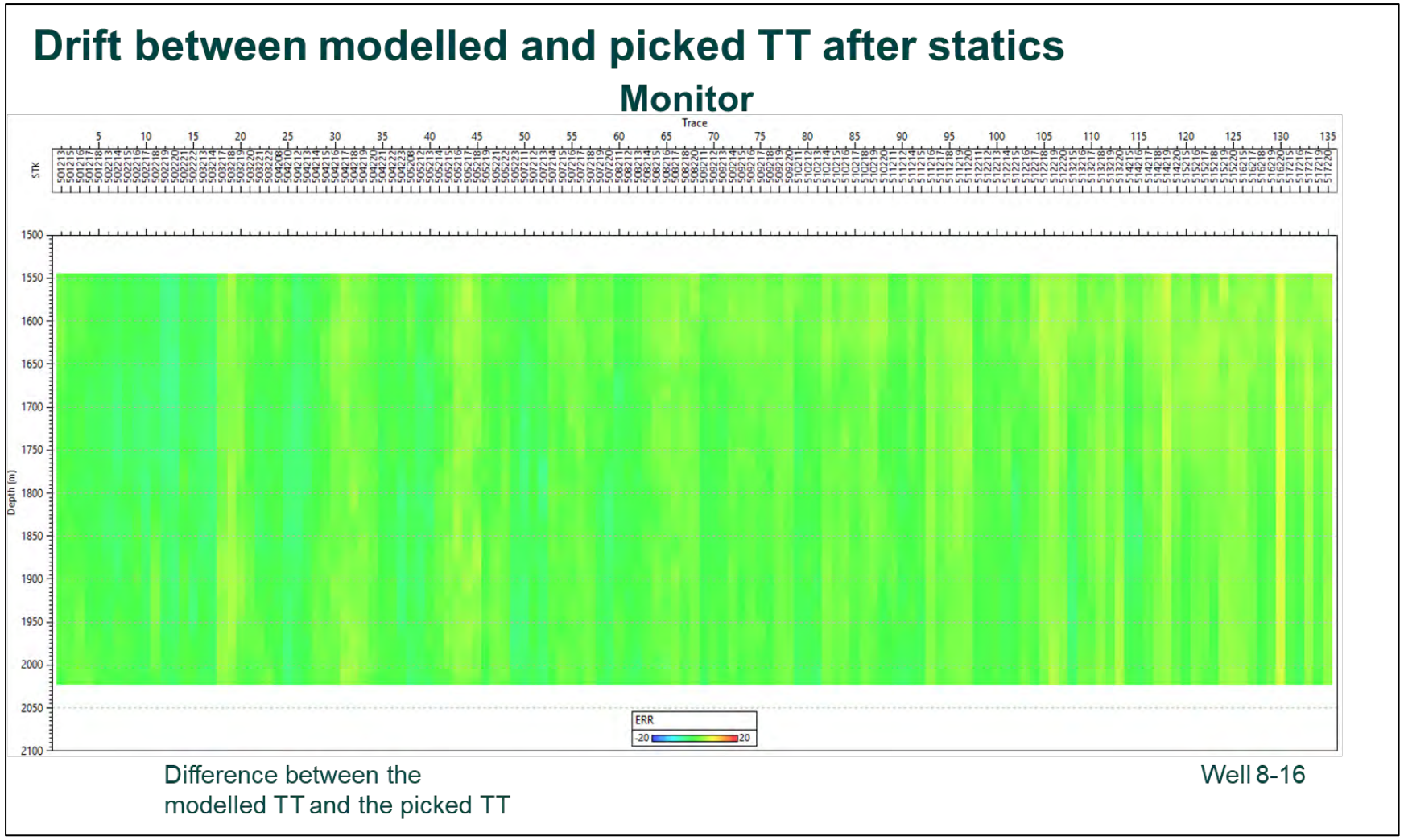


*Figure 9-56. Drift between modelled and picked TT after statics – Monitor.*

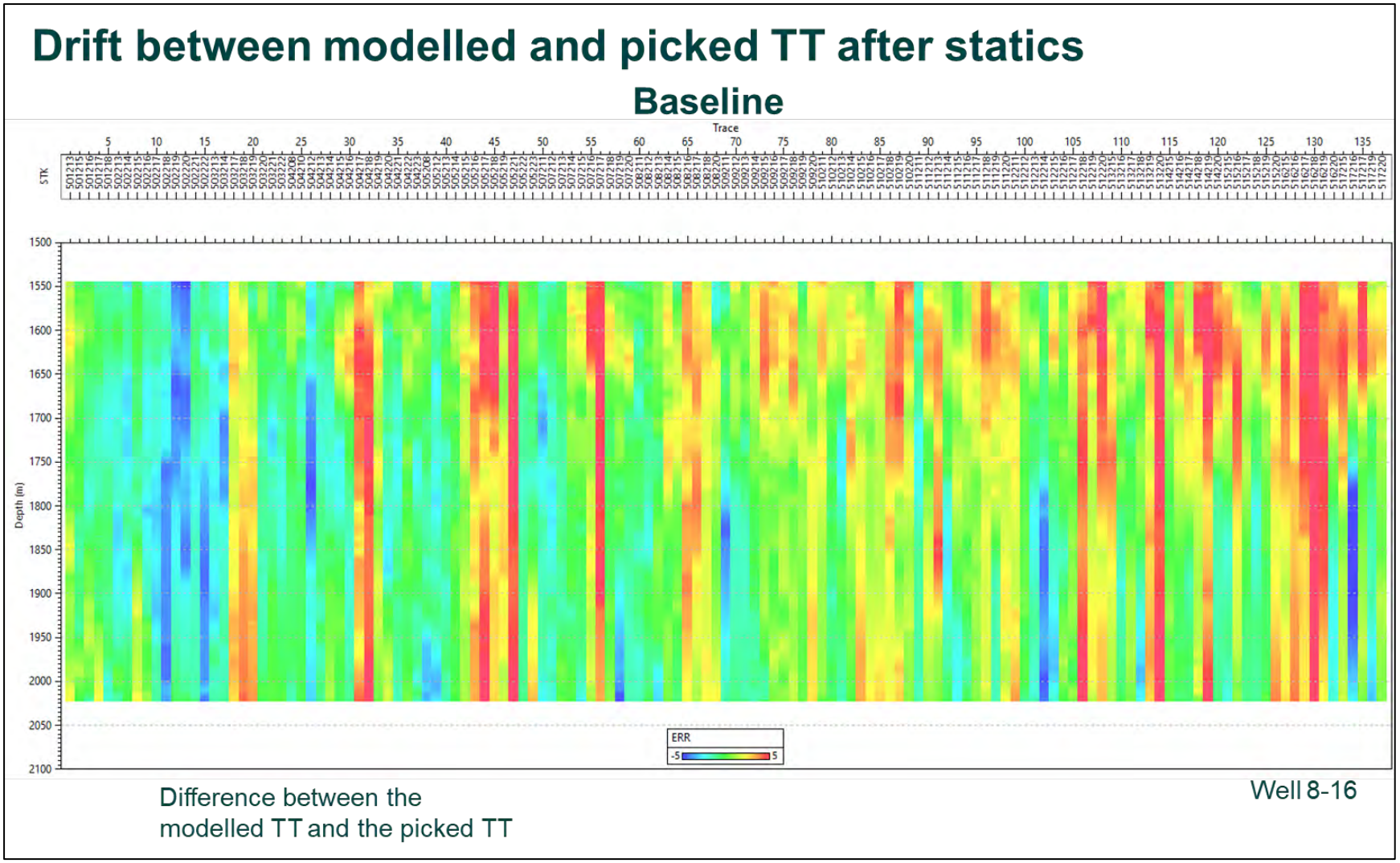


*Figure 9-57. Drift between modelled and picked TT after statics – Baseline.*

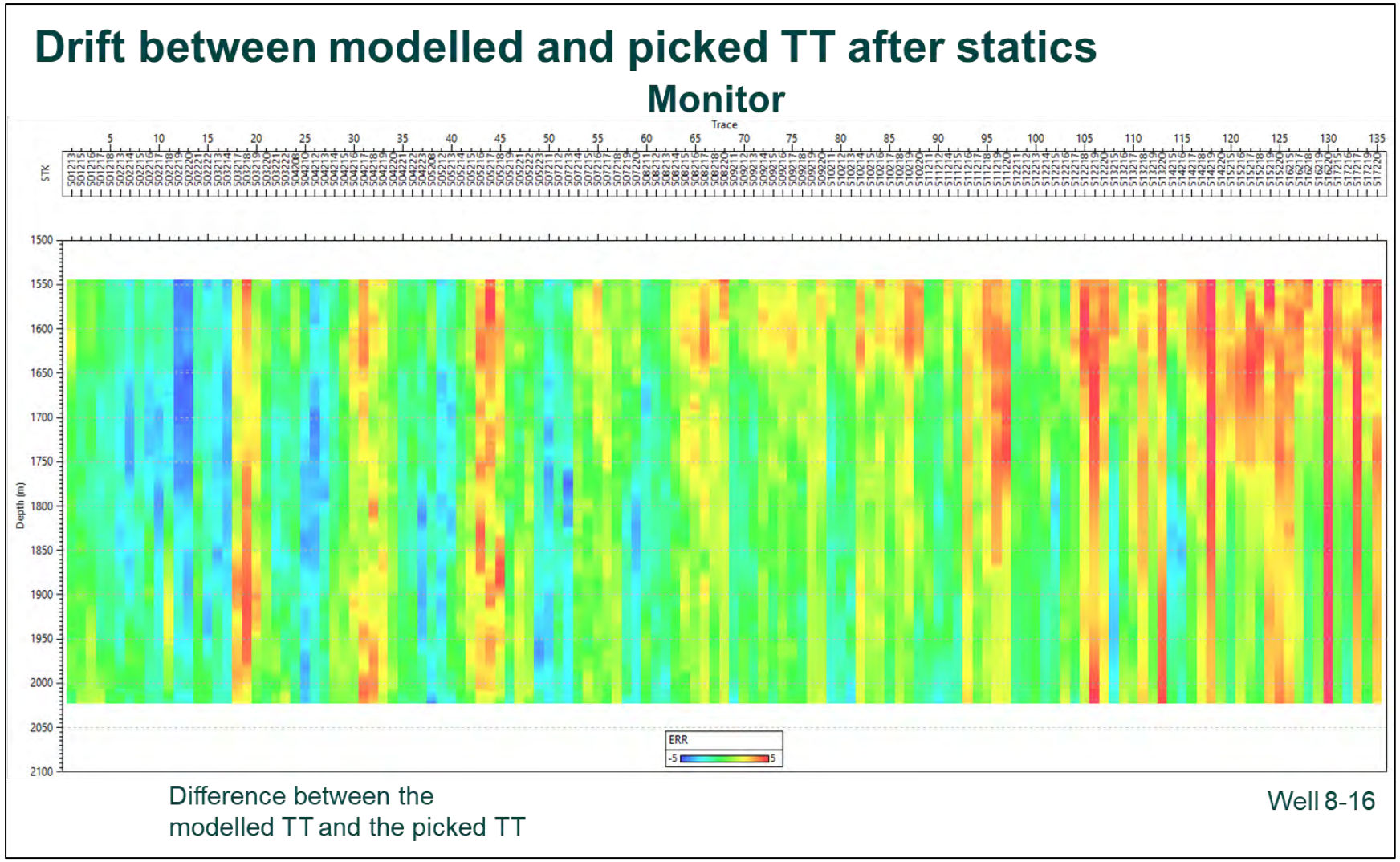


*Figure 9-58. Drift between modelled and picked TT after statics – Monitor.*

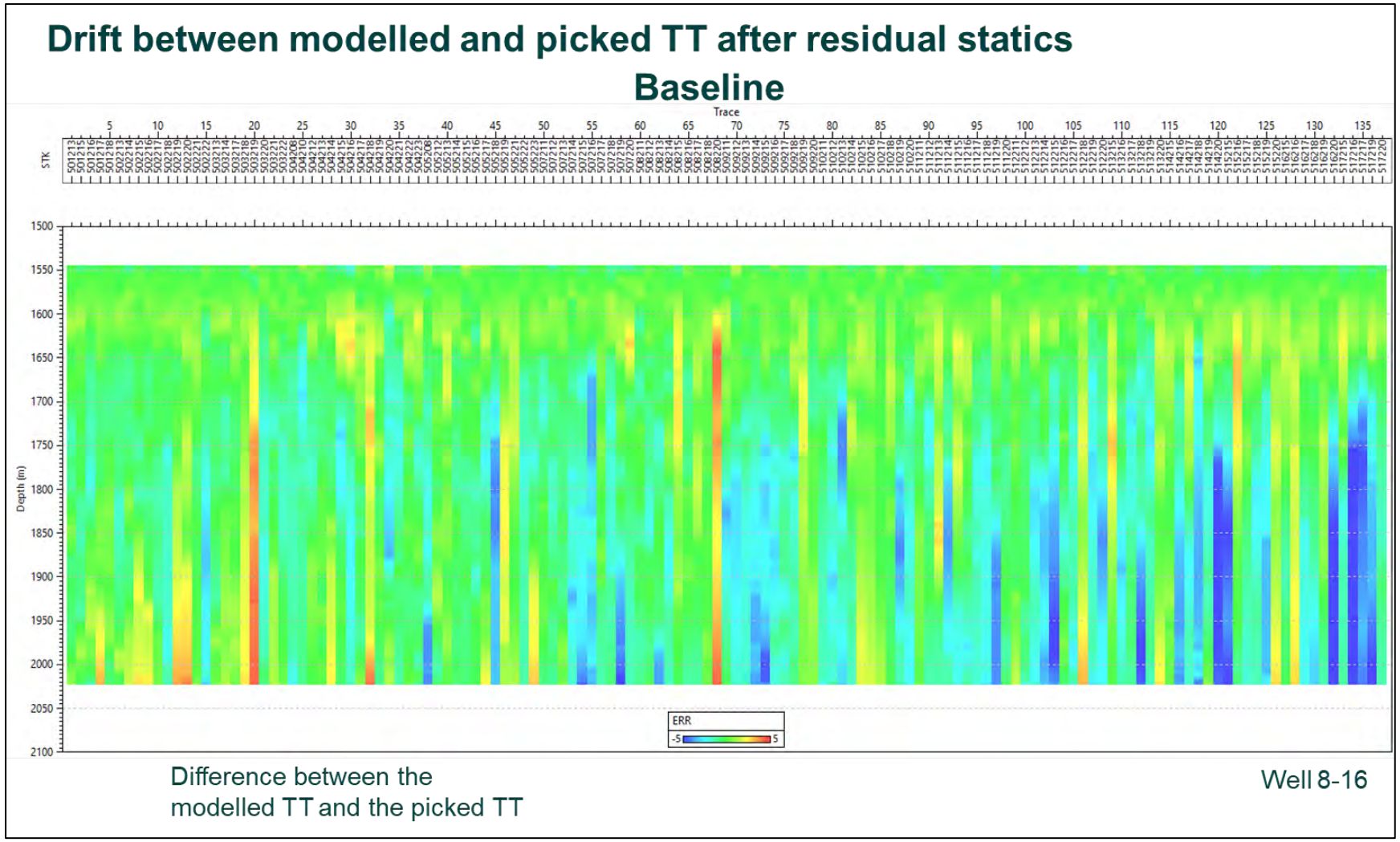


*Figure 9-59. Drift between modelled and picked TT after residual statics – Baseline.*

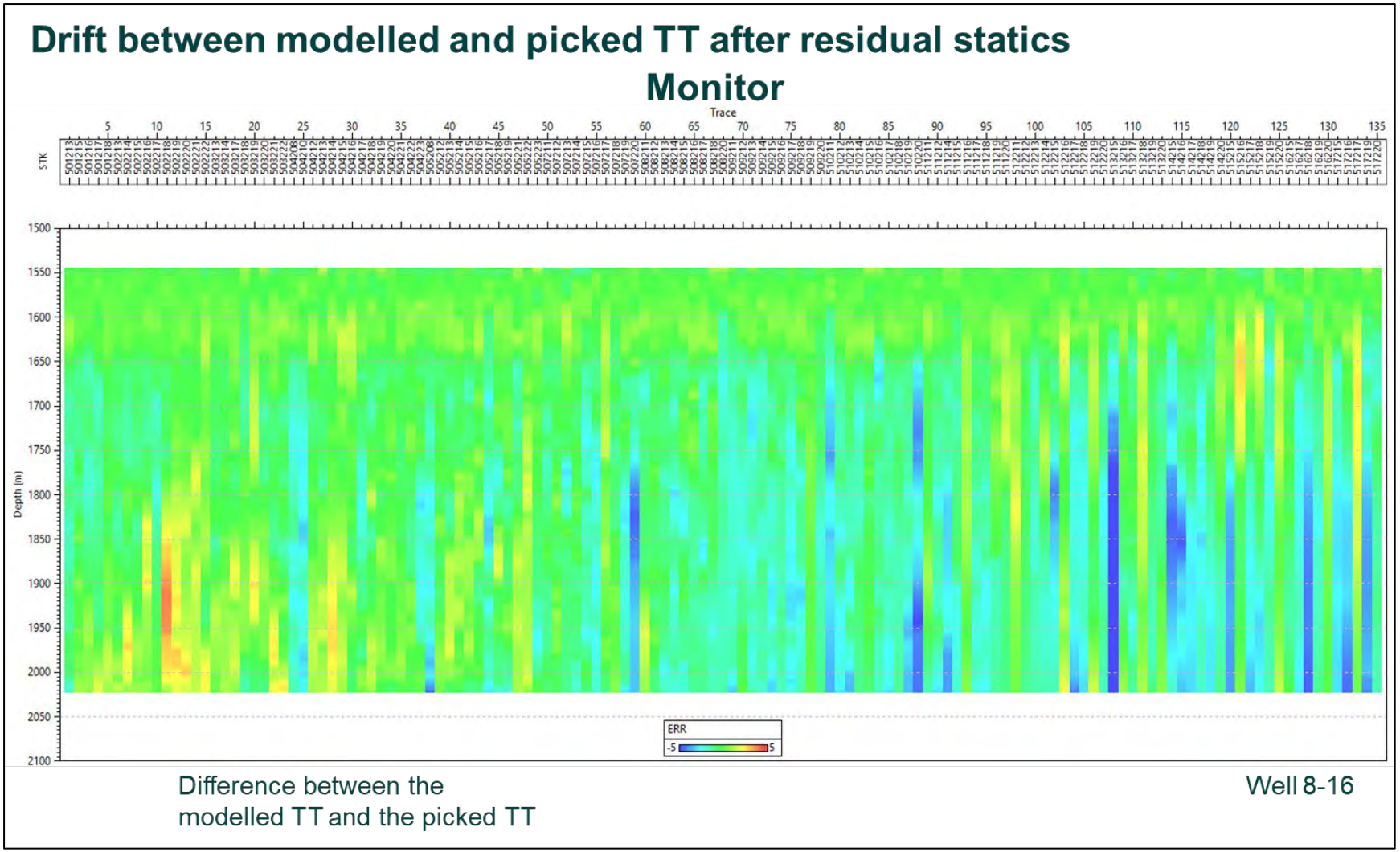


*Figure 9-60. Drift between modelled and picked TT after residual statics – Monitor.*

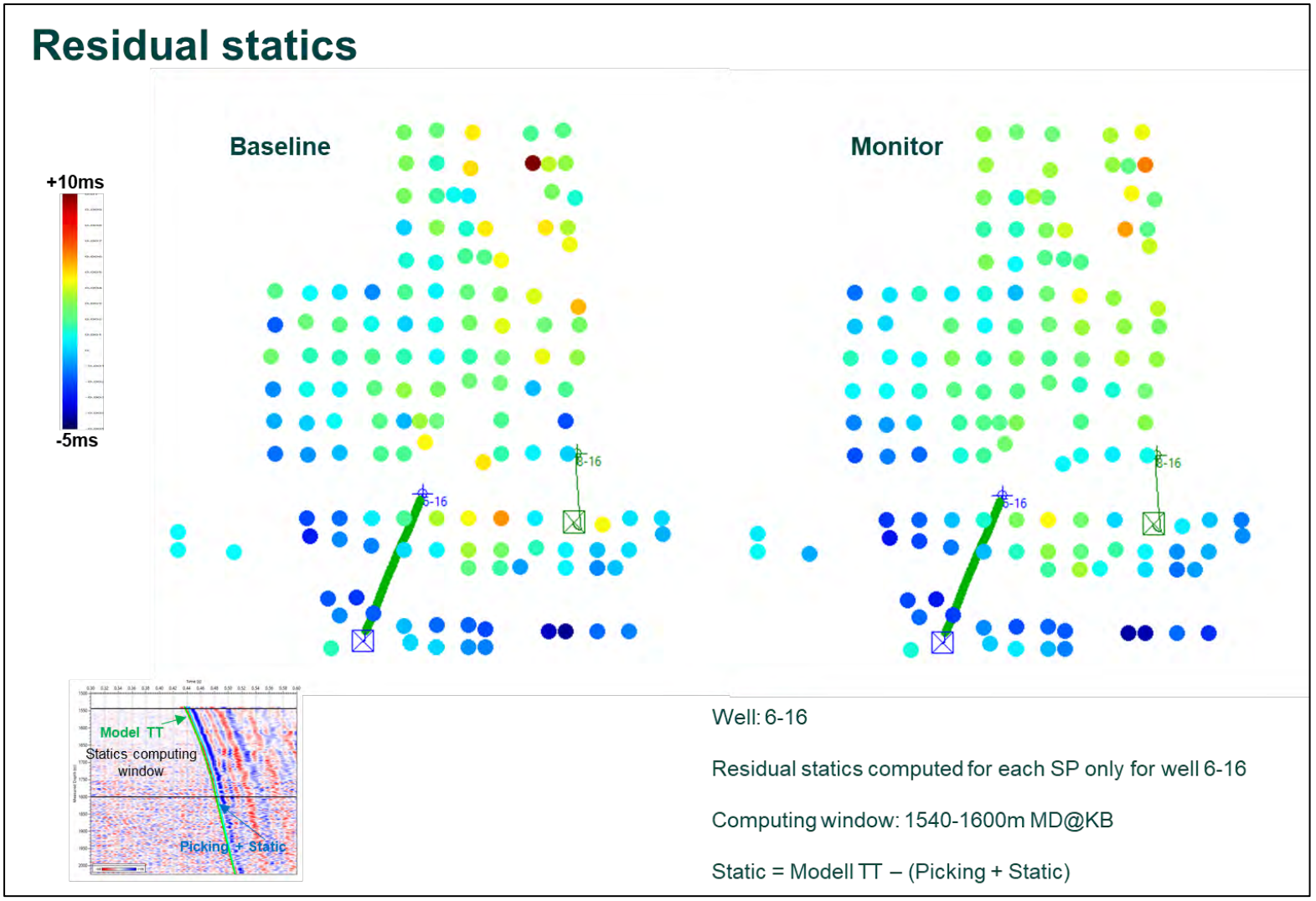


*Figure 9-61. Statics - Plane view with statics for each SP. Using the statics computed based on the well 6-16 data, the remaining error is still significant. Residual statics were computed by averaging the error over the 1540 m – 1600 m MD interval (Fig. 9.61 bottom left). Residual static shift values were calculated separately for the baseline and monitor surveys (Fig. 9.61).*

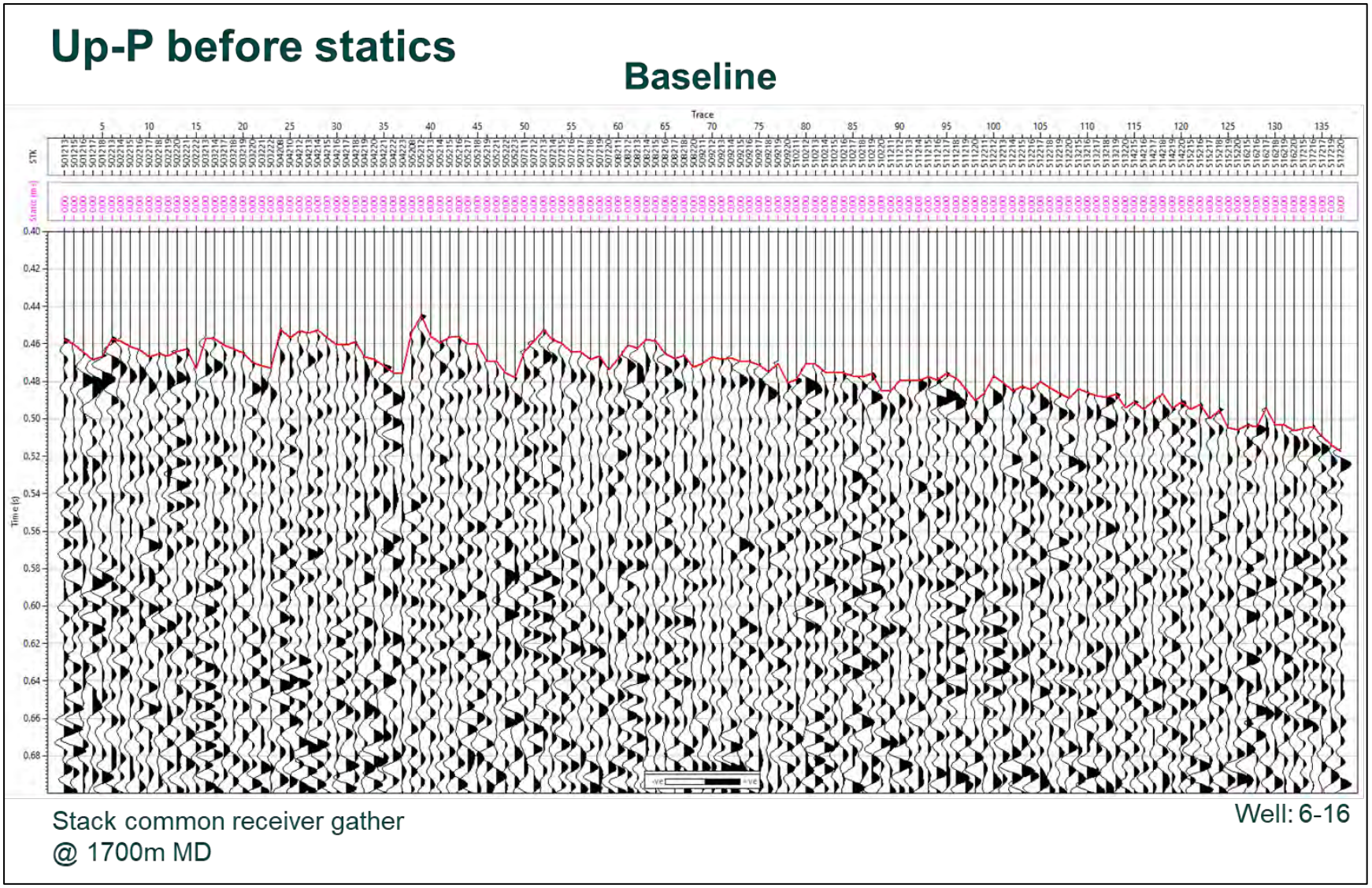


*Figure 9-62. Up-P before statics - Common receiver gather – Baseline.*

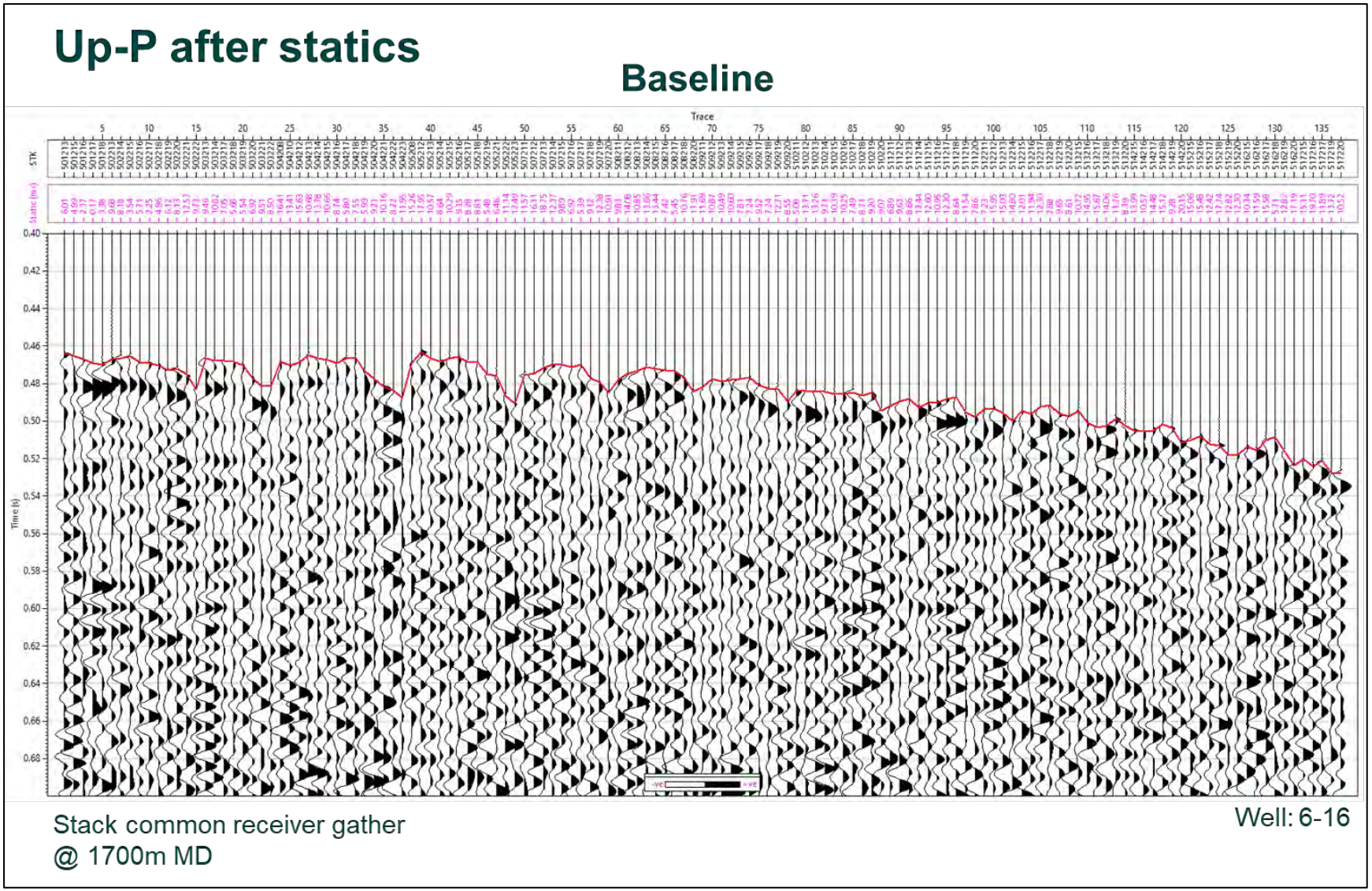


*Figure 9-63. Up-P after statics - Common receiver gather – Baseline.*

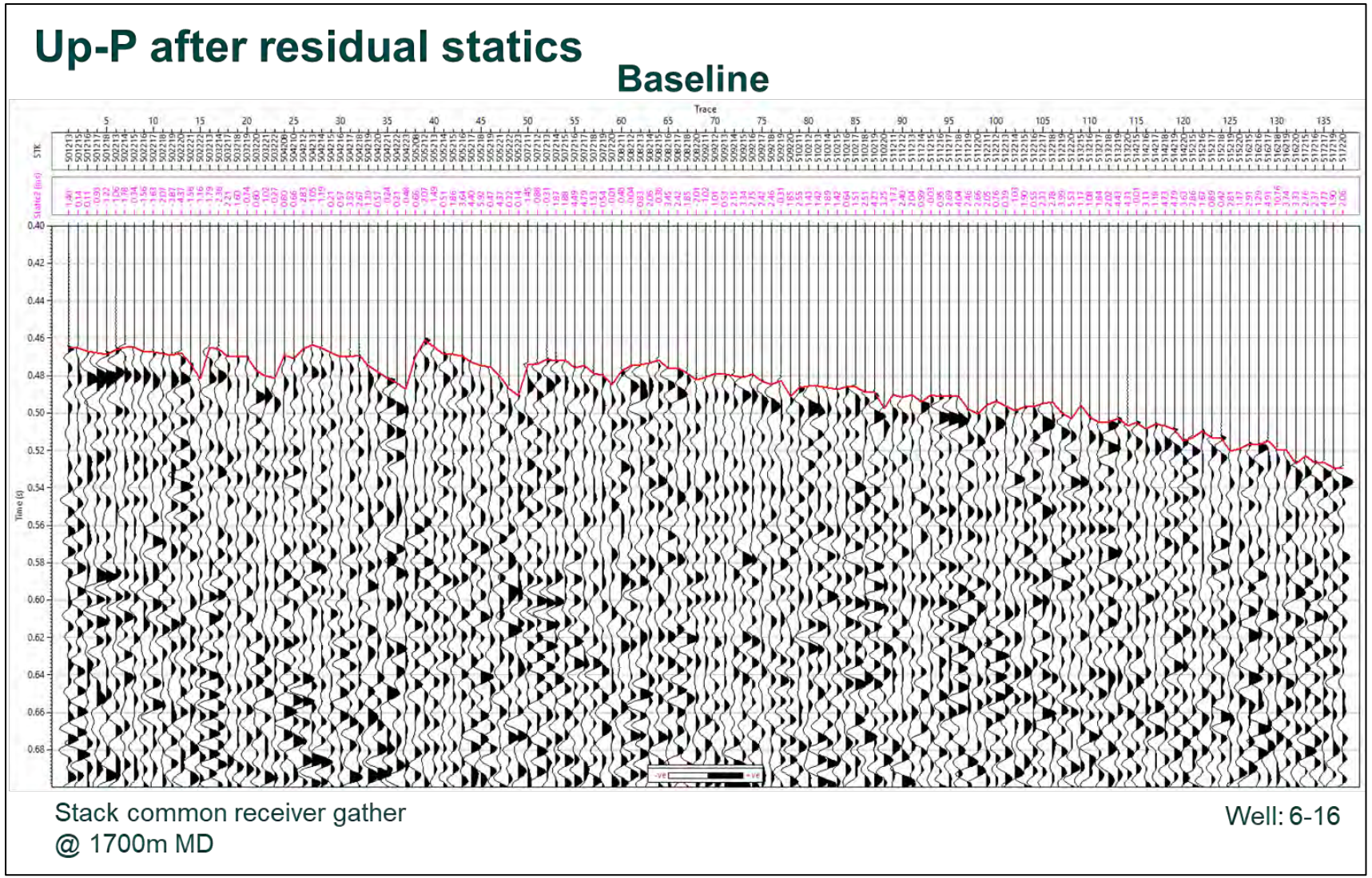


*Figure 9-64. Up-P after residual statics - Common receiver gather – Baseline. This figure shows the baseline Up P common receiver gather at 1700 m MD after the residual statics correction.*

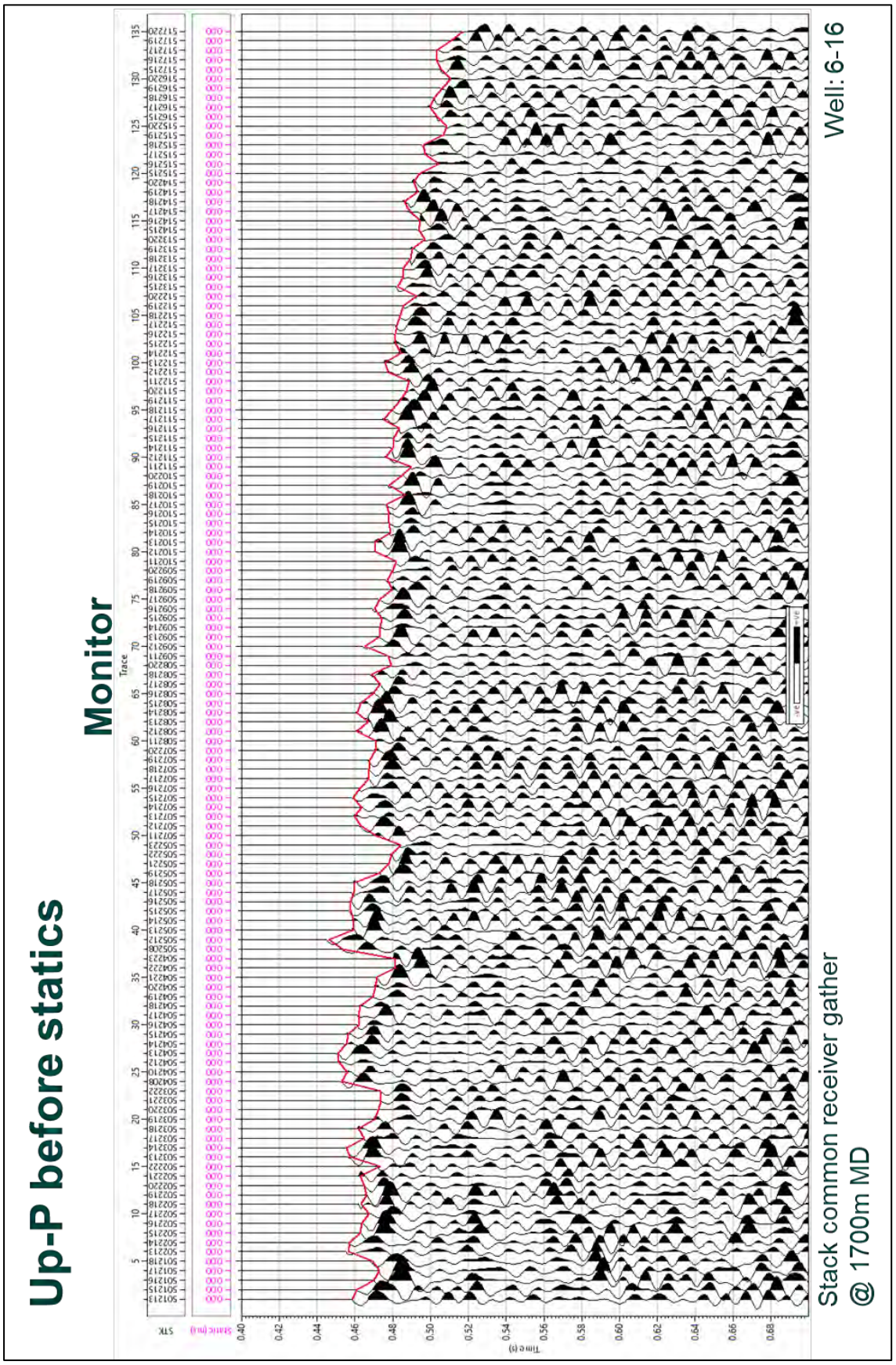


*Figure 9-65. Up-P before statics - Common receiver gather – Monitor.*

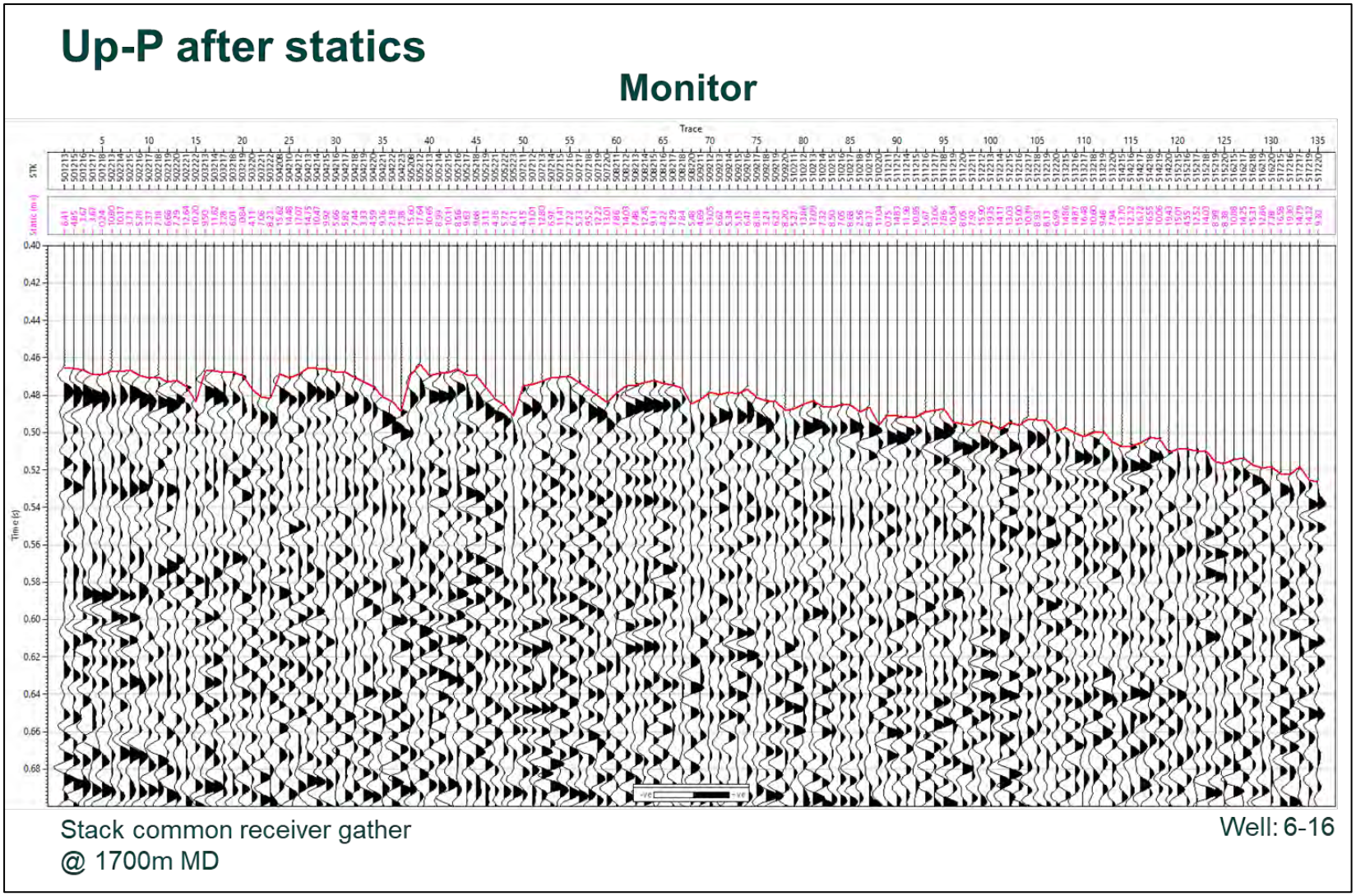


*Figure 9-66. Up-P after statics - Common receiver gather – Monitor.*

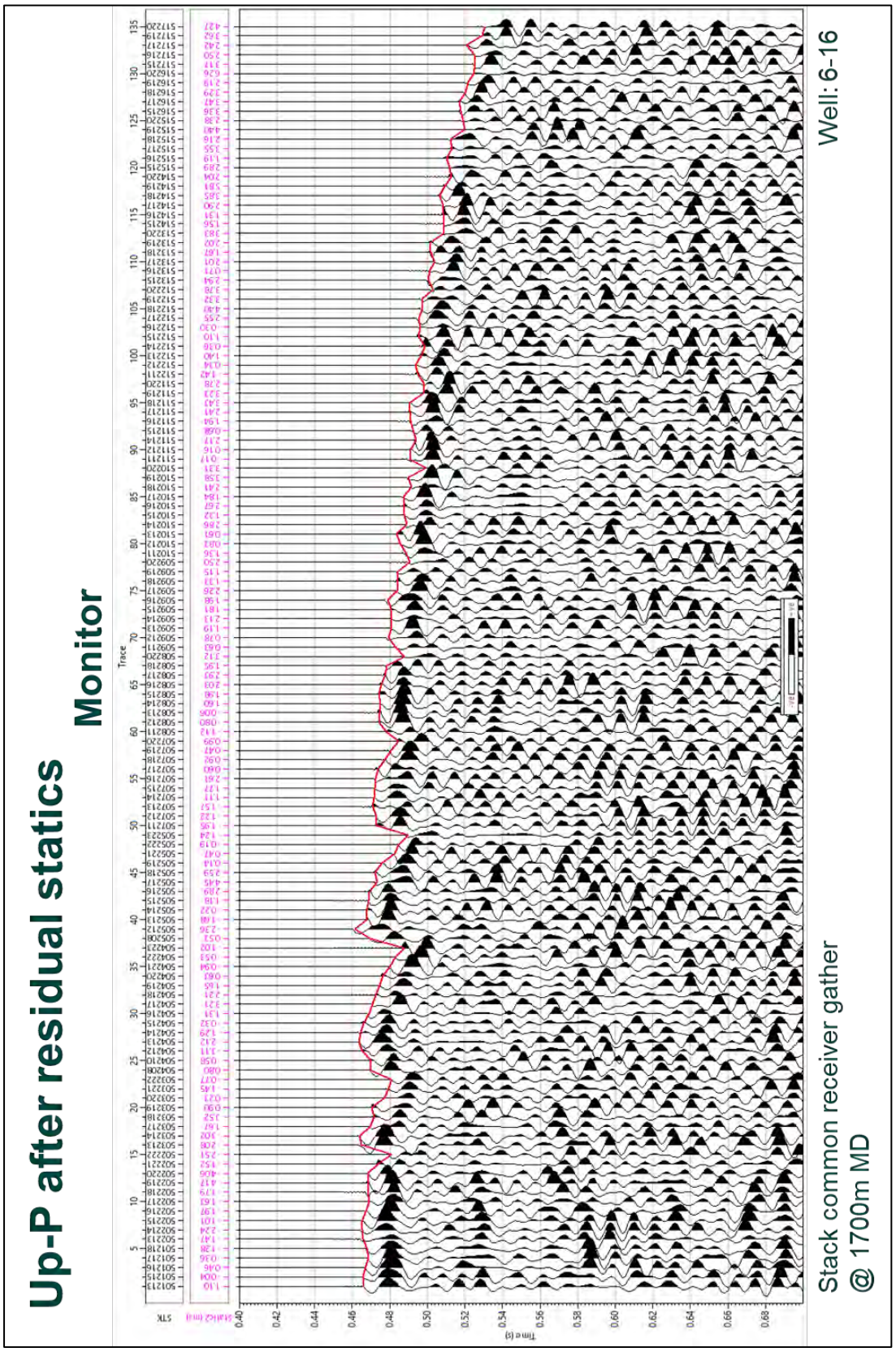


*Figure 9-67. Up-P after residual statics - Common receiver gather – Monitor.*

# 10 Velocity Model

This section describes the 3D velocity model building and calibration. The same model was used to image both surveys. Ray-tracing is performed to map the shot point reflectivity. The velocity model was ray-traced to generate the modelled TT used to guide the picking and during the data processing (sections 7 to 9).

A flat layer model was computed based on the geological markers and the well 6-16 acoustic logs. The layer boundaries were defined at significant changes of the log velocity profile (Fig. 10-1).

The acoustic logs (Fig. 10-1 graphs 1 and 2) were converted to velocity (Fig. 10-1 graphs 3 and 4). For each layer the compressional velocity, shear velocity and density values were computed by averaging the log velocity and density data (Fig. 10-1 black curves).

The dynamite charge elevation values are between 385 m and 406 m above MSL and the vibroseis GL elevation values range from 392 m to 406 m above MSL. In the shallow part of the velocity model two additional layers at 410 m above MSL (above the sources elevation) and at 380 m above MSL (below the sources elevation) were added. After the velocity model calibration with the well 8-16 ZVSP profile, a Vp value of 1100 m/s (550 m/s for Vs) was chosen for this layer.

The velocity model layer called “Below SP” in table 10-1 covers mainly unconsolidated Glacial formations. The expected velocity profile of this layer follows a profile close to a gradient increase in velocities. The velocities inside a gradient layer are defined by the following expressions:

$$V_p = V_p0 + \left(k_p(TVDSD - TVDSD_0)\right)$$

$$V_s = V_s0 + \left(k_s(TVDSD - TVDSD_0)\right)$$

where $V_p$ and $V_s$ are the compressional and shear velocities at TVDSD; TVDSD is the vertical depth referred to the model datum; $V_p0$ and $V_s0$ are the starting velocities at $TVDSD_0$ reference point; $k_p$ and $k_s$ are the gradients.

Over 2000 iterations were computed with random values of Vp (800 m/s – 2200 m/s range) and kp (0 – 10 range) for the “Below SP” velocity model layer. All these models were ray-traced and the difference between the model TT and the picked TT was computed for all the vibroseis source locations. For each iteration a Root Mean Square (RMS) difference value was computed over a defined interval.

Figure 10-2 shows a scatter plot of the average model TT – picked TT difference RMS after the random iterations for well 6-16. Only the data above the A2 Carbonate (1000 m to 1725 m MD) were considered. On the vertical axis is $V_p0$, on the horizontal axis is $k_p$ (scaled by 100) and the RMS value is colour coded. Lower error values are presented in dark blue. The minimum RMS follows two linear trends (blue line) with the intersection around $V_p0$ = 1200 m/s and $k_p$ = 6.0.

Figure 10-3 presents the same analysis as above considering only the data form well 8-16 over 1000 m – 1650 m MD interval. The minimum RMS trend is marked by the green line.

In figure 10-4 only well 8-16 SP 506220 data are displayed (closer to well 8-16 trajectory). The minimum RMS trend is marked on this plot by a brown line. Figure 10-5 shows the same information as figure 10-4 with well 6-16 (Fig. 10-2) and well 8-16 (Fig. 10-3) overlaid. All the RMS minimum trend lines converged to a $V_p0$ value of 1200 m/s and a $k_p$ value of 6.0. Those values were used for the “Below SP” layer in the final velocity model (Fig. 10-6).

Figure 10-7 presents in track 2 the well 8-16 ZVSP velocity profile and the final model velocity profile after ray tracing. The first track shows the drift between the model TT and the picked TT and on the third graph is the well 8-16 ZVSP stack with the picks in light blue and the model TT in light green. The maximum drift is below 1 ms which is below the seismic sampling.

In figure 10-8 is a 3D display of the final velocity model. The compressional velocity is represented in the Rainbow colour scale.

| Name | TVD below MSL | Compressional | | Shear | | Anisotropy | |
|---|---|---|---|---|---|---|---|
| | | Vp | kp | Vs | ks | ε | δ |
| Model Start | -500 | 340 | | 170 | | 0.00 | 0.00 |
| Above SP | -410 | 1100 | | 550 | | 0.00 | 0.00 |
| Below SP | -380 | 1200 | 6.00 | 600 | 3.00 | 0.00 | 0.00 |
| Sunbury | -102 | 2944 | | 1422 | | 0.00 | 0.00 |
| Traverse | 99 | 4959 | | 2484 | | 0.00 | 0.00 |
| Bell_Sh | 296 | 2928 | | 1103 | | 0.00 | 0.00 |
| Dundee | 316 | 4900 | | 2314 | | 0.00 | 0.00 |
| B_Detroit_R_Salt | 532 | 5683 | | 3100 | | 0.00 | 0.00 |
| Above Bass_Islands | 786 | 6063 | | 3313 | | 0.00 | 0.00 |
| Salina_G Shale | 921 | 4483 | | 2430 | | 0.00 | 0.00 |
| Salina_F Salt | 1145 | 4228 | | 2295 | | 0.00 | 0.00 |
| Salina_B Salt | 1227 | 4602 | | 2510 | | 0.00 | 0.00 |
| A2_Carb | 1317 | 6140 | | 3338 | | 0.00 | 0.00 |
| Below Wells TD | 1800 | 6140 | | 3338 | | 0.00 | 0.00 |

*Table 10-18 Final velocity model*

The final velocity model was ray traced to map the shot points reflectivity which is used in the depth imaging. At Salina G top layer the conversion from P to S was modelled. The shear TT was used to enhance the Down S wavefield during wavefield separation (Chapter 8). The P-P reflection points at A2 Carbonate layer for the vibroseis source location is presented in figure 10-9 and for the dynamite source locations in figure 10-10.

Figure 10-11 shows the vibroseis data reflection-point loci for a receiver at approximately 1540 m MD for well 6-16 (left) and for a receiver at approximately 1350 m MD for well 8-16 (right). Figure 10-12 presents the same information for the dynamite SP.

| Title | Description | Figure |
|---|---|---|
| **10 Velocity Model** | | |
| Velocity Model Build | Using well 6-16 acoustic logs | **10.1** |
| Average Model-Picking RMS – Well 6-16 | All the offset | **10.2** |
| Average Model-Picking RMS – Well 8-16 | All the offset | **10.3** |
| Average Model-Picking RMS – Well 8-16 ZVSP | SP 506220 close to well trajectory | **10.4** |
| Average Model-Picking RMS | Well 6-16, well 8-16 and well 8-16 ZVSP | **10.5** |
| Velocity Model Parameters | Final velocity model | **10.6** |
| Well 8-16 ZVSP Velocity Profile | Velocity model QC | **10.7** |
| Velocity Model | 3D view | **10.8** |
| Ray tracing – Vibroseis | 3D view | **10.9** |
| Ray tracing – Dynamite | 3D view | **10.10** |
| Ray tracing – Vibroseis | Loci field | **10.11** |
| Ray tracing – Dynamite | Loci field | **10.12** |

*Table 10-19 Velocity model figures*

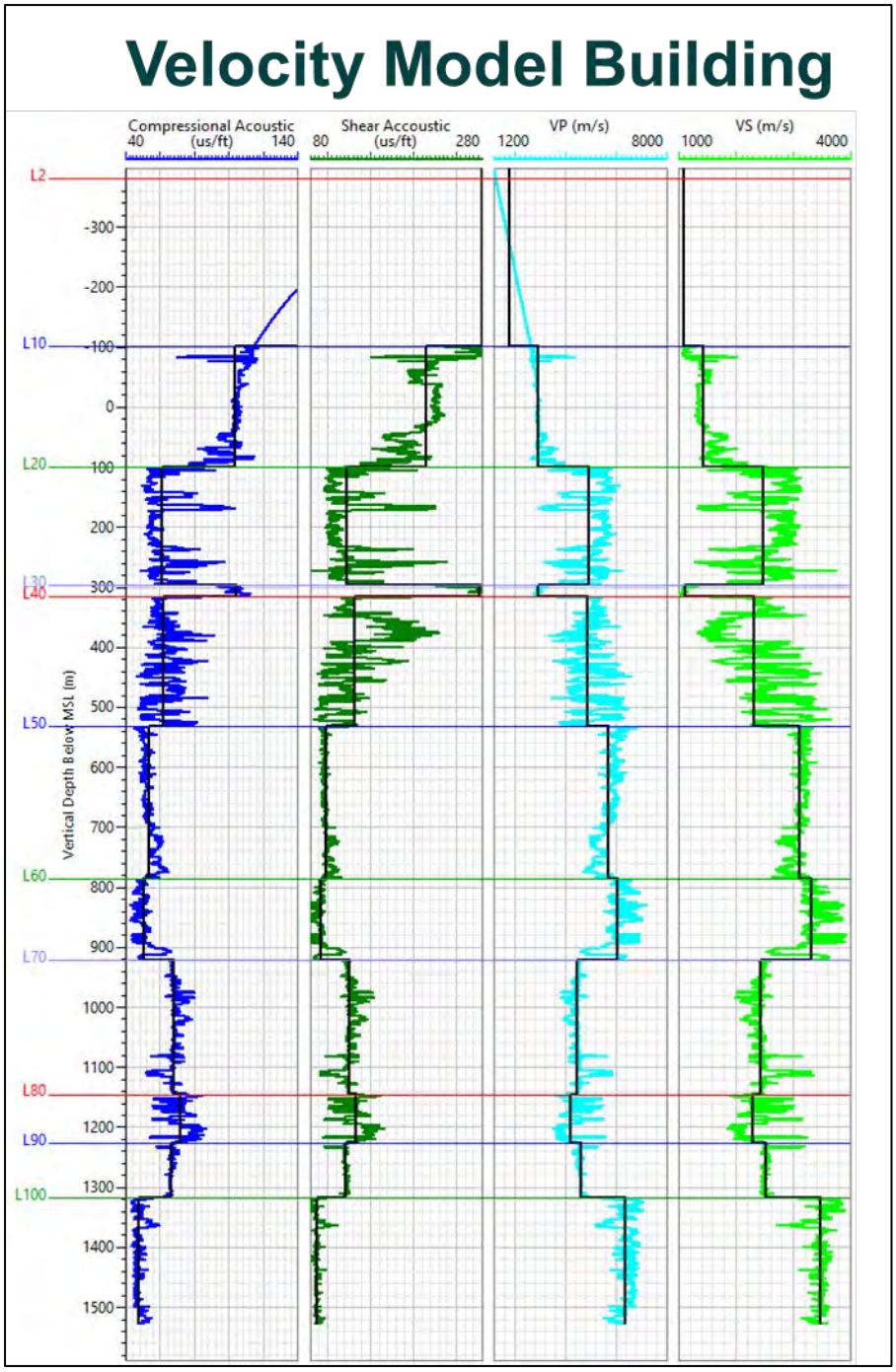


*Figure 10-1. Velocity Model Build - Using well 6-16 acoustic logs.*

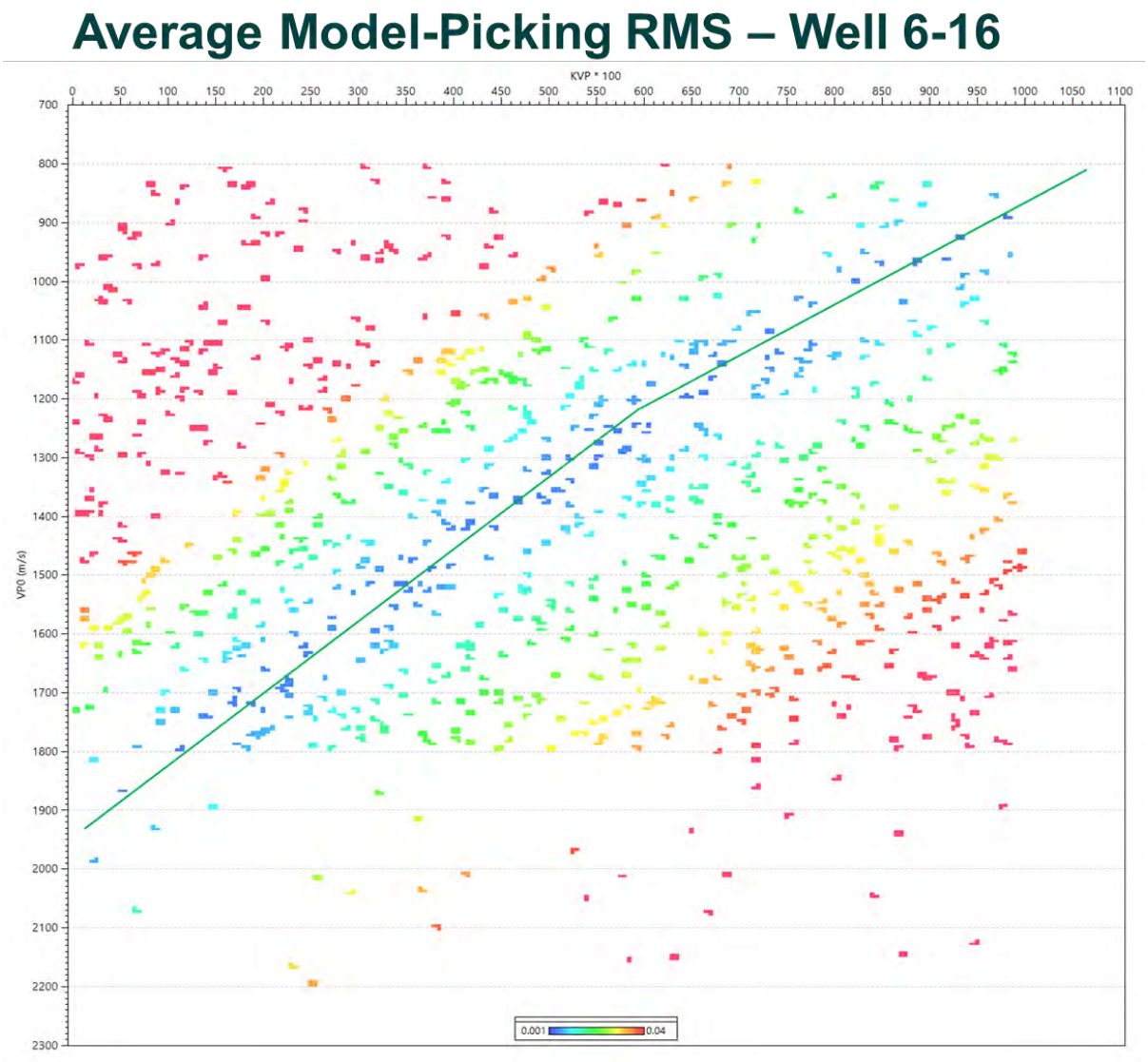


*Figure 10-2. Average Model-Picking RMS – Well 6-16 - All the offset. This figure shows a scatter plot of the average model TT – picked TT difference RMS after the random iterations for well 6-16. Only the data above the A2 Carbonate (1000 m to 1725 m MD) were considered. On the vertical axis is $V_p0$, on the horizontal axis is $k_p$ (scaled by 100) and the RMS value is colour coded. Lower error values are presented in dark blue. The minimum RMS follows two linear trends (blue line) with the intersection around $V_p0$ = 1200 m/s and $k_p$ = 6.0.*

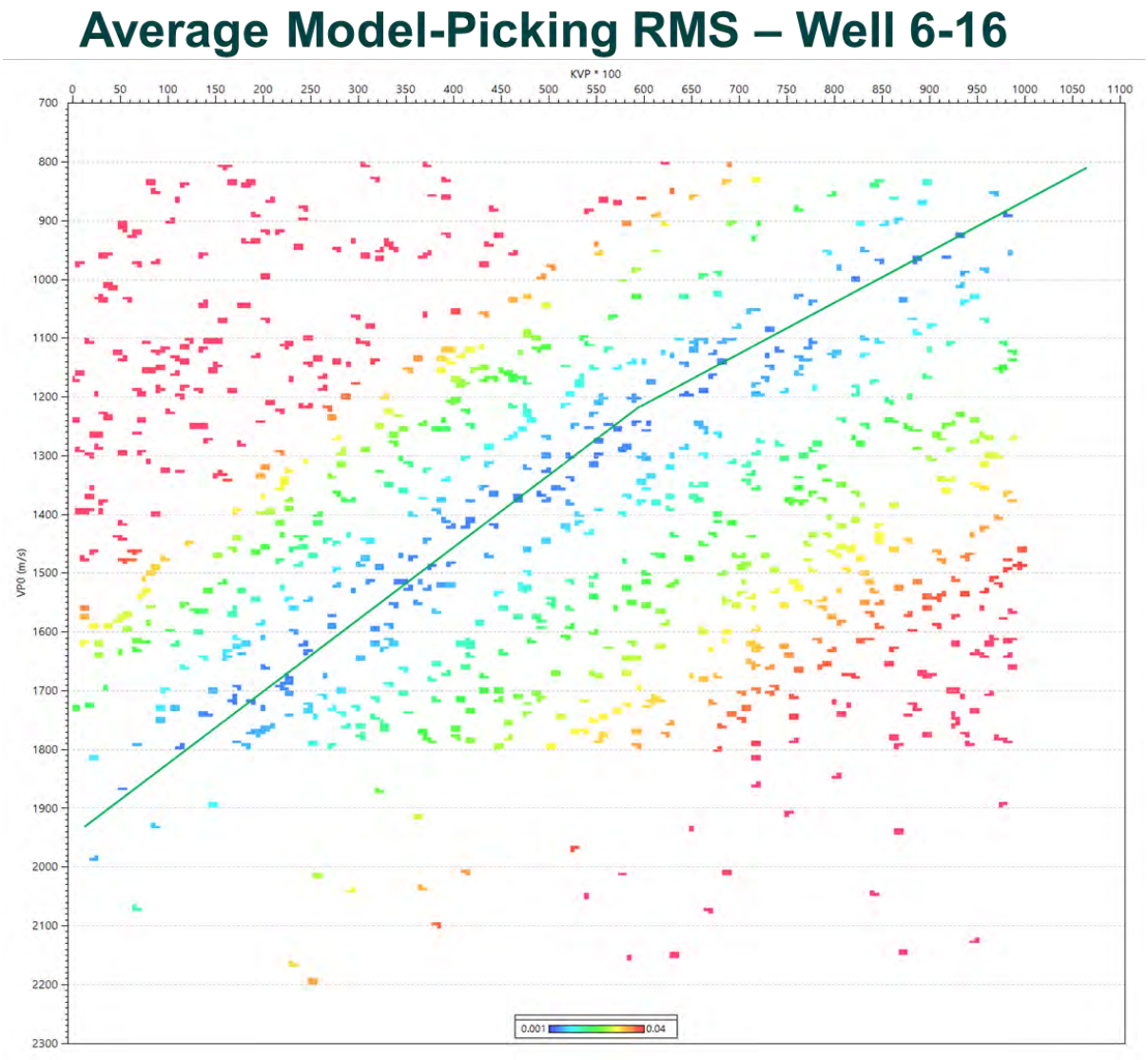


*Figure 10-3. Average Model-Picking RMS – Well 6-16 - All the offset. Figure 10.3 presents the same analysis as above considering only the data form well 6-16 over 1000 m – 1650 m MD interval. The minimum RMS trend is marked by the green line.*

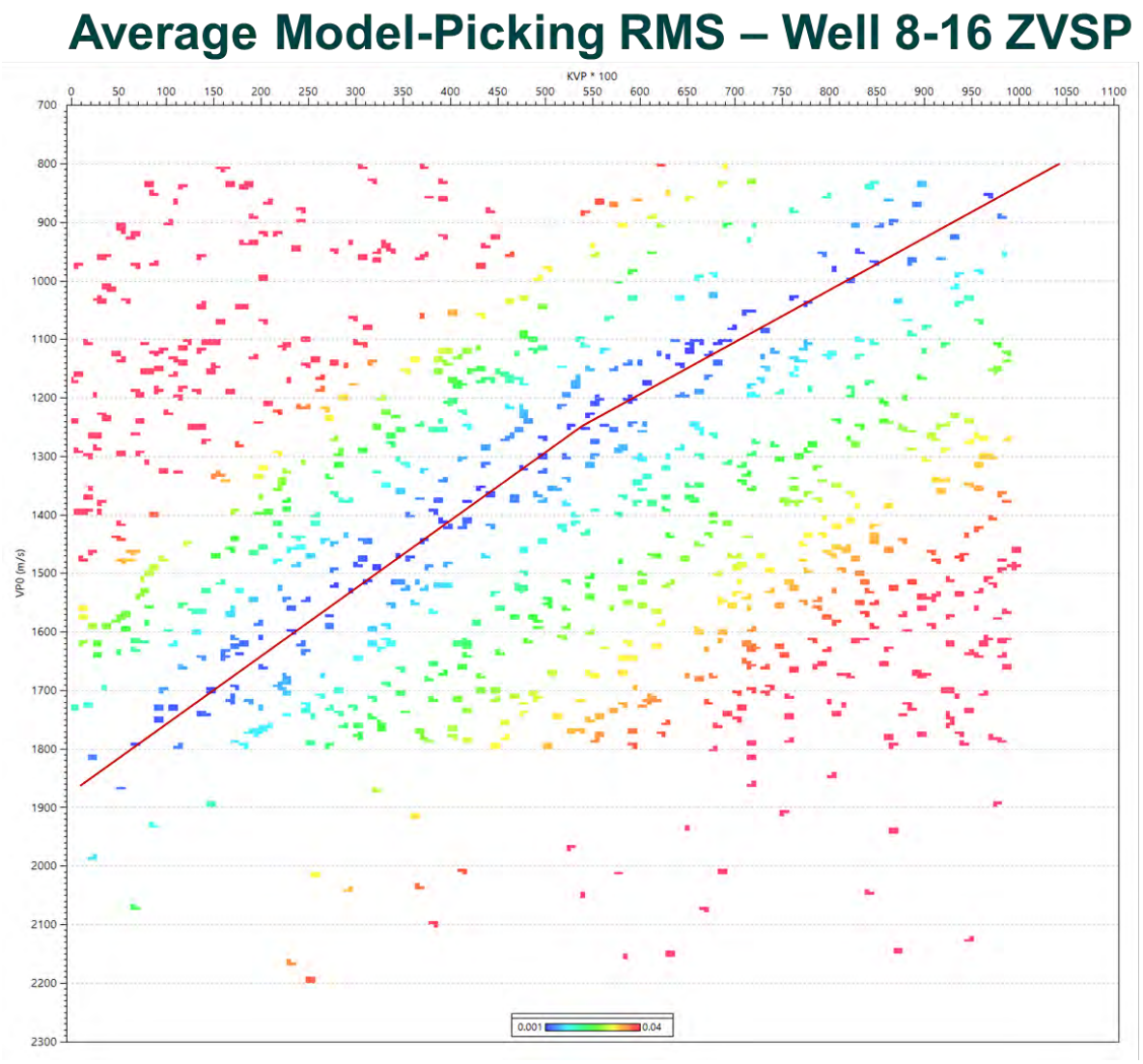


*Figure 10-4. Average Model-Picking RMS – Well 8-16 ZVSP - SP 506220 close to well trajectory. In this figure only well 8-16 SP 506220 data are displayed (closer to well 8-16 trajectory). The minimum RMS trend is marked on this plot by a brown line.*

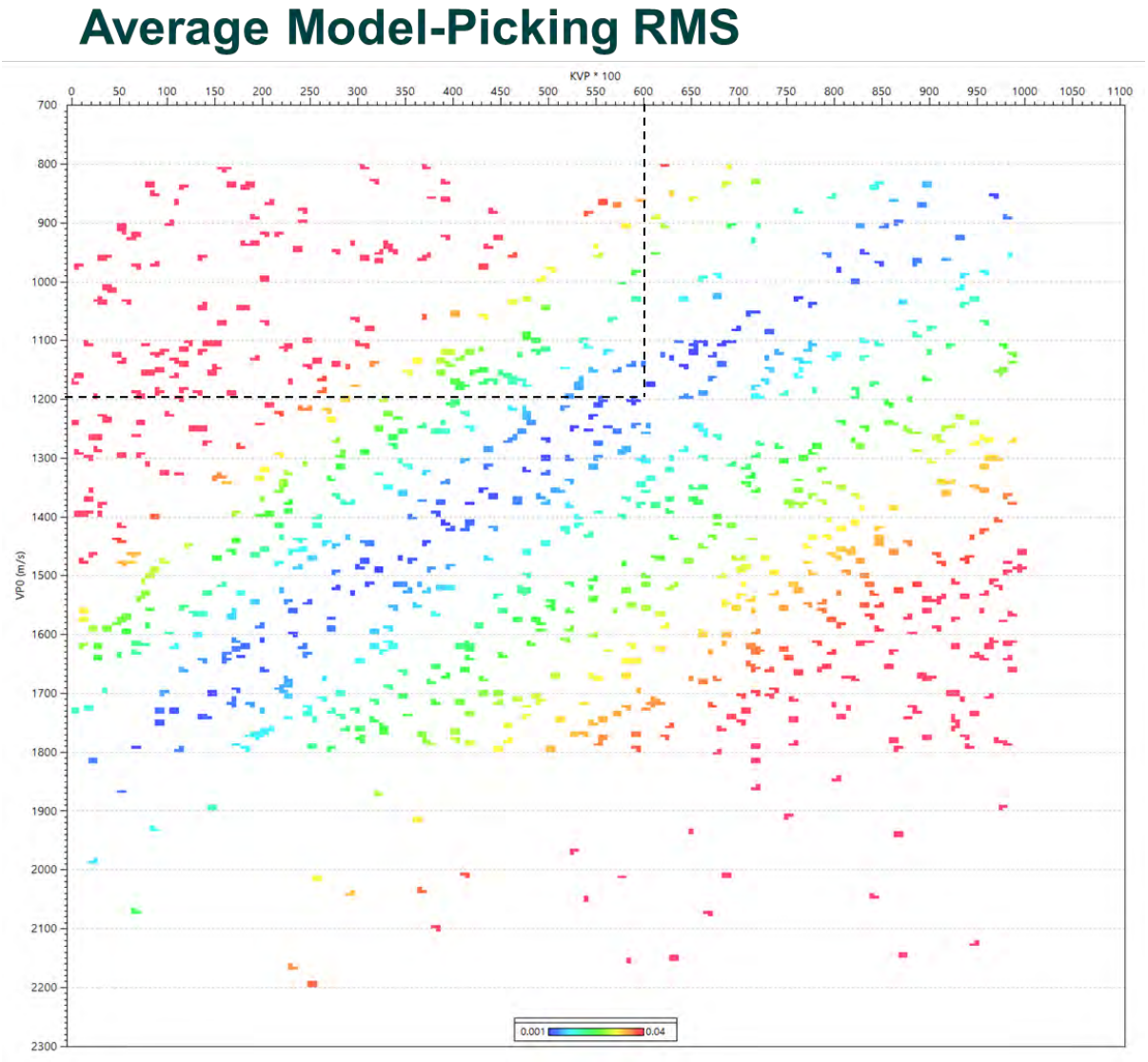


*Figure 10-5. Average Model-Picking RMS - Well 6-16, well 8-16 and well 8-16 ZVSP. Figure 10.5 shows the same information as figure 10.4 with well 6-16 (Fig. 10-2) and well 8-16 (Fig. 10.3) overlaid.*

# Velocity Model Parameters

| | | Compressional | | Shear | | Anisotropy | |
|---|---|---|---|---|---|---|---|
| Layer | TVD@MSL | Vp | kp | Vs | ks | ε | δ |
| Model Start | -500 | 340 | | 170 | | 0.00 | 0.00 |
| Above SP | -410 | 1100 | | 550 | | 0.00 | 0.00 |
| Below SP | -380 | 1200 | 6.00 | 600 | 3.00 | 0.00 | 0.00 |
| Sunbury | -102 | 2944 | | 1422 | | 0.00 | 0.00 |
| Traverse | 99 | 4959 | | 2484 | | 0.00 | 0.00 |
| Bell_Sh | 296 | 2928 | | 1103 | | 0.00 | 0.00 |
| Dundee | 316 | 4900 | | 2314 | | 0.00 | 0.00 |
| B_Detroit_R_Salt | 532 | 5683 | | 3100 | | 0.00 | 0.00 |
| Above Bass_Islands | 786 | 6063 | | 3313 | | 0.00 | 0.00 |
| Salina_G Shale | 921 | 4483 | | 2430 | | 0.00 | 0.00 |
| Salina_F Salt | 1145 | 4228 | | 2295 | | 0.00 | 0.00 |
| Salina_B Salt | 1227 | 4602 | | 2510 | | 0.00 | 0.00 |
| A2_Carb | 1317 | 6140 | | 3338 | | 0.00 | 0.00 |
| Below Wells TD | 1800 | 6140 | | 3338 | | 0.00 | 0.00 |

- Flat Layers Model
- Calibrate using 6-16 logs
- Line Spacing: 25m
- Cross-Line Spacing: 25m
- InLines: 52
- Xlines: 96

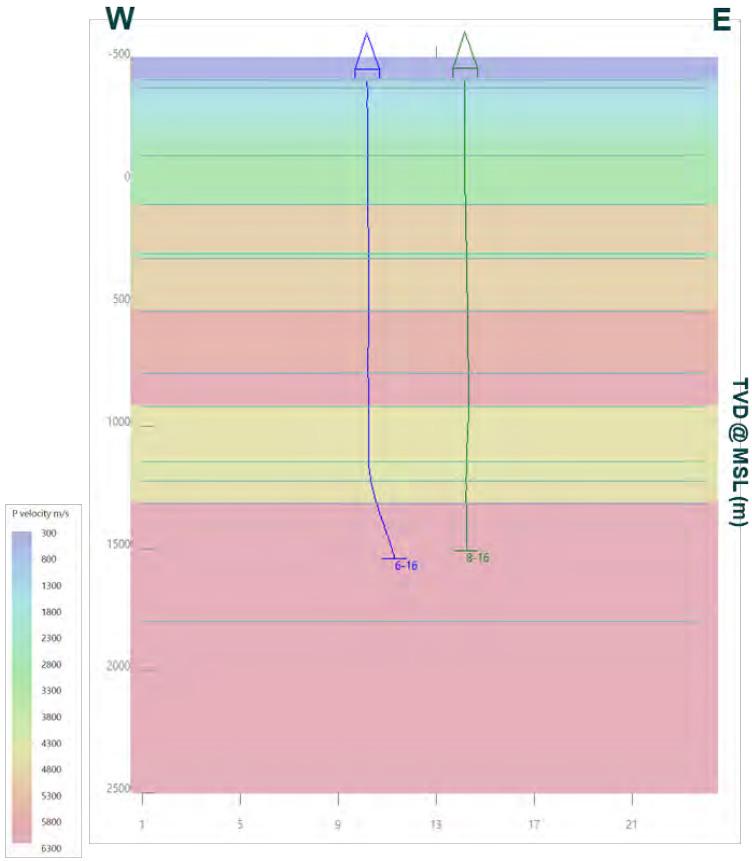


*Figure 10-6. Velocity Model Parameters - Final velocity model. All the RMS minimum trend lines converged to a $V_p0$ value of 1200 m/s and a $k_p$ value of 6.0. Those values were used for the "Below SP" layer in the final velocity model.*

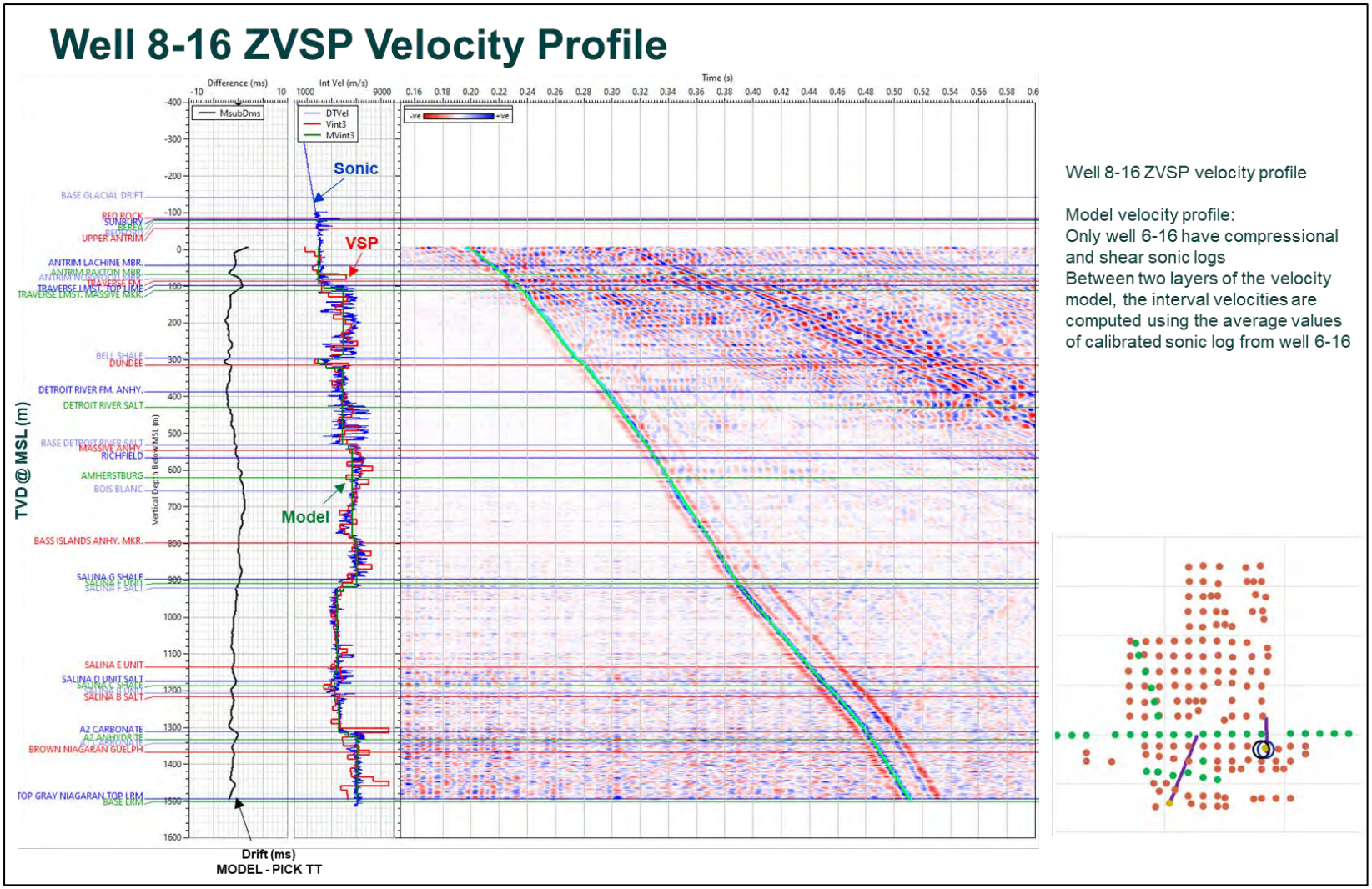


*Figure 10-7. Well 8-16 ZVSP Velocity Profile - Velocity model QC. This figure presents in track 2 the well 8-16 ZVSP velocity profile and the final model velocity profile after ray tracing. The first track shows the drift between the model TT and the picked TT and on the third graph is the well 8-16 ZVSP stack with the picks in light blue and the model TT in light green. The maximum drift is below 1 ms which is below the seismic sampling.*

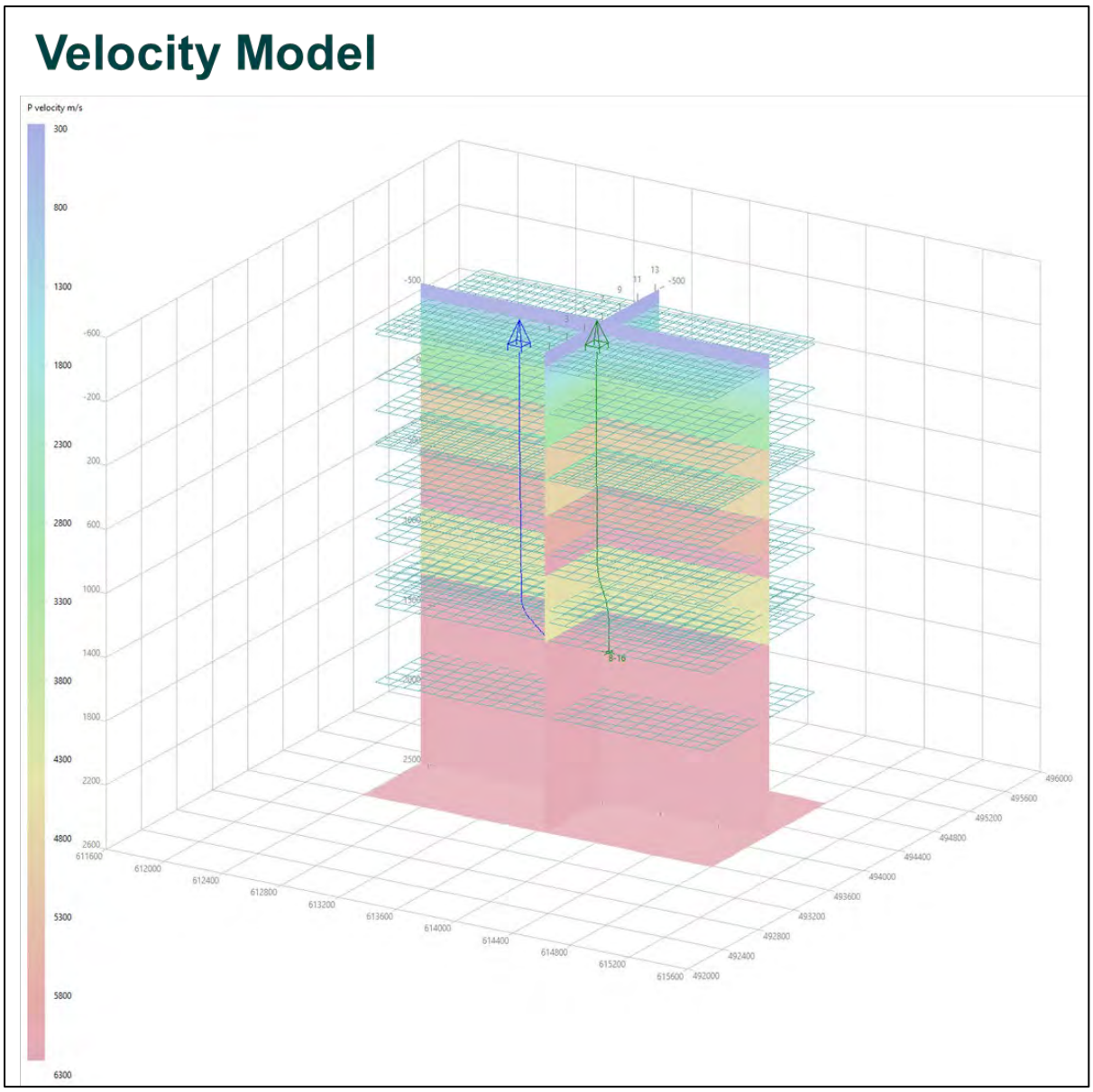


*Figure 10-8. Velocity Model - 3D view. In figure 10.8 is a 3D display of the final velocity model. The compressional velocity is represented in the Rainbow colour scale.*

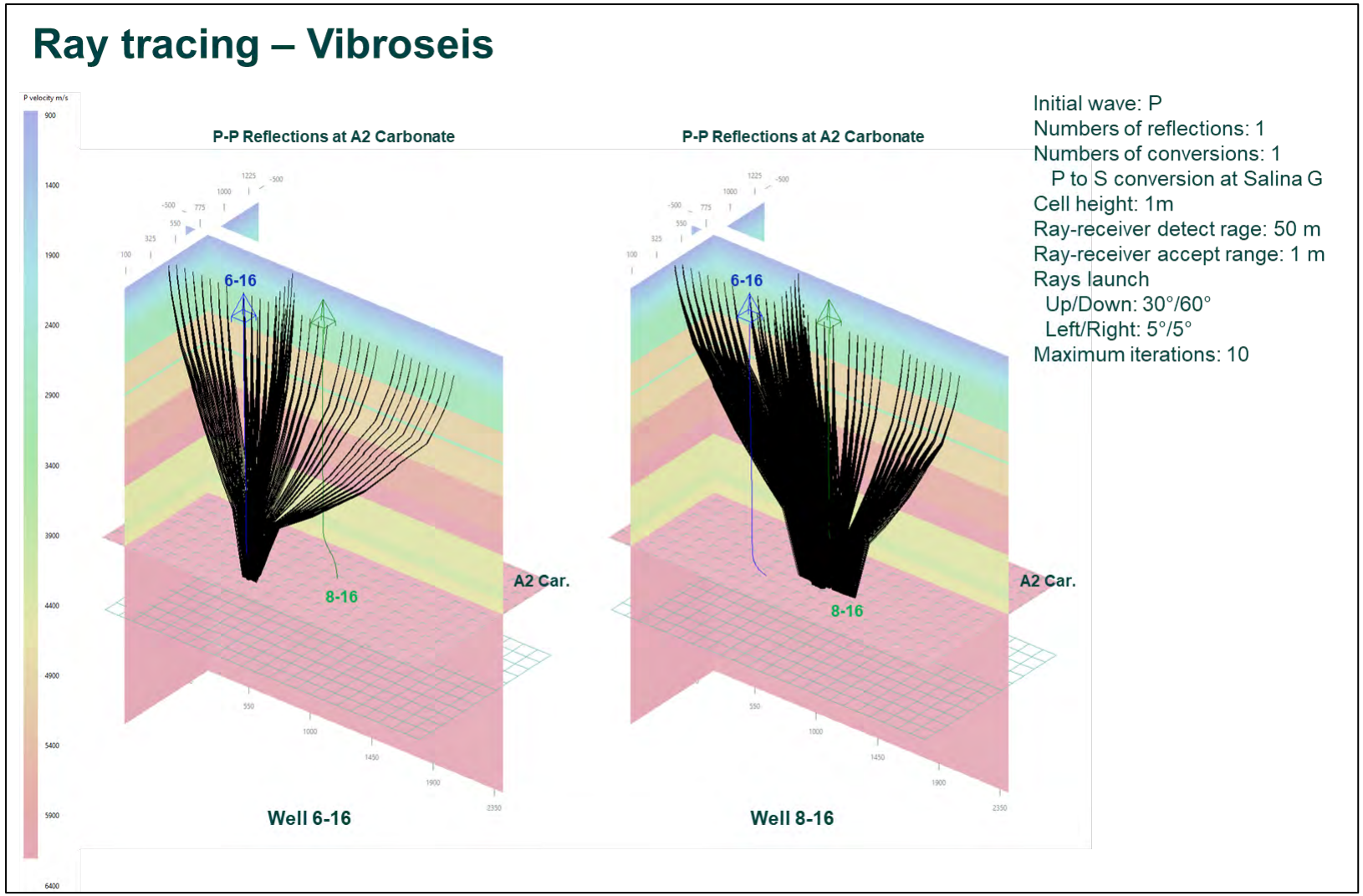


*Figure 10-9. Ray tracing – Vibroseis - 3D view.*

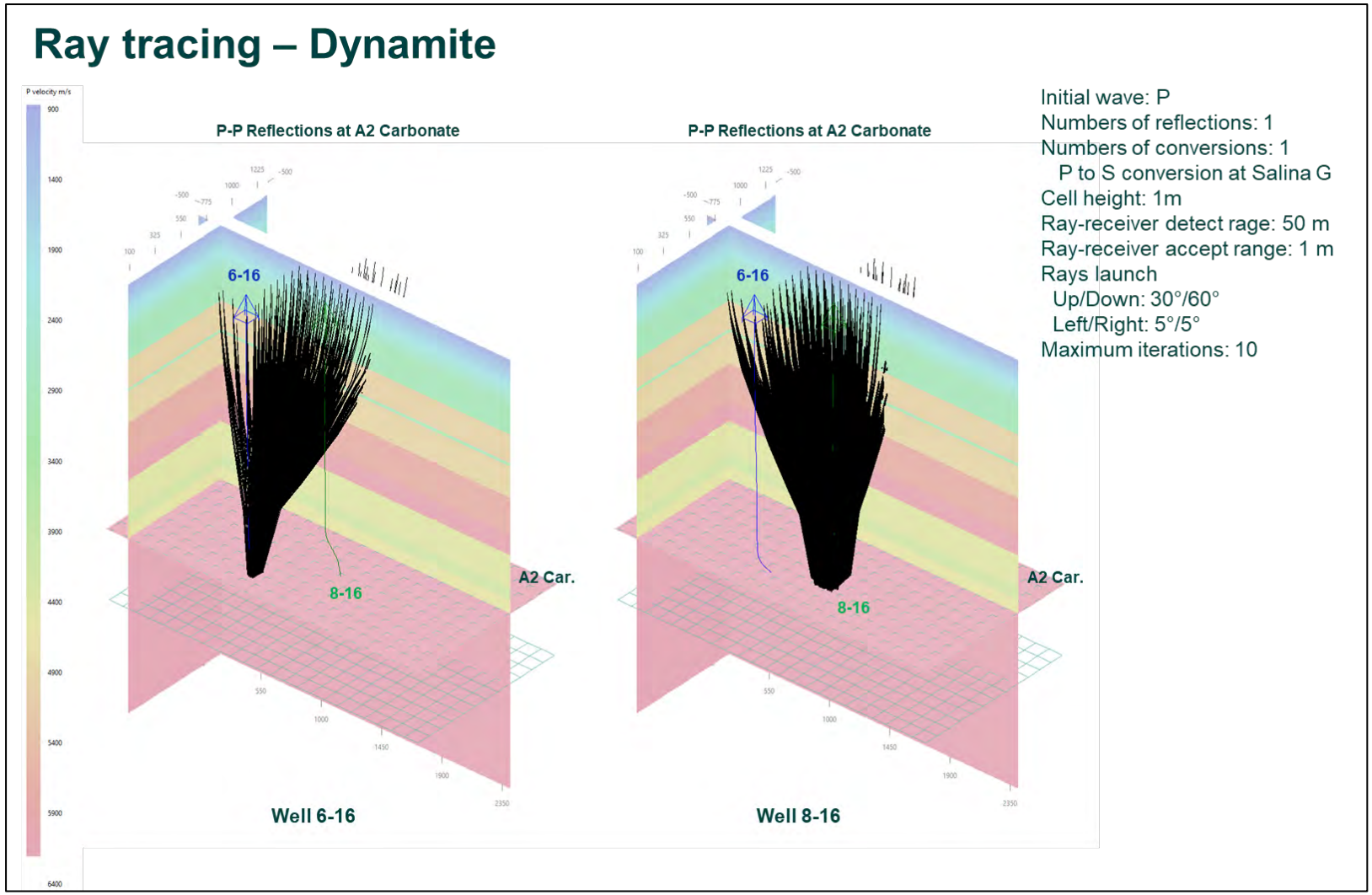


*Figure 10-10. Ray tracing – Dynamite - 3D view.*

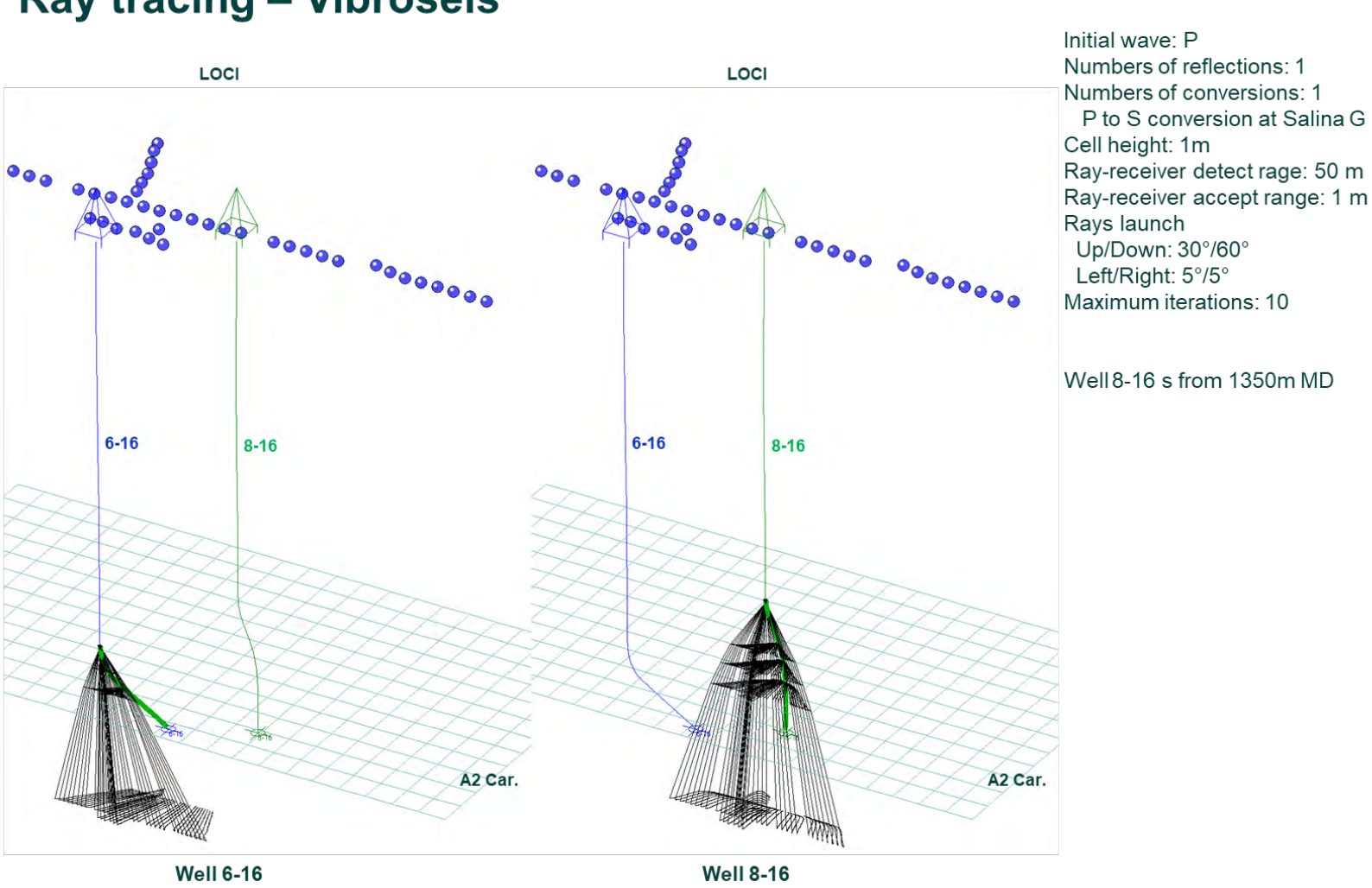


*Figure 10-11. Ray tracing – Vibroseis - Loci field. This figure shows the vibroseis data reflection-point loci for a receiver at approximately 1540 m MD for well 6-16 (left) and for a receiver at approximately 1350 m MD for well 8-16 (right).*

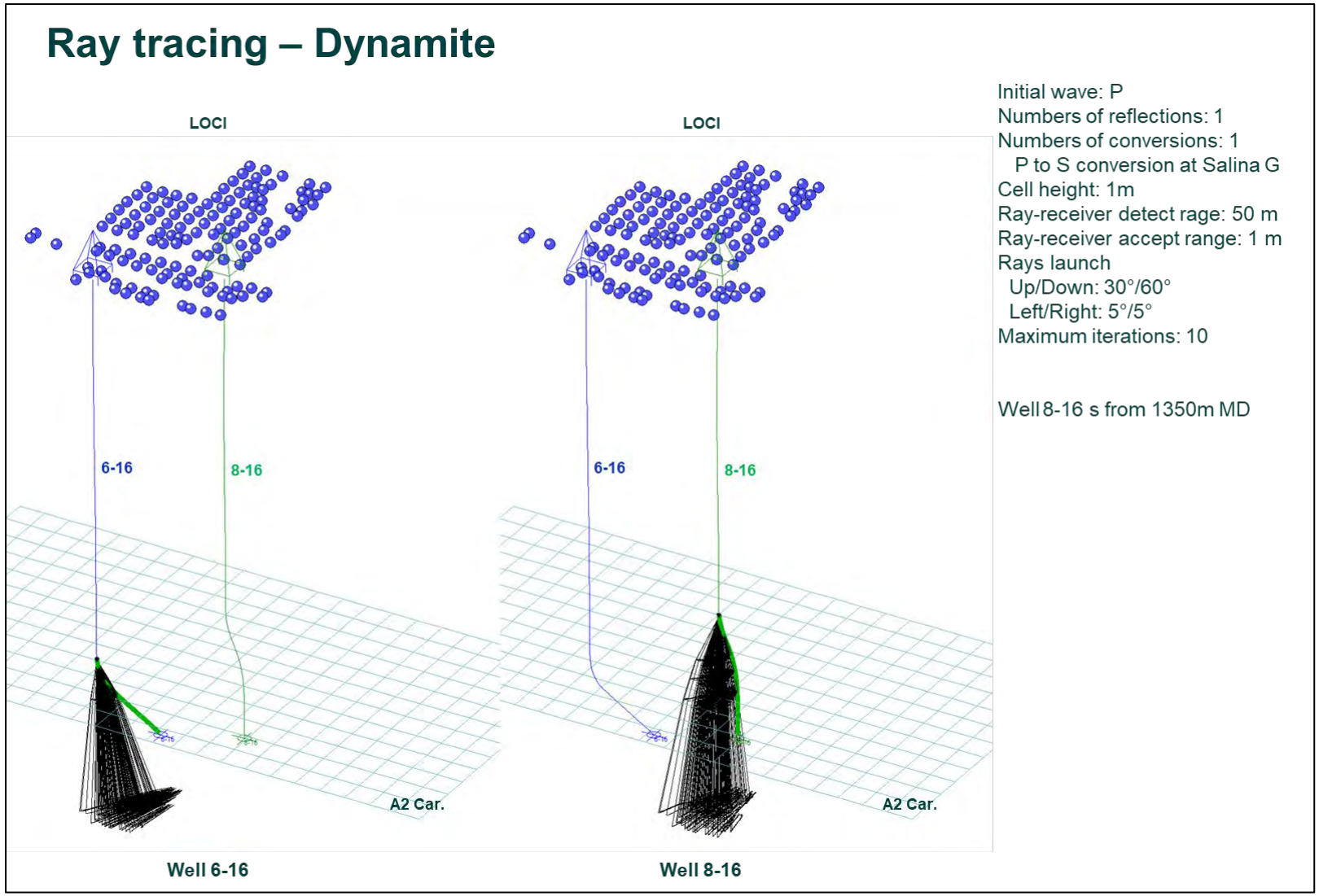


*Figure 10-12. Ray tracing – Dynamite - Loci field. Figure 10.12 presents the same information for the dynamite SP. A smooth loci field was generated without defective profile.*

# 11 Imaging

The recorded data in time are relocated in space using the loci field computed after the velocity model ray-tracing (section 10). The vibroseis and dynamite data was migrated separately. The well 6-16 and well 8-16 data were 3D migrated together. A 3D image was obtained for the baseline survey and a separate image for the monitor survey. Also, a 3D cube of amplitude difference between the monitor and baseline images was computed.

## 11.1 Vibroseis

### 11.1.1 Pre-migrate

Figure 11-1 shows the well 6-16 baseline deconvolved Up P wavefield, for SP 506216 (near well 6-16 TD), SP 506224 (mid offset to east) and SP 506230 (far offset to east). A 5,10-70,90 Hz BPF was applied to the input data (Fig. 11-2).

Using the mapped loci reflectivity, the data is mapped from recorded time to vertical-depth below SRD; this procedure we called “pre-migrate”. The amplitude response of a DAS cable is maximum for rays arriving along the axis of the cable and conversely minimum for rays arriving perpendicular to the cable. An estimate of the reflected rays incidence angle at the cable is inferred from ray-tracing and this angle is used to calculate a correction for the amplitude recorded at the modelled arrival time. A DAS cos-squared amplitude correction is applied and the data is resampled at 2 m.

Figure 11-3 presents the baseline SP 506216 (near well 6-16 TD), SP 506224 (mid offset to east) and SP 506230 (far offset to east) after pre-migrate correction. A 5,10-70,90 Hz BPF was applied to the baseline data (Fig. 11-4). Figure 11-5 shows the same data as figure 11-4 but for the monitor survey. The seismic structural response at the top of the reef is similar between the baseline and the monitor survey, but it starts to degrade below 1400 m TVDMSL, especially for far offsets, due to the lower SNR. The baseline survey with a lower SNR than the monitor survey presents a lower structural response coherency between shots.

Assuming that the strong reflector at the top of the reef is not affected by the $CO_2$ injection, a depth correction between the baseline (Fig. 11-6 panel 1) and monitor (Fig. 11-6 panel 2) pre-migrate data was performed SP by SP. From the baseline pre-migrate data a corridor stack is computed in a short window of 20 m to 70 m away from the FB. A depth shift profile for the best correlation was achieved (Fig. 11-6 panel 6) by cross correlating the baseline corridor stack (Fig. 11-6 track 3 and track 5 in red) and the monitor corridor stack (Fig. 11-6 track 4 and track 5 in blue). A static shift value per SP was obtained by averaging the shift in a 1290 m – 1360 m TVDMSL window. The monitor pre-migrate data was shifted to match the baseline data (Fig. 11-6 panel 8). Figure 11-7 shows the static shift computed after the baseline – monitor pre-migrate data cross-correlation. The maximum shift is less than 4 m which is below the seismic resolution.

The numbers of sweeps per location are different between the baseline and the monitor survey; the SNR for the same SP is also quite different between the baseline and monitor survey. After deconvolution the Up P wavefield is scaled depending on the Down P amplitudes. This results in the baseline and monitor having a different amplitude scaling. To correct this effect the amplitudes of the monitor SP was scaled to the baseline amplitudes level using the data outside the area where we expect a time-lapse effect due to the $CO_2$ injection. The baseline and monitor corridor stack were extracted in a window from 20 m to 70 m away from the FB. On each corridor stack the RMS amplitude value was computed in a window from 1305 m to 1350 m TVDMSL (above the reservoir). The monitor SP scaling factor was computed as the ratio between the baseline RMS and the monitor

RMS (Fig. 11-10 right). Figures 11-8 and 11-9 present the SP 506207 before and after the amplitude scaling. The scaling factors for each SP are presented in figure 11-10.

Figure 11-11 shows the well 8-16 baseline deconvolved Up P wavefield, for SP 506203 (far offset to the west), SP 506210 (mid offset to west) and SP 506220 (close to the well). A 5,10-70,90 Hz BPF was applied to the input data (Fig. 11-12).

Figure 11-13 presents the baseline SP 506203 (far offset to the west), SP 506210 (mid offset to west) and SP 506220 (close to the well) after pre-migrate correction. A 5,10-70,90 Hz BPF was applied to the data (Fig. 11-14). Figure 11-15 shows the same data as figure 11-14 but for the monitor survey. As with well 6-16 data, at well 8-16 the seismic structural response at the top of the reef is similar between the baseline and the monitor survey, but it starts to degrade below 1400 m TVDMSL, especially for far offsets (the SNR decreases with the offset).

A similar cross-correlation process for depth correction between the baseline and the monitor pre-migrate data was applied to the well 8-16 data. As the A2 Carbonate top reflection is shallow at well 8-16, the cross-correlation analysis window for well 8-18 was 1270 m – 1340 m TVDMSL. Figure 11-17 shows the static shift computed after the well 8-16 baseline – monitor pre-migrate data cross-correlation. The maximum shift is less than 4 m which is below the seismic resolution.

For well 8-16 data the scaling factor was computed using the RMS values extracted from the baseline and monitor NMO corridor stacks over the 1285 m to 1330 m TVDMSL interval (Fig. 11-20 right). Figures 11-18 and 11-19 present the SP 506207 before and after the amplitude scaling. The scaling factors for each SP are presented in figure 11-20.

### 11.1.2 Data selection

Some SPs have a very low SNR especially for the baseline survey. Figure 11-21 shows the well 6-16 baseline SNR for two adjacent SP. The SP 506215 (Fig. 11-21 right top) present a low SNR (1.28) while the neighbour SP 405216 has a better SNR value. The same SP shows a much better SNR for the monitor survey (Fig. 11-22). Similar to well 8-16 data, the baseline SP 506220 has an average SNR value of 1.6 which is much lower than the neighbour SP 506222 SNR average value (Fig. 11-23). In figure 11-24, the same SP as in the figure 11-17 has a better SNR for the monitor survey. The first graph from figures 11-21 to 11-24 (right) shows the SNR computed on each channel in black and the average value in red.

Before migration only the SPs with average SNR value above 1.5 for well 6-16 and above 1.6 for well 8-16 data were used. When a SP data were removed from one survey the same SP data were removed from the other survey even if the second SP SNR was above the threshold. Figures 11-25 and 11-26 show the SPs before and after data selection.

Figure 11-27 shows on the top left the A2 Carbonate reflection point incidence angle after P-P ray tracing (Fig. 11-27 right). Due to the well trajectory and receiver and source positions, the area covered by the image is close to the wells. The incidence angle is maximum 37.2°. Also, in some areas data with different incidence angles are stacked.

During the migration the pre-migrate data will be stacked into the 3D migration grid. Each cell will sum up a different number of data points depending on the cell grid size, the migration aperture and the receiver and source positions. The number of data points from each cell is called bin density.

Common Depth Points (CDP) mapping is a migration with 0° aperture, imaging only the reflection points. Figure 11-27 shows the CDP bin density for in-line 750 (close to well 8-16 – mid top image), cross-line 1880 (close to well 6-16 – mid bottom image), depth slice 1320 (at A2 Carbonate top – top left image) and depth 1380 (below Brown Niagaran top – bottom left image). Picture 11-23 shows the same bin density slices but for migration with 3.5° aperture. For well 8-16, due to the well trajectory shape, the nosier data from above 1350 m MD (Fig. 11-28 and 11-29 top right) will mix with the data

recorded by the receivers close to the image points. Restricting the migration only to the receiver data below 1350 m MD will have a relatively small impact on the extent of the image-covered area (Fig. 11-30 and 11-31).

### 11.1.3 Migration

Several migration tests were performed to quantify the impact of the static corrections and the baseline-monitor survey data cross-correlation on the depth images (Fig. 11-32 to 11-34). The final migration image with a 3.5° aperture (10° aperture for the image points near receivers) and a threshold of minimum bin density per cell of 50, is presented in figure 11-35. Figures 11-32 to 11-35 show on the top in-line 750 (close to well 8-16) and on the bottom cross-line 1180 (close to well 6-16). On the left is the baseline survey image, in the middle is the monitor survey image and on the right is the acoustic impedance amplitude difference between the monitor and the baseline image.

The residual static correction applied to well 6-16 data aligned the image data near well 6-16 (Fig. 11-32) and the monitor shift after the cross-correlation lower the artefacts near the image edge visible on the amplitude difference (Fig. 11-34 right).

The migration aperture takes into account the Fresnel zone (the fact that the reflection points are not specular). Increasing the migration aperture to 3.5° (Fig. 11-35) will thus fill the gaps seen in the CDP mapping image.

## 11.2 Dynamite

### 11.2.1 Pre-migrate

Figure 11-36 shows the well 6-16 dynamite baseline deconvolved Up P wavefield, for SP 502213 (near well 6-16 TD), SP 507216 (mid offset to north) and SP 515220 (far offset to north-east). Figure 11-37 shows the SP data after a 5,10-70,90 Hz BPF was applied.

Figure 11-38 presents the baseline SP 502213 (near well 6-16 TD), SP 507216 (mid offset to north) and SP 515220 (far offset to north-east) after pre-migration. A 5,10-70,90 Hz BPF was applied to the data (Fig. 11-39). Figure 11-40 shows the same data as in figure 11-39 for the monitor survey. Only the near offset data shows a similarity between the baseline and monitor survey. While the A2 Carbonate is visible on the monitor survey, on the baseline survey the same SP is too noisy and the A2 Carbonate reflector is not visible.

Figure 11-41 shows the well 8-16 baseline deconvolved Up P wavefield, for SP 503222 (close to the well), SP 508214 (mid offset to north-west) and SP 515215 (far offset to north). A 5,10-70,90 Hz BPF was applied to the data (Fig. 11-42).

Figure 11-43 presents the baseline SP 503222 (close to the well), SP 508214 (mid offset to north-west) and SP 515215 (far offset to north) after pre-migration. A 5,10-70,90 Hz BPF was applied to the data (Fig. 11-44). Figure 11-45 shows the same data as figure 11-44 but for the monitor survey. Similar to well 6-16 data, the seismic structural response at the top of the reef is comparable between the baseline and the monitor survey only on the close offsets and to a certain degree to the mid offsets.

### 11.2.2 Data selection

For the migration only the SPs with an average SNR value above 1.5 were used. If a SP data were removed from one survey the same SP data were removed from the other survey even when the second SP SNR was above the threshold. Figures 11-46 and 11-47 show the SPs data before and after data selection. A second test was performed with a SNR threshold of 2.0 for the baseline data and 2.5 for the monitor data (Fig. 11-48).

Figure 11-49 shows the CDP bin density for in-line 820 (close to well 8-16 – mid top image), cross-line 1880 (close to well 6-16 – mid bottom image), depth slice 1320 (at A2 Carbonate top – top left image) and depth 1380 (below Brown Niagaran top – bottom left image). Picture 11-50 shows the same bin density slices but for migration with a 3.5° aperture. The data were limited to the receivers below 1350 m MD. The dynamite image coverage at the A2 Carbonate does not have a larger extent compared with the vibroseis data image.

### 11.2.3 Migration

Two migration tests were performed using only the dynamite data. The first test filtered the input data with SNR values below 1.5 (Fig 11-51). The second test has the SNR threshold at 2.0 for the baseline data and 2.5 for the monitor data (Fig. 11-52). Figures 11-51 and 11-52 show on the top in-line 820 (close to well 8-16) and on the bottom cross-line 1180 (close to well 6-16). On the left is the baseline survey image, in the middle is the monitor survey image and on the right is the acoustic impedance amplitude difference between the monitor and the baseline image.

As the dynamite data have low SNR the image noise level is too high in order to obtain a good correlation between the baseline and monitor survey. Near well 8-16 the impact of $CO_2$ injection is expected to be lower, but the monitor-baseline amplitude difference shows very strong artefacts (Fig. 11-51 top right). Filtering the input data up to a SNR of 2.0 for baseline and 2.5 for the monitor survey does not improve the result (Fig. 11-52).

| Title | Description | Figure |
|---|---|---|
| | | |
| **11 Imaging** | | |
| **11.1 Vibroseis** | | |
| Well 6-16 – Baseline – Deconvolved Up-P | Input data | **11.1** |
| Well 6-16 – Baseline – BPF | | **11.2** |
| Well 6-16 – Baseline – Pre-migrate | Pre-migrate | **11.3** |
| Well 6-16 – Baseline – Pre-migrate – BPF | Reduce pre-migrate artefacts | **11.4** |
| Well 6-16 – Monitor – Pre-migrate – BPF | Reduce pre-migrate artefacts | **11.5** |
| Monitor SP shift after XCorrelation – Well 6-16 | Harmonize the baseline and monitor pre-migrate data | **11.6** |
| Static shift after Pre-migrate corridor stack XCorrelation – Well 6-16 | Harmonize the baseline and monitor pre-migrate data | **11.7** |
| Well 6-16 before Scaling | Pre-migrate and corridor stack | **11.8** |
| Well 6-16 after Scaling | Baseline / Monitor scaling factor | **11.9** |
| Monitor Scaling factor– Well 6-16 | For each SP | **11.10** |
| Well 8-16 – Baseline – Deconvolved Up-P | Input data | **11.11** |
| Well 8-16 – Baseline – BPF | | **11.12** |
| Well 8-16 – Baseline – Pre-migrate | Pre-migrate | **11.13** |
| Well 8-16 – Baseline – Pre-migrate – BPF | Reduce pre-migrate artefacts | **11.14** |
| Well 8-16 – Monitor – Pre-migrate – BPF | Reduce pre-migrate artefacts | **11.15** |
| Monitor SP shift after XCorrelation – Well 8-16 | Harmonize the baseline and monitor pre-migrate data | **11.16** |
| Static shift after Pre-migrate corridor stack XCorrelation – Well 8-16 | Harmonize the baseline and monitor pre-migrate data | **11.17** |
| Well 8-16 before Scaling | Pre-migrate and corridor stack | **11.18** |
| Well 8-16 after Scaling | Baseline / Monitor scaling factor | **11.19** |
| Monitor Scaling factor– Well 8-16 | For each SP | **11.20** |
| Signal to noise ratio – Baseline | Well 6-16 – for data selection | **11.21** |
| Signal to noise ratio – Monitor | Well 6-16 – for data selection | **11.22** |
| Signal to noise ratio – Baseline | Well 8-16 – for data selection | **11.23** |
| Signal to noise ratio – Monitor | Well 8-16 – for data selection | **11.24** |
| Signal to noise ratio | Before data selection | **11.25** |

| Title | Description | Figure |
|---|---|---|
| Signal to noise ratio threshold | After data selection | **11.26** |
| Incidence angle at A2 Carbonate | P-P reflection points | **11.27** |
| Bin density – CDP mapping | Before data selection | **11.28** |
| Bin density – Migration | Before data selection | **11.29** |
| Bin density – CDP mapping – data below 1350m MD | After data selection | **11.30** |
| Bin density – Migration – data below 1350m MD | After data selection | **11.31** |
| 3D Migration – Test 1 | Statics applied | **11.32** |
| 3D Migration – Test 2 | Residual statics applied | **11.33** |
| 3D Migration – Test 3 | Cross-correlation shift applied | **11.34** |
| Final 3D Migration | Final vibroseis data image | **11.35** |
| | | |
| **11.2 Dynamite** | | |
| Well 6-16 – Baseline – Deconvolved Up-P | Input data | **11.36** |
| Well 6-16 – Baseline – BPF | | **11.37** |
| Well 6-16 – Baseline – Pre-migrate | Pre-migrate | **11.38** |
| Well 6-16 – Baseline – Pre-migrate – BPF | Reduce pre-migrate artefacts | **11.39** |
| Well 6-16 – Monitor – Pre-migrate – BPF | Reduce pre-migrate artefacts | **11.40** |
| Well 8-16 – Baseline – Deconvolved Up-P | Input data | **11.41** |
| Well 8-16 – Baseline – BPF | | **11.42** |
| Well 8-16 – Baseline – Pre-migrate | Pre-migrate | **11.43** |
| Well 8-16 – Baseline – Pre-migrate – BPF | Reduce pre-migrate artefacts | **11.44** |
| Well 8-16 – Monitor – Pre-migrate – BPF | Reduce pre-migrate artefacts | **11.45** |
| Signal to Noise Ratio | Before data selection | **11.46** |
| Signal to noise ratio threshold | After data selection (threshold 1.5) | **11.47** |
| Signal to noise ratio threshold | After data selection (threshold 2.0/2.5) | **11.48** |
| Bin density – CDP mapping – data below 1350m MD | After data selection | **11.49** |
| Bin density – Migration – data below 1350m MD | After data selection | **11.50** |
| 3D Migration – Test 1 | SNR threshold 1.5 | **11.51** |
| 3D Migration – Test 2 | SNR threshold 2.0/2.5 | **11.52** |

*Table 11-20 Imaging figures*

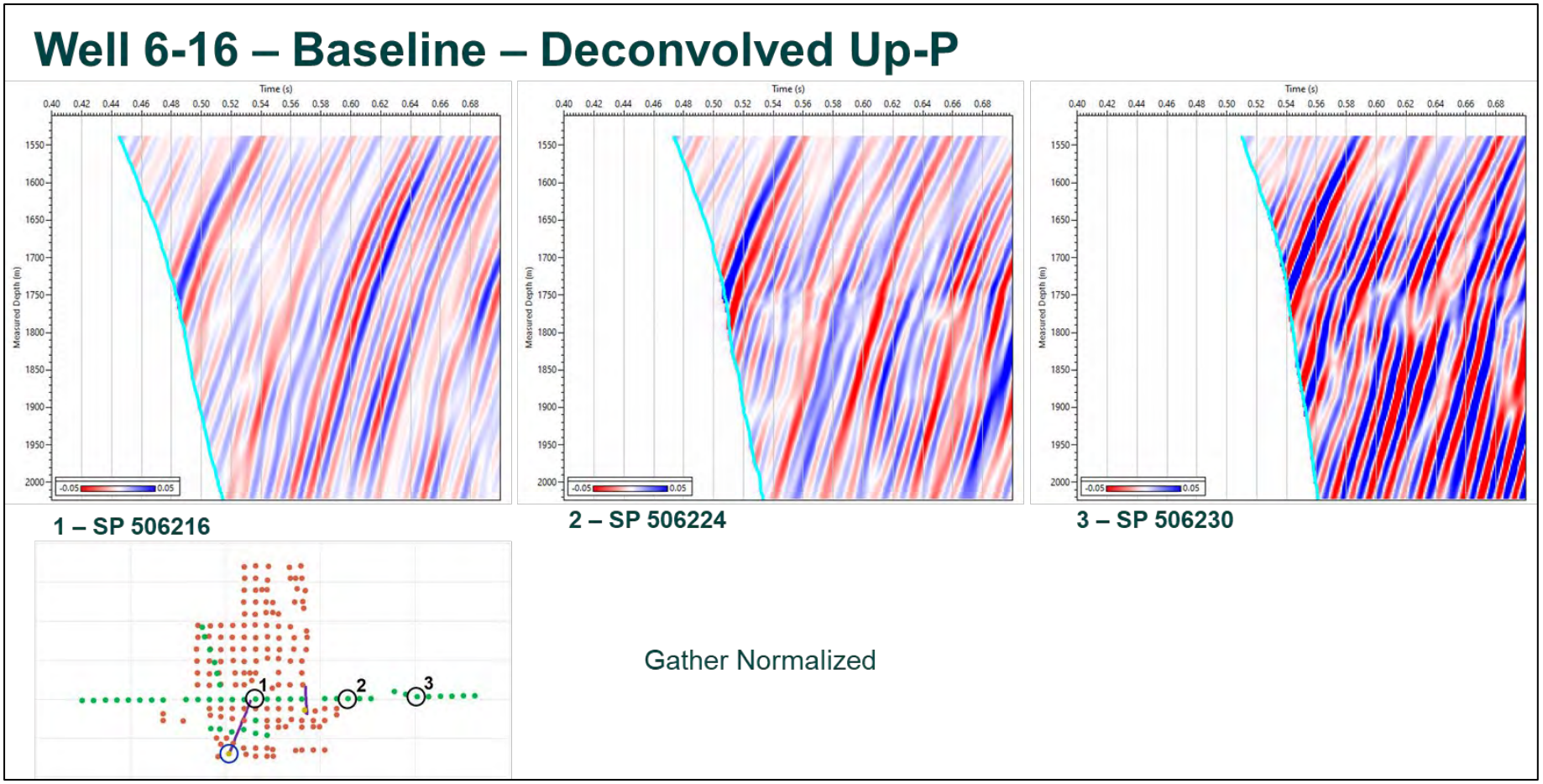


*Figure 11-1. Well 6-16 – Baseline – Deconvolved Up-P. Input data. This figure shows the well 6-16 baseline deconvolved Up P wavefield, for SP 506216 (near well 6-16 TD), SP 506224 (mid offset to east) and SP 506230 (far offset to east).*

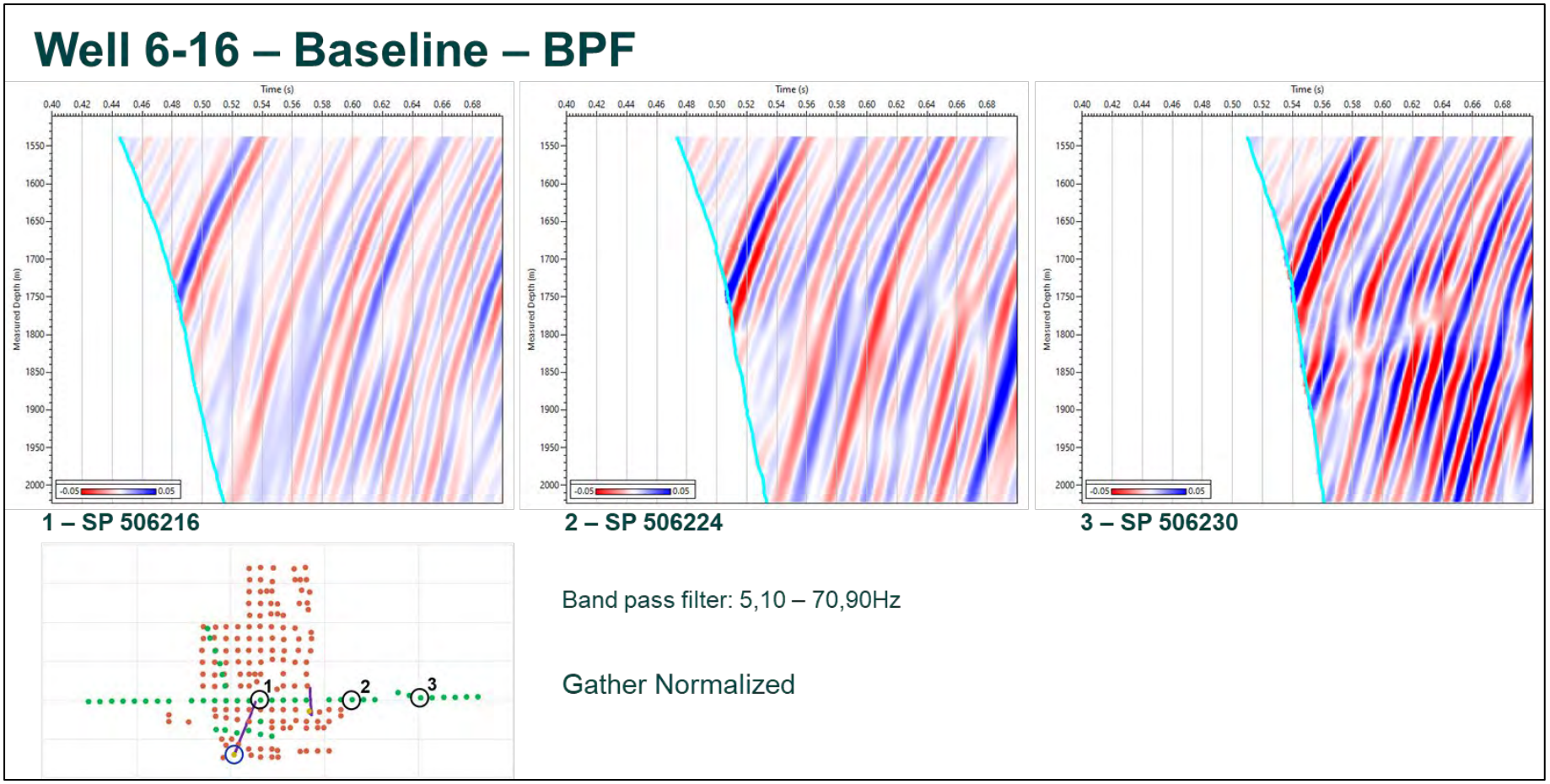


*Figure 11-2. Well 6-16 – Baseline – BPF. A 5,10-70,90 Hz BPF was applied to the input data.*

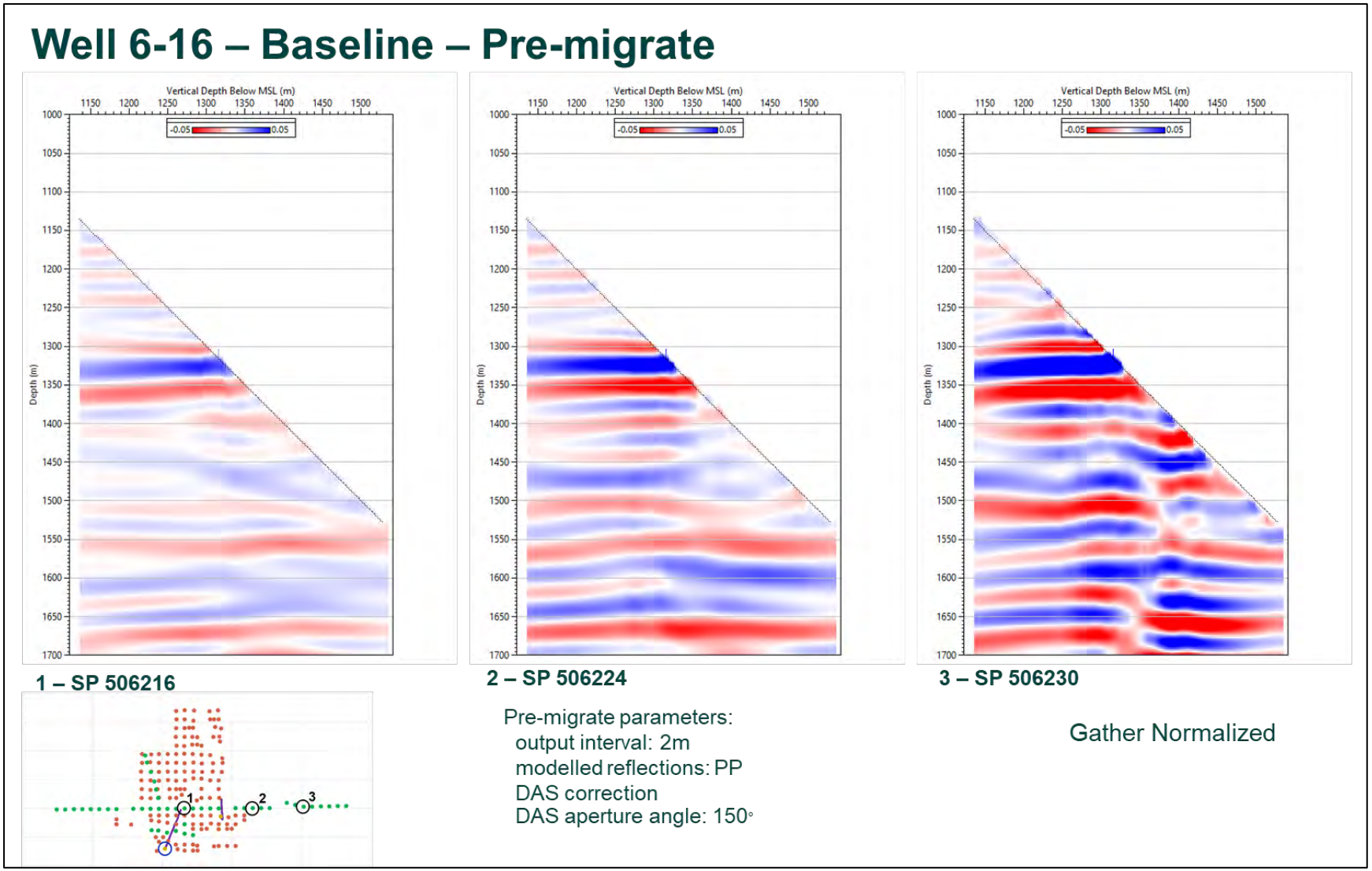


*Figure 11-3. Well 6-16 – Baseline – Pre-migrate. Figure 11.3 presents the baseline SP 506216 (near well 6-16 TD), SP 506224 (mid offset to east) and SP 506230 (far offset to east) after pre-migrate correction.*

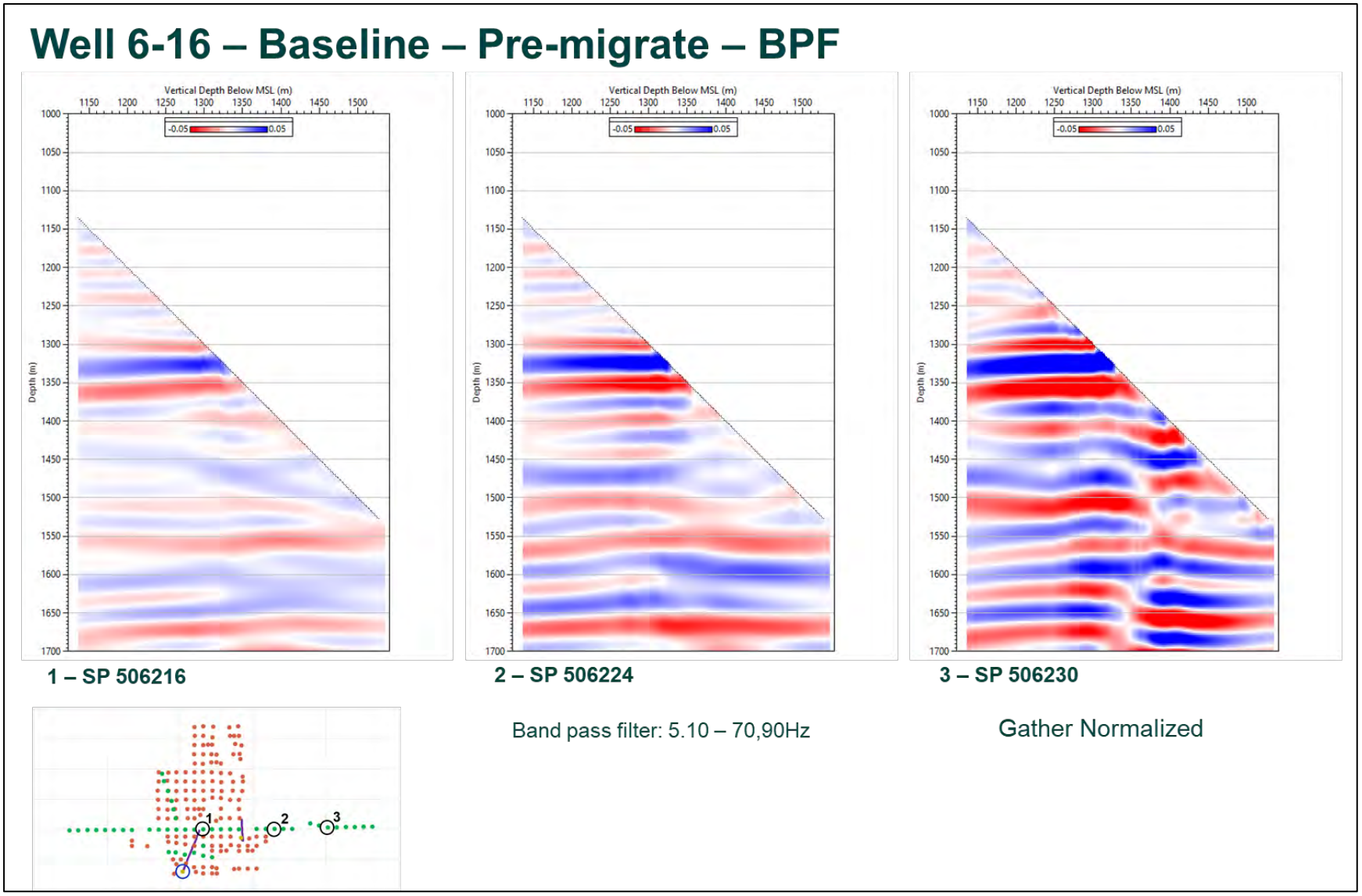


*Figure 11-4. Well 6-16 – Baseline – Pre-migrate – BPF - Reduce pre-migrate artefacts. A 5,10-70,90 Hz BPF was applied to the baseline data.*

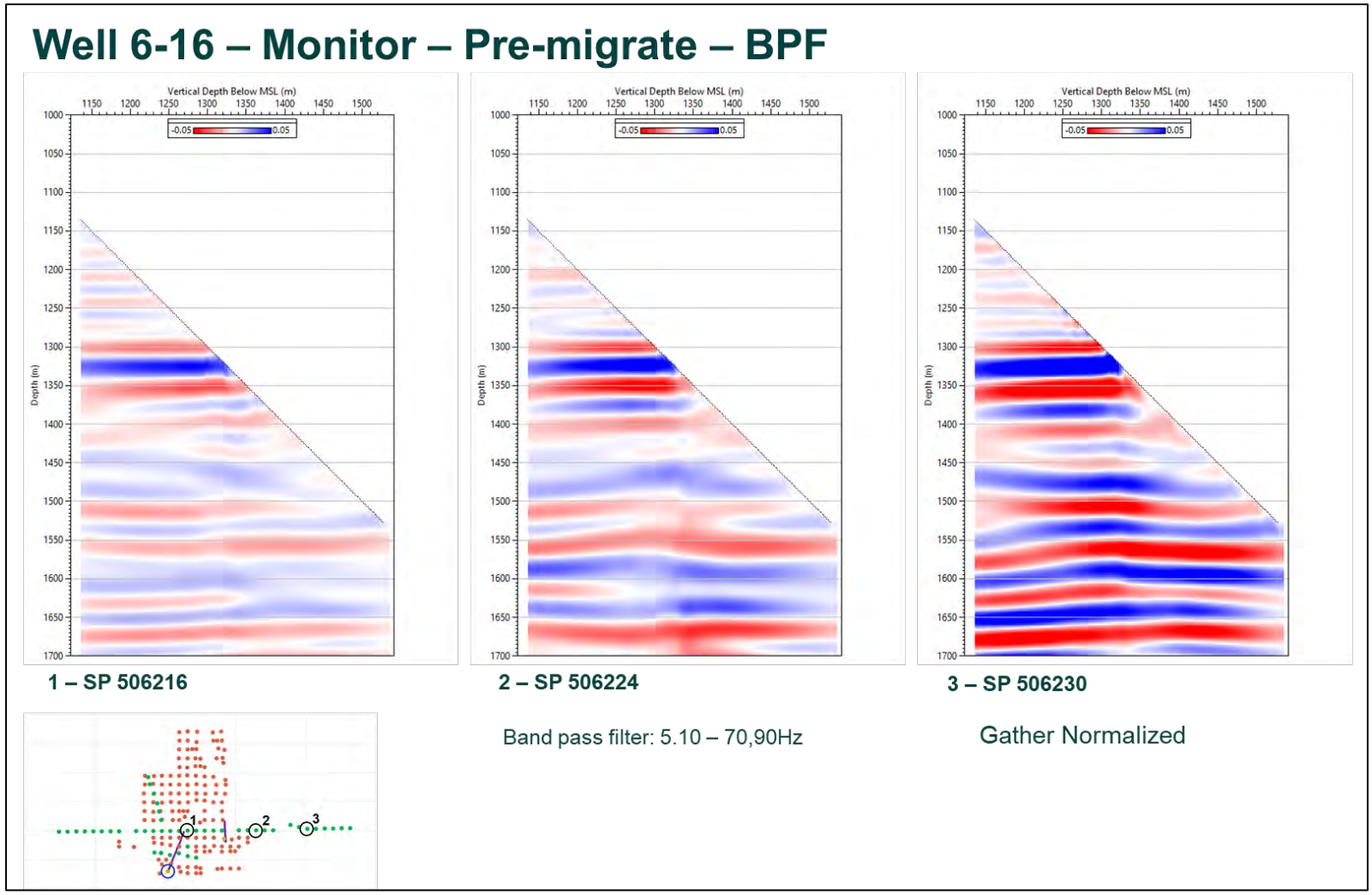


*Figure 11-5. Well 6-16 – Monitor – Pre-migrate – BPF - Reduce pre-migrate artefacts. This figure shows the same data as figure 11.4 but for the monitor survey. The seismic structural response at the top of the reef is similar between the baseline and the monitor survey, but it starts to degrade below 1400 m TVDMSL, especially for far offsets, due to the lower SNR. The baseline survey with a lower SNR than the monitor survey presents a lower structural response coherency between shots.*

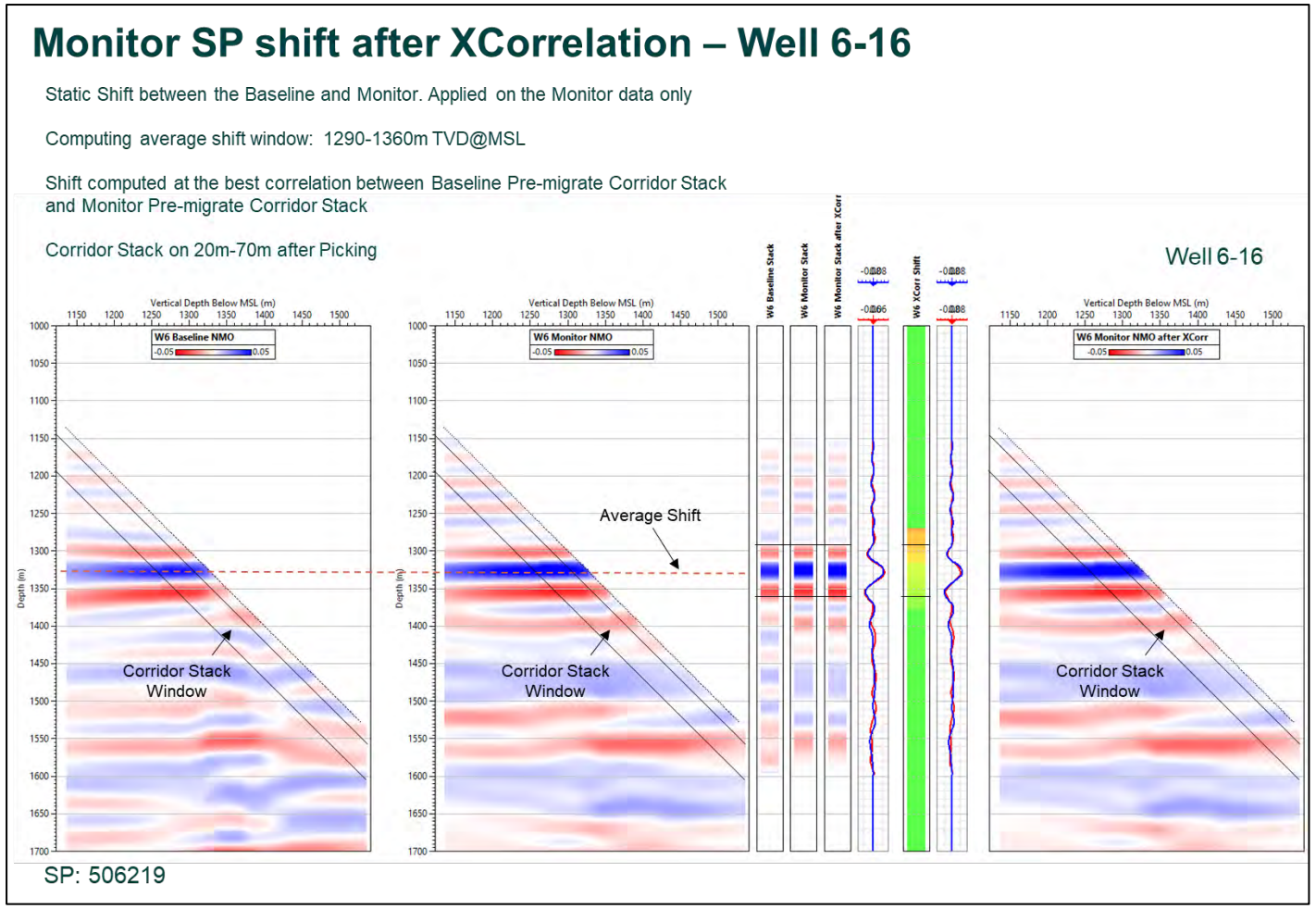


*Figure 11-6. Monitor SP shift after XCorrelation – Well 6-16 - Harmonize the baseline and monitor pre-migrate data. Assuming that the strong reflector at the top of the reef is not affected by the $CO_2$ injection, a depth correction between the baseline (Fig. 11.6 panel 1) and monitor (Fig. 11.6 panel 2) pre-migrate data was performed SP by SP. From the baseline pre-migrate data a corridor stack is computed in a short window of 20 m to 70 m away from the FB. A depth shift profile for the best correlation was achieved (Fig. 11.6 panel 6) by cross correlating the baseline corridor stack (Fig. 11.6 track 3 and track 5 in red) and the monitor corridor stack (Fig. 11.6 track 4 and track 5 in blue). A static shift value per SP was obtained by averaging the shift in a 1290 m – 1360 m TVDMSL window. The monitor pre-migrate data was shifted to match the baseline data (Fig. 11.6 panel 8).*

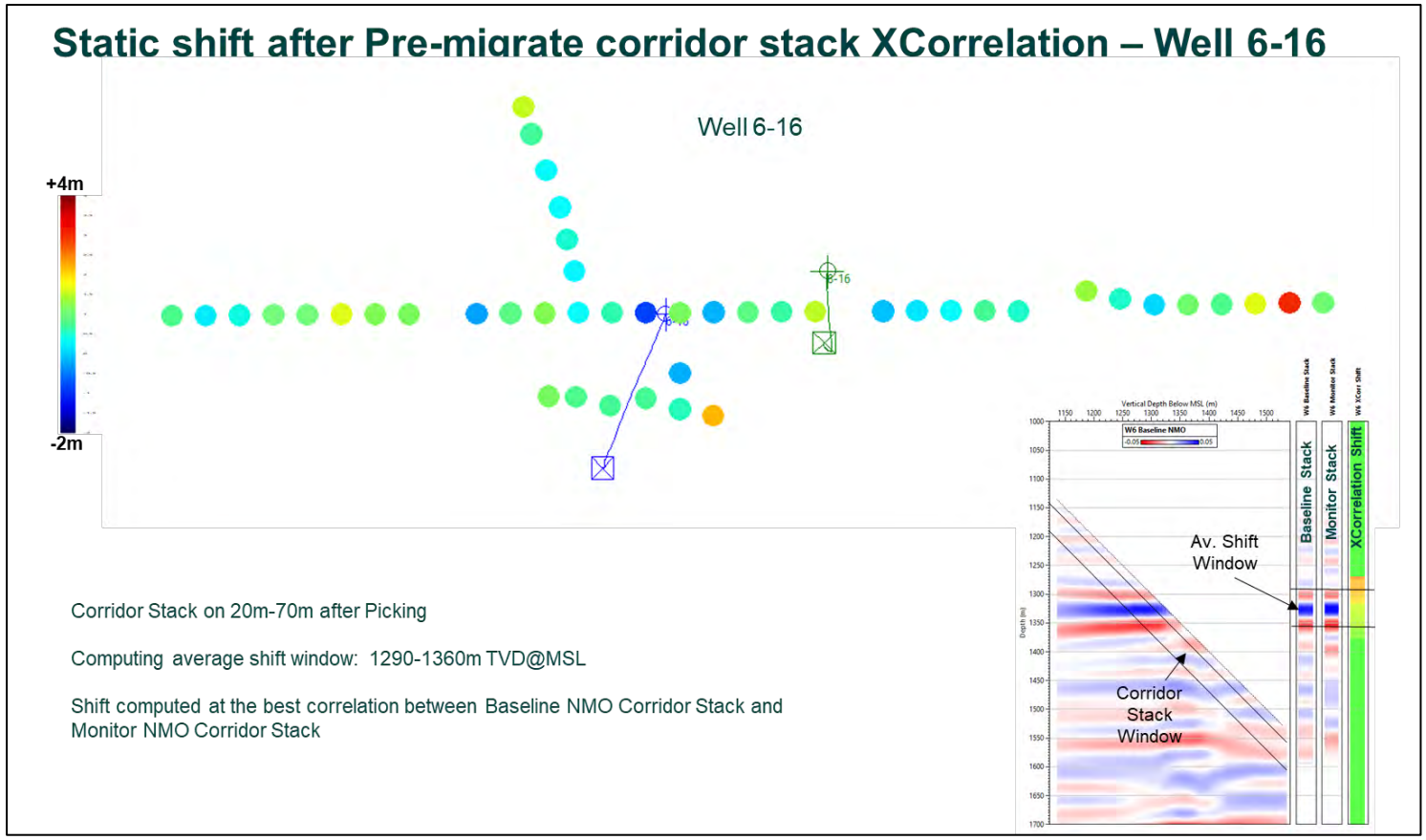


*Figure 11-7. Static shift after Pre-migrate corridor stack XCorrelation – Well 6-16 - Harmonize the baseline and monitor pre-migrate data. Figure 11.7 shows the static shift computed after the baseline – monitor pre-migrate data cross-correlation. The maximum shift is less than 4 m which is below the seismic resolution.*

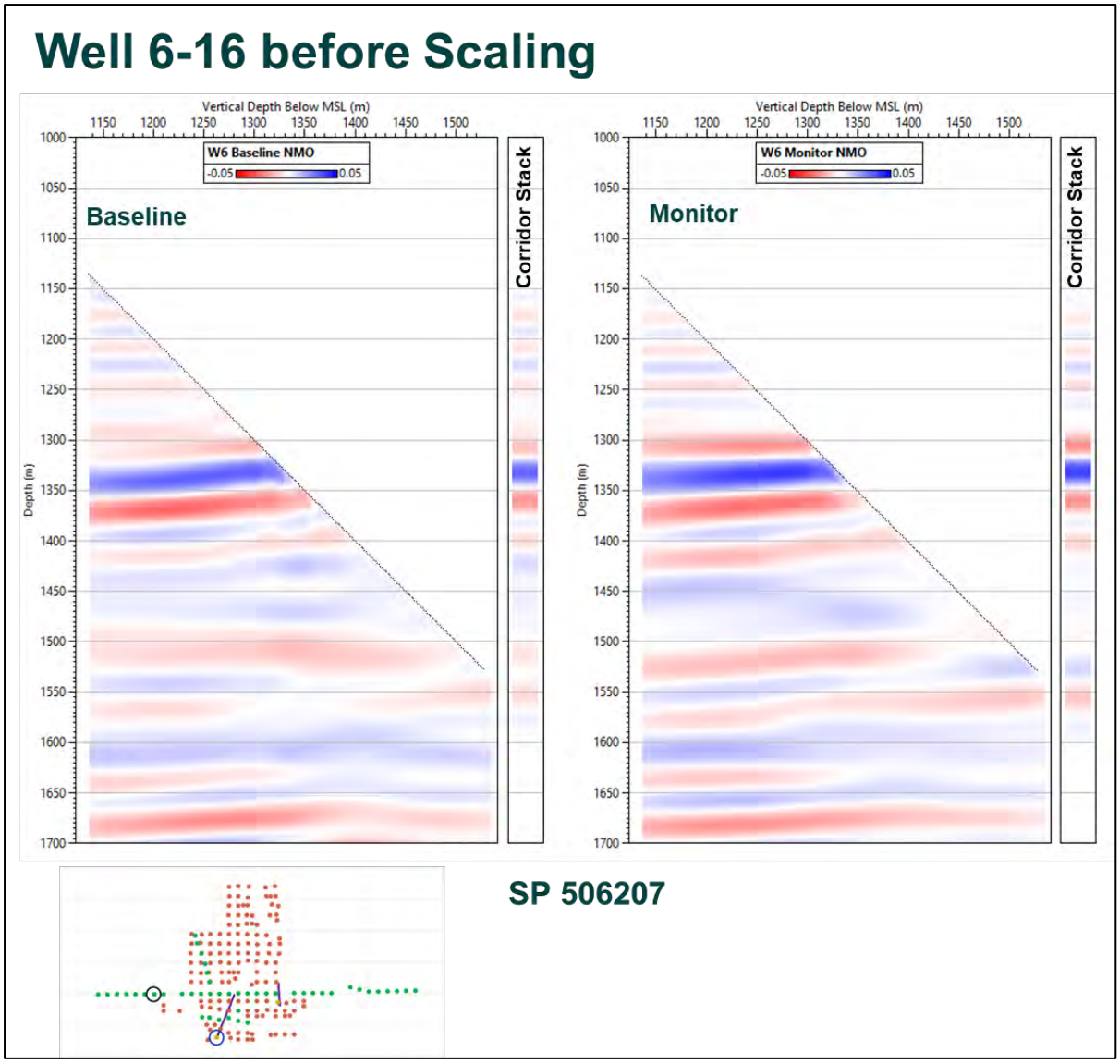


*Figure 11-8. Well 6-16 before Scaling - Pre-migrate and corridor stack.*

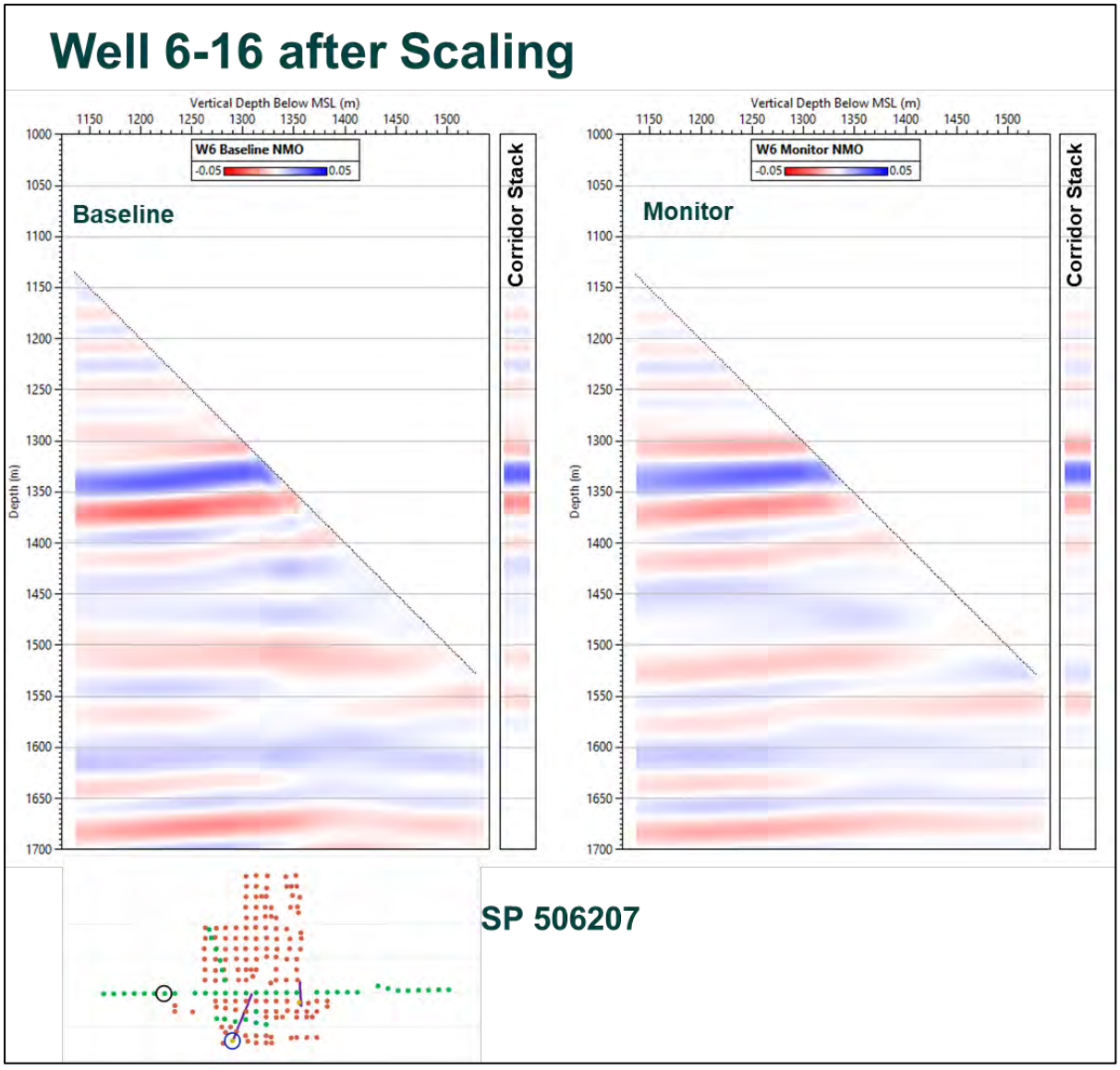


*Figure 11-9. Well 6-16 after Scaling - Baseline / Monitor scaling factor.*

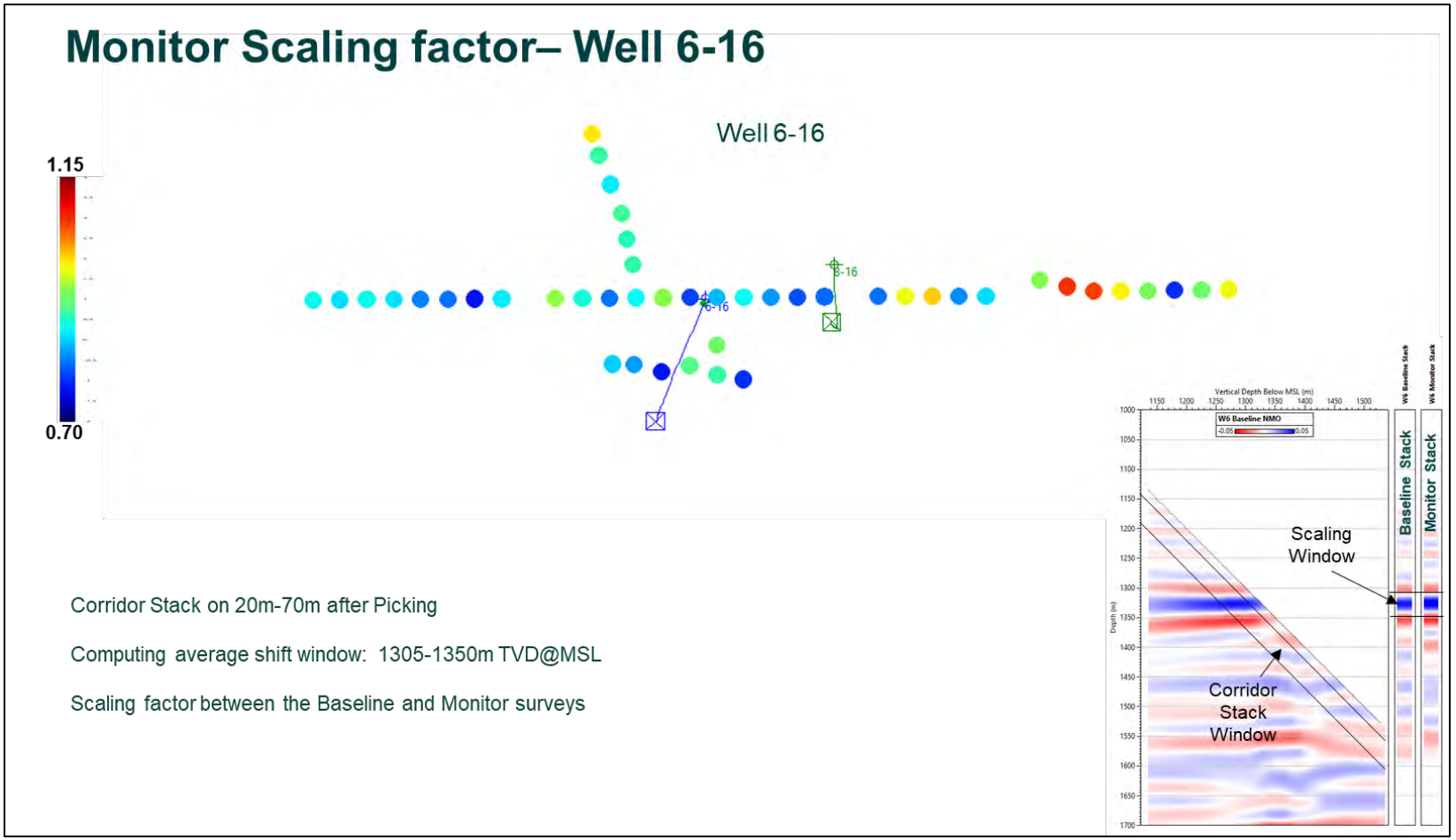


*Figure 11-10. Monitor Scaling factor– Well 6-16 - For each SP. The numbers of sweeps per location are different between the baseline and the monitor survey; the SNR for the same SP is also quite different between the baseline and monitor survey. After deconvolution the Up P wavefield is scaled depending on the Down P amplitudes. This results in the baseline and monitor having a different amplitude scaling. To correct this effect the amplitudes of the monitor SP was scaled to the baseline amplitudes level using the data outside the area where we expect a time-lapse effect due to the $CO_2$ injection. The baseline and monitor corridor stack were extracted in a window from 20 m to 70 m away from the FB. On each corridor stack the RMS amplitude value was computed in a window from 1305 m to 1350 m TVDMSL (above the reservoir). The monitor SP scaling factor was computed as the ratio between the baseline RMS and the monitor RMS (Fig. 11.10 right).*

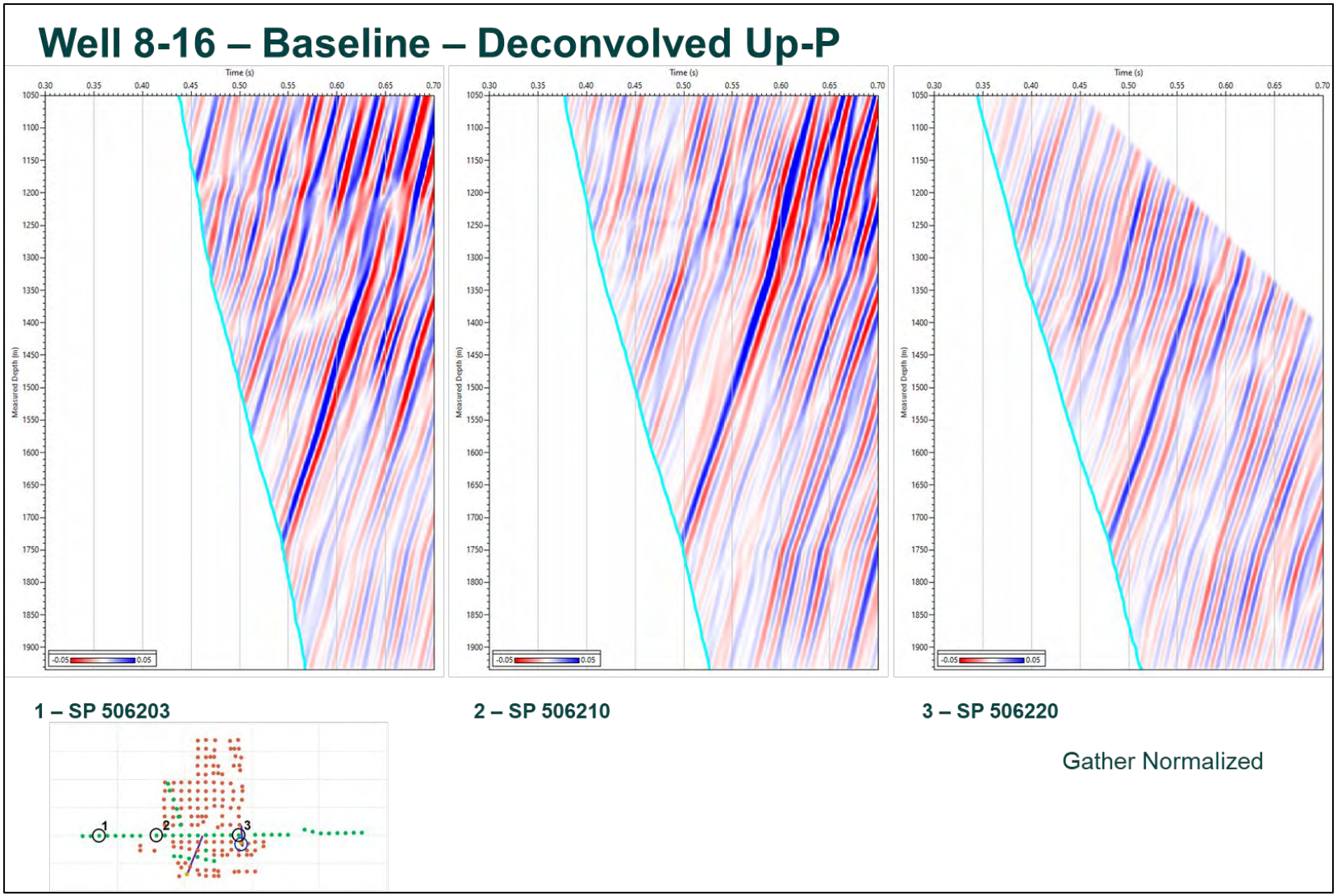


*Figure 11-11. Well 8-16 – Baseline – Deconvolved Up-P - Input data. This figure shows the well 8-16 baseline deconvolved Up P wavefield, for SP 506203 (far offset to the west), SP 506210 (mid offset to west) and SP 506220 (close to the well).*

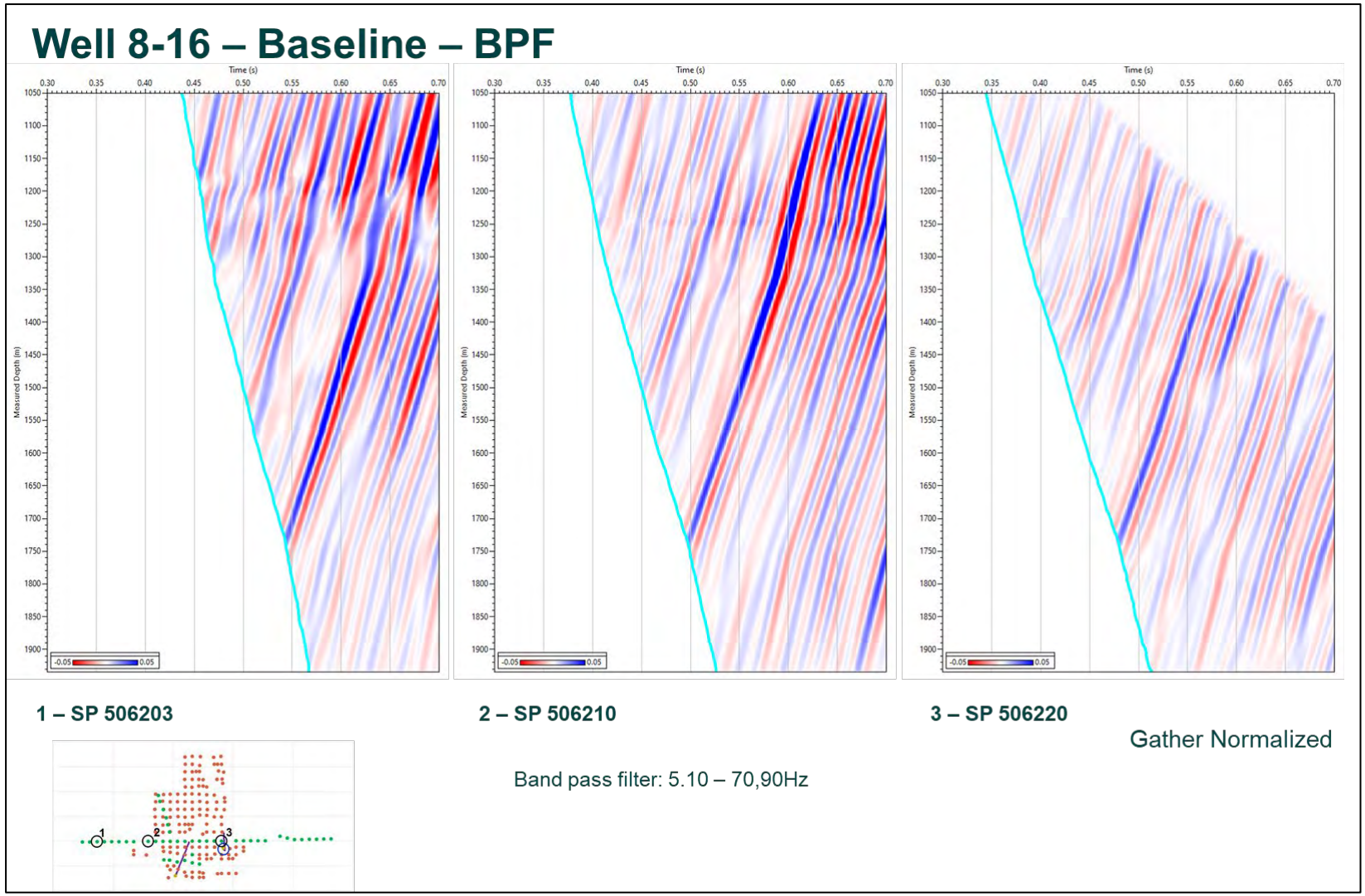


*Figure 11-12. Well 8-16 – Baseline – BPF. A 5,10-70,90 Hz BPF was applied to the input data.*

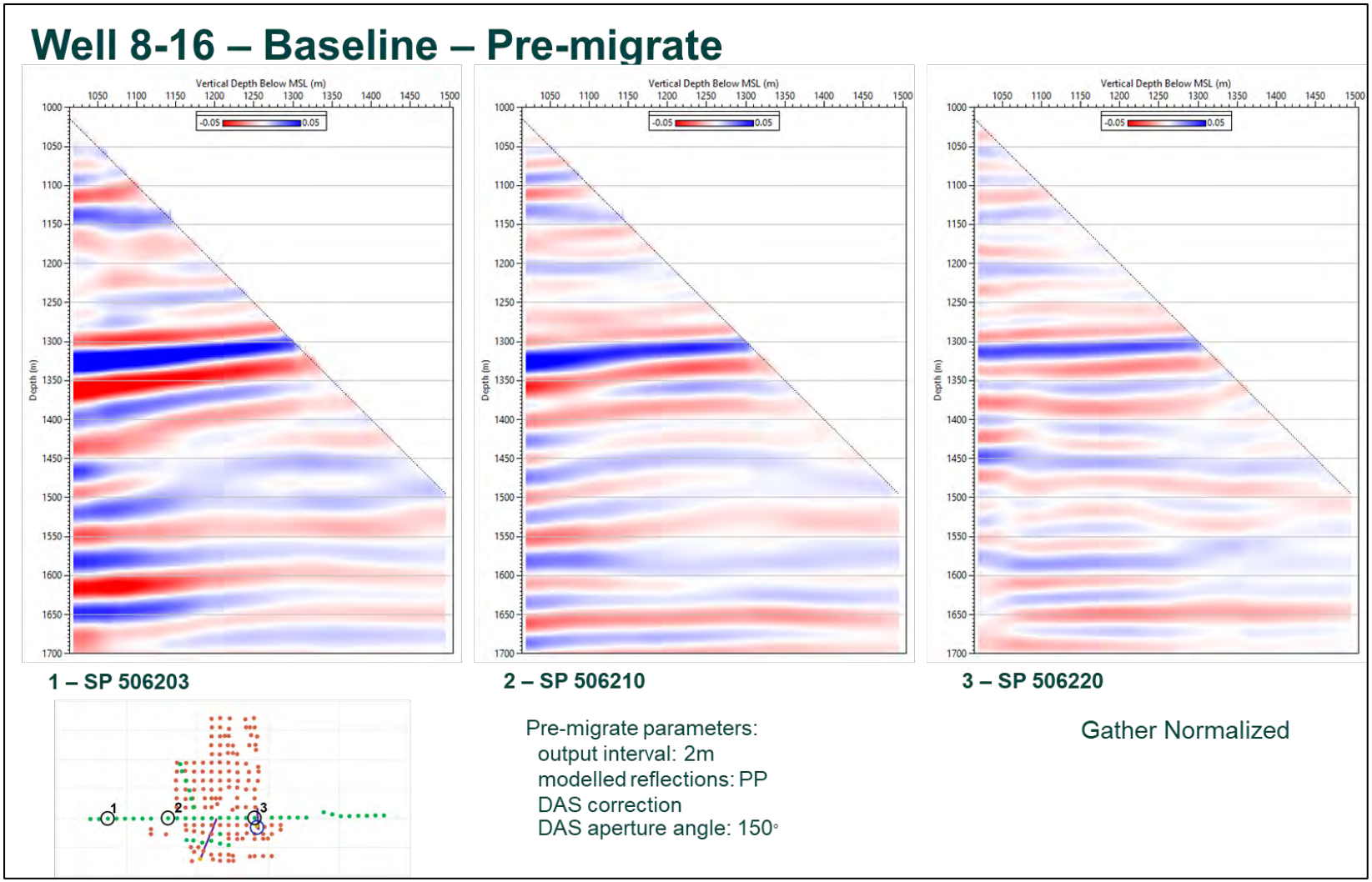


*Figure 11-13. Well 8-16 – Baseline – Pre-migrate - Pre-migrate. This presents the baseline SP 506203 (far offset to the west), SP 506210 (mid offset to west) and SP 506220 (close to the well) after pre-migrate correction.*

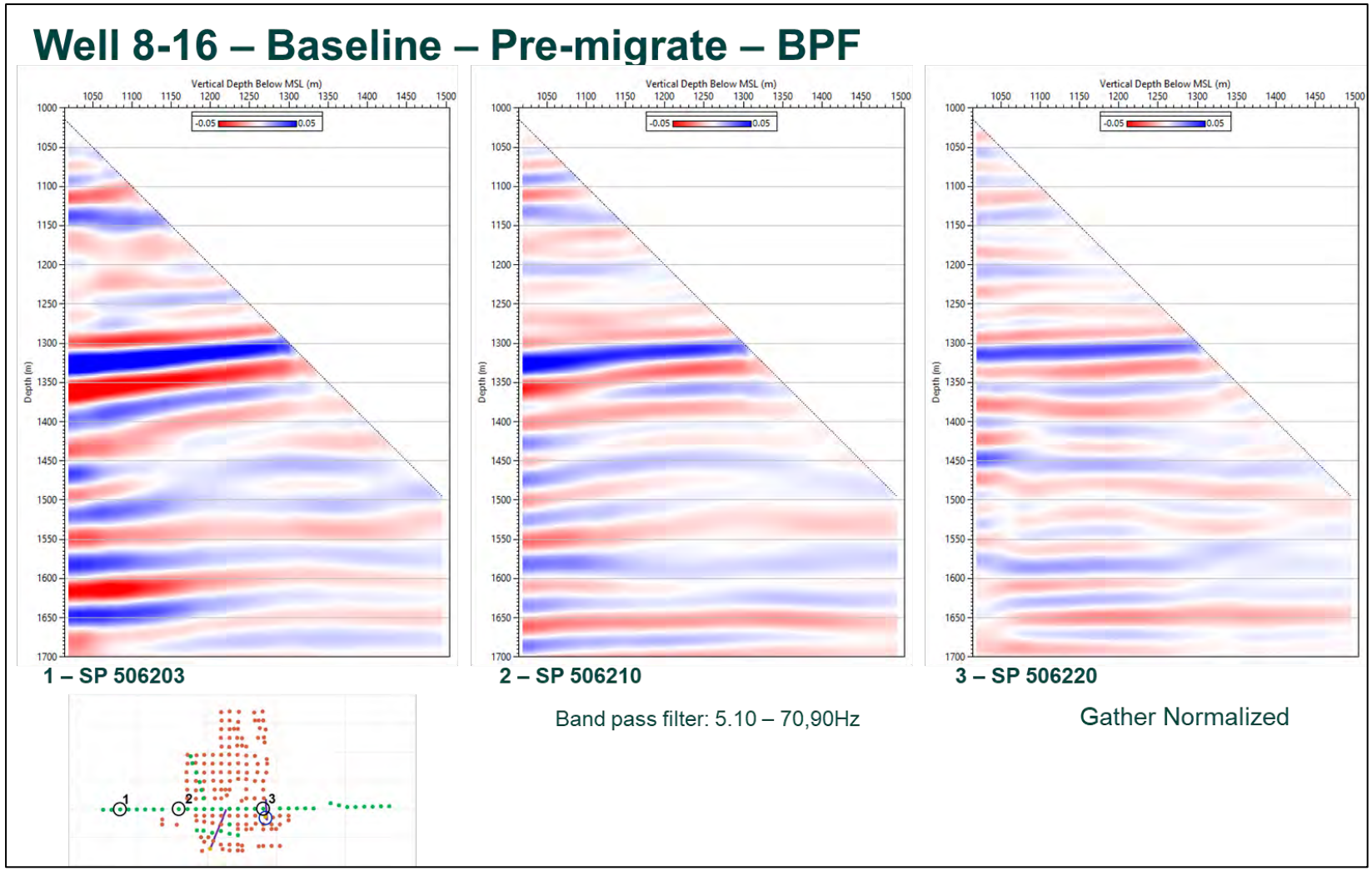


*Figure 11-14. Well 8-16 – Baseline – Pre-migrate – BPF - Reduce pre-migrate artefacts. A 5,10-70,90 Hz BPF was applied to the data.*

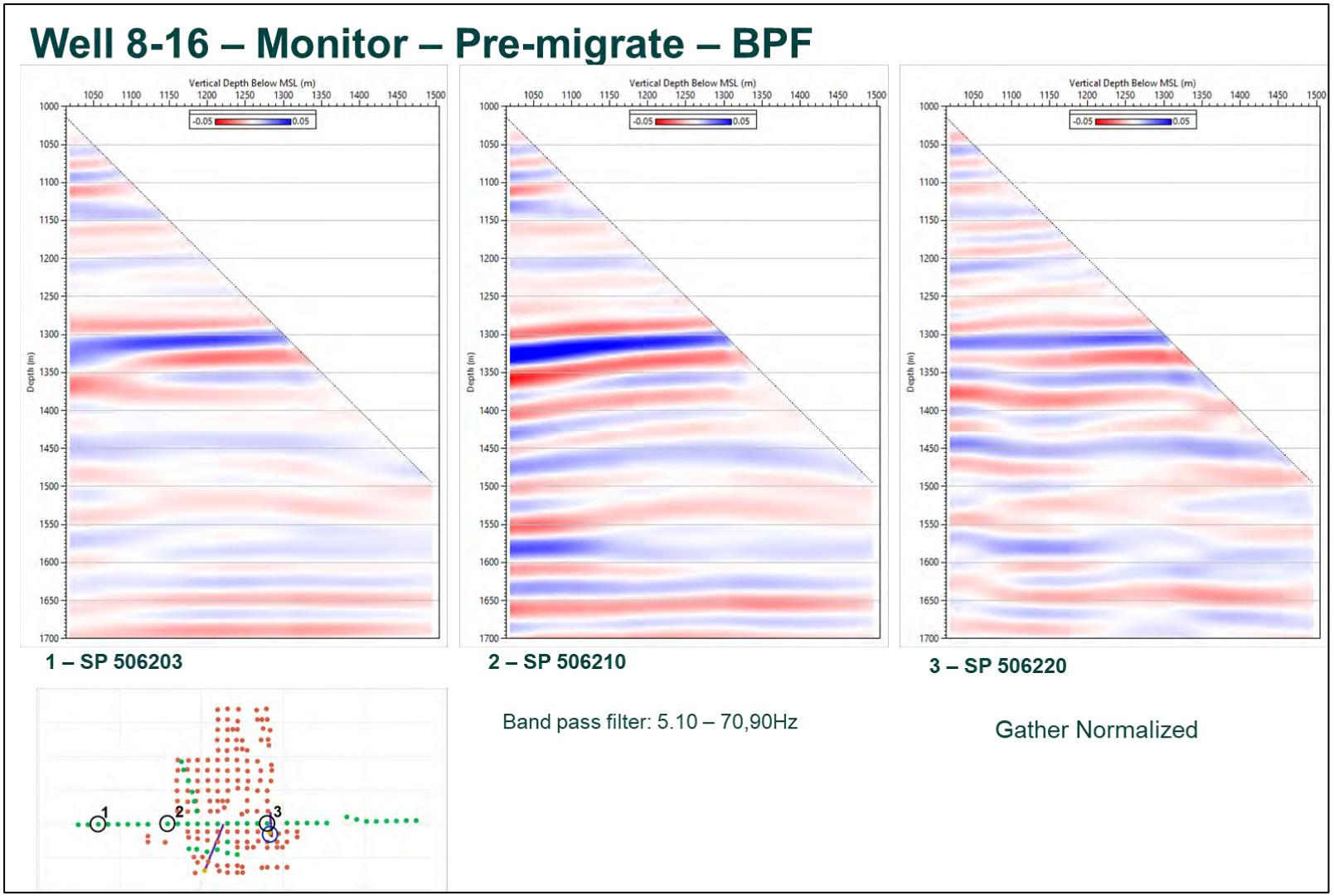


*Figure 11-15. Well 8-16 – Monitor – Pre-migrate – BPF - Reduce pre-migrate artefacts. Figure 11.15 shows the same data as figure 11.14 but for the monitor survey. As with well 6-16 data, at well 8-16 the seismic structural response at the top of the reef is similar between the baseline and the monitor survey, but it starts to degrade below 1400 m TVDMSL, especially for far offsets (the SNR decreases with the offset).*

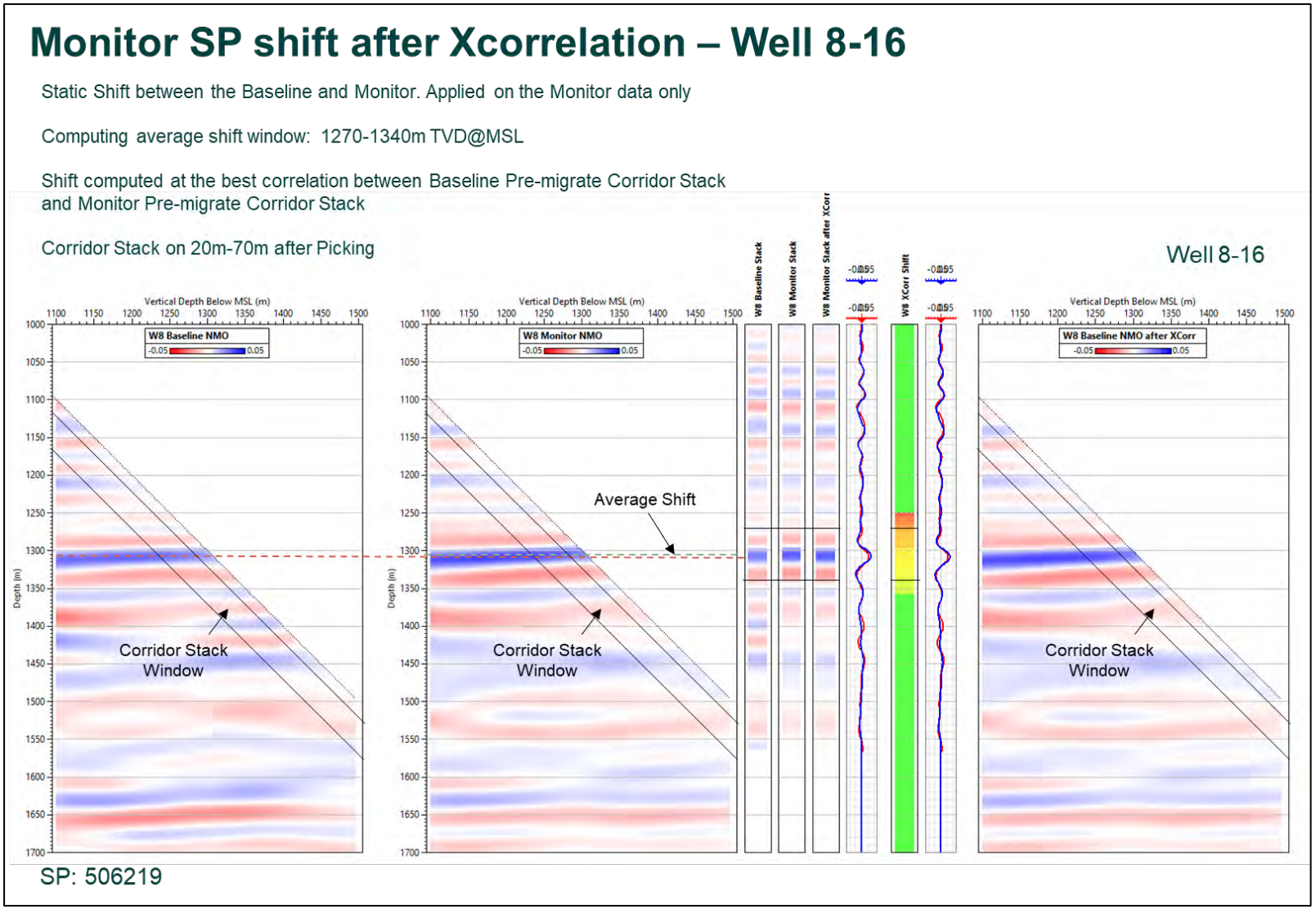


*Figure 11-16. Monitor SP shift after XCorrelation – Well 8-16 - Harmonize the baseline and monitor pre-migrate data.*

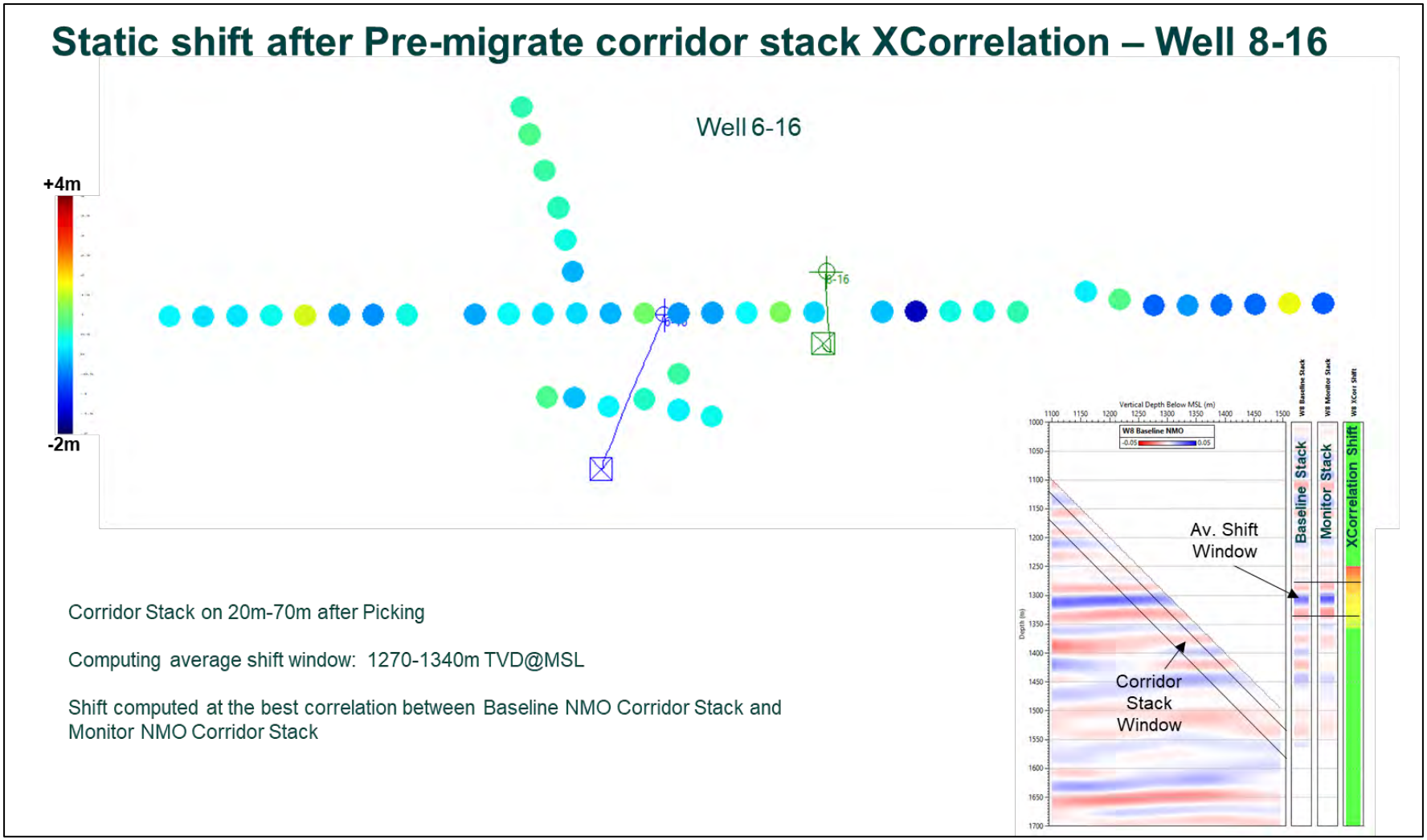


*Figure 11-17. Static shift after Pre-migrate corridor stack XCorrelation – Well 8-16 - Harmonize the baseline and monitor pre-migrate data. A similar cross-correlation process for depth correction between the baseline and the monitor pre-migrate data was applied to the well 8-16 data. As the A2 Carbonate top reflection is shallow at well 8-16, the cross-correlation analysis window for well 8-18 was 1270 m – 1340 m TVDMSL. Figure 11.17 shows the static shift computed after the well 8-16 baseline – monitor pre-migrate data cross-correlation. The maximum shift is less than 4 m which is below the seismic resolution.*

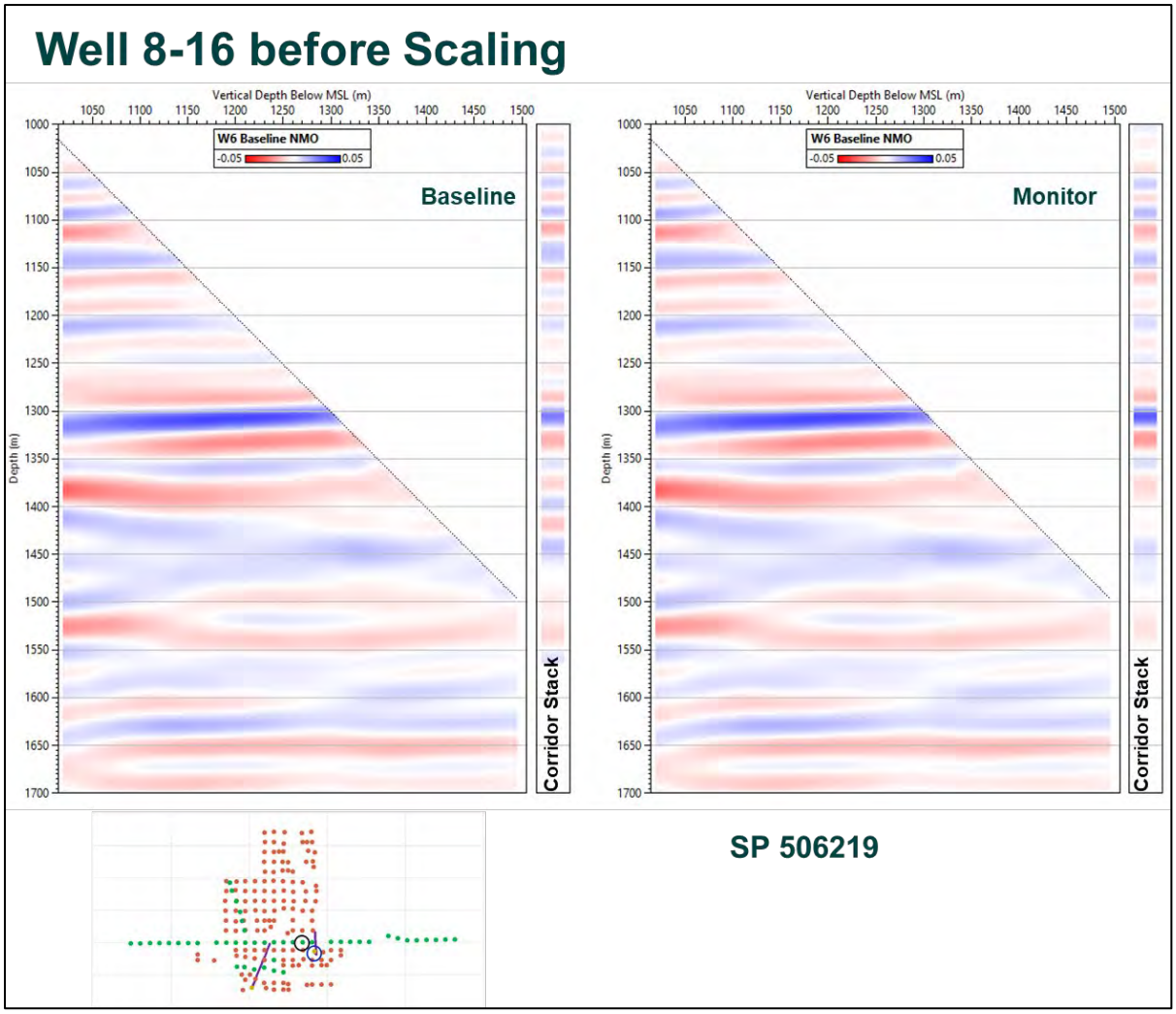


*Figure 11-18. Well 8-16 before Scaling - Pre-migrate and corridor stack.*

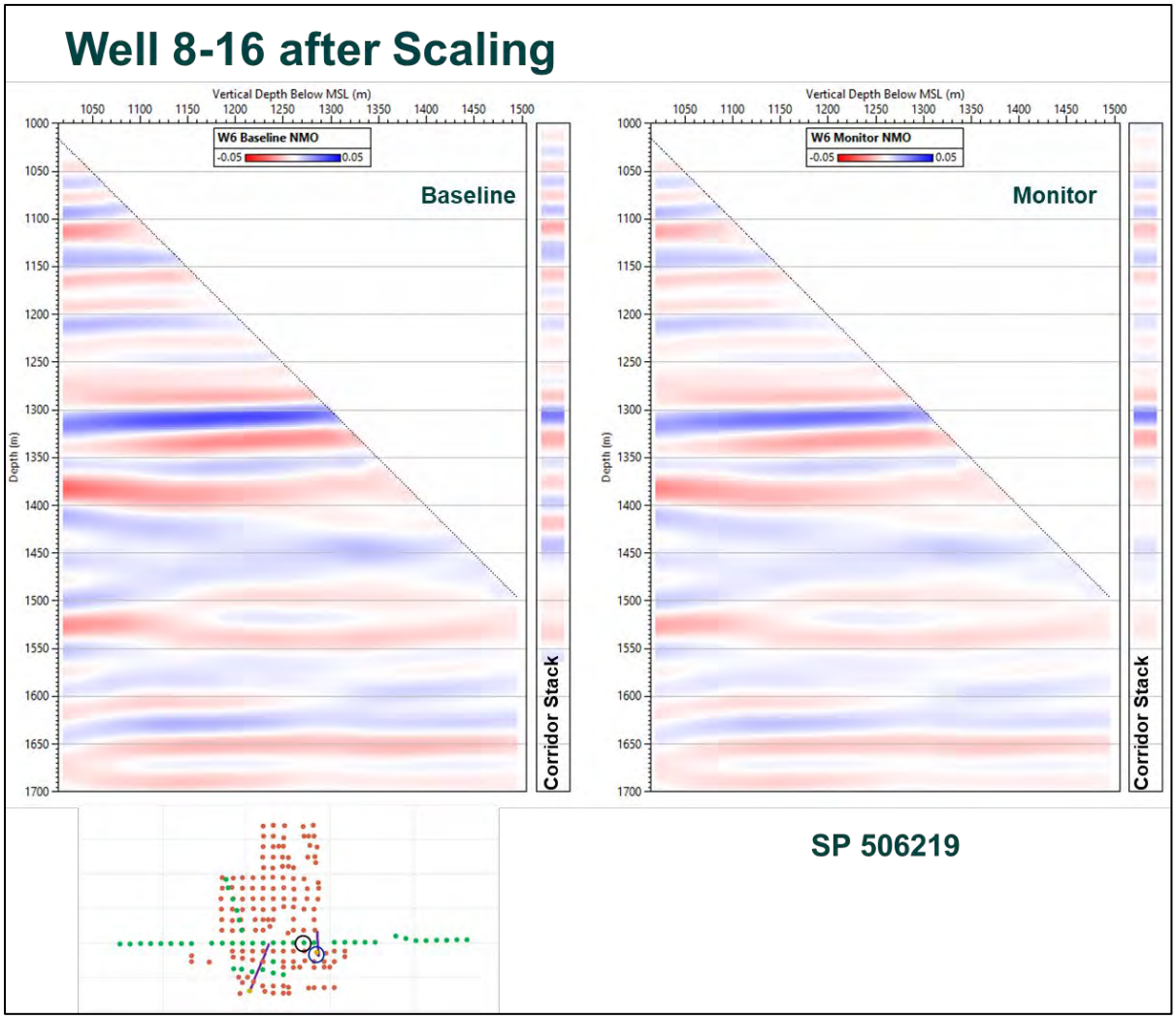


*Figure 11-19. Well 8-16 after Scaling - Baseline / Monitor scaling factor.*

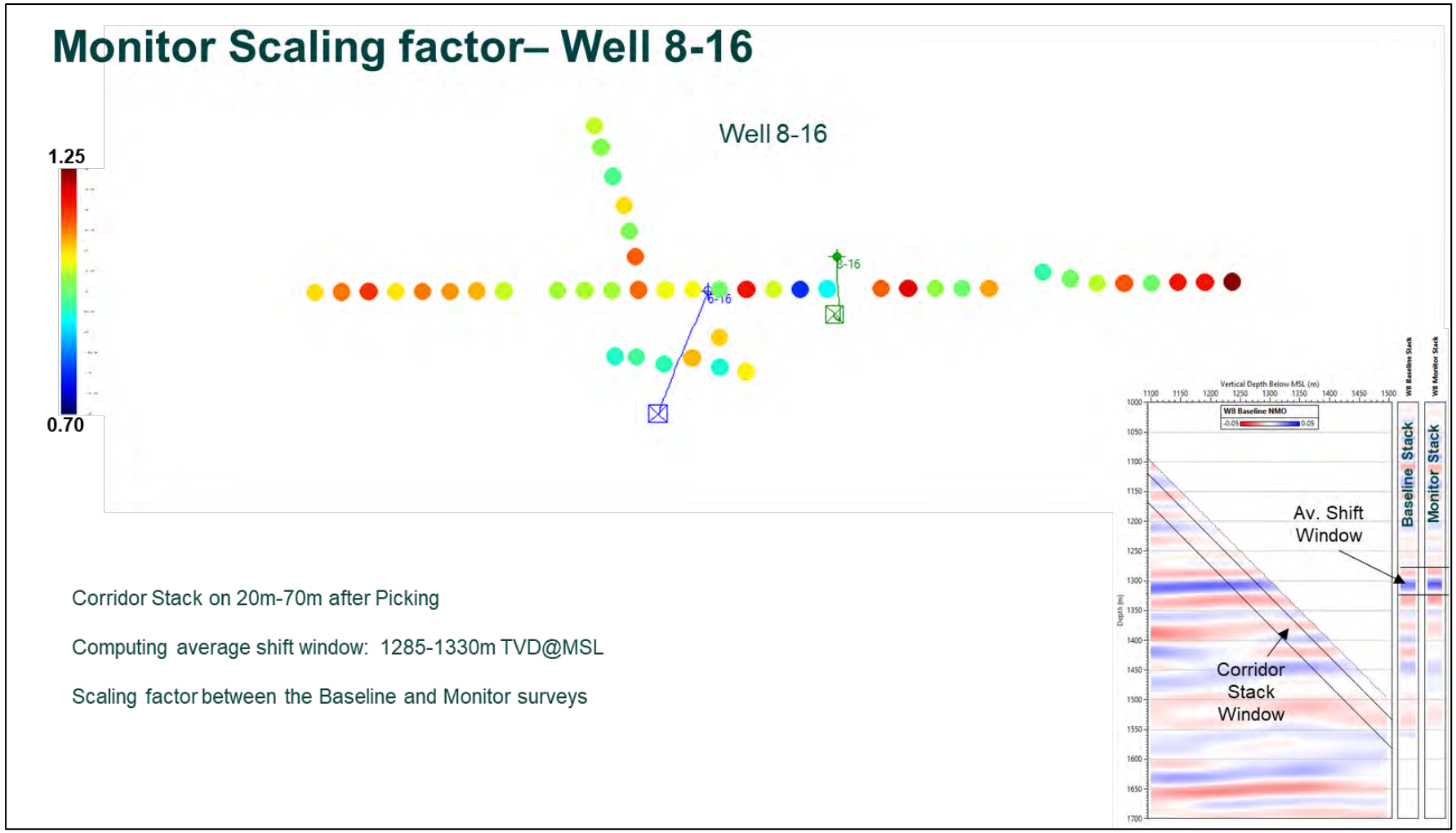


*Figure 11-20. Monitor Scaling factor– Well 8-16 - For each SP. For well 8-16 data the scaling factor was computed using the RMS values extracted from the baseline and monitor NMO corridor stacks over the 1285 m to 1330 m TVDMSL interval (Fig. 11.20 right).*

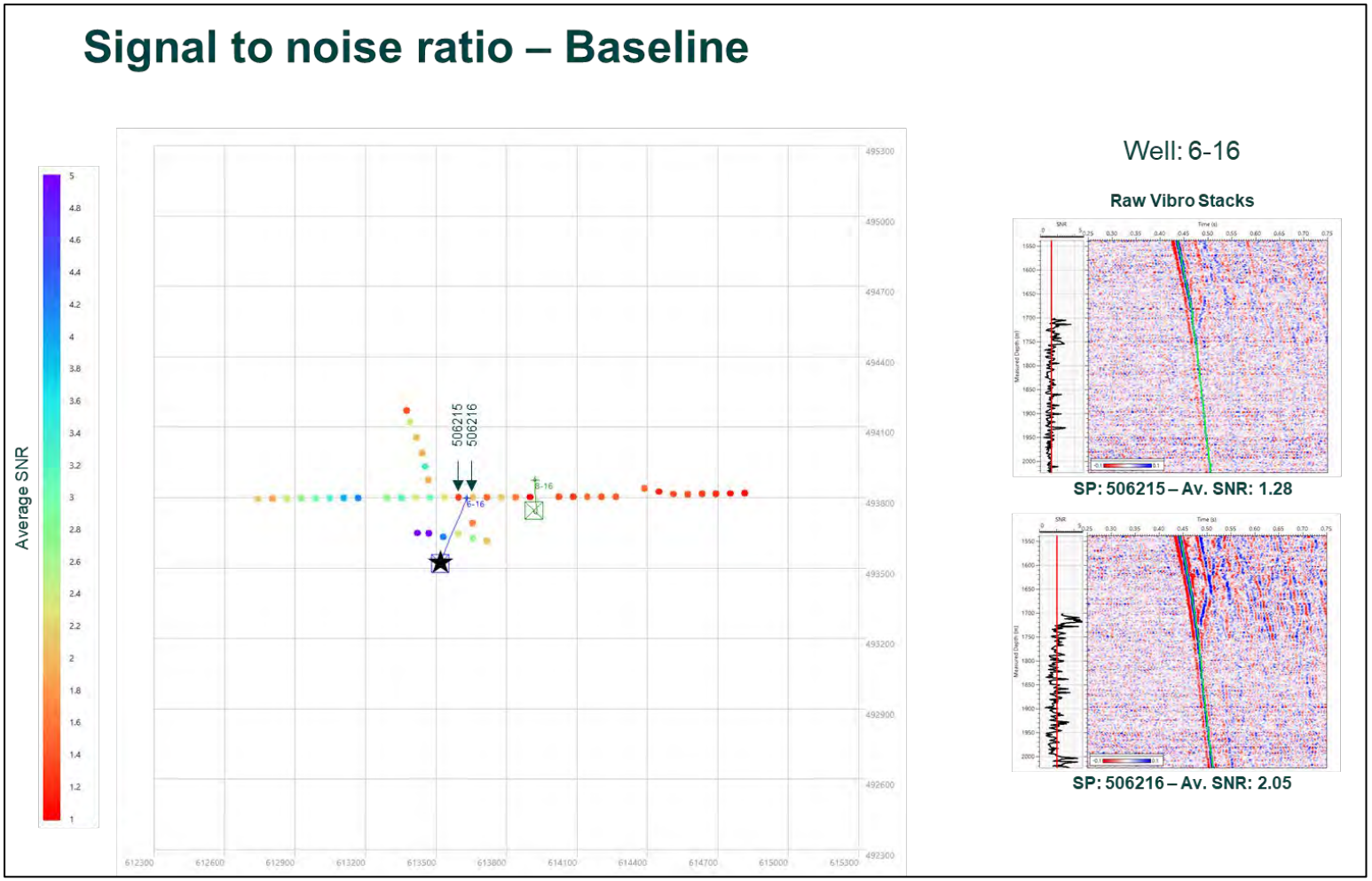


*Figure 11-21. Signal to noise ratio – Baseline - Well 6-16 – for data selection. Some SPs have a very low SNR especially for the baseline survey. Figure 11-21 shows the well 6-16 baseline SNR for two adjacent SP. The SP 506215 (Fig. 11-21 right top) present a low SNR (1.28) while the neighbour SP 506216 has a better SNR value.*

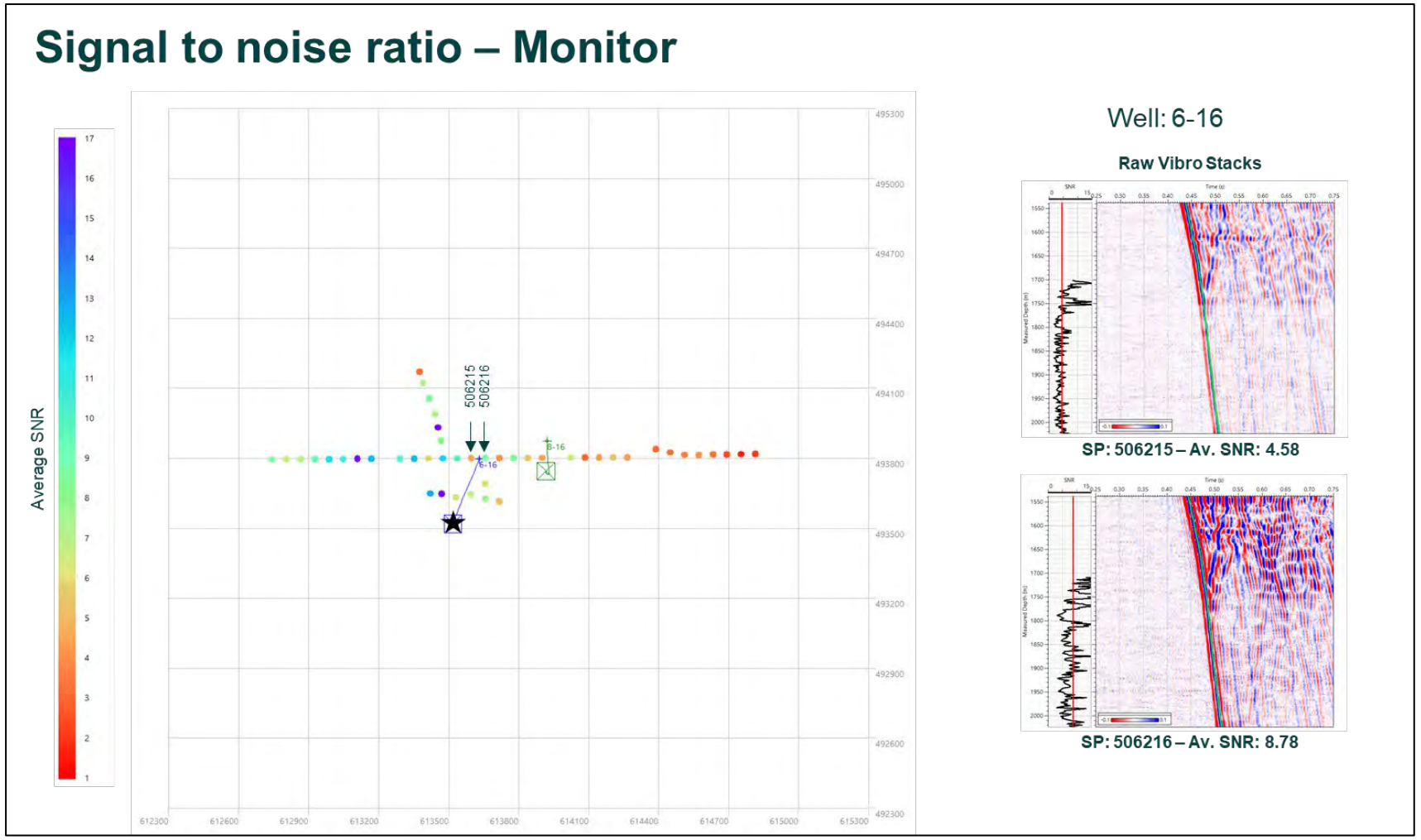


*Figure 11-22. Signal to noise ratio – Monitor - Well 6-16 – for data selection. The same SP shows a much better SNR for the monitor survey.*

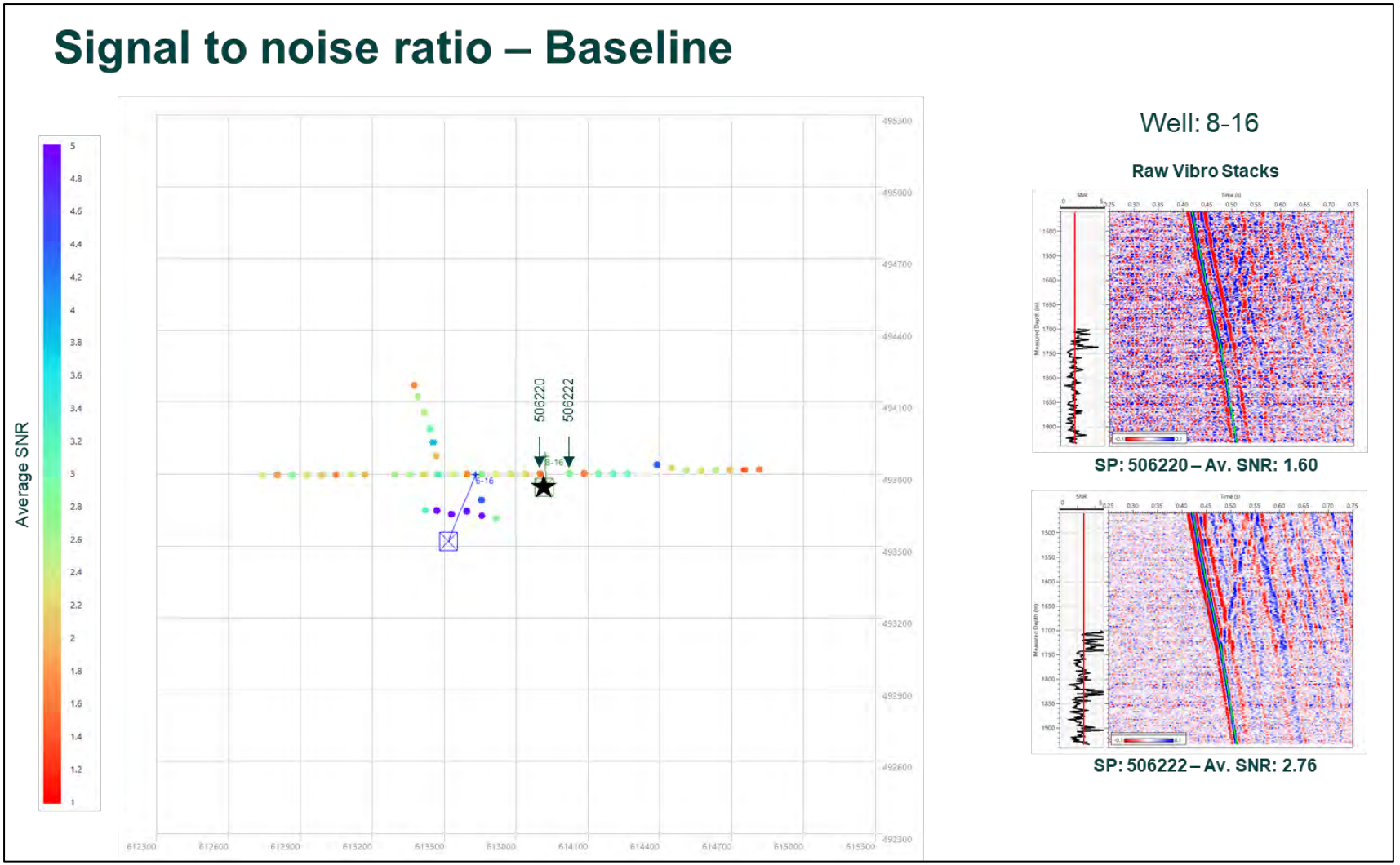


*Figure 11-23. Signal to noise ratio – Baseline - Well 8-16 – for data selection. Similar to well 8-16 data, the baseline SP 506220 has an average SNR value of 1.6 which is much lower than the neighbour SP 506222 SNR average value.*

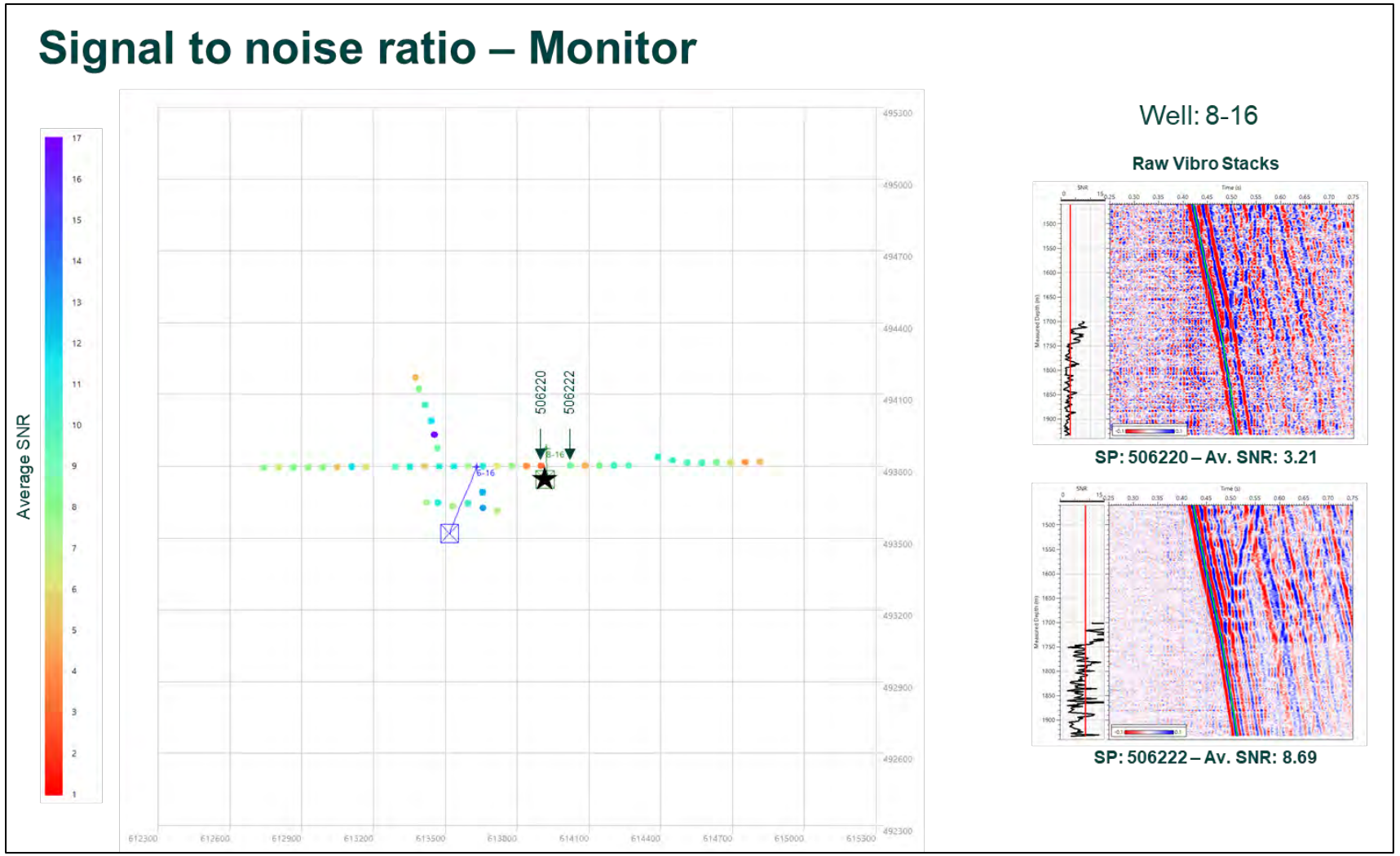


*Figure 11-24. Signal to noise ratio – Monitor - Well 8-16 – for data selection. In figure 11.24, the same SP as in the figure 11.17 has a better SNR for the monitor survey.*

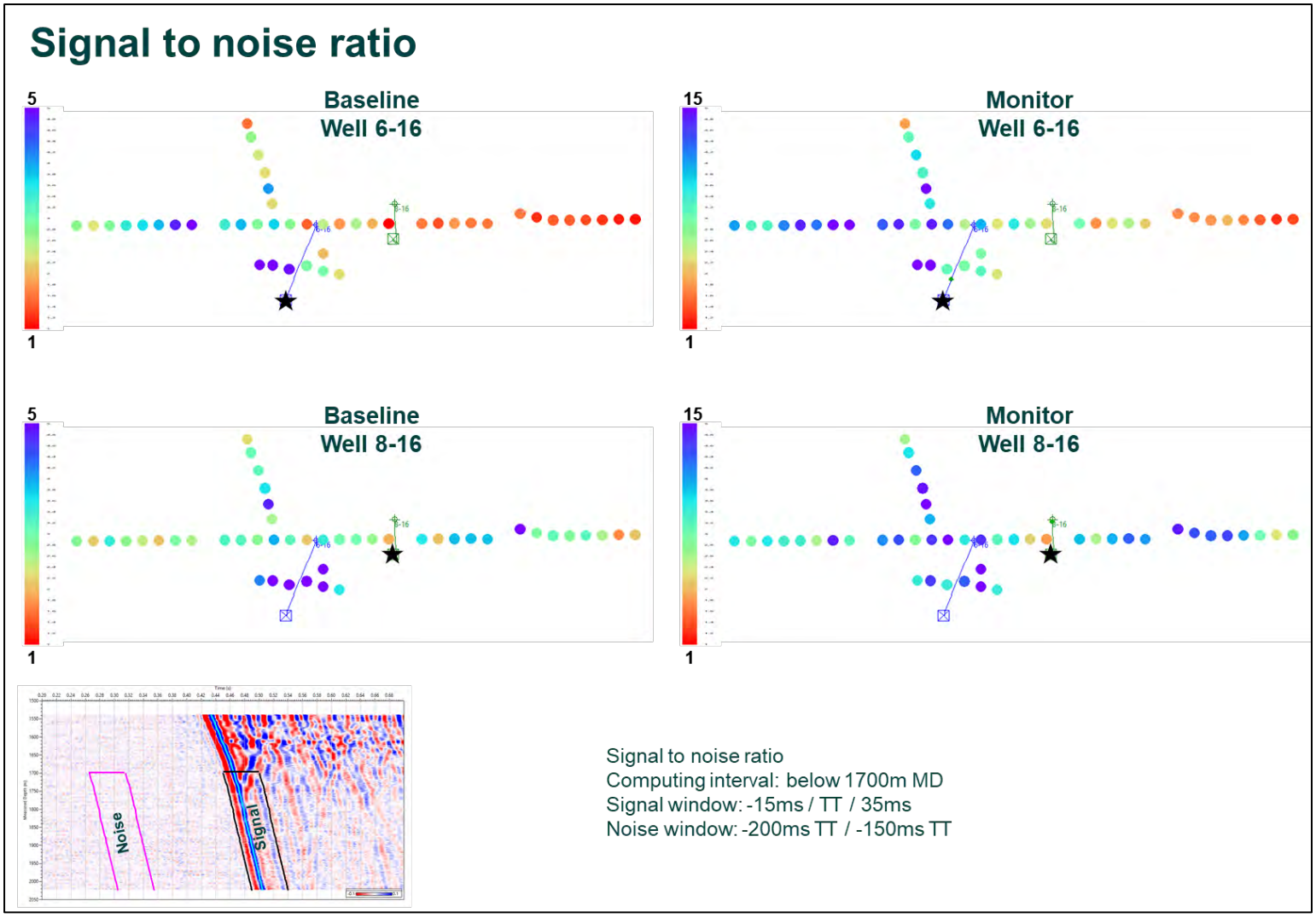


*Figure 11-25. Signal to noise ratio - Before data selection.*

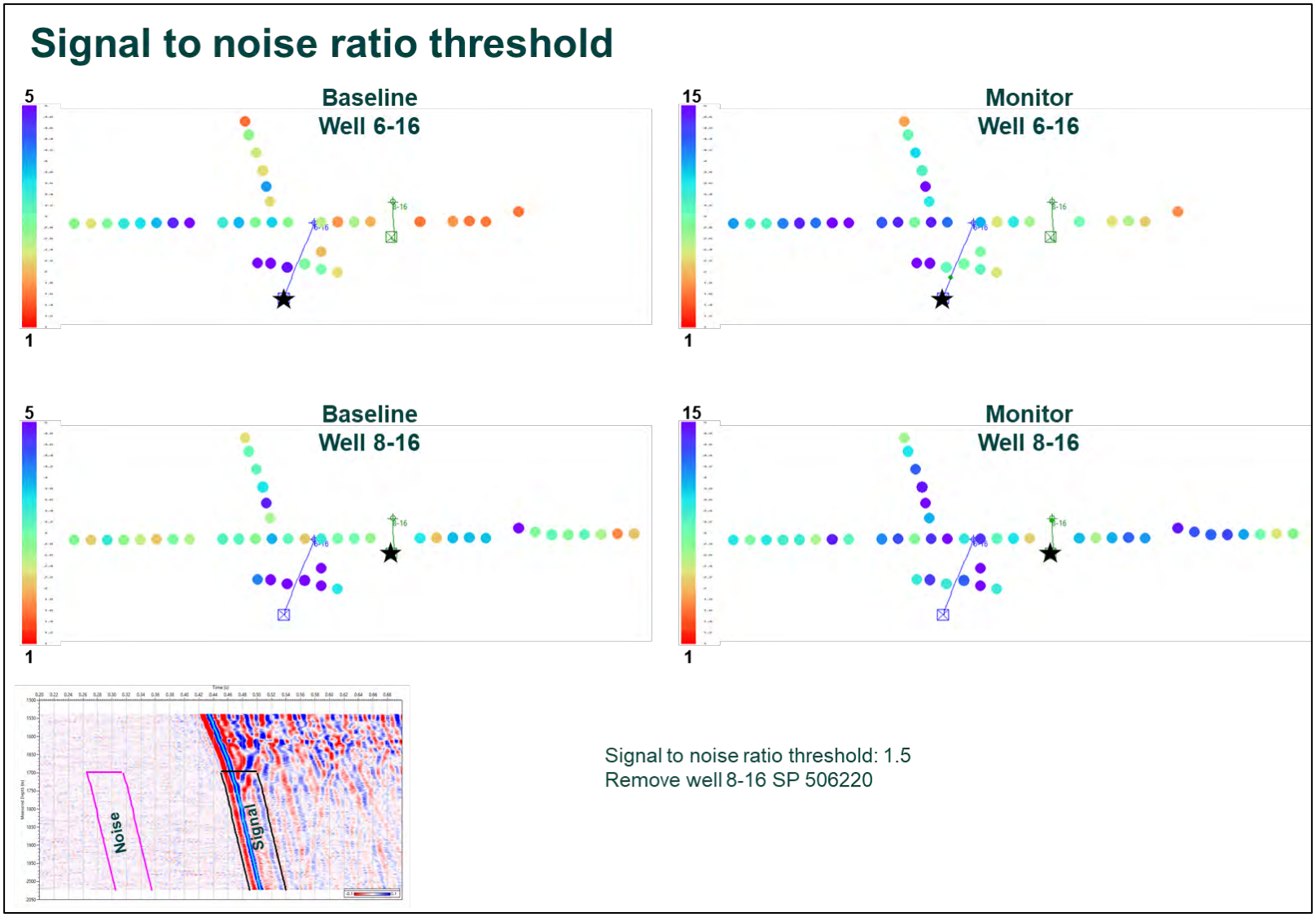


*Figure 11-26. Signal to noise ratio threshold - After data selection.*

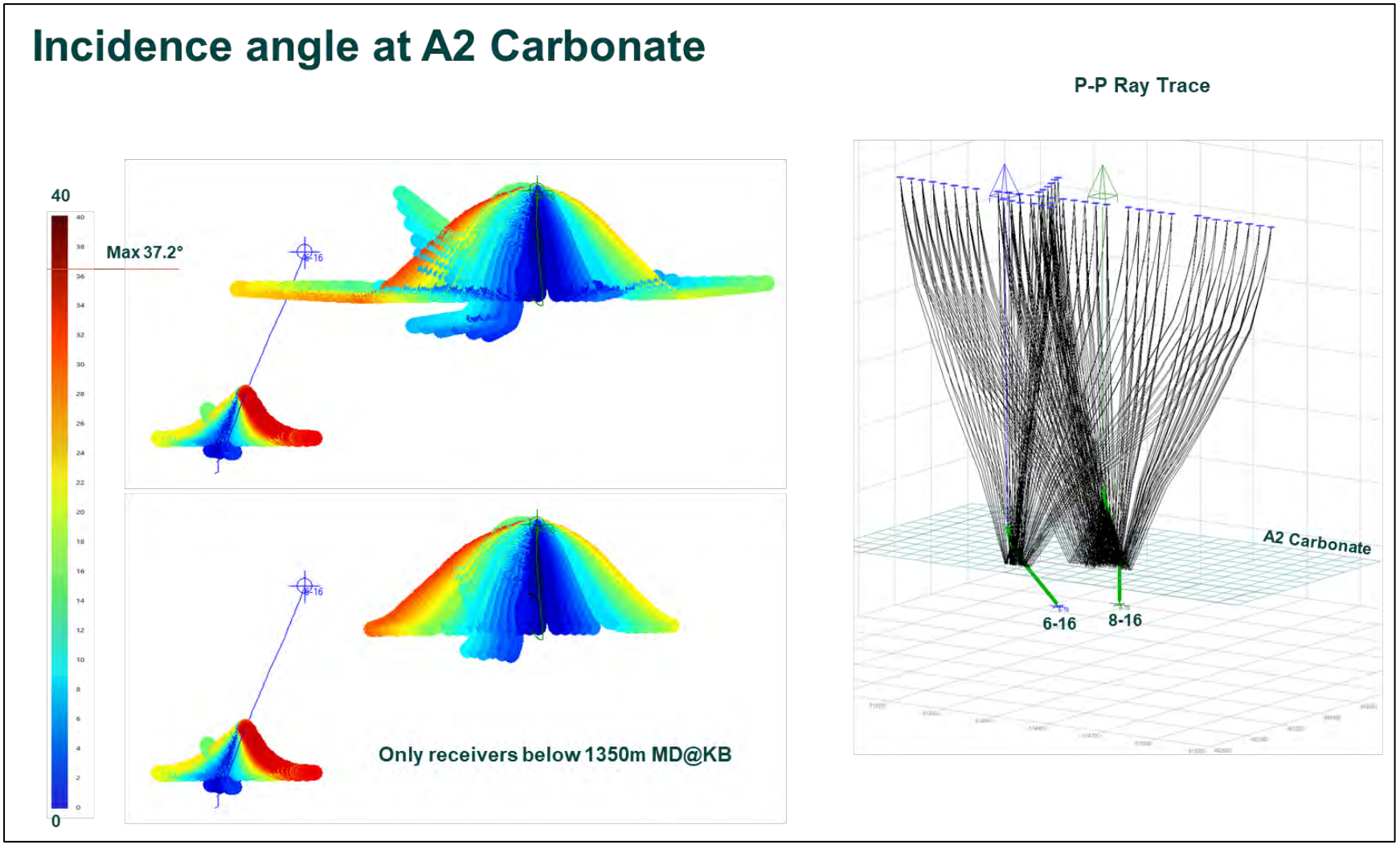


*Figure 11-27. Incidence angle at A2 Carbonate - P-P reflection points. This figure shows on the top left the A2 Carbonate reflection point incidence angle after P-P ray tracing (Fig. 11.27 right). Due to the well trajectory and receiver and source positions, the area covered by the image is close to the wells. The incidence angle is maximum 37.2°. Also, in some area data with different incidence angle are mixing.*

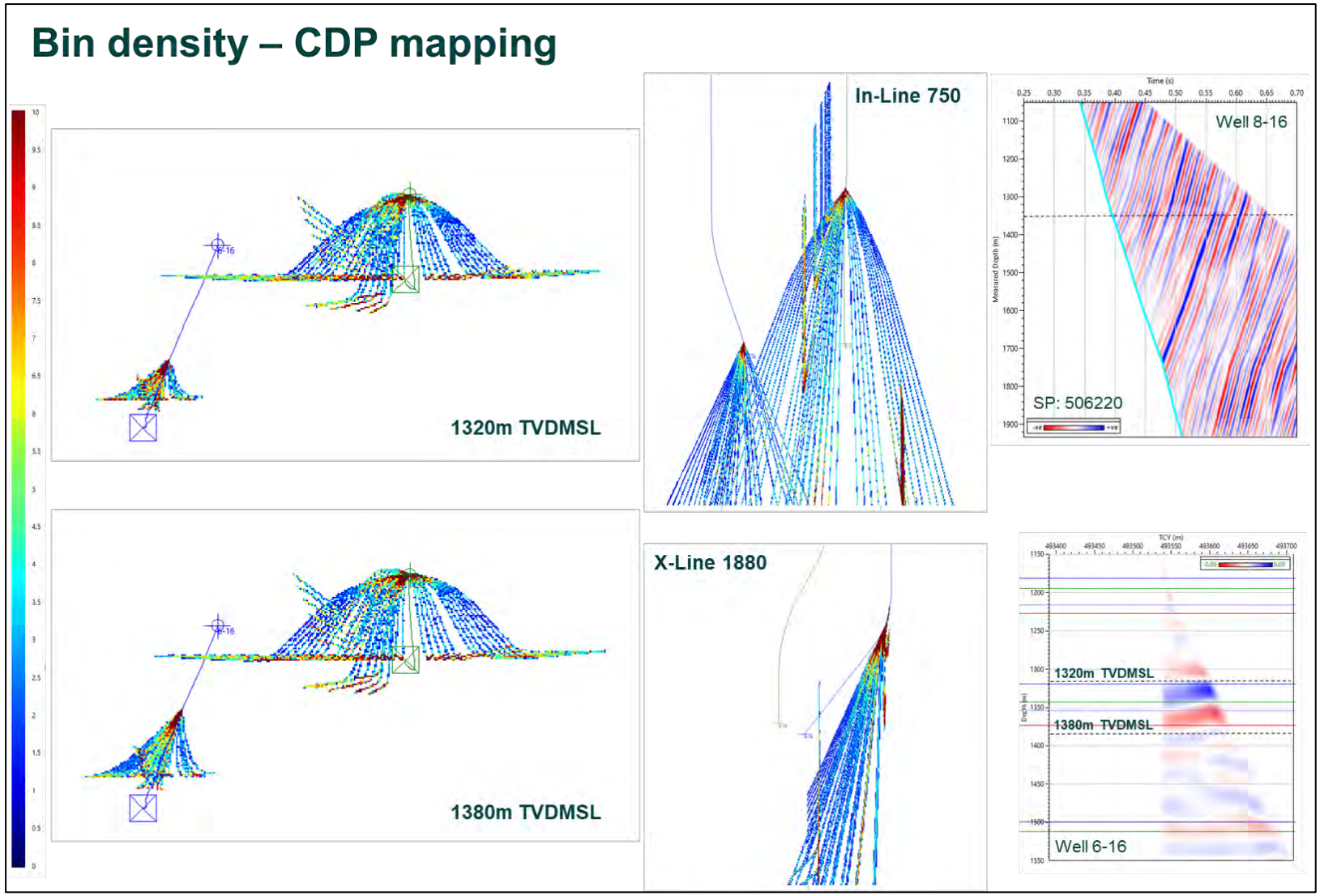


*Figure 11-28. Bin density – CDP mapping - Before data selection.*

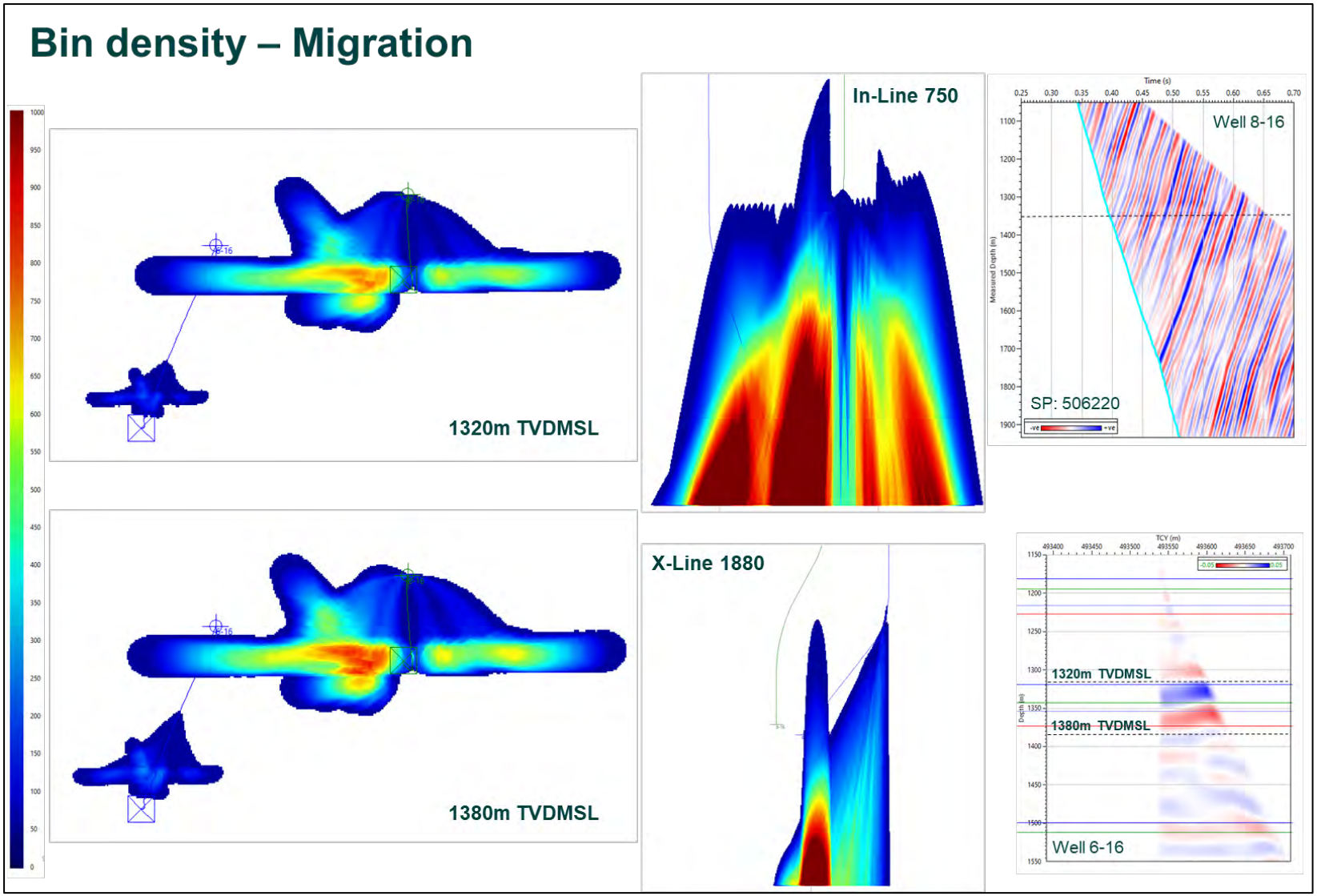


*Figure 11-29. Bin density – Migration - Before data selection.*

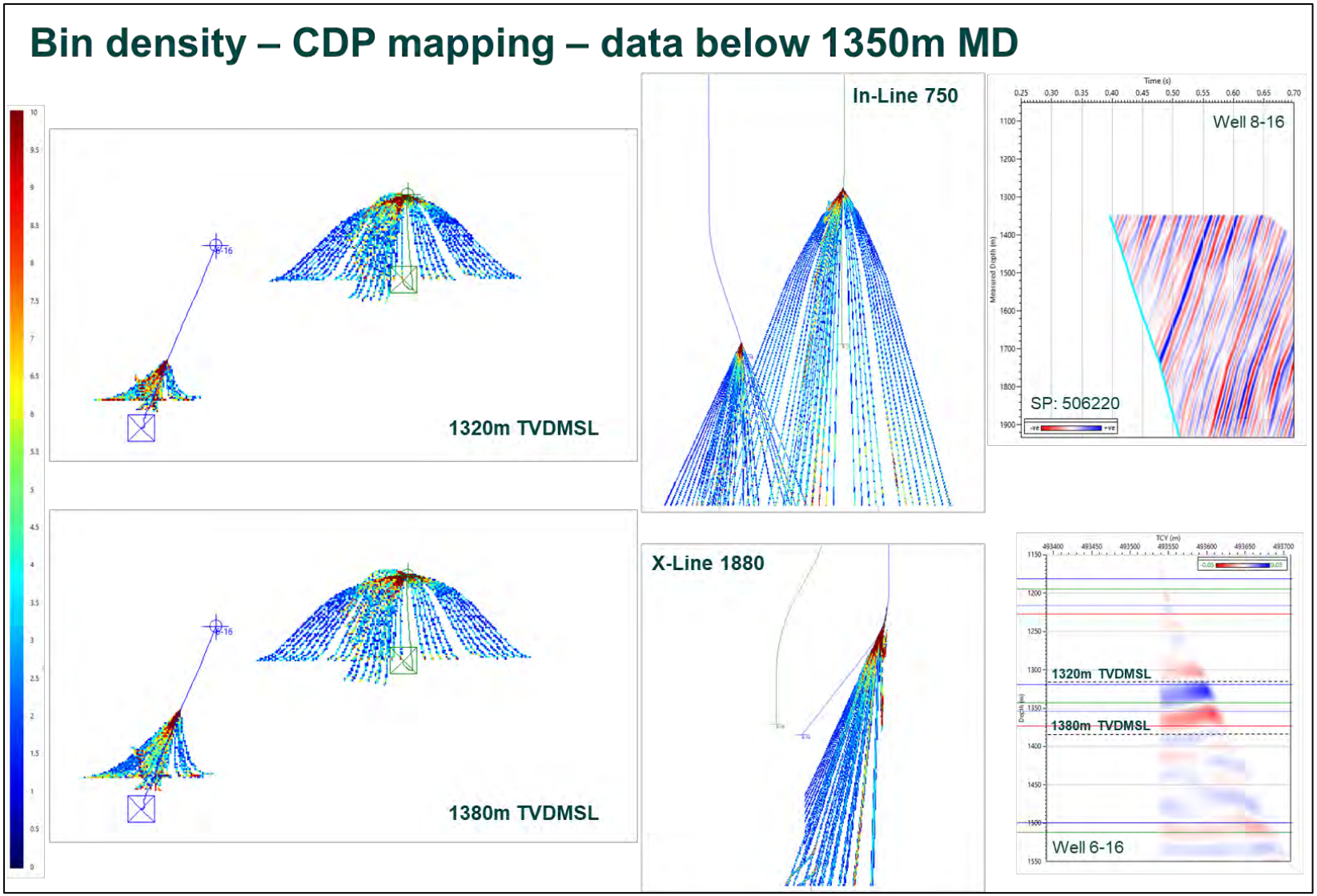


*Figure 11-30. Bin density – CDP mapping – data below 1350m MD - After data selection.*

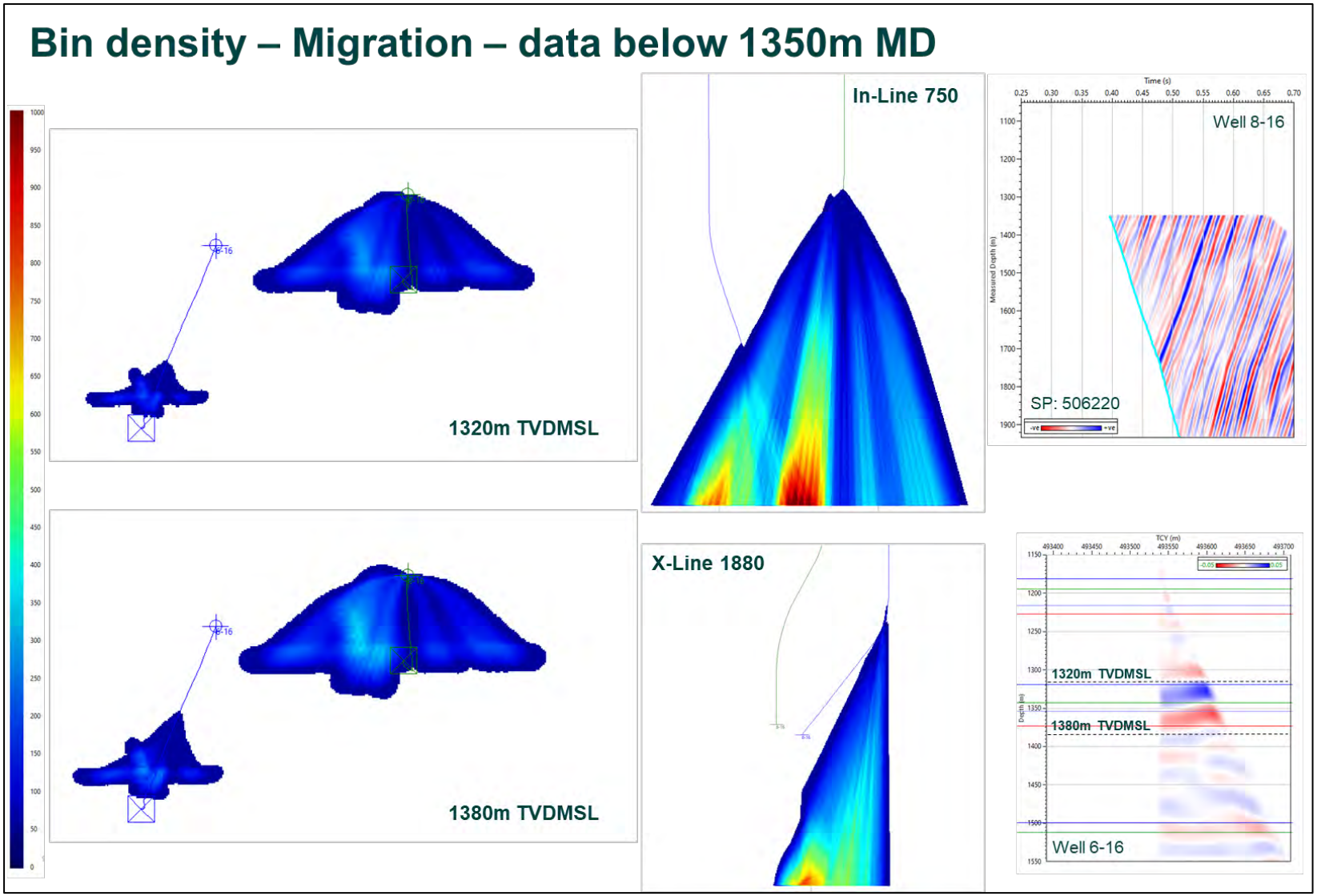


*Figure 11-31. Bin density – Migration – data below 1350m MD - After data selection.*

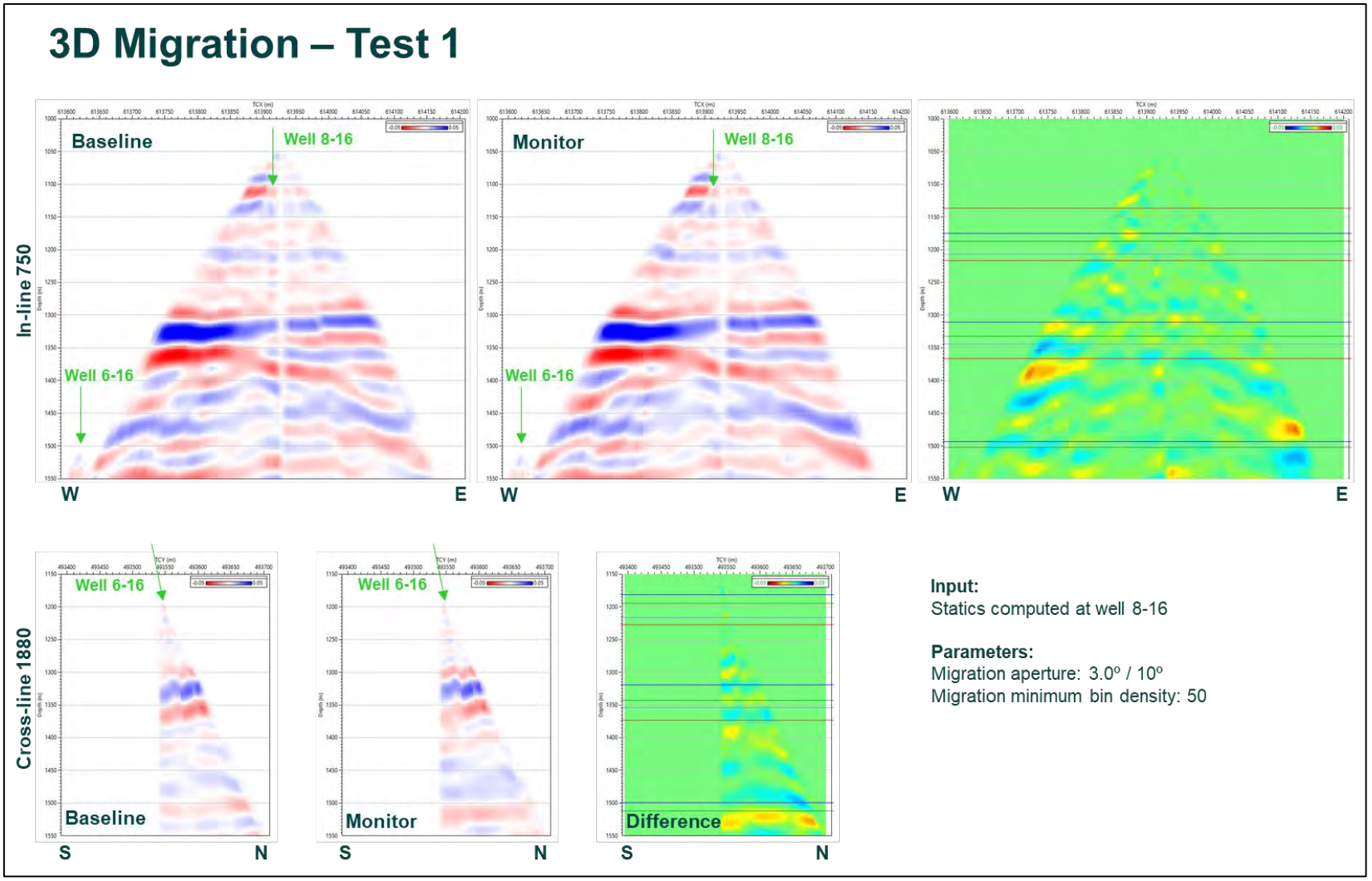


*Figure 11-32. 3D Migration – Test 1 - Statics applied.*

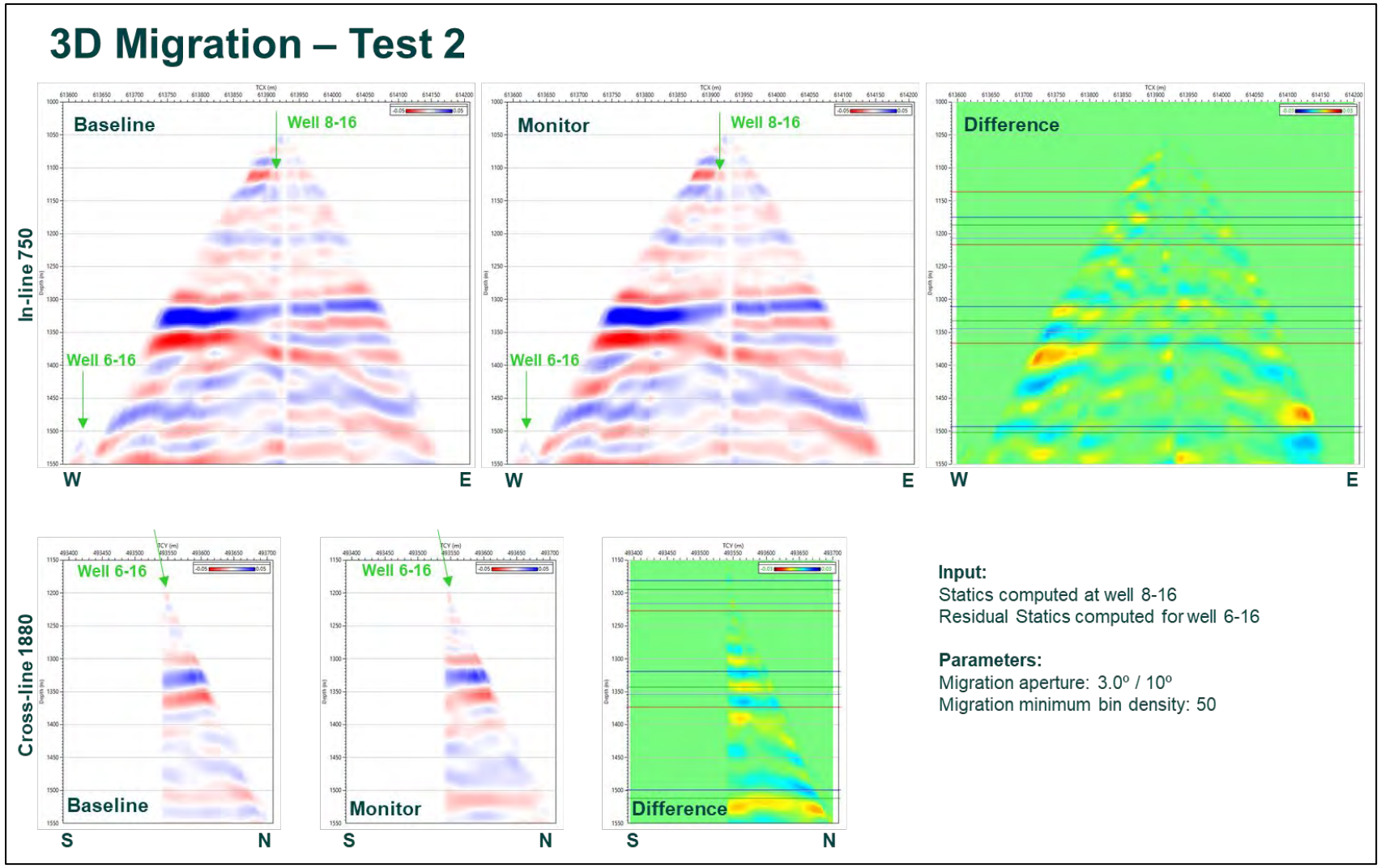


*Figure 11-33. 3D Migration – Test 2 - Residual statics applied.*

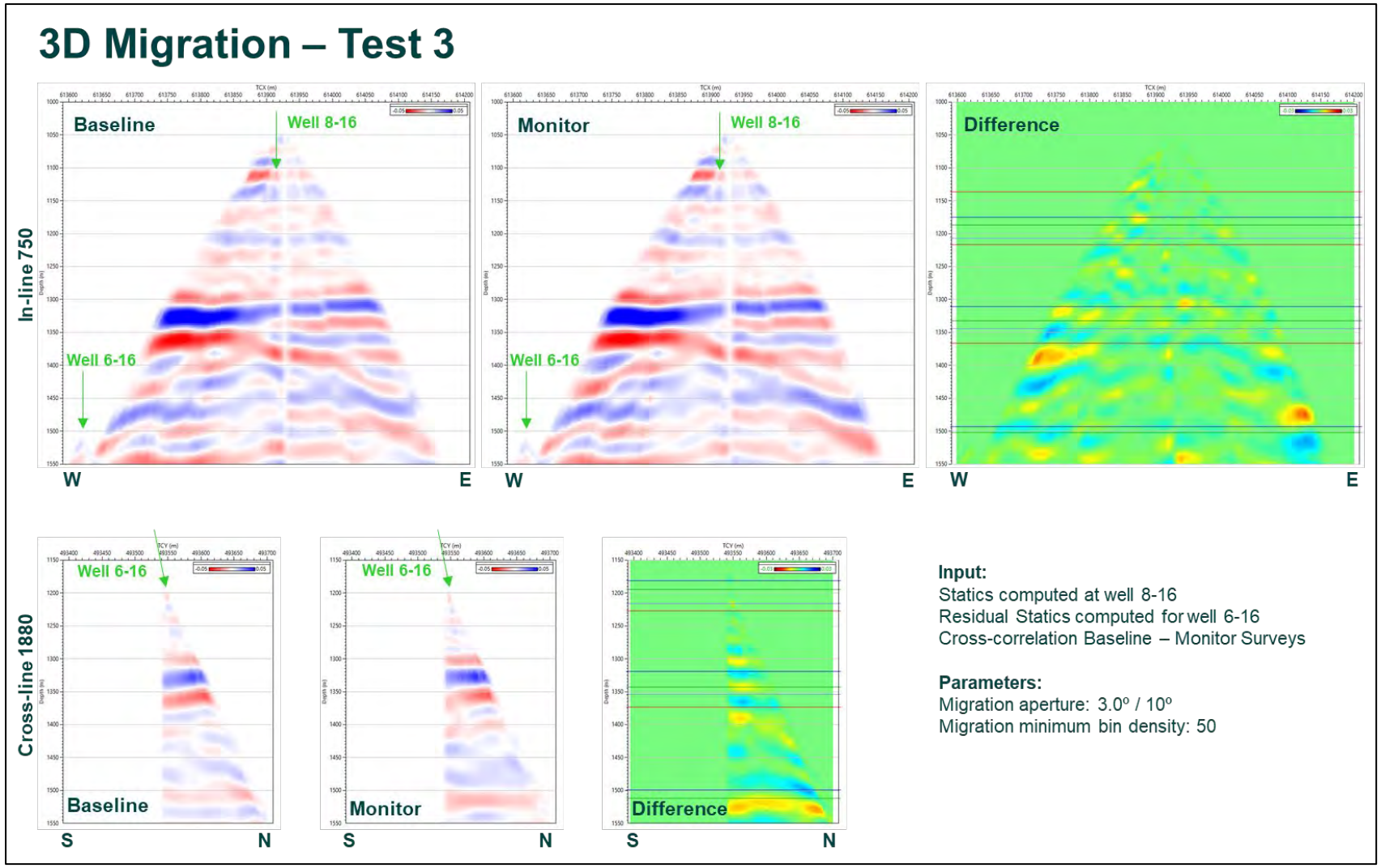


*Figure 11-34. 3D Migration – Test 3 - Cross-correlation shift applied.*

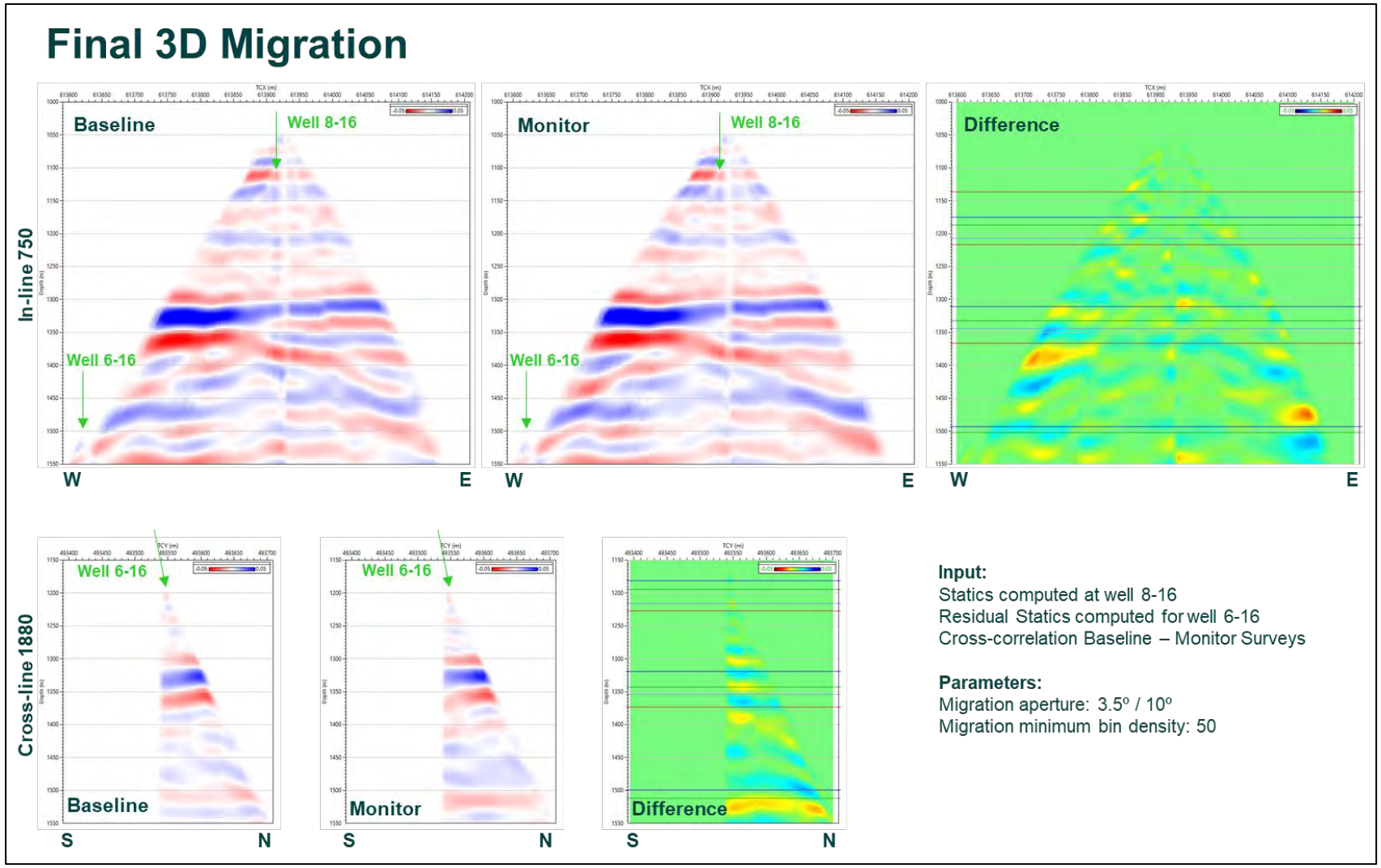


*Figure 11-35. Final 3D Migration - Final vibroseis data image. The final migration image with a 3.5° aperture (10° aperture for the image points near receivers) and a threshold of minimum bin density per cell of 50, is presented in figure 11.35.*

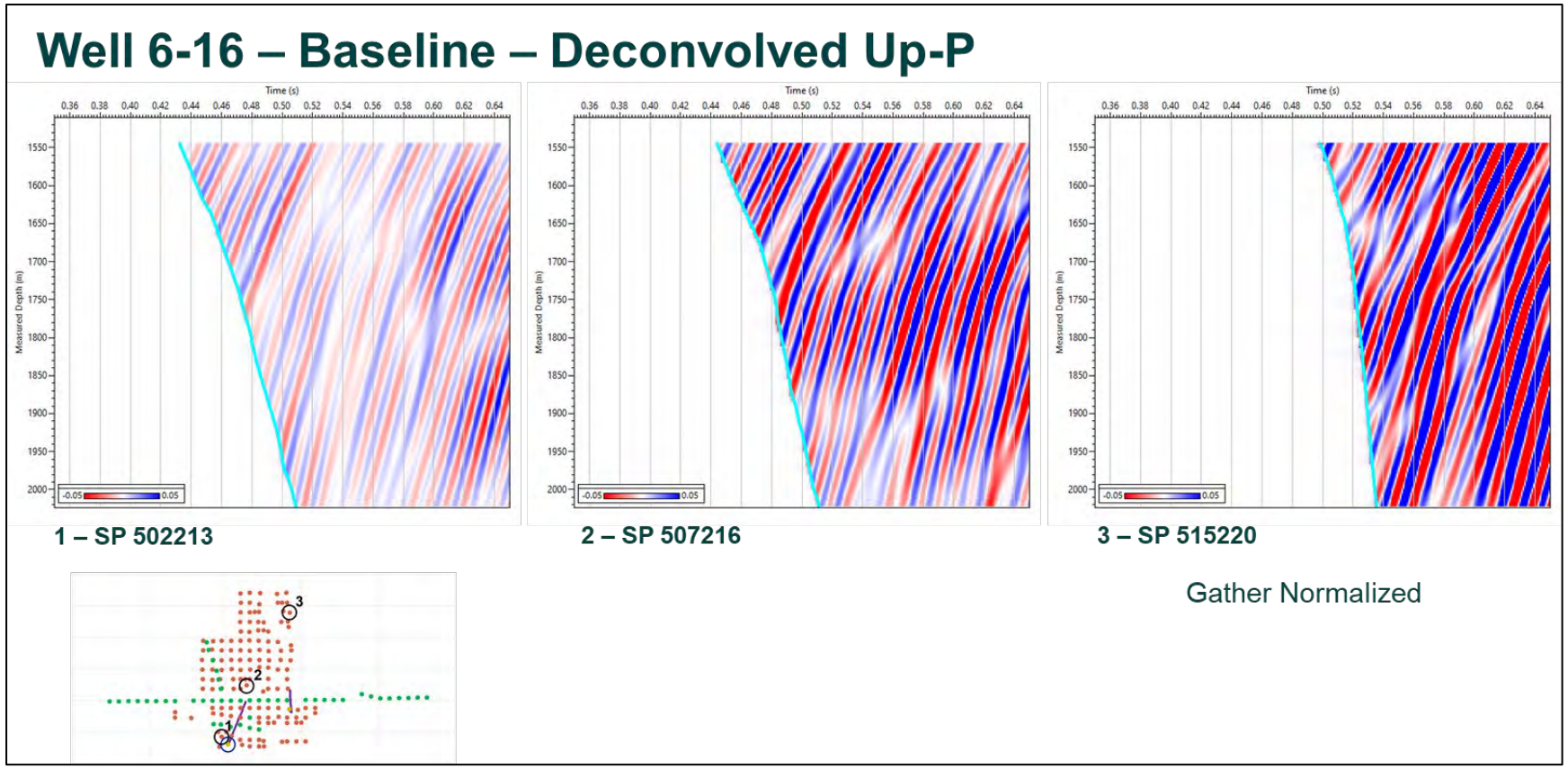


*Figure 11-36. Well 6-16 – Baseline – Deconvolved Up-P - Input data. This figure shows the well 6-16 dynamite baseline deconvolved Up P wavefield, for SP 502213 (near well 6-16 TD), SP 507216 (mid offset to north) and SP 515220 (far offset to north-east).*

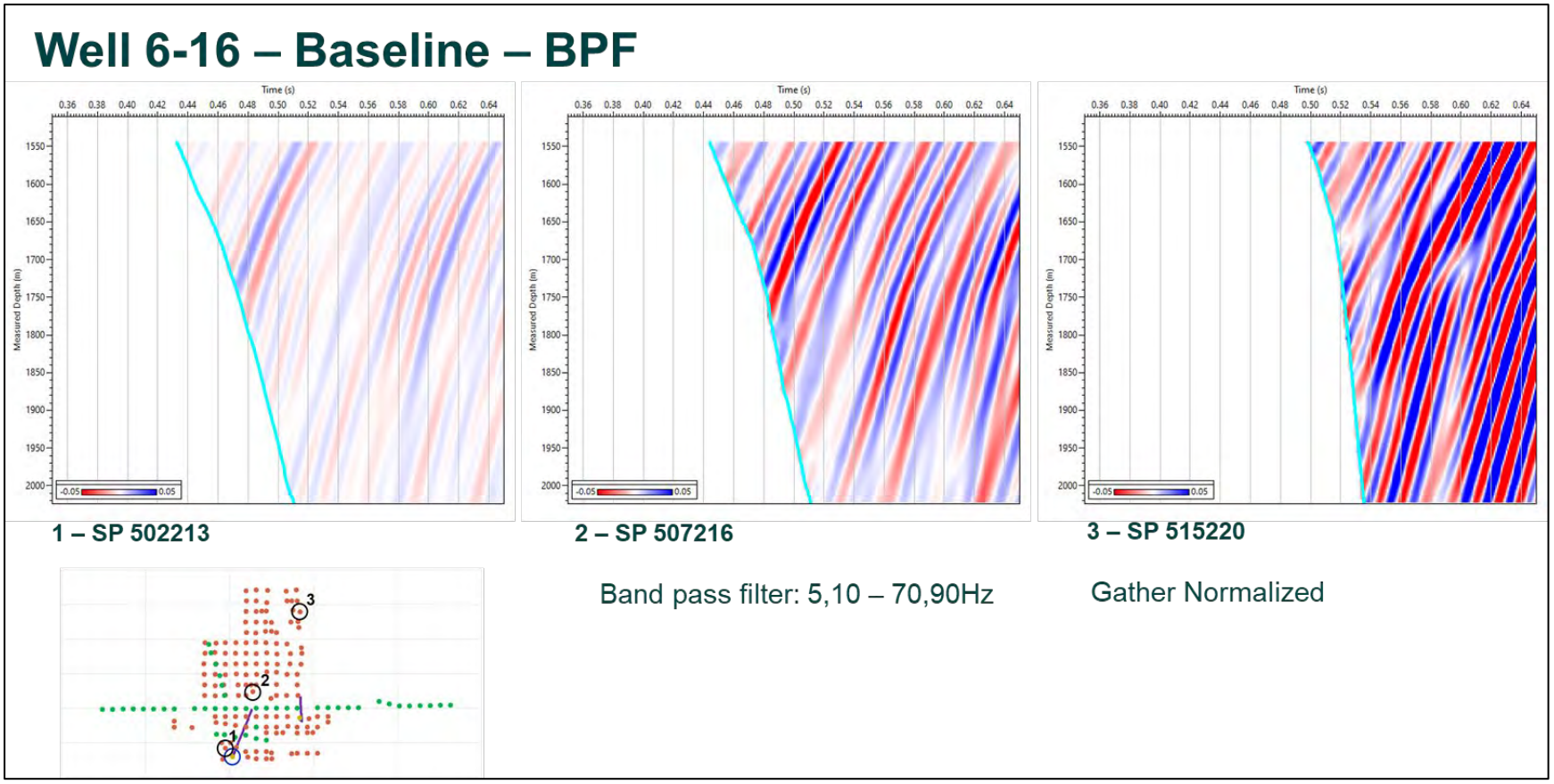


*Figure 11-37. Well 6-16 – Baseline – BPF. Figure 11.37 shows the SP data after a 5,10-70,90 Hz BPF was applied.*

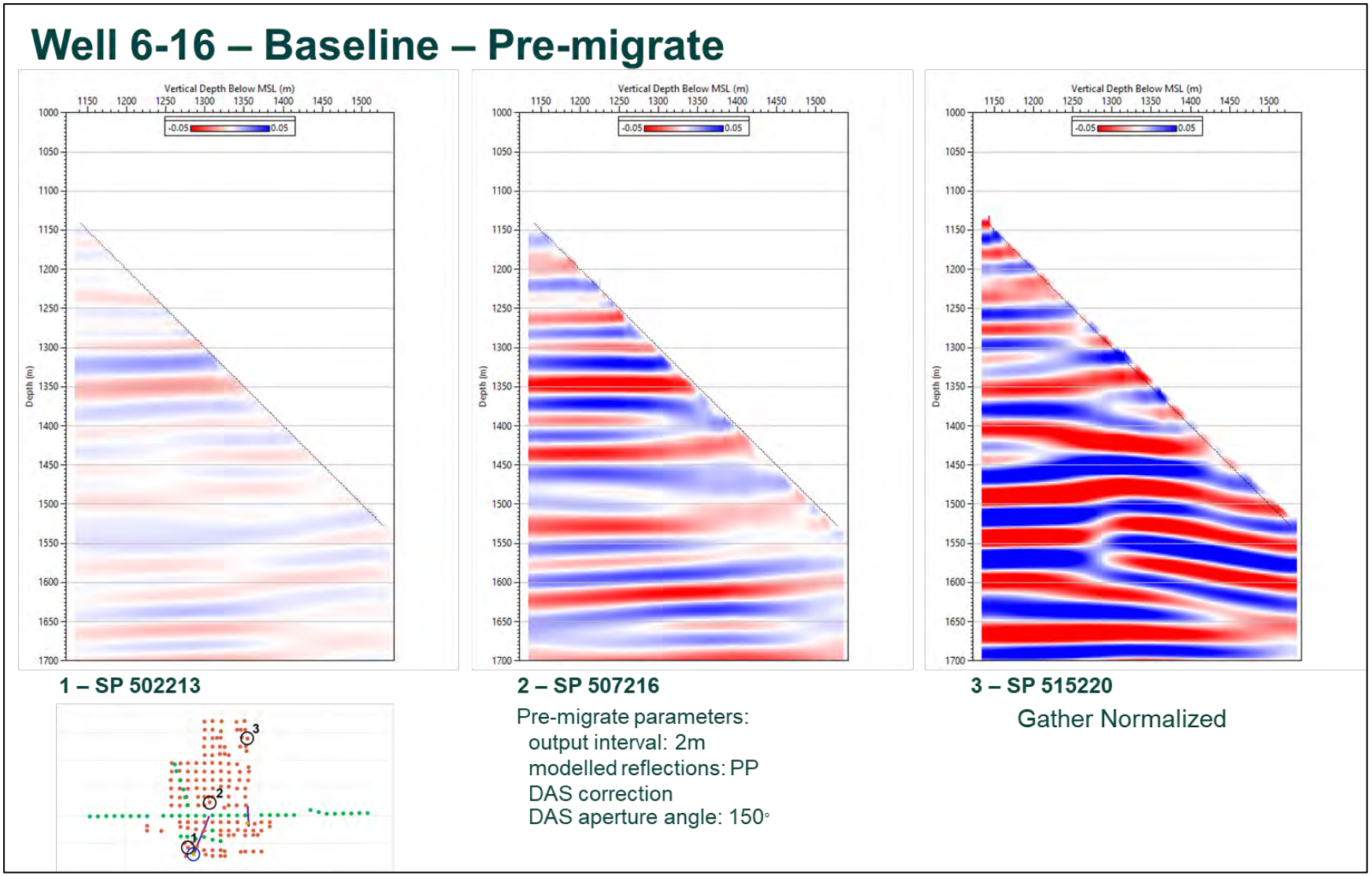


*Figure 11-38. Well 6-16 – Baseline – Pre-migrate - Pre-migrate. This figure presents the baseline SP 502213 (near well 6-16 TD), SP 507216 (mid offset to north) and SP 515220 (far offset to north-east) after pre-migration.*

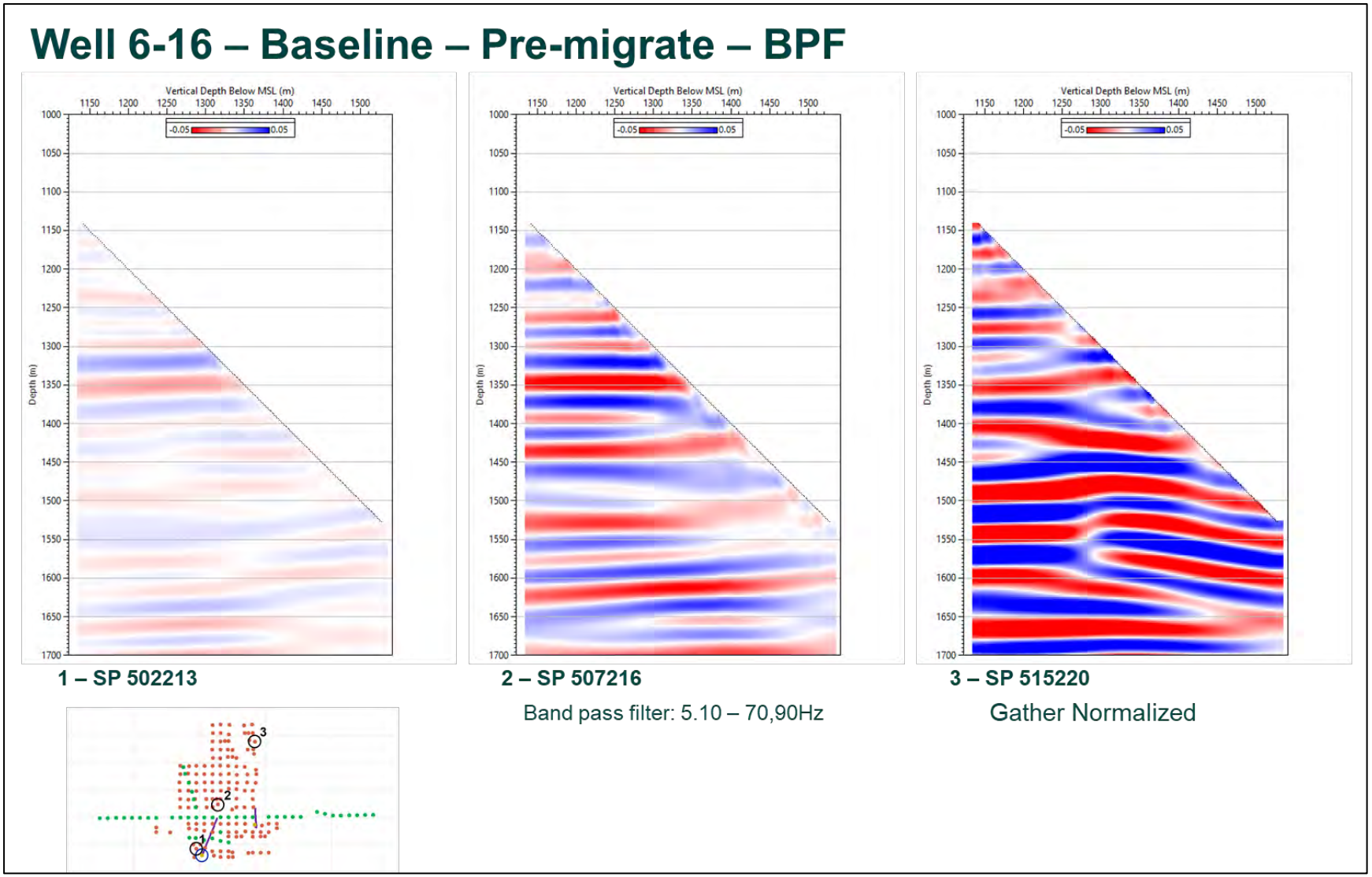


*Figure 11-39. Well 6-16 – Baseline – Pre-migrate – BPF - Reduce pre-migrate artefacts. A 5,10-70,90 Hz BPF was applied to the data.*

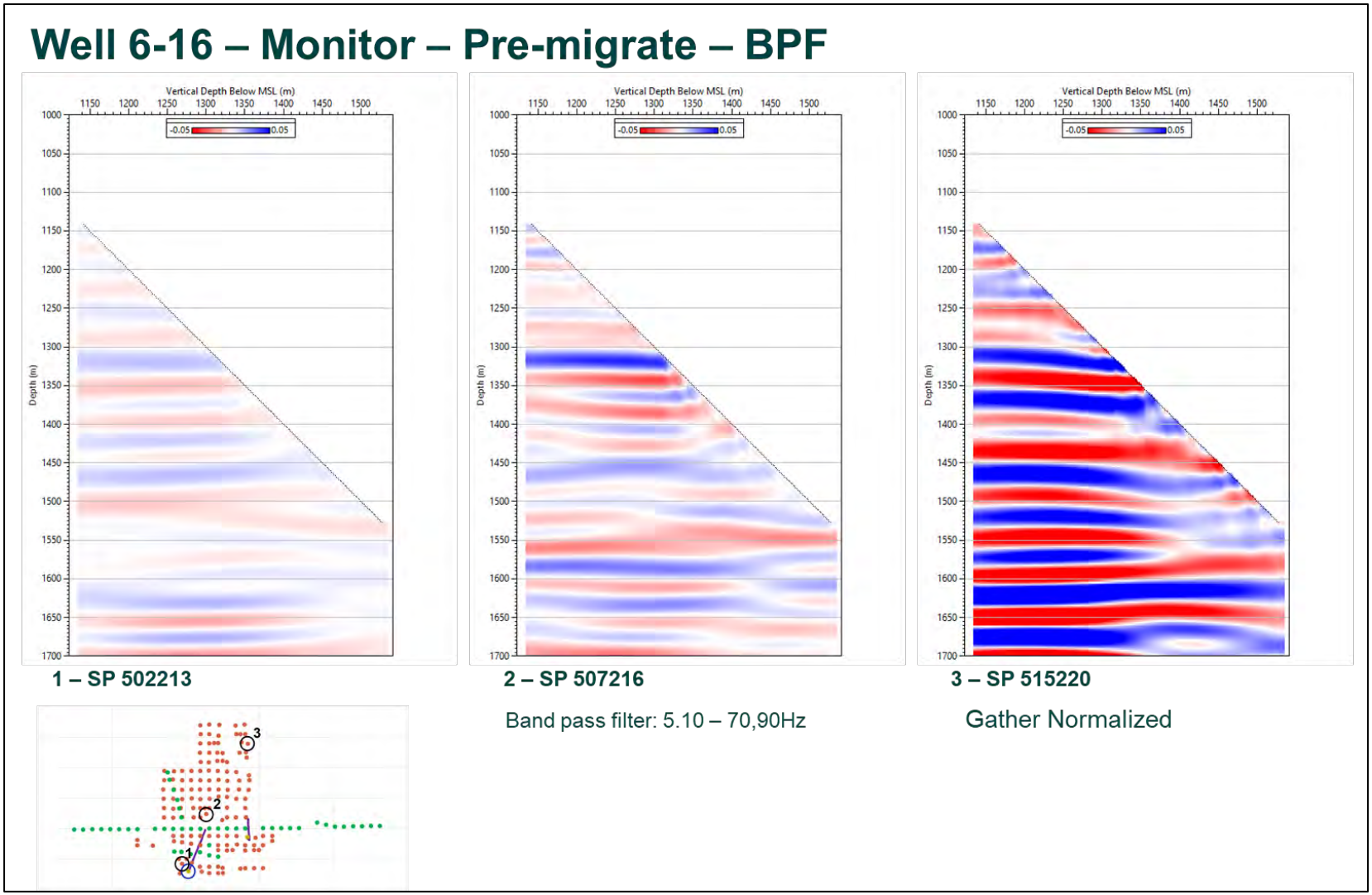


*Figure 11-40. Well 6-16 – Monitor – Pre-migrate – BPF - Reduce pre-migrate artefacts. Figure 11.40 shows the same data as in figure 11.39 for the monitor survey. Only the near offset data shows a similarity between the baseline and monitor survey. While the A2 Carbonate is visible on the monitor survey, on the baseline survey the same SP is too noisy and the A2 Carbonate reflector is not visible.*

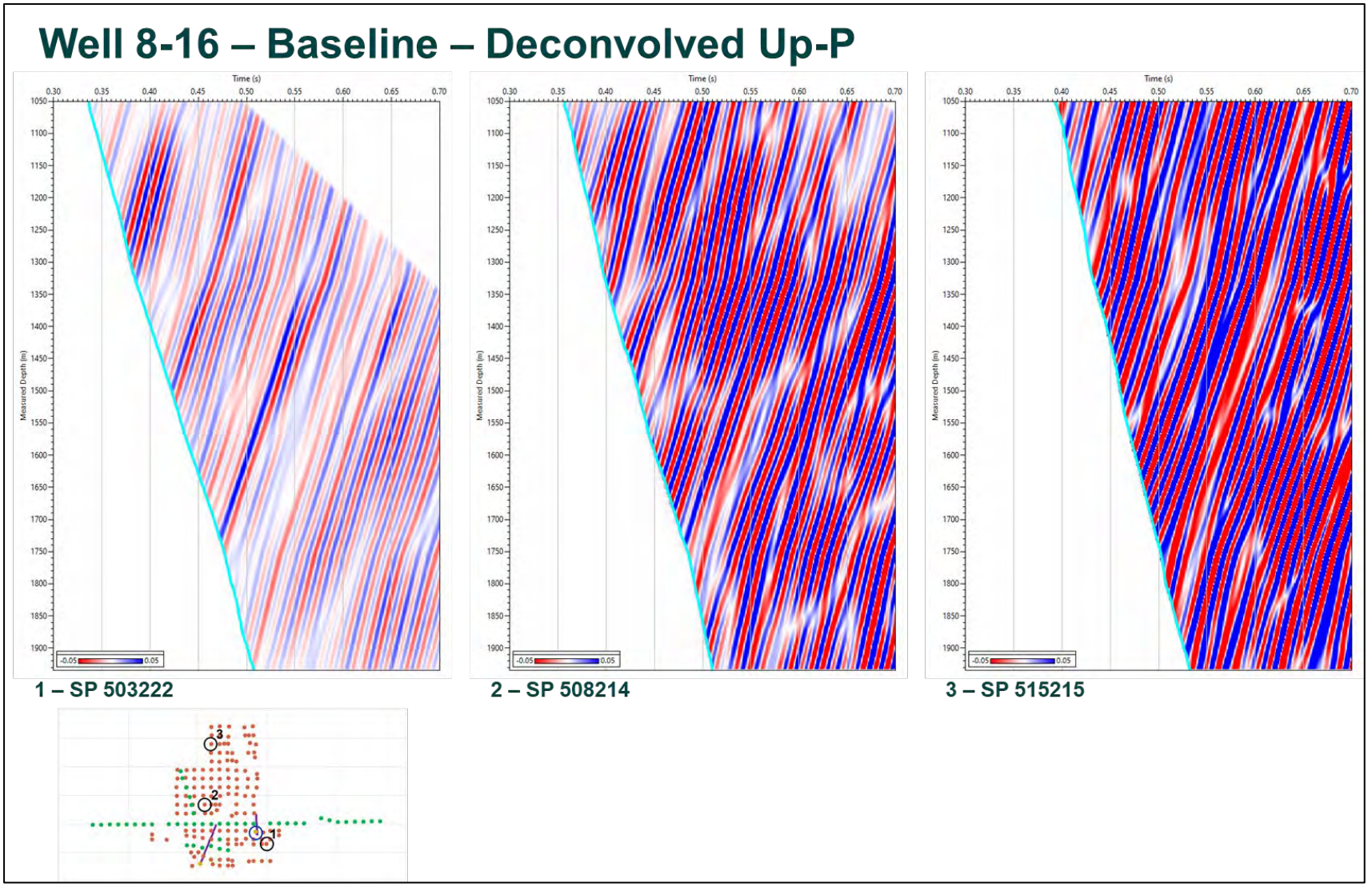


*Figure 11-41. Well 8-16 – Baseline – Deconvolved Up-P - Input data. This figure shows the well 8-16 baseline deconvolved Up P wavefield, for SP 503222 (close to the well), SP 508214 (mid offset to north-west) and SP 515215 (far offset to north).*

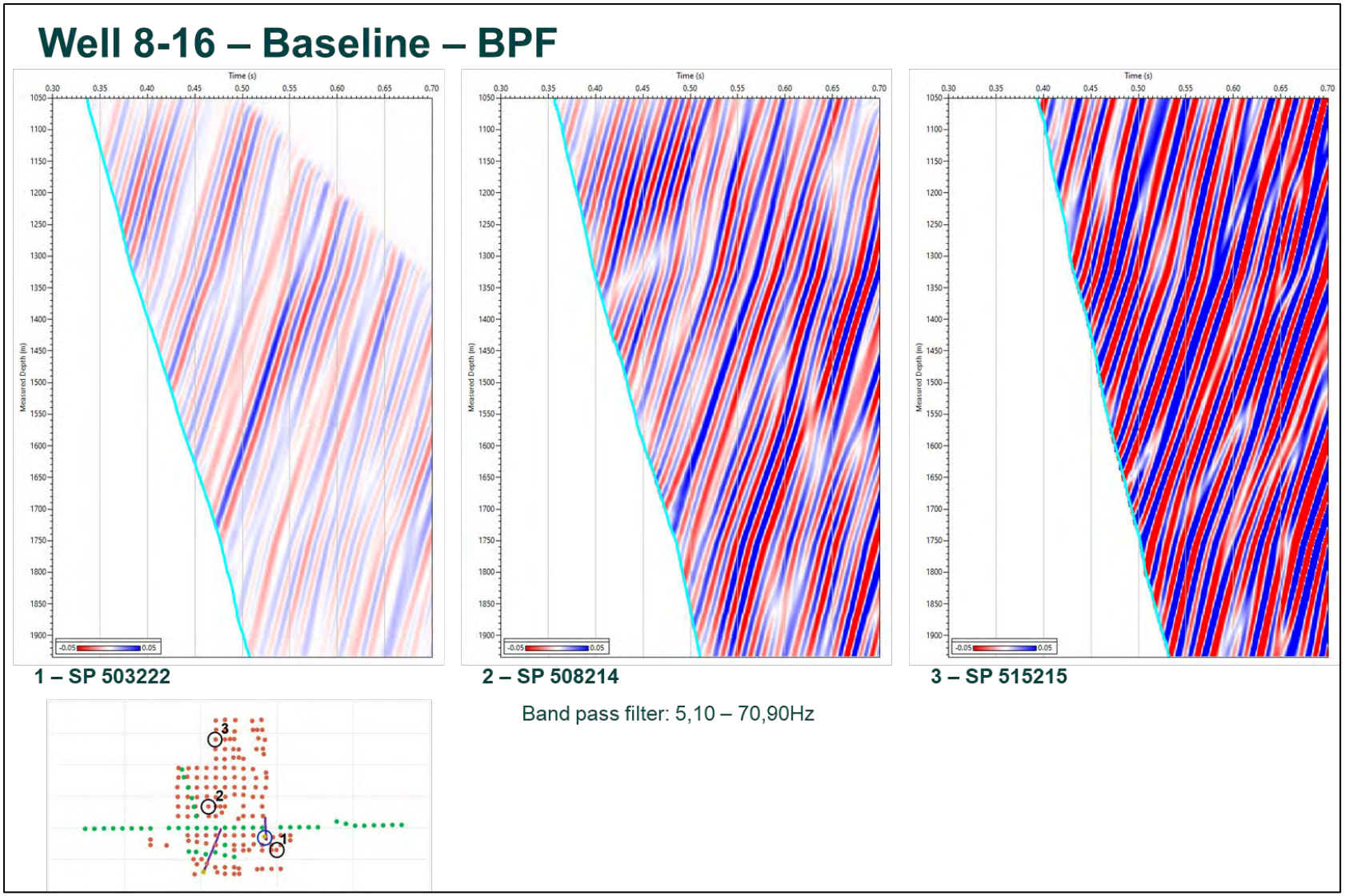


*Figure 11-42. Well 8-16 – Baseline – BPF. A 5,10-70,90 Hz BPF was applied to the data.*

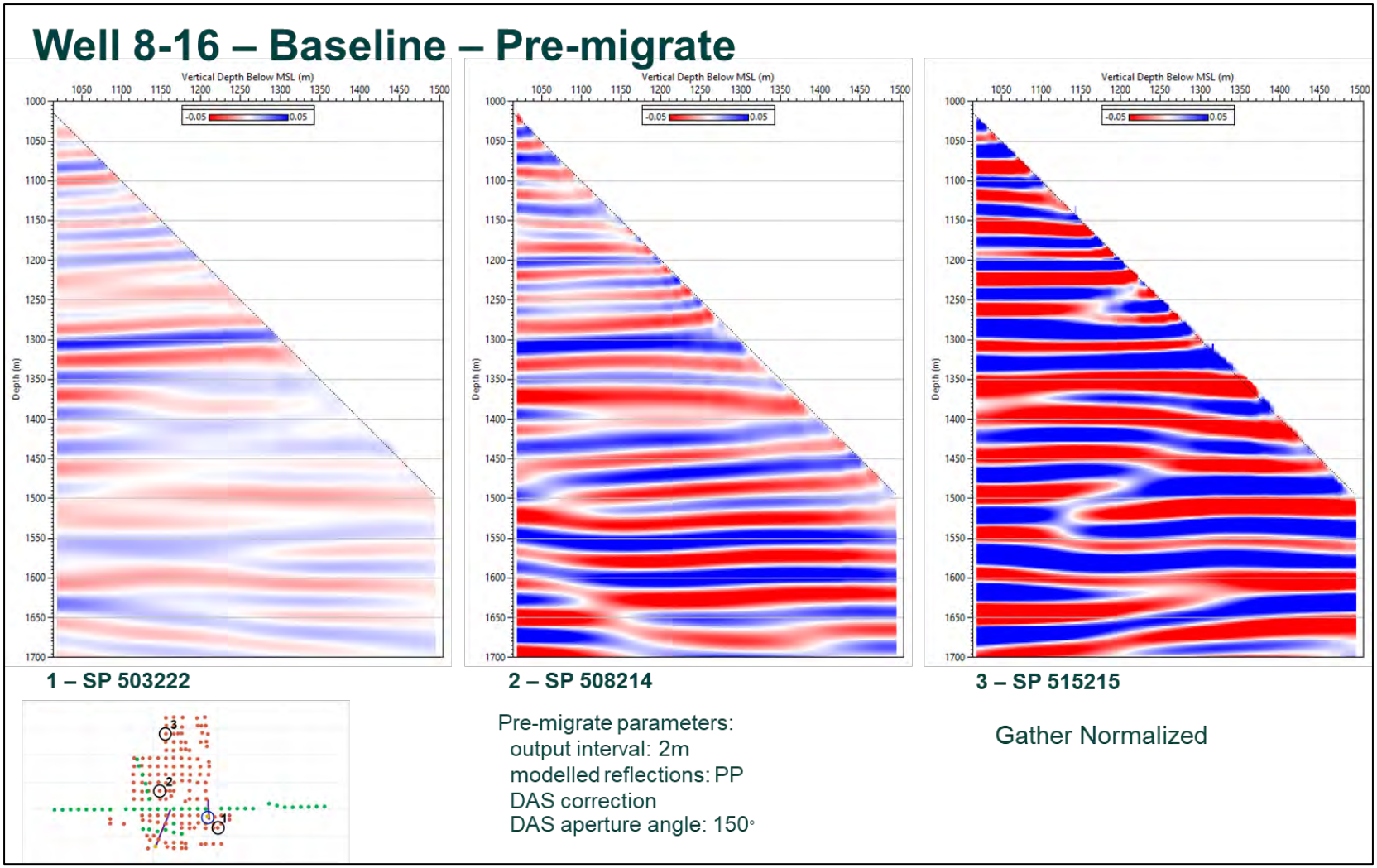


*Figure 11-43. Well 8-16 – Baseline – Pre-migrate. This figure presents the baseline SP 503222 (close to the well), SP 508214 (mid offset to north-west) and SP 515215 (far offset to north) after pre-migration.*

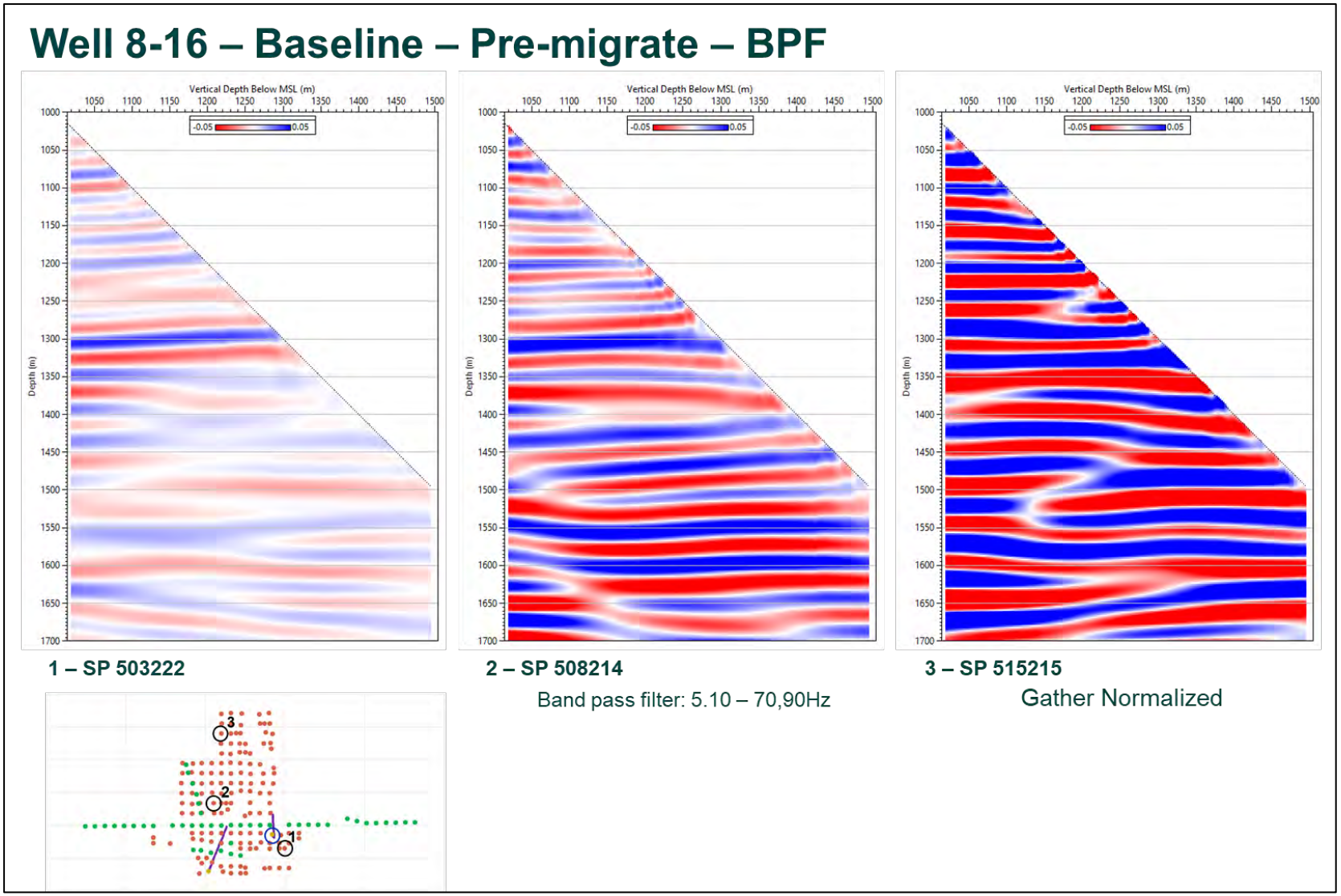


*Figure 11-44. Well 8-16 – Baseline – Pre-migrate – BPF - Reduce pre-migrate artefacts. A 5,10-70,90 Hz BPF was applied to the data.*

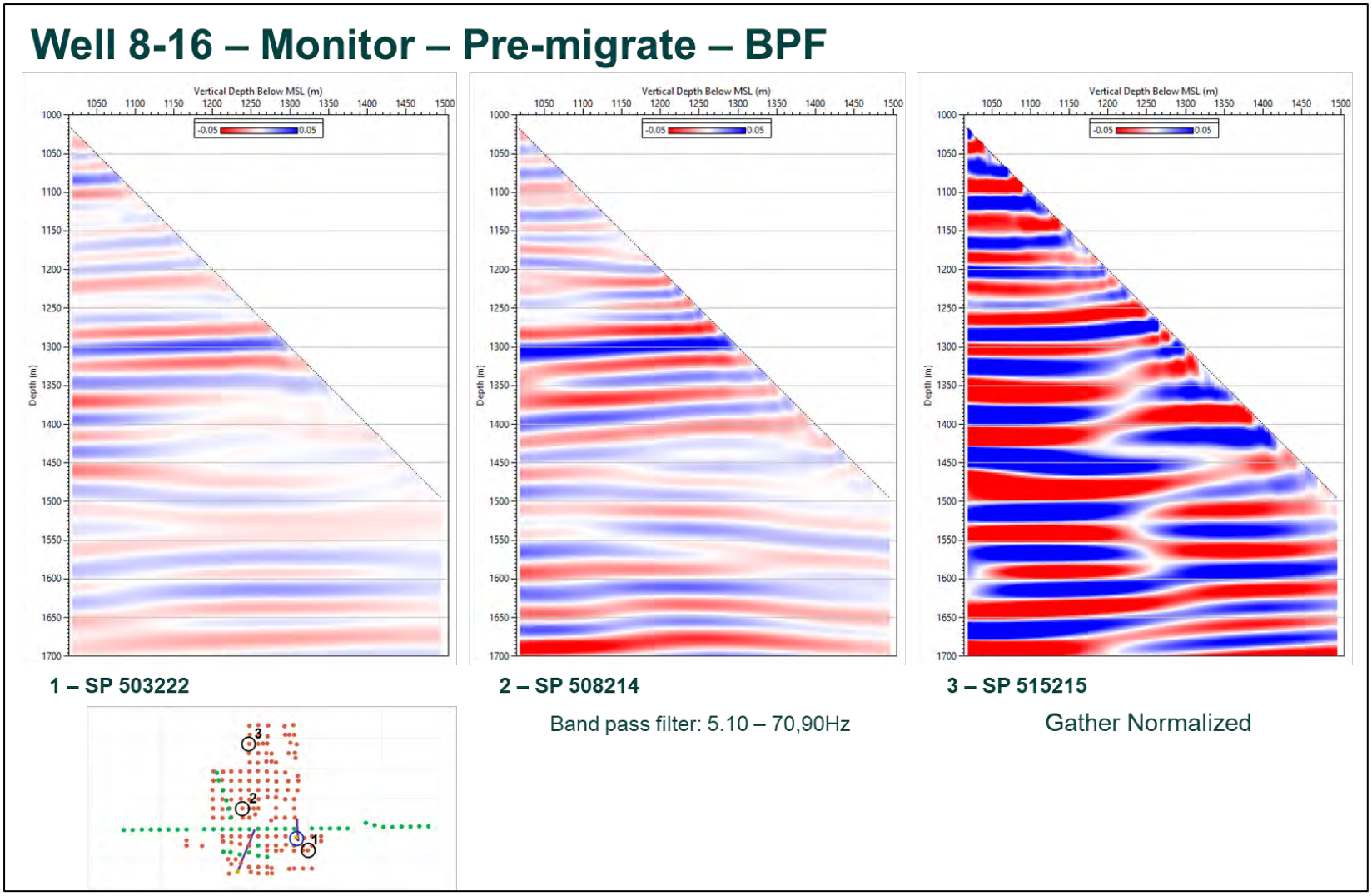


*Figure 11-45. Well 8-16 – Monitor – Pre-migrate – BPF - Reduce pre-migrate artefacts. Figure 11.45 shows the same data as figure 11.44 but for the monitor survey. Similar to well 6-16 data, the seismic structural response at the top of the reef is comparable between the baseline and the monitor survey only on the close offsets and to a certain degree to the mid offsets.*

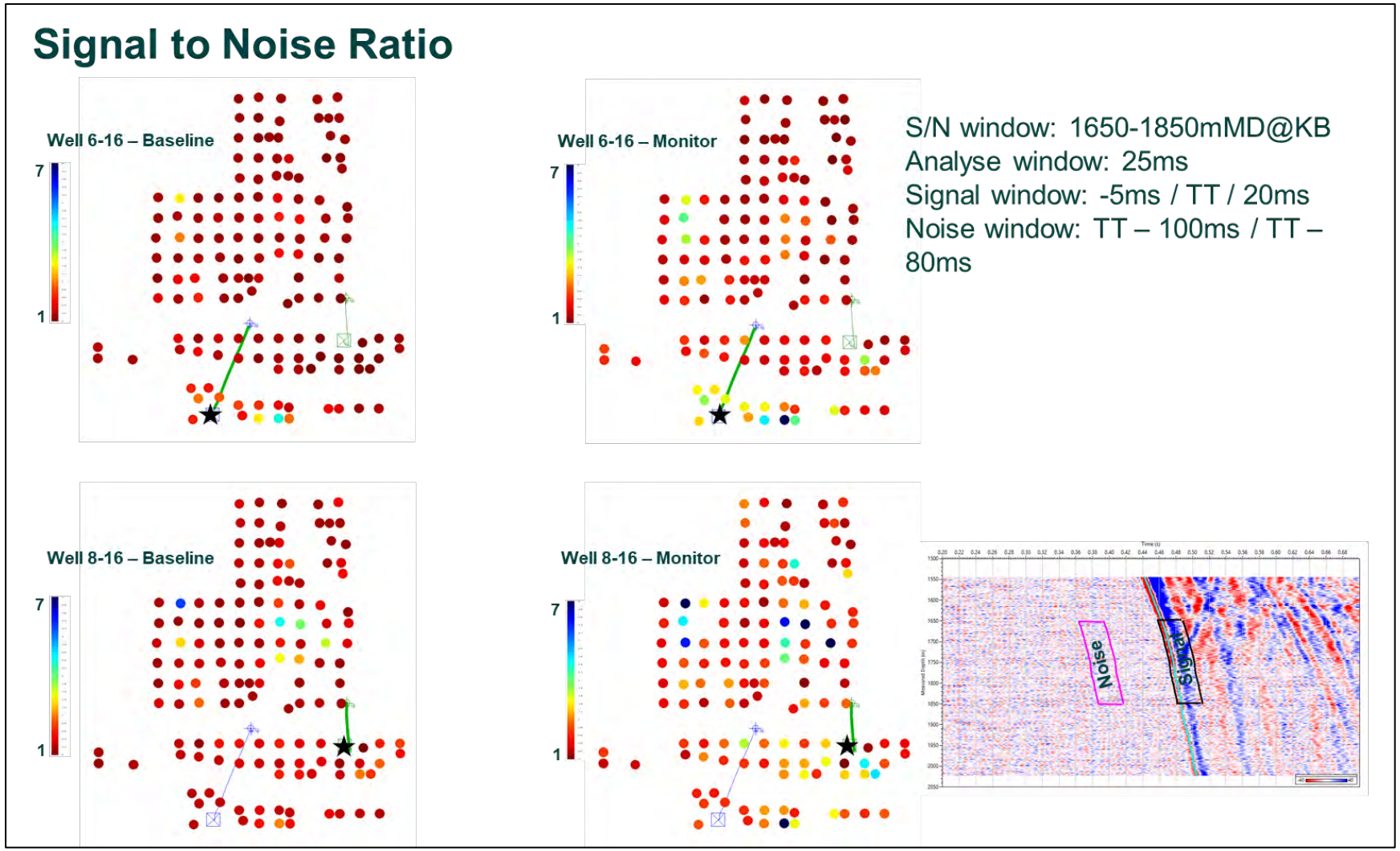


*Figure 11-46. Signal to Noise Ratio - Before data selection.*

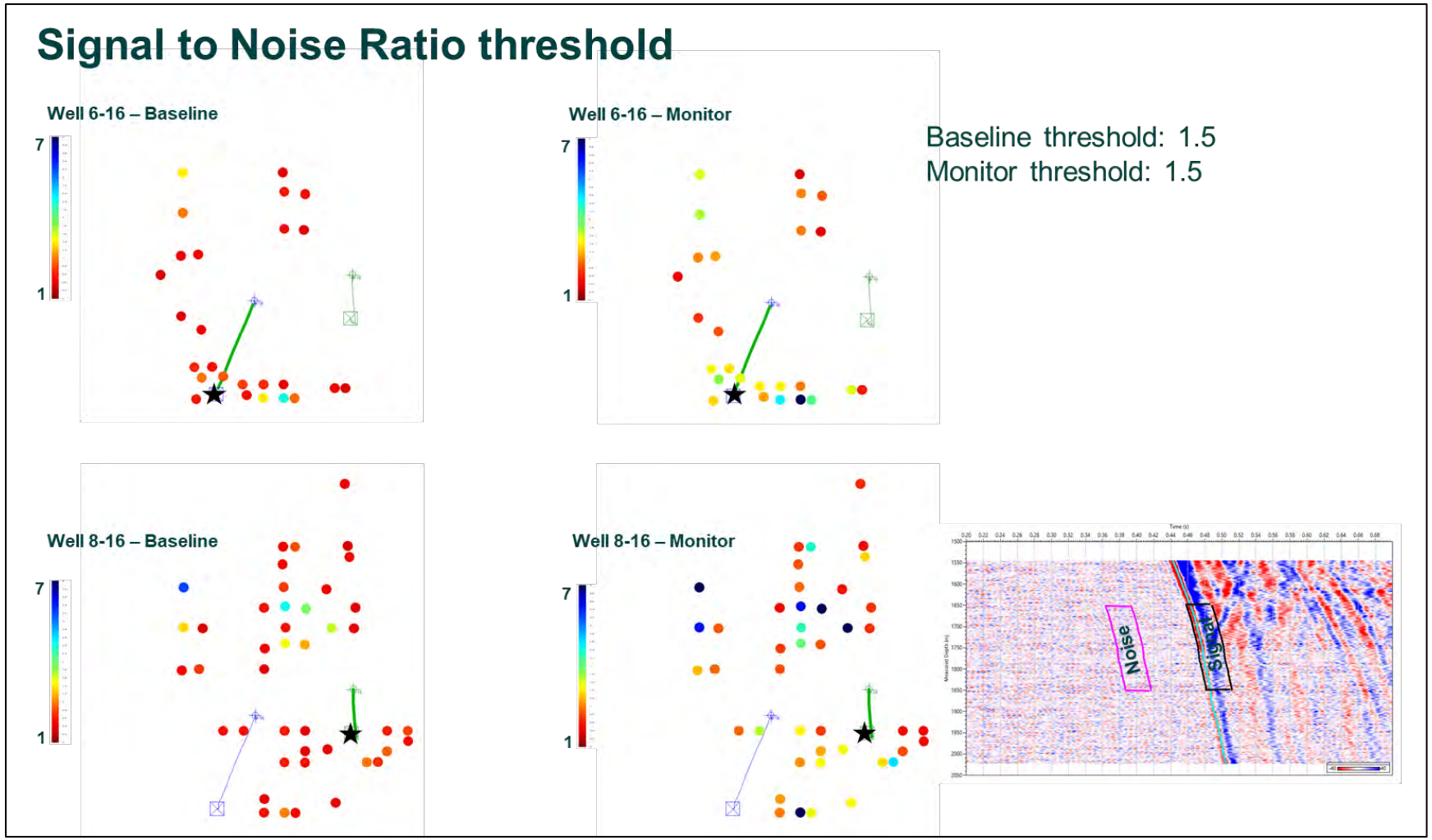


*Figure 11-47. Signal to noise ratio threshold - After data selection (threshold 1.5).*

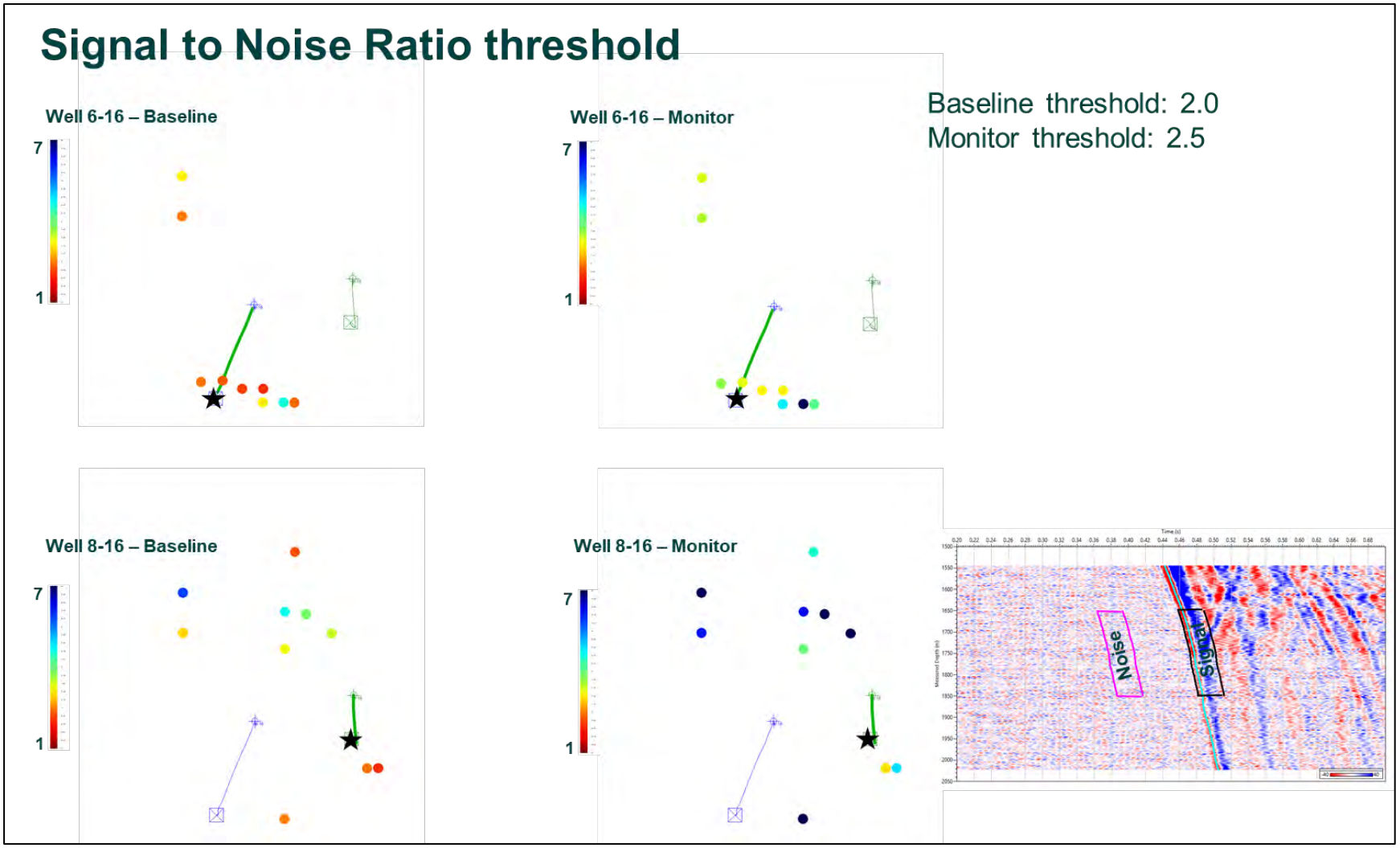


*Figure 11-48. Signal to noise ratio threshold - After data selection (threshold 2.0/2.5). A second test was performed with a SNR threshold of 2.0 for the baseline data and 2.5 for the monitor data.*

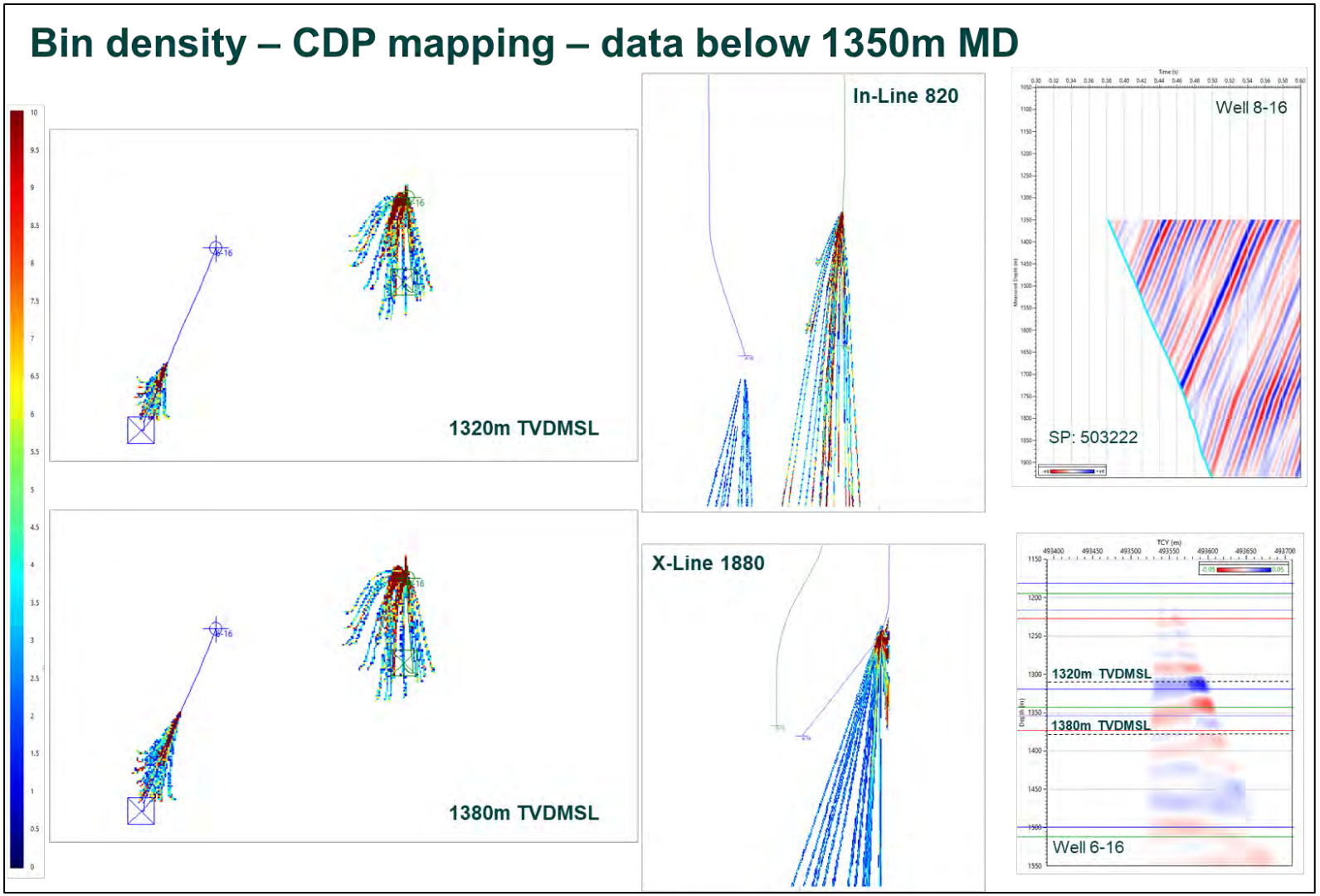


*Figure 11-49. Bin density – CDP mapping – data below 1350m MD - After data selection. This figure shows the CDP bin density for in-line 820 (close to well 8-16 – mid top image), cross-line 1880 (close to well 6-16 – mid bottom image), depth slice 1320 (at A2 Carbonate top – top left image) and depth 1380 (below Brown Niagaran top – bottom left image).*

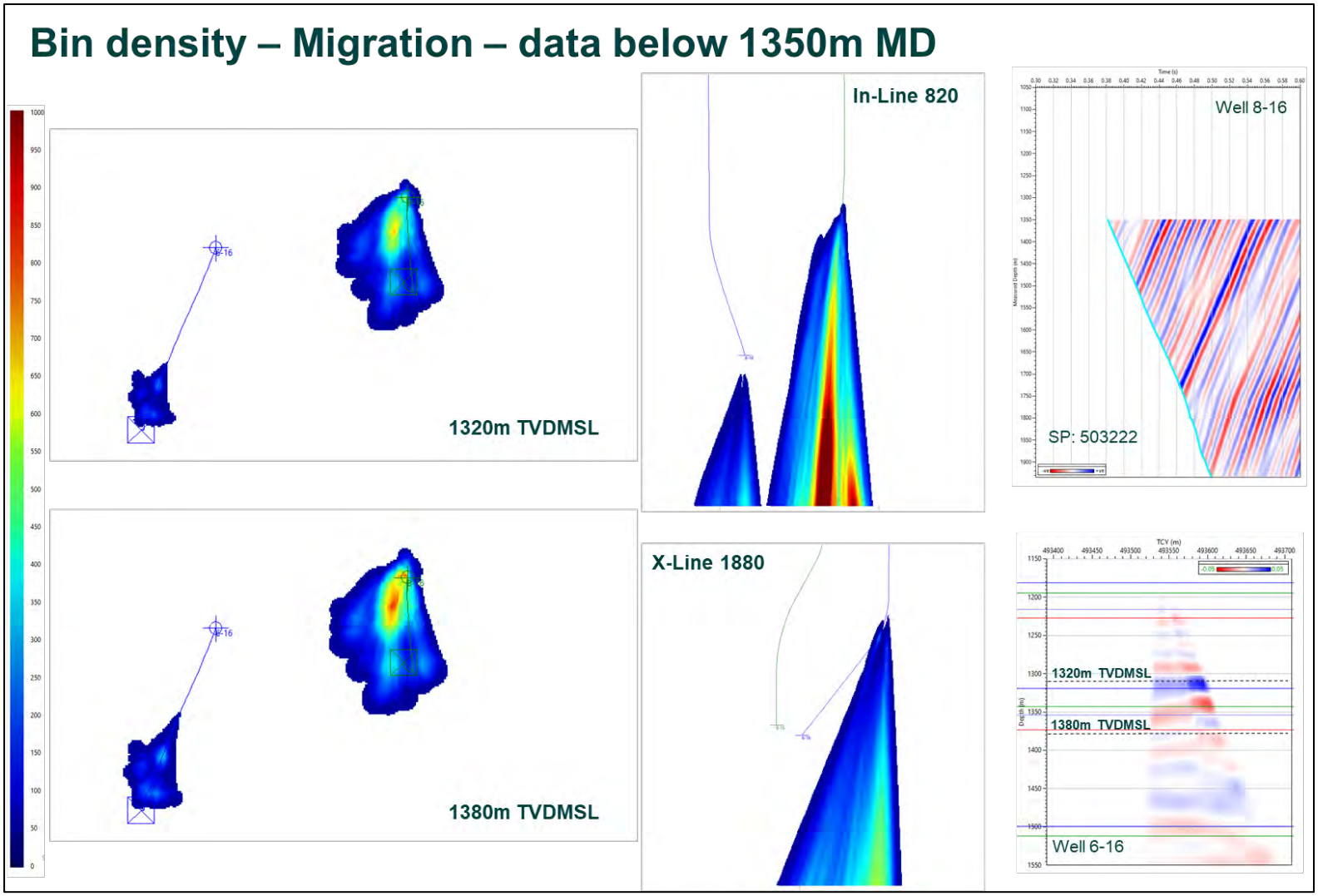


*Figure 11-50. Bin density – Migration – data below 1350m MD - After data selection. This picture shows the same bin density slices but for migration with a 3.5° aperture. The data were limited to the receivers below 1350 m MD. The dynamite image coverage at the A2 Carbonate does not have a larger extent compared with the vibroseis data image.*

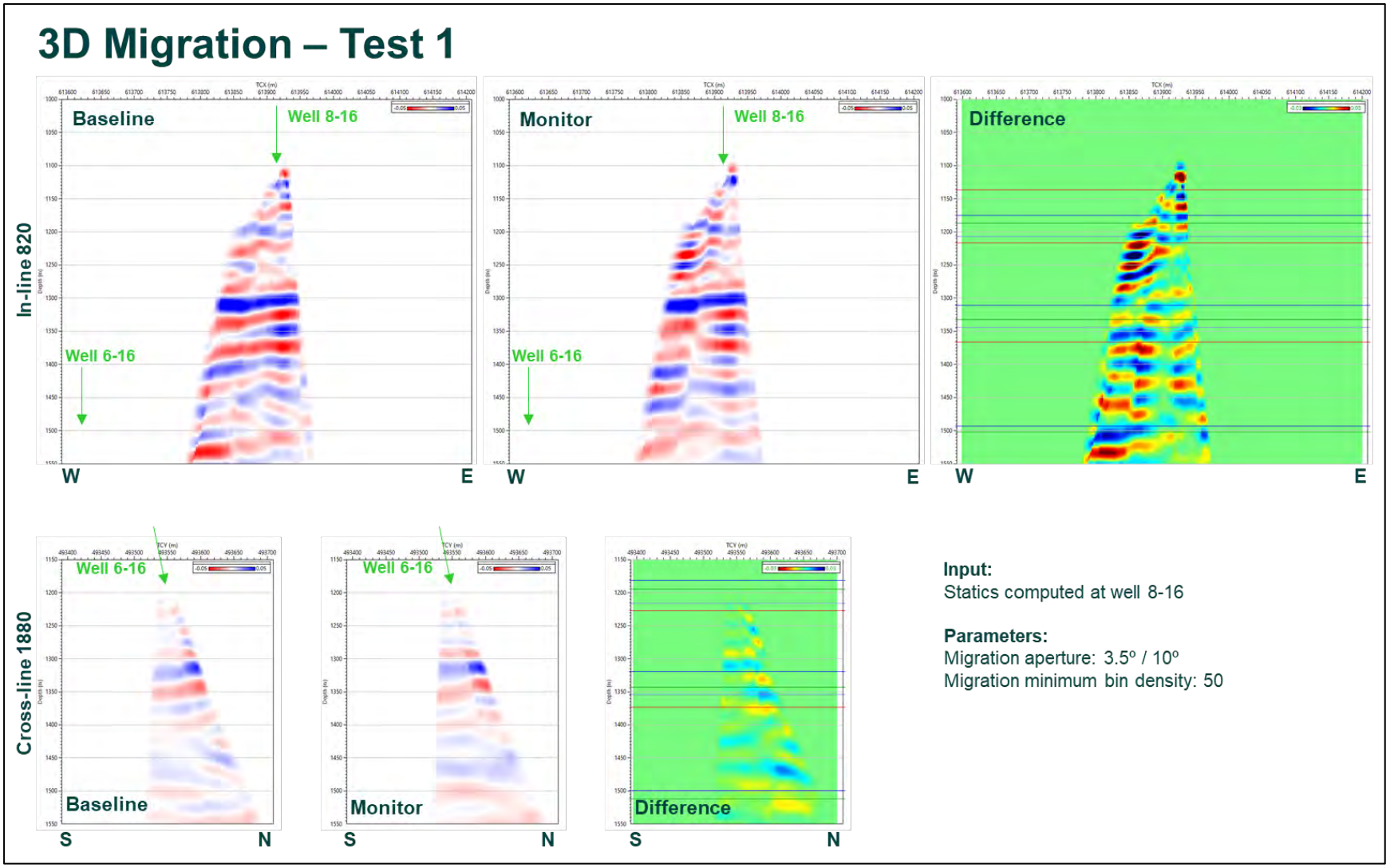


*Figure 11-51. 3D Migration – Test 1 - SNR threshold 1.5. Two migration tests were performed using only the dynamite data. The first test filtered the input data with SNR values below 1.5.*

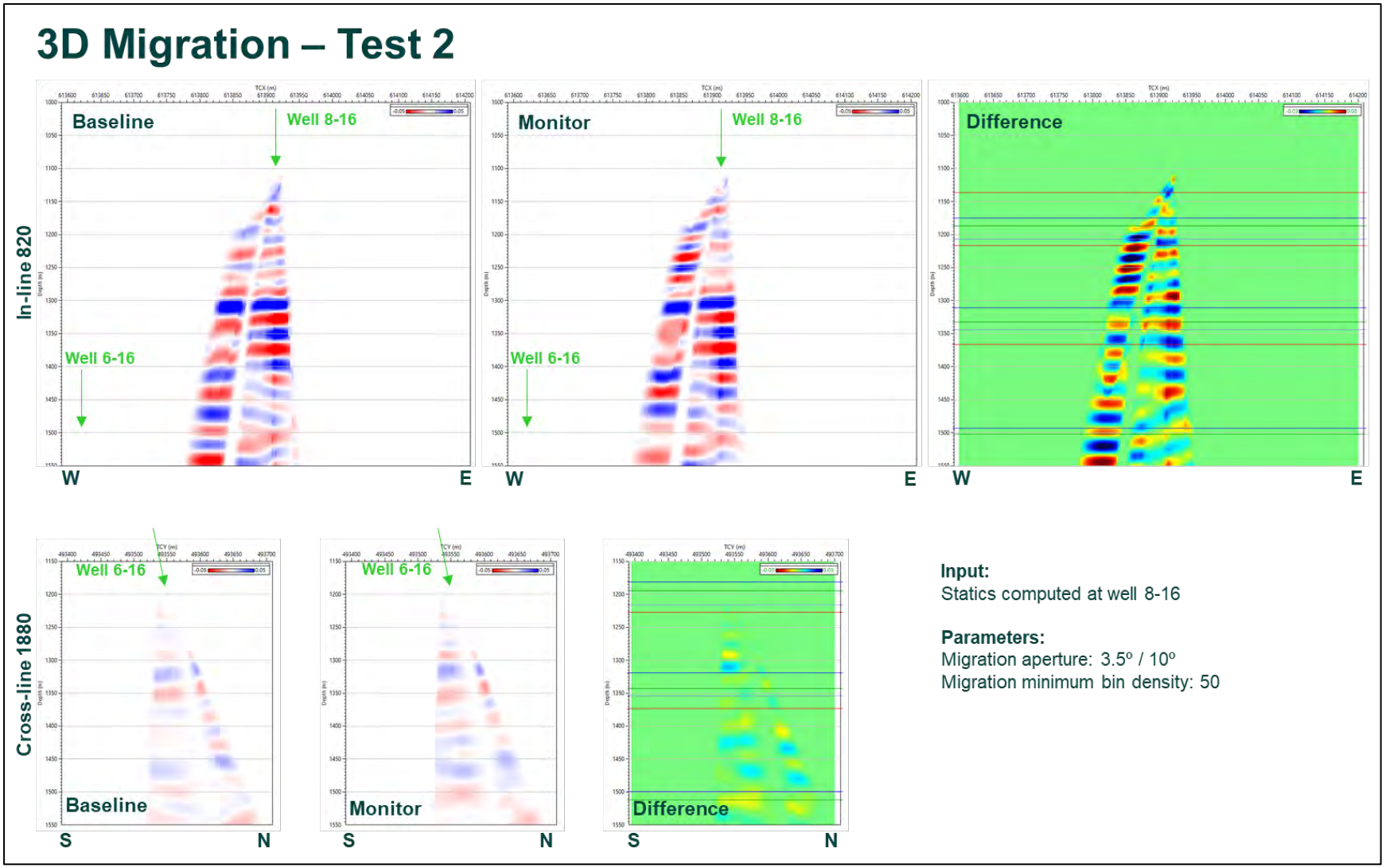


*Figure 11-52. 3D Migration – Test 2 - SNR threshold 2.0/2.5. The second test has the SNR threshold at 2.0 for the baseline data and 2.5 for the monitor data.*

# 12 Survey normalisation

Assuming that the A2 Carbonate reflector is not affected by the $CO_2$ injection, the baseline and monitor survey images were harmonized in depth and also amplitude balanced.

Figure 12-1 presents the results of the A2 Carbonate and A1 Carbonate reflection picking of the baseline and monitor 3D image data. The strong A2 Carbonate positive reflection was picked in a 1285 m – 1360 m TVDMSL window. Only the picks from the 3D cells with a minimum migration bin value of 55 were retained. The trough reflector below the A2 Carbonate was picked as A1 Carbonate in a 15 m – 45 m offset window below the A2 Carbonate. The picks were 3D smoothed.

Cross-correlation over +/-30 m windows along the A2 Carbonate picks was applied to harmonize the depth monitor image with the depth baseline image (Fig. 12-2). The result of the cross-correlation is a 3D cube of depth shifts for the best correlation between the two surveys. For each trace an average static shift was computed in a window of +/-5 m along the A2 Carbonate picks (Fig. 12-3 right). The monitor image was shifted to match the baseline data. Figures 12-3 and 12-4 show the 3D image before and after depth harmonization. After this process some artefacts in the amplitude difference data are attenuated.

Near the image edges the migration may induce some artefacts due to reduced reflection points density and noise from the far offsets. To counter this issue the data outside the A2 Carbonate coverage was muted (Fig. 12-5).

Above the reservoir we don't expect to see time-lapse effects due to the $CO_2$ injection. For this reason, the amplitude scale of the A2 Carbonate reflector should be similar between the baseline and the monitor surveys. For each trace an amplitude scaling factor was computed as the ratio between the monitor and baseline amplitudes at the A2 Carbonate reflector. The monitor image amplitudes were trace by trace balanced with the baseline survey amplitudes (Fig. 12-6).

| Title | Description | Figure |
|---|---|---|
| | | |
| **12 Survey normalisation** | | |
| Reflection picking | Final 3D image | **12.1** |
| Correlating migration images | Baseline – monitor cross-correlation | **12.2** |
| Image before harmonization | Final 3D image | **12.3** |
| Image after harmonization | | **12.4** |
| Image after edge suppress | Outside A2 Carbonate covering | **12.5** |
| Amplitude balance | At A2 Carbonate | **12.6** |

*Table 12-21 Survey normalization figures*

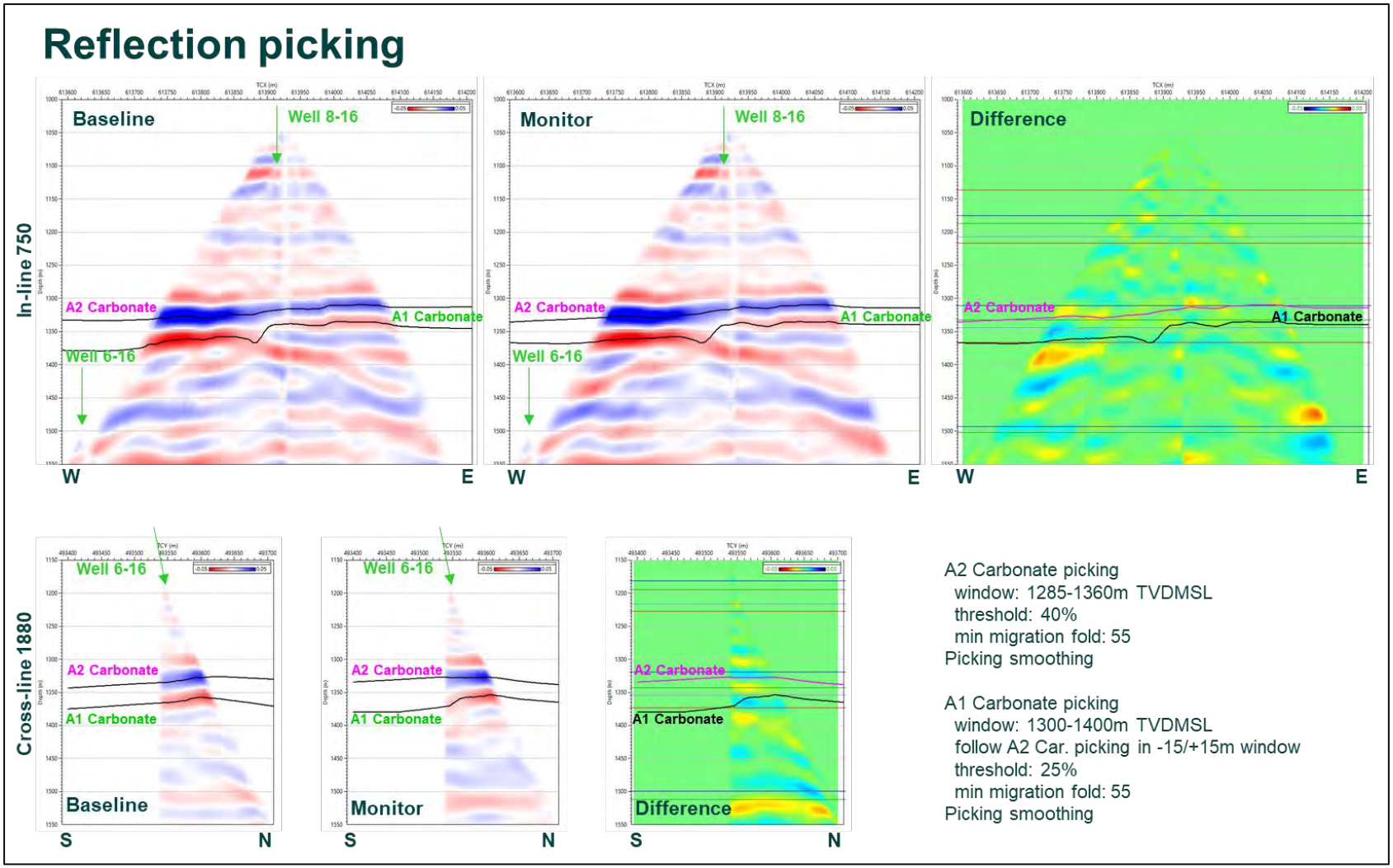


*Figure 12-1. Reflection picking - Final 3D image. Figure 12.1 presents the results of the A2 Carbonate and A1 Carbonate reflection picking of the baseline and monitor 3D image data. The strong A2 Carbonate positive reflection was picked in a 1285 m – 1360 m TVDMSL window. Only the picks from the 3D cells with a minimum migration bin value of 55 were retained. The trough reflector below the A2 Carbonate was picked as A1 Carbonate in a 15 m – 45 m offset window below the A2 Carbonate. The picks were 3D smoothed.*

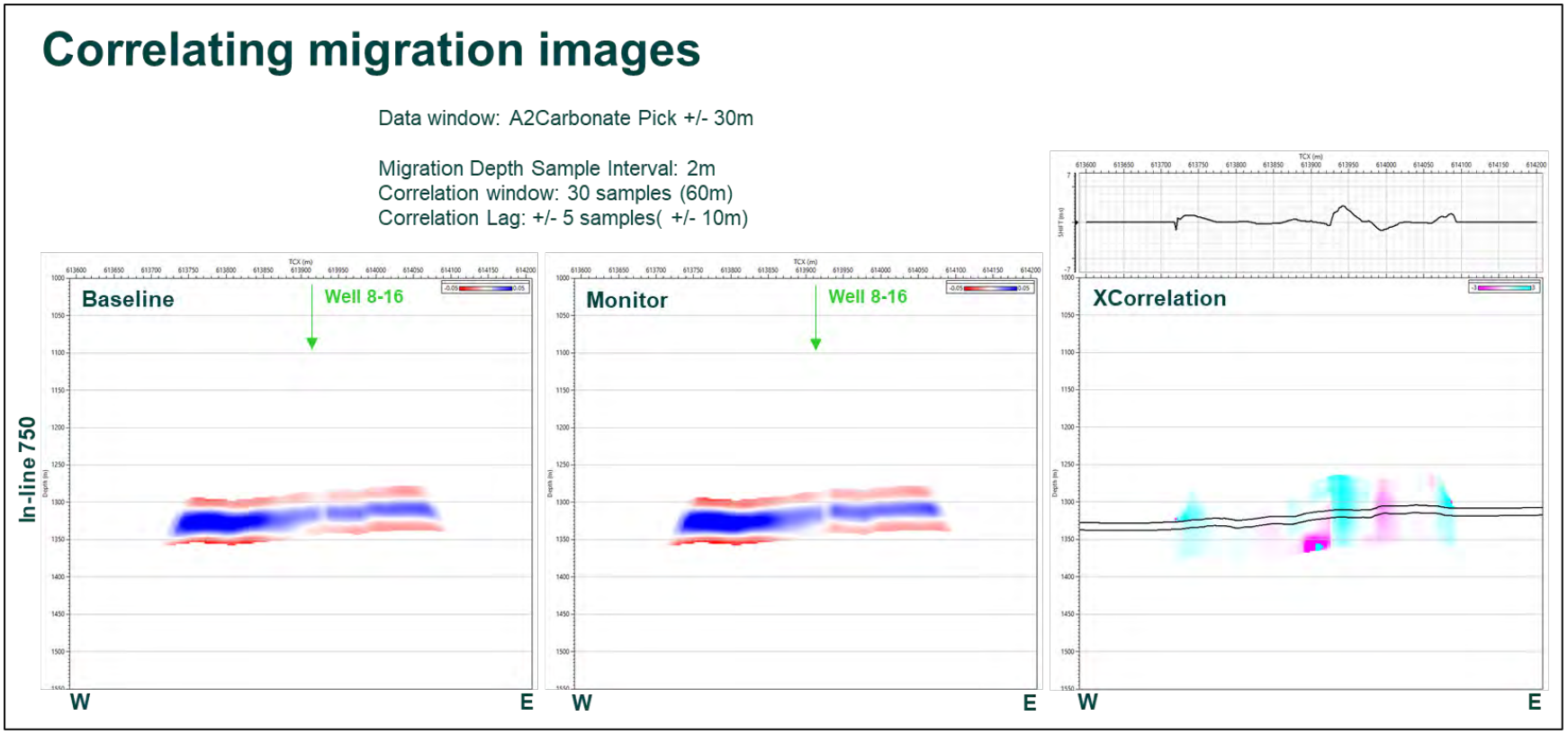


*Figure 12-2. Correlating migration images - Baseline – monitor cross-correlation. Cross-correlation over +/-30 m windows along the A2 Carbonate picks was applied to harmonize the depth monitor image with the depth baseline image. For each trace a shift value was computed and applied.*

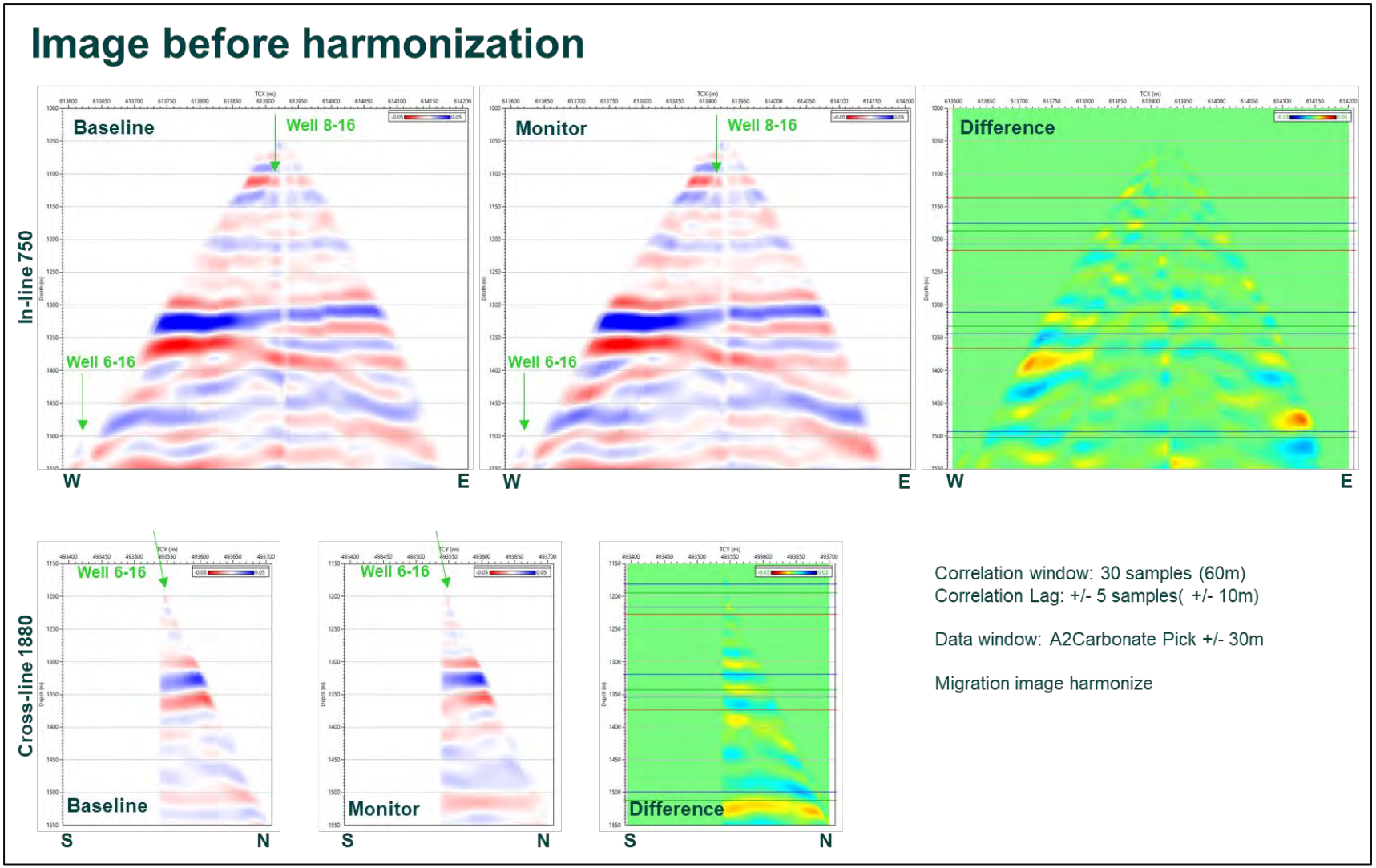


*Figure 12-3. Image before harmonization - Final 3D image. The result of the cross-correlation is a 3D cube of depth shifts for the best correlation between the two surveys. For each trace an average static shift was computed in a window of +/-5 m along the A2 Carbonate picks (Fig. 12.3 right). The monitor image was shifted to match the baseline data.*

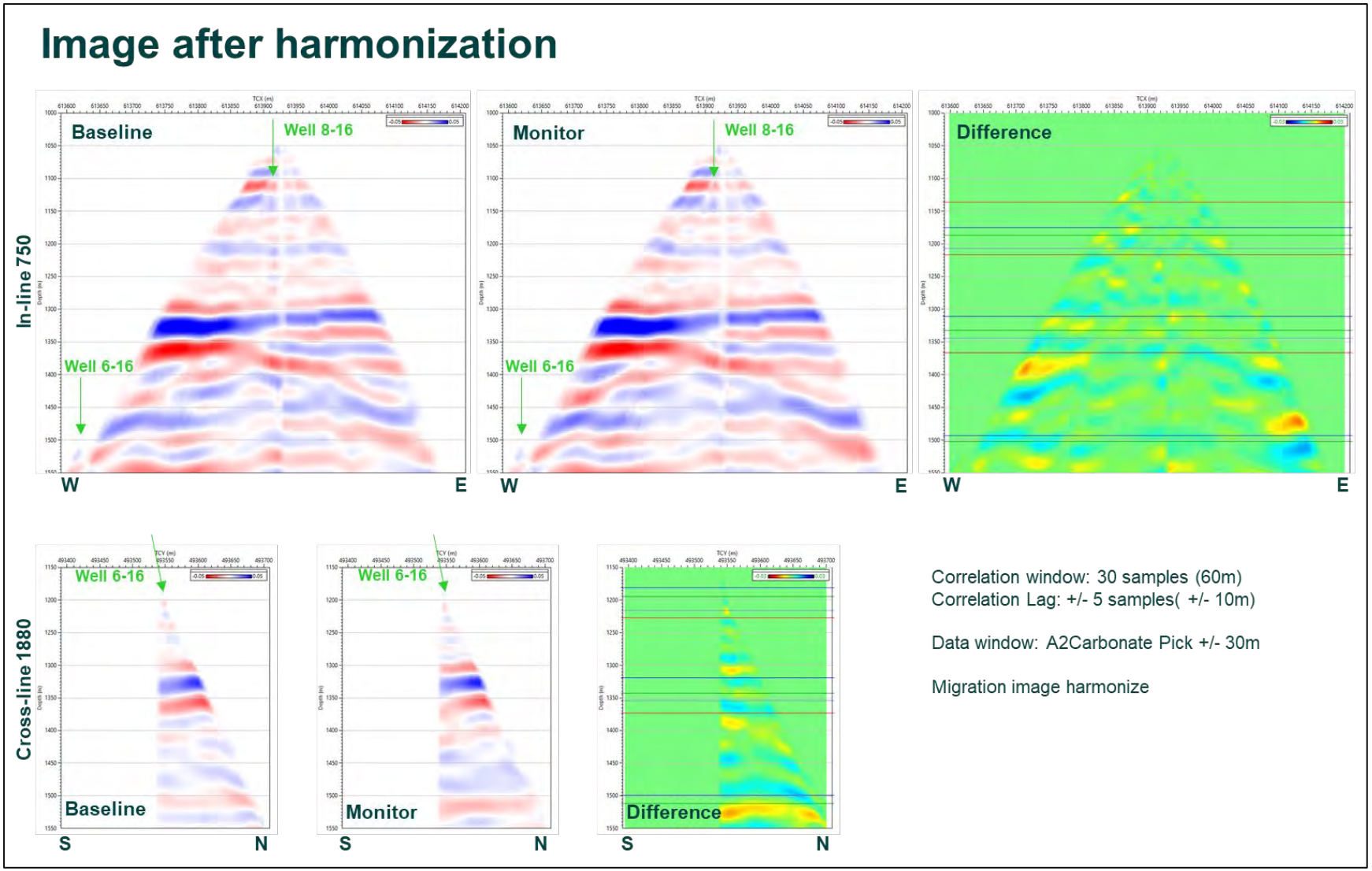


*Figure 12-4. Image after harmonization.*

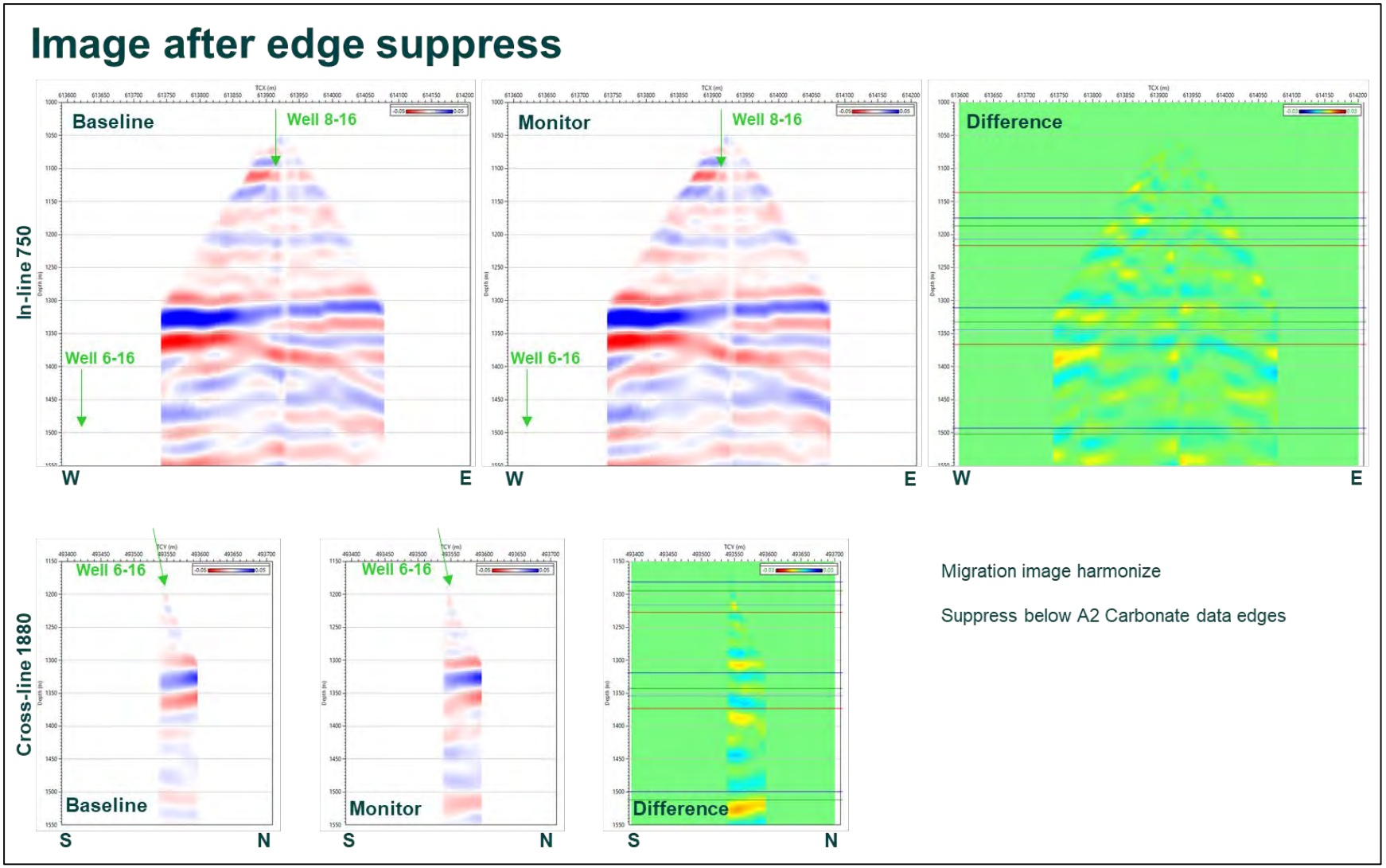


*Figure 12-5. Image after edge suppress - Outside A2 Carbonate covering. Near image edges the migration may induce some artefacts due to reduced data coverage and noise from the far offsets. To counter this issue the data outside the A2 Carbonate coverage was muted.*

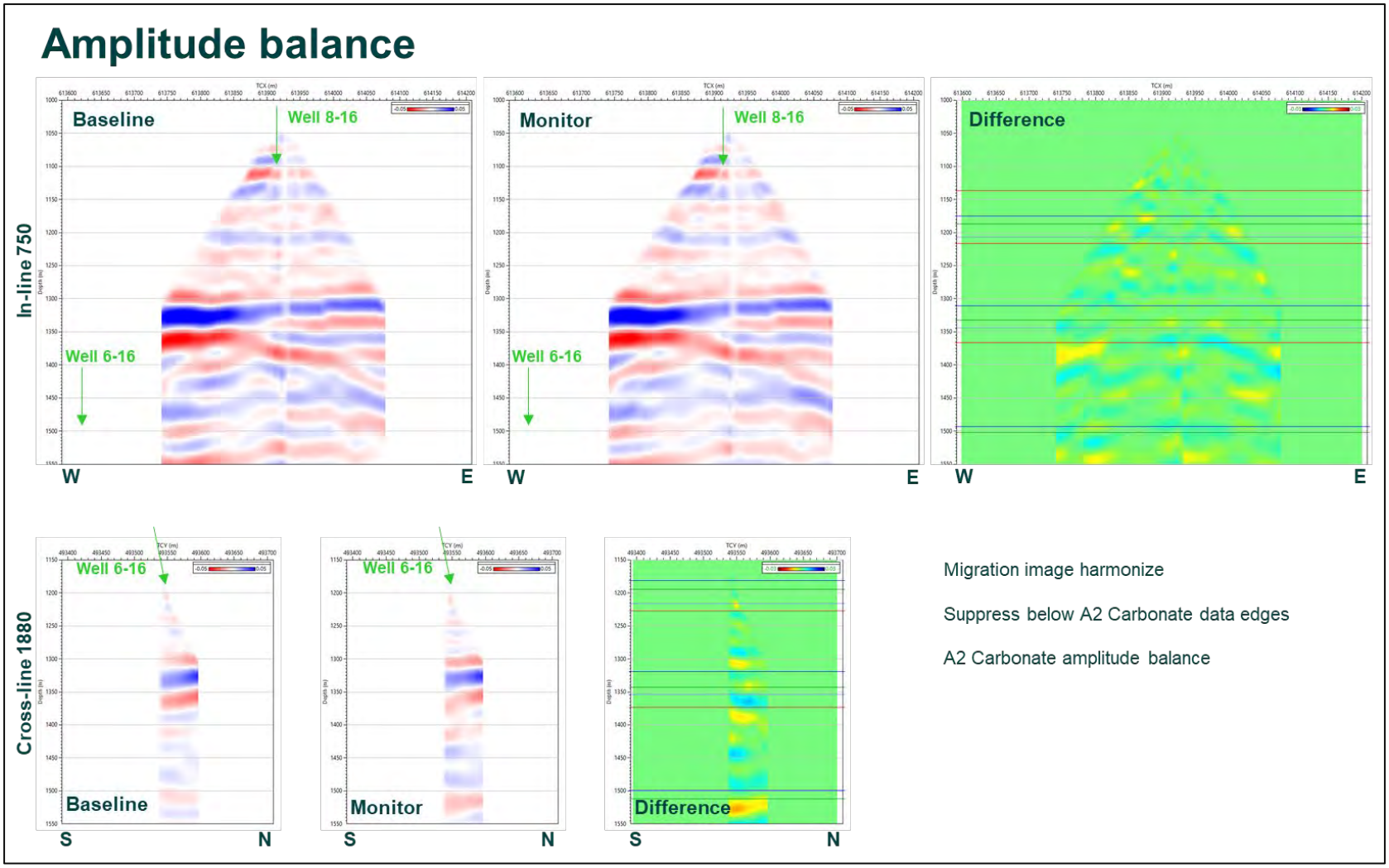


*Figure 12-6. Amplitude balance - At A2 Carbonate. Above the reservoir we don't expect to see time-lapse effects due to the $CO_2$ injection. For this reason, the amplitude scale of the A2 Carbonate reflector should be similar between the baseline and the monitor surveys. For each trace an amplitude scaling factor was computed as the ratio between the monitor and baseline amplitudes at the A2 Carbonate reflector. The monitor image amplitudes were trace by trace balanced with the baseline survey amplitudes.*

# 13 Synthetic models

Battelle has performed lab tests on reservoir cores to estimate the $CO_2$ injection impact on reservoir properties. The increase in reservoir pressure will result in a Vp and a Vs decrease of up to 5%. To estimate the expected seismic response of the $CO_2$ injection into the carbonate reservoir, several scenarios were modelled and analysed. The models were built using the well logs and information from the lab tests.

Figure 13-1 presents the model build based on the well 6-16 acoustic and density logs recorded after the well was drilled, before the baseline seismic acquisition. It is a 7 layers 1D model with constant velocity and density layers. For each layer the velocity and density values were computed by averaging the well log over the interval (black step line on top of the well log).

Seven different cases of $CO_2$ injection impact on the formation velocity and density were considered (Fig. 13-2). Case 0 is the baseline, in cases 1 and 2 the velocity was decreased by 1% and respectively 6% in the A1 Carbonate and Brown Niagaran layers. Case 3 is similar to case 2, but adds a 1% decrease in velocity at the A2 Carbonate layer. For the Cases 4 to 6 only the density varies. In case 4 there is a 2% increase in density at the A1 Carbonate and Brown Niagaran layers, case 5 has a 5% increase in density in the same layers and case 6 has a 5% increase in density at the A1 Carbonate and Brown Niagaran and a 1% increase at the A2 Carbonate layer. The last case varies the velocity and density in the same time: 6% decrease in velocity and increase in density at the A1 Carbonate and Brown Niagaran and 1% decrease in velocity and increase in density at A2 Carbonate.

The Zoeppritz equations describes seismic wave energy partitioning at an interface, for example the boundary between two layers with different properties. The equations relate the amplitude of the incident P-waves to the reflected and refracted P and S waves at a plane interface for a given angle of incidence.

The analysis was done to study the impact of the offset on the reflector amplitude. If the effect is significant then the migrated image may be affected by stacking together shots with different amplitude response. As the response depends on the velocity (P and S) it may have an impact on the time laps results.

Figure 13-3 shows the model on the left and the reflection magnitude vs incidence angle on the right. At the A2 Carbonate top there is a slight decrease of the P response with the incident angle and above 40° incidence angle all the P energy is refracted. Also, above 25° incidence angle the P to S reflectivity is stronger compare with P to P. For the top of A1 Carbonate, the P to P response is almost flat with the P to S response greater than the P to P response for incidence angles above 25°. The thickens of the A2 Anhydrite is small and because the difference in velocity and density is not significant compared to the A2 Carbonate layer, the reflection coefficient is very small. The interface at top Brown Niagaran shows a P to P critical incidence angle at 60°.

Case 1 is presented in figure 13-4. In the left image, in the first graph are the well logs and the well perforations (blue dots), in the second graph are the compressional velocity (baseline in blue and adjusted log light blue) and the average velocity (baseline in red and adjusted log in magenta). In the third graph of the left image is the density log and average density.

In the middle image are the synthetic seismograms computed based only on the well log data. Synthetic generation was explained in figure 7-24. The acoustic impedance (Z) is computed as the product between Vp and density. The reflection coefficient is defined as: (Z2 – Z1) / (Z2 + Z1). The reflection coefficient (RC) looks like a series of spikes (with infinite bandwidth in frequency domain).

The RC spectrum is filtered up to the seismic bandwidth resulting in a seismic trace similar to the trace recorded by the seismic survey. The first panel of the middle picture shows in red the synthetic seismogram computed using the original logs (“baseline” survey), in the second panel in blue is the synthetic seismogram computed using the altered logs (“monitor” survey), the third track shows the “baseline” and “monitor” synthetic seismogram overlapped and the fourth track shows the difference between the “monitor” and “baseline” synthetic seismogram.

Decreasing the A1 Carbonate and Brown Niagaran velocity by 1% will slightly increase the wavelet length below the A2 Anhydrite (as the velocity decrease, the travel time becomes longer) and increasing the reflectivity of the A1 Carbonate as the difference in velocity between the A2 Anhydrite and the A1 Carbonate become higher (Fig. 13-4 right). An average ratio of 0.03 was computed between the RMS of the monitor – baseline difference and the RMS of the baseline synthetic over the 550-600 ms window.

Decreasing the A1 Carbonate and Brown Niagaran velocity by 6% further increase the wavelet length below the A2 Anhydrite (Fig. 13-5 – Case 2). The A1 Carbonate amplitude is higher due to a larger difference in velocity between the A2 Anhydrite and the A1 Carbonate. The P reflection magnitude become stronger than the S response at A1 Carbonate (Fig. 13-5 right). The RMS ratio of the difference to the baseline is 0.06.

By adding a 1% velocity increase in the A2 Carbonate layer (Fig. 13-6 – Case 3) the amplitude response at the A2 Carbonate top will slightly decrease, but is increasing the phase difference below. Also, the RMS ratio of the difference to the baseline increased to 0.17.

For Case 1 to 3 the differences between the “baseline” and “monitor” are mainly due to a phase shift increase between the two.

In Case 4, changes in density will affect only the amplitude response and will not stretch or contract the wave in time (Fig. 13-7). Increasing the A1 Carbonate and Brown Niagaran formation density by 2% has a negligible effect on the seismic response and it will be very hard to detect by a time laps survey. The reflection magnitude at the A1 Carbonate will slightly decrease as the density difference between the A1 Carbonate and the A2 Anhydrite decreases. The RMS ratio between the difference and the baseline is 0.04.

Figure 13-8 presents Case 5, where the density of the A1 Carbonate and Brown Niagaran increases by 5%. This has a more visible impact on the amplitude response at the A1 Carbonate level. The S response at the A1 Carbonate is lower and close to the P response at a high angle of incidence (Fig. 13-8 right). The RMS ratio between the difference and the baseline increase to 0.10.

Increasing with 1% the density of the A2 Carbonate presented in case 6 (Fig. 13-9), would not be detected by a seismic survey. The P and S response at the A2 anhydrite is close to 0. The RMS ratio between the difference and the baseline remain at 0.10.

By combining the velocity and density adjustments in the same time (Case 7) will generate a significant difference and this is mainly due to the stretch of the “monitor” synthetic (Fig. 13-10),but lower compare with case 3 as the velocity decrease generate an amplitude increase and the density decrease generate amplitude decrease. The A2 Anhydrite reflection magnitude is 0 below 40° incidence angles and A1 Carbonate “monitor” response is lower in amplitude compare with the “baseline” synthetic. The ratio of RMS difference vs RMS baseline is 0.09.

The Zoeppritz graphs do not show significant amplitude variation with angle. For this reason we can stack data from different incidence angles.

Figure 13-11 presents a composite with synthetic seismograms and the monitor – baseline synthetic seismogram differences for all cases. The difference trace is more perceptible by plotting in the

rainbow colour scale. The composite confirms that changes in velocity can be detected due to a change in the wavelet shape, but the changes in density are difficult to detect in the seismic data.

The synthetic ZVSP cases were compared with the recorded SP data located close to the well (Vibroseis SP 101216 and SP 101214). Figures 13-12 and 13-13 show in the first panel the baseline pre-migrated shot point gather, in the second panel the baseline corridor stack (computed by summing the pre-migrate data in a 20 m – 70 m window relative to the FB), in the third panel the monitor pre-migrate data after amplitude scaling, in the fourth panel the monitor corridor stack, in the fifth panel the difference between the monitor and the baseline corridor stack and in the sixth panel the case 7 synthetic difference. As the synthetic data were computed in time and the pre-migrated data are in depth, the synthetic data were scaled and positioned to match the pre-migrate data in the reservoir interval.

Most of the pre-migrate corridor stacks differences are probable due to the noise as differences are also presented above the reservoir depth. Nevertheless, along the A2 and A1 Carbonate intervals, the monitor-baseline differences show similarities with the synthetic cases (changes in velocity). This is a qualitative comparison as the amplitude differences of the real and synthetic data are not scaled in the same way.

| Title | Description | Figure |
|---|---|---|
| | | |
| **13 Synthetic models** | | |
| Velocity model | Using well 6-16 logs | **13.1** |
| Synthetic cases | Property changes | **13.2** |
| Synthetic case 0 | “Baseline” | **13.3** |
| Synthetic case 1 | 1% velocity change | **13.4** |
| Synthetic case 2 | 6% velocity change | **13.5** |
| Synthetic case 3 | 6% and 1% velocity change | **13.6** |
| Synthetic case 4 | 2% density change | **13.7** |
| Synthetic case 5 | 5% density change | **13.8** |
| Synthetic case 6 | 5% and 1% density change | **13.9** |
| Synthetic case 7 | 6% and 1% velocity and density change | **13.10** |
| Synthetic seismograms and the difference case - baseline | All cases result composite plot | **13.11** |

*Table 13-22 Synthetic models figures*

# Velocity model

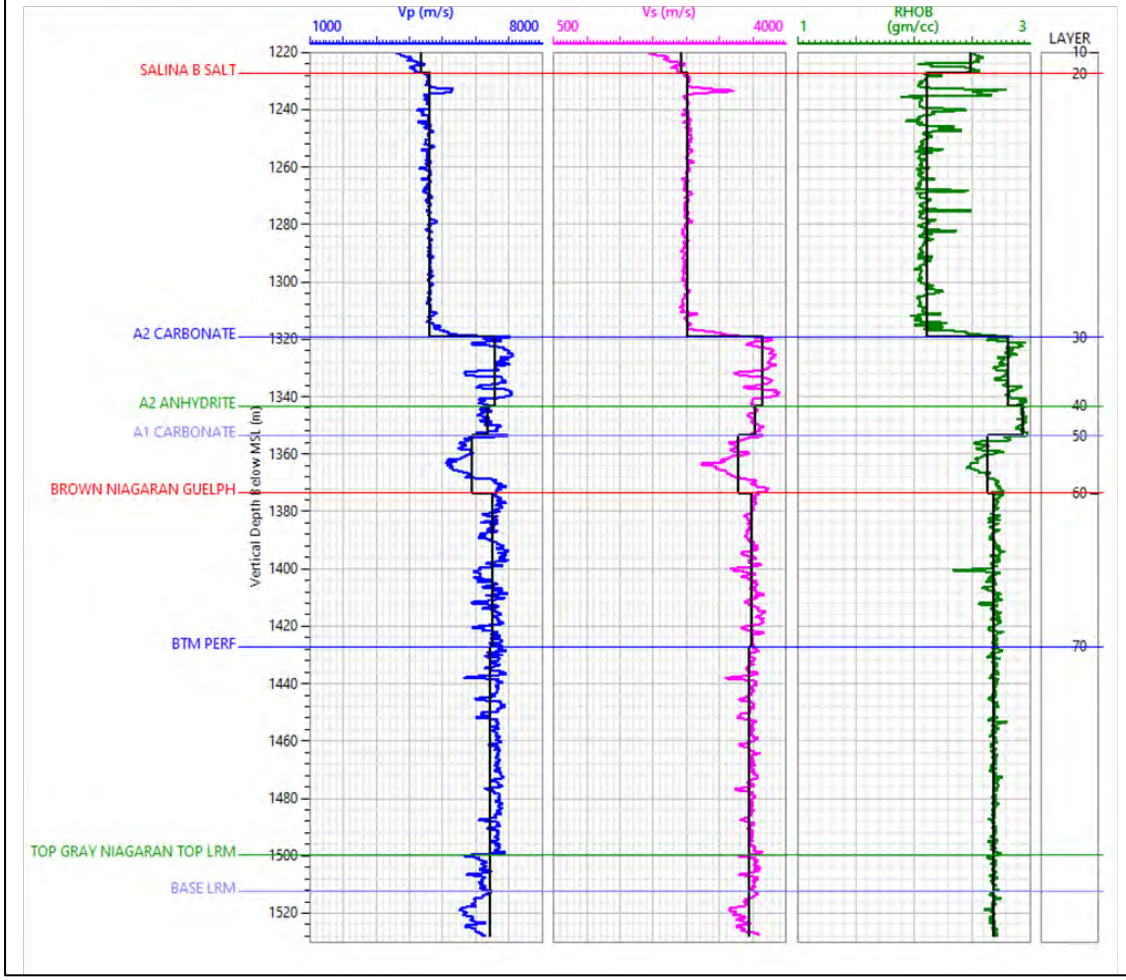


1D velocity model
Number of layers: 7
Average interval velocity and average density based on the well 6-16 logs

| Name | Model layers | |
|---|---|---|
| | MD@KB | TVD@MSL |
| | m | m |
| SALINA B UNIT | 1622 | 1216 |
| SALINA B SALT | 1634 | 1227 |
| A2 CARBONATE | 1749 | 1319 |
| A2 ANHYDRITE | 1780 | 1343 |
| A1 CARBONATE | 1793 | 1354 |
| BROWN NIAGARAN/GUELPH | 1820 | 1374 |
| BTM PERF | 1890 | 1427 |

*Figure 13-1. Velocity model - Using well 6-16 logs. This figure presents the model build based on the well 6-16 acoustic and density logs recorded after the well was drilled, before the baseline seismic acquisition. It is a 7 layers 1D model with constant velocity and density layers. For each layer the velocity and density values were computed by averaging the well log over the interval (black step line on top of the well log).*

# Synthetic cases

| Name | Model layers | | Case 0 | | Case 1 | | Case 2 | | Case 3 | | Case 4 | | Case 5 | | Case 6 | | Case 7 | |
|---|---|---|---|---|---|---|---|---|---|---|---|---|---|---|---|---|---|---|
| | MD@KB | TVD@MSL | Alter Velocity | Alter Density | Alter Velocity | Alter Density | Alter Velocity | Alter Density | Alter Velocity | Alter Density | Alter Velocity | Alter Density | Alter Velocity | Alter Density | Alter Velocity | Alter Density | Alter Velocity | Alter Density |
| | m | m | % | % | % | % | % | % | % | % | % | % | % | % | % | % | % | % |
| SALINA B UNIT | 1622 | 1216 | 0 | 0 | 0 | 0 | 0 | 0 | 0 | 0 | 0 | 0 | 0 | 0 | 0 | 0 | 0 | 0 |
| SALINA B SALT | 1634 | 1227 | 0 | 0 | 0 | 0 | 0 | 0 | 0 | 0 | 0 | 0 | 0 | 0 | 0 | 0 | 0 | 0 |
| A2 CARBONATE | 1749 | 1319 | 0 | 0 | 0 | 0 | 0 | 0 | -1 | 0 | 0 | 0 | 0 | 0 | 0 | 1 | 1 | 5 |
| A2 ANHYDRITE | 1780 | 1343 | 0 | 0 | 0 | 0 | 0 | 0 | 0 | 0 | 0 | 0 | 0 | 0 | 0 | 0 | 0 | 0 |
| A1 CARBONATE | 1793 | 1354 | 0 | 0 | -1 | 0 | --6 | 0 | -6 | 0 | 0 | 2 | 0 | 5 | 0 | 5 | 6 | 5 |
| BROWN NIAGARAN/GUELPH | 1820 | 1374 | 0 | 0 | -1 | 0 | 6 | 0 | -6 | 0 | 0 | 2 | 0 | 5 | 0 | 5 | 6 | 5 |
| BTM PERF | 1890 | 1427 | 0 | 0 | 0 | 0 | 0 | 0 | 0 | 0 | 0 | 0 | 0 | 0 | 0 | 0 | 0 | 0 |

*Figure 13-2. Synthetic cases - Property changes. Seven different cases of $CO_2$ injection impact on the formation velocity and density were considered. Case 0 is the baseline, in cases 1 and 2 the velocity was decreased by 1% and respectively 6% in the A1 Carbonate and Brown Niagaran layers. Case 3 is similar with case 2 but is adding a 1% decrease in velocity at the A2 Carbonate layer. For the Cases 4 to 6 only the density varies. In case 4 there is a 2% increase in density at the A1 Carbonate and Brown Niagaran layers, case 5 has a 5% increase in density in the same layers and case 6 has a 5% increase in density at the A1 Carbonate and Brown Niagaran and a 1% increase at the A2 Carbonate layer. The last case varies the velocity and density in the same time: 6% decrease in velocity and increase in density at the A1 Carbonate and Brown Niagaran and 1% decrease in velocity and increase in density at A2 Carbonate.*

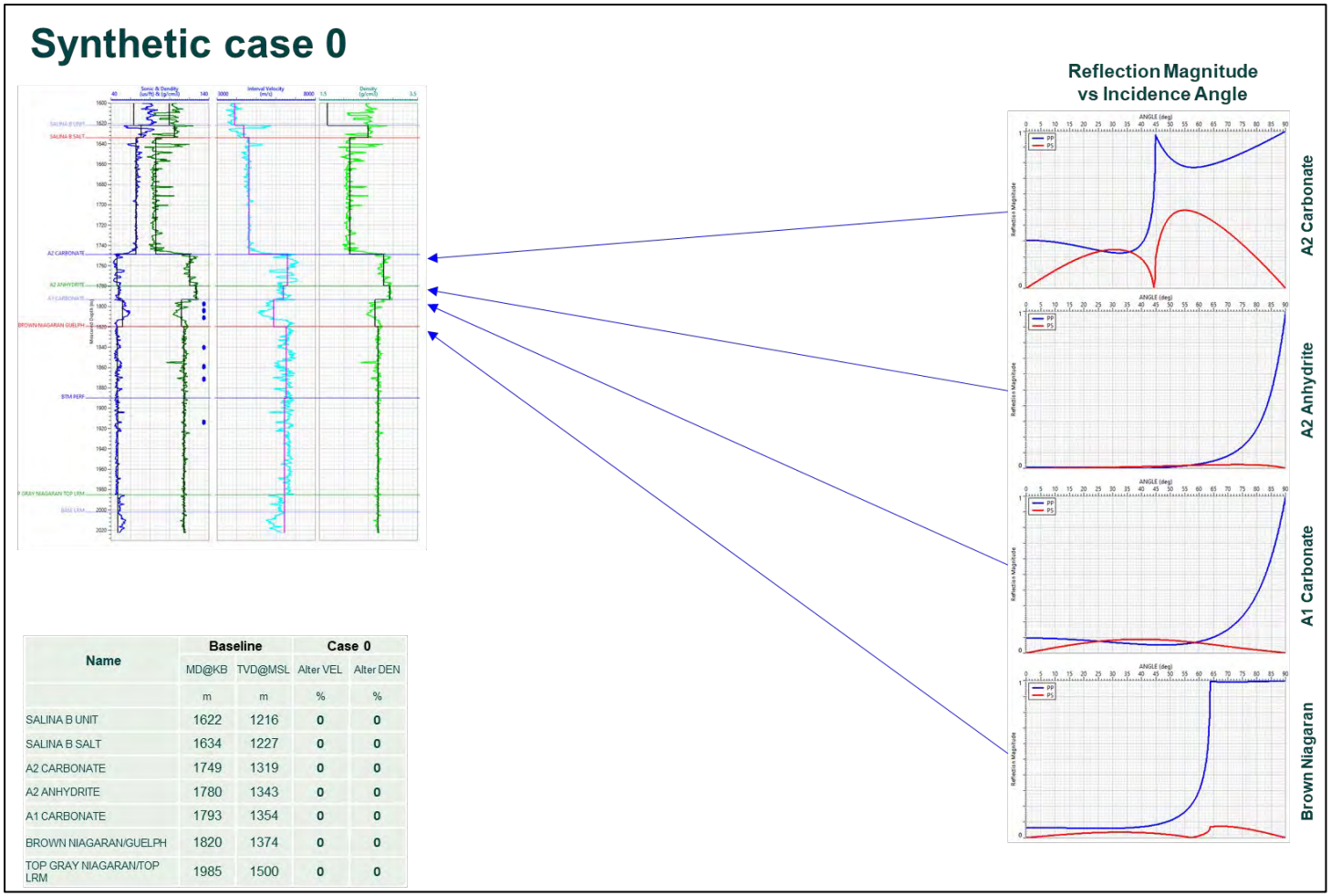


| Name | Baseline | | Case 0 | |
|---|---|---|---|---|
| | MD@KB | TVD@MSL | Alter VEL | Alter DEN |
| | m | m | % | % |
| SALINA B UNIT | 1622 | 1216 | 0 | 0 |
| SALINA B SALT | 1634 | 1227 | 0 | 0 |
| A2 CARBONATE | 1749 | 1319 | 0 | 0 |
| A2 ANHYDRITE | 1780 | 1343 | 0 | 0 |
| A1 CARBONATE | 1793 | 1354 | 0 | 0 |
| BROWN NIAGARAN/GUELPH | 1820 | 1374 | 0 | 0 |
| TOP GRAY NIAGARAN/TOP LRM | 1985 | 1500 | 0 | 0 |

*Figure 13-3. Synthetic case 0 - "Baseline". This figure shows the model on the left and the reflection magnitude vs incidence angle on the right. At the A2 Carbonate top there is a slight decrease of the P response with the incident angle and above 40° incidence angle all the P energy is refracted. Also, above 25° incidence angle the P to S reflectivity is stronger compare with P to P. For the top of A1 Carbonate, the P to P response is almost flat with the P to S response greater than the P to P response for incidence angles above 25°. The thickens of the A2 Anhydrite is small and because the difference in velocity and density is not significant compared to the A2 Carbonate layer, the reflection coefficient is very small. The interface at top Brown Niagaran shows a P to P critical incidence angle at 60°.*

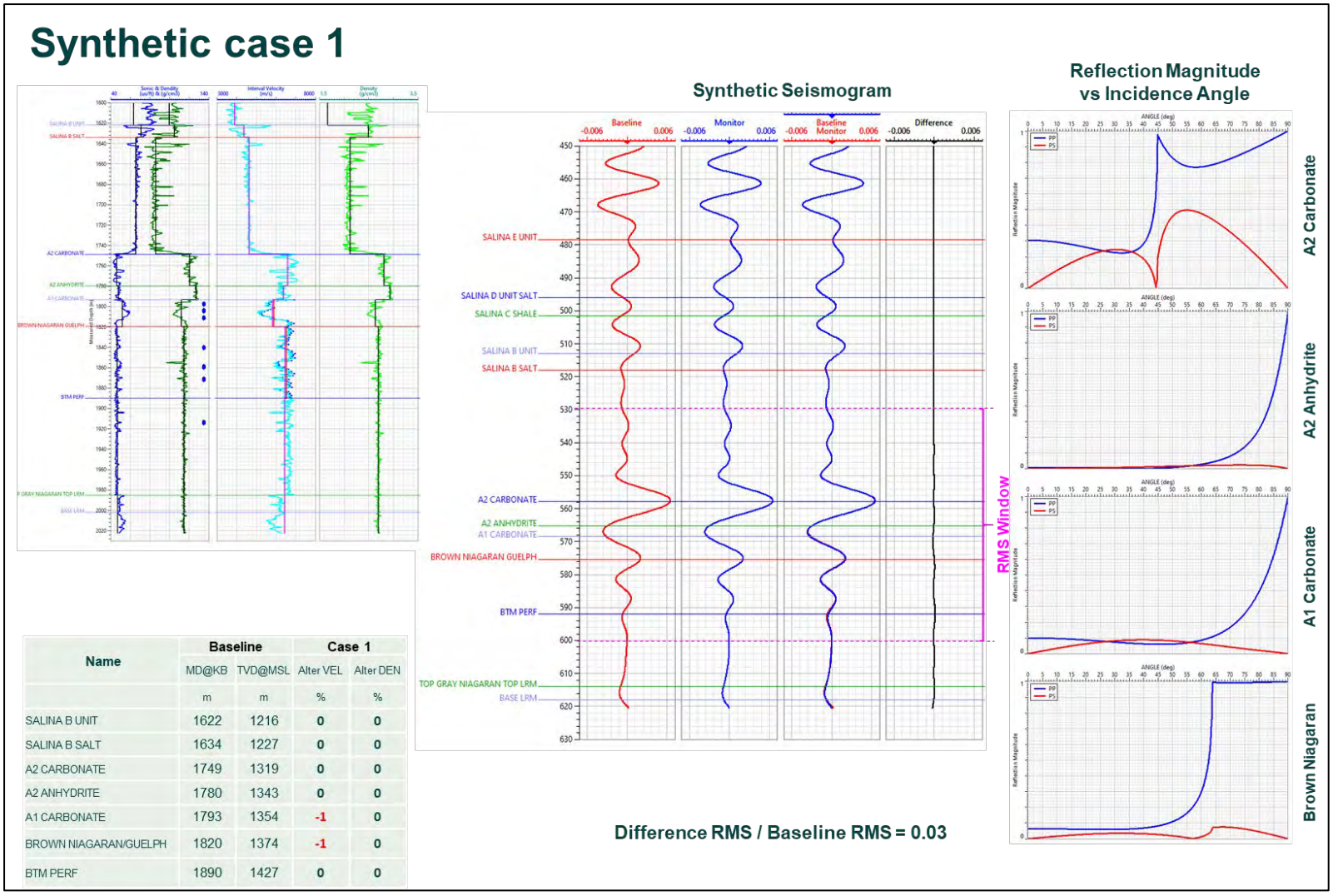


| Name | Baseline | | Case 1 | |
|---|---|---|---|---|
| | MD@KB | TVD@MSL | Alter VEL | Alter DEN |
| | m | m | % | % |
| SALINA B UNIT | 1622 | 1216 | 0 | 0 |
| SALINA B SALT | 1634 | 1227 | 0 | 0 |
| A2 CARBONATE | 1749 | 1319 | 0 | 0 |
| A2 ANHYDRITE | 1780 | 1343 | 0 | 0 |
| A1 CARBONATE | 1793 | 1354 | -1 | 0 |
| BROWN NIAGARAN/GUELPH | 1820 | 1374 | -1 | 0 |
| BTM PERF | 1890 | 1427 | 0 | 0 |

*Figure 13-4. Synthetic case 1 - 1% velocity change. Case 1 is presented in figure 13.4. In the left image, in the first graph are the well logs and the well perforations (blue dots), in the second graph are the compressional velocity (baseline in blue and adjusted log light blue) and the average velocity (baseline in red and adjusted log in magenta). In the third graph of the left image is the density log and average density.*

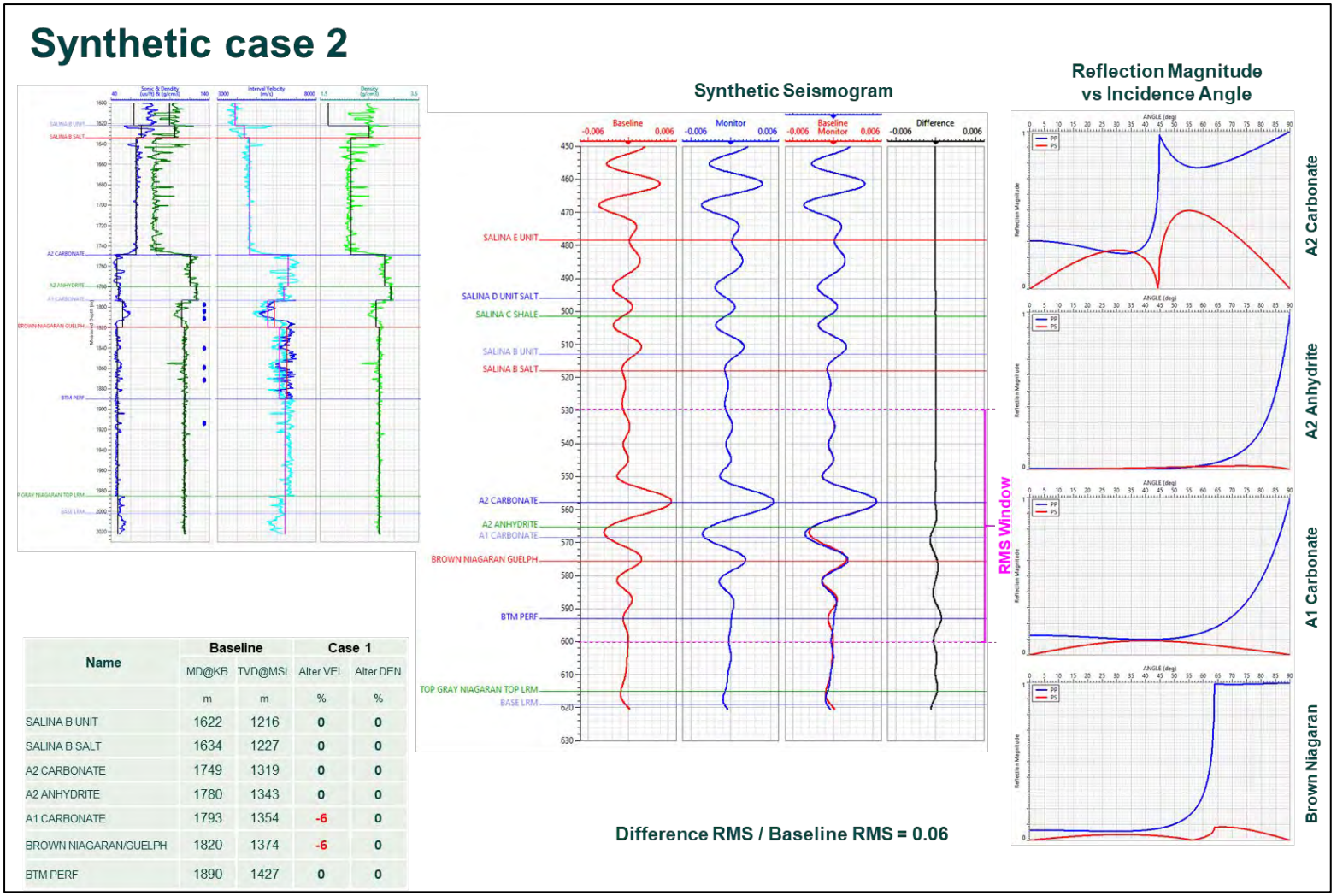


| Name | Baseline | | Case 1 | |
|---|---|---|---|---|
| | MD@KB | TVD@MSL | Alter VEL | Alter DEN |
| | m | m | % | % |
| SALINA B UNIT | 1622 | 1216 | 0 | 0 |
| SALINA B SALT | 1634 | 1227 | 0 | 0 |
| A2 CARBONATE | 1749 | 1319 | 0 | 0 |
| A2 ANHYDRITE | 1780 | 1343 | 0 | 0 |
| A1 CARBONATE | 1793 | 1354 | -6 | 0 |
| BROWN NIAGARAN/GUELPH | 1820 | 1374 | -6 | 0 |
| BTM PERF | 1890 | 1427 | 0 | 0 |

*Figure 13-5. Synthetic case 2 - 6% velocity change. Decreasing the A1 Carbonate and Brown Niagaran velocity by 6% further increase the wavelet length below the A2 Anhydrite (Fig. 13-5 – Case 2). The A1 Carbonate amplitude is higher due to a larger difference in velocity between the A2 Anhydrite and the A1 Carbonate. The P reflection magnitude become stronger than the S response at A1 Carbonate (Fig. 13-5 right). The RMS ratio of the difference to the baseline is 0.29.*

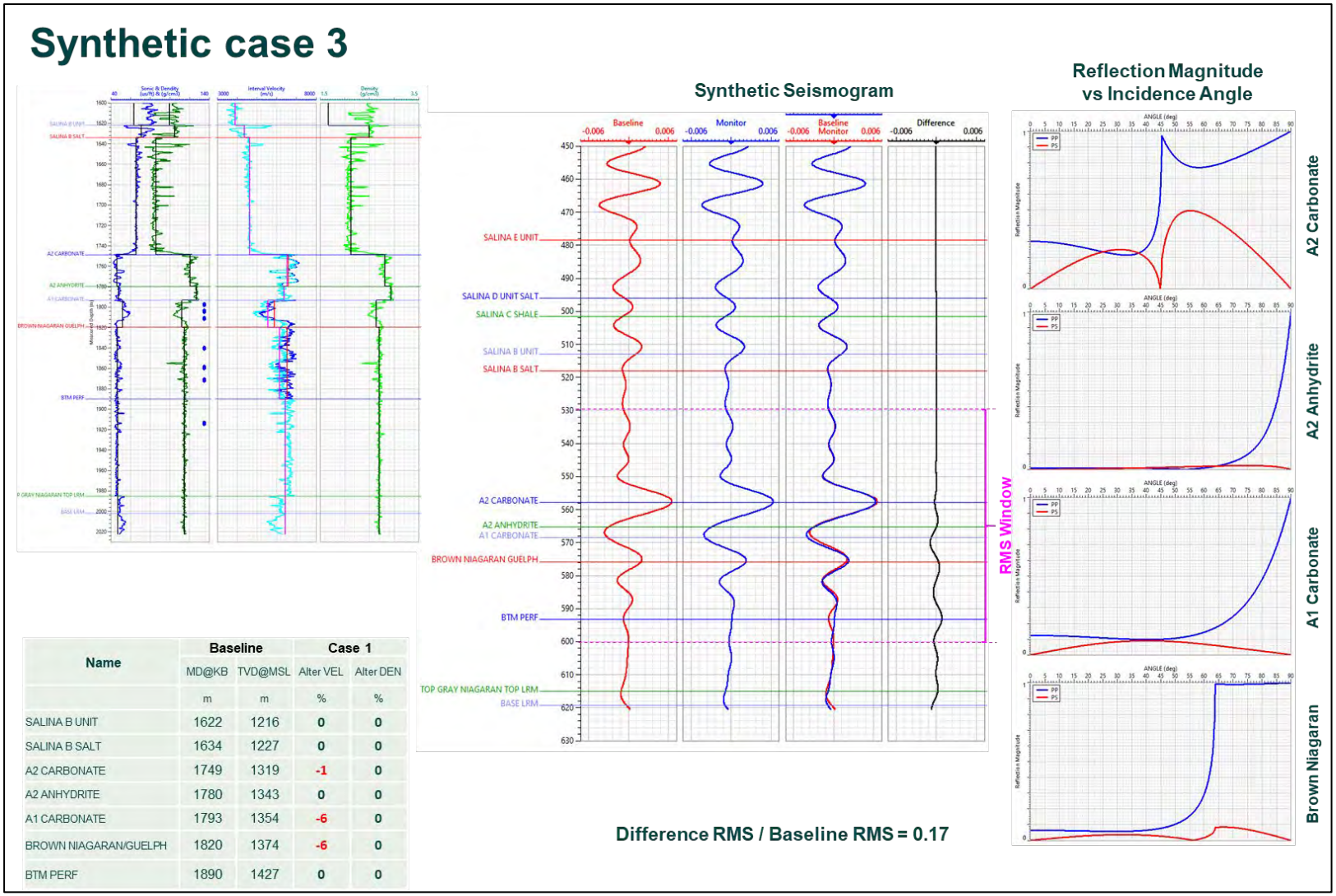


| Name | Baseline | | Case 1 | |
|---|---|---|---|---|
| | MD@KB | TVD@MSL | Alter VEL | Alter DEN |
| | m | m | % | % |
| SALINA B UNIT | 1622 | 1216 | 0 | 0 |
| SALINA B SALT | 1634 | 1227 | 0 | 0 |
| A2 CARBONATE | 1749 | 1319 | -1 | 0 |
| A2 ANHYDRITE | 1780 | 1343 | 0 | 0 |
| A1 CARBONATE | 1793 | 1354 | -6 | 0 |
| BROWN NIAGARAN/GUELPH | 1820 | 1374 | -6 | 0 |
| BTM PERF | 1890 | 1427 | 0 | 0 |

*Figure 13-6. Synthetic case 3 - 6% and 1% velocity change. By adding a 1% velocity increase in the A2 Carbonate layer (Fig. 13-6 – Case 3) the amplitude response at the A2 Carbonate top will slightly decrease but is increasing the amplitude response below.*

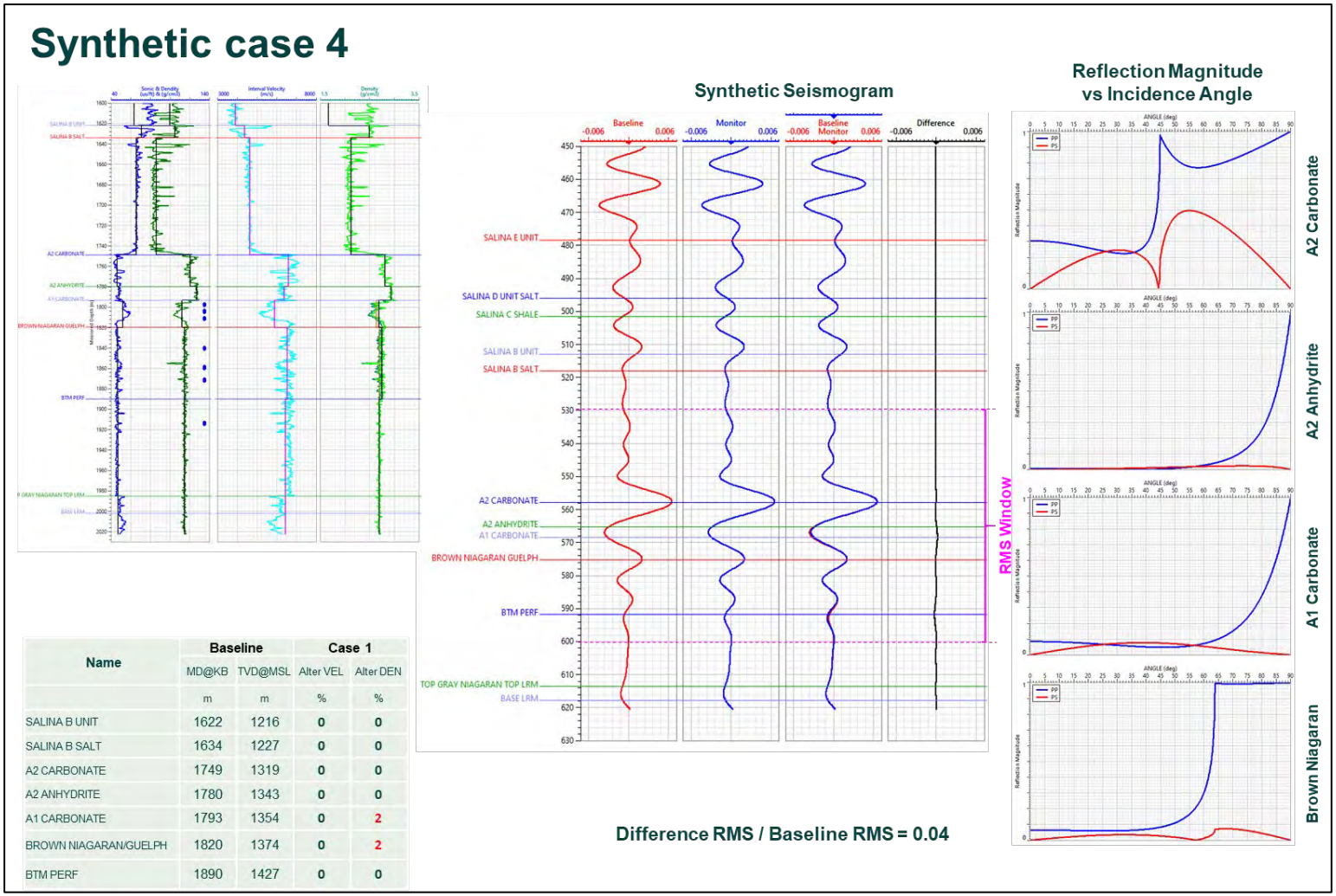


| Name | Baseline | | Case 1 | |
|---|---|---|---|---|
| | MD@KB | TVD@MSL | Alter VEL | Alter DEN |
| | m | m | % | % |
| SALINA B UNIT | 1622 | 1216 | 0 | 0 |
| SALINA B SALT | 1634 | 1227 | 0 | 0 |
| A2 CARBONATE | 1749 | 1319 | 0 | 0 |
| A2 ANHYDRITE | 1780 | 1343 | 0 | 0 |
| A1 CARBONATE | 1793 | 1354 | 0 | 2 |
| BROWN NIAGARAN/GUELPH | 1820 | 1374 | 0 | 2 |
| BTM PERF | 1890 | 1427 | 0 | 0 |

*Figure 13-7. Synthetic case 4 - 2% density change. In Case 4, changes in density will affect only the amplitude response and will not stretch or contract the wave in time (Fig. 13.7). Increasing the A1 Carbonate and Brown Niagaran formation density by 2% has a negligible effect on the seismic response and it will be very hard to detect by a time laps survey. The reflection magnitude at the A1 Carbonate will slightly decrease as the density difference between the A1 Carbonate and the A2 Anhydrite decreases. The RMS ratio between the difference and the baseline is close to 0.*

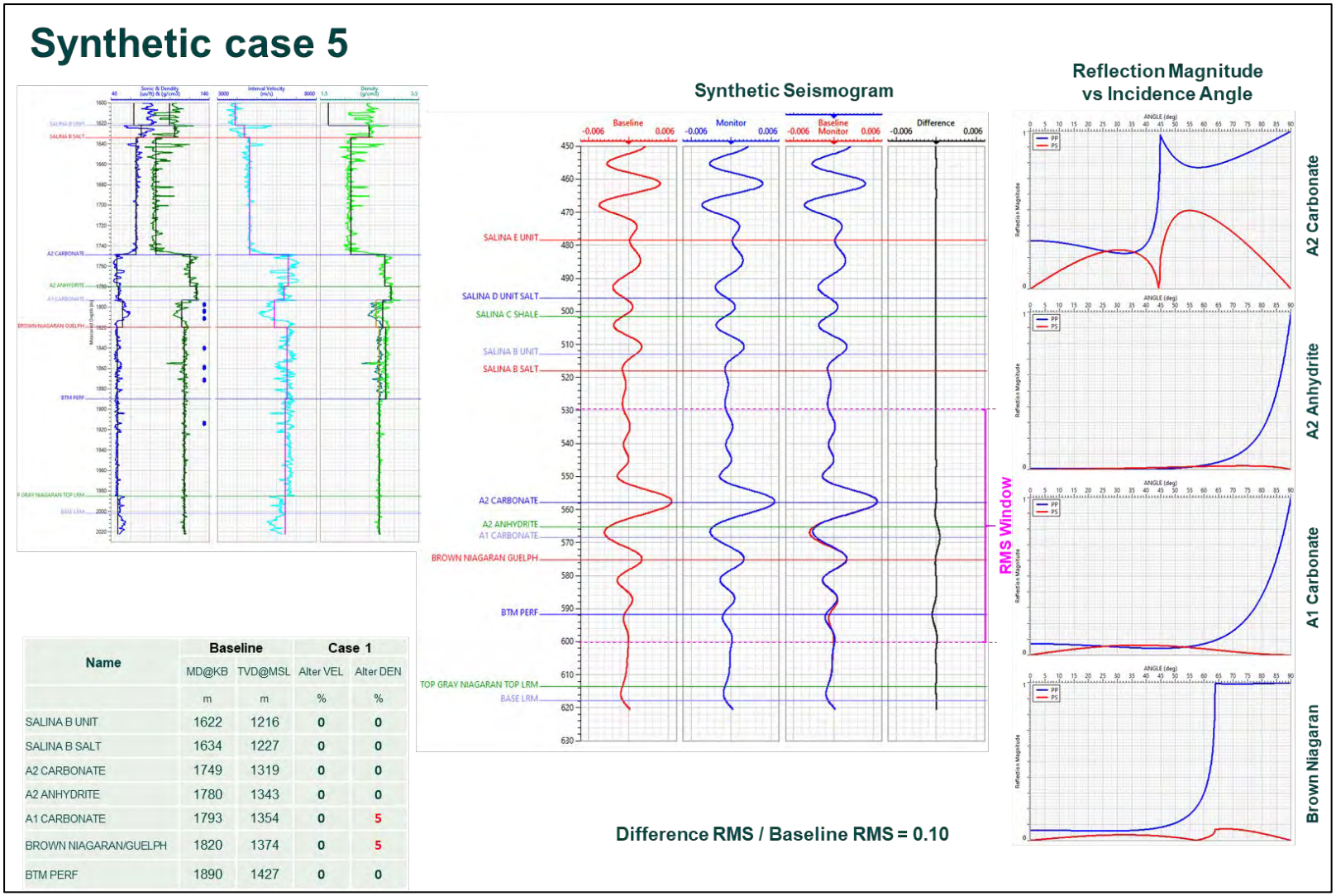


| Name | Baseline | | Case 1 | |
|---|---|---|---|---|
| | MD@KB | TVD@MSL | Alter VEL | Alter DEN |
| | m | m | % | % |
| SALINA B UNIT | 1622 | 1216 | 0 | 0 |
| SALINA B SALT | 1634 | 1227 | 0 | 0 |
| A2 CARBONATE | 1749 | 1319 | 0 | 0 |
| A2 ANHYDRITE | 1780 | 1343 | 0 | 0 |
| A1 CARBONATE | 1793 | 1354 | 0 | 5 |
| BROWN NIAGARAN/GUELPH | 1820 | 1374 | 0 | 5 |
| BTM PERF | 1890 | 1427 | 0 | 0 |

*Figure 13-8. Synthetic case 5 - 5% density change. Figure 13.8 presents Case 5, where the density of the A1 Carbonate and Brown Niagaran increases by 5%. This has no impact on the amplitude response at the A1 Carbonate level. The S response at the A1 Carbonate is lower and close to the P response at a high angle of incidence (Fig. 13-8 right).*

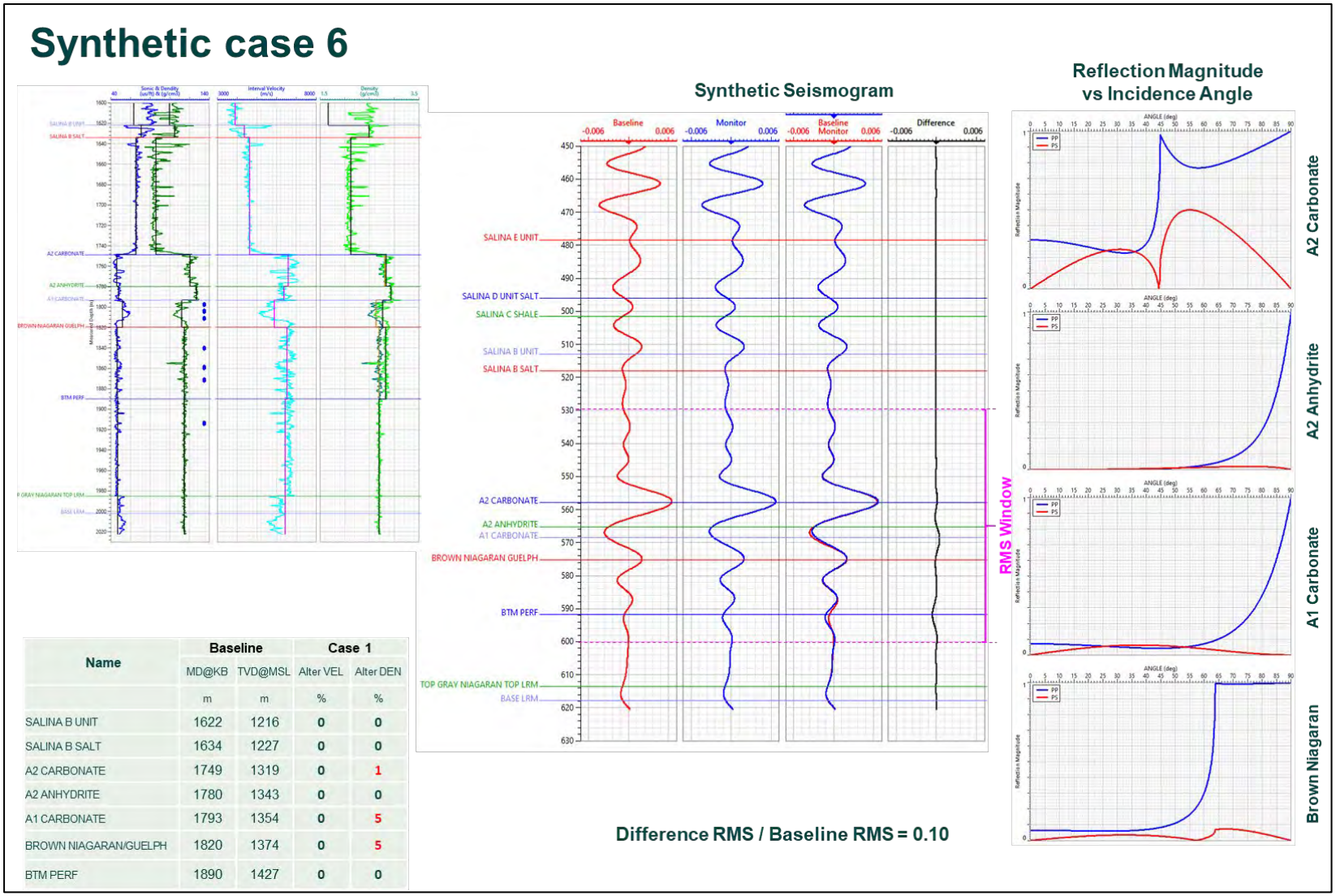


| Name | Baseline | | Case 1 | |
|---|---|---|---|---|
| | MD@KB | TVD@MSL | Alter VEL | Alter DEN |
| | m | m | % | % |
| SALINA B UNIT | 1622 | 1216 | 0 | 0 |
| SALINA B SALT | 1634 | 1227 | 0 | 0 |
| A2 CARBONATE | 1749 | 1319 | 0 | 1 |
| A2 ANHYDRITE | 1780 | 1343 | 0 | 0 |
| A1 CARBONATE | 1793 | 1354 | 0 | 5 |
| BROWN NIAGARAN/GUELPH | 1820 | 1374 | 0 | 5 |
| BTM PERF | 1890 | 1427 | 0 | 0 |

*Figure 13-9. Synthetic case 6 - 5% and 1% density change. Increasing with 1% the density of the A2 Carbonate presented in case 6 (Fig. 13.9), would not be detected by a seismic survey. The P and S response at the A2 anhydrite is close to 0.*

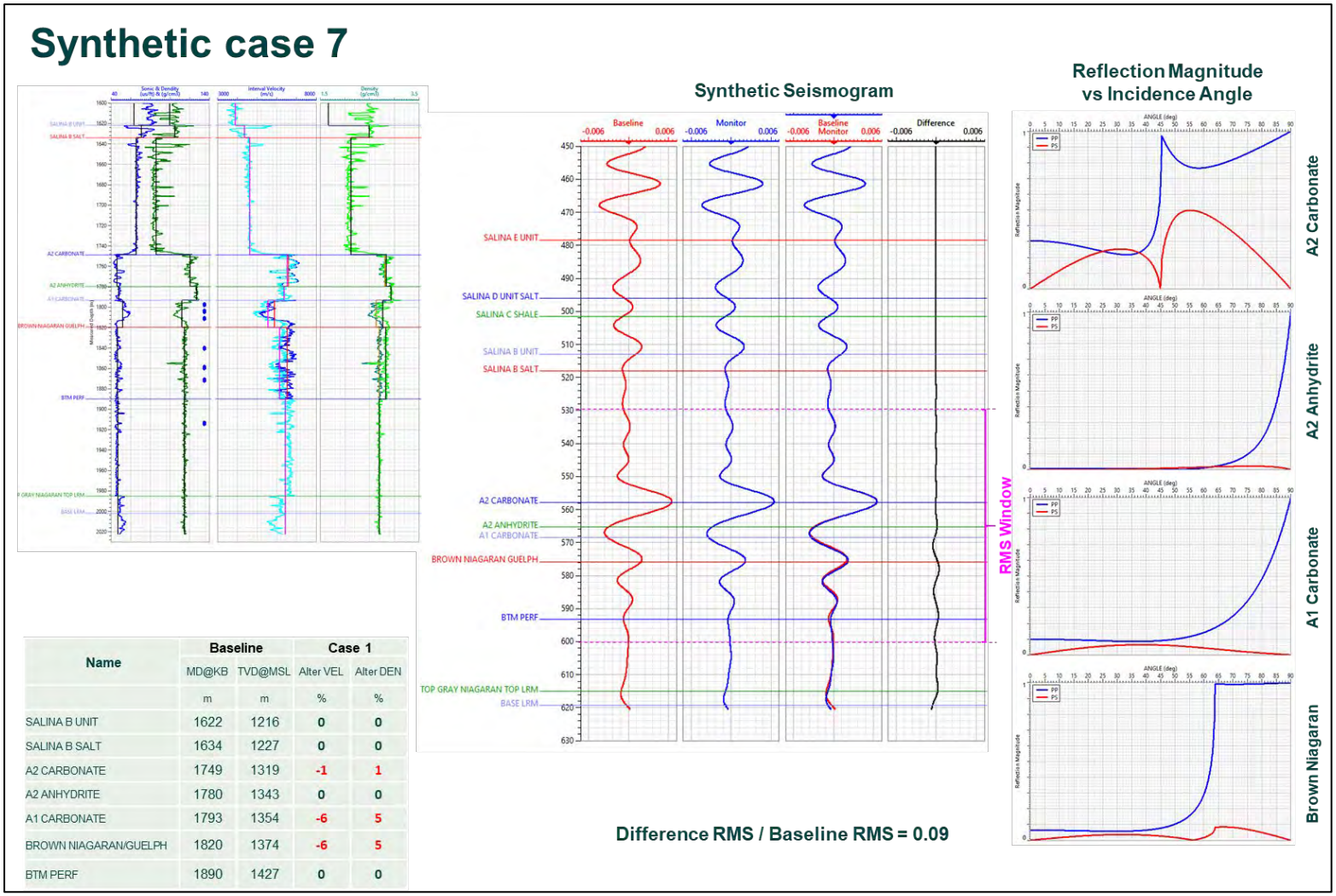


| Name | Baseline | | Case 1 | |
|---|---|---|---|---|
| | MD@KB | TVD@MSL | Alter VEL | Alter DEN |
| | m | m | % | % |
| SALINA B UNIT | 1622 | 1216 | 0 | 0 |
| SALINA B SALT | 1634 | 1227 | 0 | 0 |
| A2 CARBONATE | 1749 | 1319 | -1 | 1 |
| A2 ANHYDRITE | 1780 | 1343 | 0 | 0 |
| A1 CARBONATE | 1793 | 1354 | -6 | 5 |
| BROWN NIAGARAN/GUELPH | 1820 | 1374 | -6 | 5 |
| BTM PERF | 1890 | 1427 | 0 | 0 |

*Figure 13-10. Synthetic case 7 - 6% and 1% velocity and density change. By combining the velocity and density adjustments in the same time (Case 7) will generate a significant difference and this is mainly due to the stretch of the "monitor" synthetic (Fig. 13-10). The A2 Anhydrite reflection magnitude is 0 below 40° incidence angles and A1 Carbonate "monitor" response is lower in amplitude compare with the "baseline" synthetic. The ratio of RMS difference vs RMS baseline is 0.34.*

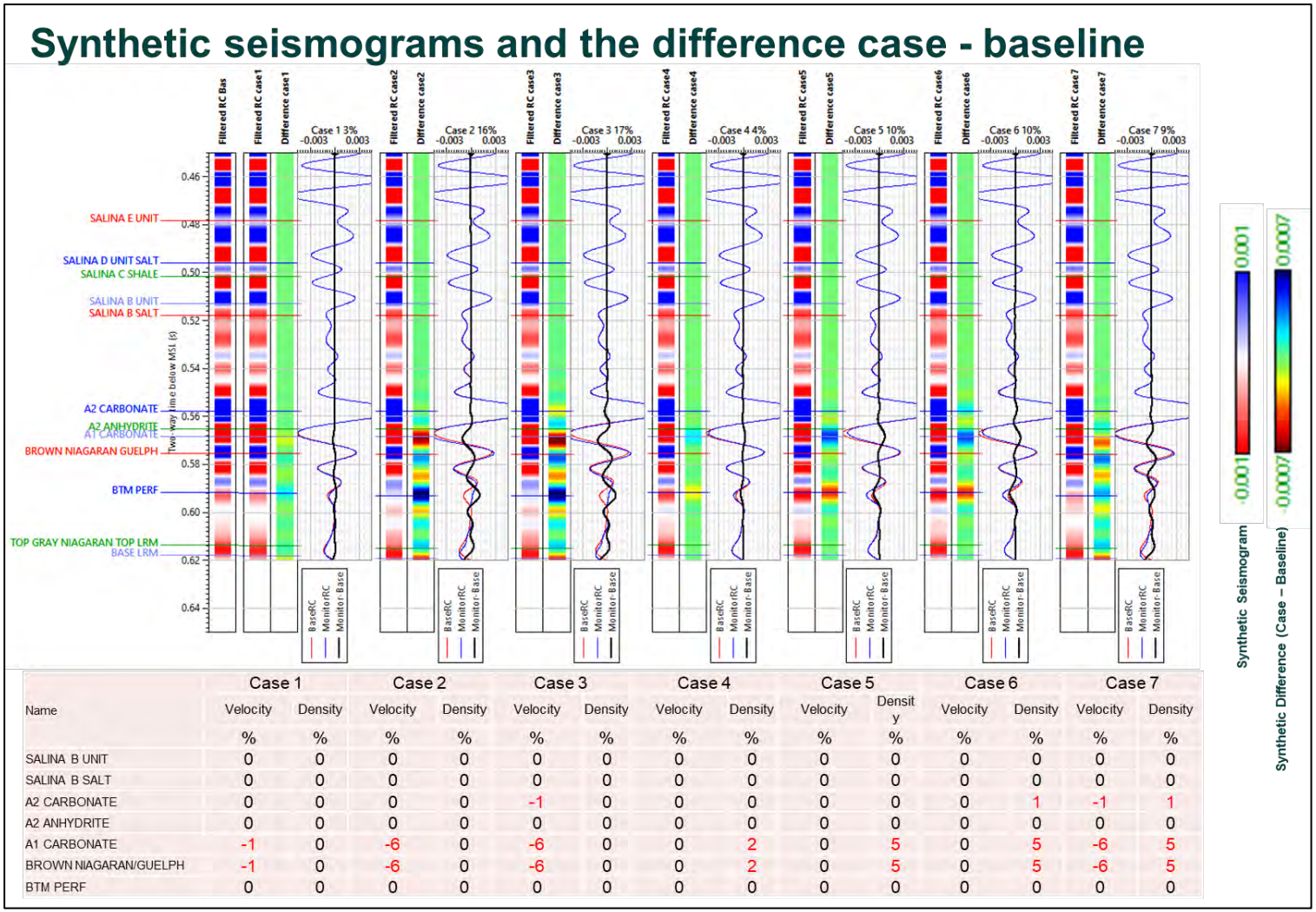


| Name | Case 1 | | Case 2 | | Case 3 | | Case 4 | | Case 5 | | Case 6 | | Case 7 | |
|---|---|---|---|---|---|---|---|---|---|---|---|---|---|---|
| | Velocity | Density | Velocity | Density | Velocity | Density | Velocity | Density | Velocity | Density | Velocity | Density | Velocity | Density |
| | % | % | % | % | % | % | % | % | % | % | % | % | % | % |
| SALINA B UNIT | 0 | 0 | 0 | 0 | 0 | 0 | 0 | 0 | 0 | 0 | 0 | 0 | 0 | 0 |
| SALINA B SALT | 0 | 0 | 0 | 0 | 0 | 0 | 0 | 0 | 0 | 0 | 0 | 0 | 0 | 0 |
| A2 CARBONATE | 0 | 0 | 0 | 0 | -1 | 0 | 0 | 0 | 0 | 0 | 0 | 1 | -1 | 1 |
| A2 ANHYDRITE | 0 | 0 | 0 | 0 | 0 | 0 | 0 | 0 | 0 | 0 | 0 | 0 | 0 | 0 |
| A1 CARBONATE | -1 | 0 | -6 | 0 | -6 | 0 | 0 | 2 | 0 | 5 | 0 | 5 | -6 | 5 |
| BROWN NIAGARAN/GUELPH | -1 | 0 | -6 | 0 | -6 | 0 | 0 | 2 | 0 | 5 | 0 | 5 | -6 | 5 |
| BTM PERF | 0 | 0 | 0 | 0 | 0 | 0 | 0 | 0 | 0 | 0 | 0 | 0 | 0 | 0 |

*Figure 13-11. Synthetic seismograms and the difference case – baseline - All cases result composite plot. This figure presents a composite with synthetic seismograms and the monitor – baseline synthetic seismogram differences for all cases. The difference trace is more perceptible by plotting in the rainbow colour scale. The composite confirms that changes in velocity can be detected due to a change in the wavelet shape, but the changes in density are difficult to detect in the seismic data.*

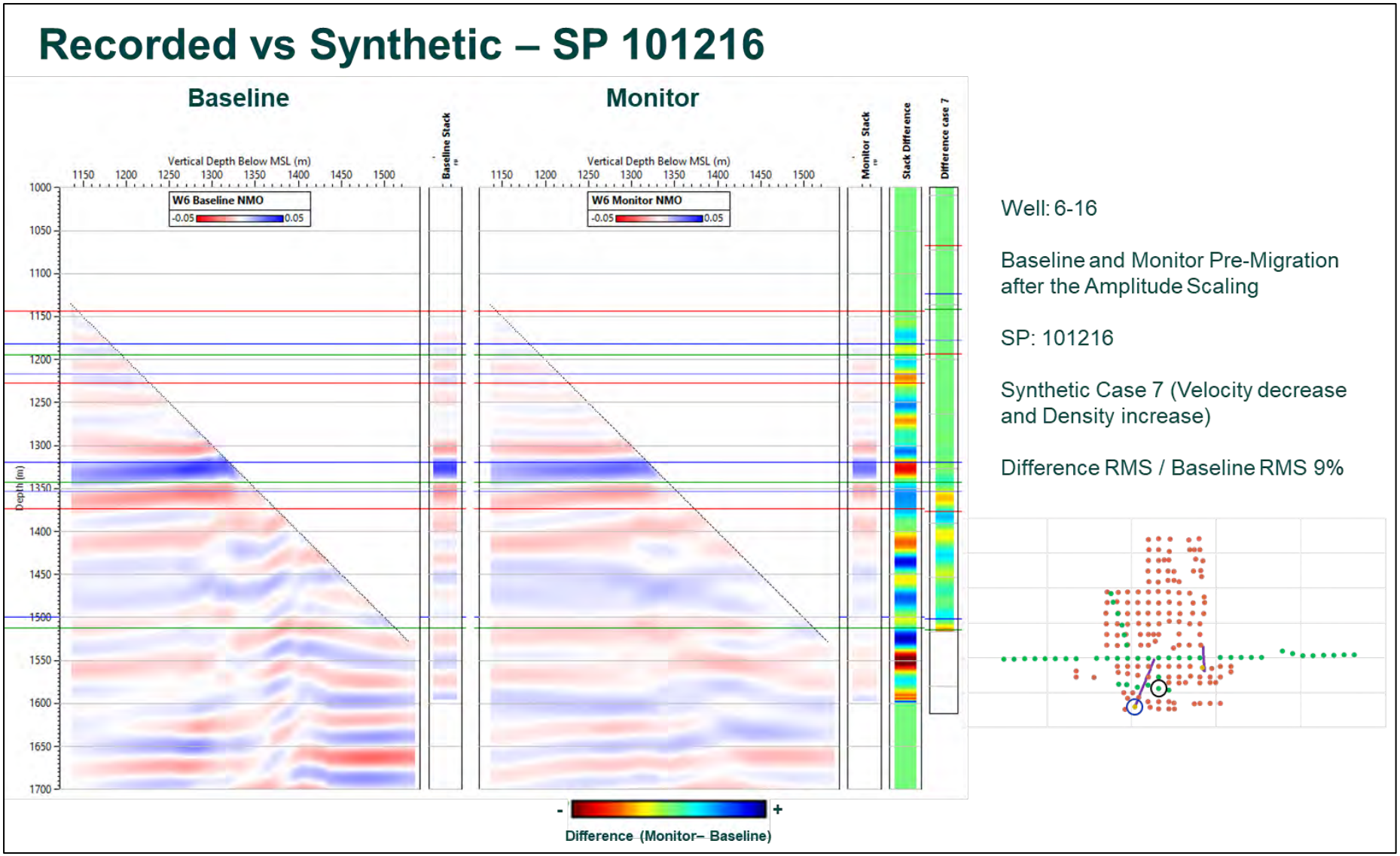


*Figure 13-12. Synthetic ZVSP compared with the recorded SP data located close to the well for Vibroseis SP 101216.*

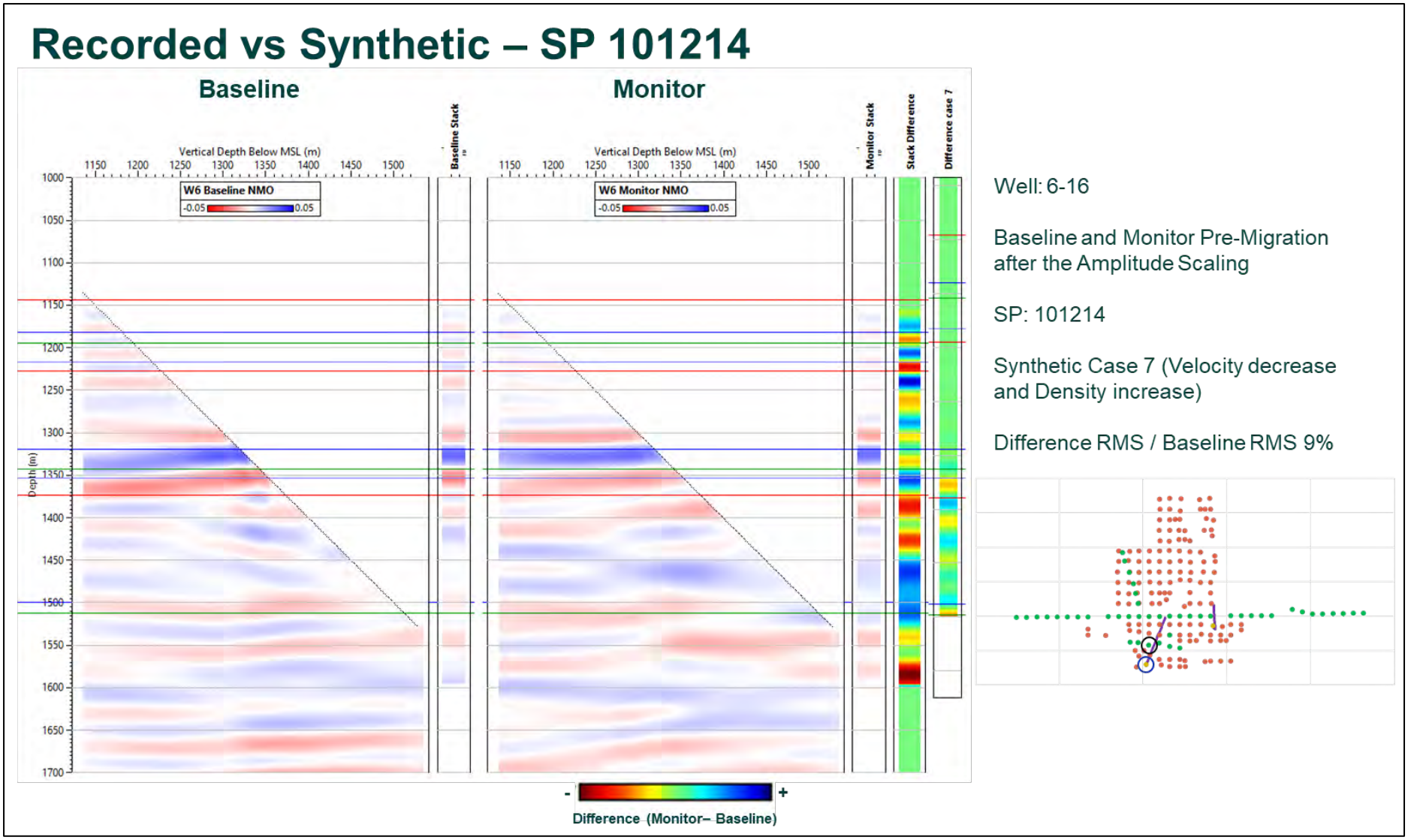


*Figure 13-13. Synthetic ZVSP compared with the recorded SP data located close to the well for Vibroseis SP 101214.*

# 14 Time-lapse analyses

Due to the low SNR of the input data the dynamite data images are highly contaminated by artefacts, for this reason the time-lapse analysis was performed only using the vibroseis image data.

Figure 14-1 shows the final baseline and monitor migrated image. On the top is In-line 750 (close to well 8-16) having the baseline on the left, the monitor in the centre and on the right the amplitude difference between the monitor and the baseline. On the bottom is the cross-line 1880 (near well 6-16) with the baseline on the left, monitor images in the centre and the amplitude difference on the right. The baseline and the monitor surveys present the same structural features. The amplitude differences are larger on the cross-line near well 6-16 compared to the in-line near well 8-16.

In figure 14-2 are presented different In-lines extracted from the monitor – baseline amplitude difference 3D cube. On the top left is a monitor – baseline amplitude difference time slice at 1320 m TVD MSL (at the A2 Carbonate level). The In-line 700 amplitude difference shows some additional artefacts compared to the northern In-lines. In general, higher amplitude differences are noticed in the data close to well 6-18 compared to the data close to well 6-16.

Several monitor – baseline amplitude difference cross-lines are presented in figure 14-3. The cross-lines close to well 6-16 perforations (stars on the top left) show bigger differences compared with the cross-lines far from well 6-16 perforations.

The amplitude difference from figure 14-4 was extracted along several 3D slices parallel to the A1 Carbonate surface. On the top centre is the amplitude difference extracted along the A1 Carbonate 3D surface. On the top right is the amplitude difference extracted along the 3D surface parallel and 20 m deeper than the A1 Carbonate 3D surface. Similarly, on the bottom image are the amplitude differences along 40 m, 60 m and 80 m offset surfaces. The images don't show a clear $CO_2$ plume delineation.

A better way to quantify the amplitude difference is to compute the difference amplitude RMS over a short window (from 5 m above to 5 m below the surface). Figure 14-5 presents the difference amplitude RMS with the centre of the analysis window at the A1 Carbonate 3D surface (top centre) and at 10 m, 20 m, 40 m and 60 m below the A1 Carbonate 3D surface. It is not a clear delineation, but higher RMS values are noticed close to the well 6-16 perforations.

| Title | Description | Figure |
|---|---|---|
| | | |
| **14 Time-lapse analyses** | | |
| Final baseline and monitor images | | **14.1** |
| Amplitude difference – In-lines | | **14.2** |
| Amplitude difference – Cross-lines | | **14.3** |
| Amplitude difference along A1 Carbonate | At and below A1 Carbonate surface | **14.4** |
| RMS amplitude difference along A1 Carbonate | Inside +/- 5 m window | **14.5** |

*Table 14-23 Time-lapse analyses figures*

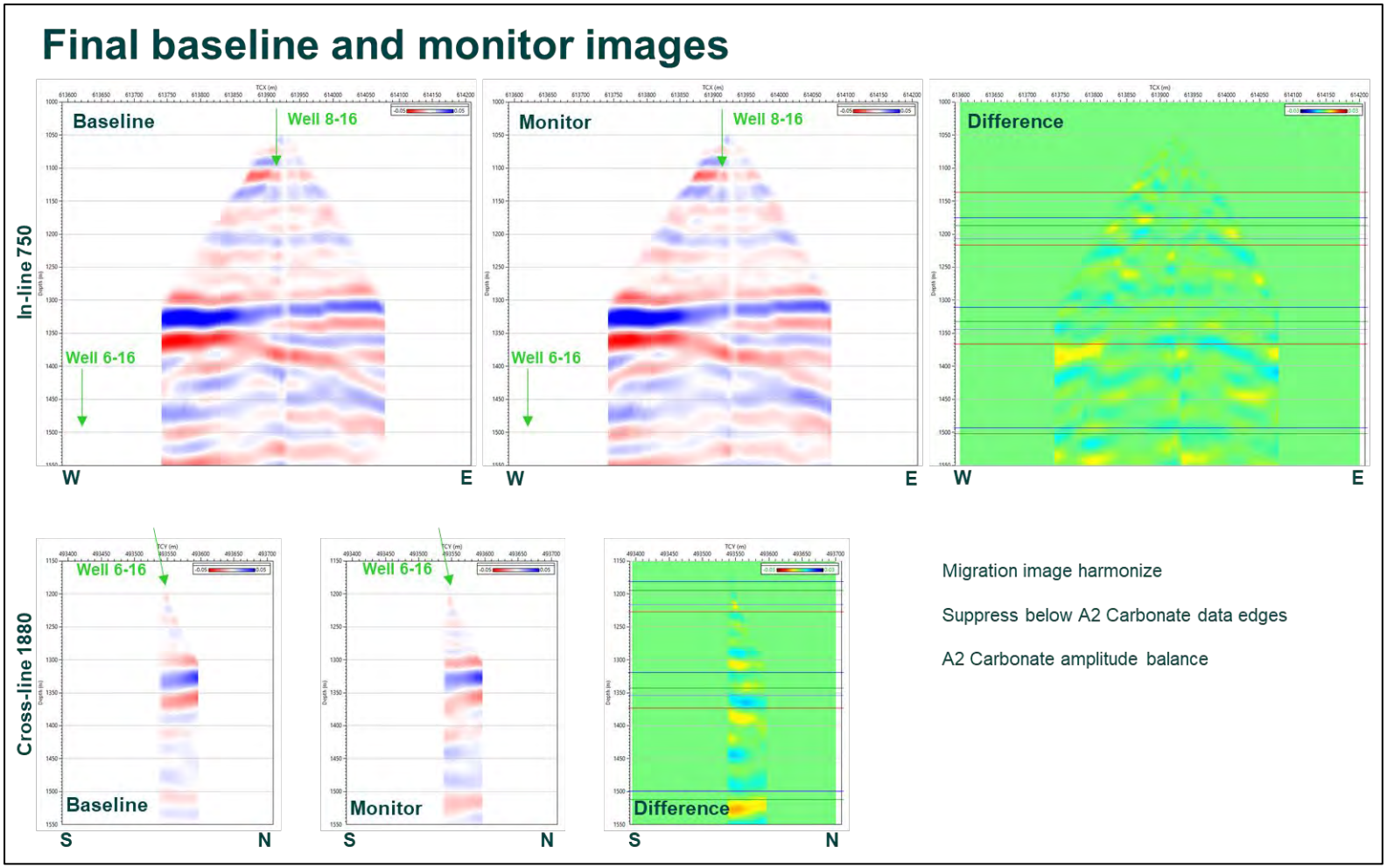


*Figure 14-1. Final baseline and monitor images. Due to the low SNR of the input data the dynamite data images are highly contaminated by artefacts, for this reason the time-lapse analysis was performed only using the vibroseis image data. Figure 14.1 shows the final baseline and monitor migrated image. On the top is In-line 750 (close to well 8-16) having the baseline on the left, the monitor in the centre and on the right the amplitude difference between the monitor and the baseline. On the bottom is the cross-line 1880 (near well 6-16) with the baseline on the left, monitor images in the centre and the amplitude difference on the right. The baseline and the monitor surveys present the same structural features. The amplitude differences are larger on the cross-line near well 6-16 compared to the in-line near well 8-16.*

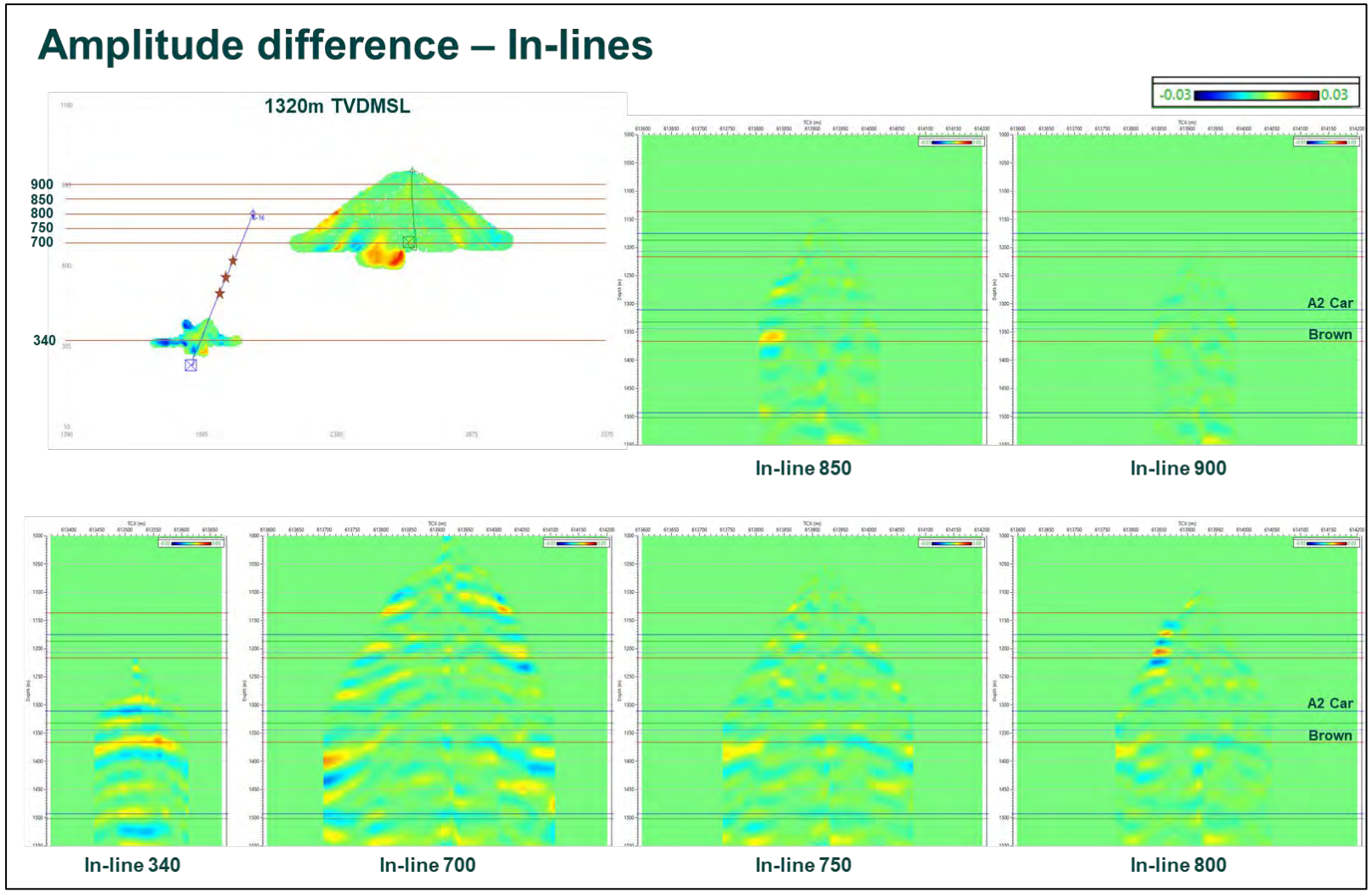


*Figure 14-2. Amplitude difference – In-lines. In figure 14-2 are presented different In-lines extracted from the monitor – baseline amplitude difference 3D cube. On the top left is a monitor – baseline amplitude difference time slice at 1320 m TVD MSL (at the A2 Carbonate level). The In-line 700 amplitude difference shows some additional artefacts compared to the northern In-lines. In general, higher amplitude differences are noticed in the data close to well 8-16 compared to the data close to well 6-16.*

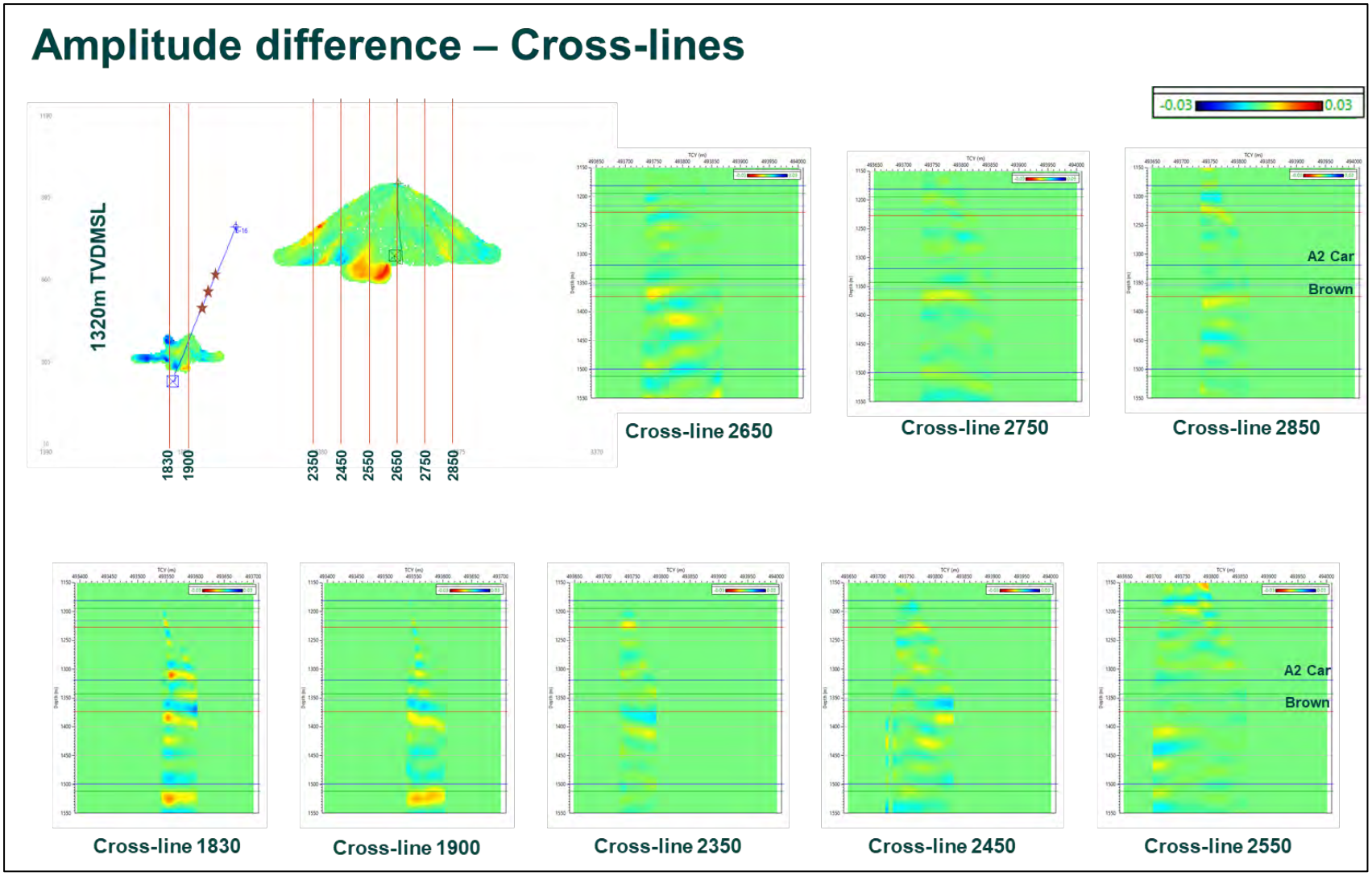


*Figure 14-3. Amplitude difference – Cross-lines. Several monitor – baseline amplitude difference cross-lines are presented in figure 14.3. The cross-lines close to well 6-16 perforations (stars on the top left) show bigger differences compared with the cross-lines far from well 6-16 perforations.*

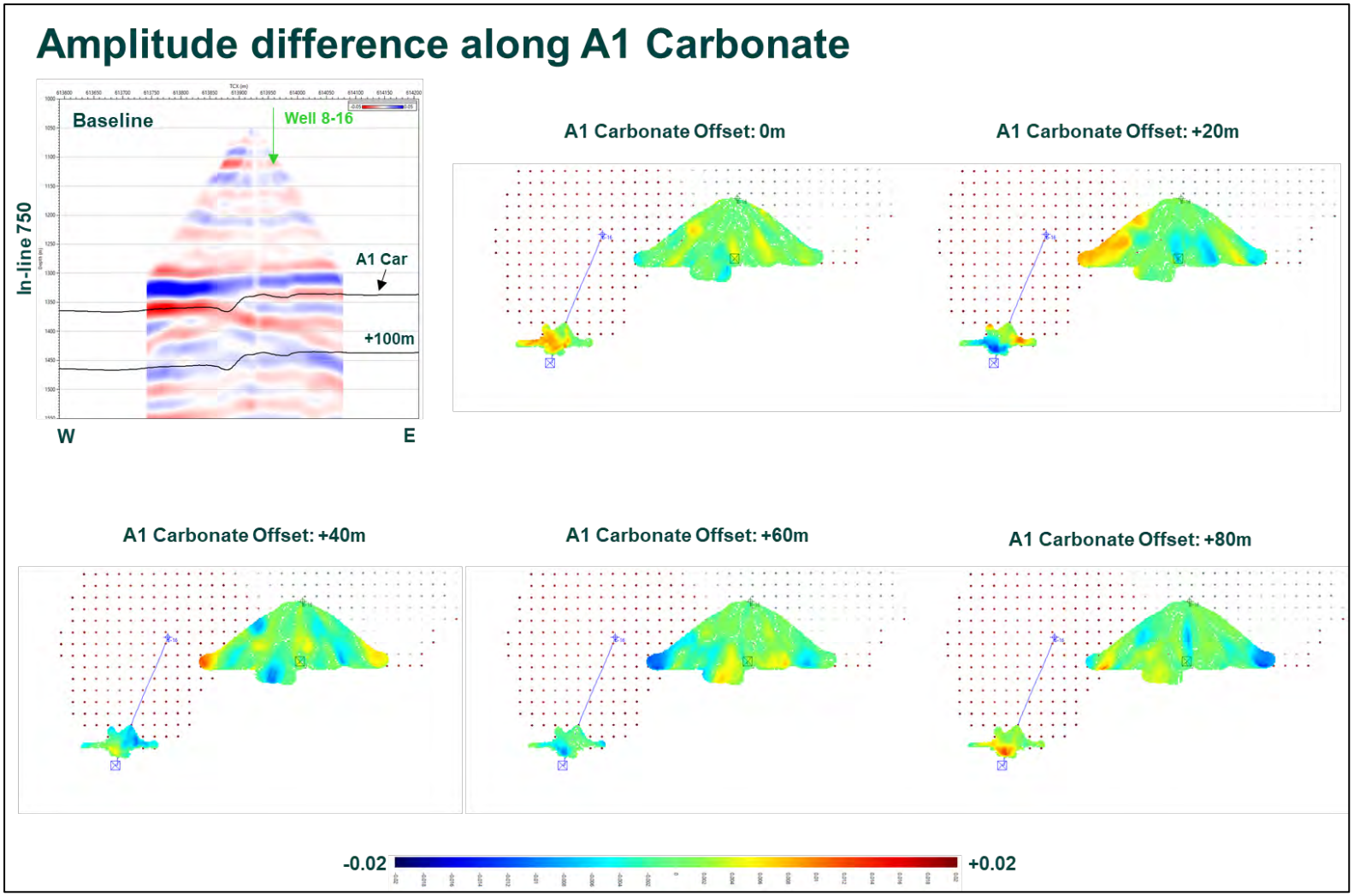


*Figure 14-4. Amplitude difference along A1 Carbonate - At and below A1 Carbonate surface. The amplitude difference from figure 14.4 was extracted along several 3D slices parallel to the A1 Carbonate surface. On the top centre is the amplitude difference extracted along the A1 Carbonate 3D surface. On the top right is the amplitude difference extracted along the 3D surface parallel and 20 m dipper than the A1 Carbonate 3D surface. Similarly, on the bottom image are the amplitude differences along 40 m, 60 m and 80 m offset surfaces. The images don't show a clear $CO_2$ plume delineation.*

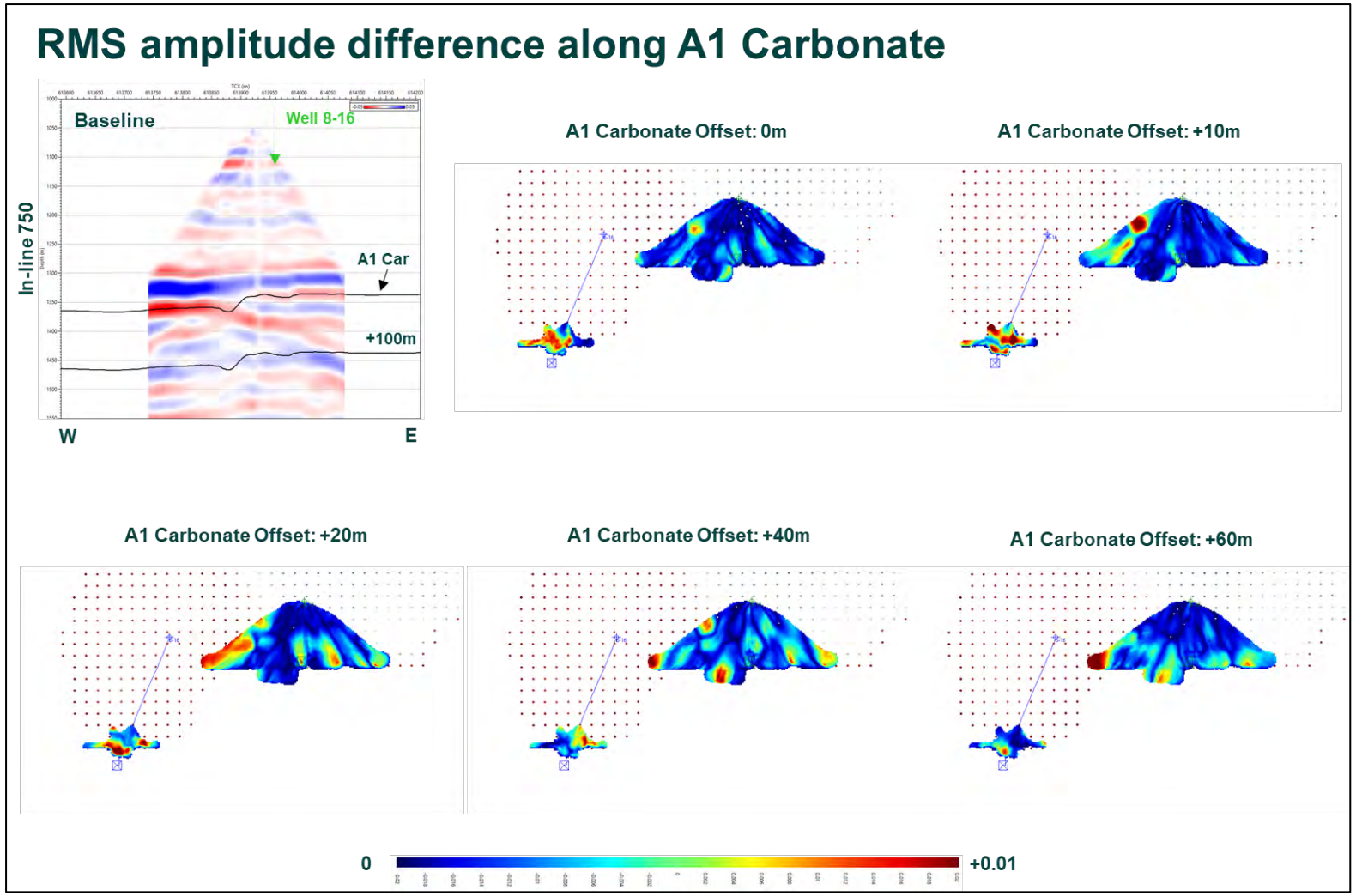


*Figure 14-5. RMS amplitude difference along A1 Carbonate - Inside +/- 5 m window. A better way to quantify the amplitude difference is to compute the difference amplitude RMS over a short window (from 5 m above to 5 m below the surface). Figure 14.5 presents the difference amplitude RMS with the centre of the analysis window at the A1 Carbonate 3D surface (top centre) and at 10 m, 20 m, 40 m and 60 m below the A1 Carbonate 3D surface. It is not a clear delineation, but higher RMS values are noticed close to the well 6-16 perforations.*

# 15 Conclusions

The Chester 16 DAS VSP time-lapse baseline and monitor surveys were processed to generate 3D images. These images cover the areas close to the injection well 6-16 and monitor well 8-16. The native measurement recorded by the DAS surveys is in strain rate. Conversions from strain rate to particle velocity (geophone equivalent) measurements may introduce additional artefacts in the data. To avoid this effect, the data was processed in native strain rate units.

The dynamite data from both surveys have a low SNR, possibly due to the high energy absorption in the glacial breccia. For this reason, the dynamite baseline and monitor images do not have coherent reflectivity, structure or amplitude response. The time-lapse analysis was therefore focussed only on the vibroseis data which has better SNR.

When the well deviation is close to vertical, the data are affected by ringing, probably because the production casing is only cemented at the bottom of the well. The injection well 6-16 additionally has injection tubing that, together with the uncemented casing, results in severe ringing in the vertical section of the well. For the time-lapse analysis we were looking for rather small changes in the seismic response and any such changes would be easily swamped by ringing. We therefore could only use the higher quality data from the bottom part of the wells.

During the monitor survey the number of sweeps per SP was twice that of the baseline survey, resulting in a higher SNR for the monitor survey. Also, the monitor raw data has a slightly better SNR compared to the baseline raw data. Probably this is related to different weather conditions.

The ZVSP source location was acquired only during the monitor survey. The time to depth relationship therefore was derived from the measurements acquired near well 8-16 during the monitor survey.

The shallow formation below the GL appears to exhibit lateral variations in velocity. To align the data with the velocity model, an extensive static correction workflow was applied before the 3D imaging. Also, the monitor data was aligned with the baseline data by comparing areas where 4D effects were not expected.

Lab tests had been performed by Battelle on the A1 Carbonate and Brown Niagaran core samples to measure the changes in velocity and density due to increases in gas pressure. We used the results of these tests to model the expected time-lapse seismic response over a number of different combinations of changes in velocity and/or density. This modelling showed that due to the high acoustic velocity in carbonates and the small thickness of the reservoir, any time-lapse effects due to $CO_2$ injection would be difficult to detect and would require a very good signal to noise level. The modelling also showed that changes in velocity would be easier to detect than changes in density.

The shot points located near well 6-16 are expected to have the best seismic response as the travel paths are shorter and the image points are closer to the receivers. The time-lapse analysis of these shot points however shows amplitude differences also above the reservoir, suggesting that the observed differences are probably due to the noise.

The 3D time-lapse analysis shows differences between the monitor and baseline surveys. Part of the difference is considered to be due to the noisier baseline survey data. The differences are higher in the area close to the injection well perforations thus it is considered that some may also be due to the $CO_2$ injection. The image is limited to areas close to the wells and so the $CO_2$ plume cannot be delineated.

Due to the limited receiver interval in the injection well 6-16, the image does not extend to the reservoir area between the wells close to the perforations.

# 16 Input data and references

The following files were provided to Silxa (VSProwess) by Battelle or Core Energy. After the data processing was completed, the files were collected on a portable hard drive that was provided to Battelle.

***Raw data***

Baseline survey – well 6-16 – Dynamite (161 files):
TDMS\2017_Survey\Well_6-16\6-16_Dynamite_All_TDMS\

Baseline survey – well 8-16 – Dynamite (161 files):
TDMS\2017_Survey\Well_8-16\TDMS\8-16_Dynamite_All_TDMS\

Baseline survey – well 6-16 – Vibroseis (271 files):
TDMS\2017_Survey\Well_6-16\6-16_Vibe_All_TDMS\

Baseline survey – well 8-16 – Vibroseis (271 files):
TDMS\2017_Survey\Well_8-16\TDMS\8-16_Vibe_All_TDMS\

Monitor survey – well 6-16 – Vibroseis Tests and ZVSP (93 files):
TDMS\2018_Survey\Well_6-16\08_20_2018\Test_Sweeps

Monitor survey – well 8-16 – Vibroseis Tests and ZVSP (94 files):
TDMS\2018_Survey\Well_8-16\08_20_2018\Test_Sweeps

Monitor survey – well 6-16 – Dynamite (145 files):
TDMS\2018_Survey\Well_6-16\08_22_2018\

Monitor survey – well 8-16 – Dynamite (145 files):
TDMS\2018_Survey\Well_8-16\08_22_2018\

Monitor survey – well 6-16 – Vibroseis (606 files):
TDMS\2018_Survey\Well_6-16\08_21_2018\

Monitor survey – well 8-16 – Vibroseis (606 files):
TDMS\2018_Survey\Well_8-16\08_21_2018\

***Well position***

Well 6-16: Well\ 6-16 Northing-Easting.pdf
Well 8-16: Well\ 8-16 Northing-Easting.pdf

***Well deviation***

Well\Deviation\Original\Well_6-16\Chester 6-16 PILOT txt A.D.pdf
Well\Deviation\Original\Well_6-16\ Chester 8-16 and 6-16 trajectory .xlsx

***Source position***

Baseline survey:
Navigation\2017_Edited_Emerson_files\ Chester16DasVspGPSViewPositions.ASC

Monitor survey:
Navigation\2018_Edited_Emerson_files\ Chester 16 Das VSP REDO 8_22_2018_FINAL_PSSCSV.ASC

Baseline survey – Dynamite:
Navigation\Chester 16 DAS VSP.xlsx
Navigation\Chester 16 DAS VSP Shot.sp1

Baseline survey – Dynamite & Vibroseis:
Navigation\Chester 16 DAS VSP Source points 22117final.xlsx
Navigation\Chester 16 DAS VSP Source points 22117final+MEK.xlsx

***Interpreted horizons***

Interpreted_horizons\ HORIZONS FOR SILIXA over chester 16 reef.csv

***Well tops***

Well 6-16: Well\Markers\Original\PN 61189 Tops Sheet, Top-Bottom.xlsx
Well 8-16: Well\Markers\Original\PN 61186 Tops Sheet, Top-Bottom.xlsx

***Well logs***

Well\Logs_used_for_processing\CORE_CHESTER_16_UNIT_6_16_XMAC_TI.las
Well\Logs_used_for_processing\ 12_2_16_BATTELLE_CHESTER_16_8_16_POROSITY_RESISTIVITY.las
Well\Logs_used_for_processing\ CHESTER16_8_16_RUN2_FULL_SUITE_24_JAN_2017.las
Source points 22117final+MEK.xlsx

***Interpreted horizons***

Interpreted_horizons\ HORIZONS FOR SILIXA over chester 16 reef.csv

***Well tops***

Well 6-16: Well\Markers\Original\PN 61189 Tops Sheet, Top-Bottom.xlsx
Well 8-16: Well\Markers\Original\PN 61186 Tops Sheet, Top-Bottom.xlsx

***Well logs***

Well\Logs_used_for_processing\CORE_CHESTER_16_UNIT_6_16_XMAC_TI.las
Well\Logs_used_for_processing\ 12_2_16_BATTELLE_CHESTER_16_8_16_POROSITY_RESISTIVITY.las
Well\Logs_used_for_processing\ CHESTER16_8_16_RUN2_FULL_SUITE_24_JAN_2017.las

# 17 Output Data

The data processing generated several output files, which are identified below. All files were provided to Battelle on a portable hard drive.

***SEGYs***

Baseline survey – Vibroseis data – 3D image:
Final_data\Imaging\Battele_Baseline_Vib_3D_Image.sgy

Monitor survey – Vibroseis data – 3D image:
Final_data\Imaging\Battele_Monitor_Vib_3D_Image.sgy

Monitor-Baseline – Vibroseis data – Acoustic impedance amplitude difference:
Final_data\Imaging\Battele_Vib_3D_Image_Difference.sgy

Monitor-Baseline – Vibroseis data – RMS of Acoustic impedance amplitude difference along the A1 Carbonate surface:
Final_data\Imaging\Battele_Vib_3D_Image_RMS_Difference_A1Carbonate.sgy

Well 6-16 – ZVSP corridor stack:
Final_data\ZVSP\Battelle_Well_6-16_ZVSP_Corridor_Stack.sgy

Well 8-16 – ZVSP deconvolved enhanced Up-P in OWT:
Final_data\ZVSP\Battelle_Well_8-16_ZVSP_Deconvolved_Enhanced_Up-P.sgy

Well 8-16 – ZVSP deconvolved enhanced Up-P in TWT:
Final_data\ZVSP\Battelle_Well_8-16_ZVSP_Deconvolved_Enhanced_Up-P_TWT.sgy

Well 8-16 – ZVSP corridor stack:
Final_data\ZVSP\Battelle_Well_8-16_ZVSP_Corridor_Stack.sgy

Well 6-16 – Synthetic seismogram:
Final_data\Calibrated_Logs_and_Synthetic_Seismograms\Battelle_Well_6-16_Synthetic_Seismogram.sgy

Well 8-16 – Synthetic seismogram:
Final_data\Calibrated_Logs_and_Synthetic_Seismograms\Battelle_Well_8-16_Synthetic_Seismogram.sgy

***Well logs***

1 Well 6-16 – Calibrated logs in depth:
2 Final_data\Calibrated_Logs_and_Synthetic_Seismograms\Battelle_Well_6-16_Calibrated_log_depth.las
3
4 Well 6-16 – Acoustic impedance and reflection coefficients in TWT:
5 Final_data\Calibrated_Logs_and_Synthetic_Seismograms\Battelle_Well_6-16_Reflection_coeficients.las

Well 8-16 – Calibrated logs in depth:
Final_data\Calibrated_Logs_and_Synthetic_Seismograms\Battelle_Well_8-16_Calibrated_log_depth.las

Well 8-16 – Acoustic impedance and reflection coefficients in TWT:
Final_data\ Calibrated_Logs_and_Synthetic_Seismograms\Battelle_Well_8-16_Reflection_coeficients.las
Well 6-16 – Modelled case 0 – Baseline:
Final_data\Synthetic_Cases\Battelle_Well_6-16_Synthetic_Case_0.csv

Well 6-16 – Modelled case 1:
Final_data\Synthetic_Cases\Battelle_Well_6-16_Synthetic_Case_1.csv

Well 6-16 – Modelled case 2:
Final_data\Synthetic_Cases\Battelle_Well_6-16_Synthetic_Case_2.csv

Well 6-16 – Modelled case 3:
Final_data\Synthetic_Cases\Battelle_Well_6-16_Synthetic_Case_3.csv

Well 6-16 – Modelled case 4:
Final_data\Synthetic_Cases\Battelle_Well_6-16_Synthetic_Case_4.csv

Well 6-16 – Modelled case 5:
Final_data\Synthetic_Cases\Battelle_Well_6-16_Synthetic_Case_5.csv

Well 6-16 – Modelled case 6:
Final_data\Synthetic_Cases\Battelle_Well_6-16_Synthetic_Case_6.csv

Well 6-16 – Modelled case 7:
Final_data\Synthetic_Cases\Battelle_Well_6-16_Synthetic_Case_7.csv

### *Listings*

Well 8-16 – ZVSP time to depth table:
Report\Battelle_8-16_Time_Depth_2018_ZVSP8.xlsx

# Appendix B.
# Source Records

**Table B-1. Vibroseis Source Record**

| Point Number | Northing (meters) | Easting (meters) | Elevation (meters) | Force[a] | Location |
|---|---|---|---|---|---|
| 101212 | 613421.64 | 493648.4 | 398.46 | Full | Field In-Fill Point |
| 101213 | 613471.12 | 493647.48 | 398.62 | Full | Field In-Fill Point |
| 101214 | 613532.04 | 493631.78 | 398.44 | Full | Field In-Fill Point |
| 101215 | 613596.45 | 493645.18 | 399.91 | Full | Field In-Fill Point |
| 101216 | 613658.49 | 493625.01 | 402.31 | Full | Field In-Fill Point |
| 101217 | 613718.31 | 493614.1 | 401.51 | Full | Field In-Fill Point |
| 504216 | 613657.99 | 493690.62 | 402.45 | Full | Field, co-located with dynamite shot point |
| 506201 | 612743.61 | 493793.88 | 398.14 | Full | McCoy Road |
| 506202 | 612804.57 | 493794.24 | 398.12 | Reduced | McCoy Road |
| 506203 | 612865.46 | 493794.73 | 398.3 | Reduced | McCoy Road |
| 506204 | 612926.47 | 493795.08 | 397.44 | Full | McCoy Road |
| 506205 | 612987.41 | 493795.61 | 395.58 | Full | McCoy Road |
| 506206 | 613048.45 | 493796.16 | 393.17 | Full | McCoy Road |
| 506207 | 613109.36 | 493796.51 | 392.2 | Full | McCoy Road |
| 506208 | 613170.42 | 493796.53 | 392.94 | Full | McCoy Road |
| 506209 | 613231.45 | 493797.38 | 393.98 | Did Not Acquire | McCoy Road |
| 506210 | 613292.12 | 493797.87 | 394.85 | Reduced | McCoy Road |
| 506211 | 613353.22 | 493798.08 | 396.24 | Full | McCoy Road |
| 506212 | 613414.11 | 493798.53 | 397.91 | Full | McCoy Road |
| 506213 | 613475.05 | 493798.87 | 399.23 | Full | McCoy Road |
| 506214 | 613536.16 | 493799.03 | 399.94 | Full | McCoy Road |
| 506215 | 613597.07 | 493799.27 | 400.68 | Full | McCoy Road |
| 506216 | 613658.08 | 493799.52 | 401.79 | Full | McCoy Road |
| 506217 | 613719.06 | 493799.8 | 402.55 | Full | McCoy Road |
| 506218 | 613779.86 | 493800.19 | 402.95 | Full | McCoy Road |
| 506219 | 613840.95 | 493800.62 | 403.56 | Full | McCoy Road |
| 506220 | 613901.82 | 493801.22 | 404.26 | Full | McCoy Road |
| 506221 | 613962.85 | 493801.55 | 404.77 | Did Not Acquire | McCoy Road |
| 506222 | 614023.82 | 493801.93 | 404.96 | Reduced | McCoy Road |
| 506223 | 614084.72 | 493802.47 | 404.75 | Reduced | McCoy Road |
| 506224[b] | 614145.76 (see comment) | 493802.64 (see comment) | 404.25 | Full | McCoy Road |
| 506225 | 614206.55 | 493802.94 | 403.75 | Reduced | McCoy Road |
| 506226 | 614267.64 | 493801.87 | 403.54 | Full | McCoy Road |
| 506227 | 614328.6 | 493802.99 | 403.3 | Did Not Acquire | McCoy Road |
| 506228 | 614389.35 | 493838.84 | 403.68 | Full | SR 32 |
| 506229 | 614450.5 | 493824.18 | 402.83 | Full | SR 32 |
| 506230 | 614511.45 | 493813.86 | 403.67 | Full | SR 32 |

| Point Number | Northing (meters) | Easting (meters) | Elevation (meters) | Force[a] | Location |
|---|---|---|---|---|---|
| 506231 | 614572.44 | 493813.7 | 404.26 | Full | SR 32 |
| 506232 | 614633.45 | 493814.66 | 404.46 | Reduced | SR 32 |
| 506233 | 614694.18 | 493815.65 | 404.4 | Reduced | SR 32 |
| 506234 | 614755.27 | 493816.55 | 403.8 | Reduced | SR 32 |
| 506235 | 614816.2 | 493817.33 | 402.56 | Full | SR 32 |
| 507113 | 613468.72 | 493874.4 | 399.05 | Full | Dirt road |
| 508113 | 613454.4 | 493931.29 | 399.81 | Full | Dirt road |
| 509112 | 613442.05 | 493989.54 | 401.75 | Full | Dirt road |
| 510112 | 613417.33 | 494055.73 | 408.17 | Full | Dirt road |
| 511112 | 613390.26 | 494121.52 | 405.52 | Full | Dirt road |
| 512111 | 613375.97 | 494170.64 | 405.14 | Full | Dirt road |

a. Full force is 78% of maximum capability of vibroseis trucks; reduced force is 40% of maximum. For full force, five sweeps were performed; For reduced force, ten sweeps were performed. All sweeps 30 seconds, 10-140 HZ. All points acquired using three vibroseis trucks.
b. Point 506224 moved ~ 65 ft east of surveyed point

**Table B- 2. Dynamite Source Records**

| Point Number | Northing (meters) | Easting (meters) | Elevation (meters) | Load (kg) | Hole Depth (ft) | Comment |
|---|---|---|---|---|---|---|
| 501213 | 613458.96 | 493504.97 | 398.24 | 1.0 | 20 | --- |
| 501215 | 613608.83 | 493516.66 | 398.82 | 1.0 | 20 | --- |
| 501216 | 613657.92 | 493507.86 | 399.26 | 1.0 | 20 | --- |
| 501217 | 613718.93 | 493508.36 | 399.24 | 1.0 | 20 | --- |
| 501218 | 613750.93 | 493507.63 | 398.78 | 1.0 | 20 | --- |
| 502213 | 613475.27 | 493568.46 | 399.16 | 1.0 | 20 | --- |
| 502214 | 613539.13 | 493572.29 | 398.73 | 1.0 | 20 | --- |
| 502215 | 613596.65 | 493548.44 | 399.15 | 1.0 | 20 | --- |
| 502216 | 613658.66 | 493548.56 | 400.29 | 1.0 | 20 | --- |
| 502217 | 613718.33 | 493548.6 | 399.74 | 1.0 | 20 | --- |
| 502218 | 613749.97 | 493541.14 | 398.91 | 1.0 | 20 | --- |
| 502219 | 613870.41 | 493537.35 | 395.65 | 1.0 | 20 | --- |
| 502220 | 613902.09 | 493537.74 | 393.17 | 1.0 | 20 | --- |
| 502221 | 613963.31 | 493538.38 | 396.11 | 1.0 | 20 | --- |
| 502222 | 614023.15 | 493538.16 | 400.54 | 1.0 | 20 | --- |
| 503213 | 613453.18 | 493599.52 | 398.19 | 1.0 | 20 | --- |
| 503214 | 613506.25 | 493601 | 398.51 | 1.0 | 20 | --- |
| 503217 | 613718.04 | 493657.71 | 402.29 | 1.0 | 20 | --- |
| 503218 | 613779.25 | 493657.14 | 401.11 | 1.0 | 20 | --- |
| 503219 | 613816.81 | 493659.29 | 401.58 | 1.0 | 20 | --- |
| 503220 | 613902.42 | 493656.64 | 401.88 | 1.0 | 20 | --- |
| 503221 | 613963.38 | 493657.86 | 401.6 | 1.0 | 20 | --- |
| 503222 | 613995.62 | 493658.4 | 400.94 | 1.0 | 20 | --- |

| Point Number | Northing (meters) | Easting (meters) | Elevation (meters) | Load (kg) | Hole Depth (ft) | Comment |
|---|---|---|---|---|---|---|
| 504208 | 613170.48 | 493690.92 | 391.24 | 0.5 | 20 | --- |
| 504210 | 613276.2 | 493686.84 | 397.2 | 1.0 | 20 | --- |
| 504212 | 613419.19 | 493717.54 | 396.86 | 1.0 | 20 | --- |
| 504213 | 613474.24 | 493711.13 | 395.98 | 1.0 | 20 | --- |
| 504214 | 613535.21 | 493700.35 | 398.34 | 1.0 | 20 | --- |
| 504215 | 613597.01 | 493690.63 | 400.39 | 1.0 | 20 | --- |
| 504216 | 613657.99 | 493690.62 | 402.45 | 1.0 | 20 | *co-located with vibroseis point* |
| 504217 | 613719 | 493690.63 | 402.61 | 1.0 | 20 | --- |
| 504218 | 613779.93 | 493690.63 | 401.66 | 1.0 | 20 | --- |
| 504219 | 613846.21 | 493696.33 | 402.26 | 1.0 | 20 | --- |
| 504220 | 613901.8 | 493690.64 | 401.81 | 1.0 | 20 | --- |
| 504221 | 613962.8 | 493690.61 | 402.14 | 1.0 | 20 | --- |
| 504222 | 614023.16 | 493690.45 | 401.6 | 1.0 | 20 | --- |
| 504223 | 614085.74 | 493720.54 | 401.65 | 1.0 | 20 | --- |
| 505208 | 613170.25 | 493724.54 | 391.49 | 1.0 | 20 | --- |
| 505212 | 613414.21 | 493751.55 | 391.83 | 1.0 | 20 | --- |
| 505213 | 613475.12 | 493751.53 | 399.09 | 1.0 | 20 | --- |
| 505214 | 613536.09 | 493751.53 | 400.69 | 1.0 | 20 | --- |
| 505215 | 613597.02 | 493751.56 | 401.37 | 1.0 | 20 | --- |
| 505216 | 613657.98 | 493751.53 | 401.65 | 1.0 | 20 | --- |
| 505217 | 613719.01 | 493751.56 | 402.61 | 1.0 | 20 | --- |
| 505218 | 613779.89 | 493751.51 | 401.87 | 1.0 | 20 | --- |
| 505219 | 613844.94 | 493751.52 | 403.63 | 1.0 | 20 | --- |
| 505221 | 613973.43 | 493738.53 | 402.98 | 1.0 | 20 | --- |
| 505222 | 614023.8 | 493751.53 | 403.17 | 1.0 | 20 | --- |
| 505223 | 614084.71 | 493751.53 | 403.76 | 1.0 | 20 | --- |
| 507211 | 613352.9 | 493873.87 | 398.67 | 1.0 | 20 | --- |
| 507212 | 613414.59 | 493871.58 | 401.07 | 1.0 | 20 | --- |
| 507213 | 613475.28 | 493875.38 | 399.48 | 1.0 | 20 | --- |
| 507214 | 613553.48 | 493873.54 | 400.57 | 1.0 | 20 | --- |
| 507215 | 613596.98 | 493873.53 | 399.34 | 0.5 | 20 | --- |
| 507216 | 613637.83 | 493895.52 | 400.23 | 0.5 | 20 | --- |
| 507217 | 613746.72 | 493857.26 | 402.19 | 0.5 | 20 | --- |
| 507218 | 613780.33 | 493873.52 | 402.91 | 0.5 | 20 | --- |
| 507219 | 613840.56 | 493874.65 | 403.56 | 0.5 | 20 | --- |
| 507220 | 613906.79 | 493873.17 | 404.68 | 0.5 | 20 | --- |
| 508211 | 613351.37 | 493934.58 | 400.64 | 1.0 | 20 | --- |
| 508212 | 613413.73 | 493930.71 | 399.51 | 1.0 | 20 | --- |
| 508213 | 613464.5 | 493934.46 | 399.94 | 1.0 | 20 | --- |
| 508214 | 613550.74 | 493934.45 | 400.07 | 1.0 | 20 | --- |

| Point Number | Northing (meters) | Easting (meters) | Elevation (meters) | Load (kg) | Hole Depth (ft) | Comment |
|---|---|---|---|---|---|---|
| 508215 | 613597.02 | 493934.41 | 400.76 | 1.0 | 20 | --- |
| 508216 | 613627.93 | 493934.45 | 401.77 | 0.5 | 20 | --- |
| 508217 | 613658.12 | 493934.5 | 402.01 | 0.5 | 20 | --- |
| 508218 | 613779.78 | 493936.32 | 402.09 | 0.5 | 20 | --- |
| 508220 | 613902.64 | 493934.65 | 404.67 | 0.5 | 20 | --- |
| 509211 | 613348.52 | 493996.02 | 402.61 | 1.0 | 20 | --- |
| 509212 | 613414.23 | 493995.95 | 401.14 | 1.0 | 20 | --- |
| 509213 | 613475.76 | 493994.71 | 401.76 | 1.0 | 20 | --- |
| 509214 | 613541.25 | 493997.97 | 402.55 | 1.0 | 20 | --- |
| 509215 | 613597.02 | 493993.56 | 403.57 | 1.0 | 20 | --- |
| 509216 | 613660.04 | 493995.93 | 401.22 | 1.0 | 20 | --- |
| 509217 | 613720.41 | 494010.99 | 403.67 | 1.0 | 20 | --- |
| 509218 | 613778.73 | 494007.87 | 404.69 | 1.0 | 20 | --- |
| 509219 | 613841.15 | 493996.13 | 402.75 | 0.5 | 20 | --- |
| 509220 | 613901.88 | 493995.15 | 405.89 | 0.5 | 20 | --- |
| 510211 | 613346.22 | 494056.53 | 403.43 | 1.0 | 20 | --- |
| 510212 | 613419.07 | 494058.23 | 403.57 | 1.0 | 20 | --- |
| 510213 | 613475.67 | 494055.72 | 403.04 | 1.0 | 20 | --- |
| 510214 | 613537.61 | 494056.39 | 408.13 | 1.0 | 20 | --- |
| 510215 | 613596.18 | 494057.57 | 407.37 | 1.0 | 20 | --- |
| 510216 | 613658.02 | 494056.29 | 406.34 | 1.0 | 20 | --- |
| 510217 | 613721.53 | 494057.63 | 404.52 | 1.0 | 20 | --- |
| 510218 | 613782.98 | 494054.05 | 407.53 | 1.0 | 20 | --- |
| 510219 | 613859.25 | 494056.9 | 402.92 | 0.5 | 20 | --- |
| 510220 | 613925.11 | 494055.74 | 407.04 | 1.0 | 20 | --- |
| 511211 | 613353.37 | 494117.55 | 404.32 | 1.0 | 20 | --- |
| 511212 | 613411.99 | 494123.57 | 405.38 | 1.0 | 20 | --- |
| 511213 | 613475.08 | 494117.35 | 407.67 | 1.0 | 20 | --- |
| 511214 | 613535.51 | 494118.19 | 409.76 | 1.0 | 20 | --- |
| 511215 | 613599.04 | 494118.56 | 407.19 | 1.0 | 20 | --- |
| 511216 | 613657.72 | 494117.03 | 408.19 | 1.0 | 20 | --- |
| 511217 | 613720.51 | 494121.39 | 404.4 | 0.5 | 20 | --- |
| 511218 | 613782.91 | 494114.09 | 403.26 | 1.0 | 20 | --- |
| 511219 | 613862.15 | 494116.24 | 408.24 | 0.5 | 20 | --- |
| 511220 | 613929.47 | 494117.15 | 407.34 | 1.0 | 20 | --- |
| 512211 | 613353.35 | 494180.02 | 405.57 | 1.0 | 20 | --- |
| 512212 | 613418.94 | 494177.25 | 404.72 | 1.0 | 20 | --- |
| 512213 | 613475.09 | 494178.3 | 406.95 | 1.0 | 20 | --- |
| 512214 | 613537.35 | 494178.74 | 411.92 | 1.0 | 20 | --- |
| 512215 | 613598.24 | 494179.53 | 407.01 | 1.0 | 20 | --- |
| 512216 | 613656.66 | 494181.61 | 407.84 | 1.0 | 20 | --- |

| Point Number | Northing (meters) | Easting (meters) | Elevation (meters) | Load (kg) | Hole Depth (ft) | Comment |
|---|---|---|---|---|---|---|
| 512217 | 613715.94 | 494178.26 | 403.8 | 0.5 | 20 | --- |
| 512218 | 613779.49 | 494175.26 | 404.73 | 0.5 | 20 | --- |
| 512219 | 613843.01 | 494171.65 | 405.25 | 1.0 | 20 | --- |
| 512220 | 613927.17 | 494150.97 | 406.82 | 0.5 | 20 | --- |
| 513215 | 613600.84 | 494238.72 | 404.96 | 0.5 | 20 | --- |
| 513216 | 613657.21 | 494234.99 | 403.75 | 0.65 | 4 x 5 ft | --- |
| 513217 | 613712.85 | 494245.83 | 403.8 | 0.65 | 4 x 5 ft | --- |
| 513218 | 613748.17 | 494245.42 | 407.46 | 1.0 | 20 | --- |
| 513219 | 613779.85 | 494238.76 | 405.03 | 1.0 | 20 | --- |
| 513220 | 613911.27 | 494268.06 | 404.08 | 0.5 | 20 | --- |
| 514215 | 613596.37 | 494300.22 | 403.91 | 0.65 | 4 x 5 ft | --- |
| 514216 | 613657.99 | 494300.15 | 404.03 | 0.65 | 4 x 5 ft | --- |
| 514217 | 613714.45 | 494298.12 | 403.98 | 0.65 | 4 x 5 ft | --- |
| 514218 | 613750.17 | 494297.91 | 403.76 | 0.65 | 4 x 5 ft | --- |
| 514219 | 613864.31 | 494299.96 | 404.52 | 0.5 | 20 | --- |
| 514220 | 613906.63 | 494300.43 | 403.57 | 0.65 | 4 x 5 ft | --- |
| 515215 | 613597.05 | 494361.11 | 403.97 | 0.65 | 4 x 5 ft | --- |
| 515216 | 613658 | 494361.1 | 403.98 | 0.65 | 4 x 5 ft | --- |
| 515217 | 613690.68 | 494363.12 | 404.11 | 0.65 | 4 x 5 ft | --- |
| 515218 | 613718.06 | 494361.51 | 403.8 | 0.65 | 4 x 5 ft | --- |
| 515219 | 613876.35 | 494367.93 | 403.5 | 0.65 | 4 x 5 ft | --- |
| 515220 | 613920.38 | 494356.83 | 404.55 | 0.65 | 4 x 5 ft | --- |
| 516215 | 613600.69 | 494422.16 | 403.78 | 0.65 | 4 x 5 ft | Footnote a |
| 516216 | 613657.97 | 494422.08 | 404.01 | 0.65 | 4 x 5 ft | Footnote a |
| 516217 | 613721.9 | 494411.72 | 404.57 | 1.0 | 20 | |
| 516218 | 613841.17 | 494421.7 | 404.26 | 1.0 | 20 | |
| 516219 | 613870.87 | 494421.29 | 404.63 | 1.0 | 20 | |
| 516220 | 613902.51 | 494421.63 | 404.82 | 0.65 | 4 x 5 ft | |
| 517215 | 613597.01 | 494479.93 | 403.91 | 0.65 | 4 x 5 ft | Footnote a |
| 517216 | 613658.43 | 494484.41 | 403.7 | 0.65 | 4 x 5 ft | Footnote a |
| 517217 | 613726.54 | 494481.33 | 405.8 | 1.0 | 20 | |
| 517219 | 613836.76 | 494478.39 | 407.23 | 1.0 | 20 | |
| 517220 | 613897.53 | 494484.86 | 406.02 | 1.0 | 20 | |

a. These were repeated (i.e., done twice) during the baseline survey but only once during the repeat survey